Universitat de Girona

BIOINSPIRED LIGANDS AND MODEL SUBSTRATES FOR THE MECHANISTIC ELUCIDATION OF OXYGEN ACTIVATION AND CROSS-COUPLING REACTIONS MEDIATED BY FIRST-ROW TRANSITION METALS

Carla Magallón Gubau

Universitat de Girona

Doctoral Thesis

BIOINSPIRED LIGANDS AND MODEL SUBSTRATES FOR THE MECHANISTIC ELUCIDATION OF OXYGEN ACTIVATION AND CROSS-COUPLING REACTIONS MEDIATED BY FIRST-ROW TRANSITION METALS

Carla Magallón Gubau

2021

Doctoral programme in Chemistry

Supervised by: Dr. Xavi Ribas Salamaña and Dr. Anna Company Casadevall

Tutor: Dr. Xavi Ribas Salamaña

Presented in partial fulfilment of the requirements for a doctoral degree from the University of Girona

Universitat de Girona

Dr. Xavi Ribas Salamaña and Dr. Anna Company Casadevall of Universitat de Girona,

WE DECLARE:

That the thesis entitled "Bioinspired ligands and model substrates for the mechanistic elucidation of oxygen activation and cross-coupling reactions mediated by first-row transition metals", presented by Carla Magallón Gubau to obtain a doctoral degree, has been completed under our supervision and meets the requirements to opt for an International Doctorate.

For all intents and purposes, we hereby sign this document.

Dr. Xavi Ribas Salamaña

Dr. Anna Company Casadevall

Girona, 29th November, 2021

"Every now and then one's mind is stretched by a new idea or sensation,
and never shrinks back to its former dimensions"

Oliver Wendell Holmes, Sr.

"It is our choices that show what we truly are,
far more than our abilities"

Albus Dumbledore

FULL LIST OF PUBLICATIONS

This thesis is based on a compendium of the following publications:

CHAPTER III

"Preparation of a Coordinatively Saturated μ-η^2:η^2-peroxodicopper(II) compound"
C. Magallón, J. Serrano-Plana, S. Roldán-Gómez, X. Ribas, M. Costas, A. Company*
Inorg. Chim. Acta, **2018**, *481*, 166 – 170 (Impact factor: 2.545; Inorganic chemistry, Q2)

CHAPTER IV

"Mechanistic Insights into the *ortho*-Defluorination-Hydroxylation of 2-Halophenolates Promoted by a Bis(μ-oxo)dicopper(III) Complex"
P.Besalú-Sala,[‡] C. Magallón,[‡] M. Costas,* A. Company*, J. M. Luis*
Inorg. Chem., **2020**, *59*, 23, 17018 – 17027 (Impact factor: 5.165; Chemistry (miscellaneous), Q1)

CHAPTER V

"Well-Defined Aryl-Fe^{II} Complexes in Cross-Coupling and C–H Activation Processes"
C. Magallón, O. Planas, S. Roldán-Gómez, J. M. Luis, A. Company*, X. Ribas*
Organometallics, **2021**, *40*, 9, 1195 – 1200 (Impact factor: 3.876; Inorganic chemistry, Q1)

CHAPTER VI

"Organometallic Ni(II), Ni(III) and Ni(IV) Complexes Relevant to Carbon-Carbon and Carbon-Oxygen Bond Formation Reactions"
C. Magallón, L. Griego, C. H. Hu, A. Company*, X. Ribas*, L. M. Mirica*
Inorg. Chem. Front., **2022**, DOI: 10.1039/d1qi01486b. (Impact factor: 6.569; Inorganic chemistry, Q1)

Publications not included in this thesis:

"Spectroscopic and reactivity comparisons between nonheme oxoiron(IV) and oxoiron(V) species bearing the same ancillary ligand".
V. Dantignana, J. Serrano-Plana, A. Draksharapu, C. Magallón, S. Banerjee, R. Fan, I. Gamba, Y. Guo, L. Que Jr.,* M. Costas,* A. Company.*
J. Am. Chem. Soc. **2019**, *141*, 38, 15078-15091

LIST OF ABBREVIATIONS

Å	Ångström
AcOEt	Ethyl acetate
AcOH	Acetic acid
Ar	Aryl
atm	Atmosphere
B	Base
BDE	Bond dissociation energy
cat	Catalyst
CF_3	Trifluoromethyl group
CO	Carbon monoxide
COD	1,5-Cyclooctadiene
COSY	Homonuclear correlation spectroscopy
CMD	Concerted metalation-deprotonation
Cp	cyclopentadiene
Cp*	1,2,3,4,5-pentamethylcyclopentadiene
CV	Cyclic voltammetry
DCIB	dichloroisobutane
DCM	dichloromethane
DFP	difluorophenolate
DFT	Density functional theory
DG	Directing group
DMF	*N, N*-dimethylformamide
dmpe	1,2-bis(dimethylphoshino)ethane
DMSO	Dimethylsulfoxide
dppen	1,2-bis(diphenylphoshino)ethane
E^+	electrophile
e^-	electron
EA	Elemental analysis
EDG	Electron-donating group
EPR	Electron paramagnetic resonance
equiv	Equivalent
ESI-MS	Electrospray ionization mass spectrometry
Et	Ethyl
EtOH	Ethanol
EWG	Electron-withdrawing group
FT-IR	Fourier transform infrared spectroscopy
GC	Gas chromatography
h	hour
H	Hydrogen
$HClO_4$	Perchloric acid
His	Histidine residue
HMBC	Heteronuclear multiple-bond correlation spectroscopy

HNO_3	Nitric acid
HOMO	Highest occupied molecular orbital
HR-ESI-MS	High-resolution electrospray ionization mass spectrometry
HR-MS	High-resolution mass spectrometry
HSQC	Heteronuclear single-quantum correlation spectroscopy
h*v*	The energy of photons
Hz	Hertz
*i*Bu	*Iso*-butyl
*i*Pr	*Iso*-propyl
*i*PrOH	*Iso*-propanol
Kcal	Kilocalorie
L	Ligand
LMCT	Ligand to metal charge transfer
LUMO	Lowest unoccupied molecular orbital
M	Metal
Me	Methyl
MeOH	Methanol
MeCN	Acetonitrile
MHz	Mega Hertz
min	Minutes
mL	Millilitre
mM	Millimolar
MO	Molecular orbital
MW	Molecular weight
MS	Mass spectrometry
MS/MS	Tandem mass spectrometry
*n*Bu	*n*-butyl
n.d.	Not detected
NFTPT	*N*-Fluoro-2, 4,6-trimethylpyridinium triflate
NHC	*N*-heterocyclic carbene
nm	nanometers
NMP	*N*-methylpyrrolidone
NMR	Nuclear magnetic resonance
NOESY	Nuclear overhauser effect spectroscopy
Nu	Nucleophile
O	Bis(μ-oxo)dicopper(III)
OAT	Oxygen atom transfer
OTf	CF_3SO_3 anion or triflate anion
ox	oxidant
Ox. Add.	Oxidative addition
p.	Page
PCy_3	Tricyclohexylphosphine
Ph	Phenyl
Phen	1,10-phenanthroline
PEt_3	Triethylphosphine

$PhI(OAc)_2$	Iodobenzene diacetate
PMe_3	Trimethylphosphine
PPh_3	Triphenylphosphine
ppm	Part per million
py	Pyridine
QTOF	Quadrupole time-of-flight
Ref.	Reference
r.t.	Room temperature
SET	Single electron transfer
S_EAr	Electrophilic aromatic substitution
S_N	Nucleophilic substitution
^SP	μ-η2:η2-peroxodicopper(II)
T	Temperature
tacn	Triazacyclononane
^tBu	*Tert*-butyl
TEMPO	2,2,6,6-Tetramethylpiperidin-1-yl)oxyl
TDTT	*S*-(trifluoromethyl)dibenzothiophenium triflate
THF	Tetrahydrofurane
TMB	1,3,5-trimethoxybenzene
TMEDA	tetramethylethylenediamine
TOCKSY	Total correlation spectroscopy
Tol	Toluene
TON	Turn over number
^TP	*Trans*-μ-1,2-peroxodicopper(III)
Ts	Tosyl
TS	Transition state
UV-Vis	Ultraviolet-Visible spectroscopy
V	Volts
XANES	X-ray absorption near edge structure
XAS	X-ray absorption spectroscopy
XRD	X-ray diffraction

Als meus pares,

a l'Aleix,

i especialment a tu, avi.

ACKNOWLEDGEMENTS

This work would not have been possible without the following collaborations:

- Serveis Tècnics de Recerca (STR) from Universitat de Girona for technical support, with especial remark to Dr. Laura Gómez, Xavi Fontrodona and Dr. Sergio Gil, for their dedication in setting up the mass spectrometer, the X-ray diffractometer, and selected NMR experiments, respectively.
- Dr. Josep Maria Luis, Dr. Steven Roldán Gómez and Pau Besalú Sala from the Institut de Química Computacional i Catàlisi of Univeristat de Girona for the theoretical studies.
- Prof. Dr. Miquel Costas for the collaborative research in the studies of bioinspired copper systems for oxygen activation.
- Prof. Dr. Liviu M. Mirica, and his co-workers, for hosting and supervision, and collaborative research in the mechanistic investigations the organometallic nickel redox reactivity during my scientific visit at the University of Illinois at Urbana-Champaign.
- Financial support by:
  - Universtitat de Girona: IF-UdG-2017 PhD fellowship, MOB19 mobility grant
  - Spanish Ministry of Science: CTQ2016-77989_P, PID2019-104498GB-I00.

TABLE OF CONTENTS

GRAPHICAL ABSTRACT

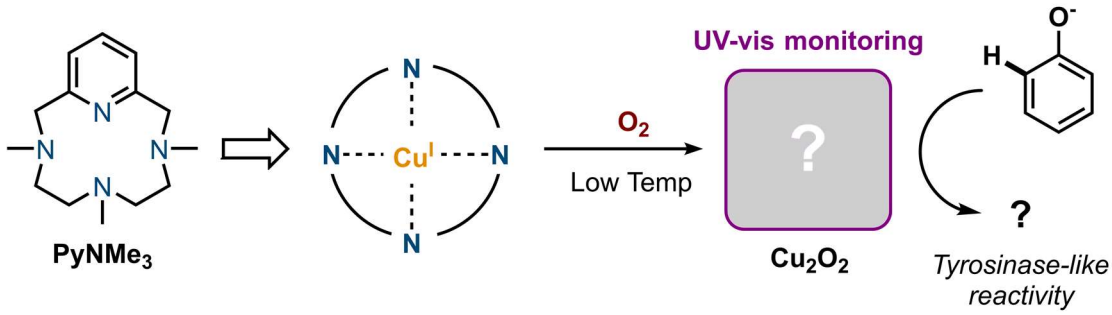

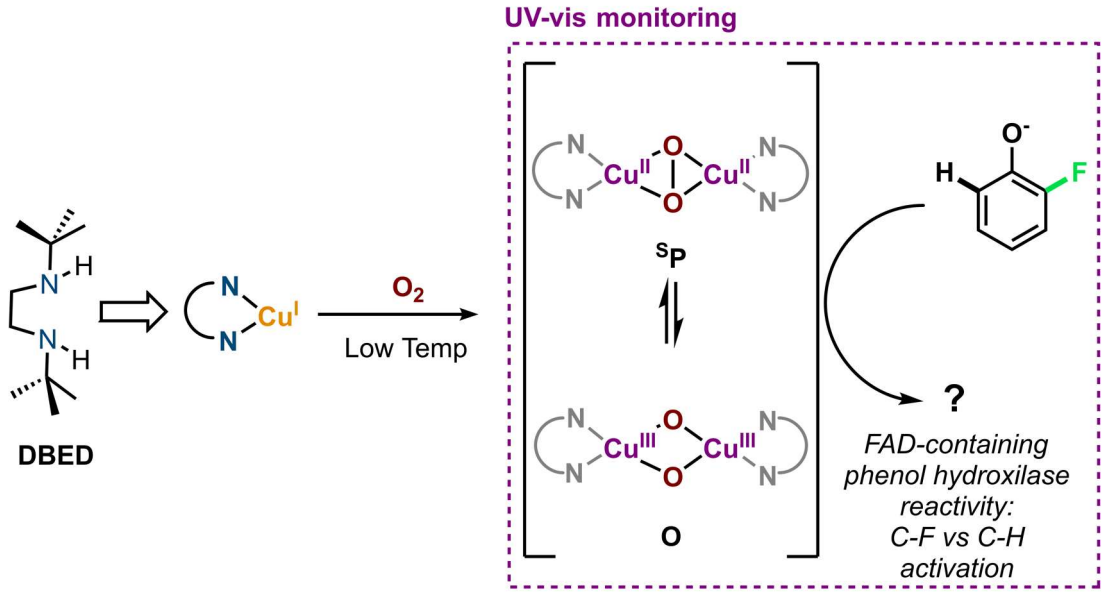

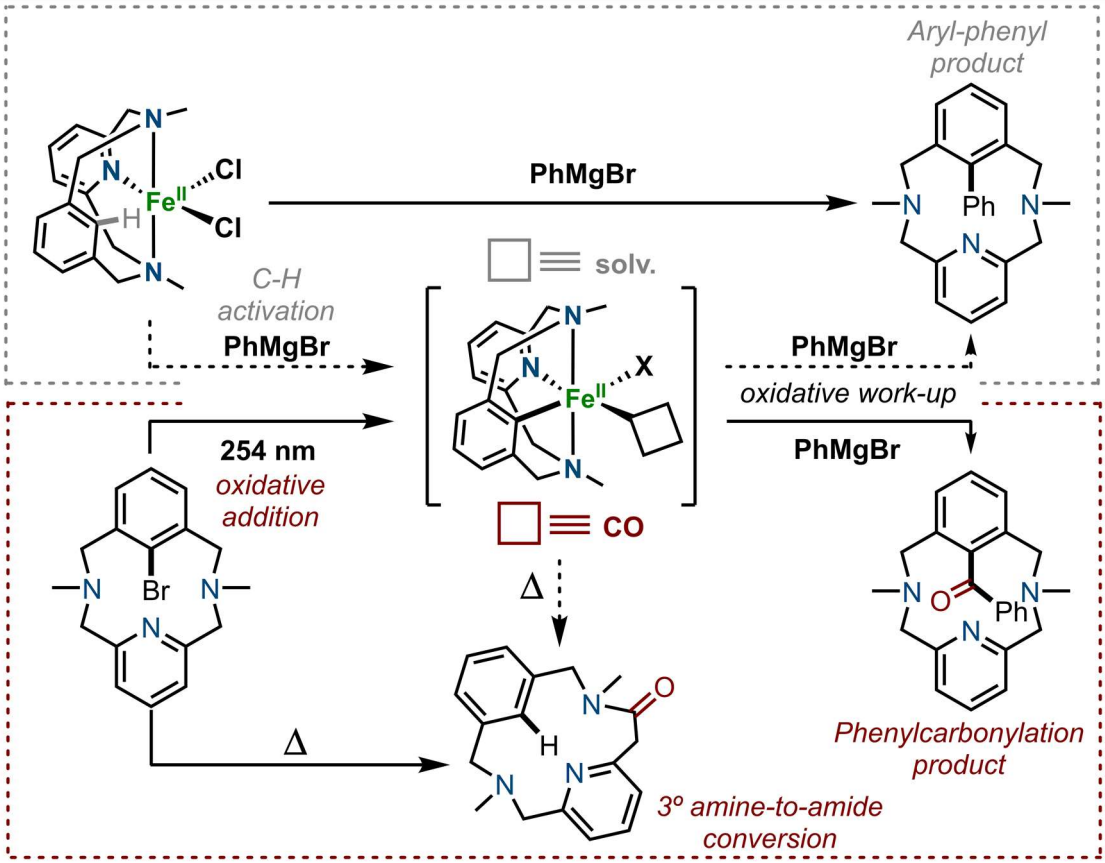

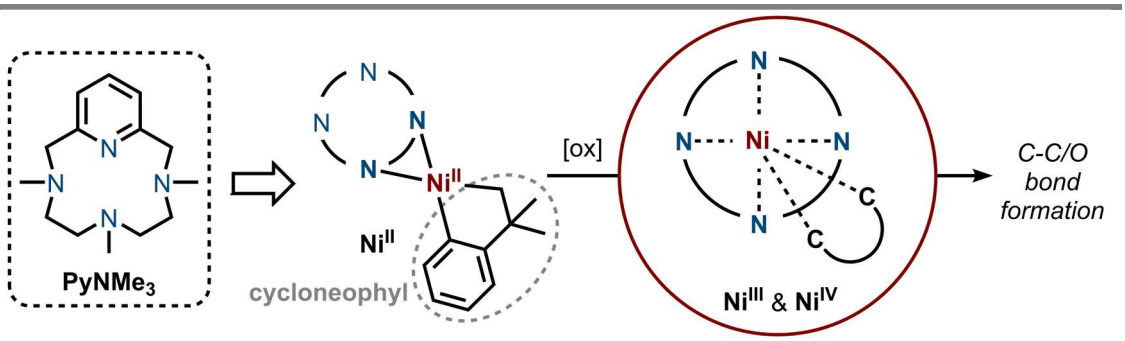

LIST OF FIGURES

LIST OF TABLES

LIST OF SCHEMES

SUMMARY

Nowadays, one of the main goals in organic chemistry and fine industry is the development of new synthetic methodologies for the preparation of life-relevant products in a sustainable manner. The use of first-row transition-metals to mediate these transformations has drastically revolutionized the field. In order to develop efficient protocols, mechanistic understanding of the steps that occur in each transformation is required. For first-row transition-metal mediated transformations, this fundamental knowledge is usually scarce due to the elusive character of the intermediate species formed *in situ* and to the different reaction pathways that can occur depending on the reaction conditions applied. This doctoral dissertation is focused on the mechanistic understanding of different reactions mediated by first-row transition-metals using specially designed ligands to stabilize the otherwise very reactive intermediate species.

The first part of this thesis deals with reactivity of two copper systems bearing bioinspired ligands for the activation of molecular oxygen. First, we developed a copper complex bearing a macrocyclic ligand to mimic the activity of the tyrosinase enzyme, which consists in the *ortho*-hydroxylation of phenolic substrates. We were able to detect a side-on peroxodicopper(II) species, yet no oxidative reactivity was observed because it was coordinatively congested. Then, we studied the detailed mechanism of another copper system for oxygen activation previously developed by Stack and co-workers, which is able to perform the *ortho*-defluorination-hydroxylation of 2-fluorophenol derivatives.

In the second part of this thesis we turned our attention to C-C and C-O bond forming reactions mediated by organometallic iron and nickel complexes. We explored the reactivity of a well-defined aryl-iron(II) complex bearing a macrocyclic model substrate with phenyl Grignard reagent, obtaining the phenylcarbonylation C-C product stemming from the insertion of one CO ligand to the phenyl group prior to the reductive elimination step to release the final organic coupling product. Moreover, upon applying different reaction conditions an unprecedented tertiary-amine-to-amide conversion of a cyclic substrate is observed. Subsequently, the synthesis and redox reactivity of well-defined organometallic nickel(II), nickel(III) and nickel(IV) complexes is explored towards the formation of new C-C or C-O bonds by using oxygen-transfer oxidants.

RESUM

Actualment, un dels objectius principals en química orgànica i la indústria és el desenvolupament de noves síntesis per la preparació de productes biològicament rellevants de forma sostenible. L'ús de metalls de la primera sèrie de transició per efectuar aquestes transformacions ha revolucionat dràsticament el camp. Per tal de desenvolupar protocols eficients cal entendre a tarvés de quin mecanisme té lloc per cada transformació. En les reaccions catalitzades per metalls de la primea sèrie de transició aquests coneixements fonamentals sovint són escassos degut a que els intermedis formats *in situ* són esquius i a l'existència de diferents vies de reacció que es donen en funció de les condicions aplicades. Aquesta tesi doctoral se centra en entendre el mecanisme de diferents reaccions efectuades per metalls de la primera sèrie de transició mitjançant l'ús de lligands especialment dissenyats per estabilitzar els intermedis de reacció, que d'altra manera són altament reactius.

La primera part de la tesi estudia la reactivitat de dos sistemes de coure amb lligands bioinspirats per l'activació d'oxigen. En primer lloc vam desenvolupar un complex de coure amb un lligand macrocíclic per mimetitzar la reactivitat de l'enzim tirosinasa, la qual consisteix en la hidroxilació de substrats fenòlics. Tot i que vam poder detectar un intermedi "side-on peroxodicoure(II)", aquest no va desenvolupar cap tipus d'oxidació ja que no té posicions de coordinació lliures. Aleshores, vam estudiar detalladament el mecanisme d'un altre sistema de coure, prèviament descrit pel grup de Stack, que és capaç d'efectuar l'*orto*-hidroxilació d'enllaços C-F en compostos derivats del 2-fluorofenol.

En la segona part d'aquesta tesis vam enfocar el nostre estudi cap a les reaccions per formar enllaços C-C i C-O mitjançant complexos organometàl·lics ben definits de ferro i níquel. Vam explorar la reactivitat d'un complex aril-ferro(II) coordinat a un substrat model macrocíclic amb reactiu fenil Grignard, obtenint el producte de fenilcarbonilació C-C provinent de la inserció d'un lligand CO al grup fenil just abans del pas d'eliminació reductiva que allibera el producte final. A més, a l'aplicar diferents condicions de reacció es va observar una conversió d'amina-a-amida terciària sense precedents en substrats cíclics. Finalment, es va estudiar la síntesi i reactivitat redox d'uns complexos organometàl·lics de níquel(II), níquel(III) i níquel(IV) per la formació de nous enllaços C-C o C-O amb oxidants amb transferència d'oxigen.

RESUMEN

Actualmente, uno de los objetivos principales en química orgánica y la industria es el desarrollo de nuevas síntesis para la preparación de productos biológicamente relevantes de forma sostenible. El uso de metales de la primera serie de transición para efectuar estas transformaciones ha revolucionado drásticamente el campo. Para desarrollar protocolos eficientes es necesario entender el mecanismo operativo para cada transformación. En las reacciones catalizadas por metales de la primera serie de transición estos conocimientos básicos a menudo son escasos debido a que los intermedios formados *in situ* son esquivos, así como a las diferentes vías de reacción que se dan según las condiciones aplicadas. Esta tesis doctoral se focaliza en entender el mecanismo de diferentes reacciones efectuadas por metales de la primera serie de transición mediante el uso de ligandos especialmente diseñados para estabilizar las especies intermedias altamente reactivas.

La primera parte de la tesis estudia la reactividad de dos sistemas de cobre con ligandos bioinspirados capaces de realizar la activación de oxígeno. Primero, desarrollamos un complejo de cobre con un ligando macrocíclico para mimetizar la reactividad de la enzima tirosinasa, que consiste en la hidroxilación de sustratos fenólicos. Aunque pudimos detectar un intermedio "side-on peroxodicobre(II)", éste no desarrolló ningún tipo de oxidación puesto que está coordinativamente saturado. A continuación, estudiamos detalladamente el mecanismo de otro sistema de cobre, previamente descrito por el grupo de Stack, que es capaz de realizar la orto-hidroxilación de enlaces C-F en compuestos derivados del 2-fluorofenol.

En la segunda parte de esta tesis cambiamos nuestro estudio hacia las reacciones para formar enlaces C-C y C-O mediante complejos organometálicos bien definidos de hierro y níquel. Exploramos la reactividad de un complejo arilo-Fe(II) junto a un sustrato modelo macrocíclico con reactivo fenilo Grignard, obteniendo el producto de fenilcarbonilación C-C proveniente de la inserción de un ligando CO en el grupo fenilo justo antes del paso de eliminación reductiva que libera el producto final. Además, al aplicar diferentes condiciones de reacción se observó una conversión de amina-a-amida terciaria sin precedentes en sustratos cíclicos. Por último, se estudió la síntesis y reactividad redox de unos complejos organometálicos de Ni(II), Ni(III) y Ni(IV) para la formación de enlaces C-C/O con oxidantes con transferencia de oxígeno.

Chapter I. General introduction

I.1 SUSTAINABLE CHALLENGES IN ORGANIC SYNTHESIS

The discovery and development of new synthetic methodologies to enhance efficiency, atom and step economy in current organic transformations is one of the main goals for synthetic chemists to build up chemical complexity in molecules. Life-relevant products such as pharmaceuticals, agrochemicals, polymers, and natural products can be obtained from relatively simple organic scaffolds.[1] These compounds have a high percentage of C-C, C-H and C-Heteroatom bonds, and therefore the activation and/or functionalization of these bonds has gained significant attention over the last decades in order to build up molecular complexity. Current industrial processes involve reagents such as organometallic compounds, superacid electrophiles, stoichiometric oxidants, carbocations or free radicals.[2] However, the functionalization of these ubiquitous bonds is far from trivial and often requires harsh reaction conditions (high temperatures, toxic reagents, etc.), which result in expensive methodologies with undesirable waste generation, in addition to the production of unwanted side-products.

Some of the problems mentioned above can be solved with the use of transition metal-based catalysts. Indeed, their use has drastically revolutionized organic synthesis, and this is now a field of paramount interest. The use of catalysts enables transformations that would not be easy or not even feasible by traditional methodologies.[3-6] These strategies range from organocatalysis to supramolecular chemistry, being transition metal catalysts the most widely used. Nonetheless, in order to develop novel, efficient and ecofriendly synthetic procedures, detailed studies on the mechanism of operation of these transformations must be undertaken. These mechanistic studies can proceed either via direct probes by isolating and characterizing intermediate species using different spectroscopic or spectrometric techniques (single crystal X-ray diffraction, nuclear magnetic resonance, mass spectrometry, EPR, vibrational spectroscopy, etc), or alternatively via indirect probes involving isotope labelling experiments, kinetic studies or the use of radical traps among others. A deep mechanistic knowledge of most of these catalytic transformations remains a challenging feature as they often proceed through very unstable and highly reactive species, which are particularly difficult to isolate or even detect.

In this thesis, mechanistic investigations have been performed on three different first-row transition metal-based approaches which can be divided in two blocks: (i) the oxidation or

oxygenation of hydrocarbons using bioinspired copper systems in tandem with a *green* oxidant such as molecular oxygen (Section I.3), and (ii) the *cross-coupling* (and C-H activation) *reaction* mediated by first-row transition metals like iron and nickel (Section I.4).

I.2 MECHANISTIC STUDIES: THE MACROCYCLIC APPROACH

As described above, gaining knowledge on the underlying pathways behind metal-based catalytic transformations would open new doors for both improvement of previously reported methodologies and the development of new protocols. Whether direct or indirect methods are performed to elucidate and comprehend at a molecular level the nature of the reactive species involved in reaction mechanisms, one strategy commonly used by our and other research groups and in this particular thesis is the so-called *macrocyclic approach*. This strategy consists in the use of model ligands and/or substrates which can bind to the metal center (model system) in order to stabilize these otherwise elusive intermediate species. In particular, model systems used for the study of oxidation or oxygenation of hydrocarbons are usually inspired by the ones found in nature (bioinspired), such as metalloenzymes (this will be further explained in Section I.2.1). These model ligands and/or substrates are usually tri- or tetradentate nitrogen-based macrocycles of different ring sizes, structure and functionalities depending on the metal they hold (Figure I.1).

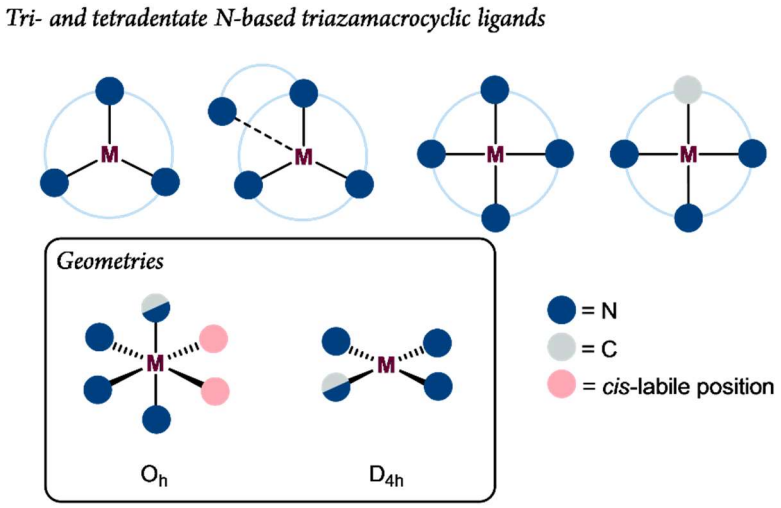

Figure I.1 Schematic representation of tri- or tetradentate *N*-based macrocyclic model ligands or substrates. Inset: Typical octahedral and square planar coordination geometries for these model ligands.

In our group triazacyclononane-type ligands have been used to stabilize high-valent manganese-oxo[7], iron-oxo[8-13], iron-nitrido[14] and iron-tosylimido[15] intermediate species. These ligands are aza-crown ethers with the general formula $(C_2H_4NR)_3$, which consist of a cyclononane where three equidistant methylene groups have been replaced with NR groups (R = H, pyridine, methyl, etc.) (Scheme I.1a). Depending on the amine substituents the ligand can be tri- (*i.e.,* R = H, Me, etc), tetra- (*i.e.,* R = 2H/Me and py) or pentadentate (*i.e.,* R = H/Me and 2py). Another macrocyclic ligand platform, $PyNMe_3$, developed in our group has been successfully employed to stabilize high-valent iron(IV)/iron(V)-oxo[16, 17] species and cobalt-peroxo[18] species. This tetradentate N-based macrocyclic ligand binds through one pyridine and three aliphatic amines, which upon coordination to the metal center leaves two *cis*-labile positions available to interact with exogenous ligands (Scheme I.1b). Thus, all these features make it a suitable ligand to stabilize high-valent complexes such as metal-oxygen intermediate species.

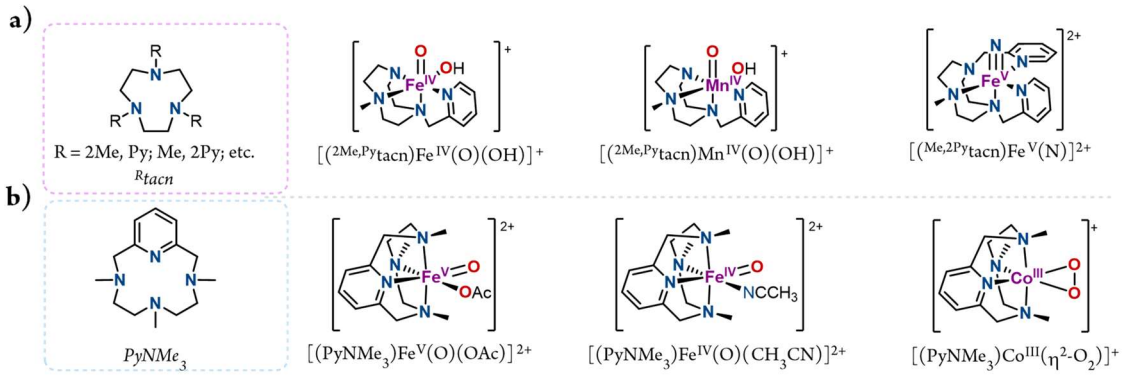

Scheme I.1 High-valent complexes stabilized and detected with a) ^{R}tacn ligand and b) $PyNMe_3$ ligand.

Also in our group, Ribas and co-workers developed a series of macrocyclic scaffolds in order to trap organometallic intermediates, otherwise non-detectable, relevant for cross-coupling transformations. These model substrates are triazamacrocyclic-type ligands that contain aryl-halide or arene moieties. One of these ligands, that consists of an aryl-H/halide moiety and three aliphatic amines, was demonstrated to stabilize a series of aryl-metal complexes (Cu(III)[19-22], Ag(III)[23] and Ni(II)[24, 25]) (Figure I.2a). Another version of these model substrates, which consists of an arene moiety with two aliphatic amines and a pyridine, was useful to trap aryl-cobalt(III) and aryl-rhodium(III) complexes[26] and a masked carbene aryl-cobalt(III) complex[27] (Figure I.2b).

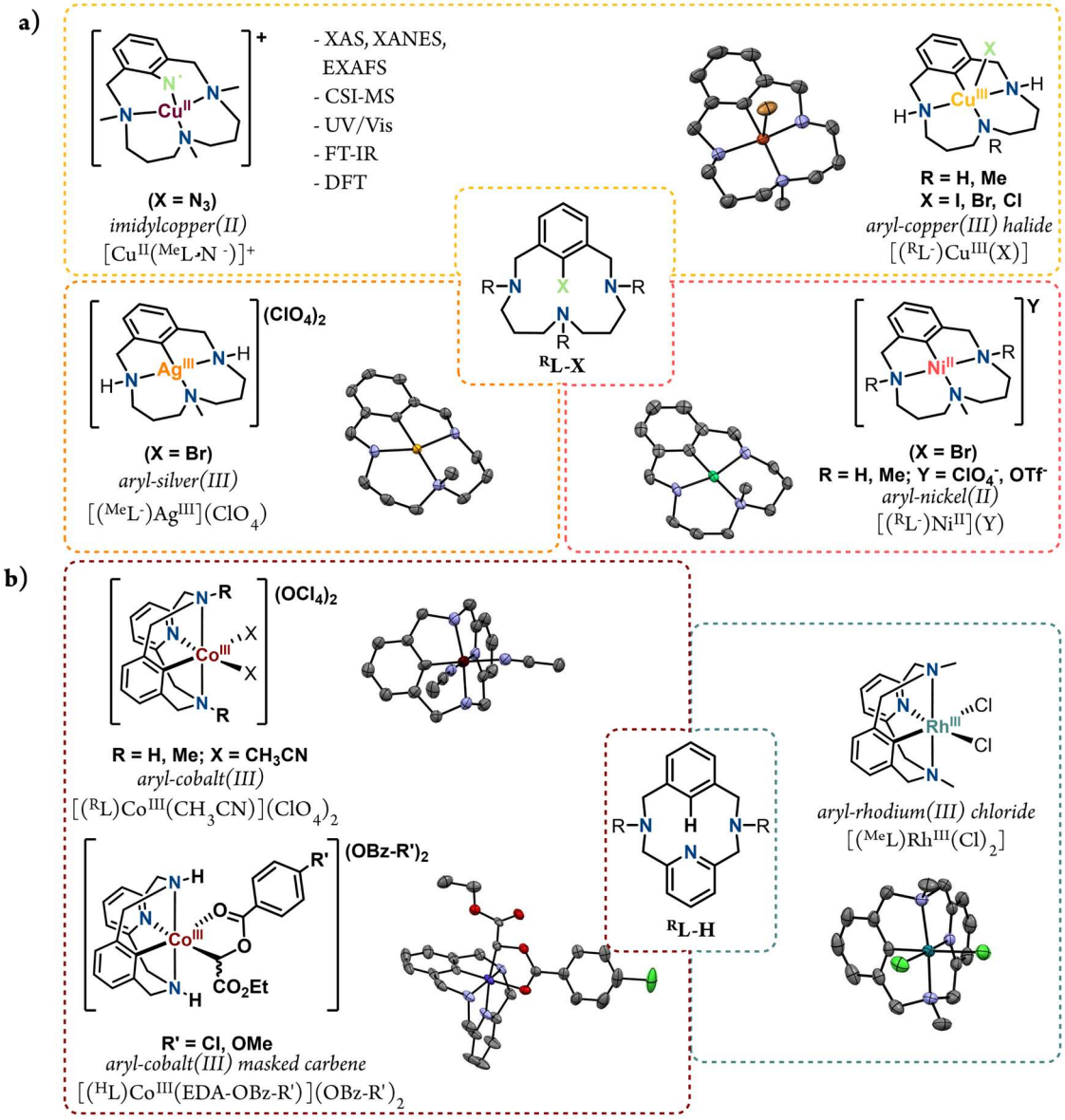

Figure I.2 Organometallic complexes isolated with a) ^{R}L-X model substrate and b) ^{R}L-H model substrate.

I.2.1 Biomimetic model systems

Metalloenzymes are very efficient catalysts and so understanding their mechanism of operation is of great interest to build up new catalysts. However, working with the entire protein is a tough task due to the complexity of these structures and the difficulty to purify and obtain proteins in large quantities. To simplify the study of these systems, chemists focus their attention on the active site, where the metal center is found and most chemical reactions occur. Per se, *biomimetics* is the study and development of synthetic systems which purpose is to imitate the formation, function, or structure of biological substances and materials, and biological mechanisms and processes. So, from this definition it can be said that two main objectives can

be drawn from this approach: i) imitating the function of an enzyme involved in a chemical transformation and so being able to reproduce its reactivity; ii) gaining insight into the biological system by affording mechanistic, structural and spectroscopic information. In this regard, the bioinorganic strategy for studying active sites consists in developing low molecular weight transition metal complexes, in which the metal is bound in a similar environment to that found in the enzyme (Figure I.3).

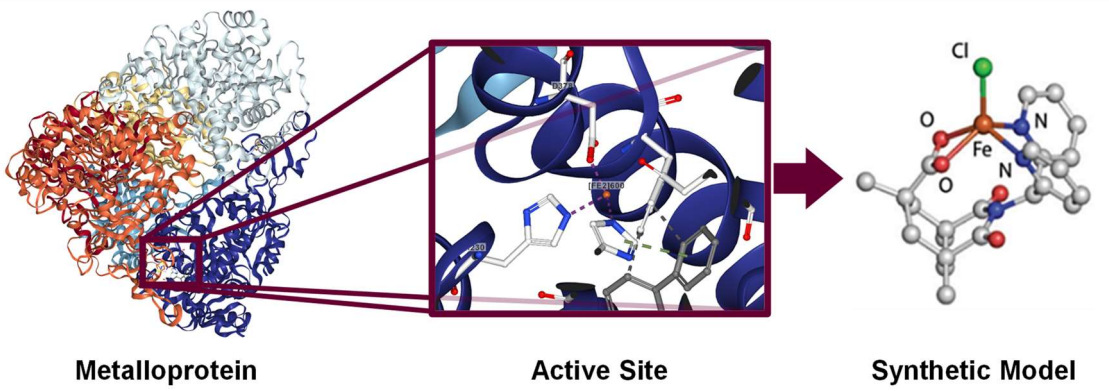

Figure I.3 Biomimetic approach: from a metalloprotein to a synthetic model.

Transition metals are prime candidates for catalysis as their ability to give and take electrons translates into a wide variety of oxidation states, which give them their chemical properties. Moreover, from the perspective of green chemistry, first-row transition metals (Mn, Fe, Co, Ni and Cu) are earth abundant and less toxic in comparison to their second and third-row transition metal counterparts. Overall, the development of model systems offers a chance to understand, reproduce the chemistry performed by the original enzymes and develop new synthetic systems.[28, 29]

I.3 BIOINSPIRED COPPER-BASED OXIDATIONS WITH DIOXYGEN

As mentioned in section I, the functionalization of inactivated C-H bonds is a very powerful reaction as hydrocarbons are a major source of feedstocks. The selective functionalization of these ubiquitous bonds could allow for further derivatizations. However, these transformations are very challenging due to the inert nature of these C-H bonds. This lack of reactivity arises from the fact that hydrocarbons are held together via strong and non-polarized C-H and C-C bonds.[30] Moreover, selectivity issues add up to this chemical inertness because, as mentioned before, these bonds are basically present in any organic molecule. One of the most desirable

functionalities to be introduced in hydrocarbons for their further transformations are oxygen-containing groups. For this reason, oxidation and oxygenation reactions are gaining great attention from synthetic researchers.[31-33]

At present, owing to environmental reasons, efforts are being directed towards the development of catalytic processes (in substitution to stoichiometric ones) in order to reduce waste generation and diminish the use of harmful oxidants (*i.e. meta*-chloroperbenzoic acid, sodium hypochlorite, permanganate, etc.). These stoichiometric oxidants are being outdated due to their noxiousness, the intolerable amounts of toxic waste generated, high reaction temperatures and long reaction times. In addition, these reactions exhibit low selectivities and poor yields. Thus, taking into account environmental and economic costs, and as outlined before, these methodologies are being substituted by catalytic processes which involve transition-metal based catalysts in tandem with *greener* (less toxic) and cheaper oxidants. So, following the sustainability trends for these reactions, the ideal green oxidant should be readily available, environmentally friendly and with a high content of active oxygen to meet high atom economy. These requirements are fulfilled by dioxygen or hydrogen peroxide (Table I.1).[34]

Table I.1 Commonly used oxidants in organic synthesis and their respective by-products ordered according to their percentage of active oxygen.

Oxidant	% Active Oxygen*	By-product
O_2	100.0 / 50.0	- / H_2O
H_2O_2	47.0	H_2O
N_2O	36.4	N_2
O_3	33.3	O_2
$KMnO_4$	30.4	Mn(II) salts
HNO_3	25.0	NO_x
CrO_3	24.0	Cr(III) salts
NaOCl	21.6	NaCl
CH_3CO_3H	21.1	CH_3CO_2H
***m*-CPBA**	9.3	*m*-CBA
PhIO	7.3	PhI

*The mass amount of oxygen transferred to the substrate with respect to the total mass of the oxidant.

Nature is and has been a source of inspiration for the development of biomimetic or bioinspired methodologies, as we can find this kind of transformations happening spontaneously in our environment in an efficient manner under mild reaction conditions. Indeed, metalloenzymes

use dioxygen to perform an extensive range of highly selective oxidation and oxygenation reactions, with the involvement of redox processes together with proton transfers.[29] However, the reaction mechanism through which these transformations take place is most of the times arduous to model. As a consequence, the need for the development of new strategies to mimic the activity of metalloenzymes is still very remarkable.

I.3.1 O_2 activation: the ideal oxidant

Dioxygen plays a very important role in our life as it is the terminal electron acceptor in aerobic processes such as cellular respiration, which enables the biosynthesis of energy-rich substrates used through the metabolism.[35] Another function of molecular oxygen in aerobic biological systems involves enzymes that can convert O_2 into highly specialized oxidizing species used to catalyze the synthesis of relevant biomolecules and the degradation of xenobiotics. Moreover, as shown in Table I.1, dioxygen is the ideal oxidant to be employed for oxidation reactions: due to its high abundance and readily availability it becomes a cheap oxidant, and it offers high atom economy as its active oxygen content is 100% (or 50% with just water as by-product).

Nevertheless, molecular oxygen itself does not act as an oxidant at room temperature. If this was the case, atmospheric O_2 would spontaneously react with all the organic molecules producing carbon dioxide and water. In fact, this reaction is exothermic, so favored from a thermodynamic point of view. Thus, the lack of reactivity of dioxygen is explained by the unfavorable kinetics, which is dictated by the electronic structure of O_2 (Figure I.4a, left). Dioxygen is a triplet molecule in its ground state (S=1, two unpaired electrons in the antibonding molecular orbitals π_{2px}^* and π_{2py}^*). Since most organic molecules are closed-shell molecules (S=0), the reaction with O_2 is a spin-forbidden process.[36]

Despite these thermodynamic limitations, biological systems are constantly using O_2 as an oxidant to carry out oxidative processes. This finds an explanation in the fact that nature has strategies to overcome the low reactivity of molecular oxygen by the interaction with molecules containing unpaired electrons such as radicals (S=1/2) or paramagnetic transition metals (S≥1/2) (Figure I.4a, right). An evidence of this is that there are enzymes containing a transition metal in their active site which can bind and activate dioxygen by transforming it into more

reactive species such as superoxides (O_2^-, S=1/2) or peroxides (O_2^{2-}, S=0) that will easily react with organic substrates in a controlled manner.[37, 38]

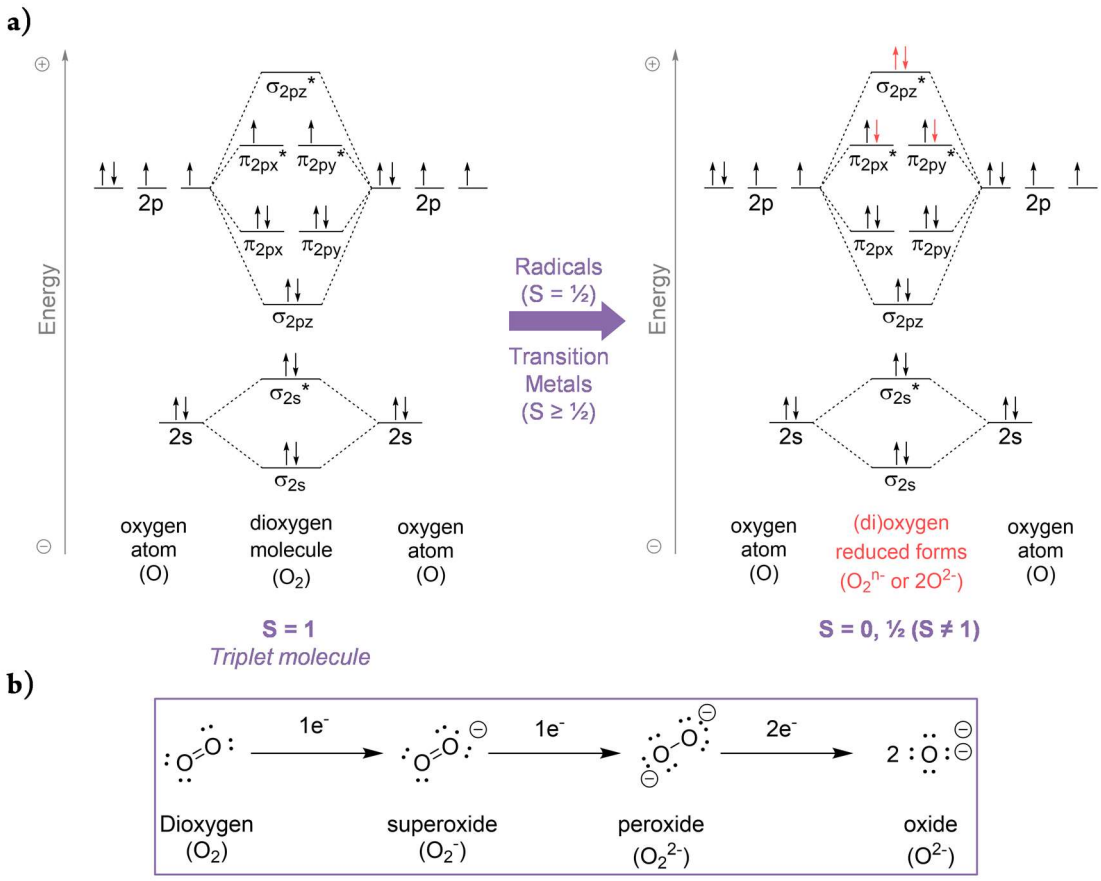

Figure I.4 a) Activation of molecular oxygen to give its active reduced forms, and b) reduction of molecular oxygen to yield its reduced forms.

As depicted in Figure I.4b, the activation of O_2 involves its reduction by one, two or four electrons. In nature the origin of these electrons is quite diverse: the organic substrate itself, a co-substrate, a cofactor or a transition metal (in the case of metalloproteins). From a bioinorganic point of view, this last case is the most interesting because earth abundant transition metals such as iron and copper are found in the active site of metalloenzymes.[36] For example, Rieske dioxygenases contain a mononuclear iron center in their active site that activates O_2 to perform the *syn*-dihydroxylation of arenes (Scheme I.2, top),[37, 39, 40] while tyrosinase presents a dinuclear copper center in its active site responsible for the O_2 reduction coupled with the *ortho*-hydroxylation of phenols to catechols which are the precursors of melanin (Scheme I.2, bottom).[28]

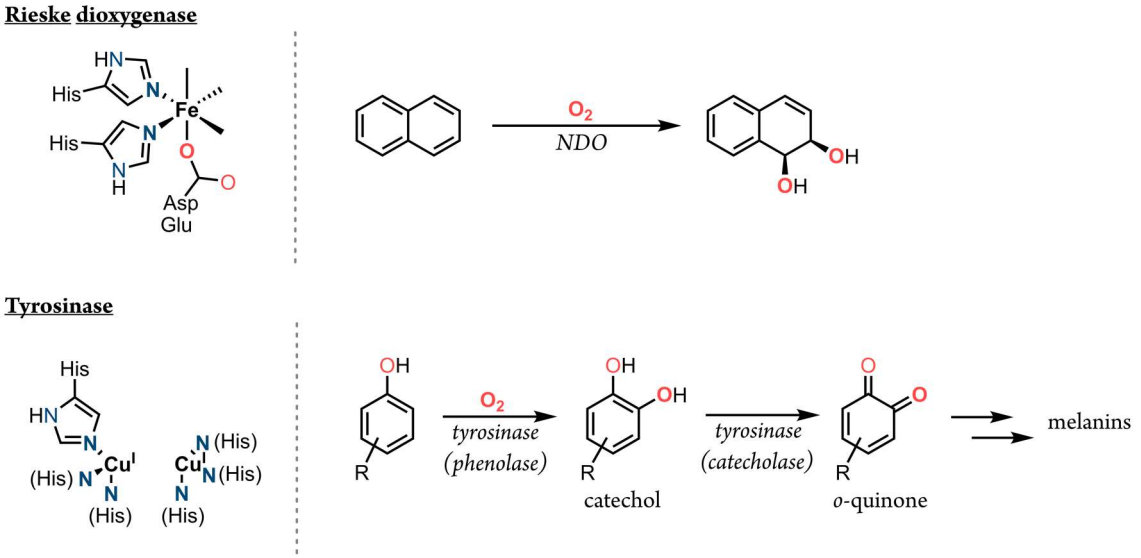

Scheme I.2 Top: reduced form of the Rieske Dioxygenase active center (mononuclear non-heme iron-containing metalloprotein) which uses O_2 as oxidant for the *syn*-dihydroxylation of arenes (Naphthalene dioxygenase, NDO). Bottom: reduced form of the tyrosinase active center (dinuclear copper-containing metalloprotein), which uses O_2 as oxidant in the *ortho*-hydroxylation of phenols (Phenolase).

I.3.2 Copper oxygenases

It is well established that copper is an essential element found in trace amounts in most living systems. It can be found in metalloenzymes with mononuclear or coupled multinuclear configurations involved in intricate redox processes.[28, 41] The most common oxidation states of copper in biological systems are +1 and +2 so it is considered a one electron shuttle. As for the +3 oxidation state, it is believed to be present in highly reactive intermediate species in some enzymatic reactions. Nevertheless, due to the highly positive Cu^{II} / Cu^{III} redox potential, Cu^{III} oxidation state is considered to be unreachable in natural systems and so far it has not been directly detected in nature, although it has been proposed to be involved in the mechanism of some systems such as particulate methane monooxygenase (pMMO).[42, 43]

In general, the structure of the active site of copper-based metalloproteins enables to accommodate the structural changes it suffers when the copper center changes its oxidation state. Thus, the structure of the active center is flexible to tolerate these conformational changes but robust enough to prevent side reactions to occur. In addition, the binding pocket around the active site is also tailored for the interaction of the metallic center with a unique substrate in a specific orientation. Finally, yet importantly, the second coordination sphere plays a key role optimizing the orientation of the substrate via non-covalent interactions towards the active site.

The high variety of copper species is translated in the broad range of biological reactions that they catalyze: binding and activation of small molecules (*i.e.*, CO_2, CO, NO_x, O_2) usually coupled to electron transfer reactions, superoxide disproportionation and four electron water reduction. However, the main roles of copper are found in electron transfer mechanisms, O_2 activation (followed by substrate oxidation/oxygenation) and transport of molecular oxygen.[44] At present, it is known that copper proteins involved in dioxygen binding and activation operate through the (reversible) formation of reactive intermediates such as superoxides, peroxides or oxides, which have been characterized by resonance Raman and UV-vis spectroscopy.[45] The most relevant spectroscopically characterized copper-dioxygen intermediates are summarized in Table I.2. Different coordination modes and stoichiometries have been described for these $Cu:O_2$ intermediate species (Table I.2). By far, the most studied family is the one with a $Cu:O_2$ stoichiometry of 2:1. In this group, four different intermediate species (**^{T}P**, **^{C}P**, **^{S}P** and **O**) are known, containing copper centers in the oxidation state +2 or +3. Biomimetic studies on mono- and multinuclear copper oxidases and oxygenases have not been as successful as those on dinuclear copper proteins.[46, 47] Importantly, a number of these intermediates has been characterized with the use of model systems, and a separate section will be devoted to them (see Section I.3.3).

Table I.2 Different $Cu^{n+}:O_2$ intermediate species reported in literature.

Oxidation state	**Cu:O$_2$ ratio** 1:1	2:1	3:1
Cu^{II}	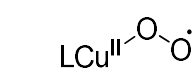 superoxo η^1 end-on (**^{E}S**)	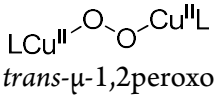 *trans*-μ-1,2peroxo (**^{T}P**)	
		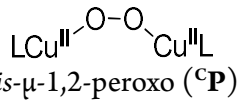 *cis*-μ-1,2-peroxo (**^{C}P**)	
	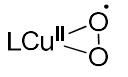 superoxo η^2 side-on (**^{S}S**)	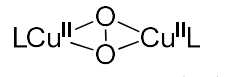 μ-η^2:η^2-peroxo (**^{S}P**)	
$Cu^{II/III}$			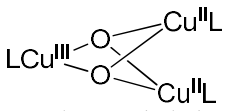 bis(μ$_3$-oxo) (**T**)
Cu^{III}	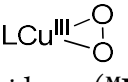 η^2 side-on (**^{M}P**)	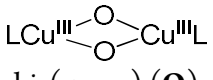 bis(μ-oxo) (**O**)	

Specially for this thesis, attention will be devoted on two of the most studied examples of copper-containing proteins, which are tyrosinase and hemocyanin. Both proteins have almost identical active sites: the reduced form is constituted by two copper(I) atoms, each one coordinated to three histidine residues. Moreover, in the oxygenated form dioxygen is reduced to form a peroxide species which binds between two copper(II) centers in a side-on configuration(**^{S}P**, O_2^{2-}) (Table I.2). Although both proteins have very similar active sites, their biological functions are very different due to the polypeptidic chain that surrounds the active site.[48, 49] Hemocyanin serves as a reversible dioxygen carrier in some arthropods and mollusks (analogous to the hemoglobin in vertebrates) because the interaction of external substrates with the active site is inhibited by the steric hindrance imposed by the protein domain (Scheme I.3b); in contrast, the active site in tyrosinase is closer to the molecular surface thus facilitating the interaction with an exogenous substrate. Given this close interaction, tyrosinase acts as a monooxygenase enzyme performing the *ortho*-hydroxylation of phenols to give catechols and further oxidation to quinones, which are the precursors of melanin (Scheme I.3a).[28]

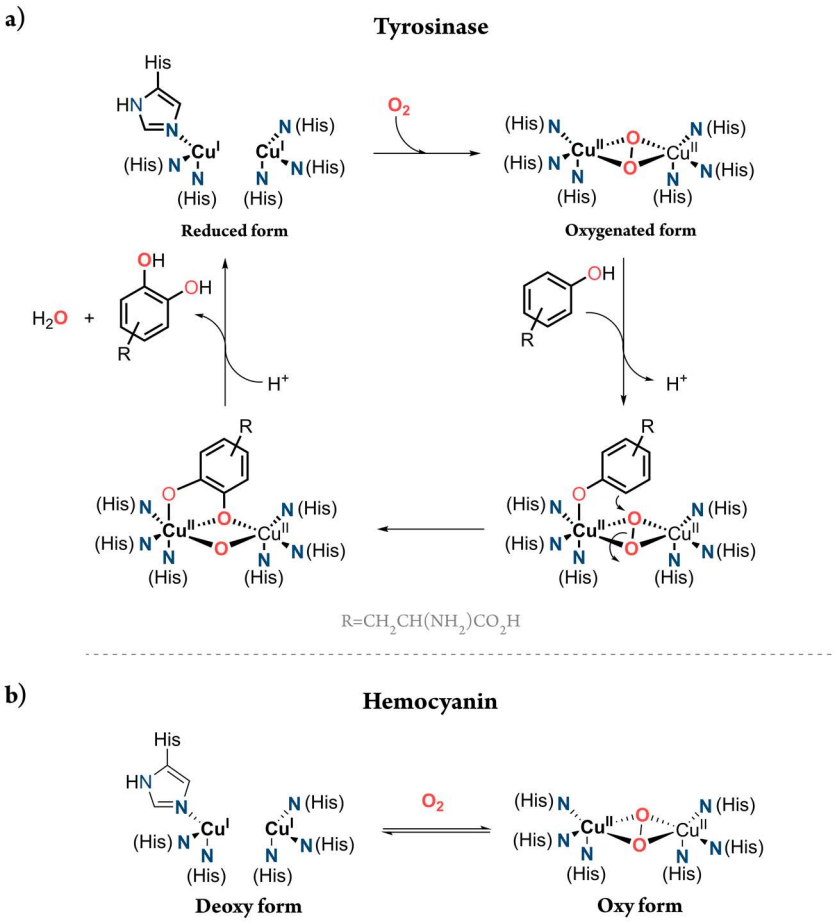

Scheme I.3 a) Proposed mechanism for the hydroxylation of phenols by tyrosinase, and b) deoxy and oxy form of hemocyanin upon dioxygen binding.

I.3.3 Copper bioinspired oxidations

As mentioned above, model systems have been crucial to characterize copper-dioxygen Cu:O_2 2:1 intermediate species.[45] These model systems have been obtained with different approaches. One of the methodologies consists in the synthesis of a ligand with two binding sites in order to hold two metal centers. An alternative strategy, which is the one used in this thesis, relies on the preparation of a mononuclear metal complex (LM, L = ligand with one binding site for a single metal) that reacts with O_2 to obtain a metal-dioxygen adduct (LM-O_2) that further reacts with another mononuclear metal complex (L'M') to yield a dinuclear metal-dioxygen adduct (LM-O_2-L'M').[47, 50, 51] Regardless of the strategy used to synthetize these model systems, the final goal is to characterize and, if possible, isolate this Cu:O_2 2:1 species in order to gain mechanistic insight. However, these transient species are thermally unstable and the use of low-temperatures to spectroscopically characterize these copper-oxygen adducts is often required.[47, 51]

This thesis will focus on models that mimic the enzymes tyrosinase and hemocyanin. Even though the structures of these enzymes are nowadays well established by X-ray diffraction, some key aspects of their mechanisms of action are still unclear. In this sense, as shown in the previous section, the use of models has proven successful to shed light in this type of chemistry and to perform selective oxidation of organic substrates. As tyrosinase and hemocyanin have a histidine-rich environment, reproduction of the structure and functionality of these enzymes requires copper atoms being surrounded by ligands containing nitrogen atoms (secondary and tertiary amines, pyridines, imidazoles…).[28, 46, 47, 52]

The first synthetically prepared Cu_2O_2 species capable of mimicking the reactivity of tyrosinase was reported by the group of Casella.[53] It consisted in a dicopper complex bearing the dinucleating ligand L66 that binds to the metal through an aliphatic amine and two benzimidazole units. Reaction of $[Cu^{I}_2(L66)]^{2+}$ with O_2 at low temperature (-80 °C) gave a species whose spectroscopic characterization was fully consistent with a ^{S}**P** compound. Subsequent reaction of this transient Cu_2O_2 adduct with *p*-carbomethoxyphenolate at low temperature resulted in the corresponding catechol product (Scheme I.4).

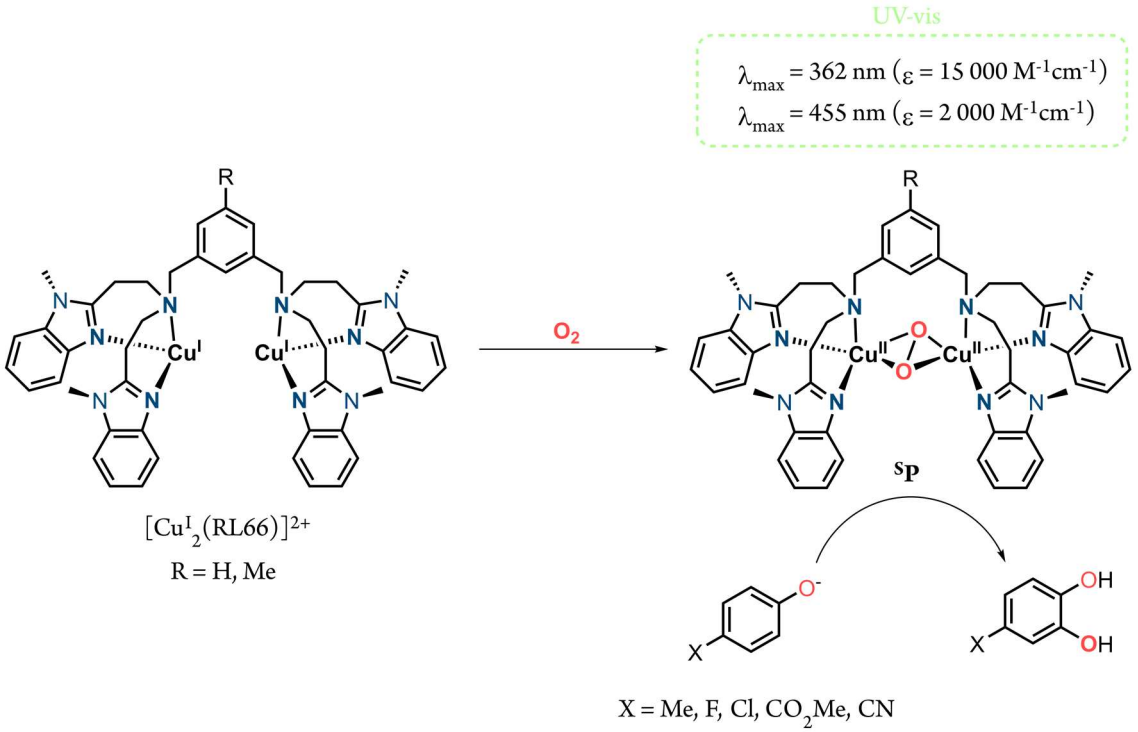

Scheme I.4 Reported synthetic ^{S}**P** species using the dinucleating ^{R}L66 ligand that performs the *ortho*-hydroxylation of phenolates.

Remarkably, Stack and co-workers reported that Cu_2-bis(μ-oxo) species (**O**) could also perform the *ortho*-hydroxylation of phenols, thus mimicking tyrosinase-like reactivity.[54-56] In this work they used a bidentate *N*-based mononucleating ligand, *N,N'*-ditertbutylethylenediamine (DBED), to form the corresponding mononuclear copper(I) complex, $[Cu^{I}(DBEB)]^{+}$. In this case, reaction with molecular oxygen at -80 °C yields the corresponding ^{S}**P** species, characterized by UV-vis and rRaman spectroscopy. However, when the reaction of this Cu_2O_2 adduct with 3,5-di-*tert*-butylphenolate was monitored by UV-vis spectroscopy at extremely low temperatures (-120 °C), the formation of a new transient species was observed and assigned to a bis(μ-oxo) core (**O**) with a coordinated phenolic substrate (Scheme I.5). Indeed, this result has caused intense discussion because the existence of a rapid equilibrium between a ^{S}**P** and **O** species hampers the assignment of the true hydroxylating species in natural and synthetic systems.

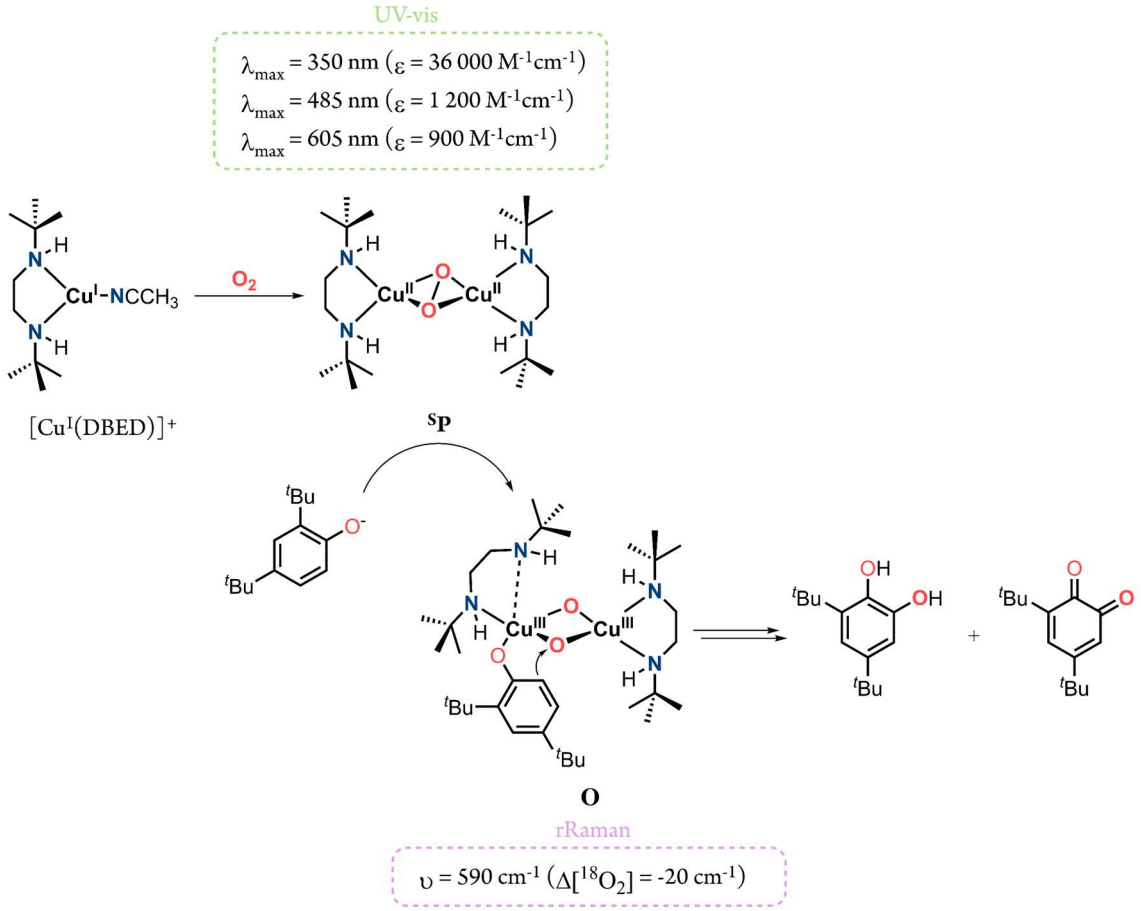

Scheme I.5 Schematic representation of the reaction of $[Cu^{I}(DBED)]^{+}$ using dioxygen and phenolates to generate a ^{S}**P** and a **O** species, respectively.

In a work done by our group, the key role played by the flexibility of the ligand to hold the conformational changes that the copper center suffers when changing the oxidation state among dioxygen binding and activation is demonstrated.[57] A dinucleating *N*-based ligand, *m*-XYL^{MeAN}, was used, consisting of two binding triamine sites connected by a single *meta*-xylyl group. The metal centers in the corresponding dicopper(I) complex, $[Cu^{I}_{2}(m\text{-}XYL^{MeAN})]^{2+}$, coordinate through the three aliphatic amines presenting a distorted trigonal planar geometry, similarly to the coordination sphere found in tyrosinase. $[Cu^{I}_{2}(m\text{-}XYL^{MeAN})]^{2+}$ readily reacts with O_2 at low temperature affording a bis(μ-oxo) core (**O**), trapped and spectroscopically characterized by UV-vis and rRaman spectroscopy, which is the species responsible for the *ortho*-hydroxylation of *para*-substituted phenolates (Scheme I.6, left). Moreover, and very remarkably, another work performed in our group by Company, Costas and co-workers demonstrated the ability of this system for the selective cleavage of *ortho*-C-F bonds in phenolate substrates (Scheme I.6, right).[58] This is a very important contribution from a mechanistic perspective as tyrosinase is known to operate through a ^{S}**P** species for the *ortho*-hydroxylation of phenols. However,

tyrosinase is not capable of hydroxylating 2-fluorophenols as these substrates inhibit its enzymatic activity. The enzymes responsible for the hydroxylation of 2-fluorophenols by cleaving the C-F bond are FAD-dependent phenol hydroxylases. Thus, this reactivity opens new doors to oxidative cleavage of C-F bonds, which are very challenging to break due to their inertness and also for their applications in fluorinated organic compound degradation (pharmaceuticals and agrochemicals) to lower their bioaccumulation.

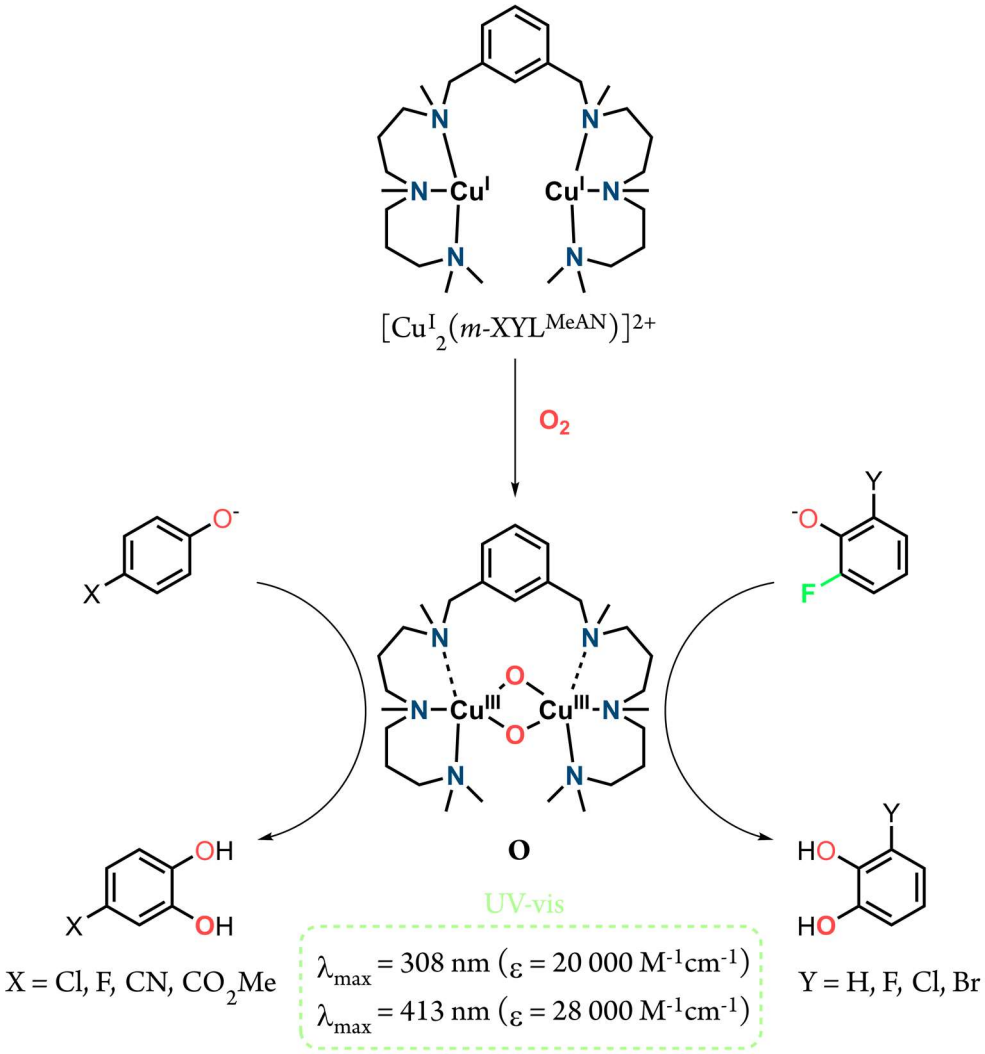

Scheme I.6 Recaction of [Cu$^{I}_{2}$(*m*-XYL^{MeAN})]$^{2+}$ towards O_2 to generate the **O** species and subsequent reaction of this with phenolates (left) and 2-fluorophenolates (right) to yield the corresponding catechols.

I.4 CROSS COUPLING REACTIONS

Cross-coupling chemistry consists in the assembly of two coupling partners assisted by a transition metal promoter (Scheme I.7a). These transformations have been known for more than a century, but they became very popular in the seventies when the first reactions catalyzed by palladium were reported.[59-61] Thenceforward, cross-coupling reactions have become a revolution in the area of organic synthesis as they have provided synthetic chemists with valuable means to build-up complexity in relevant molecules such as pharmaceuticals, agrochemicals, polymers and other compounds with extensive industrial applications.[62-64] In fact, the impact of palladium-catalyzed C-C couplings was recognized in 2010 with the Nobel Prize in Chemistry awarded to Akira Suzuki, Ei-ichi Negishi and Richard F. Heck.[65] These early palladium-based methodologies were restricted to the coupling of aryl and vinyl halides as the electrophile counterparts, with organometallic reagents as the nucleophilic partners. Nonetheless, this was a way to obtain in one step scaffolds such as biaryls, aryl-alkenyls, aryl-alkynyls, conjugated alkenes, etc. which until then could only be prepared by multistep reactions.[66] The general mechanism for palladium-catalyzed cross-coupling reactions (Scheme I.7b) starts with an oxidative addition of the organic (pseudo)halide (electrophilic coupling partner) to the metal catalyst. After that, the nucleophilic coupling partner (usually an organometallic reagent) undergoes transmetalation to the metal catalyst. From here, the organic moieties of both coupling fragments are covalently bound to the same palladium center. The last step is the reductive elimination of the organic moieties of the two coupling partners to achieve the new organic product via a new C-C bond formation and the recovery and regeneration of the metal catalyst to restart the catalytic cycle.[61]

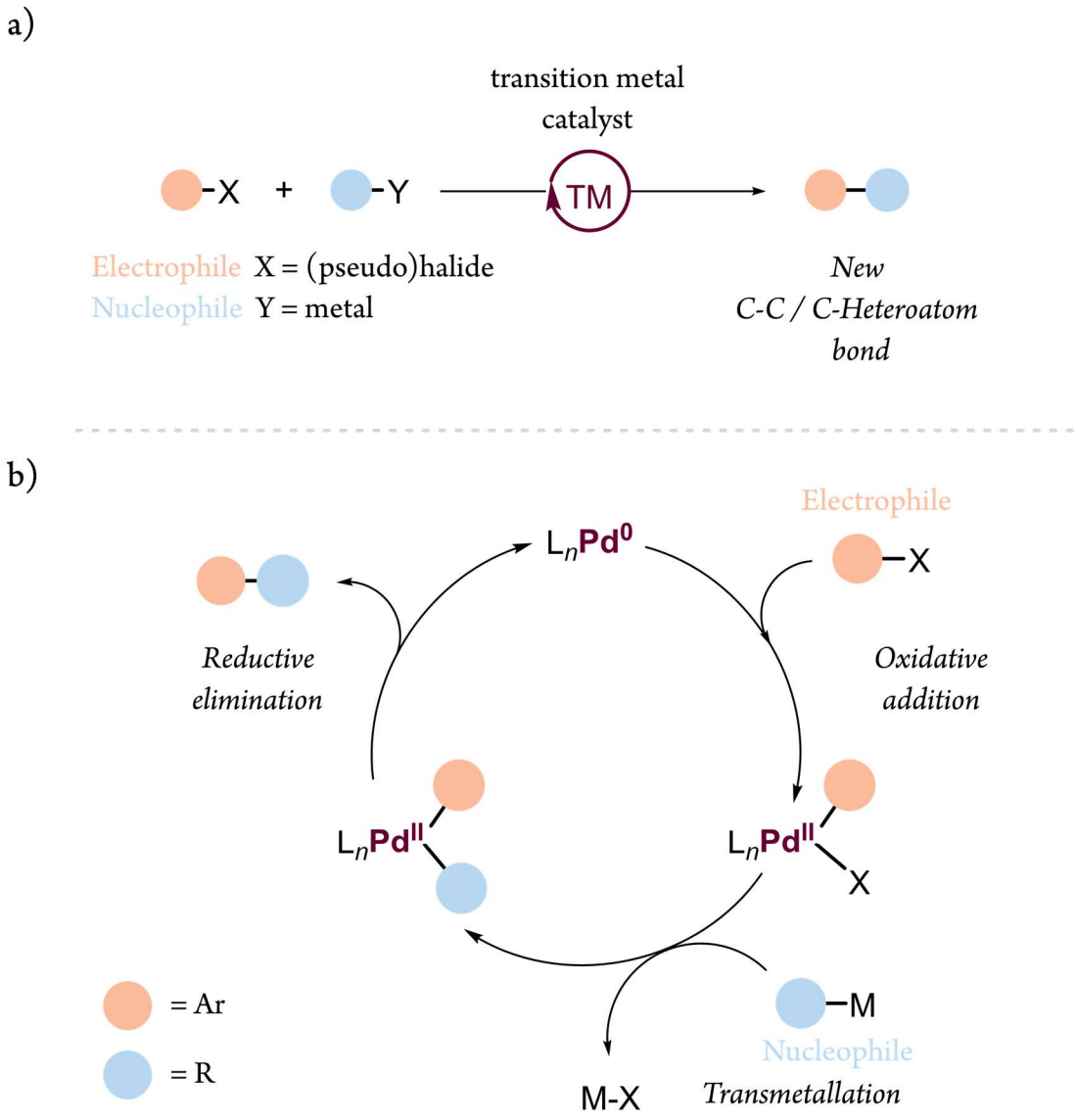

Scheme I.7 a) Schematic and general representation of a cross-coupling reaction, and b) general mechanism for palladium cross-coupling reactions.

It was not until the early nineties that Hartwig and Buchwald upgraded the field of palladium-catalyzed cross-coupling reactions by developing protocols for the formation of new C-N bonds, specifically for the arylation of amines, and so broadening the architectures accessible by cross-coupling to an ample choice of aromatic amines (Scheme I.8).[67, 68] Over the years, the development of new systems for C-heteroatom cross-coupling transformations is on the rise, allowing to expand the scope of coupling partners to amine-, sulfide- and oxygen-based nucleophiles and aryl halides.[69, 70]

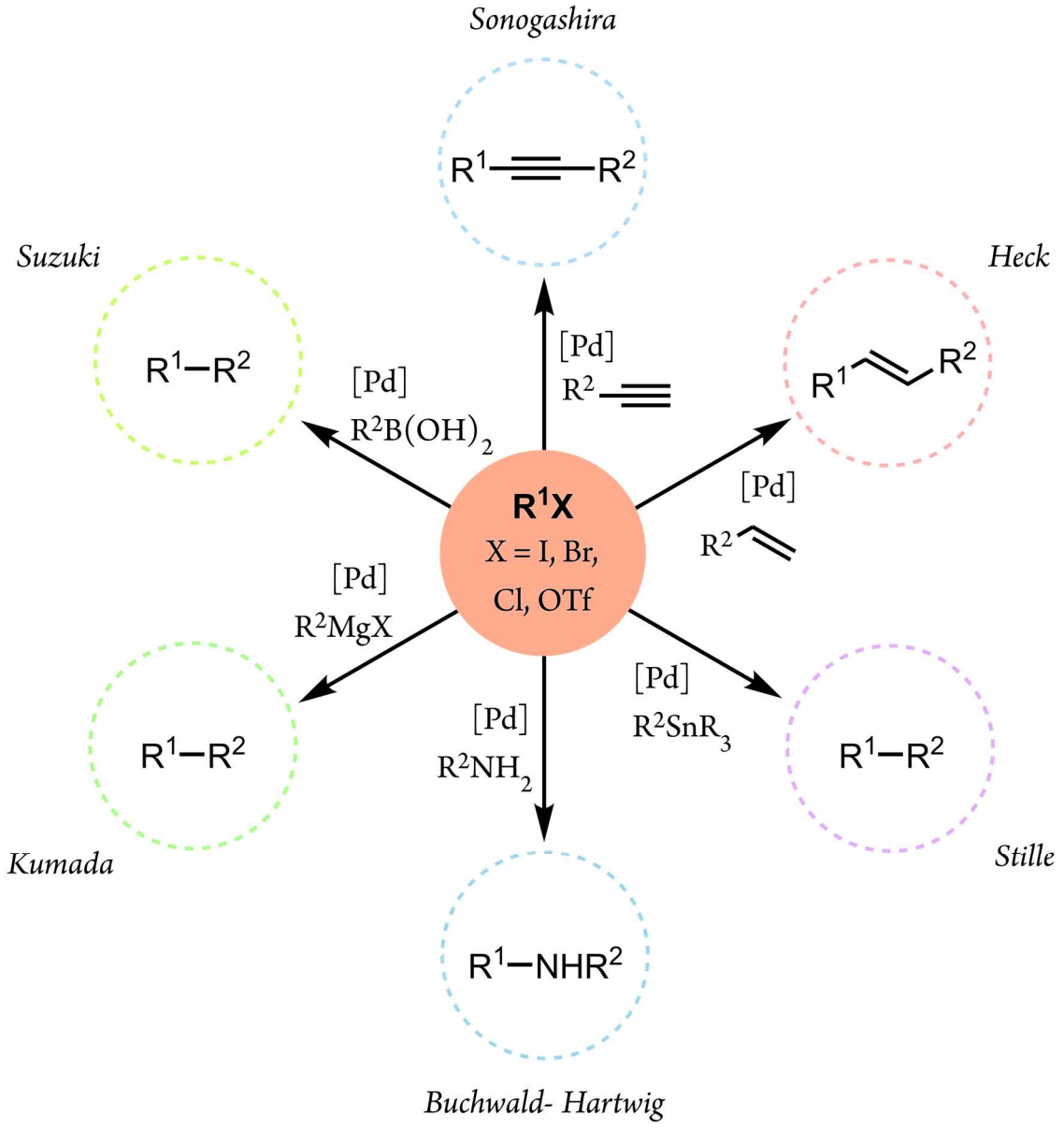

Scheme I.8 Selected examples of the most relevant C–C and C-Heteroatom bond forming cross-coupling and Heck reactions.

In summary, cross-coupling reactions constitute one of the most successful ways to build new C-C bonds as well as C-Heteroatom bonds.[71] Improvement of traditional cross-coupling procedures would require avoiding the prefunctionalization step of the substrate, as direct cross-coupling reactions of C-H bonds would afford greener and more sustainable approaches, as is described below.[72]

I.4.1 C-H activation: the strategy towards sustainability

The need of functionalized coupling partners in cross-coupling reactions imposes an important drawback for these transformations. That is, most of the fuels, chemicals and materials are obtained from petroleum feedstocks, which mainly consist of saturated and unsaturated hydrocarbons, and therefore derivatization of these precursors is needed before the coupling reaction. Therefore, the direct use of hydrocarbons in coupling reactions is highly desirable, as it would simplify reaction schemes and improve atom economy. However, the exploitation of such resources is impeded by the lack of reactivity of carbon-hydrogen bonds, as shown by their bond dissociation energies of 100 kcal/mol in alkanes and 110 kcal/mol in arenes and olefins.[30] Consequently, harsh conditions and reagents have traditionally been employed to achieve the functionalization of C-H bonds in industry.[2] The use of these conditions became especially troublesome more than twenty years ago, when the establishment of the *12 Principles of Green Chemistry* triggered chemists towards the pursuit of new synthetic routes and materials while preserving natural resources.[73] This situation improved with the introduction of transition-metal catalysis, which, as mentioned in the previous section, opened new perspectives in this area.[6] Specifically, the possibility of directly introducing a new functionality through a selective metal-mediated C-H bond cleavage (C-H bond activation) is a highly appealing strategy as, in comparison with *cross-coupling reactions*, it avoids the requirement for prefunctionalization of both partners (Scheme I.9).[73]

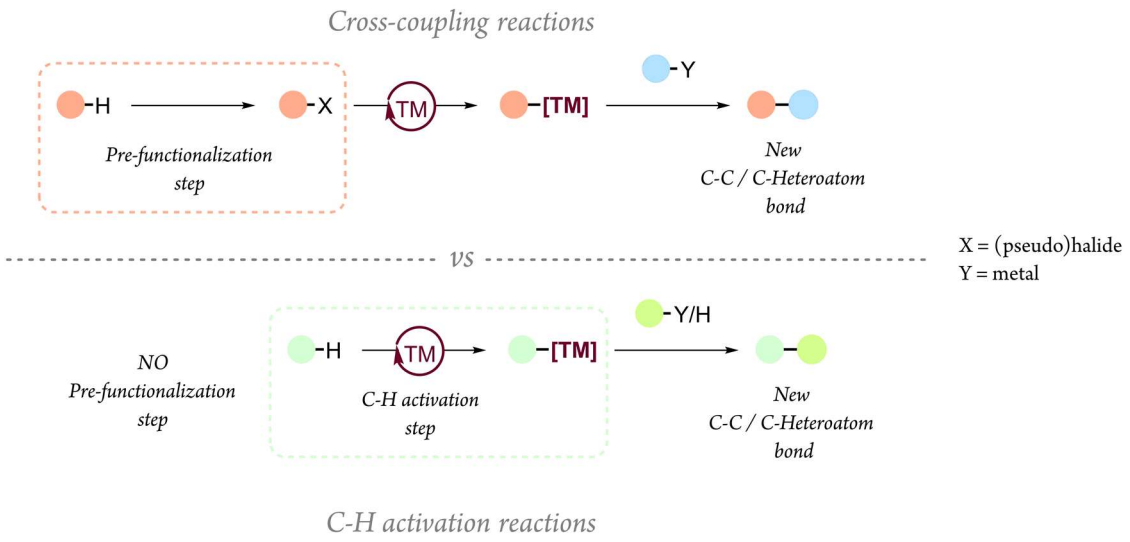

Scheme I.9 Advantages of C-H activation and functionalization reactions in comparison with cross-coupling reactions.

Going deeper into the general mechanism of "C-H activation", formally the term *activation* involves the cleavage of the C-H bond by means of a metal center and so the formation of an organometallic species (metal-C bond), which can be further functionalized by another coupling partner/reagent to release the final organic product. In other words, the concept of *C-H Activation* implies the interaction of the substrate's C-H bond directly with the metal-reagent or catalyst.[74] In this *organometallic approach*, the metal-carbon intermediate is formed, after the C-H bond cleavage, through an inner-sphere mechanism. On the contrary, the outer-sphere mechanism or *coordination chemistry approach* consists in high-valent metals with activated ligands (X = oxo, carbene, nitrene, imido …), and these activated ligands are the ones which will interact with the C-H bond either via radicals pathways (hydrogen atom abstraction) or direct insertion (Scheme I.10).[75-77]

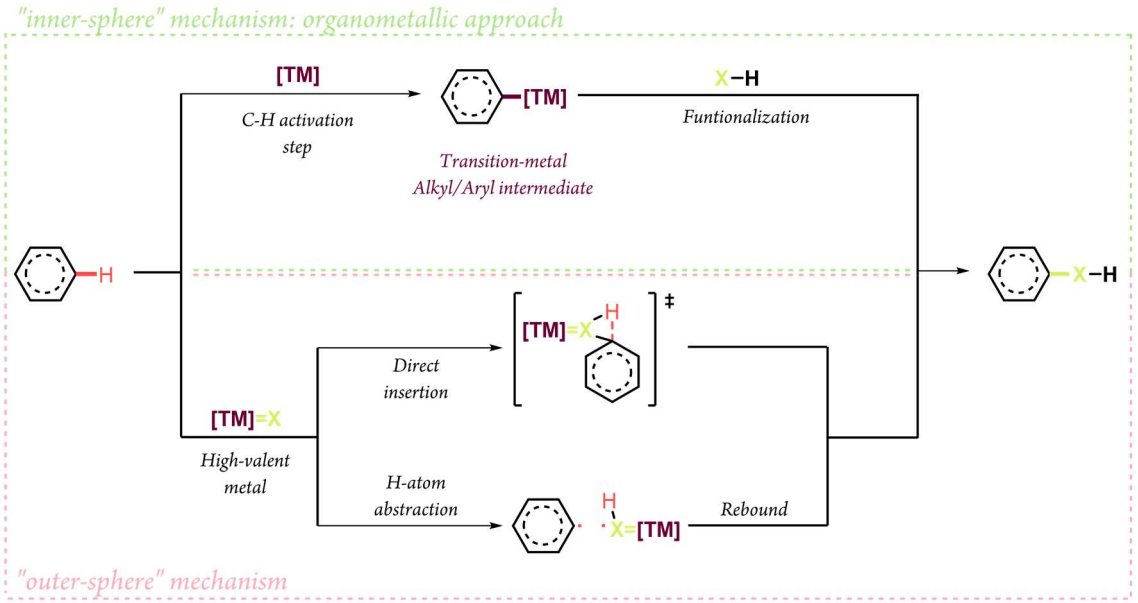

Scheme I.10 Inner sphere mechanism (top) and outer sphere mechanism (bottom) for C-H functionalization transformations.

Over the past decades, important breakthroughs have been accomplished in the field and nowadays different C-H activation protocols have been put forward. However, similarly to the cross-coupling reaction, these were mostly based on scarce precious metals.

I.4.2 Drawbacks and alternatives

In spite of the extraordinary results obtained with palladium systems and other precious metals for both C-H activation and cross-coupling reactions, several disadvantages began to arise, such as the high costs and toxicity related to the employment and removal of these second-row transition-metal based catalysts. From this need, several new procedures have evolved for the substitution of palladium-based systems by other more sustainable and less expensive first-row transition metals, which have proved efficiently successful for these types of transformations.[4, 78-81] For instance, the natural abundance of first-row transition metals is approximately 32% for Fe, 0.88% for Co, 1.8% for Ni and 0.31% for Cu.[4] Consequently, the organic chemists' community shifted its attention to the use of earth-abundant first-row transition metals such as the ones mentioned above, as they have lower toxicity and are less expensive.[82]

In this thesis, we focus our attention on catalysts based on iron and nickel, which will be explained in more detail in sections I.4.3 and I.4.4, respectively.

I.4.3 Iron-mediated cross-coupling and C-H activation reactions

Iron is considered one of the most relevant metals in nature as it is the most abundant transition metal in the earth's crust, it is cheap and non-toxic. Moreover, iron is tightly related to the life of many living systems and its versatility is unique as demonstrated by the presence of this metal in the active center of a wide variety of metalloenzymes. In this line, iron complexes have huge potential for their application in homogeneous organic transformations due to its various reachable oxidation states and high availability.[72]

The study of iron is one of the oldest fields in chemistry, and the development of organic chemistry mediated by iron has never been ceased due to its advances and relevance. Two fields in which the development of iron catalysis is now fundamental are cross-coupling reactions and C-H activation reactions.[83]

I.4.3.1 Iron-mediated cross-coupling chemistry

Prof. Jay Kochi, considered one of the pioneers in the field of iron-based cross-coupling transformations, proved in the seventies that naked ferric salts could catalyze the formation of C-C bonds between alkenyl halides and Grignard reagents in a stereoselective manner (Scheme I.11).[84-86] Although these pioneer works demonstrated huge potential for further development, iron catalysis was kept in the shadow of late transition metals cross-coupling for decades, as the latter were easier to handle (bench-stable catalysis).

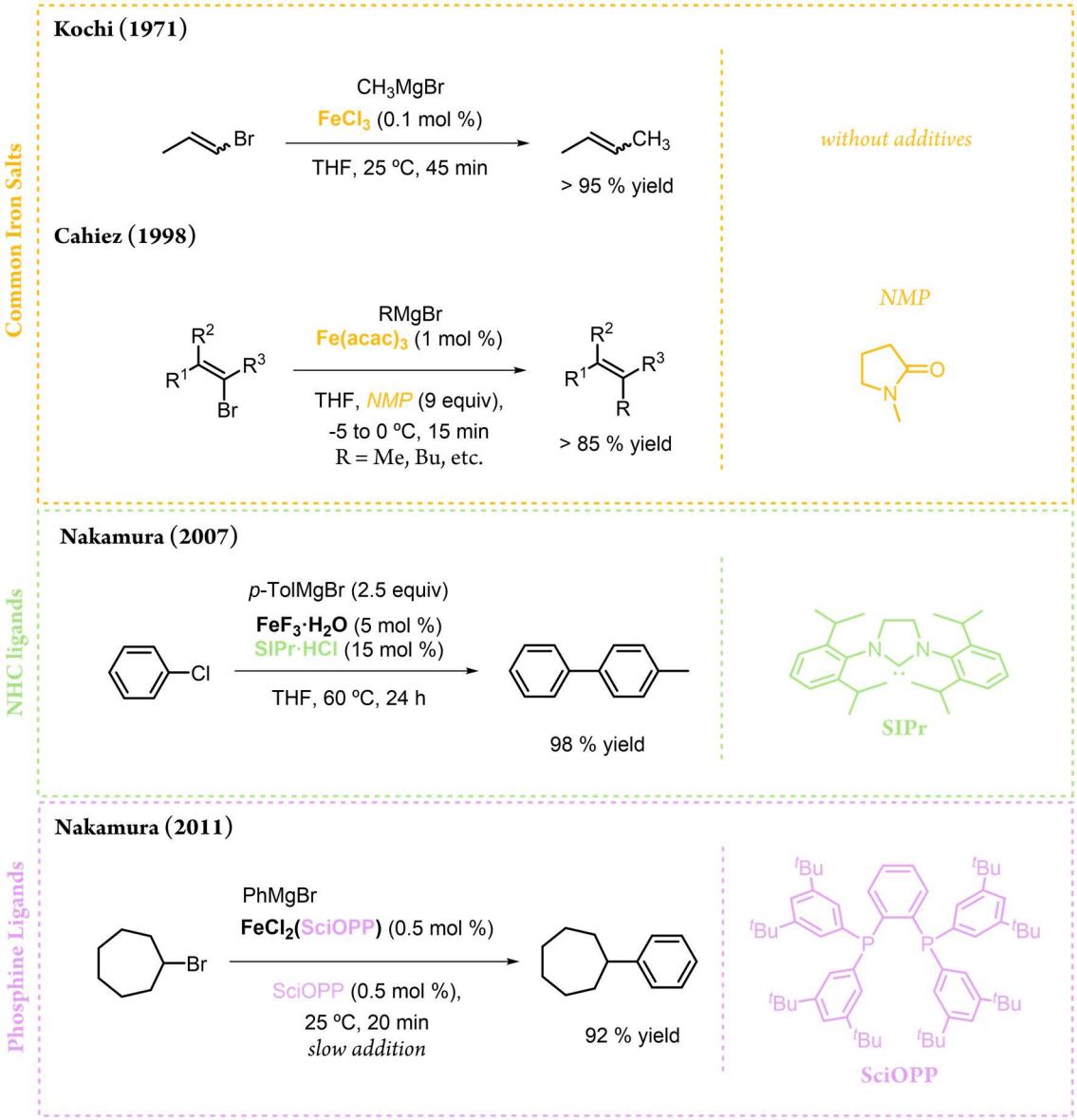

Scheme I.11 Selected examples of iron-catalysed cross-coupling reactions using naked iron salts, additives, NHC or phosphine ligands.

There are many methodological studies on iron-catalyzed cross-coupling reactions. The metal center can consist of iron-naked salts[84-87] to metal complexes in which elaborated ligands (such

as bisamine,[88-90] N-heterocyclic carbene[91-95] and bisphosphine[96-102] ligands) and additives[103] were used (Scheme I.11). However, there is a lack of mechanistic studies and most reported mechanisms rely on hypothesis based on transient data, such as spectroscopy, while characterization of intermediates has been rather scarce.[104, 105]

I.4.3.2 Iron-mediated C-H activation

At present, the field of iron-mediated C-H activation is very extensive, and there is a plethora of methodological studies. A full review of the field is beyond the scope of the present thesis introduction, and therefore this section will be focused only in the arylation of arenes with organometallic reagents, as this is the reaction that is covered in Chapter V of this thesis.

The field of C-H activation has seen important advances with the use of iron catalysts. In 2008, Nakamura and co-workers reported the first iron-catalysed C-H activation. In this seminal work, the authors achieved the *ortho*-arylation of α-benzoquinoline using phenylzinc reagents generated *in situ* from phenyl Grignard reagents together with $ZnCl_2$ in the presence of 1,10-phenantroline as ligand and 1,2-dichloroisobutane (DCIB) as the optimal oxidant (Scheme I.12). In the following years the scope of the reaction was expanded by using different aryl-zinc reagents and different substrates.[106, 107] Afterwards, the methodology was improved in terms of sustainability, by substitution of the expensive organodichloride-type oxidant, by a most desirable oxidant such as molecular oxygen.[108] Nowadays a wide range of protocols have been reported involving different substrates and organometallic coupling partners.[109-115]

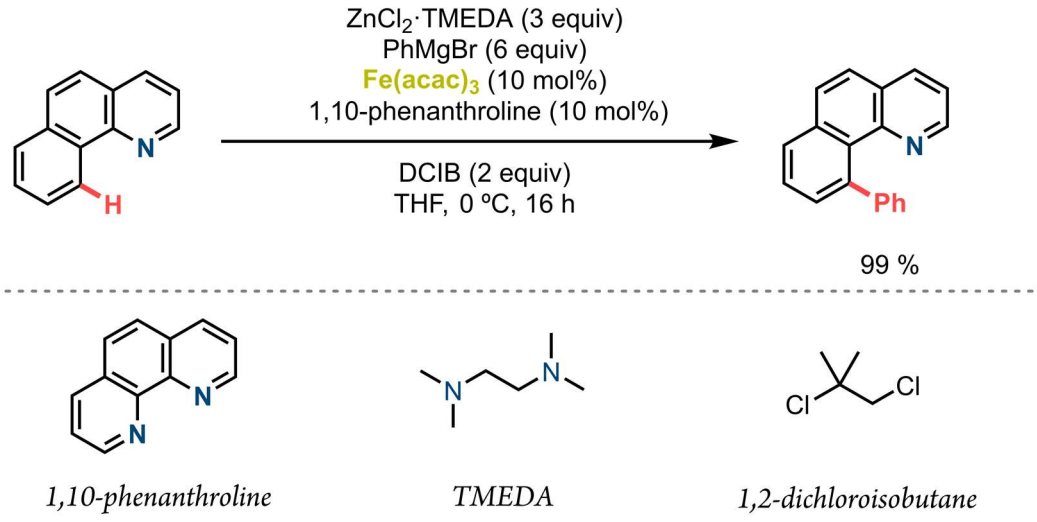

Scheme I.12 Iron-catalysed arylation of α-benzoquinoline with phenyl Grignard reagent and DCIB as oxidant reported by Nakamura and co-workers in 2008.

Remarkably, from the perspective of mechanistic proposals, in 2011, a new methodology was described by Nakamura's group that allowed the use of Grignard reagents directly as coupling partners (slowly added and at low temperature), without the need for the *in situ* generation of the organozinc reagent.[116] In order to get deeper insight into the mechanism of this iron-catalyzed C-H activation and functionalization, the authors of this work conducted several mechanistic studies which allowed them to propose a four-step catalytic cycle: (i) reversible N-coordination of the pyridyl moiety (substrate) to the previously generated aryliron species; (ii) irreversible ferracycle formation by *ortho*-C-H bond cleavage together with arene elimination; (iii) oxidation of the ferracycle with DCIB to trigger the reductive elimination step and release of the final coupling product; and (iv) regeneration of the active catalytic species via transmetallation of the previously formed dichloroiron species with aryl Grignard reagent. To further support the experimental mechanistic studies and elucidate the reaction mechanism, Chen and co-workers performed theoretical calculations, which uncovered a two-state reactivity (TSR, very briefly explained in section I.4.3.3) of the organoiron species to cleave the C-H bond.[117]

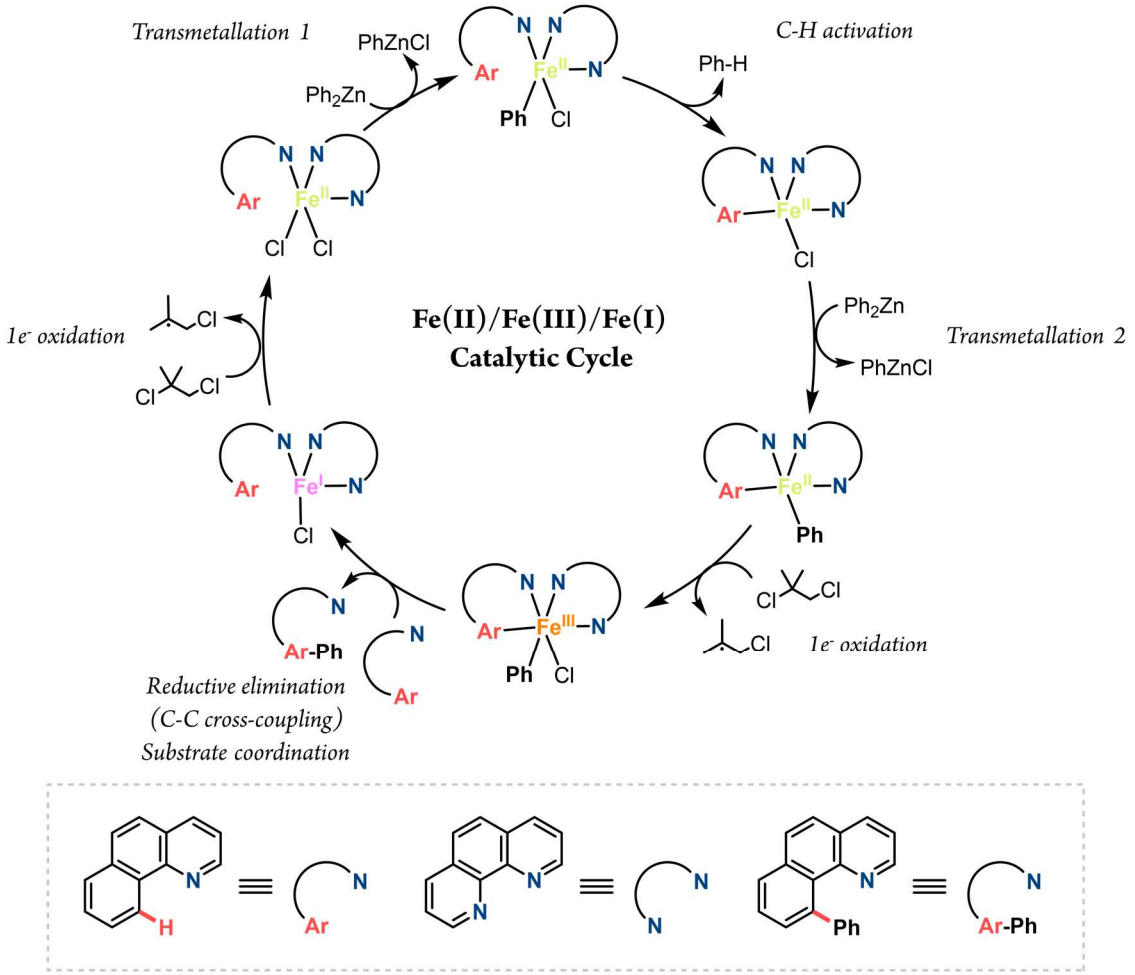

Scheme I.13 Schematic representation of the proposed mechanism via Fe(II)/Fe(III)/Fe(I) for C-H activation/C-C cross-coupling reactions.

These results led to the conclusion that organoiron can effectively perform C-H activation via deprotonation if the metal is in +2 or +3 oxidation state. However, when the organoiron is in 0 or +1 oxidation state it is less likely to promote the cleavage of the C-H bond through an oxidative addition as they react reversibly with arene C-H bonds and with dihydrogen.[118-120] Based on that, generally the mechanism can proceed either via Fe(II)/Fe(III)/Fe(I) (Scheme I.13) or Fe(III)/Fe(I) (Scheme I.14) catalytic cycles.

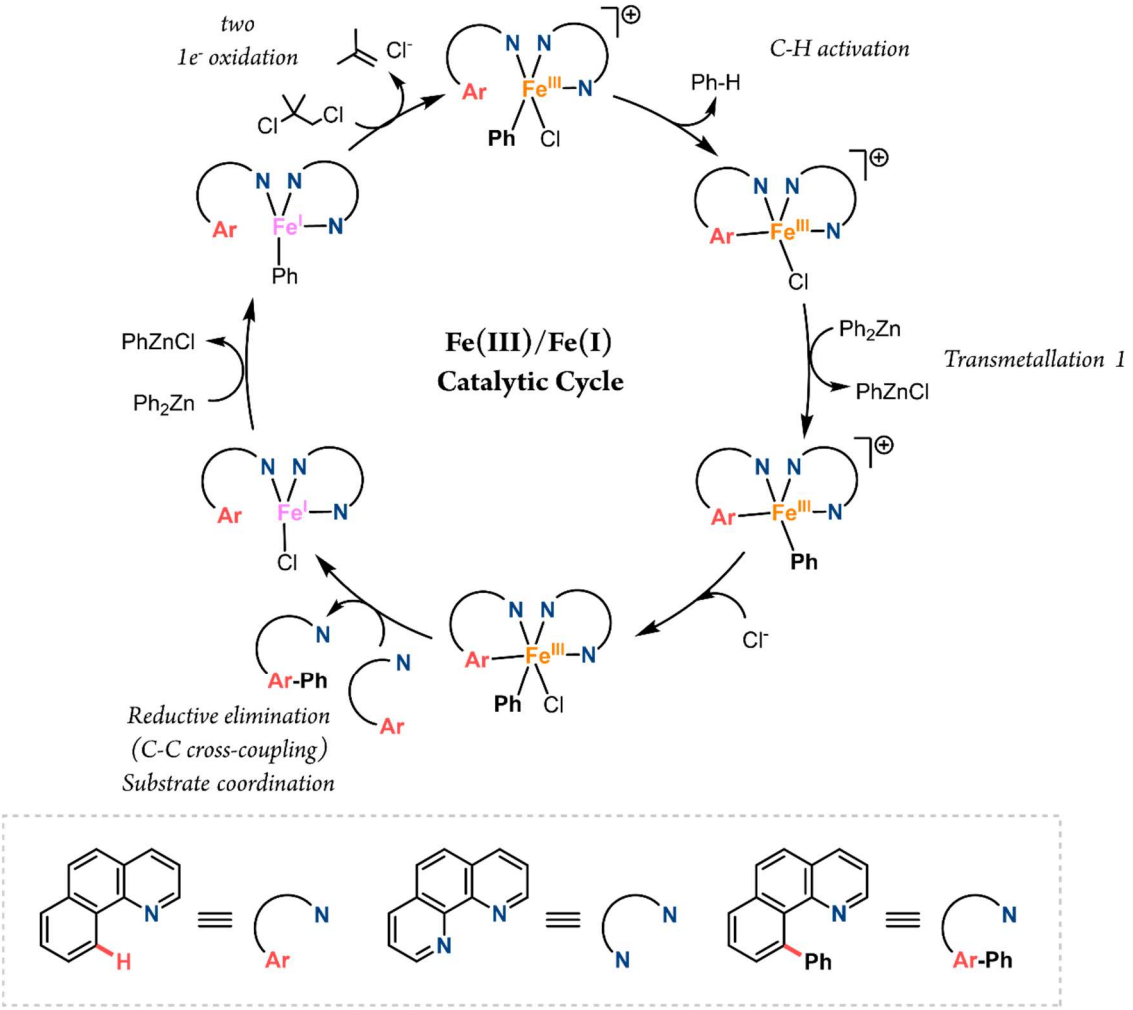

Scheme I.14 Schematic representation of the proposed mechanism via Fe(III)/Fe(I) for C-H activation / C-C cross-coupling reactions.

Interestingly in terms of sustainability, in 2019 the group of Ackermann described a "greener" approach under mild conditions and a DCIB-free procedure in which the reductive elimination step was electrochemically induced (Scheme I.15).[121] Thus, this work states for the first example of environmentally friendly electrochemical iron-catalyzed C-H activation.

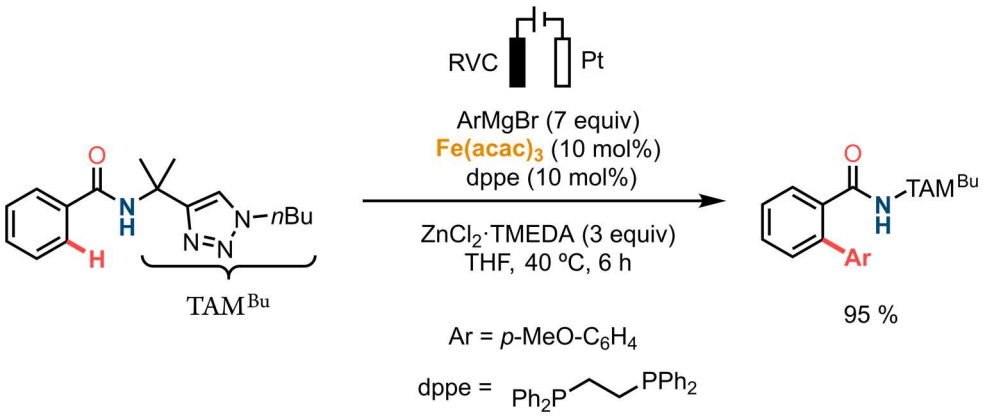

Scheme I.15 First example of iron-electro-catalysed C-H arylation under mild conditions.

I.4.3.3 Mechanistic understanding

As described above, iron-based cross-coupling reactions and C-H activation have attracted considerable research interest due to the major advantages in comparison with noble-metal cross-coupling transformations. Even though these methodologic studies have proven successful in terms of efficiency for these transformations, the underlying mechanisms and the structures of the key active species have remained elusive and scarcely described.[83]

The absence of such insight is ascribed to the struggles found when studying iron-mediated reactions. Application of conventional characterization techniques such as nuclear magnetic resonance (NMR) spectroscopy is not plausible due to the large number of paramagnetic species that are formed *in situ*.[122] Indirect physical-organic probes, including kinetic studies, radical-clock trials and deuterium labeling experiments constitute the main source of information to get a deeper understanding of the fundamental mechanisms of many of these transformations.[83] Yet, an in-depth knowledge of the systems is restricted due to the lack of direct evidence of *in situ* generated iron species.[123, 124]

In order to address these limitations, different strategies are required compared to those employed to investigate the mechanisms and speciation of C-H activation and cross-coupling transformations catalyzed by noble metals. For example, in comparison with palladium-based cross-couplings, iron-mediated cross-couplings can occur within a wider range of redox couples (*i.e.,* Fe(I)/Fe(III),[85] Fe(0)/Fe(II),[89] Fe(-II)/Fe(0),[124] and Fe(II)/Fe(III)[125]) (Scheme I.16).[124, 126]

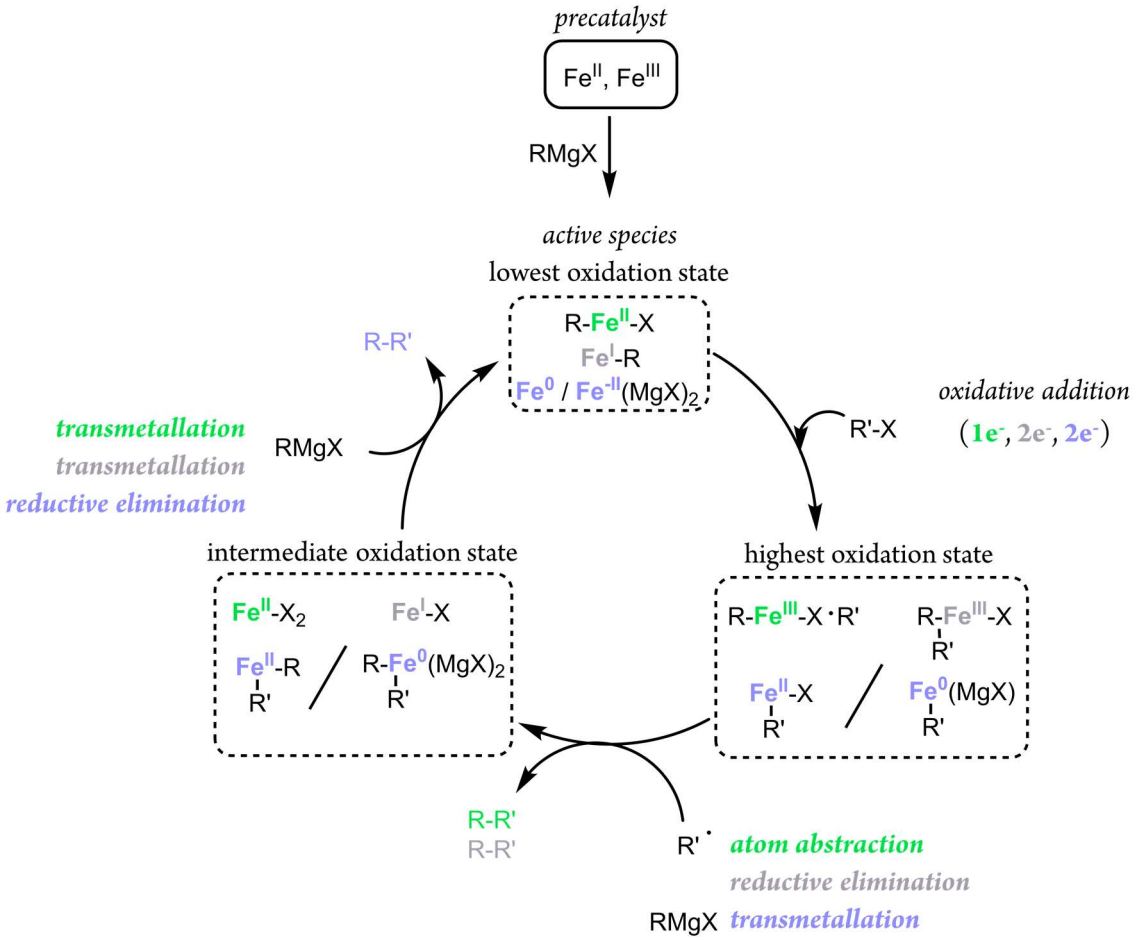

Scheme I.16 General scheme for iron-mediated cross-coupling catalytic cycles based on the redox couples involved: Fe(I)/Fe(III), Fe(0)/Fe(II), Fe(-II)/Fe(0), and Fe(II)/Fe(III).

Due to the numerous oxidation and spin states that iron can adopt in these transformations, a generalized mechanism has not certainly been proposed. Moreover, in the case of iron it is known that different spin states of a given intermediate can coexist and undergo different reactivity. These spin state changes on the iron intermediates can happen due conformational alterations (geometry, ligands, oxidation state…) during the reaction course and are known as the *Two-State Reactivity* (TSR). Very briefly, the TSR is considered when a given spin state change on a given transition state lowers the energy barrier from one intermediate to the next one (Figure I.5).[127-129]

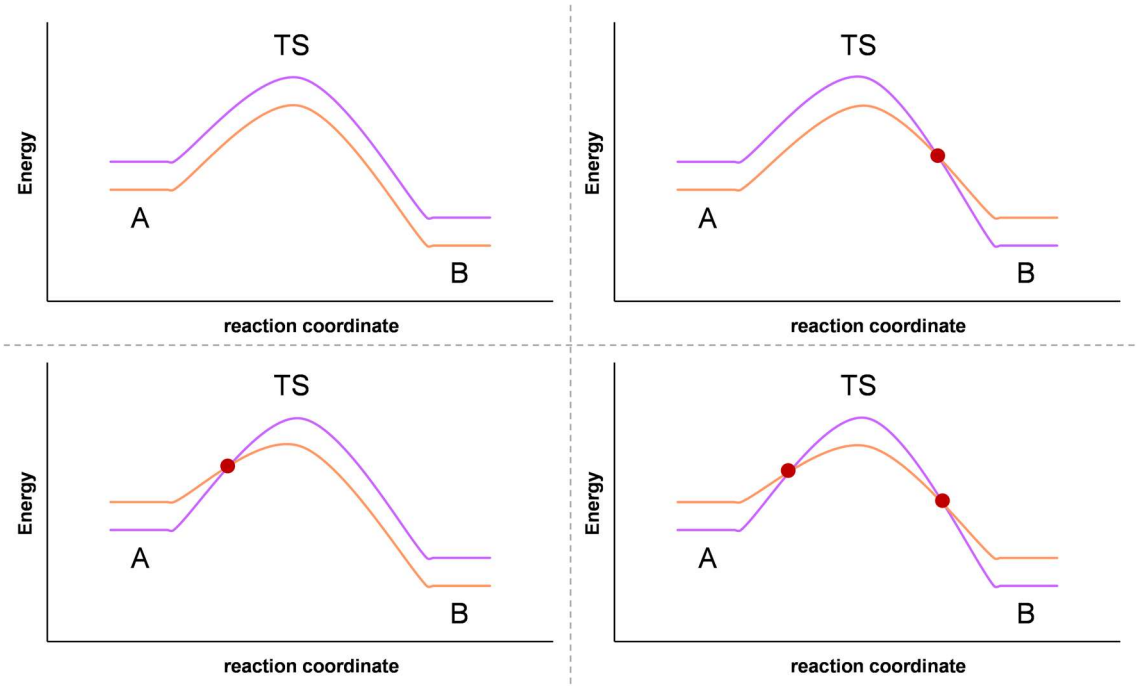

Figure I.5 Different spin-state scenarios possible for the reaction coordinates given by the TSR affording smaller activation barriers. The purple and orange curves represent different spin states, and the red dots represent spin inversions.

As mentioned above, the generation of paramagnetic iron species not only challenges the reaction monitoring by NMR spectroscopy, but it also precludes a precise quantification. In addition, most commonly these reactive organoiron species are very sensitive to air, moisture and temperature, so that they are difficult to handle, and strict control of reaction conditions and parameters is required.

In order to address all these complications, physical-inorganic spectroscopic methods, such as ^{57}Fe Mössbauer spectroscopy, electron paramagnetic resonance (EPR) and magnetic circular dichroism (MCD) spectroscopy, in combination with X-ray absorption spectroscopy (XAS), have been successfully utilized.[83, 130-134] Moreover, additional techniques such as theoretical calculations together with X-ray diffraction (XRD) have allowed to further elucidate the coordination environment of the iron active species and to get mechanistic insights of the corresponding transformation (Figure I.6).[135-137]

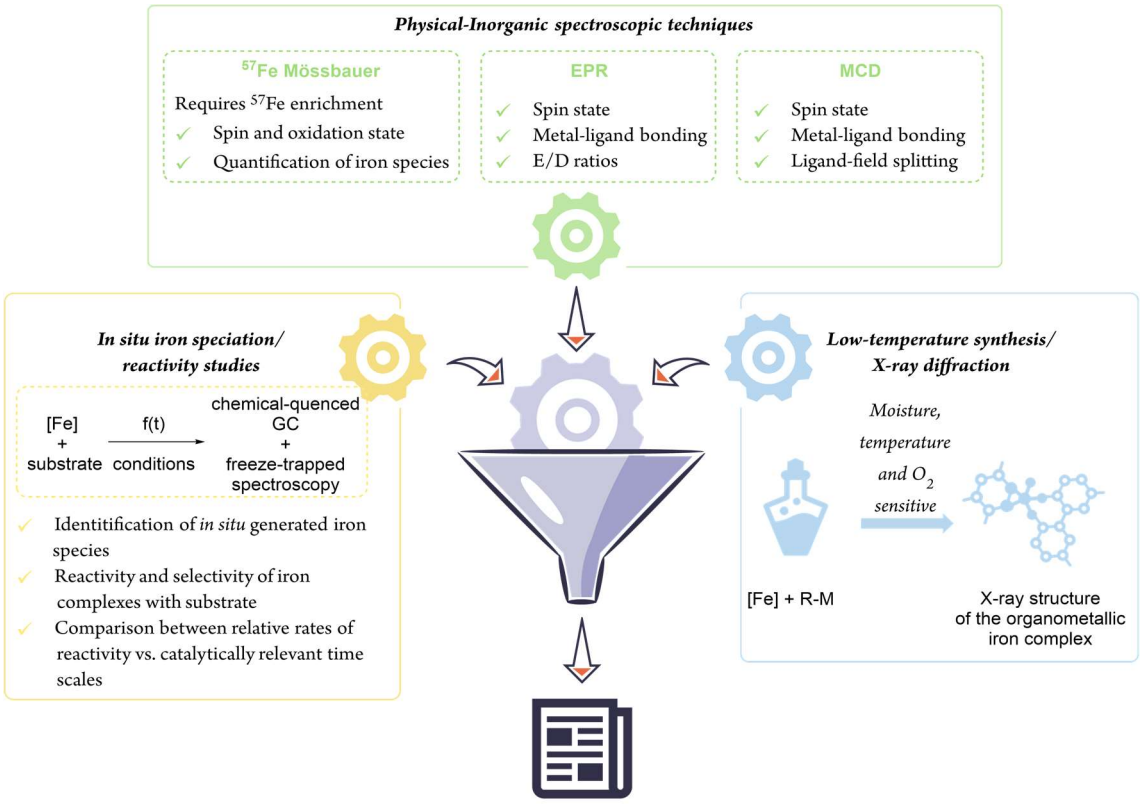

Figure I.6 Representation of the iron-mechanistic toolbox using a combination of physical-inorganic spectroscopies, concurrent iron speciation reactivity studies and low-temperature synthesis of organometallic iron complexes.

In the past decade, relevant advances in gaining insight into the mechanism of these reactions were achieved by trapping key alkyl or aryl organoiron species. A myriad of organoiron complexes have been reported in the literature since the 1960s (see the upcoming sections I.4.3.3.1 and I.4.3.3.2), including those coming from the activation of C-H bonds, and from the activation of C-(pseudo)halide bonds. Still, in the specific case of aryl-iron complexes bearing directing groups attached to the substrate, detection of such ferracycle species has remained elusive for a long time and only limited spectroscopic characterization has been described.

I.4.3.3.1 Organoiron complexes via C-X activation

All cross-coupling reactions start with a C-halogen bond activation, and thus gaining knowledge on how iron-mediated C-X bond activation works is of vital importance in order to develop new iron catalysts. Considerable efforts have been devoted to the characterization of reaction intermediates. However, the process towards the elucidation of the underlying mechanism behind iron-catalyzed cross-coupling reactions has evolved much slower than those of analogous palladium catalyzed reactions. Indeed, while in the latter case the reactions are known

to proceed via net two-electron steps (oxidative-addition / transmetalation / reductive-elimination),[138] iron catalyzed reactions can also proceed via polar and radical pathways.[139, 140] Formation of radical species represents a fundamental problem in experimental mechanistic investigations, as these species are prompt to decomposition and their spectroscopic characterization is significantly more complex than for closed-shell compounds. Furthermore, in some cases in which iron is in the +2 or +3 oxidation state, pre-activation of the catalyst is required by transmetallation with an organometallic reagent and subsequent reductive elimination (homocoupling) to generate the active iron(0) or iron(I) species which can then undergo C-X bond activation.[83, 141-147]

In the case of iron, addition of aryl- or alkyl-halides to reduced iron complexes usually proceeds via a radical halogen-atom abstraction which results in the one-electron oxidized iron complex and the organic radical fragment, thus posing difficulties for a proper characterization of the iron species.[91, 92, 130, 131, 148-152] Therefore, modification of the reaction conditions to favor polar mechanisms has been an enduring challenge in the field, and the synthesis of low valent and reduced iron complexes which enable net two-electron oxidative addition of aryl- and alkyl-halides has become fundamental for enhancing mechanistic insights.[122, 139, 140]

An approach that has proven especially successful is the use of strong-field ligands like CO, which allows for the net two-electron oxidative addition of organic halides to iron.[153-156] In 1988 Zanazzi and co-workers could isolate a series of alkyl and/or η^2-acyl iron(II) iodide complexes bearing CO and phosphine ligands upon reaction of the corresponding iron(0) precursors and alkyl iodides (Scheme I.17).[157] Interestingly, the stability of these species was attributed not only to the use of strong-field ligands, but also to the steric hindrance of the phosphine substituents.

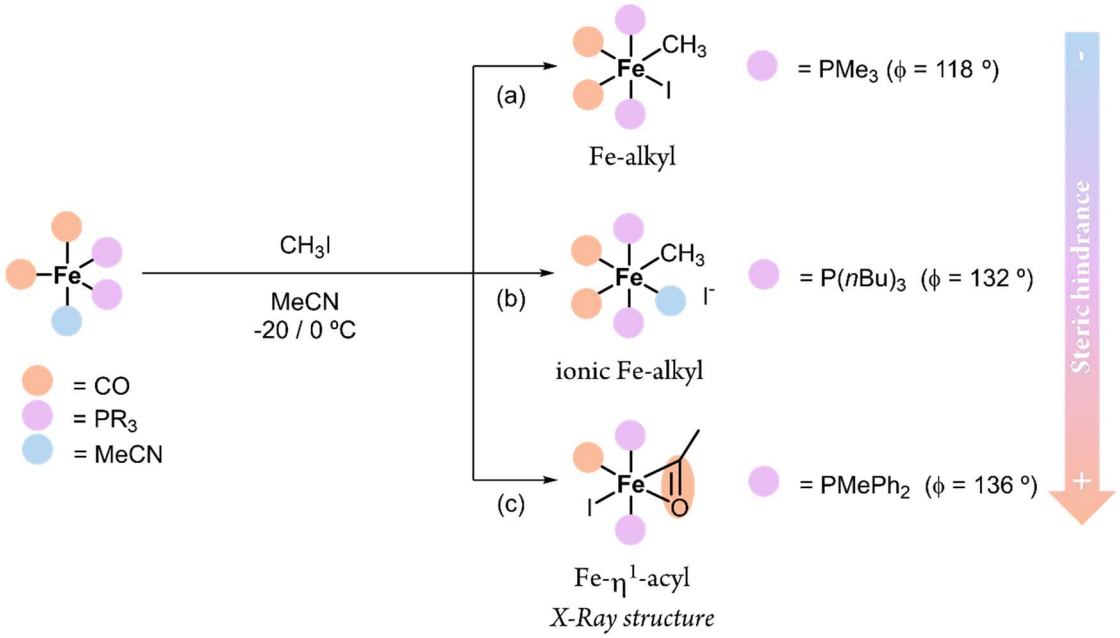

Scheme I.17 Synthesis of a) alkyl-Fe(II), b) ionic alkyl-Fe(II), and c) η^1-acyl-Fe(II) bearing strong-field ligands such as carbon monoxide and phosphines via oxidative addition. Larger cone angles (ϕ) of the phosphine ligands favours the ionic- and acyl-type complexes due to steric effects.

Another strategy that proved successful was the use of specially designed ligands with haloaryl moieties with directing groups (Figure I.7a). In 2009, Sun and co-workers reported the first structures of aryl-iron(II) chloride complexes formed via oxidative addition.[158] In this case, the authors used *ortho*-directing groups to stabilize the intermediates (Figure I.7b). Later in 2010, Nishiyama and co-workers described a similar example of aryl-Fe(II) complex via oxidative addition using an *ortho*-directing substrate and strong field ligands (Figure I.7c).[159]

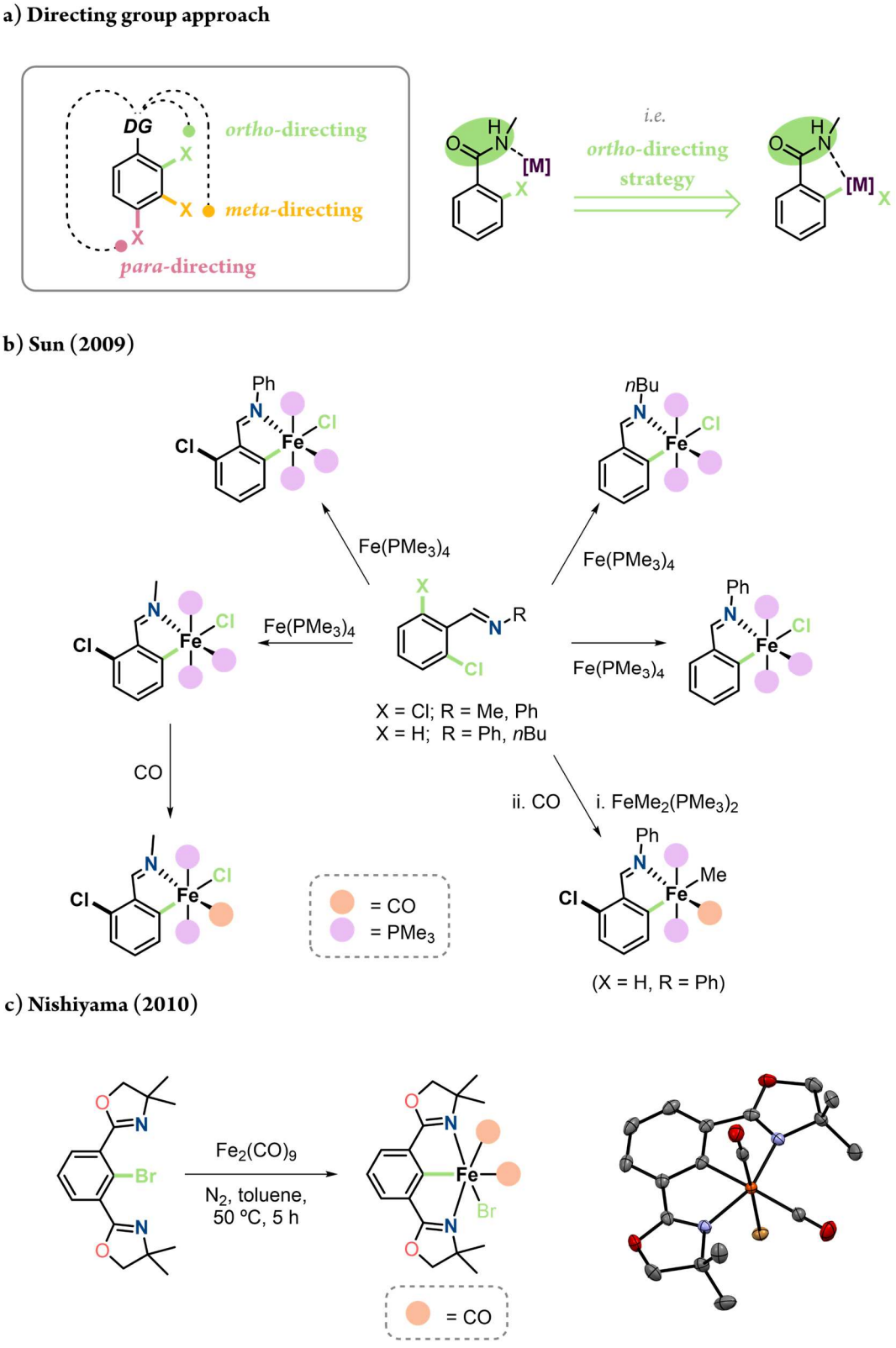

Figure I.7 a) General scheme of the directing group approach for the activation of *ortho*-, *meta*- and *para*-positions of aryl-X groups. Example of an *ortho*-directing group strategy; b) Isolated and XRD characterized aryl-Fe(II) complexes obtained via polar oxidative addition using a phenylimine substrate for the *ortho*-directing group strategy together with strong field ligands such as trimethyl phosphine and carbon monoxide, and c) Isolated and XRD characterized aryl-Fe(II) complexes obtained via polar oxidative addition using a (oxazolinyl)phenyl substrate for the *ortho*-directing group strategy together with carbon monoxide as strong field ligand.

The most recent breakthrough occurred very recently in 2021, when Chirik and co-workers prepared an iron(0) complex bearing an (arylimidazole-2-ylidene)pyridine and dinitrogen ligands capable of undergoing formal two-electron oxidative addition of both aryl- and alkyl-halides (Figure I.8).[160] The resulting organometallic iron(II) halide complexes were successfully isolated. Mechanistic investigations combining competition experiments, radical clock trials and stereochemical probes were also performed. The performance of a net two-electron transformation was attributed to the strong ligand field around the iron center provided by the electrodonating carbene pincer ligand. Nevertheless, experiments with radical clocks and deuterium labeling probes suggested a radical pathway in the case of alkyl halides, even though the resulting iron complexes are very similar to those obtained via two-electron oxidative addition processes.

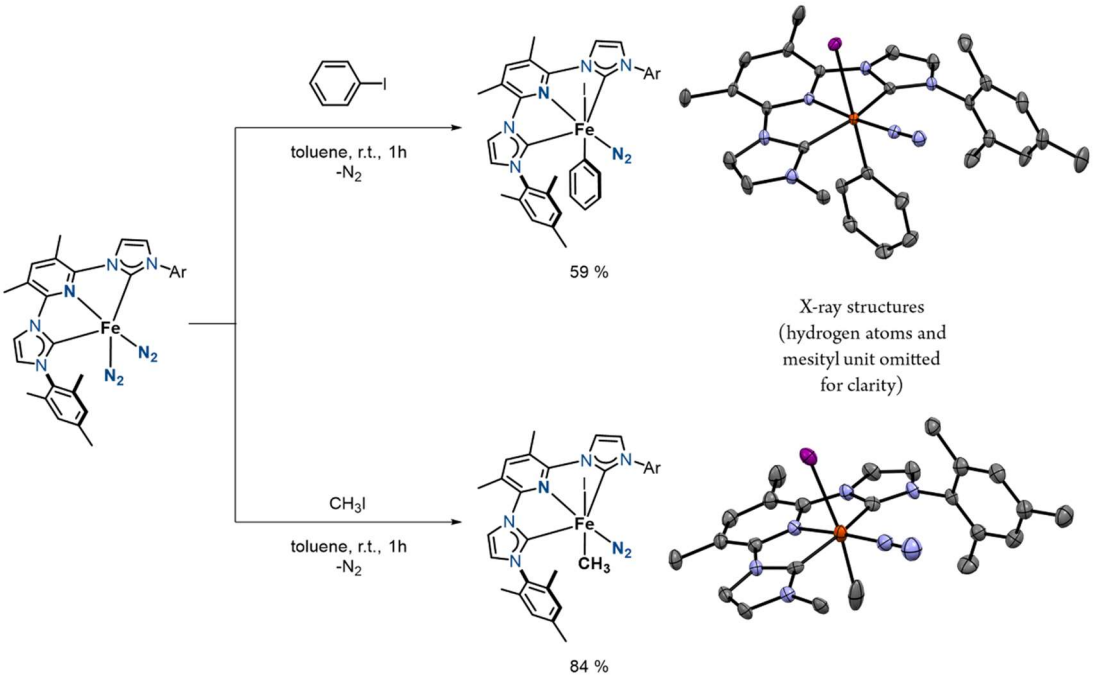

Figure I.8 Isolated and XRD characterized aryl- and alkyl-Fe(II) complexes obtained via oxidative addition of the phenyl and methyl iodide, respectively, towards the corresponding iron(0) precursor using a carbene pincer ligand that provides a strong field ligand environment to stabilize the resulting organometallic iron(II) complexes (Chirik 2021).

Despite the recent achievements, synthesis of iron compounds able to undergo polar reactivity still poses a big challenge. Synthesis of such compounds would not only bring better understanding of the mechanism but would also allow for the development of less expensive and more sustainable iron-catalyzed cross-coupling transformations.

I.4.3.3.2 Aryl-iron intermediates via C-H activation

Generation of low-valent aryl-Fe species from a C-H activation can occur through two different processes depending on the oxidation state of the starting iron complex: (1) oxidative addition at an iron(0) center to yield the corresponding aryl-Fe hydride, or (2) via transmetalation at an iron(II/III) center where the R group is the responsible for removing the hydrogen atom as a proton (σ-bond metathesis or deprotonative metalation, the organic moiety of the organometallic reagent acts as a base).[161] In some cases concerted metalation-deprotonation (CMD) by an iron(II) center has been also proposed (Scheme I.18).[162]

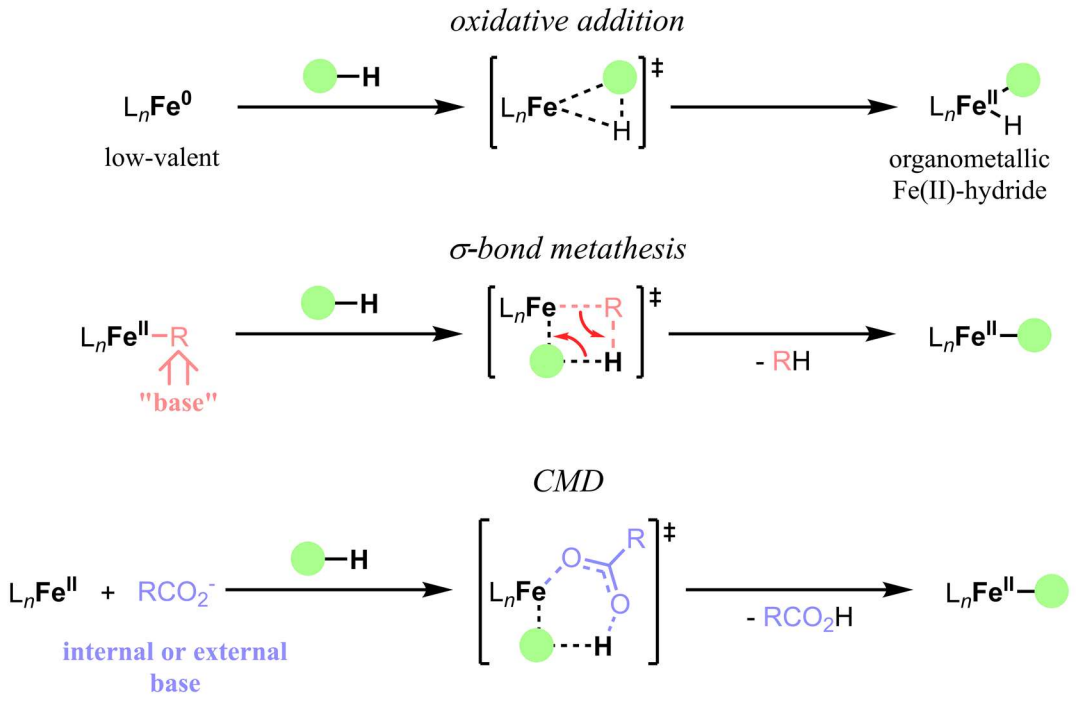

Scheme I.18 Described C-H activation mechanisms mediated by iron: oxidative addition to a low valent iron complex to generate the corresponding organoiron hydride complex, σ-bond metathesis where the organic group (R) of the initial iron complex acts as an internal base to remove the proton, and concerted metalation deprotonation with an internal or an external base to remove the proton.

An early example of an organoiron complex obtained via C-H activation was reported by Hata *et al.* in 1968.[163] UV light irradiation of an ethylene-iron(0) complex bearing 1,2-bis(diphenylphosphino)ethane (dppe) ligands, [Fe(dppe)$_2$·C$_2$H$_4$], results in the generation of a hydride ferracycle complex, with the iron center in the +2 oxidation state, and loss of ethylene gas. This transformation proceeds via an oxidative addition of one of the phenyl hydrogen atoms in *ortho* from the dppe ligand to the iron(0) center (Scheme I.19). Since then, other similar examples of organoiron complexes bearing phosphine/phosphite-based ligands[120, 164-169] or carbonyl ligands[170-177] obtained via oxidative addition have been reported in literature.

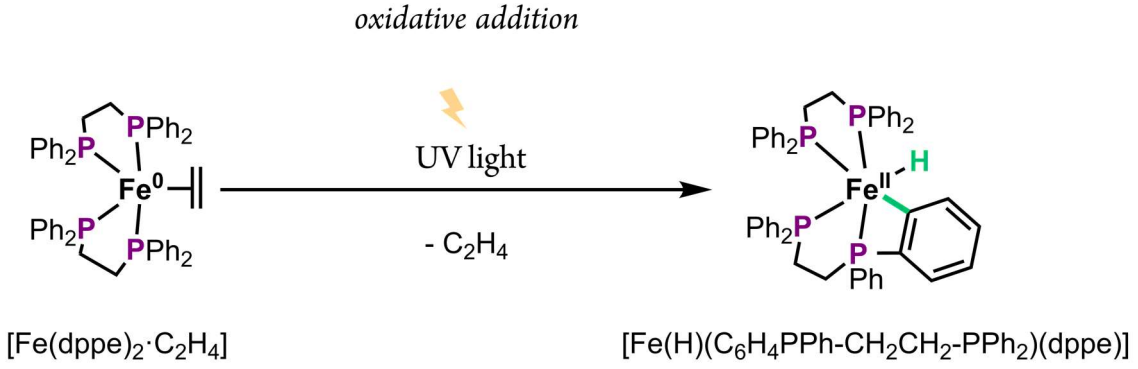

Scheme I.19 Reaction of $[Fe(dppe)_2{\cdot}C_2H_4]$ under UV light to generate the corresponding ferracycle hydride complex by oxidative addition of one of the *ortho*-C-H in the phenyl groups from the dppe ligand.

In 2009 Camandali and co-workers described a work in which a dimethyl-iron(II) complex bearing trimethylphosphine ligands, $FeMe_2(PMe_3)_4$, reacts with benzophenone imine to form an *ortho*-methylated iron(II) hydride complex.[178] In this case, the mechanism of this transformation involves three main steps. Opening, the benzophenone imine substrate coordinates by ligand exchange (decoordination of one trimethylphosphine ligand). Then, *ortho*-ferration via σ-bond metathesis, in which one of the methyl ligands acts as a base to deprotonate the phenyl C-H bond and subsequent release of methane. After that, reductive elimination occurs and a new C-methyl bond is formed and a new iron(0) complex bearing trimethylphosphine ligands, $Fe(PMe_3)_3$. Finally, the new iron(0) complex undergoes oxidative addition to another accessible C-H bond from the previously formed product resulting in an *ortho*-methylated hydride iron(II) ferracycle (Scheme I.20).

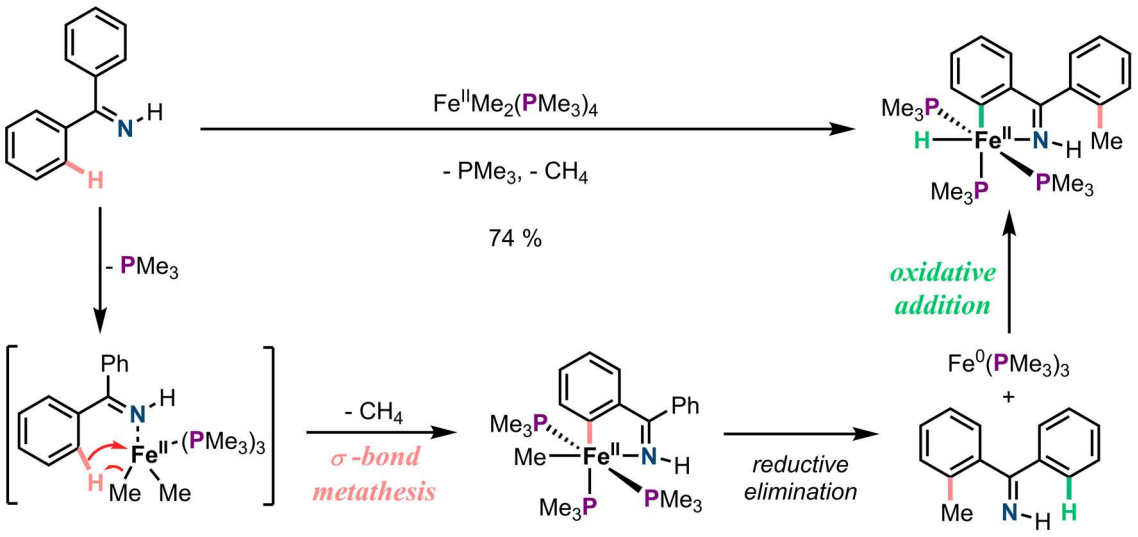

Scheme I.20 Synthesis of an *ortho*-methylated Fe(II) hydride complex via C-H activation involving first a σ-bond metathesis and then an oxidative addition.

The above-mentioned examples correspond to stoichiometric C-H activation processes via organoiron complexes. The first direct empirical evidence of a catalytically relevant organoiron intermediate in C-H activation was not reported until recently by Neidig and Ackermann.[132] Their investigations shed light into the mechanism and structure of key cyclometalated iron species active in triazole-assisted C-H activation and C-arylation transformations, a methodological work previously reported by Ackermann in 2014.[113] To do so, they performed freeze-trapped ^{57}Fe Mössbauer spectroscopy and single-crystal X-ray crystallography together with reactivity studies. They were able to trap the organoiron species formed right after the C-H activation step which was identified as a low-spin iron(II) dimer. Most remarkably, they could also identify the organometallic iron compound formed upon reation with a phenyl Grignard reagent which corresponds to a diamagnetic iron(II)-bisaryl dimer (Figure I.9).

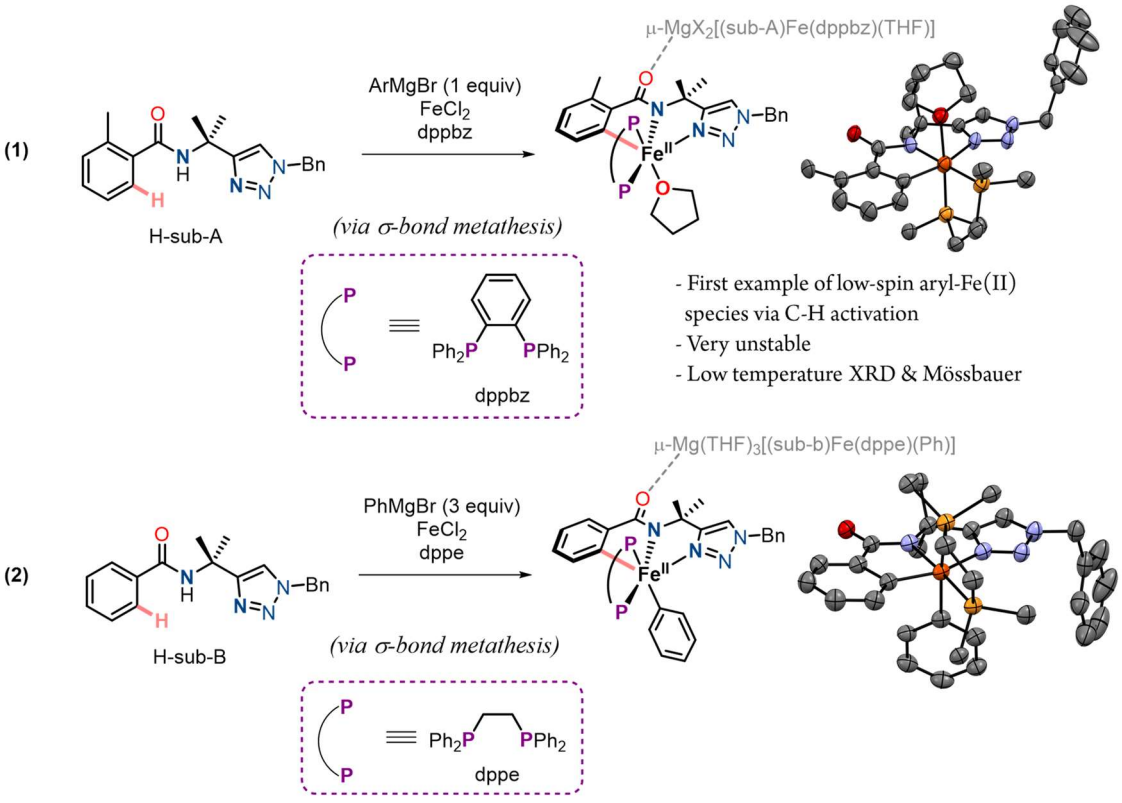

Figure I.9 (1) Synthesis of the aryl-Fe(II) dimer formed right after the C-H activation step using one equivalent of Grignard reagent, and (2) formation of the bisaryl-Fe(II) dimer using three equivalents of Grignard reagent. Hydrogen atoms and some of the carbon atoms from the diphosphine ligands of the X-ray structures have been omitted for clarity.

In 2020, Ackermann and co-workers reported the isolation of an aryl-iron(II)-hydride via oxidative addition of the phenone substrate to an iron(0) precursor, $Fe(PMe_3)_4$, under mild conditions (Figure I.10). In this contribution the Ackermann group studied the hydroarylation

of allenes using phenone substrates. This transformation proceeds with excellent *ortho*-regioselectivity near the carbonyl group.[179]

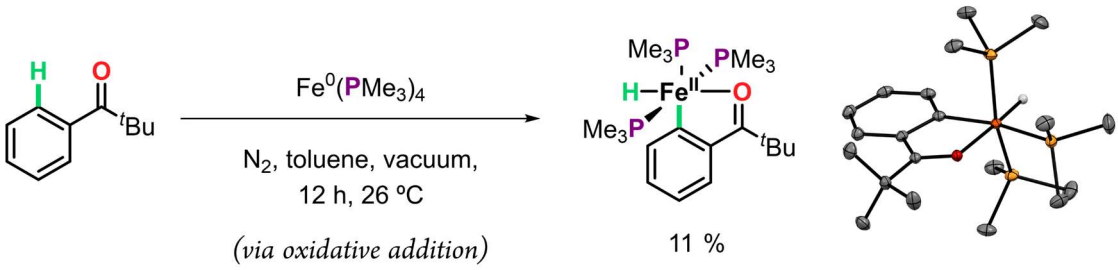

Figure I.10 Synthesis of aryl-Fe(II) hydride complex via oxidative addition to an iron(0) source. All hydrogen atoms (except the Fe-H) have been omitted for clarity.

I.4.4 Nickel-mediated cross-coupling reactions

The use of nickel in organometallic chemistry comes before many other metals as it was isolated in 1751 and Wilke was able to shed light into the structure and reactivity of different nickel complexes, including that of $Ni(COD)_2$ and olefin oligomerization, in 1899.[180] In 1912 the scientist Paul Sabatier was awarded with the Nobel Prize in Chemistry for his groundbreaking work on nickel-mediated ethylene hydrogenation. Then, in the seventies, the use of nickel was expanded to cross-coupling transformations and reactions of alkenes and alkynes (nucleophilic allylation, oligomerization, cycloisomerization and reductive couplings). However, the development of nickel-based protocols was limited by the extensive use of palladium-based catalysts for many years. It was not until the past decade, that the need for the substitution of palladium for a less expensive and more sustainable candidate such as nickel occurred. Since then, nickel chemistry has experienced a period of special interest both academically and industrially. Thus, nickel has become a synthetically important metal that is able to catalyze a broad range of challenging transformations and huge improvements have been made in the area of nickel catalysis over the last decade.[181-184] Nevertheless, nickel catalysis has not made profit from the same exhaustive mechanistic organometallic studies as palladium.[181]

As before stated, the popularity of nickel catalysts is in part attributed to its high natural abundance in the Earth's crust which results in its low cost (roughly 2000 times cheaper than palladium) and high sustainability.[184] In terms of chemical properties, nickel is an attractive metal as in most of the cases it has demonstrated complimentary and/or increased reactivity

when compared to its group 10 counterparts. This can be due to the relative electropositivity of nickel which makes the oxidative addition step more feasible than for Pd and Pt based systems.[184] One example would be cross-coupling reactions that involve the cleavage of C-F bonds,[185-189] tertiary alkyl halides[190-192] and tertiary phenol derivatives[183, 193-196] (Scheme I.21).

a) C-F activation (*Chatani, 2011*)

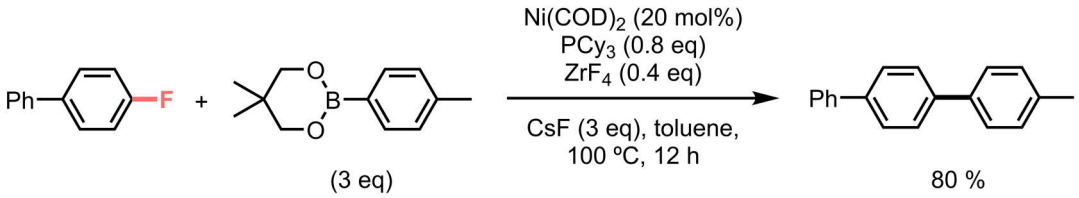

b) Activation of tertiary alkyl halides (*Fu, 2013*)

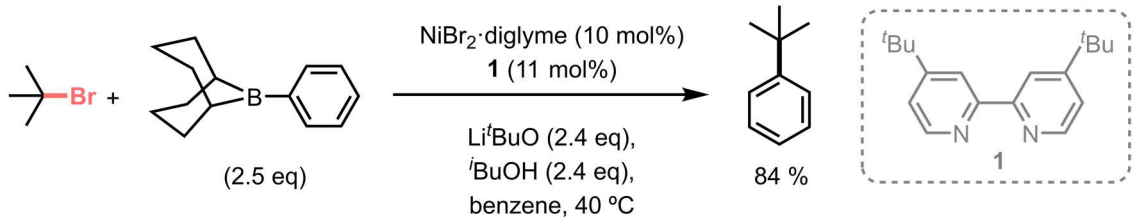

c) Activation of tertiary phenol derivatives (*Dankwardt, 2004*)

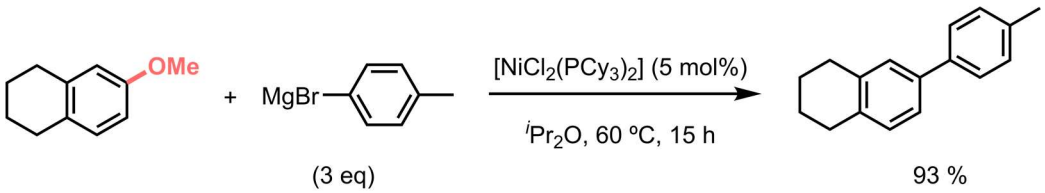

Scheme I.21 Selected examples of Ni-catalyzed cross-coupling reactions of a) C-F bond activation, b) tertiary alkyl halides activation, and c) tertiary phenol derivatives activation.

Another feature that enriches the chemistry performed by nickel is that not only it can perform two electron processes as Pd and Pt (*i.e.,* M(0), M(II) and M(IV) species), but also one electron events, making all nickel oxidation states (*i.e.,* Ni(0), Ni(I), Ni(II), Ni(III) and Ni(IV)) mechanistically accessible.[197] However, this fact also complicates nickel's mechanistic studies due to the formation of paramagnetic species in comparison with the well-known and established processes held by palladium-based catalysts. For this reason, specific key facts of its reactivity, particularly in the higher oxidation states, remain rather obscure. Nevertheless, different mechanistic cycles have been commonly proposed: (i) Ni(0)/Ni(II), (ii) Ni(I)/Ni(II)/Ni(III) or Ni(I)/Ni(III), and more rarely (iii) Ni(II)/Ni(IV) (Scheme I.22).[156, 159]

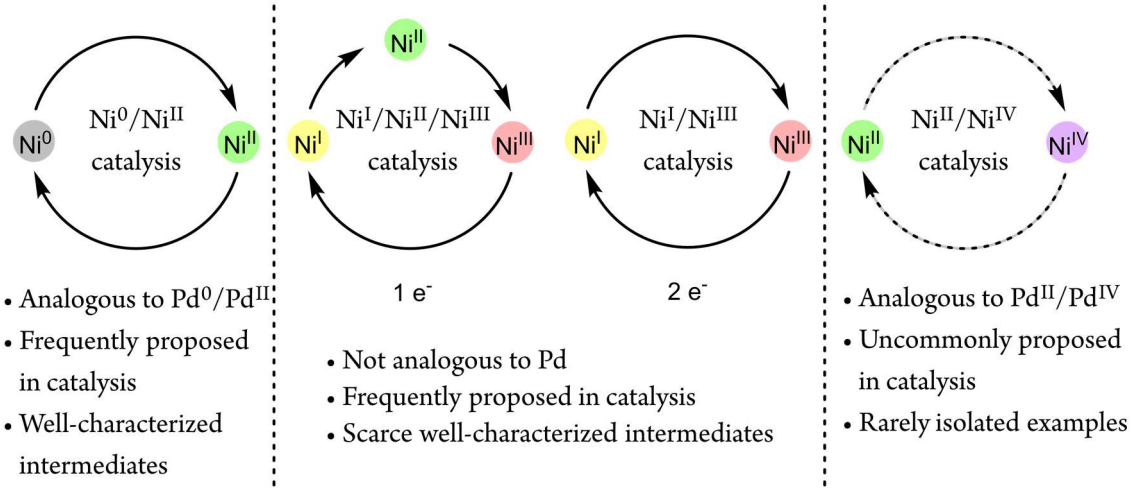

Scheme I.22 Commonly proposed Ni(0)/Ni(II), Ni(I)/Ni(II)/Ni(III) and Ni(I)/Ni(III) catalytic cycles and rarely invoked Ni(II)/Ni(IV) catalytic cycle, and comparison with Pd chemistry.

Even though nickel catalysis has grown significantly over the past decade, challenges for forecasting and controlling the operative mechanistic routes persist. Thereby, conducting systematic studies on organonickel complexes will enable deeper mechanistic understanding and help in the improvement of already existing bond-forming reactions and development of much more difficult new transformations.

I.4.4.1 High-valent organometallic nickel chemistry

It has been mechanistically well-stablished and demonstrated that the lower oxidation states of nickel (Ni(0), Ni(I) and Ni(II)) are catalytic intermediate species in many types of C-C and C-Heteroatom bond-forming transformations.[198-200] Instead, nickel(III)[201-206] and nickel(IV) species[207-214] have not been proposed as catalytic intermediates in nickel-mediated cross-coupling reactions until more recently. These higher oxidation states of nickel can undergo transformations that are not achievable by low-valent nickel species or other metal ions. For this reason, lots of efforts are being devoted in elucidating the underlying reactivity of nickel(III) and nickel(IV) complexes by means of both stoichiometric and catalytic studies.

Nickel(III) species are commonly invoked as catalytically competent intermediates in nickel-mediated cross-coupling transformations, yet studies that support these hypotheses remain scarce. In the late 70s, Kochi reported the first contribution that provided indirect evidence for the involvement of a Ni(III) intermediate species by stoichiometrically studying the oxidative C-C bond formation reaction starting from an organometallic Ni(II) complex (Scheme

I.23a).[198] Later in 1995, Hillhouse and co-workers conducted a similar study but this time through and oxidative C-N bond-forming transformation (Scheme I.23b).[215] Nevertheless, the first organonickel(III) complex was not isolated until 1983 by Van Koten and co-workers. To do so, they used a pincer ligand to stabilize the nickel(III) center (Scheme I.23c).[216] Later in 2009, Sanford's group proved the ability of this species to undergo C-Br reductive elimination (Scheme I.23c).[217]

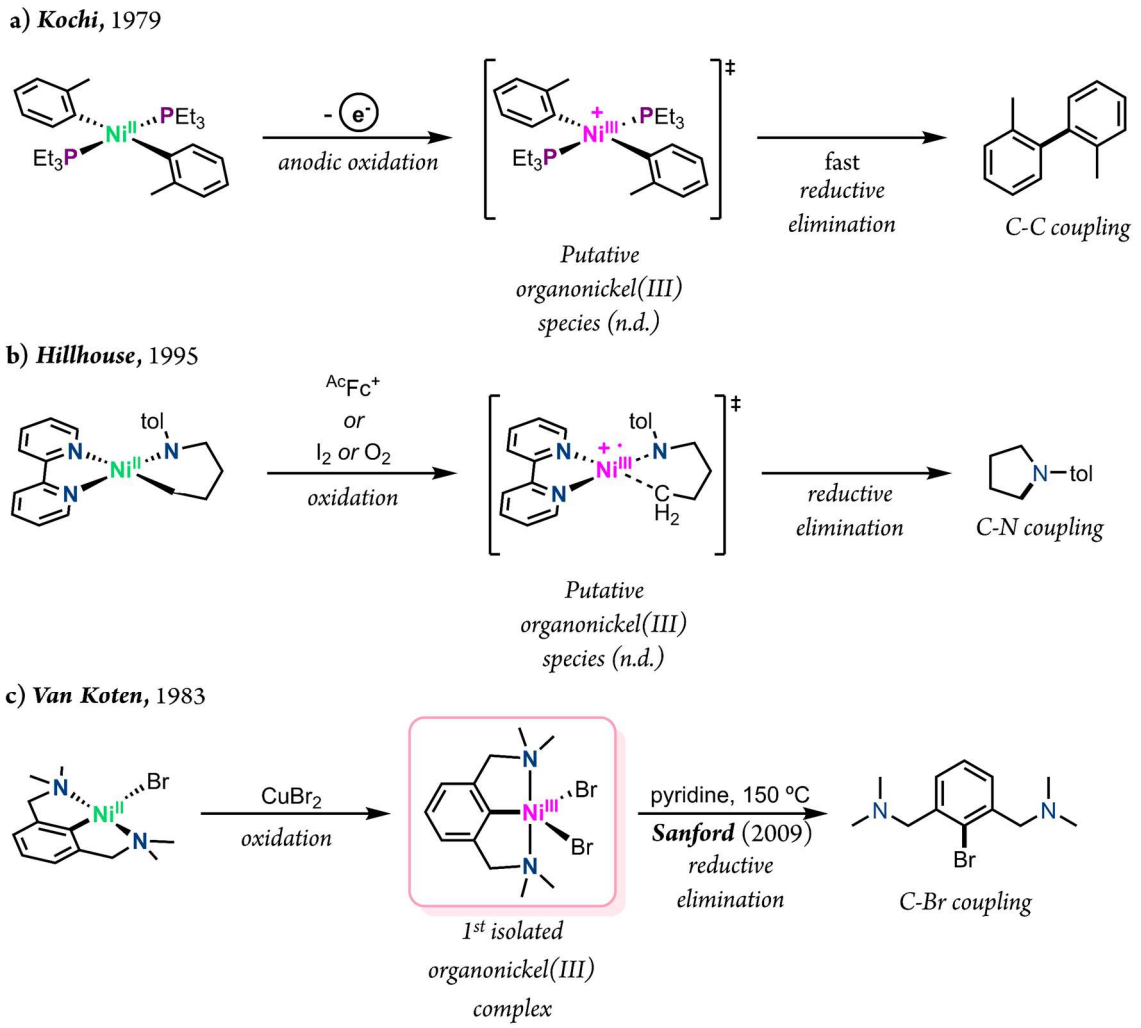

Scheme I.23 a) and b) selected contributions with reactivity on nickel-mediated cross-coupling reactions via proposed organonickel(III) intermediates, in which a 1electron oxidant is added to the Ni(II) precursor which results in the formation of the organic coupling product, thus indicating the putative formation of a Ni(III) intermediate species. c) First isolated organonickel(III) complex and reactivity studies towards C-Br bond-forming reactions.

The above-mentioned contributions were a springboard for the upcoming investigations in the area of organometallic Ni(III) complexes relevant for cross-coupling catalysis. In the past decade, the group of Mirica has been able to isolate several organonickel(III) complexes. For this purpose, they employed tri- and tetradentate N-based macrocyclic ligands to stabilize

nickel(III) centers together with different carbon-donor ligands such as aryl groups, methyl groups and the cycloneophyl ligand (a special cyclic alkyl/aryl carbon-donor ligand with no β-hydrogens which prevents from undesired side reactions such as β-hydride elimination, -CH_2CMe_2-*o*-C_6H_4-). In addition, they performed reactivity studies that demonstrated that these nickel(III) complexes were able to promote C-C and C-Heteroatom bond formation transformations under mild conditions (Figure I.11).[218-221]

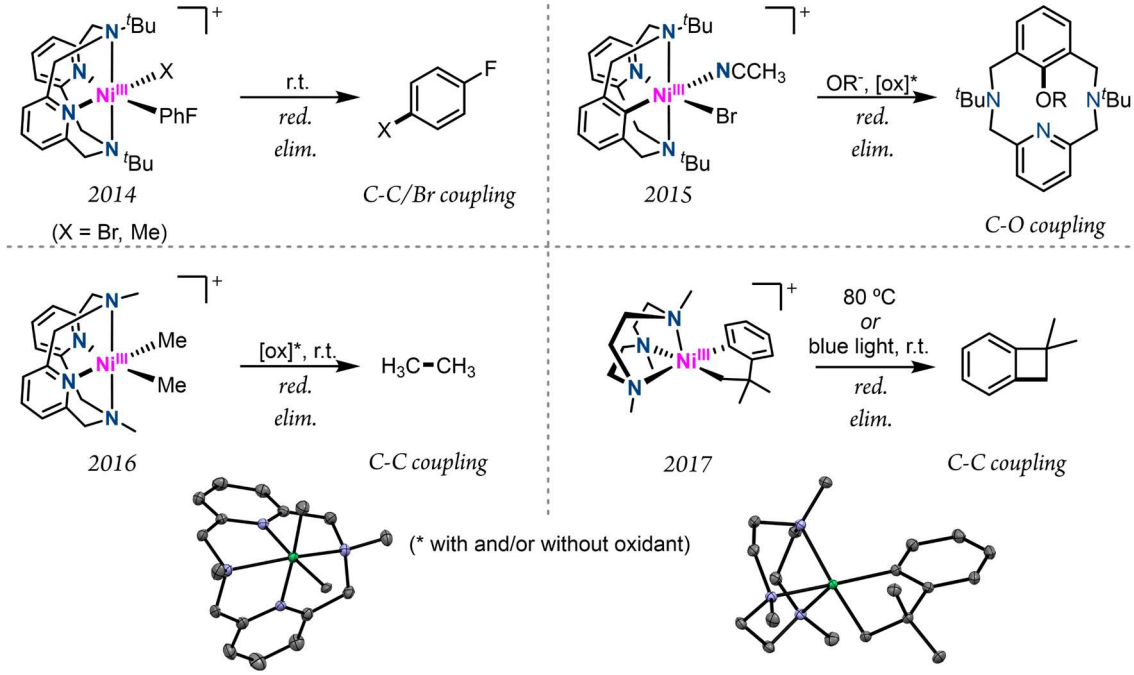

Figure I.11 Examples of recently isolated well-defined organonickel(III) complexes relevant for cross-coupling transformations by the Mirica group.

Sanford and co-workers also provided great contribution in the field by isolating several organonickel(III) complexes bearing a facial tridentate tris(pyrazolyl)borate ligand (Tp) and performing reductive elimination studies relevant for nickel-catalyzed C-C bond forming reactions (Scheme I.24).[222] In all cases, the organonickel(III) complexes thermally decomposed under mild conditions to yield the corresponding C-C coupling product. Moreover, and by means of mechanistic studies, they demonstrated that the final coupling products occurred directly from the nickel(III) species.

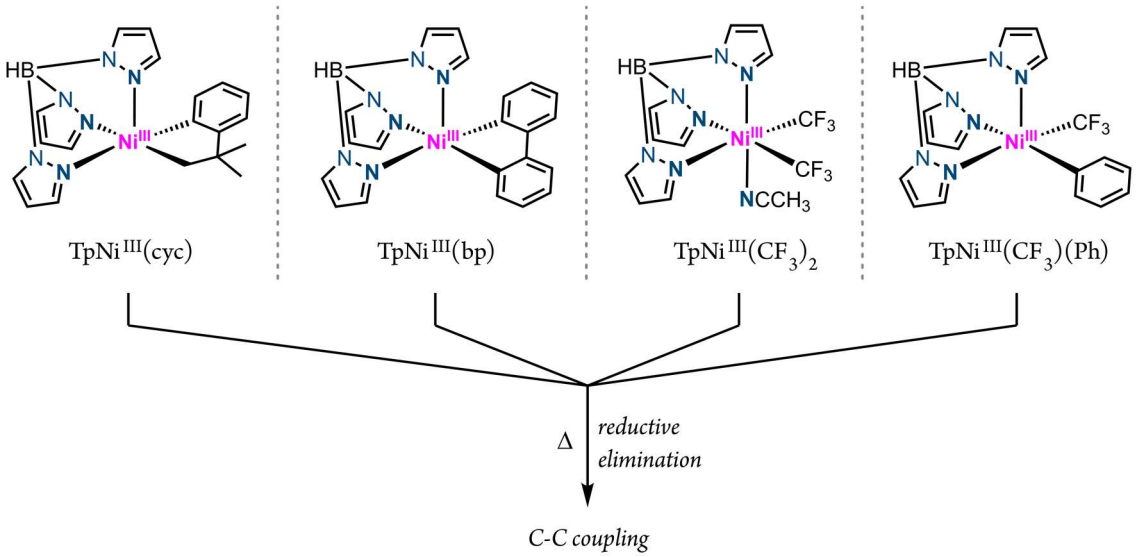

Scheme I.24 Isolated organonickel(III) complexes by Sanford and co-workers and subsequent thermolysis studies yields to C-C bond-forming products by reductive elimination, respectively.

Even though all these seminal works have supplied excellent evidences for the involvement of nickel(III) species in nickel-mediated cross-coupling transformations, much more is yet to be known about this oxidation state.

Oppositely to organometallic nickel(III) species, which has been usually invoked as a catalytically active intermediate for cross-coupling transformations, nickel(IV) is not often proposed and was believed to be inaccessible under usual reaction conditions. Nonetheless, since the recent discovery of the reactivity performed by Pd(IV) and Pt(IV) species a new window was opened to study the related capability of Ni(IV) to promote difficult transformations.[223-226] The first example of isolated organonickel(IV) complex was reported in 1994 by Klein and co-workers, via oxidation of the corresponding Ni(II) precursor with methyl iodide (Scheme I.25).[227] Even though no reactivity studies were performed, this work demonstrated that organonickel(IV) species were accessible and could be investigated employing the appropriate conditions. From then, other examples of organonickel(IV) complexes were isolated by Dimitrov and Nuckolls, using very specific carbon-donor ligands to stabilize the metal center (Scheme I.25).[228, 229] Nevertheless, these ligands did not allow the investigation of catalytically important cross-coupling and bond-forming transformations.

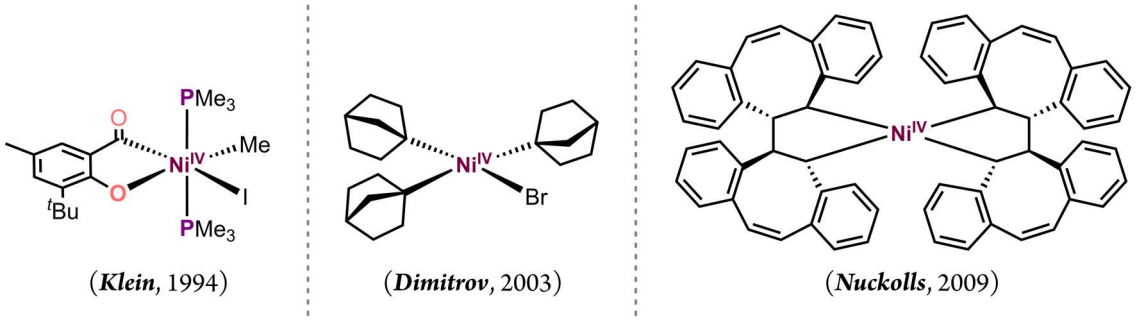

(***Klein***, 1994) (***Dimitrov***, 2003) (***Nuckolls***, 2009)

Scheme I.25 First isolated organonickel(IV) complexes.

It has not been until more recently that organonickel(IV) complexes relevant for cross-coupling reactions have been isolated by using specially designed ligands and selected reaction conditions. In 2015, the group of Sanford reported the isolation of an organonickel(IV) complex bearing a facial tridentate N-based ligand (tris(2-pyridyl)methane, Py_3CH), a trifluoromethyl ligand and a cycloneophyl ligand.[230] To synthesize this organonickel(IV) the corresponding organonickel(II) precursor was oxidized by two electrons with a "CF_3^+" source. Moreover, its reactivity was tested towards exogenous acetate to afford the C-O coupling product, and also upon thermolysis to yield the reductive elimination C-C bond forming product (Figure I.12). This work was a stepping stone to gather all the information needed to isolate a series of organonickel(IV) complexes by changing some variables in a well-designed and controlled manner. In most of the cases they used the Tp ligand together with different stabilizing carbon-donor ligands (biphenylene, cycloneophyl, etc.), trifluoromethyl groups and aryl electrophiles.[231-236] They also performed reductive elimination as well as coupling with exogenous nucleophiles achieving coupling products in good yields. This supports the initial hypotheses that organonickel(IV) complexes are catalytically competent for cross-coupling transformations.

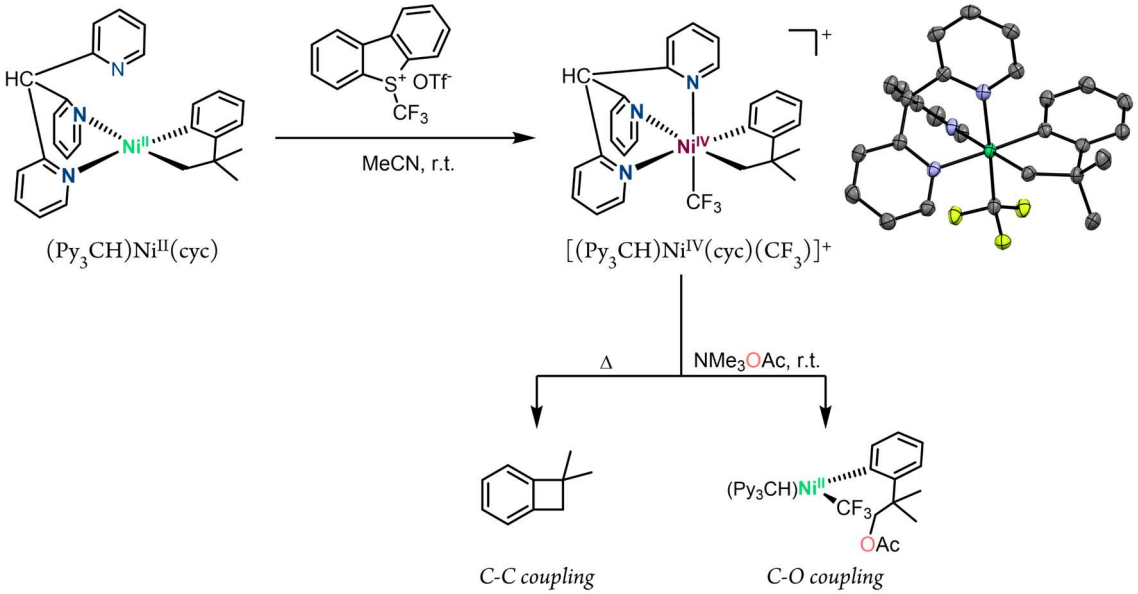

Figure I.12 Synthesis, X-ray structure and reactivity of the organonickel(IV) complex isolated by Sanford and co-workers.

Following this line, the group of Mirica also provided seminal contribution in isolating a well-defined organonickel(IV) complex relevant for cross-coupling transformations. In this case they used a tridentate N-based macrocyclic ligand (N,N,N-trimethyl-triazacyclononane, ^{Me}tacn) to provide a stable environment to the metal center, and cycloneophyl as the bis-carbon-donor ligand.[219] In addition, they performed reactivity studies regarding reductive elimination, C-C, C-O and C-Cl bond forming reactions (Figure I.13).

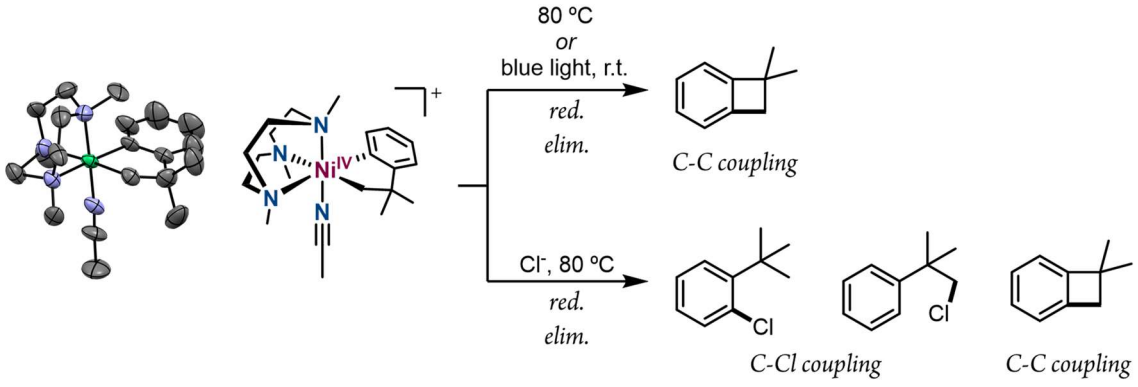

Figure I.13 X-ray structure of the isolated organonickel(IV) complex reported by Mirica and co-workers and reductive elimination reactivity studies upon thermolysis and chlorination, respectively.

I.4.4.1.1 High-valent organonickel complexes via C-H activation

Nickel-mediated C-H activation/functionalization reactions have drawn great attention in the past decade due to the low-cost of Ni-based catalysts and to the many advantages in terms of green chemistry that provides direct C-H functionalization over traditional cross-coupling

transformations. For these reasons, the scientific community has devoted a lot of efforts in developing methodologies for $Csp^{2/3}$-H activation and functionalization transformations mediated by nickel(II) catalysts.[207, 237-239] Nevertheless, there are only scarce examples of $Csp^{2/3}$-H activation/functionalization transformations performed by high-valent nickel complexes analogously to its group 10 high-valent counterparts.

In order to gain insight into the feasibility of this transformation and inspired by the emerging studies on Pd(IV) C-H activation, some fundamental studies have been published on well-defined high-oxidation state organonickel complexes obtained via C-H activation. In 2016, the group of Mirica reported the characterization of an organonickel(III) complex obtained via C-H activation under mild conditions.[240] In order to stabilize the high-valent intermediate species, they used a modified version of their previously used tetradentate N-based pyridinophane ligand by replacing one of the pyridine moieties for an aryl group as a carbon-donor source where the C-H activation will take place following a directing group strategy. They also reported reactivity studies towards aromatic cyanoalkylation of the model substrate through double C-H activation mediated by the organonickel(III) complex (Scheme I.26a).

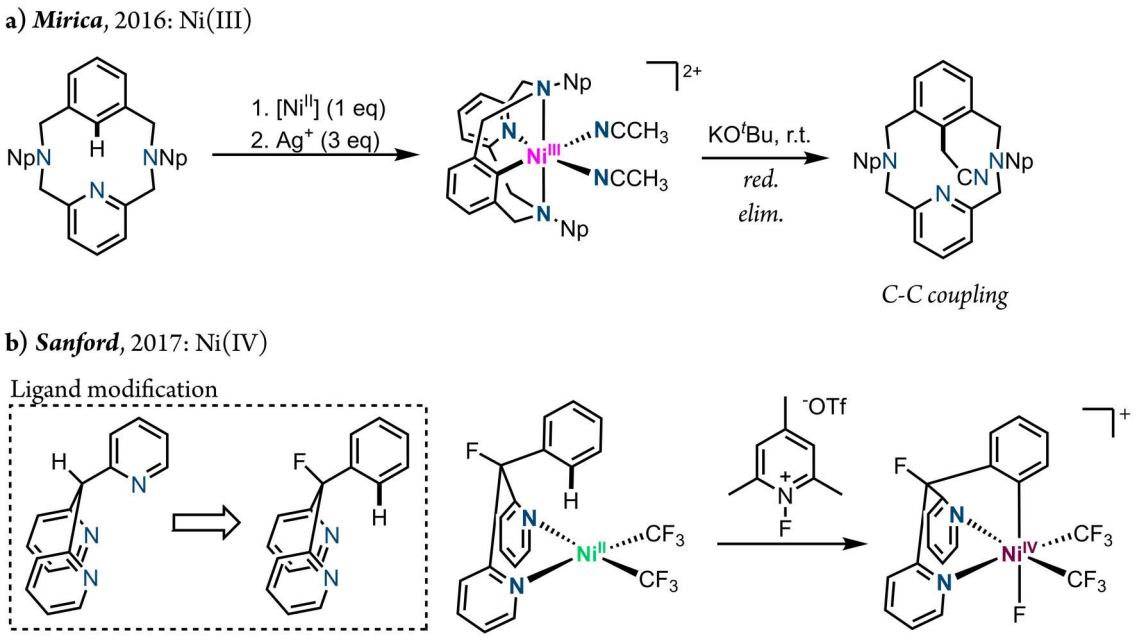

Scheme I.26 a) Isolated organonickel(III) complex obtained via C-H activation and reactivity studies towards cyanoalkylation by Mirica and co-workers, and b) isolated organonickel(IV) complex via C-H activation by Sanford and co-workers.

One year later, Sanford and co-workers reported a well-defined organonickel(IV) complex obtained by C-H activation under mild conditions. In this case, they modified their previously

used Py_3CH ligand by replacing one of the pyridine arms by an aryl moiety in order to promote a directed C-H activation, and trifluoromethyl groups as supporting ligands (Scheme I.26b).[241] Yet, the authors note that with the gathered information and experimental evidences, the involvement of an undetected organonickel(III) intermediate in the C-H cleavage step cannot be discarded based on previously reported literature.

Overall, the knowledge acquired in all these investigations will serve as a trampoline to the discovery of new transformations involving high-valent nickel intermediate species in C-H activation and functionalization transformations such as the ones reported by Sanford in 2019.[234, 242]

I.5 REFERENCES

1. J. Yamaguchi, A. D. Yamaguchi and K. Itami, *Angew. Chem. Int. Ed.*, 2012, **51**, 8960-9009.
2. J. Sommer and J. Bukala, *Acc. Chem. Res.*, 1993, **26**, 370-376.
3. R. H. Crabtree, *The Organometallic Chemistry of the Transition Metals*, Wiley, New York, 7th edn., 2009.
4. B. Su, Z.-C. Cao and Z.-J. Shi, *Acc. Chem. Res.*, 2015, **48**, 886-896.
5. B. M. Trost and L. C. Czabaniuk, *Angew. Chem. Int. Ed.*, 2014, **53**, 2826-2851.
6. G. Dyker, *Angew. Chem. Int. Ed.*, 1999, **38**, 1698-1712.
7. I. Garcia-Bosch, A. Company, C. W. Cady, S. Styring, W. R. Browne, X. Ribas and M. Costas, *Angew. Chem. Int. Ed.*, 2011, **50**, 5648-5653.
8. I. Prat, J. S. Mathieson, M. Güell, X. Ribas, J. M. Luis, L. Cronin and M. Costas, *Nature Chemistry*, 2011, **3**, 788-793.
9. J. L. Fillol, Z. Codolà, I. Garcia-Bosch, L. Gómez, J. J. Pla and M. Costas, *Nat. Chem.*, 2011, **3**, 807-813.
10. A. Company, I. Prat, J. R. Frisch, D. R. Mas-Ballesté, M. Güell, G. Juhász, X. Ribas, D. E. Münck, J. M. Luis, L. Que Jr. and M. Costas, *Chem. Eur. J.*, 2011, **17**, 1622-1634.
11. Z. Codolà, I. Garcia-Bosch, F. Acuña-Parés, I. Prat, J. M. Luis, M. Costas and J. Lloret-Fillol, *Chem. Eur. J.*, 2013, **19**, 8042-8047.
12. A. Company, G. Sabenya, M. González-Béjar, L. Gómez, M. Clémancey, G. Blondin, A. J. Jasniewski, M. Puri, W. R. Browne, J.-M. Latour, L. Que, M. Costas, J. Pérez-Prieto and J. Lloret-Fillol, *J. Am. Chem. Soc.*, 2014, **136**, 4624-4633.
13. E. Andris, J. Jašík, L. Gómez, M. Costas and J. Roithová, *Angew. Chem. Int. Ed.*, 2016, **55**, 3637-3641.
14. G. Sabenya, L. Lázaro, I. Gamba, V. Martin-Diaconescu, E. Andris, T. Weyhermüller, F. Neese, J. Roithova, E. Bill, J. Lloret-Fillol and M. Costas, *J. Am. Chem. Soc.*, 2017, **139**, 9168-9177.
15. G. Sabenya, I. Gamba, L. Gómez, M. Clémancey, J. R. Frisch, E. J. Klinker, G. Blondin, S. Torelli, L. Que, V. Martin-Diaconescu, J.-M. Latour, J. Lloret-Fillol and M. Costas, *Chem. Sci.*, 2019, **10**, 9513-9529.
16. J. Serrano-Plana, A. Aguinaco, R. Belda, E. García-España, M. G. Basallote, A. Company and M. Costas, *Angew. Chem. Int. Ed.*, 2016, **55**, 6310-6314.
17. J. Serrano-Plana, W. N. Oloo, L. Acosta-Rueda, K. K. Meier, B. Verdejo, E. García-España, M. G. Basallote, E. Münck, L. Que, A. Company and M. Costas, *J. Am. Chem. Soc.*, 2015, **137**, 15833-15842.
18. B. Shin, K. D. Sutherlin, T. Ohta, T. Ogura, E. I. Solomon and J. Cho, *Inorg. Chem.*, 2016, **55**, 12391-12399.
19. X. Ribas, D. A. Jackson, B. Donnadieu, J. Mahía, T. Parella, R. Xifra, B. Hedman, K. O. Hodgson, A. Llobet and T. D. P. Stack, *Angew. Chem. Int. Ed.*, 2002, **41**, 2991-2994.
20. A. Casitas, A. E. King, T. Parella, M. Costas, S. S. Stahl and X. Ribas, *Chem. Sci.*, 2010, **1**, 326-330.
21. A. Casitas, M. Canta, M. Solà, M. Costas and X. Ribas, *J. Am. Chem. Soc.*, 2011, **133**, 19386-19392.

22. T. Corona, L. Ribas, M. Rovira, E. R. Farquhar, X. Ribas, K. Ray and A. Company, *Angew. Chem. Int. Ed.*, 2016, **55**, 14005-14008.
23. M. Font, F. Acuña-Parés, T. Parella, J. Serra, J. M. Luis, J. Lloret-Fillol, M. Costas and X. Ribas, *Nat. Commun.*, 2014, **5**, 4373.
24. X. Ribas, C. Calle, A. Poater, A. Casitas, L. Gómez, R. Xifra, T. Parella, J. Benet-Buchholz, A. Schweiger, G. Mitrikas, M. Solà, A. Llobet and T. D. P. Stack, *J. Am. Chem. Soc.*, 2010, **132**, 12299-12306.
25. M. Rovira, S. Roldán-Gómez, V. Martin-Diaconescu, C. J. Whiteoak, A. Company, J. M. Luis and X. Ribas, *Chem. Eur. J.*, 2017, **23**, 11662-11668.
26. O. Planas, C. J. Whiteoak, V. Martin-Diaconescu, I. Gamba, J. M. Luis, T. Parella, A. Company and X. Ribas, *J. Am. Chem. Soc.*, 2016, **138**, 14388-14397.
27. O. Planas, S. Roldán-Gómez, V. Martin-Diaconescu, T. Parella, J. M. Luis, A. Company and X. Ribas, *J. Am. Chem. Soc.*, 2017, **139**, 14649-14655.
28. B. Pignataro, *Ideas in Chemistry and Molecular Sciences*, Wiley VCH, Weinheim, Germany, 2006.
29. B. Meunier, *Biomimetic Oxidations Catalyzed by Transition Metal Complexes*, Imperial College Press, London, 2000.
30. E. V. Anslyn and D. A. Dougherty, *Modern Physical Organic Chemistry*, University Science Books, Sausalito, CA, 2006.
31. O. Y. Lyakin, R. V. Ottenbacher, K. P. Bryliakov and E. P. Talsi, *ACS Catal.*, 2012, **2**, 1196-1202.
32. Y. Morimoto, S. Bunno, N. Fujieda, H. Sugimoto and S. Itoh, *J. Am. Chem. Soc.*, 2015, **137**, 5867-5870.
33. S. Palavicini, A. Granata, E. Monzani and L. Casella, *J. Am. Chem. Soc.*, 2005, **127**, 18031-18036.
34. J.-E. Bäckvall, *Modern Oxidation Methods*, Wiley VCH, Weinheim, Germany, 2010.
35. G. L. Semenza, *Science*, 2007, **318**, 62-64.
36. E. G. Kovaleva and J. D. Lipscomb, *Nat. Chem. Biol.*, 2008, **4**, 186-193.
37. M. Costas, M. P. Mehn, M. P. Jensen and L. Que, *Chem. Rev.*, 2004, **104**, 939-986.
38. W. B. Tolman, *Activation of Small Molecules*, Wiley VCH, Weinheim, Germany, 2006.
39. E. L. Hegg and L. Que, Jr., *Eur. J. Biochem.*, 1997, **250**, 625-629.
40. K. D. Koehntop, J. P. Emerson and L. Que, Jr., *J. Biol. Inorg. Chem.*, 2005, **10**, 87-93.
41. W. Kaim, B. Schwederski and A. Klein, *Bioinorganic Chemistry: Inorganic Elements in the Chemistry of Life*, John Wiley & Sons, Inc, Chichester, 2013.
42. L. Que, *Physical Methods in Bioinorganic Chemistry: Spectroscopy and Magnetism*, University Science Books, Sausalito, CA, 2000.
43. K. Yoshizawa and Y. Shiota, *J. Am. Chem. Soc.*, 2006, **128**, 9873-9881.
44. S. J. Lippard and J. M. Berg, *Principles of Bioinorganic Chemistry*, University Science Books, Mill Valley, CA, 1994.
45. S. Schindler, *Eur. J. Inorg. Chem.*, 2000, **2000**, 2311-2326.
46. E. A. Lewis and W. B. Tolman, *Chem. Rev.*, 2004, **104**, 1047-1076.
47. L. M. Mirica, X. Ottenwaelder and T. D. P. Stack, *Chem. Rev.*, 2004, **104**, 1013-1046.
48. M. E. Cuff, K. I. Miller, K. E. van Holde and W. A. Hendrickson, *J. Mol. Biol.*, 1998, **278**, 855-870.
49. Y. Matoba, T. Kumagai, A. Yamamoto, H. Yoshitsu and M. Sugiyama, *J. Biol. Chem.*, 2006, **281**, 8981-8990.

50. I. Garcia-Bosch, X. Ribas and M. Costas, *Eur. J. Inorg. Chem.*, 2012, **2012**, 179-187.
51. J. Serrano-Plana, I. Garcia-Bosch, A. Company and M. Costas, *Acc. Chem. Res.*, 2015, **48**, 2397-2406.
52. L. Q. Hatcher and K. D. Karlin, *J. Biol. Inorg. Chem.*, 2004, **9**, 669-683.
53. L. Santagostini, M. Gullotti, E. Monzani, L. Casella, R. Dillinger and F. Tuczek, *Chem. Eur. J.*, 2000, **6**, 519-522.
54. L. M. Mirica, D. J. Rudd, M. A. Vance, E. I. Solomon, K. O. Hodgson, B. Hedman and T. D. P. Stack, *J. Am. Chem. Soc.*, 2006, **128**, 2654-2665.
55. L. M. Mirica, M. Vance, D. J. Rudd, B. Hedman, K. O. Hodgson, E. I. Solomon and T. D. P. Stack, *J. Am. Chem. Soc.*, 2002, **124**, 9332-9333.
56. L. M. Mirica, M. Vance, D. J. Rudd, B. Hedman, K. O. Hodgson, E. I. Solomon and T. D. P. Stack, *Science*, 2005, **308**, 1890.
57. A. Company, D. Lamata, A. Poater, M. Solà, E. V. Rybak-Akimova, L. Que, X. Fontrodona, T. Parella, A. Llobet and M. Costas, *Inorg. Chem.*, 2006, **45**, 5239-5241.
58. J. Serrano-Plana, I. Garcia-Bosch, R. Miyake, M. Costas and A. Company, *Angew. Chem. Int. Ed.*, 2014, **53**, 9608-9612.
59. K. Masanori, K. Masayuki and M. Toshihiko, *Chem. Lett.*, 1983, **12**, 927-928.
60. S. L. Buchwald, *Acc. Chem. Res.*, 2008, **41**, 1439-1439.
61. J. F. Hartwig, *Nature*, 2008, **455**, 314-322.
62. S. L. Buchwald, C. Mauger, G. Mignani and U. Scholz, *Adv. Synth. Catal.*, 2006, **348**, 23-39.
63. J. Magano and J. R. Dunetz, *Chem. Rev.*, 2011, **111**, 2177-2250.
64. B. Schlummer and U. Scholz, *Adv. Synth. Catal.*, 2004, **346**, 1599-1626.
65. C. C. C. Johansson Seechurn, M. O. Kitching, T. J. Colacot and V. Snieckus, *Angew. Chem. Int. Ed.*, 2012, **51**, 5062-5085.
66. J.-P. Corbet and G. Mignani, *Chem. Rev.*, 2006, **106**, 2651-2710.
67. A. S. Guram and S. L. Buchwald, *J. Am. Chem. Soc.*, 1994, **116**, 7901-7902.
68. F. Paul, J. Patt and J. F. Hartwig, *J. Am. Chem. Soc.*, 1994, **116**, 5969-5970.
69. J. F. Hartwig, *Acc. Chem. Res.*, 1998, **31**, 852-860.
70. J. P. Wolfe, S. Wagaw, J.-F. Marcoux and S. L. Buchwald, *Acc. Chem. Res.*, 1998, **31**, 805-818.
71. J. Hassan, M. Sévignon, C. Gozzi, E. Schulz and M. Lemaire, *Chem. Rev.*, 2002, **102**, 1359-1470.
72. C.-L. Sun, B.-J. Li and Z.-J. Shi, *Chem. Rev.*, 2011, **111**, 1293-1314.
73. T. Dalton, T. Faber and F. Glorius, *ACS Cent. Sci.*, 2021, **7**, 245-261.
74. K. Morikawa, W. S. Benedict and H. S. Taylor, *J. Am. Chem. Soc.*, 1936, **58**, 1445-1449.
75. G. Olivo, O. Cussó and M. Costas, *Chem. Asian J.*, 2016, **11**, 3148-3158.
76. E. P. Talsi and K. P. Bryliakov, *Coord. Chem. Rev.*, 2012, **256**, 1418-1434.
77. M. Beller and C. Bolm, *Transition Merals for Organic Synthesis: Building Blocks and Fine Chemicals*, Wiley, New York, 2nd edn., 2008.
78. J. Miao and H. Ge, *Eur. J. Org. Chem.*, 2015, **2015**, 7859-7868.
79. I. P. Beletskaya and V. P. Ananikov, *Chem. Rev.*, 2011, **111**, 1596-1636.
80. J. D. Hayler, D. K. Leahy and E. M. Simmons, *Organometallics*, 2019, **38**, 36-46.
81. T. Laird, *Organic Process Research & Development*, 2012, **16**, 1-2.
82. K. S. Egorova and V. P. Ananikov, *Angew. Chem. Int. Ed.*, 2016, **55**, 12150-12162.
83. J. D. Sears, P. G. N. Neate and M. L. Neidig, *J. Am. Chem. Soc.*, 2018, **140**, 11872-11883.

84. S. M. Neumann and J. K. Kochi, *J. Org. Chem.*, 1975, **40**, 599-606.
85. R. S. Smith and J. K. Kochi, *J. Org. Chem.*, 1976, **41**, 502-509.
86. M. Tamura and J. K. Kochi, *J. Am. Chem. Soc.*, 1971, **93**, 1487-1489.
87. T. Nagano and T. Hayashi, *Org. Lett.*, 2004, **6**, 1297-1299.
88. M. Nakamura, K. Matsuo, S. Ito and E. Nakamura, *J. Am. Chem. Soc.*, 2004, **126**, 3686-3687.
89. G. Cahiez, C. Duplais and A. Moyeux, *Org. Lett.*, 2007, **9**, 3253-3254.
90. A. Guérinot, S. Reymond and J. Cossy, *Angew. Chem. Int. Ed.*, 2007, **46**, 6521-6524.
91. R. B. Bedford, M. Betham, D. W. Bruce, A. A. Danopoulos, R. M. Frost and M. Hird, *J. Org. Chem.*, 2006, **71**, 1104-1110.
92. T. Hatakeyama and M. Nakamura, *J. Am. Chem. Soc.*, 2007, **129**, 9844-9845.
93. T. Hatakeyama, S. Hashimoto, K. Ishizuka and M. Nakamura, *J. Am. Chem. Soc.*, 2009, **131**, 11949-11963.
94. S. K. Ghorai, M. Jin, T. Hatakeyama and M. Nakamura, *Org. Lett.*, 2012, **14**, 1066-1069.
95. M. Guisán-Ceinos, F. Tato, E. Buñuel, P. Calle and D. J. Cárdenas, *Chem. Sci.*, 2013, **4**, 1098-1104.
96. R. B. Bedford, M. Huwe and M. C. Wilkinson, *Chem. Commun.*, 2009, 600-602.
97. T. Hatakeyama, Y. Kondo, Y.-i. Fujiwara, H. Takaya, S. Ito, E. Nakamura and M. Nakamura, *Chem. Commun.*, 2009, DOI: 10.1039/B820879D, 1216-1218.
98. T. Hatakeyama, T. Hashimoto, Y. Kondo, Y. Fujiwara, H. Seike, H. Takaya, Y. Tamada, T. Ono and M. Nakamura, *J. Am. Chem. Soc.*, 2010, **132**, 10674-10676.
99. T. Hatakeyama, Y. Okada, Y. Yoshimoto and M. Nakamura, *Angew. Chem. Int. Ed.*, 2011, **50**, 10973-10976.
100. H. Takuji, F. Yu-ichi, O. Yoshihiro, I. Takuma, H. Toru, K. Shintaro, O. Kazuki, T. Hikaru and N. Masaharu, *Chem. Lett.*, 2011, **40**, 1030-1032.
101. C. J. Adams, R. B. Bedford, E. Carter, N. J. Gower, M. F. Haddow, J. N. Harvey, M. Huwe, M. Á. Cartes, S. M. Mansell, C. Mendoza, D. M. Murphy, E. C. Neeve and J. Nunn, *J. Am. Chem. Soc.*, 2012, **134**, 10333-10336.
102. R. B. Bedford, E. Carter, P. M. Cogswell, N. J. Gower, M. F. Haddow, J. N. Harvey, D. M. Murphy, E. C. Neeve and J. Nunn, *Angew. Chem. Int. Ed.*, 2013, **52**, 1285-1288.
103. G. Cahiez and H. Avedissian, *Synthesis*, 1998, **1998**, 1199-1205.
104. M. Jin, L. Adak and M. Nakamura, *J. Am. Chem. Soc.*, 2015, **137**, 7128-7134.
105. H. M. O'Brien, M. Manzotti, R. D. Abrams, D. Elorriaga, H. A. Sparkes, S. A. Davis and R. B. Bedford, *Nat. Catal.*, 2018, **1**, 429-437.
106. J. Norinder, A. Matsumoto, N. Yoshikai and E. Nakamura, *J. Am. Chem. Soc.*, 2008, **130**, 5858-5859.
107. N. Yoshikai, A. Matsumoto, J. Norinder and E. Nakamura, *Angew. Chem. Int. Ed.*, 2009, **48**, 2925-2928.
108. N. Yoshikai, A. Matsumoto, J. Norinder and E. Nakamura, *Synlett*, 2010, **2010**, 313-316.
109. J. Wen, S. Qin, L.-F. Ma, L. Dong, J. Zhang, S.-S. Liu, Y.-S. Duan, S.-Y. Chen, C.-W. Hu and X.-Q. Yu, *Org. Lett.*, 2010, **12**, 2694-2697.
110. J. Wen, J. Zhang, S.-Y. Chen, J. Li and X.-Q. Yu, *Angew. Chem. Int. Ed.*, 2008, **47**, 8897-8900.
111. L. Ilies, E. Konno, Q. Chen and E. Nakamura, *Asian J. Org. Chem.*, 2012, **1**, 142-145.
112. J. J. Sirois, R. Davis and B. DeBoef, *Org. Lett.*, 2014, **16**, 868-871.

113. Q. Gu, H. H. Al Mamari, K. Graczyk, E. Diers and L. Ackermann, *Angew. Chem. Int. Ed.*, 2014, **53**, 3868-3871.
114. R. Shang, L. Ilies, S. Asako and E. Nakamura, *J. Am. Chem. Soc.*, 2014, **136**, 14349-14352.
115. Z. Shen, G. Cera, T. Haven and L. Ackermann, *Org. Lett.*, 2017, **19**, 3795-3798.
116. N. Yoshikai, S. Asako, T. Yamakawa, L. Ilies and E. Nakamura, *Chem. Asian J.*, 2011, **6**, 3059-3065.
117. Y. Sun, H. Tang, K. Chen, L. Hu, J. Yao, S. Shaik and H. Chen, *J. Am. Chem. Soc.*, 2016, **138**, 3715-3730.
118. C. A. Tolman, S. D. Ittel, A. D. English and J. P. Jesson, *J. Am. Chem. Soc.*, 1978, **100**, 4080-4089.
119. C. A. Tolman, S. D. Ittel, A. D. English and J. P. Jesson, *J. Am. Chem. Soc.*, 1979, **101**, 1742-1751.
120. M. V. Baker and L. D. Field, *J. Am. Chem. Soc.*, 1986, **108**, 7433-7434.
121. C. Zhu, M. Stangier, J. C. A. Oliveira, L. Massignan and L. Ackermann, *Chem. Eur. J.*, 2019, **25**, 16382-16389.
122. A. Fürstner, *ACS Cent. Sci.*, 2016, **2**, 778-789.
123. F. Alois and M. Rubén, *Chem. Lett.*, 2005, **34**, 624-629.
124. B. D. Sherry and A. Fürstner, *Acc. Chem. Res.*, 2008, **41**, 1500-1511.
125. D. Noda, Y. Sunada, T. Hatakeyama, M. Nakamura and H. Nagashima, *J. Am. Chem. Soc.*, 2009, **131**, 6078-6079.
126. T. L. Mako and J. A. Byers, *Inorg. Chem. Front.*, 2016, **3**, 766-790.
127. D. Schröder, S. Shaik and H. Schwarz, *Acc. Chem. Res.*, 2000, **33**, 139-145.
128. W. I. Dzik, W. Böhmer and B. de Bruin, in *Spin States in Biochemistry and Inorganic Chemistry*, 2015, John Wiley & Sons, 103-129.
129. S. A. Lutz, A. K. Hickey, Y. Gao, C.-H. Chen and J. M. Smith, *J. Am. Chem. Soc.*, 2020, **142**, 15527-15535.
130. S. L. Daifuku, M. H. Al-Afyouni, B. E. R. Snyder, J. L. Kneebone and M. L. Neidig, *J. Am. Chem. Soc.*, 2014, **136**, 9132-9143.
131. S. L. Daifuku, J. L. Kneebone, B. E. R. Snyder and M. L. Neidig, *J. Am. Chem. Soc.*, 2015, **137**, 11432-11444.
132. T. E. Boddie, S. H. Carpenter, T. M. Baker, J. C. DeMuth, G. Cera, W. W. Brennessel, L. Ackermann and M. L. Neidig, *J. Am. Chem. Soc.*, 2019, **141**, 12338-12345.
133. M. L. Neidig, S. H. Carpenter, D. J. Curran, J. C. DeMuth, V. E. Fleischauer, T. E. Iannuzzi, P. G. N. Neate, J. D. Sears and N. J. Wolford, *Acc. Chem. Res.*, 2019, **52**, 140-150.
134. P. G. N. Neate, M. D. Greenhalgh, W. W. Brennessel, S. P. Thomas and M. L. Neidig, *J. Am. Chem. Soc.*, 2019, **141**, 10099-10108.
135. K. L. Fillman, J. A. Przyojski, M. H. Al-Afyouni, Z. J. Tonzetich and M. L. Neidig, *Chem. Sci.*, 2015, **6**, 1178-1188.
136. J. L. Kneebone, V. E. Fleischauer, S. L. Daifuku, A. A. Shaps, J. M. Bailey, T. E. Iannuzzi and M. L. Neidig, *Inorg. Chem.*, 2016, **55**, 272-282.
137. J. Mo, T. Müller, J. C. A. Oliveira, S. Demeshko, F. Meyer and L. Ackermann, *Angew. Chem. Int. Ed.*, 2019, **58**, 12874-12878.
138. A. Biffis, P. Centomo, A. Del Zotto and M. Zecca, *Chem. Rev.*, 2018, **118**, 2249-2295.
139. R. B. Bedford, *Acc. Chem. Res.*, 2015, **48**, 1485-1493.
140. R. Arevalo and P. J. Chirik, *J. Am. Chem. Soc.*, 2019, **141**, 9106-9123.

141. A. Fürstner, A. Leitner, M. Méndez and H. Krause, *J. Am. Chem. Soc.*, 2002, **124**, 13856-13863.
142. R. Martin and A. Fürstner, *Angew. Chem. Int. Ed.*, 2004, **43**, 3955-3957.
143. B. Scheiper, M. Bonnekessel, H. Krause and A. Fürstner, *J. Org. Chem.*, 2004, **69**, 3943-3949.
144. A. Fürstner, R. Martin, H. Krause, G. Seidel, R. Goddard and C. W. Lehmann, *J. Am. Chem. Soc.*, 2008, **130**, 8773-8787.
145. G. Lefèvre and A. Jutand, *Chem. Eur. J.*, 2014, **20**, 4796-4805.
146. S. B. Muñoz, S. L. Daifuku, W. W. Brennessel and M. L. Neidig, *J. Am. Chem. Soc.*, 2016, **138**, 7492-7495.
147. S. B. Muñoz III, S. L. Daifuku, J. D. Sears, T. M. Baker, S. H. Carpenter, W. W. Brennessel and M. L. Neidig, *Angew. Chem. Int. Ed.*, 2018, **57**, 6496-6500.
148. H. Lehmkuhl, G. Mehler, R. Benn, A. Rufiǹska, G. Schroth, C. Krüger and E. Raabe, *Chem. Ber.*, 1987, **120**, 1987-2002.
149. D. H. Hill, M. A. Parvez and A. Sen, *J. Am. Chem. Soc.*, 1994, **116**, 2889-2901.
150. Y.-Y. Chua and H. A. Duong, *Chem. Commun.*, 2014, **50**, 8424-8427.
151. Y. Liu, J. Xiao, L. Wang, Y. Song and L. Deng, *Organometallics*, 2015, **34**, 599-605.
152. J. A. Przyojski, K. P. Veggeberg, H. D. Arman and Z. J. Tonzetich, *ACS Catal.*, 2015, **5**, 5938-5946.
153. P. L. Bock, D. J. Boschetto, J. R. Rasmussen, J. P. Demers and G. M. Whitesides, *J. Am. Chem. Soc.*, 1974, **96**, 2814-2825.
154. J. P. Collman, R. G. Finke, J. N. Cawse and J. I. Brauman, *J. Am. Chem. Soc.*, 1977, **99**, 2515-2526.
155. R. Birk, H. Berke, G. Huttner and L. Zsolnai, *Chem. Ber.*, 1988, **121**, 1557-1564.
156. S. C. Wright and M. C. Baird, *J. Am. Chem. Soc.*, 1985, **107**, 6899-6902.
157. G. Cardaci, G. Bellachioma and P. Zanazzi, *Organometallics*, 1988, **7**, 172-180.
158. Y. Shi, M. Li, Q. Hu, X. Li and H. Sun, *Organometallics*, 2009, **28**, 2206-2210.
159. S. Hosokawa, J.-i. Ito and H. Nishiyama, *Organometallics*, 2010, **29**, 5773-5775.
160. S. M. Rummelt, P. O. Peterson, H. Zhong and P. J. Chirik, *J. Am. Chem. Soc.*, 2021, **143**, 5928-5936.
161. R. Shang, L. Ilies and E. Nakamura, *Chem. Rev.*, 2017, **117**, 9086-9139.
162. S. H. Wunderlich and P. Knochel, *Angew. Chem. Int. Ed.*, 2009, **48**, 9717-9720.
163. G. Hata, H. Kondo and A. Miyake, *J. Am. Chem. Soc.*, 1968, **90**, 2278-2281.
164. G. Cerveau, E. Colomer and R. Corriu, *J. Organomet. Chem.*, 1977, **136**, 349-353.
165. S. D. Ittel, C. A. Tolman, A. D. English and J. P. Jesson, *J. Am. Chem. Soc.*, 1978, **100**, 7577-7585.
166. M. K. Whittlesey, R. J. Mawby, R. Osman, R. N. Perutz, L. D. Field, M. P. Wilkinson and M. W. George, *J. Am. Chem. Soc.*, 1993, **115**, 8627-8637.
167. H. Azizian and R. H. Morris, *Inorg. Chem.*, 1983, **22**, 6-9.
168. S. D. Ittel, C. A. Tolman, P. J. Krusic, A. D. English and J. P. Jesson, *Inorg. Chem.*, 1978, **17**, 3432-3438.
169. B. J. Jackson, D. C. Najera, E. M. Matson, T. J. Woods, J. A. Bertke and A. R. Fout, *Organometallics*, 2019, **38**, 2943-2952.
170. M. M. Bagga, P. L. Pauson, F. J. Preston and R. I. Reed, *Chem. Commun. (London)*, 1965, 543-544.
171. P. E. Baikie and O. S. Mills, *Chem. Commun. (London)*, 1966, 707-708.

172. W. T. Flannigan, G. R. Knox and P. L. Pauson, *J. Chem. Soc. C Org.*, 1969, 2077-2080.
173. M. M. Bagga, W. T. Flannigan, G. R. Knox, P. L. Pauson, F. J. Preston and R. I. Reed, *J. Chem. Soc. C Org.*, 1968, 36-40.
174. M. M. Bagga, W. T. Flannigan, G. R. Knox and P. L. Pauson, *J. Chem. Soc. C Org.*, 1969, DOI: 10.1039/J39690001534, 1534-1537.
175. D.-L. Wang, W.-S. Hwang, L.-C. Liang, L.-I. Wang, L. Lee and M. Y. Chiang, *Organometallics*, 1997, **16**, 3109-3113.
176. W. Imhof, *Organometallics*, 1999, **18**, 4845-4855.
177. T. Jia, C. Zhao, R. He, H. Chen and C. Wang, *Angew. Chem. Int. Ed.*, 2016, **55**, 5268-5271.
178. S. Camadanli, R. Beck, U. Flörke and H.-F. Klein, *Organometallics*, 2009, **28**, 2300-2310.
179. A. M. Messinis, L. H. Finger, L. Hu and L. Ackermann, *J. Am. Chem. Soc.*, 2020, **142**, 13102-13111.
180. G. Wilke, *Angew. Chem. Int. Ed.*, 1988, **27**, 185-206.
181. V. P. Ananikov, *ACS Catal.*, 2015, **5**, 1964-1971.
182. A. de Meijere and F. Diederich, *Metal-Catalyized Cross-Coupling Reactions*, Wiley VCH, Weinheim, 2004.
183. B. M. Rosen, K. W. Quasdorf, D. A. Wilson, N. Zhang, A.-M. Resmerita, N. K. Garg and V. Percec, *Chem. Rev.*, 2011, **111**, 1346-1416.
184. S. Z. Tasker, E. A. Standley and T. F. Jamison, *Nature*, 2014, **509**, 299-309.
185. M. Tobisu, T. Xu, T. Shimasaki and N. Chatani, *J. Am. Chem. Soc.*, 2011, **133**, 19505-19511.
186. L. Capdevila, T. H. Meyer, S. Roldán-Gómez, J. M. Luis, L. Ackermann and X. Ribas, *ACS Catal.*, 2019, **9**, 11074-11081.
187. V. Müller, D. Ghorai, L. Capdevila, A. M. Messinis, X. Ribas and L. Ackermann, *Org. Lett.*, 2020, **22**, 7034-7040.
188. J. Terao, H. Todo, H. Watabe, A. Ikumi, Y. Shinohara and N. Kambe, *Pure Appl. Chem.*, 2008, **80**, 941-951.
189. O. Eisenstein, J. Milani and R. N. Perutz, *Chem. Rev.*, 2017, **117**, 8710-8753.
190. S. L. Zultanski and G. C. Fu, *J. Am. Chem. Soc.*, 2013, **135**, 624-627.
191. E. Serrano and R. Martin, *Angew. Chem. Int. Ed.*, 2016, **55**, 11207-11211.
192. C. K. Chu, Y. Liang and G. C. Fu, *J. Am. Chem. Soc.*, 2016, **138**, 6404-6407.
193. T. Mesganaw and N. K. Garg, *Organic Process Research & Development*, 2013, **17**, 29-39.
194. J. W. Dankwardt, *Angew. Chem. Int. Ed.*, 2004, **43**, 2428-2432.
195. B.-J. Li, D.-G. Yu, C.-L. Sun and Z.-J. Shi, *Chem. Eur. J.*, 2011, **17**, 1728-1759.
196. M. Tobisu and N. Chatani, *Top. Curr. Chem.*, 2016, **374**, 41.
197. X. Hu, *Chem. Sci.*, 2011, **2**, 1867-1886.
198. T. T. Tsou and J. K. Kochi, *J. Am. Chem. Soc.*, 1979, **101**, 6319-6332.
199. C. A. Laskowski, D. J. Bungum, S. M. Baldwin, S. A. Del Ciello, V. M. Iluc and G. L. Hillhouse, *J. Am. Chem. Soc.*, 2013, **135**, 18272-18275.
200. J. Cornella, E. Gómez-Bengoa and R. Martin, *J. Am. Chem. Soc.*, 2013, **135**, 1997-2009.
201. A. Joshi-Pangu, C.-Y. Wang and M. R. Biscoe, *J. Am. Chem. Soc.*, 2011, **133**, 8478-8481.
202. A. S. Dudnik and G. C. Fu, *J. Am. Chem. Soc.*, 2012, **134**, 10693-10697.
203. N. D. Schley and G. C. Fu, *J. Am. Chem. Soc.*, 2014, **136**, 16588-16593.
204. J. C. Tellis, D. N. Primer and G. A. Molander, *Science*, 2014, **345**, 433-436.

205. Z. Zuo, D. T. Ahneman, L. Chu, J. A. Terrett, A. G. Doyle and D. W. C. MacMillan, *Science*, 2014, **345**, 437-440.
206. J. Cornella, J. T. Edwards, T. Qin, S. Kawamura, J. Wang, C.-M. Pan, R. Gianatassio, M. Schmidt, M. D. Eastgate and P. S. Baran, *J. Am. Chem. Soc.*, 2016, **138**, 2174-2177.
207. L. C. M. Castro and N. Chatani, *Chem. Lett.*, 2015, **44**, 410-421.
208. Y. Aihara, M. Tobisu, Y. Fukumoto and N. Chatani, *J. Am. Chem. Soc.*, 2014, **136**, 15509-15512.
209. X. Yang, G. Shan, L. Wang and Y. Rao, *Tetrahedron Lett.*, 2016, **57**, 819-836.
210. Z. Ruan, S. Lackner and L. Ackermann, *Angew. Chem. Int. Ed.*, 2016, **55**, 3153-3157.
211. M. Iyanaga, Y. Aihara and N. Chatani, *J. Org. Chem.*, 2014, **79**, 11933-11939.
212. Y. Aihara and N. Chatani, *J. Am. Chem. Soc.*, 2013, **135**, 5308-5311.
213. Y. Aihara and N. Chatani, *J. Am. Chem. Soc.*, 2014, **136**, 898-901.
214. S.-Y. Yan, Y.-J. Liu, B. Liu, Y.-H. Liu, Z.-Z. Zhang and B.-F. Shi, *Chem. Commun.*, 2015, **51**, 7341-7344.
215. K. Koo and G. L. Hillhouse, *Organometallics*, 1995, **14**, 4421-4423.
216. D. M. Grove, G. Van Koten, R. Zoet, N. W. Murrall and A. J. Welch, *J. Am. Chem. Soc.*, 1983, **105**, 1379-1380.
217. A. T. Higgs, P. J. Zinn, S. J. Simmons and M. S. Sanford, *Organometallics*, 2009, **28**, 6142-6144.
218. J. W. Schultz, K. Fuchigami, B. Zheng, N. P. Rath and L. M. Mirica, *J. Am. Chem. Soc.*, 2016, **138**, 12928-12934.
219. M. B. Watson, N. P. Rath and L. M. Mirica, *J. Am. Chem. Soc.*, 2017, **139**, 35-38.
220. B. Zheng, F. Tang, J. Luo, J. W. Schultz, N. P. Rath and L. M. Mirica, *J. Am. Chem. Soc.*, 2014, **136**, 6499-6504.
221. W. Zhou, J. W. Schultz, N. P. Rath and L. M. Mirica, *J. Am. Chem. Soc.*, 2015, **137**, 7604-7607.
222. J. R. Bour, N. M. Camasso, E. A. Meucci, J. W. Kampf, A. J. Canty and M. S. Sanford, *J. Am. Chem. Soc.*, 2016, **138**, 16105-16111.
223. A. J. Hickman and M. S. Sanford, *Nature*, 2012, **484**, 177-185.
224. S. R. Whitfield and M. S. Sanford, *J. Am. Chem. Soc.*, 2007, **129**, 15142-15143.
225. A. R. Dick, J. W. Kampf and M. S. Sanford, *J. Am. Chem. Soc.*, 2005, **127**, 12790-12791.
226. Y. Ye, N. D. Ball, J. W. Kampf and M. S. Sanford, *J. Am. Chem. Soc.*, 2010, **132**, 14682-14687.
227. H.-F. Klein, A. Bickelhaupt, T. Jung and G. Cordier, *Organometallics*, 1994, **13**, 2557-2559.
228. V. Dimitrov and A. Linden, *Angew. Chem. Int. Ed.*, 2003, **42**, 2631-2633.
229. M. Carnes, D. Buccella, J. Y.-C. Chen, A. P. Ramirez, N. J. Turro, C. Nuckolls and M. Steigerwald, *Angew. Chem. Int. Ed.*, 2009, **48**, 290-294.
230. N. M. Camasso and M. S. Sanford, *Science*, 2015, **347**, 1218-1220.
231. J. R. Bour, N. M. Camasso and M. S. Sanford, *J. Am. Chem. Soc.*, 2015, **137**, 8034-8037.
232. N. M. Camasso, A. J. Canty, A. Ariafard and M. S. Sanford, *Organometallics*, 2017, **36**, 4382-4393.
233. E. A. Meucci, N. M. Camasso and M. S. Sanford, *Organometallics*, 2017, **36**, 247-250.
234. E. A. Meucci, S. N. Nguyen, N. M. Camasso, E. Chong, A. Ariafard, A. J. Canty and M. S. Sanford, *J. Am. Chem. Soc.*, 2019, **141**, 12872-12879.

235. E. A. Meucci, A. Ariafard, A. J. Canty, J. W. Kampf and M. S. Sanford, *J. Am. Chem. Soc.*, 2019, **141**, 13261-13267.
236. J. R. Bour, D. M. Ferguson, E. J. McClain, J. W. Kampf and M. S. Sanford, *J. Am. Chem. Soc.*, 2019, **141**, 8914-8920.
237. J. Yamaguchi, K. Muto and K. Itami, *Top. Curr. Chem.*, 2016, **374**, 55.
238. N. Chatani, in *C-H Bond Activation and Catalytic Functionalization II*, Springer, 2015.
239. P. Roy, J. R. Bour, J. W. Kampf and M. S. Sanford, *J. Am. Chem. Soc.*, 2019, **141**, 17382-17387.
240. W. Zhou, S. Zheng, J. W. Schultz, N. P. Rath and L. M. Mirica, *J. Am. Chem. Soc.*, 2016, **138**, 5777-5780.
241. E. Chong, J. W. Kampf, A. Ariafard, A. J. Canty and M. S. Sanford, *J. Am. Chem. Soc.*, 2017, **139**, 6058-6061.
242. C. C. Roberts, E. Chong, J. W. Kampf, A. J. Canty, A. Ariafard and M. S. Sanford, *J. Am. Chem. Soc.*, 2019, **141**, 19513-19520.

Chapter II. Objectives

In this thesis, within the context of the development of new synthetic methodologies mediated by Earth-abundant first-row transition metals, mechanistic investigations of important transformations have been performed: (i) the oxidation or oxygenation of C-H and C-F bonds using bioinspired copper systems in tandem with a *green* oxidant such as molecular oxygen (Chapters III and IV), and (ii) the *cross-coupling* (and C-H activation) *reaction* mediated by first-row transition metals like iron and nickel (Chapters V and VI).

The first part of this thesis will be aimed to the study of O_2-activating copper enzymes such as tyrosinase (Chapter III) and FAD-containing phenol hydroxylase (Chapter IV).

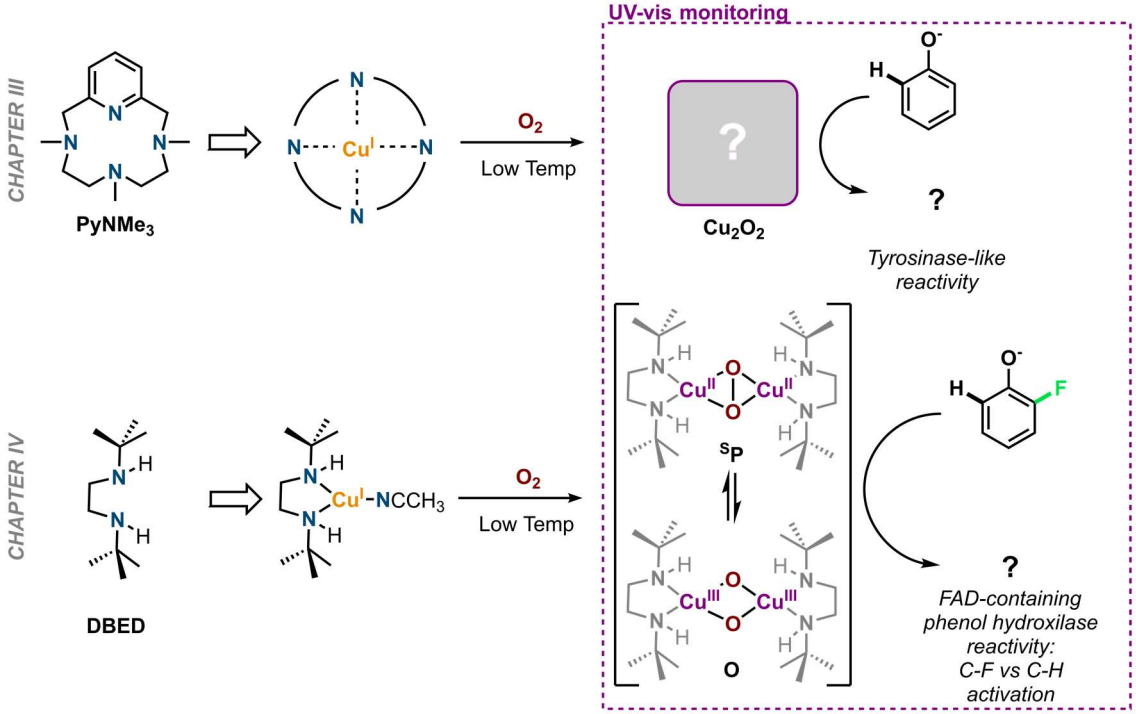

Scheme II.1 Schematic representation of the objectives corresponding to the first part of this thesis (top: Chapter III, and bottom: Chapter IV): copper complexes for O_2-activation and substrate oxidation using bioinspired model ligands.

To this end, in Chapter III we will develop a new bioinspired copper(I) complex capable of mimicking the reactivity of tyrosinase upon dioxygen exposure. We envision the use of the $PyNMe_3$ ligand to mimic the nitrogen-rich environment found in the active site of tyrosinase. This tetradentate nitrogen-based 12-membered macrocyclic ligand was previously used by Company, Costas and coworkers to stabilize high-valent iron-oxo species. If the corresponding mononuclear copper(I) complex can be obtained, its reactivity towards O_2 at low temperature will be explored with the aim of trapping and characterizing any Cu_2:O_2 adduct formed. Finally,

to ensure that this system is a functional model of tyrosinase, the hydroxylation of phenolate derivatives by the *in situ* generated copper-oxygen adduct will also be studied (Scheme II.1, top).

In Chapter IV we will explore further the reactivity of a Cu_2:O_2 adduct reported by Stack and coworkers generated al low temperature. This system is supported by a bidentate nitrogen-based ligand, and upon exposing the corresponding copper(I) complex to dioxygen at low temperatures the ^{s}**P** species is observed by UV-vis spectroscopy. Moreover, when adding a phenolate, the **O** species with the phenolate coordinated is also be detected. Given the fact that both the ^{s}**P** and the **O** species are observable for this system, the main goal is to explore if this functional model of tyrosinase can also perform the challenging *ortho*-defluorination-hydroxylation of 2-fluorophenols, in contrast to tyrosinase which activity is inhibited in the presence of C-F bonds (Scheme II.1, bottom).

The second part of this thesis will be focused on the organometallic chemistry mediated by iron (Chapter V) and nickel (Chapter VI) with carefully designed model substrates that will provide the metal center with a more stable environment for its isolation and characterization.

In Chapter V, we will use 12-membered macrocyclic model substrate to study the iron-mediated C-H activation pathway using a Grignard reagent as coupling partner. This model platform was previously used to isolate and characterize high-valent organometallic palladium, nickel and cobalt complexes. Given this precedent, and due to the lack of mechanistic information in the field of organometallic iron chemistry, the aim of this work is to be able to isolate a well-defined aryl-iron(II) complex, characterize it and study its reactivity towards Grignard reagents. If successfully achieved, this new family of well-defined aryl-iron(II) complexes could serve as a stepping stone for unraveling the underlying mechanism of other iron-mediated transformations in the field of organometallic chemistry (Scheme II.2, top).

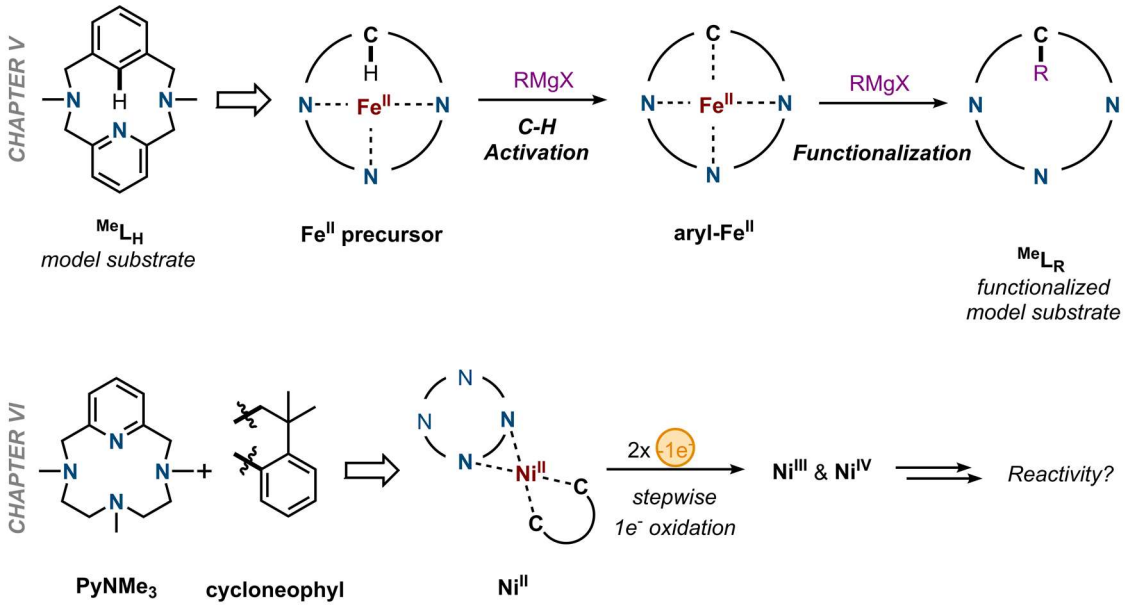

Scheme II.2 Schematic representation of the objectives corresponding to the second part of this thesis (top: Chapter V, and bottom: Chapter VI): isolation of organometallic iron and nickel complexes bearing model substrates and model ligands relevant for C-H activation and cross-coupling transformations.

Finally, in Chapter VI we envision the use of the $PyNMe_3$ ligand together with a bis-carbon-donor ligand such as cycloneophyl to isolate and characterize an organometallic low-valent nickel(II) complex and its corresponding high-valent nickel(III) and nickel(IV) analogues via stepwise one-electron oxidation. Noteworthy, $PyNMe_3$ has never been used to stabilize organometallic complexes. This system is interesting due to the non-symmetric arrangement provided by the two ligands which will allow for the study of the *trans-effect*. Moreover, the reactivity of the different species in the presence of oxidants towards the formation of new C-C or C-O bonds will also be investigated, in order to shed more light into the presumed involvement of organometallic nickel(IV) species in nickel-mediated cross-coupling reactions (Scheme II.2, bottom).

Chapter III. Preparation of a Coordinatively Saturated μ-η²:η²-Peroxodicopper(II) Compound

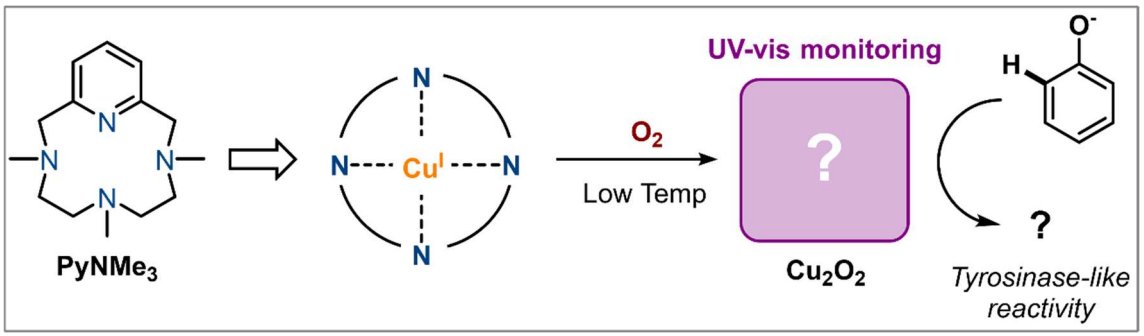

This chapter corresponds to the following publication:

Reprinted from *Inorg. Chim. Acta, 481,* Carla Magallón, Joan Serrano-Plana, Steven Roldán-Gómez, Xavi Ribas, Miquel Costas, Anna Company*, Preparation of a Coordinatively Saturated μ-η²:η²-Peroxodicopper(II) Compound, 166 – 170

Inorganica Chimica Acta 481 (2018) 166–170

Contents lists available at ScienceDirect

Inorganica Chimica Acta

journal homepage: www.elsevier.com/locate/ica

Preparation of a coordinatively saturated μ-η²:η²-peroxodicopper(II) compound

Carla Magallón, Joan Serrano-Plana, Steven Roldán-Gómez, Xavi Ribas, Miquel Costas, Anna Company *

Grup de Química Bioinspirada, Supramolecular i Catàlisi (QBIS-CAT), Institut de Química Computacional i Catàlisi (IQCC), Departament de Química, Universitat de Girona, C/ M Aurèlia Capmany 69, E-17003 Girona, Catalonia, Spain

ARTICLE INFO

Article history:
Received 14 July 2017
Received in revised form 28 August 2017
Accepted 31 August 2017
Available online 6 September 2017

Keywords:
Copper
Dioxygen
Bioinorganic chemistry
Metastable species
Oxygenases

ABSTRACT

The synthesis and solution characterization of the mononuclear copper(I) complex $[Cu^{I}(PyNMe_3)(CH_3CN)]^+$ (**1**) is described. This compound presents a C_s symmetric architecture as ascertained by NMR spectroscopy and corroborated by DFT calculations. The reactivity of **1** towards O_2 in a CH_3CN:THF 1:19 mixture at −100 °C was monitored by UV–vis spectroscopy, which evidenced the formation of a new species (**2**) with a highly intense absorption at 353 nm (ε > 17200 M^{-1} cm^{-1}) that was not stable even at this low temperature ($t_{1/2}$ = 6 min at −100 °C). This spectroscopic signature is characteristic of μ-η²:η²-peroxodicopper(II) complexes, which typically exhibit one single intense absorption between 340 and 380 nm. Despite the fact that such species are involved in the catalytic cycle of tyrosinase, a copper-based enzyme that *ortho*-hydroxylates phenols, attempts to hydroxylate phenolates by **2** turned out to be unsuccessful. Most probably, the rigid macrocyclic tetradentate architecture of the $PyNMe_3$ ligand hinders simultaneous peroxide and phenolate coordination in the same copper center, a necessary step prior to the *ortho*-hydroxylation of this substrate.

1. Introduction

Copper-containing proteins are one of the most relevant subgroups of O_2-activating enzymes [1,2]. Their reaction mechanism usually entails the reductive activation of O_2 by a copper(I) center to form copper-dioxygen adducts (Cu_n:O_2) in which the oxidation state of the metal center is +2 or +3 and the O_2 moiety has been reduced to superoxide, peroxide or oxide moieties. These Cu_n:O_2 adducts are key intermediates in the catalytic cycle of the enzymes and they are directly involved in the oxidation/oxygenation of organic substrates [3,4]. However, their intrinsic reactivity turns them into elusive species which are difficult to trap and characterize. In this context, a particularly valuable strategy to get information about such compounds involves the synthesis, characterization, and detailed evaluation of the reactivity of discrete molecules that contain copper–oxygen moieties [5–7]. Such small molecular bioinspired models serve as platforms to unravel key aspects about the structure and electronic properties of these biologically relevant Cu_n:O_2 adducts.

These studies have enabled the characterization of a myriad of copper-dioxygen adducts, ranging from mononuclear centers to multinuclear or heterometallic configurations. In most cases, neutral N-based ligands combining tertiary amines, imines or heterocyclic amines (pyridines, pyrazoles, imidazoles) constitute the coordination environment around the copper center. In the present work, we use a tetradentate nitrogen-based marocyclic ligand ($PyNMe_3$), which coordinates the metal center through three aliphatic nitrogens and one pyridine (Fig. 1). We will study the ability of $PyNMe_3$ to coordinate to copper(I) and the binding and activation of O_2 by the resulting copper(I) complex. Noteworthy, $PyNMe_3$ has been previously used in our laboratory for the synthesis of high-valent iron-oxygen species [8,9], and later Cho et al. reported its use for the synthesis of mononuclear (hydro)peroxidocobalt(III) species [10].

2. Experimental section

2.1. Materials and methods

Anhydrous solvents were purchased from Scharlau or Sigma-Aldrich and used as received. Reagents were of commercially available reagent quality. Ligand $PyNMe_3$ was synthesized following previously reported procedures [8,9].

NMR spectra were recorded on Bruker Ultrashield Avance III400 and Ultrashield DPX300 spectrometers. Mass spectra were

* Corresponding author.
E-mail address: anna.company@udg.edu (A. Company).

http://dx.doi.org/10.1016/j.ica.2017.08.061
0020-1693/

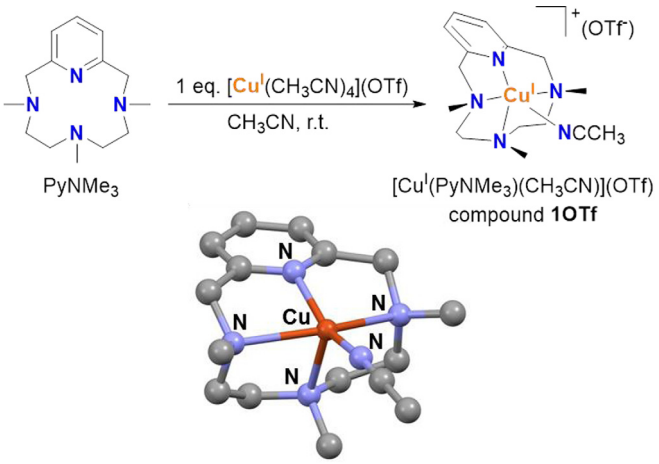

Fig. 1. Synthesis of $[Cu^{I}(PyNMe_3)(CH_3CN)](OTf)$ (**1OTf**) by reaction of $PyNMe_3$ with 1 equiv $[Cu^{I}(CH_3CN)_4](OTf)$ along with the DFT computed structure for **1**.

performed by electrospray ionization in a high-resolution mass spectrometer Bruker micrOTOF QII (Q-TOF) with a quadrupole analyzer with positive and negative ionization modes. UV–vis spectroscopy was performed on an Agilent 8453 UV–vis spectrophotometer with 1 cm quartz cells and low temperature control was achieved with a cryostat from Unisoku Scientific Instruments (Japan).

2.2. Synthesis of $[Cu^{I}(PyNMe_3)(CH_3CN)](OTf)$ (**1OTf**)

In the glovebox, $PyNMe_3$ (4.6 mg, 0.02 mmols) was dissolved in anhydrous CH_3CN (1 mL) and $[Cu^{I}(CH_3CN)_4](OTf)$ (OTf = trifluoromethanesulfonate) (7.0 mg, 0.02 mmols) was added directly as a solid. The resulting yellow mixture was stirred for 5 min. Spectroscopic and mass spectrometry analyses of the resulting solution indicated the formation of the title compound. CD_3CN was used as solvent for the NMR characterization of **1OTf**. ^{1}H-NMR (CD_3CN, 400 MHz, 298 K) δ, ppm: 7.76 (t, J = 7.8 Hz, 1H), 7.21 (d, J = 7.8 Hz, 2H), 3.95 (d, J = 15.2 Hz, 2H), 3.59 (d, J = 15.2 Hz, 2H), 2.68 (s, 6H), 2.58 (m, 2H), 2.47 (s, 3H), 2.32 (m, 2H), 2.23 (m, 2H), 1.83 (m, 2H); ^{13}C-NMR (CD_3CN, 400 MHz, 298 K) δ, ppm: 156.72, 137.81, 122.37, 63.34, 56.10, 53.93, 45.94, 44.28. HR-MS (m/z): Calc. for $[Cu^{I}(PyNMe_3)]^+$ 311.1291, found 311.1319; calc. for $[Cu^{I}(PyNMe_3)(CH_3CN)]^+$ 352.1557, found 352.1535.

2.3. Reaction of $[Cu^{I}(PyNMe_3)(CH_3CN)](OTf)$ (**1OTf**) with O_2

Samples of **1OTf** to monitor its reaction with O_2 by UV–vis spectroscopy were prepared under an inert atmosphere in the glovebox. A freshly prepared 20 mM solution of **1OTf** in CH_3CN (see above) was diluted 10 times to afford a 2 mM stock solution of the copper(I) complex in CH_3CN. A UV–Vis cuvette with a cell path length of 1 cm was charged with 100 μL of the 2 mM stock solution of **1OTf** and 1.9 mL of dry THF were added. Thus, the final concentration of **1OTf** in the sample was 0.1 mM in a CH_3CN:THF 1:19 mixture. The UV–vis cuvette was capped with a septum, taken out of the glovebox and placed in a Unisoku thermostated cell holder designed for low-temperature experiments at 173 K. After reaching thermal equilibrium a UV–vis spectrum of the starting complex was recorded. Dioxygen was injected into the cell with a balloon and a needle through the septum causing immediate reaction.

2.4. DFT calculations

All calculations were performed with the *Gaussian 09* package [11]. The B3LYP level of theory [12–15] and the 6-311G(d) basis set [16–20] were used to optimize the geometries and calculate the frequencies of each structure. Empirical dispersion was included with the Grimme's GD3BJ model [21] and solvation effects in acetonitrile were taken into account with the PCM-SMD model [22]. Also, under the same conditions, Single Point Energy (SPE) computations were performed with the cc-pVTZ basis set [23,24], a more flexible basis set, to obtain more accurate energy values. Additionally, a correcting factor in the Gibbs energy was included to compensate the change from gas-phase standard concentration of 1 atm to 1 M gas-phase standard concentration (+1.89 kcal mol^{-1} for the species and +3.64 kcal mol^{-1} for the acetonitrile, which is defined as the solvent).

3. Results and discussion

3.1. Synthesis and characterization of $[Cu^{I}(PyNMe_3)(CH_3CN)](OTf)$ (**1OTf**)

1OTf was synthesized by mixing equimolar amounts of $[Cu^{I}(CH_3CN)_4](OTf)$ and $PyNMe_3$ in the glovebox at room temperature. THF, CH_2Cl_2, acetone and CH_3CN were tested as solvents. Unfortunately, the synthesis of **1OTf** in THF, CH_2Cl_2 or acetone caused the immediate disproportionation of copper(I) as evidenced by the formation of copper mirror and a deep-blue colored solution attributable to copper(II) species. Such disproportionation reactions are not uncommon in the chemistry of copper(I) and they depend on the stability of Cu^{I} relative to Cu^{II}, which is affected by both the solvent and the ligand geometry [25–29]. In contrast, CH_3CN prevented the decomposition of copper(I), and an intense yellow solution was obtained. ESI-MS analysis of this solution by high-resolution mass spectrometry afforded a clean spectrum dominated by a peak at m/z 311.1319 with a mass value and isotopic pattern fully consistent with the desired copper(I) ion $[Cu^{I}(PyNMe_3)]^+$ (Fig. S1). Attempts to crystallize or isolate this complex were unsuccessful because disproportionation of the metal complex occurred during the crystallization or isolation process even in CH_3CN.

Although an X-ray structure of this compound could not be obtained, most likely $PyNMe_3$ behaves as a tetradentate ligand as previously observed for the corresponding iron(II) and cobalt(II) compounds [9,10]. DFT calculations were performed in order to get a picture of the possible structure of the copper(I) complex (see SI). From all the calculated structures, the most stable geometry corresponded to a C_s symmetric distorted square pyramidal compound with the copper(I) center coordinated to the four nitrogens of the $PyNMe_3$ ligand and to one CH_3CN ligand (*trans* to the pyridine ring), yielding $[Cu^{I}(PyNMe_3)(CH_3CN)](OTf)$ as the general formula for the copper(I) complex of the $PyNMe_3$ ligand (**1OTf**, Fig. 1). Optimization of the structures where the CH_3CN ligand is bound *trans* to the N-methyl group always led to the formation of the isomer with the CH_3CN *trans* to the pyridine. The optimized geometry with no coordinated CH_3CN was less stable by 9.3 kcal mol^{-1} (Gibbs free energy difference, ΔG°) and no structure could be optimized with the copper(I) center ligated to two acetonitrile molecules. The optimized geometry for $[Cu^{I}(PyNMe_3)(CH_3CN)]^+$ (**1**) is in agreement with the structures reported for copper(I) complexes with other tetradentate ligands, in which a CH_3CN molecule fullfills a square-pyramidal pentadentate coordination environment [30,31]. Indeed, the high-resolution ESI-MS spectrum of **1OTf** (Fig. S1) also showed the presence of a small peak corresponding to the coordination of one CH_3CN mole-

cule to the copper center ($[Cu^{I}(PyNMe_3)(CH_3CN)]^+$, m/z 352.1535), which further supports the proposed formulation.

NMR characterization of **1OTf** could be achieved by performing its synthesis in CD_3CN and transferring the resulting solution in an NMR tube inside the glovebox. To our delight the ^1H NMR spectrum of **1OTf** exhibited well resolved signals that could be assigned with the help of ^{13}C and two-dimensional NMR experiments (no traces of unreacted $PyNMe_3$ were detected). This observation is quite remarkable because copper(I) complexes are intrinsically labile compounds (d^{10} metal ions) that tend to give fluxional structures with broadened NMR signals [31,32] In this case, the $PyNMe_3$ ligand confers certain rigidity to the metal center, so that well resolved signals are observed.

According to the NMR data compound **1OTf** presents a C_s symmetry, which is consistent with the computed structure (Fig. 1). This is also in agreement with the C_s symmetry previously observed for paramagnetic $[Fe^{II}(PyNMe_3)(CH_3CN)_2](OTf)_2$ and $[Co^{II}(PyNMe_3)(CH_3CN)_2](OTf)_2$ complexes [9,10], suggesting that a similar folding and coordination of the $PyNMe_3$ ligand may be taking place around the copper(I) system. Accordingly, the aromatic region consists of a triplet at 7.76 ppm and a doublet at 7.21 ppm corresponding to the γ proton and to the two equivalent β protons of the pyridine ring, respectively. The four methylenic protons next to the pyridine appear as two well defined doublets at 3.95 and 3.60 ppm, indicating that the two protons on the same carbon are diastereotopic, while two equivalent N-methyl groups appear as a singlet at 2.68 ppm and the other N-methyl unit at 2.47 ppm (Fig. 2). Assignment of the methylenic protons between the aliphatic nitrogens, which appear as four different multiplets in the 2.6–1.8 ppm range, was more complicated. However, with the help of a NOESY experiment the interactions of some of these protons with one of the two singlets of the methyl groups could be observed (Fig. 3a). These through-space correlations together with an HSQC experiment (Figs. 3b and S3) allowed the allocation of these protons on a particular carbon center of the $PyNMe_3$ structure and their orientation with respect to the methyl groups could be unequivocally established (see assignments in Fig. 2).

3.2. Reaction of $[Cu^{I}(PyNMe_3)(CH_3CN)](OTf)$ (**1OTf**) with O_2

As copper-dioxygen adducts are known to be intensely colored compounds, the reaction of compound **1OTf** towards O_2 was monitored by UV–vis spectroscopy at low temperature. Initial attempts were performed at −40 °C and using CH_3CN as solvent, but no absorption band that could be attributed to the formation of a copper-dioxygen adduct was observed. Instead, direct oxidation of **1OTf** to copper(II) was observed. In an attempt to further lower the temperature and trap a putative copper-dioxygen adduct, solvents with lower melting points were used. As detailed above, the use of THF, CH_2Cl_2 or acetone as solvents caused the immediate decomposition of **1OTf**, so that the presence of a certain proportion of CH_3CN was necessary in order to keep the nature of the starting reagent. After optimization, we found that reaction of **1OTf** with O_2 at −100 °C in a CH_3CN:THF 1:19 solvent mixture caused an immediate color change from yellow to deep brown, which was accompanied by the appearance of an intense absorption band at λ_{max} = 353 nm (ε > 17200 M^{-1} cm^{-1} per Cu dimer) in the UV–vis spectrum (Fig. 4). This new species (**2**) reached its maximum

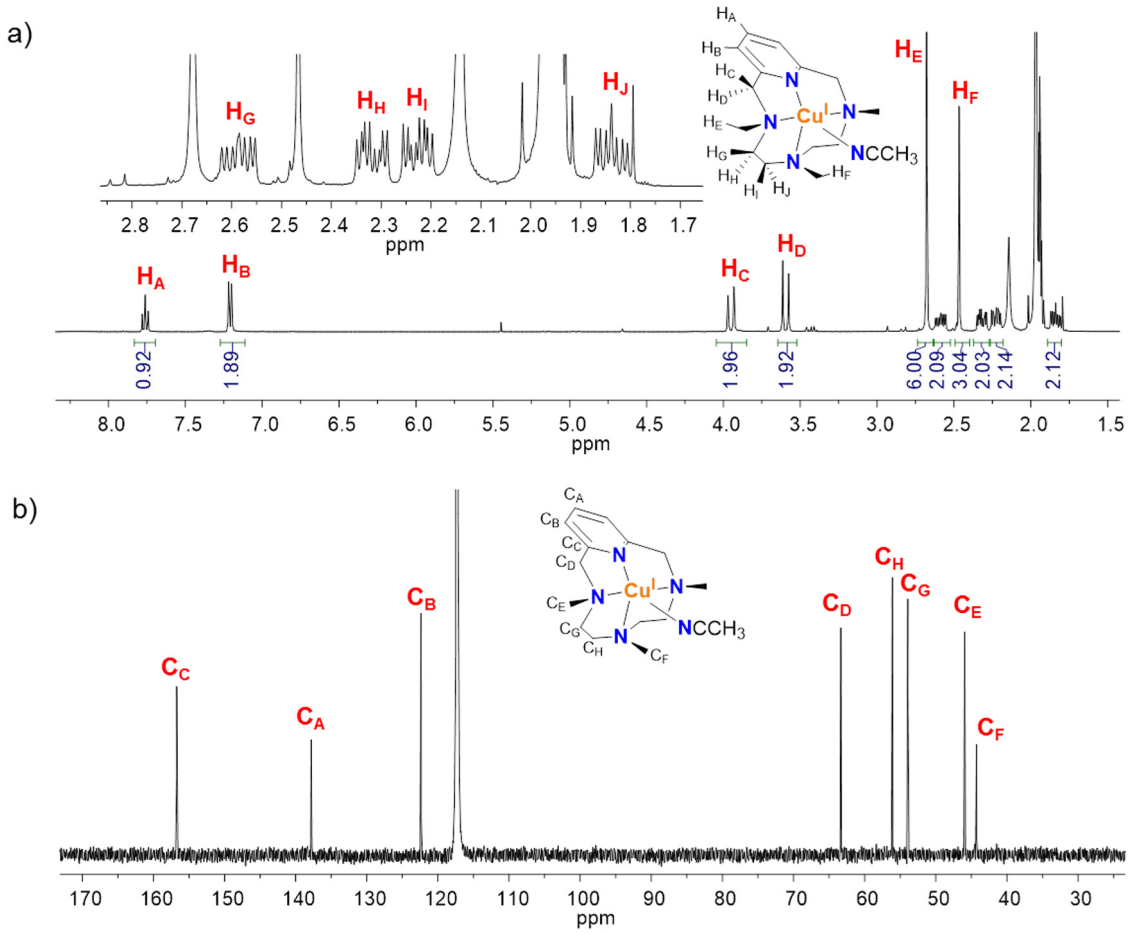

Fig. 2. ^1H-NMR (a) and ^{13}C-NMR (b) spectra of $[Cu^{I}(PyNMe_3)(CH_3CN)](OTf)$ (**1OTf**) in CD_3CN at 298 K.

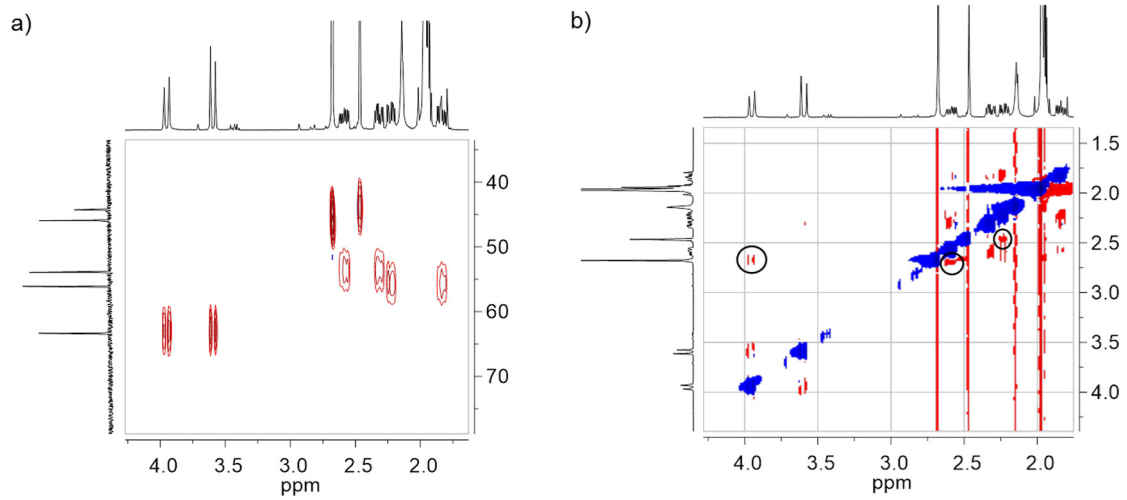

Fig. 3. a) Expanded view of the HSQC spectrum of [Cu^{I}(PyNMe$_3$)(CH$_3$CN)](OTf) (**1OTf**) in CD$_3$CN at 298 K. b) Expanded view of the NOESY spectrum of [Cu^{I}(PyNMe$_3$)(CH$_3$CN)](OTf) (**1OTf**) in CD$_3$CN at 298 K. Remarkable NOESY cross-peaks are circled.

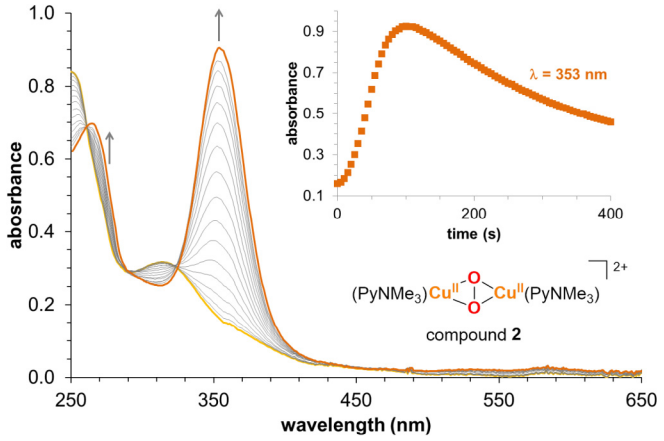

Fig. 4. UV–vis spectra corresponding to the reaction of [Cu^{I}(PyNMe$_3$)(CH$_3$CN)](OTf) (**1OTf**, 0.1 mM) with O$_2$ in a CH$_3$CN:THF 1:19 solvent mixture at −100 °C. Inset: time trace of the band at λ_{max} = 353 nm.

absorbance after 120 s but it immediately decomposed ($t_{1/2}$ = 6 min at −100 °C). By analogy to previously reported Cu$_n$:O$_2$ systems, **2** may correspond to a μ-η^2:η^2-peroxodicopper(II) (**^{S}P**) complex, which typically exhibit one single intense absorption band between 340 and 380 nm [6]. This species would be formed by reaction of two molecules of **1** with a single O$_2$ molecule. MS analysis of the reaction mixture after the self-decay of **2** indicated the formation of copper(II) species coordinated to the unchanged PyNMe$_3$ ligand.

^{S}P species are often considered the arene hydroxylating agent in tyrosinase [33], which catalyzes the *ortho*-hydroxylation of phenols to catechols and subsequent two-electron oxidation to *ortho*-quinones using molecular O$_2$ as oxidant. The biological relevance of **^{S}P** compounds has also been substantiated by model systems [34–41], although isomerization towards the bis(μ-oxo) dicopper(III) isomer has been also proposed to precede arene hydroxylation [42–46]. In order to check if **2** behaved as a functional model of tyrosinase, its reaction with sodium *para*-chlorophenolate was monitored by UV–vis spectroscopy. Upon maximum formation of **2**, a THF solution containing 10 equiv of sodium *para*-chlorophenolate was added into the cuvette. This caused the fast decay of the characteristic band of **2** at 353 nm. Unfortunately, analysis of the crude did not show the presence of any catechol product, indicating that compound **2** fails in eliciting tyrosinase-like reactivity. Most probably, the rigid tetradentate PyNMe$_3$ ligand strongly coordinates to the copper center, affording a coordinatively saturated **^{S}P** unit. This prevents simultaneous binding of peroxide and the phenolic substrate to the same copper center, a mandatory requirement necessary for the attack of the peroxide unit over the aromatic ring. A similar situation has been observed in **^{S}P** species derived from 1,4,7-tri-*tert*-butyl-1,4,7-triazacyclononane ring, in which the steric hindrance imposed by the ligand makes the copper center inaccessible to phenolates, and thus tyrosinase-like reactivity is not detected [47]. In the case of **2**, the interaction of the phenolic substrate causes the unproductive decomposition of the **^{S}P** unit without substrate hydroxylation. As a matter of fact, **^{S}P** species usually bear tridentate or bidentate nitrogen-based ligands that leave room for interaction with the substrate [7,34]. In the same line, the typical electrophilic sulfide oxidation carried out by **^{S}P** compounds was not observed for **2** and the addition of 4-methoxythioanisole to **2** only afforded 2% of the corresponding sulfoxide oxidation product.

4. Conclusions

In this work we have described the synthesis and characterization of the copper(I) complex [Cu^{I}(PyNMe$_3$)(CH$_3$CN)](OTf) (**1OTf**). Despite the fact that no crystal structure has been obtained for this compound, comprehensive NMR analyses together with DFT calculations have allowed to unequivocally establish the structure of this compound in solution. Remarkably, **1OTf** is highly reactive with O$_2$ at low temperature and this reaction leads to the formation of a μ-η^2:η^2-peroxodicopper(II) (**2**) as ascertained by UV–vis spectroscopy. Despite the fact that such species are known to be key intermediates in the mechanism of reaction of the copper enzyme tyrosinase, in the current system no phenol *ortho*-hydroxylation analogous to that observed for the enzyme has been detected. We speculate that the rigid tetradentate structure of the PyNMe$_3$ ligand affords a coordinatively saturated **^{S}P** species with no capacity to coordinate any exogenous substrate, which contrasts with the lower coordination numbers of tyrosinase functional models. Compound **2** constitutes the first example of a **^{S}P** species with a tetradentate N-based ligand and adds to the growing family of bioinspired copper(I) complexes capable of stabilizing Cu$_2$:O$_2$ adducts, which are biologically relevant.

Acknowledgements

We acknowledge financial support from the European Research Council for the Starting Grant Project ERC-2011-StG-277801 to X.R. and from MINECO of Spain for project CTQ2016-77989-P to A.C. and X.R., and project CTQ2015-70795-P to M.C. We also thank Generalitat de Catalunya for project 2014SGR862. X.R. and M.C. thank Generalitat de Catalunya for ICREA Academia awards.

Appendix A. Supplementary data

Supplementary data associated with this article can be found, in the online version, at http://dx.doi.org/10.1016/j.ica.2017.08.061.

References

[1] E.I. Solomon, D.E. Heppner, E.M. Johnston, J.W. Ginsbach, J. Cirera, M. Qayyum, M.T. Kieber-Emmons, C.H. Kjaergaard, R.G. Hadt, L. Tian, Chem. Rev. 114 (2014) 3659–3853.
[2] I. Bento, M.A. Carrondo, P.F. Lindley, J. Biol. Inorg. Chem. 11 (2006) 539–547.
[3] J.P. Klinman, Chem. Rev. 96 (1996) 2541–2562.
[4] E.I. Solomon, U.M. Sundaram, T.E. Machonkin, Chem. Rev. 96 (1996) 2563–2606.
[5] E.A. Lewis, W.B. Tolman, Chem. Rev. 104 (2004) 1047–1076.
[6] L.M. Mirica, X. Ottenwaelder, T.D.P. Stack, Chem. Rev. 104 (2004) 1013–1046.
[7] C.E. Elwell, N.L. Gagnon, B.D. Neisen, D. Dhar, A.D. Spaeth, G.M. Yee, W.B. Tolman, Chem. Rev. 117 (2017) 2059–2107.
[8] J. Serrano-Plana, A. Aguinaco, R. Belda, E. García-España, M.G. Basallote, A. Company, M. Costas, Angew. Chem. Int. Ed. 55 (2016) 6310–6314.
[9] J. Serrano-Plana, W.N. Oloo, L. Acosta-Rueda, K.K. Meier, B. Verdejo, E. García-España, M.G. Basallote, E. Münck, L. Que, A. Company, M. Costas, J. Am. Chem. Soc. 137 (2015) 15833–15842.
[10] B. Shin, K.D. Sutherlin, T. Ohta, T. Ogura, E.I. Solomon, J. Cho, Inorg. Chem. 55 (2016) 12391–12399.
[11] M.J. Frisch, G.W. Trucks, H.B. Schlegel, G.E. Scuseria, M.A. Robb, J.R. Cheeseman, G. Scalmani, V. Barone, B. Mennucci, G.A. Petersson, H. Nakatsuji, M. Caricato, X. Li, H.P. Hratchian, A.F. Izmaylov, J. Bloino, G. Zheng, J.L. Sonnenberg, M. Hada, M. Ehara, K. Toyota, R. Fukuda, J. Hasegawa, M. Ishida, T. Nakajima, Y. Honda, O. Kitao, H. Nakai, T. Vreven, J.J.A. Montgomery, J.E. Peralta, F. Ogliaro, M. Bearpark, J.J. Heyd, E. Brothers, K.N. Kudin, V.N. Staroverov, R. Kobayashi, F. Normand, K. Raghavachari, A. Rendell, J.C. Burant, S.S. Iyengar, J. Tomasi, M. Cossi, N. Rega, J.M. Millam, M. Klene, J.E. Knox, J.B. Cross, V. Bakken, C. Adamo, J. Jaramillo, R. Gomperts, R.E. Stratmann, O. Yazyev, A.J. Austin, R. Cammi, C. Pomelli, J.W. Ochterski, R.L. Martin, K. Morokuma, V.G. Zakrzewski, G.A. Voth, P. Salvador, J.J. Dannenberg, S. Dapprich, A.D. Daniels, O. Farkas, J.B. Foresman, J.V. Ortiz, J. Cioslowski, D.J. Fox, Gaussian Inc.: Wallingford CT, 2013.
[12] A.D. Becke, J. Chem. Phys. 98 (1993) 1372–1377.
[13] C. Lee, W. Yang, R.G. Parr, Phys. Rev. B 37 (1988) 785–789.
[14] S.H. Vosko, L. Wilk, M. Nusair, Can. J. Phys. 58 (1980) 1200–1211.
[15] P.J. Stephens, F.J. Devlin, C.F. Chabalowski, M.J. Frisch, J. Phys. Chem. 98 (1994) 11623–11627.
[16] A.D. McLean, G.S. Chandler, J. Chem. Phys. 72 (1980) 5639–5648.
[17] R. Krishnan, J.S. Binkley, R. Seeger, J.A. Pople, J. Chem. Phys. 72 (1980) 650–654.
[18] A.J.H. Wachters, J. Chem. Phys. 52 (1970) 1033–1036.
[19] P.J. Hay, J. Chem. Phys. 66 (1977) 4377–4384.
[20] K. Raghavachari, G.W. Trucks, J. Chem. Phys. 91 (1989) 1062–1065.
[21] S. Grimme, S. Ehrlich, L. Goerigk, J. Comput. Chem. 32 (2011) 1456–1465.
[22] A.V. Marenich, C.J. Cramer, D.G. Truhlar, J. Phys. Chem. B 113 (2009) 6378–6396.
[23] R.A. Kendall, T.H. Dunning Jr., R. Harrison, J J. Chem. Phys. 96 (1992) 6796–6806.
[24] E.R. Davidson, Chem. Phys. Lett. 260 (1996) 514–518.
[25] M. Becker, F.W. heinemann, S. Schindler, Chem. Eur. J. 5 (1999) 3124–3129.
[26] T. Osako, Y. Ueno, Y. Tachi, S. Itoh, Inorg. Chem. 42 (2003) 8087–8097.
[27] I. Persson, J.E. Penner-Hahn, K.O. Hodgson, Inorg. Chem. 32 (1993) 2497–2501.
[28] D. Petrovic, T. Bannenberg, S. Randoll, P.G. Jones, M. Tamm, Dalton Trans. (2007) 2812–2822.
[29] F.A. Cotton, G. Wilkinson, C.A. Murillo, M. Bochmann, Advanced Inorganic Chemistry, John Wiley & Sons Inc., New York, 1999. pp. 855–856.
[30] H. Börzel, P. Comba, K.S. Hagen, M. Kerscher, H. Pritzkow, M. Schatz, S. Schindler, O. Walter, Inorg. Chem. 41 (2002) 5440–5452.
[31] Z. Tyeklar, R.R. Jacobson, N. Wei, N.N. Murthy, J. Zubieta, K.D. Karlin, J. Am. Chem. Soc. 115 (1993) 2677–2689.
[32] H. Börzel, P. Comba, K.S. Hagen, C. Katsichtis, H. Pritzkow, Chem. Eur. J. 6 (2000) 914–919.
[33] Y. Matoba, T. Kumagai, A. Yamamoto, H. Yoshitsu, M. Sugiyama, J. Biol. Chem. 281 (2006) 8981–8990.
[34] W. Keown, J.B. Gary, T.D.P. Stack, J. Biol. Inorg. Chem. 22 (2017) 289–305.
[35] J. Serrano-Plana, I. Garcia-Bosch, A. Company, M. Costas, Acc. Chem. Res. 48 (2015) 2397–2406.
[36] A. Company, in: Ideas in Chemistry and Molecular Sciences, B. Pignataro (Ed.), Wiley-VCH Verlag: Weinheim, 2010.
[37] M. Rolff, J. Schottenheim, H. Decker, F. Tuczek, Chem. Soc. Rev. 40 (2011) 4077–4098.
[38] C. Citek, C.T. Lyons, E.C. Wasinger, T.D.P. Stack, Nat. Chem. 4 (2012) 317–322.
[39] S. Itoh, H. Kumei, M. Taki, S. Nagatomo, T. Kitagawa, S. Fukuzumi, J. Am. Chem. Soc. 123 (2001) 6708–6709.
[40] L. Santagostini, M. Gullotti, E. Monzani, L. Casella, R. Dillinger, F. Tuczek, Chem. Eur. J. (2000) 519–522.
[41] M.S. Askari, K.V.N. Esguerra, J.-P. Lumb, X. Ottenwaelder, Inorg. Chem. 54 (2015) 8665–8672.
[42] A. Company, S. Palavicini, I. Garcia-Bosch, R. Mas-Ballesté, L. Que, E.V. Rybak-Akimova, L. Casella, X. Ribas, M. Costas, Chem. Eur. J. 14 (2008) 3535–3538.
[43] S. Herres-Pawlis, P. Verma, R. Haase, P. Kang, C.T. Lyons, E.C. Wasinger, U. Flörke, G. Henkel, T.D.P. Stack, J. Am. Chem. Soc. 131 (2009) 1154–1169.
[44] L. Chiang, W. Keown, C. Citek, E.C. Wasinger, T.D.P. Stack, Angew. Chem. Int. Ed. 55 (2016) 10453–10457.
[45] L.M. Mirica, M. Vance, D.J. Rudd, B. Hedman, K.O. Hodgson, E.I. Solomon, T.D.P. Stack, Science 308 (2005) 1890–1892.
[46] J. Becker, P. Gupta, F. Angersbach, F. Tuczek, C. Näther, M.C. Holthausen, S. Schindler, Chem. Eur. J. 21 (2015) 11735–11744.
[47] G.J. Karahalis, A. Thangavel, B. Chica, J. Bacsa, R.B. Dyer, C.C. Scarborough, Inorg. Chem. 55 (2016) 1102–1107.

Chapter IV. Mechanistic Insights into the ortho-Defluorination-Hydroxylation of 2-Halophenolates Promoted by a Bis(μ-oxo)dicopper(III) Complex

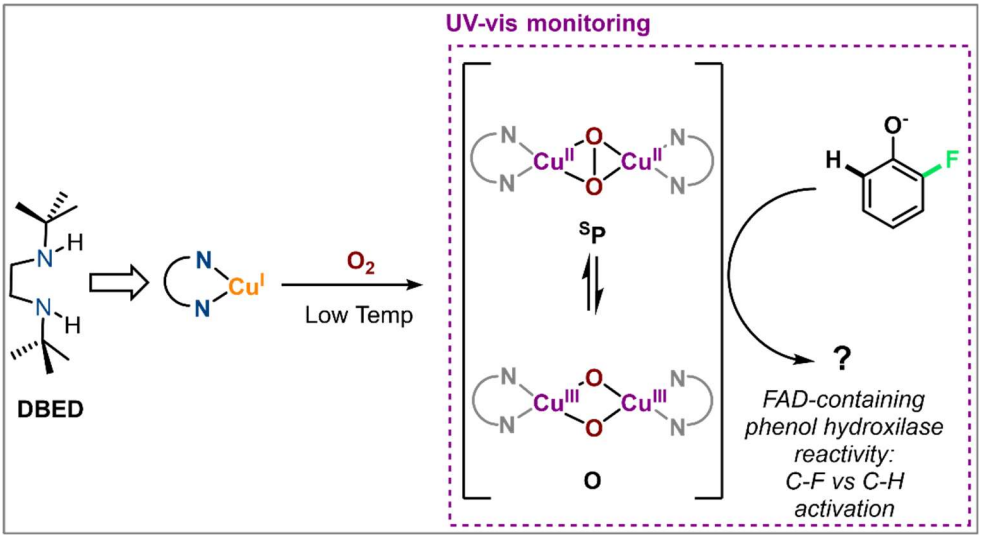

This chapter corresponds to the following publication:

Pau Besalú-Sala,[‡] Carla Magallón,[‡] Miquel Costas,* Anna Company*, Josep M. Luis* ([‡] equal contribution). Reprinted with permission from *Inorg. Chem.*, **2020**, *59*, 23, 17018 – 17027. Copyright © 2020 American Chemical Society.

Inorganic Chemistry

pubs.acs.org/IC

Article

Mechanistic Insights into the *ortho*-Defluorination-Hydroxylation of 2-Halophenolates Promoted by a Bis(μ-oxo)dicopper(III) Complex

Pau Besalú-Sala,[‡] Carla Magallón,[‡] Miquel Costas,* Anna Company,* and Josep M. Luis*

Cite This: *Inorg. Chem.* 2020, 59, 17018−17027

Read Online

ACCESS | Metrics & More | Article Recommendations | Supporting Information

ABSTRACT: C−F bonds are one of the most inert functionalities. Nevertheless, some $[Cu_2O_2]^{2+}$ species are able to defluorinate-hydroxylate *ortho*-fluorophenolates in a chemoselective manner over other *ortho*-halophenolates. Albeit it is known that such reactivity is promoted by an electrophilic attack of a $[Cu_2O_2]^{2+}$ core over the arene ring, the crucial details of the mechanism that explain the chemo- and regioselectivity of the reaction remain unknown, and it has not being determined either if $Cu^{II}_2(\eta^2{:}\eta^2\text{-}O_2)$ or $Cu^{III}_2(\mu\text{-}O)_2$ species are responsible for the initial attack on the arene. Herein, we present a combined theoretical and experimental mechanistic study to unravel the origin of the chemoselectivity of the ortho-defluorination-hydroxylation of 2-halophenolates by the $[Cu_2(O)_2(DBED)_2]^{2+}$ complex (DBED = *N*,*N*′-di-*tert*-butylethylenediamine). Our results show that the equilibria between (side-on)peroxo (**P**) and bis(μ-oxo) (**O**) isomers plays a key role in the mechanism, with the latter being the reactive species. Furthermore, on the basis of quantum-mechanical calculations, we were able to rationalize the chemoselective preference of the $[Cu_2(O)_2(DBED)_2]^{2+}$ catalyst for the C−F activation over C−Cl and C−H activations.

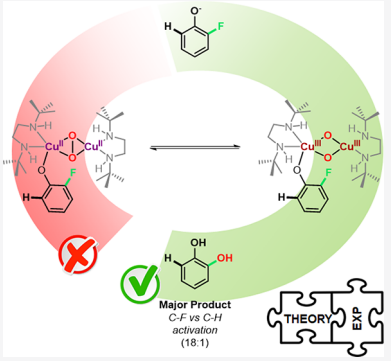

INTRODUCTION

The high electronegativity of fluorine strongly polarizes and shortens C−F bonds, reinforcing the ionic component of the chemical bond. As a consequence, the C−F bond has the largest C−X (X = F, Cl, Br, I) dissociation energy (up to 130 kcal·mol^{-1}).[1] Thus, C−F is considered the most inert organic functionality, which confers a high thermal stability to the fluorinated organic compounds. On the one hand, because of the increment of the lipophilicity caused by the fluorination, fluorinated drugs present larger in vivo residence times than their nonfluorinated counterparts.[2,3] Therefore, fluorinated compounds are of great interest in medicinal chemistry and agrochemistry.[2] In addition, fluorinated compounds are also currently in the spotlight, since their metabolization is very difficult due to the aforementioned high stability, which triggers their bioaccumulation and environmental persistence. This scenario pops up a dilemma, since we are facing two sides of the same coin. The particular properties of fluorinated organic molecules make them interesting for medicinal chemistry or agrochemistry. However, they are also responsible for their bioaccumulation and biomagnification.[4,5] Therefore, finding strategies to promote the activation and subsequent transformation of C−F bonds into more reactive functionalities is the key to facilitate the degradation of the fluorinated organic molecules.

In nature, aliphatic and aromatic fluorinated compounds can be enzymatically functionalized. In particular, the defluorination of aromatics occurs in cytochrome P450, chloroperoxidase, and flavin adenine dinucleotide (FAD)-containing phenol hydroxylases, which can convert 2-fluorophenols into the corresponding chatecols.[6−8] On the contrary, tyrosinase, which catalyzes the ortho-hydroxylation of phenols, cannot *ortho*-defluorinate-hydroxylate 2-fluorophenols.[9,10] Indeed, 2-fluorophenols inhibit the catalytic activity of tyrosinase. The active species of this enzyme consists of a ($\eta^2{:}\eta^2$-peroxo)-dicopper(II) species (**P**), which is able to hydroxylate phenols through an electrophilic aromatic substitution. Some of us have shown that bioinspired systems such as $[Cu^{III}_2(\mu\text{-}O)_2(m\text{-}XYL^{MeAN})]^{2+}$ and $[Cu_2(\mu{-}\eta^2{:}\eta^2\text{-}O_2)(DBED)_2]^{2+}$ (Figure 1) elicit the hydroxylation-defluorination of 2-fluorophenolates to give the corresponding catechols (XYL = meta-xylyl-N,N,N′,N′,N′′-pentamethyldipropylenetriamine; DBED = *N*,*N*′-di-*tert*-butylethylenediamine).[11] In contrast, other model systems such as $[Cu_2(\mu{-}\eta^2{:}\eta^2\text{-}O_2)(L^{Py2Bz})_2]^{2+}$ are unable to cleave the C−F bond. Although the peroxo (**P**) species is the most stable isomer of both $[Cu_2(\mu{-}\eta^2{:}\eta^2\text{-}O_2)(DBED)_2]^{2+}$ and $[Cu_2(\mu{-}\eta^2{:}\eta^2\text{-}O_2)(L^{Py2Bz})_2]^{2+}$, the former is in equilibrium with the bis(μ-oxo)dicopper(III) (**O**) isomer. This led us to consider that the latter isomer is the active species in the defluorination of 2-fluorophenols (Figure 1).[12−14]

Received: July 28, 2020
Published: November 6, 2020

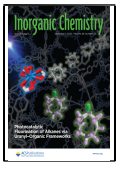

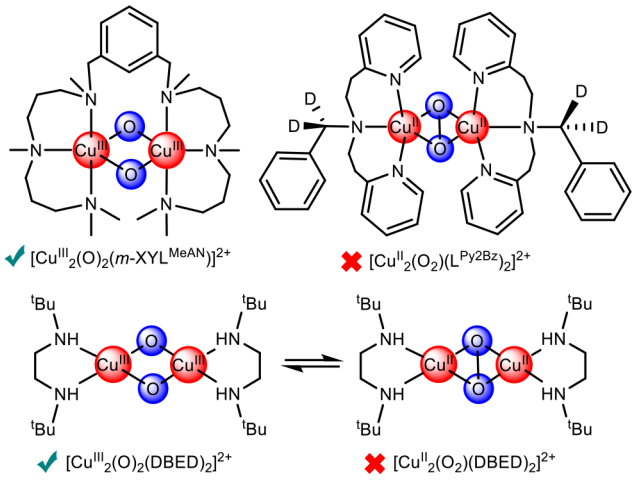

Figure 1. Three Cu_2O_2-based species. Green tick marks indicate that defluorination-hydroxylation products are obtained, whereas the red cross indicates the opposite.

In the case of $[Cu^{III}_2(\mu\text{-}O)_2(m\text{-}XYL^{MeAN})]^{2+}$ only the **O** isomer is observed,[15] further supporting the idea that this isomer is the only one competent to perform the defluorination reaction.[11] Of relevance to these observations, high-valent iron-oxo and iron-manganese species have also shown analogous reactivity.[16−20] In addition, de Visser and co-workers showed that a μ-nitrido diiron phthalocyanine complex is able to activate and hydroxylate the C−F bonds of hexafluorobenzene derivatives.[21]

In this work, theory and experiments are combined to determine the details of the mechanism of the selective ortho-hydroxylation−defluorination of 2-fluorophenolates with $[Cu_2O_2(DBED)_2]^{2+}$ (**1**), a compound first described by Stack and co-workers.[12,13] Specifically, our study was directed to address the following questions; to unravel which is the actual defluorination-oxygenation agent, either the **P** or **O** species, ($\mathbf{1}^{P}$ and **1°**, Figure 2). Both isomers have been

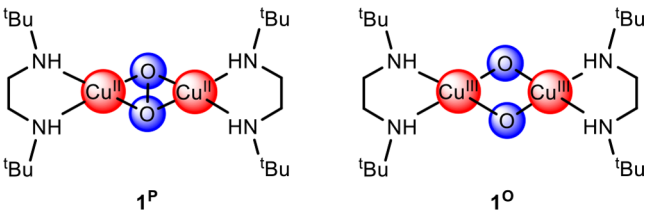

Figure 2. Schematic representation of the two studied isomers of $[Cu_2O_2(DBED)_2]^{2+}$ (**1**): the (η^2:η^2-peroxo)dicopper(II) species ($\mathbf{1}^{P}$, left) and the bis(μ-oxo)dicopper(III) species (**1°**, right).

experimentally detected for this system: The **P** isomer is generated upon reaction of the copper(I) precursor with O_2, while the **O** compound is experimentally detected upon coordination of a phenolic substrate to **P**. A second aspect to clarify is the origin of the selective oxygenation at the *ortho* C−F over the *ortho* C−H position in the reaction with 2-fluorophenols, despite the former being devised as more electron poor than the latter. Finally, the study aimed at explaining the reason for C−Cl bonds, weaker than C−F bonds, remaining unreactive.

COMPUTATIONAL DETAILS

The computationally aided modeling of $[Cu_2O_2]^{2+}$-based compounds for the defluorination-hydroxylation of fluorophenols has been exploited in the past decade, yet it is not an easy task.[22−25] Because of the high number of electrons that must be correlated, multireference methods have not been extensively used to study $[Cu_2O_2]^{2+}$ reactivity. Density functional theory (DFT) arises as a powerful alternative to study these compounds due to its good accuracy/cost balance.[26,27] However, some important considerations must be taken into account. In particular, and of high interest for the current manuscript, is that an unequivocal characterization of $[Cu_2O_2]^{2+}$ isomerization equilibria is certainly quite difficult to achieve by DFT means.[26,28,29] Whereas (end-on)peroxo/(side-on)peroxo isomerization equilibria is usually well-described by hybrid functionals, (side-on)peroxo/bis(μ-oxo) (**P**/**O**) equilibria presented by **1** is better described by pure functionals.[30] Hybrid functionals tend to understabilize bis(μ-oxo) species, the magnitude of the understabilization being proportional to the amount of exact exchange introduced in the functional definition. Therefore, we performed the DFT calculations using a pure functional. Nevertheless, the DFT results of the **P**/**O** equilibria, which have a key relevance in the present manuscript, were improved with the domain-based local pair natural orbital coupled cluster method (DLPNO-CCSD(T)) calculations, which produce more reliable predictions than DFT.[31−34]

DFT electronic structure calculations were performed with the Gaussian 09 software package[35] using the spin-unrestricted UM06-L[36] density functional. For the geometric optimizations the molecular orbitals were spanned into the Pople-type 6-311G(d) basis set[37,38] (Method A). Singlet (both open and closed shell) and triplet spin symmetries were explored, reporting always the most stable one. The nature of the stationary points was determined by analytical frequency calculations. To compute subsequent Gibbs free energy corrections, the temperature was set up at 183.15 K to simulate the experimental conditions. Furthermore, the connection between the transition state (TS) and intermediates was unambiguously established by intrinsic reaction path calculations (IRCs),[39] using the local quadratic approximation to determine the prediction step.[40] All DFT energy values were systematically improved by evaluating the electronic structures of the optimized geometries using the Dunning's correlation consistent triple-ζ basis set cc-pVTZ, suppressing the functions with higher angular momentum only for the Cu atoms (cc-pVTZ-g)[41,42] and introducing solvation (acetone) effects through the universal solvation model (SMD) (Method B).[43] Spin contamination was removed if necessary by using the following expressions[26,44,45]

$$E_{spin-corr} = \frac{E_S - aE_{(S+1)}}{1 - a} \quad (1)$$

$$a = \frac{\langle S_S^2 \rangle - S\cdot(S+1)}{\langle S_{(S+1)}^2 \rangle - S\cdot(S+1)} \quad (2)$$

where E_S and $E_{(S+1)}$ are the broken-symmetry DFT energies for the S and S+1 spin states, respectively, obtained at UM06-L/cc-pVTZ-g ∼ SMD level of theory. $\langle S_s^2 \rangle$ and $\langle S_{(s+1)}^2 \rangle$ are the expectation values of the square total spin momentum obtained at the same level of theory for the S and S+1 spin states, respectively. And $E_{spin-corr}$ is the spin-corrected DFT

https://dx.doi.org/10.1021/acs.inorgchem.0c02246
Inorg. Chem. 2020, 59, 17018−17027

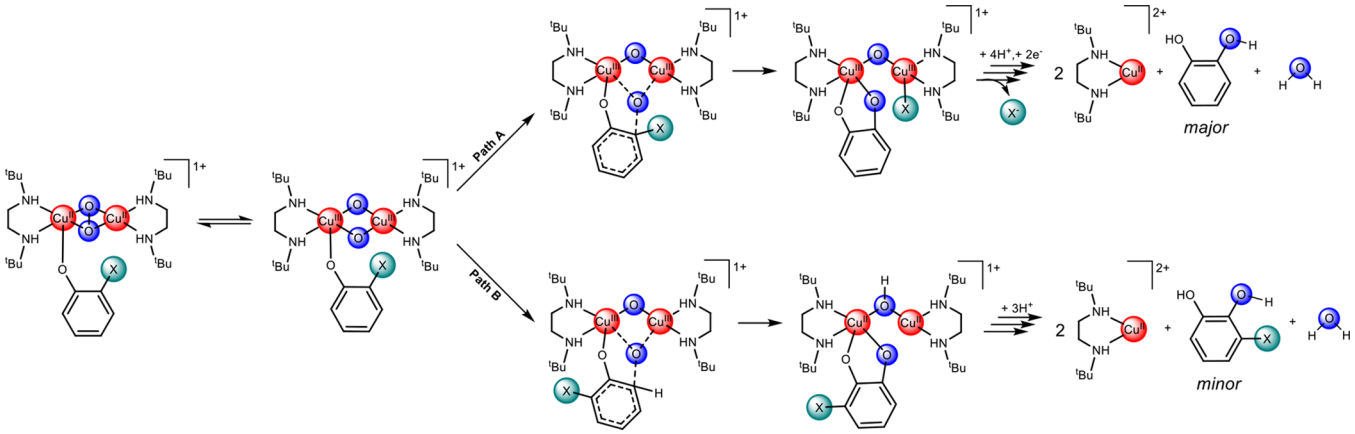

Figure 3. Schematic representation of the *ortho*-defluorination-hydroxylation reaction mechanism (Path A) and the competing *ortho*-hydroxylation reaction mechanism (Path B). The proton source in the final steps is $HClO_4$ (0.5 M). In Path A, the source of the electrons of the last step is given by an external reducing agent (ascorbate or Zn powder)[11] or, in its absence, by an intermolecular decomposition of a second Cu_2O_2 complex.

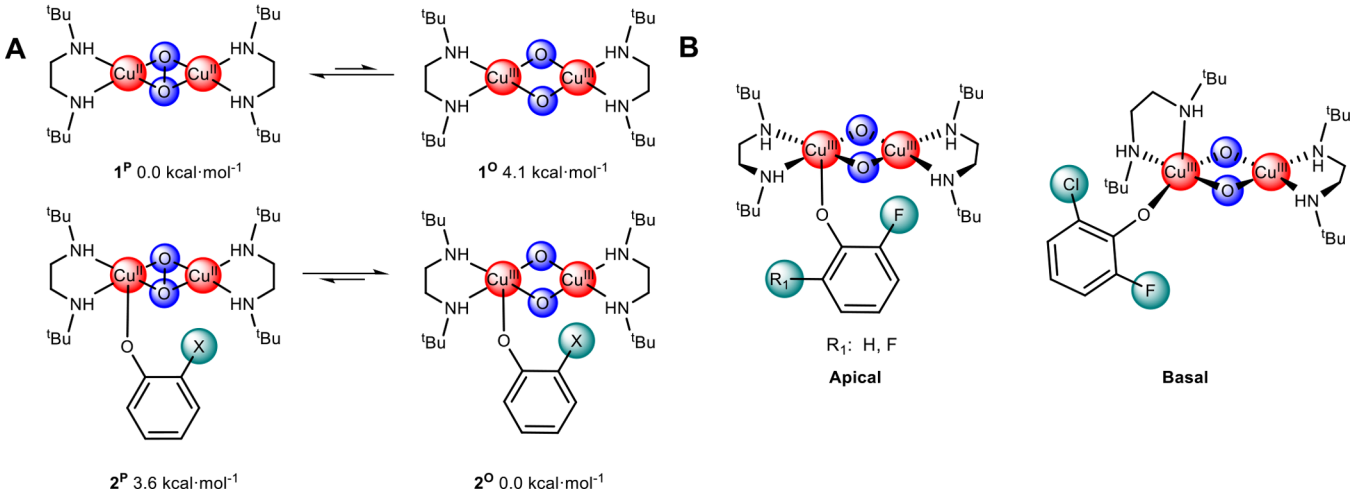

Figure 4. (A) Relative stability (kcal·mol^{-1}) of **1**^{P}/**1**° and **2**^{P}/**2**° computed at the DLPNO-CCSD(T)/cc-pVTZ ~ SMD//M06-L/6−331G(d) level. (B) Reactive **2**° conformers for 2-fluorophenolate and 2,6-difluorophenolate (apical coordination) and 6-chloro-2-fluorophenolate (basal coordination).

electronic energy. In this manner, the *a* parameter takes into account the amount of spin contamination on the S state due to the S+1 state.

ORCA 4.1.0 software package[46] was used for the domain-local pair natural orbitals coupled cluster with singles, doubles, and perturbative triples, DLPNO-CCSD(T), single-point energy calculations, together with the cc-pVTZ basis set (and cc-pVTZ as auxiliary basis) and SMD solvent corrections. Tight PNO cutoffs were set for the transformation of the orbitals into the DLPNOs. A tight self-consistent field (SCF) criterion was set for the convergence of the SCF and the coupled cluster (CC) iterations.

The values of T1 diagnostic of all DLPNO-CCSD calculations were always lower than 0.024, indicating that most of the correlation energy is captured by the DLPNO-CCSD(T) method. Therefore, there is no evidence of requiring multireferential calculations to obtain a good description of the studied species.

RESULTS AND DISCUSSION

To address the questions described at the end of the Introduction, we performed a detailed computational study of the *ortho*-defluorination-hydroxylation mechanism of 2-fluorophenolate and 2,6-difluorophenolate promoted by **1** (Figure 3).

Furthermore, we investigated the chemo-selectivity that **1** exhibits on the C−F bond activation over C−H or C−Cl bond activations for 2-fluorophenolate and 2-chloro-6-fluorophenolate. Therefore, a total of five different possible reaction paths were studied (Figure 5).

The proposed mechanism of *ortho*-defluorination-hydroxylation of 2-fluorophenolate compounds performed by **1** presents two principal steps (Figure 3). The first main step is the electrophilic attack of the $[Cu_2O_2]^{2+}$ core to the aromatic ring, which implies the pyramidalization of the attacked carbon. This C−X activation can occur at each of the two phenolate *ortho* positions, giving two possible reaction paths, Path A or Path B, which will be indicated using either A or B subscripts in the name of the intermediates and TSs. The second main step is given by the rearomatization of the substrate that leads to the catechol product either by the transfer of the halogen to one of the metals (Path A, *ortho*-defluorination-hydroxylation reaction) or through the proton abstraction by the remaining oxygen atom of the core (Path B, *ortho*-hydroxylation). Path A has some important differences

https://dx.doi.org/10.1021/acs.inorgchem.0c02246
Inorg. Chem. 2020, 59, 17018−17027

with respect to the mechanism of defluorination-hydroxylation of hexafluorobenzene catalyzed by a μ-nitrido diiron phthalocyanine complex. In the latter case a ketone intermediate is formed after a 1,2-fluoride shift, and only one transition metal is involved in the C−F activation.[21] However, in both defluorination-hydroxylation mechanisms the rearomatization of the ring plays a key role.

1 is formed in situ by the reaction of $[Cu^{I}(DBED)(CH_3CN)]^{1+}$ and atmospheric oxygen.[11] Although the most stable isomer is the species $\mathbf{1}^{\mathbf{P}}$, this compound may be in equilibrium with its bis(μ-oxo)dicopper(III) isomer, **1°**. The first requirement to elucidate the reaction mechanism is to determine which is the actual reactive species, $\mathbf{1}^{\mathbf{P}}$ or **1°**. Spectroscopic monitoring of the reaction of $\mathbf{1}^{\mathbf{P}}$ with fluorophenolates (vide infra) reveals that it proceeds via an initial phenolate binding to one of the copper atoms. Consequently, using 2-fluorophenolate as a model substrate, we computed the relative Gibbs energies of **P** and **O** isomers either without ($\mathbf{1}^{\mathbf{P}}$/**1°**) or with ($\mathbf{2}^{\mathbf{P}}$/**2°**) 2-fluorophenolate coordinated to the complex at the DLPNO-CCSD(T)/cc-pVTZ ∼ SMD//M06-L/6−331G(d) level of theory. In the absence of substrate, the $\mathbf{1}^{\mathbf{P}}$ species is 4.1 kcal·mol^{-1} more stable than **1°**. However, upon substrate coordination, this behavior is reversed, and **2°** becomes 3.6 kcal·mol^{-1} more stable than $\mathbf{2}^{\mathbf{P}}$ (Figure 4A). These results are in line with those previously described by Stack and co-workers, indicating that conversion to the **O** isomer occurs when **P** coordinates to a phenolic substrate.[12]

Thus, the DLPNO-CCSD(T) single-point calculations agree with the experimental observation that, when the Cu_2O_2 species is generated by reaction of the copper(I) precursor $[Cu^{I}(DBED)(CH_3CN)]^{+}$ with O_2, the main isomer is $\mathbf{1}^{\mathbf{P}}$. However, upon addition of the phenolic substrate in the reaction mixture, the equilibrium is shifted toward **2°**. Therefore, we placed the focus of our study on the **2°** species, although both **2°** and $\mathbf{2}^{\mathbf{P}}$ isomers were considered as possible active species of the reaction mechanism.

It is worth highlighting that, for all fluorophenolate substrates studied, both apical and basal coordination motifs (with respect to the N_2CuO_2 plane) were explored and that, in all cases, the former was the most stable. However, for the particular case of the attack over the position 6 of 6-chloro-2-fluorophenolate (Figure 5), we were only able to find the

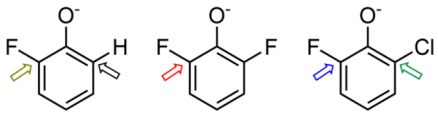

Figure 5. Five possible attacks studied in this manuscript over 2-fluorophenolate, 2,6-difluorophenolate, and 6-chloro-2-fluorophenolate.

transition state corresponding to the electrophilic attack for the isomer presenting basal coordination (Figure 4B). In this case, the activation barrier corresponding to the C−F activation, the reaction observed experimentally, is smaller than the barrier associated with a hypothetical C−Cl cleavage, which therefore is irrelevant.

The first step of the reaction corresponds to a noncovalent attractive interaction between the reactive halogen (F or Cl) with the less coordinatively saturated Cu, giving intermediate **3**. Within crystal field theory, for a square-planar Cu(III) center, all d orbitals are occupied but the $d_{x^2-y^2}$, which does not have the proper symmetry to form an apical bond. Therefore, combination of the d_{z^2} of the Cu(III) and one lone pair of the halogen leads to a nonbonding covalent interaction. However, there exists a noncovalent attractive interaction between the halogen and the Cu(III), as it can be seen in attractive interaction isosurfaces generated by the NCIPLOT[47,48] program based on the real-space analysis of the reduced density gradient (see Figure 6 and the Supporting Information).

Along with the aforementioned Cu−X interaction, the C−X bond is slightly elongated (from 1.35 to 1.38 Å). This key attractive interaction does not exist for the attack at position 6 of 2-fluorophenolate, because the proton obviously does not have a lone pair to interact with the Cu(III). Therefore, for the competing C−H *ortho*-hydroxylation reaction intermediate $\mathbf{3}_{\mathbf{H}}$ does not exist.

For all substrates, the next step of the reaction is an electrophilic attack of the $[Cu_2O_2]^{2+}$ core to the aromatic ring. This attack is ruled by the electrophilic character of the Cu, and therefore it is particularly favored in the bis(μ-oxo)-dicopper(III) **2°** isomer compared to the (η^2:η^2-peroxo)-dicopper(II) $\mathbf{2}^{\mathbf{P}}$ species (see Supporting Information for details). The highest occupied molecular orbital (HOMO) of the intermediate **3** is mainly located over the arene, which agrees with its nucleophilic character, while the lowest unoccupied molecular orbital (LUMO) is an antibonding orbital mainly placed on the $[Cu_2O_2]^{2+}$ core, which agrees with its electrophilic character (Figure 7). In the transition state of this step, which corresponds to the rate-determining step (rds) of the reaction, the C−X ($\mathbf{TS1}_{\mathbf{A}}$) or C−H ($\mathbf{TS1}_{\mathbf{B}}$) bond is elongated, while the C−O distance is shortened, and the attacked carbon of the aromatic ring is pyramidalized. The apical attack of the $[Cu_2O_2]^{2+}$ on the arene cannot be explained only with the participation of the HOMO and LUMO, and, for instance, the apical attack to the 2,6-difluorophenolate requires the participation of the HOMO−2 and LUMO+2 orbitals (Figure 7).

To confirm the electrophilic nature of the attack of the Cu_2O_2 over the aromatic ring, a Hammett plot was experimentally determined (Figure 8). Compound $\mathbf{1}^{\mathbf{P}}$ was generated at −80 °C in Me-THF (THF = tetrahydrofuran) upon reaction of the copper(I) precursor $[Cu(DBED)(CH_3CN)]^{+}$ with O_2. This process was monitored by UV−vis spectroscopy. Once $\mathbf{1}^{\mathbf{P}}$ was fully formed, the temperature was lowered to −110 °C, and the appropriate amount of sodium 2-fluoro-4-Y-phenolate (Y = Cl, F, H, CH_3) was added. This resulted in the formation of the corresponding **2°** species, in which the bis(μ-oxo) core is bound to the phenolate. The experimental characterization of **2°** was solely done by comparison of the UV−vis spectra with those of analogous species previously generated for *m*-XYL^{MeAN} systems[11] and taking into account that analogous species have been experimentally detected for the DBED system with 2-*tert*-butyl-4-Y-phenolates.[12] Decay of the UV−vis spectroscopic features of **2°** showed a first-order kinetics and could be adjusted to a single exponential function. The decay rate (k) was dependent on the nature of the para-substituent Y. Thus, plotting the logarithm of the decay rate (k) as a function of the Hammett parameter of the *para*-substituent (σ_p) resulted in a linear correlation with a negative slope (ρ = −3.5, Figure 8) indicative of an electrophilic attack over the aromatic ring, which agrees with the proposed mechanism based on

https://dx.doi.org/10.1021/acs.inorgchem.0c02246
Inorg. Chem. 2020, 59, 17018−17027

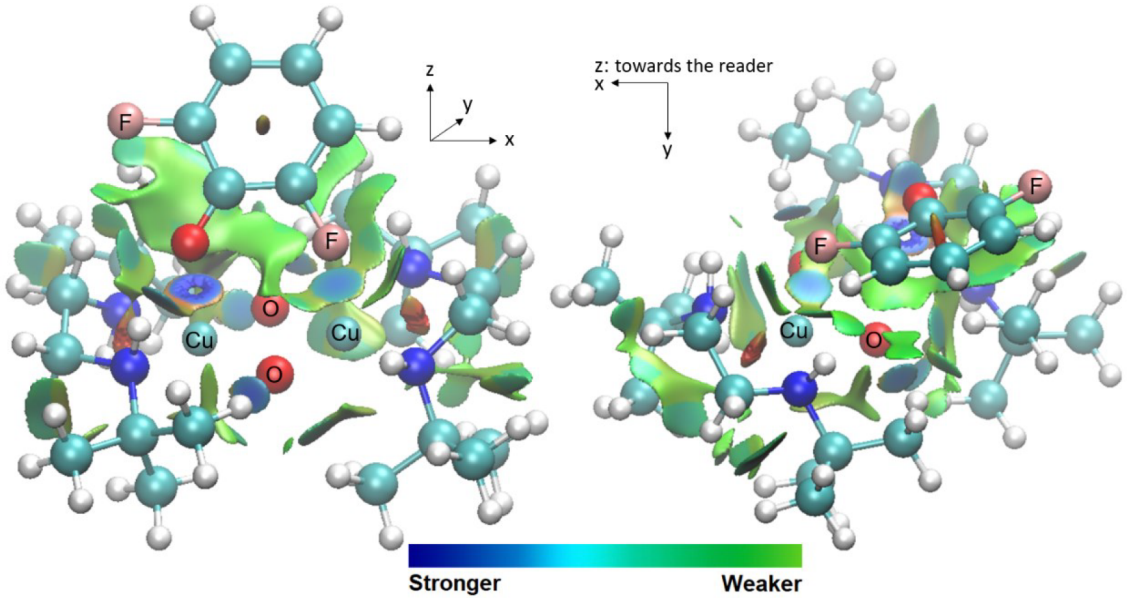

Figure 6. Two different views of the noncovalent attractive interaction isosurfaces generated by NCIPLOT for the $\mathbf{3}_{FF}$ intermediate.

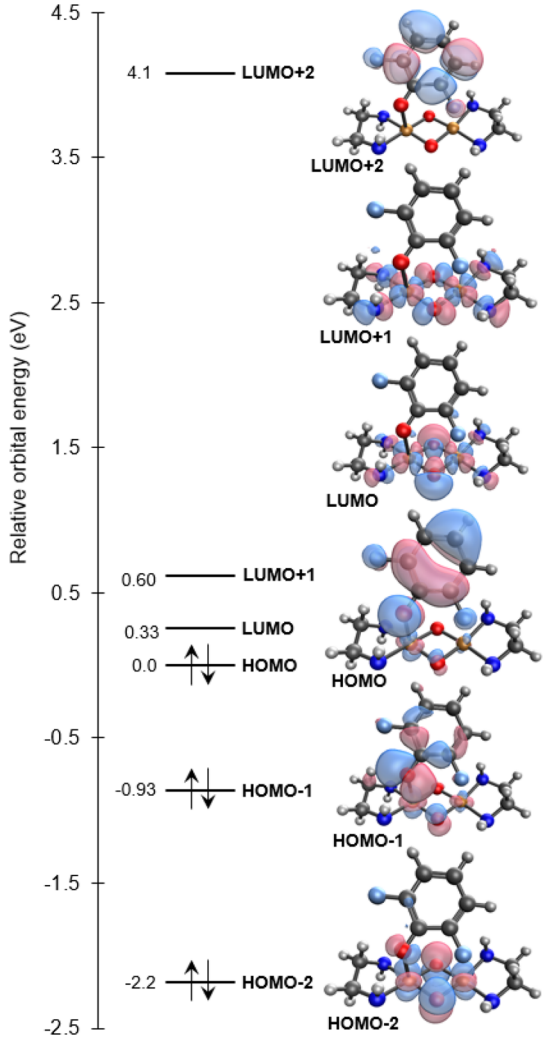

Figure 7. Molecular orbital energy diagram of the six frontier orbitals of $\mathbf{2}_F$. Copper complex simplified for clarity.

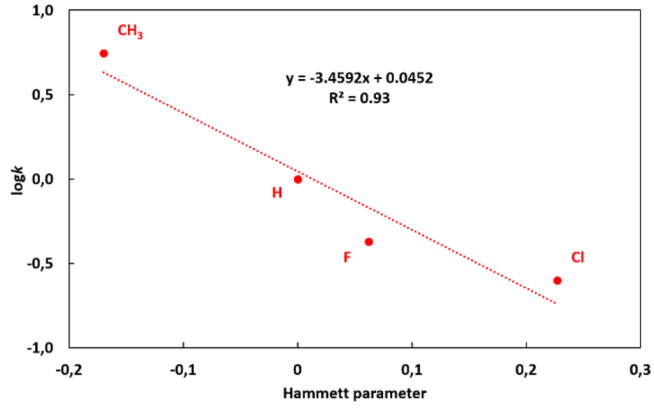

Figure 8. Experimental Hammett plot.

theoretical calculations. The calculated free-energy profile of the different mechanisms studied is shown in Figure 9.

The intermediates $\mathbf{4}_A$ (Figure 9) of Path A contain a dearomatized ring presenting one nearly sp^3 carbon bound to both the reactive oxygen from the $[Cu_2O_2]^{2+}$ core and the halogen. This halogen (either Cl or F) is strongly interacting with the closest Cu. For the attack at position 6 of 2-fluorophenolate (Path B), the intermediate $\mathbf{4}_B$ is generated (Figure 9). This intermediate presents also one nearly sp^3 carbon, but in this case, it is bound to the reactive oxygen from the $[Cu_2O_2]^{2+}$ core and one proton. The main difference of $\mathbf{4}_B$ with respect to $\mathbf{4}_A$ is that the proton cannot interact with the Cu(III), ultimately determining the reactivity of $\mathbf{4}_B$. Neither $\mathbf{4}_A$ nor $\mathbf{4}_B$ are stable intermediates and quickly rearomatize and evolve to the final product. For Path A, such a product ($\mathbf{5}_A$) is obtained through a halogen transfer from the aromatic ring to the metal. Because of the inclusion of the entropic and thermal corrections, the Gibbs energy barriers of the halogen transfers are close to zero or even negative, indicating that this step is a barrierless process. Interestingly, for the attack at the chlorine position of 2-chloro-6-fluorophenolate, the intermediate $\mathbf{4}_A$ does not exist, and $\mathbf{TS1}_A$ evolves directly to products in a

https://dx.doi.org/10.1021/acs.inorgchem.0c02246
Inorg. Chem. 2020, 59, 17018−17027

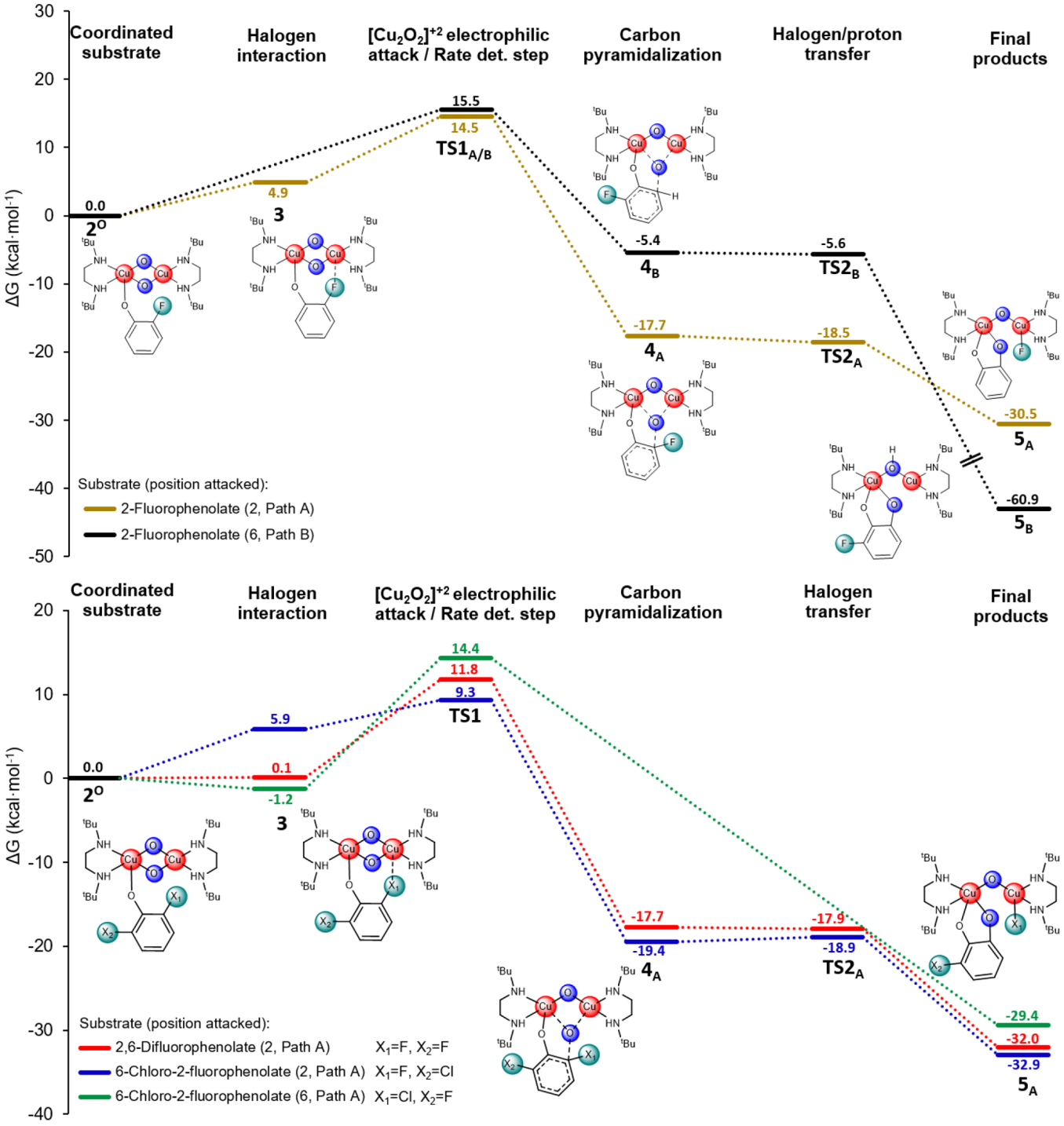

Figure 9. Calculated free-energy profiles at the UM06-L/cc-pVTZ-g ~ SMD//UM06-L/6-311G(d) level of theory for 2-fluorophenolate (top), 2,6-difluorophenolate, and 6-chloro-2-fluorophenolate (bottom) substrates. Gibbs free energies (G, in kcal·mol^{-1}) are relative to **2°**.

concerted asynchronous manner (confirmed by IRC calculations).

For the alternative *ortho* C−H oxygenation, the mechanism homologous to Path A would lead to a Cu−H species, which has not been experimentally detected. Computationally, for 2-fluorophenolate, the formation of the copper hydride is endergonic by 15 kcal·mol^{-1}. Instead, the Path B mechanism leads to a kinetically and thermodynamically favorable pathway for the *ortho*-hydroxylation of the 2-halophenolates. This path differs from Path A at intermediate $\mathbf{4_B}$, which suffers a quasi-barrierless proton transfer to the remaining oxygen of the $[Cu_2O_2]^{2+}$ core forming an OH group. In the transition state of this step ($\mathbf{TS2_B}$) the substrate rearomatizes. To do so, the nearly sp^3 carbon formed in the previous step has to become sp^2 again, releasing the proton. This proton is very close in space to the remaining O of the $[Cu_2O_2]^{2+}$ core to which it ultimately will be transferred (Figure 9, top). The formation of the final product $\mathbf{5_B}$ is highly exergonic (i.e., ΔG = −60.9 kcal·mol^{-1}).

The computed energy barriers ($\Delta G^{\ddagger}$) determined by **TS1**, from lowest to highest, are 9.3 kcal·mol^{-1} for the C−F activation of 2-chloro-6-fluorophenolate, 11.7 kcal·mol^{-1} for

https://dx.doi.org/10.1021/acs.inorgchem.0c02246
Inorg. Chem. 2020, 59, 17018−17027

the C−F activation of 2,6-difluorophenolate, 14.5 kcal·mol^{-1} for the C−F activation of 2-fluorophenolate, 15.5 kcal·mol^{-1} for the C−H activation of 2-fluorophenolate, and 15.6 kcal·mol^{-1} for the C−Cl activation of 2-chloro-6-fluorophenolate. These DFT barriers are in full agreement with observed chemoselectivities. The attack on fluoride instead of chloride in 2-chloro-6-fluorophenolate is 6.3 kcal·mol^{-1} more favorable, which is in concordance with the fact that experimentally only the *ortho*-defluorination is observed.[11] For case of 2-fluorophenolate substrate, for which both Path A and Path B are possible, the attack on C−F (Path A) is 1 kcal·mol^{-1} more favored compared with the attack on C−H (Path B), again in reasonable agreement with the fact that both products are obtained, although the *ortho*-defluorination is the major reaction (18:1 C−F vs C−H oxygenation, 38% total yield).

The precision of the computed reaction barriers was checked by experimentally measuring the decay rate of **2°** formed in the reaction of $\mathbf{1}^{\mathbf{P}}$ with sodium 2,6-difluorophenolate at different temperatures via an Eyring plot analysis (see Supporting Information for details). The experimentally derived $\Delta G^{\ddagger}_{exp}$ is 11.8 ± 0.6 kcal·mol^{-1}, which is in excellent agreement with the aforementioned computed $\Delta G^{\ddagger}_{calc}$ = 11.7 kcal·mol^{-1}. Indeed, the difference between the experimental and theoretical $\Delta G^{\ddagger}$ is far lower than the DFT or experimental errors.

Once the reactivity for the bis(μ-oxo) catalyst was understood, we computationally analyzed whether the η^2:η^2-peroxospecies could present the same reactivity. We performed linear transit calculations starting from $\mathbf{2}^{\mathbf{P}}$ and explored the electrophilic attacks from both oxygens to the aromatic ring at UM06-L/6-311G(d) level.

The energy profiles presented in Figure 10 were obtained performing *relaxed* potential energy surface (PES) scan

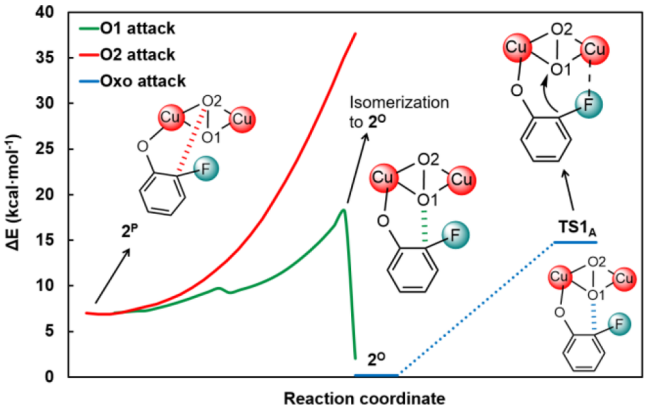

Figure 10. Schematic representation of linear transit calculations starting from $\mathbf{2}^{\mathbf{P}}$ using C−O1 (green) and C−O2 (red) distances as reaction coordinate. DBED ligand omitted for clarity.

calculations with respect to C_{sp2}−O distances. Both linear transits were targeting a transition state equivalent to $\mathbf{TS1}_{\mathbf{A}}$. At this level of theory, species $\mathbf{2}^{\mathbf{P}}$ is 7.0 kcal·mol^{-1} higher in energy than **2°**, preserving the DLPNO-CCSD(T) trends.

In the first linear transit calculation, the O1 approaches the C of the C−F bond. At the beginning of the relaxed scan the electronic energy increases ∼10 kcal·mol^{-1}. However, at the O1−C bond distance of 2.27 Å, there is a significant drop in energy corresponding to the isomerization from distorted $\mathbf{2}^{\mathbf{P}}$ to **2°**. As discussed above, **2°** may evolve until reaching the targeted $\mathbf{TS1}_{\mathbf{A}}$. Although O2 is not properly located to react with the aromatic ring, we also performed a second linear transit calculation, where the O2 approached the C of the C−F bond.

However, in this relaxed scan the energy rises ∼40 kcal·mol^{-1} without finding a structure similar to that of $\mathbf{TS1}_{\mathbf{A}}$. These two linear transit calculations further suggest that only bis(μ-oxo) isomers are able to perform the C−F activation, and then $\mathbf{2}^{\mathbf{P}}$ *should* evolve to **2°** in order to perform the electrophilic attack.

Our results also give theoretical insight about why some compounds such as $[Cu^{III}_2(O)_2(m\text{-}XYL^{MeAN})]^{2+}$ [49] and $[Cu^{II}_2(O_2)(DBED)_2]^{2+}$ (**1**) are able to perform *ortho*-defluorination-hydroxylations, whereas $[Cu^{II}_2(O_2)(L^{Py2Bz})_2]^{2+}$, which has been previously reported by Itoh,[14] does not show this chemistry. Our computations suggest that *ortho*-defluorination-hydroxylation reactions can only be performed by **O** isomers, which is the most stable species of $[Cu^{III}_2(O)_2(m\text{-}XYL^{MeAN})]^{2+}$ and **2**. On the contrary, the **P** isomer, which is the only populated stable isomer of $[Cu^{II}_2(O_2)(L^{Py2Bz})_2]^{2+}$, is unable to activate the C−F bonds of the aromatic rings. These computational results are in full concordance with the known reactivity of tyrosinase; 2-fluorophenolates are known inhibitors of oxytyrosinase, which has been spectroscopically characterized as a pure **P** species. The corresponding **O** isomer has never been detected and is computed to be at least 23 kcal·mol^{-1} higher in energy.[29]

CONCLUSIONS

In this manuscript we have explored the reaction mechanism of the ortho-dehalogenation-hydroxylation of 2-fluorophenolates by combining computational methods and experiments. By using high-level DLPNO-CCSD(T) calculations we have reproduced the experimental description of $[Cu_2O_2(DBED)_2]^{2+}$ (**1**), for which there is an equilibrium between **P** and **O** isomers, shifted toward **O** upon substrate coordination. Our coupled cluster and DFT calculations revealed that **O** is the real executor of the ortho-defluorination-hydroxylation, as it was previously suggested.[11] This fact explains why Cu_2O_2 complexes for which only the **P** isomer is stable are unable to perform defluorination-hydroxylation reactions, and it also suggests a plausible reason why tyrosinase is inhibited by 2-fluorophenols.

The full reaction mechanism was determined for three substrates (2-fluorophenolate, 2,6-difluorophenolate, and 2-chloro-6-fluorophenolate) exploring attacks of the Cu_2O_2 core at the 2 and 6 positions. Thus, we took into account also the possibility of having a competing hydroxylation over a C−H bond (Path B). In all cases, the attack of one oxygen of the $[Cu_2O_2]^{2+}$ core over the arene was the rate-determining step, while the second step was barrierless or quasi-barrierless. This result reproduces the experimental observation of the phenolate-Cu_2O_2 adduct as the last spectroscopically detectable intermediate.

The electrophilic character of the rate-determining step was elucidated by means of an experimental Hammett plot. Analysis of the frontier molecular orbitals for the substrates further confirm the electrophilic nature of the reaction.

An Eyring plot experiment for 2-fluorophenolate as substrate showed full agreement with calculations ($\Delta G^{\ddagger}_{exp}$ = 11.8 kcal·mol^{-1}; $\Delta G^{\ddagger}_{calc}$ = 11.7 kcal·mol^{-1}). The experimental chemoselectivity was rationalized on the basis of relative activation energy differences between C−F, C−H, and C−Cl activations.

https://dx.doi.org/10.1021/acs.inorgchem.0c02246
Inorg. Chem. 2020, 59, 17018−17027

In all cases, the *ortho* C−F bond is kinetically preferred over the other possible *ortho* bond (either C−Cl or C−H) explaining the observed chemoselectivity for the $[Cu_2(O)_2(DBED)_2]^{2+}$ catalyst.

The identification of the **O** isomer as the active species and the rationalization of the chemoselectivity that $[Cu_2O_2]^{2+}$ species present over specific substrates may facilitate the design of more efficient systems, eventually catalytic, and may also broaden their scope of applications.[50−53] Because of the bioinspired nature of such catalysts, they can be understood as simplified (bio)models, and therefore their relatively easy study and understanding is also helpful to acquire greater knowledge on the behavior of bigger systems such as the ubiquitous copper-based metalloproteins.

■ ASSOCIATED CONTENT

Supporting Information

The Supporting Information is available free of charge at https://pubs.acs.org/doi/10.1021/acs.inorgchem.0c02246.

Instrumentation, materials, synthesis of $[Cu^I(DBED)](SbF_6)$, preparation and reactivity of Cu_2O_2 species for UV/vis experiments, generation of $[Cu^{II}_2(\mu-\eta^2:\eta^2-O_2)(DBED)_2]^{2+}$ ($\mathbf{1^P}$) monitored by UV/vis spectroscopy, generation of $[Cu^{III}_2(\mu\text{-}O)_2(DBED)_2]^{2+}$ ($\mathbf{2^O}$) and reactivity with 2-fluorophenolates monitored by UV/vis spectroscopy, Hammett plot preparation, Eyring plot preparation, analysis and quantification of the final oxidized products for C−H versus C−F activation, noncovalent interaction (NCI) plots for the intermediates and DFT-optimized structures (PDF)

■ AUTHOR INFORMATION

Corresponding Authors

Miquel Costas − *Institut de Química Computacional i Catàlisi and Departament de Química, Universitat de Girona, 17003 Girona, Catalonia, Spain;* orcid.org/0000-0001-6326-8299; Email: miquel.costas@udg.edu

Anna Company − *Institut de Química Computacional i Catàlisi and Departament de Química, Universitat de Girona, 17003 Girona, Catalonia, Spain;* orcid.org/0000-0003-4845-4418; Email: anna.company@udg.edu

Josep M. Luis − *Institut de Química Computacional i Catàlisi and Departament de Química, Universitat de Girona, 17003 Girona, Catalonia, Spain;* orcid.org/0000-0002-2880-8680; Email: josepm.luis@udg.edu

Authors

Pau Besalú-Sala − *Institut de Química Computacional i Catàlisi and Departament de Química, Universitat de Girona, 17003 Girona, Catalonia, Spain;* orcid.org/0000-0002-0955-9762

Carla Magallón − *Institut de Química Computacional i Catàlisi and Departament de Química, Universitat de Girona, 17003 Girona, Catalonia, Spain;* orcid.org/0000-0001-6425-5238

Complete contact information is available at: https://pubs.acs.org/10.1021/acs.inorgchem.0c02246

Author Contributions

‡P.B.-S. performed all the calculations, C.M. carried out all the experiments, and both wrote the first draft of the manuscript. M.C., A.C., and J.M.L. designed and supervised the project and cowrote the manuscript. All authors contributed to the analysis of the results, and they all gave approval to the final version of the manuscript. P.B.-S. and C.M. contributed equally to this work.

Notes

The authors declare no competing financial interest.

■ ACKNOWLEDGMENTS

This work was supported with funds from the Spanish government MICINN (PGC2018-098212-B-C22 to J.M.L., PGC2018-101737-B-I00 to M.C., CTQ2016-77989-P to A.C.) and the Generalitat de Catalunya (2017SGR39 to J.M.L., 2017 SGR 00264 and ICREA Academia to M.C. and A.C.). We thank the Spanish Government for the predoctoral grant to P.B.-S. (FPU17/02058). We are also grateful for the computational time financed by the Consorci de Serveis Universitaris de Catalunya.

■ REFERENCES

(1) Lemal, D. M. Perspective on Fluorocarbon Chemistry. *J. Org. Chem.* **2004**, *69* (1), 1−11.

(2) Smart, B. E. Fluorine substituent effects (on bioactivity). *J. Fluorine Chem.* **2001**, *109* (1), 3−11.

(3) Müller, K.; Faeh, C.; Diederich, F. Fluorine in Pharmaceuticals: Looking Beyond Intuition. *Science* **2007**, *317* (5846), 1881−1886.

(4) Houde, M.; Martin, J. W.; Letcher, R. J.; Solomon, K. R.; Muir, D. C. G. Biological Monitoring of Polyfluoroalkyl Substances: A Review. *Environ. Sci. Technol.* **2006**, *40* (11), 3463−3473.

(5) Key, B. D.; Howell, R. D.; Criddle, C. S. Fluorinated Organics in the Biosphere. *Environ. Sci. Technol.* **1997**, *31* (9), 2445−2454.

(6) Bondar, V. S.; Boersma, M. G.; Golovlev, E. L.; Vervoort, J.; Van Berkel, W. J. H.; Finkelstein, Z. I.; Solyanikova, I. P.; Golovleva, L. A.; Rietjens, I. M. ^{19}F NMR study on the biodegradation of fluorophenols by various Rhodococcus species. *Biodegradation* **1998**, *9* (6), 475−486.

(7) Peelen, S.; Rietjens, I. M.; Boersma, M. G.; Vervoort, J. Conversion of phenol derivatives to hydroxylated products by phenol hydroxylase from Trichosporon cutaneum. A comparison of regioselectivity and rate of conversion with calculated molecular orbital substrate characteristics. *Eur. J. Biochem.* **1995**, *227* (1−2), 284−291.

(8) Osborne, R. L.; Raner, G. M.; Hager, L. P.; Dawson, J. H. C. fumago Chloroperoxidase is also a Dehaloperoxidase: Oxidative Dehalogenation of Halophenols. *J. Am. Chem. Soc.* **2006**, *128* (4), 1036−1037.

(9) Battaini, G.; Monzani, E.; Casella, L.; Lonardi, E.; Tepper, A. W. J. W.; Canters, G. W.; Bubacco, L. Tyrosinase-catalyzed Oxidation of Fluorophenols. *J. Biol. Chem.* **2002**, *277* (47), 44606−44612.

(10) Spada, A.; Palavicini, S.; Monzani, E.; Bubacco, L.; Casella, L. Trapping tyrosinase key active intermediate under turnover. *Dalton Trans.* **2009**, No. 33, 6468−6471.

(11) Serrano-Plana, J.; Garcia-Bosch, I.; Miyake, R.; Costas, M.; Company, A. Selective Ortho-Hydroxylation-Defluorination of 2-Fluorophenolates with a Bis(μ-oxo)dicopper(III) Species. *Angew. Chem., Int. Ed.* **2014**, *53* (36), 9608−9612.

(12) Mirica, L. M.; Vance, M.; Rudd, D. J.; Hedman, B.; Hodgson, K. O.; Solomon, E. I.; Stack, T. D. P. Tyrosinase Reactivity in a Model Complex: An Alternative Hydroxylation Mechanism. *Science* **2005**, *308* (5730), 1890−1892.

(13) Mirica, L. M.; Vance, M.; Rudd, D. J.; Hedman, B.; Hodgson, K. O.; Solomon, E. I.; Stack, T. D. P. A Stabilized μ-η^2:η^2 Peroxodicopper(II) Complex with a Secondary Diamine Ligand and Its Tyrosinase-like Reactivity. *J. Am. Chem. Soc.* **2002**, *124* (32), 9332−9333.

(14) Itoh, S.; Kumei, H.; Taki, M.; Nagatomo, S.; Kitagawa, T.; Fukuzumi, S. Oxygenation of Phenols to Catechols by A (μ-η^2:η^2-Peroxo)dicopper(II) Complex: Mechanistic Insight into the Pheno-

lase Activity of Tyrosinase. *J. Am. Chem. Soc.* **2001**, *123* (27), 6708−6709.
(15) Company, A.; Palavicini, S.; Garcia-Bosch, I.; Mas-Ballesté, R.; Que, L., Jr; Rybak-Akimova, E. V.; Casella, L.; Ribas, X.; Costas, M. Tyrosinase-Like Reactivity in a $Cu^{III}_2(\mu\text{-}O)_2$ Species. *Chem. Eur. J.* **2008**, *14* (12), 3535−3538.
(16) de Ruiter, G.; Thompson, N. B.; Takase, M. K.; Agapie, T. Intramolecular C-H and C-F Bond Oxygenation Mediated by a Putative Terminal Oxo Species in Tetranuclear Iron Complexes. *J. Am. Chem. Soc.* **2016**, *138* (5), 1486−1489.
(17) Carsch, K. M.; de Ruiter, G.; Agapie, T. Intramolecular C-H and C-F Bond Oxygenation by Site-Differentiated Tetranuclear Manganese Models of the OEC. *Inorg. Chem.* **2017**, *56* (15), 9044−9054.
(18) de Ruiter, G.; Carsch, K. M.; Takase, M. K.; Agapie, T. Selectivity of C−H versus C−F Bond Oxygenation by Homo- and Heterometallic Fe_4, Fe_3Mn, and Mn_4 Clusters. *Chem. Eur. J.* **2017**, *23* (45), 10744−10748.
(19) Colomban, C.; Kudrik, E. V.; Afanasiev, P.; Sorokin, A. B. Catalytic Defluorination of Perfluorinated Aromatics under Oxidative Conditions Using N-Bridged Diiron Phthalocyanine. *J. Am. Chem. Soc.* **2014**, *136* (32), 11321−11330.
(20) Sahu, S.; Quesne, M. G.; Davies, C. G.; Dürr, M.; Ivanović-Burmazović, I.; Siegler, M. A.; Jameson, G. N. L.; de Visser, S. P.; Goldberg, D. P. Direct Observation of a Nonheme Iron(IV)-Oxo Complex That Mediates Aromatic C-F Hydroxylation. *J. Am. Chem. Soc.* **2014**, *136* (39), 13542−13545.
(21) Colomban, C.; Tobing, A. H.; Mukherjee, G.; Sastri, C. V.; Sorokin, A. B.; de Visser, S. P. Mechanism of Oxidative Activation of Fluorinated Aromatic Compounds by N-Bridged Diiron-Phthalocyanine: What Determines the Reactivity? *Chem. Eur. J.* **2019**, *25* (63), 14320−14331.
(22) Liu, Y. F.; Yu, J. G.; Siegbahn, P. E. M.; Blomberg, M. R. A. Theoretical Study of the Oxidation of Phenolates by the $[Cu_2O_2(N,N'\text{-di-tert-butylethylenediamine})_2]^{2+}$ Complex. *Chem. Eur. J.* **2013**, *19* (6), 1942−1954.
(23) Qayyum, M. F.; Sarangi, R.; Fujisawa, K.; Stack, T. D. P.; Karlin, K. D.; Hodgson, K. O.; Hedman, B.; Solomon, E. I. L-Edge X-ray Absorption Spectroscopy and DFT Calculations on Cu_2O_2 Species: Direct Electrophilic Aromatic Attack by Side-on Peroxo Bridged Dicopper(II) Complexes. *J. Am. Chem. Soc.* **2013**, *135* (46), 17417−17431.
(24) Güell, M.; Luis, J. M.; Solà, M.; Siegbahn, P. E. M. Theoretical study of the hydroxylation of phenolates by the $Cu_2O_2(N,N'\text{-dimethylethylenediamine})_2^{2+}$ complex. *J. Biol. Inorg. Chem.* **2009**, *14* (2), 229−242.
(25) Op't Holt, B. T.; Vance, M. A.; Mirica, L. M.; Heppner, D. E.; Stack, T. D. P.; Solomon, E. I. Reaction Coordinate of a Functional Model of Tyrosinase: Spectroscopic and Computational Characterization. *J. Am. Chem. Soc.* **2009**, *131* (18), 6421−6438.
(26) Cramer, C. J.; Kinal, A.; Włoch, M.; Piecuch, P.; Gagliardi, L. Theoretical Characterization of End-On and Side-On Peroxide Coordination in Ligated Cu_2O_2 Models. *J. Phys. Chem. A* **2006**, *110* (40), 11557−11568.
(27) Cramer, C. J.; Włoch, M.; Piecuch, P.; Puzzarini, C.; Gagliardi, L. Theoretical Models on the Cu_2O_2 Torture Track: Mechanistic Implications for Oxytyrosinase and Small-Molecule Analogues. *J. Phys. Chem. A* **2006**, *110* (5), 1991−2004.
(28) Siegbahn, P. E. M. A comparison of the thermodynamics of O-O bond cleavage for dicopper complexes in enzymes and synthetic systems. *J. Biol. Inorg. Chem.* **2003**, *8* (5), 577−585.
(29) Siegbahn, P. E. M.; Wirstam, M. Is the Bis-μ-Oxo Cu_2(III,III) State an Intermediate in Tyrosinase? *J. Am. Chem. Soc.* **2001**, *123* (47), 11819−11820.
(30) Gherman, B. F.; Cramer, C. J. Quantum chemical studies of molecules incorporating a $Cu_2O_2^{2+}$ core. *Coord. Chem. Rev.* **2009**, *253* (5), 723−753.
(31) Liakos, D. G.; Guo, Y.; Neese, F. Comprehensive Benchmark Results for the Domain Based Local Pair Natural Orbital Coupled Cluster Method (DLPNO-CCSD(T)) for Closed- and Open-Shell Systems. *J. Phys. Chem. A* **2020**, *124* (1), 90−100.
(32) Goerigk, L.; Hansen, A.; Bauer, C.; Ehrlich, S.; Najibi, A.; Grimme, S. A look at the density functional theory zoo with the advanced GMTKN55 database for general main group thermochemistry, kinetics and noncovalent interactions. *Phys. Chem. Chem. Phys.* **2017**, *19* (48), 32184−32215.
(33) Sparta, M.; Neese, F. Chemical applications carried out by local pair natural orbital based coupled-cluster methods. *Chem. Soc. Rev.* **2014**, *43* (14), 5032−5041.
(34) Comba, P.; Faltermeier, D.; Krieg, S.; Martin, B.; Rajaraman, G. Spin state and reactivity of iron(iv)oxido complexes with tetradentate bispidine ligands. *Dalton Trans.* **2020**, *49* (9), 2888−2894.
(35) Frisch, M. J.; Trucks, G. W.; Schlegel, H. B.; Scuseria, G. E.; Robb, M. A.; Cheeseman, J. R.; Scalmani, G.; Barone, V.; Mennucci, B.; Petersson, G. A.; Nakatsuji, H.; Caricato, M.; Li, X.; Hratchian, H. P.; Izmaylov, A. F.; Bloino, J.; Zheng, G.; Sonnenberg, J. L.; Hada, M.; Ehara, M.; Toyota, K.; Fukuda, R.; Hasegawa, J.; Ishida, M.; Nakajima, T.; Honda, Y.; Kitao, O.; Nakai, H.; Vreven, T.; Montgomery, J. A., Jr.; Peralta, J. E.; Ogliaro, F.; Bearpark, M.; Heyd, J. J.; Brothers, E.; Kudin, K. N.; Staroverov, V. N.; Keith, T.; Kobayashi, R.; Normand, J.; Raghavachari, K.; Rendell, A.; Burant, J. C.; Iyengar, S. S.; Tomasi, J.; Cossi, M.; Rega, N.; Millam, J. M.; Klene, M.; Knox, J. E.; Cross, J. B.; Bakken, V.; Adamo, C.; Jaramillo, J.; Gomperts, R.; Stratmann, R. E.; Yazyev, O.; Austin, A. J.; Cammi, R.; Pomelli, C.; Ochterski, J. W.; Martin, R. L.; Morokuma, K.; Zakrzewski, V. G.; Voth, G. A.; Salvador, P.; Dannenberg, J. J.; Dapprich, S.; Daniels, A. D.; Farkas, O.; Foresman, J. B.; Ortiz, J. V.; Cioslowski, J.; Fox, D. J. *Gaussian 09,* Rev. E.01, Gaussian Inc., 2015.
(36) Zhao, Y.; Truhlar, D. G. A new local density functional for main-group thermochemistry, transition metal bonding, thermochemical kinetics, and noncovalent interactions. *J. Chem. Phys.* **2006**, *125* (19), 194101.
(37) Francl, M. M.; Pietro, W. J.; Hehre, W. J.; Binkley, J. S.; Gordon, M. S.; DeFrees, D. J.; Pople, J. A. Self-consistent molecular orbital methods. XXIII. A polarization-type basis set for second-row elements. *J. Chem. Phys.* **1982**, *77* (7), 3654−3665.
(38) Krishnan, R.; Binkley, J. S.; Seeger, R.; Pople, J. A. Self-consistent molecular orbital methods. XX. A basis set for correlated wave functions. *J. Chem. Phys.* **1980**, *72* (1), 650−654.
(39) Fukui, K. The path of chemical reactions - the IRC approach. *Acc. Chem. Res.* **1981**, *14* (12), 363−368.
(40) Page, M.; Doubleday, C.; McIver, J. W. Following steepest descent reaction paths. The use of higher energy derivatives with ab initio electronic structure methods. *J. Chem. Phys.* **1990**, *93* (8), 5634−5642.
(41) Dunning, T. H. Gaussian basis sets for use in correlated molecular calculations. I. The atoms boron through neon and hydrogen. *J. Chem. Phys.* **1989**, *90* (2), 1007−1023.
(42) Kendall, R. A.; Dunning, T. H.; Harrison, R. J. Electron affinities of the first-row atoms revisited. Systematic basis sets and wave functions. *J. Chem. Phys.* **1992**, *96* (9), 6796−6806.
(43) Marenich, A. V.; Cramer, C. J.; Truhlar, D. G. Universal Solvation Model Based on Solute Electron Density and on a Continuum Model of the Solvent Defined by the Bulk Dielectric Constant and Atomic Surface Tensions. *J. Phys. Chem. B* **2009**, *113* (18), 6378−6396.
(44) Yamaguchi, K.; Jensen, F.; Dorigo, A.; Houk, K. N. A spin correction procedure for unrestricted Hartree-Fock and Møller-Plesset wavefunctions for singlet diradicals and polyradicals. *Chem. Phys. Lett.* **1988**, *149* (5), 537−542.
(45) Postils, V.; Company, A.; Solà, M.; Costas, M.; Luis, J. M. Computational Insight into the Mechanism of Alkane Hydroxylation by Non-heme Fe(PyTACN) Iron Complexes. Effects of the Substrate and Solvent. *Inorg. Chem.* **2015**, *54* (17), 8223−8236.
(46) Neese, F. The ORCA program system. *Wiley Interdiscip. Rev.: Comput. Mol. Sci.* **2012**, *2* (1), 73−78.
(47) Contreras-García, J.; Johnson, E. R.; Keinan, S.; Chaudret, R.; Piquemal, J.-P.; Beratan, D. N.; Yang, W. NCIPLOT: A Program for

https://dx.doi.org/10.1021/acs.inorgchem.0c02246
Inorg. Chem. 2020, 59, 17018−17027

Plotting Noncovalent Interaction Regions. *J. Chem. Theory Comput.* **2011**, *7* (3), 625−632.
(48) Johnson, E. R.; Keinan, S.; Mori-Sánchez, P.; Contreras-García, J.; Cohen, A. J.; Yang, W. Revealing Noncovalent Interactions. *J. Am. Chem. Soc.* **2010**, *132* (18), 6498−6506.
(49) Company, A.; Lamata, D.; Poater, A.; Solà, M.; Rybak-Akimova, E. V.; Que, L.; Fontrodona, X.; Parella, T.; Llobet, A.; Costas, M. O_2 Chemistry of Dicopper Complexes with Alkyltriamine Ligands. Comparing Synergistic Effects on O_2 Binding. *Inorg. Chem.* **2006**, *45* (14), 5239−5241.
(50) Esguerra, K. V. N.; Fall, Y.; Petitjean, L.; Lumb, J.-P. Controlling the Catalytic Aerobic Oxidation of Phenols. *J. Am. Chem. Soc.* **2014**, *136*, 7662.
(51) Paul, M.; Teubner, M.; Grimm-Lebsanft, B.; Golchert, C.; Meiners, Y.; Senft, L.; Keisers, K.; Liebhauser, P.; Rosener, T.; Biebl, F.; Buchenau, S.; Naumova, M.; Murzin, V.; Krug, R.; Hoffmann, A.; Pietruszka, J.; Ivanovic-Burmazovic, I.; Rubhausen, M.; Herres-Pawlis, S. Exceptional Substrate Diversity in Oxygenation Reactions Catalyzed by a Bis(μ-oxo) Copper Complex. *Chem. - Eur. J.* **2020**, *26*, 7556.
(52) Becker, J.; Zhyhadlo, Y. Y.; Butova, E. D.; Fokin, A. A.; Schreiner, P. R.; Forster, M.; Holthausen, M. C.; Specht, P.; Schindler, S. Aerobic Aliphatic Hydroxylation Reactions by Copper Complexes: A Simple Clip-and-Cleave Concept. *Chem. - Eur. J.* **2018**, *24*, 15543.
(53) Trammell, R.; Rajabimoghadam, K.; Garcia-Bosch, I. Copper-Promoted Functionalization of Organic Molecules: From Biologically Relevant Cu2O2 Model Systems to Organometallic Transformations. *Chem. Rev.* **2019**, *119*, 2954.

https://dx.doi.org/10.1021/acs.inorgchem.0c02246
Inorg. Chem. 2020, 59, 17018−17027

Chapter V. Well-Defined Aryl-Fe^{II} Complexes in Cross-Coupling and C-H Activation Processes

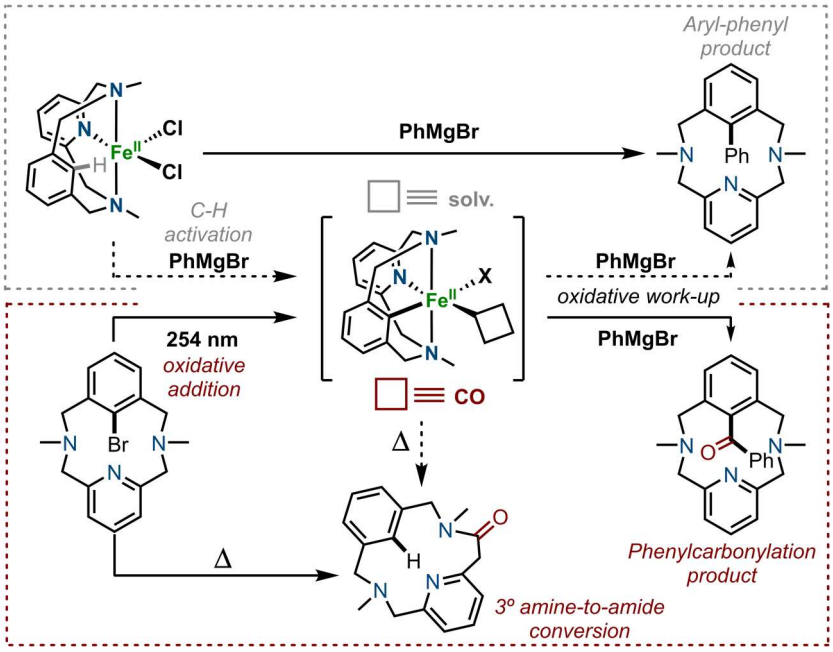

This chapter corresponds to the following publication:

Carla Magallón, Oriol Planas, Steven Roldán-Gómez, Josep M. Luis, Anna Company*, Xavi Ribas*. Reprinted with permission from *Organometallics*, **2021**, *40*, 9, 1195 – 1200. Copyright © 2021 American Chemical Society.

ORGANOMETALLICS

pubs.acs.org/Organometallics

Communication

Well-Defined Aryl-Fe^{II} Complexes in Cross-Coupling and C−H Activation Processes

Carla Magallón, Oriol Planas, Steven Roldán-Gómez, Josep M. Luis, Anna Company,* and Xavi Ribas*

Cite This: *Organometallics* 2021, 40, 1195−1200

Read Online

ACCESS | Metrics & More | Article Recommendations | Supporting Information

ABSTRACT: Herein we explore the intrinsic organometallic reactivity of iron embedded in a tetradentate N_3C macrocyclic ligand scaffold that allows the stabilization of aryl-Fe species, which are key intermediates in Fe-catalyzed cross-coupling and C−H functionalization processes. This study covers C−H activation reactions using $^{Me}L_H$ and $FeCl_2$, biaryl C−C coupling product formation through reaction with Grignard reagents, and cross-coupling reactions using $^{Me}L_{Br}$ or $^{H}L_{Br}$ in combination with $Fe^0(CO)_5$. Synthesis under light irradiation and moderate heating (50 °C) affords the aryl-Fe^{II} complexes $[Fe^{II}(Br)(^{Me}L)(CO)]$ ($\mathbf{1}^{Me}$) and $[Fe^{II}(^{H}L)(CO)_2]Br$ ($\mathbf{1}^{H}$). Exhaustive spectroscopic characterization of these rare low-spin diamagnetic species, including their crystal structures, allowed the investigation of their intrinsic reactivity.

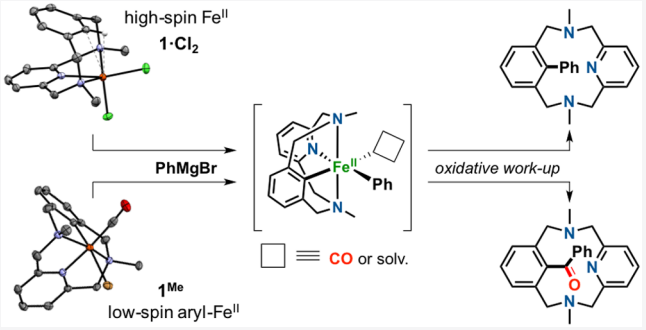

Organoiron species have been invoked for a long time in cross-coupling transformations and C−H functionalization reactions for the formation of C−C products. Early in the 1970s, Kochi reported that simple $FeCl_3$ could catalyze the methylation of haloalkenes with the use of alkyl Grignard reagents.[1,2] Since then, many reports using cheap and nontoxic iron-based catalysts have appeared, highlighting the use of *N*-methylpyrrolidine (NMP) as an additive.[3−6] More recently, the use of bisphosphine[7−9] ligands or N-heterocyclic carbene[10−13] ligands to tune the reactivity of the *in situ* formed organoiron species has allowed the development of a variety of cross-coupling C−C bond forming transformations.[14−22] Many iron-catalyzed C−H functionalization protocols have also flourished in the past decade involving C_{sp^2}−H and C_{sp^3}−H activation, C−C bond forming reactions being the vast majority,[23−25] although some examples of C−X bond formation (X = N, B, Si, O, halides) have also been reported.[26] In the past decade, important advances in understanding the mechanism of these reactions relied on trapping relevant aryl or alkyl organoiron intermediate species.[18,27−31] However, in the particular case of aryl-Fe species bearing directing groups (DG) attached to the substrate, detection of the organometallic species involved in cross-coupling or C−H activation catalysis has been quite elusive for a long time, and only scarce spectroscopic characterization has been reported. Either oxidative addition[32] at Fe^0 or σ-bond metathesis at Fe^{II} has been proposed to lead to the formation of aryl-Fe^{II} species (Scheme 1a).[32,33] Concerted metalation−deprotonation (CMD) by Fe^{II} has also been proposed in some cases.[34]

Nakamura postulated a cyclometalated iron species as the active intermediate in an arene-containing substrate using the aminoquinoline (AQ) directing group, but actual spectroscopic data on this compound were not reported.[35,36] This lack of mechanistic understanding stems from the metastable character of organoiron species together with their multiple geometries and oxidation and spin states. Recently Neidig reported a series of insightful publications in which the combination of advanced spectroscopic techniques such as Mössbauer spectroscopy and X-ray crystallography proved to be a successful strategy to identify catalytically relevant organoiron species.[37−39]

Moreover, there are very few examples of key low-spin aryl-Fe^{II} species stemming from C−H metalation in DG-bearing substrates. One of them was recently trapped by Neidig at very low temperatures using noncyclic substrates with an amide-triazole bidentate directing group (Scheme 1b).[40] Another species was reported by Ackermann featuring a cyclometalated low-spin aryl-Fe^{II}-hydride species ligated with a ketone DG and three PMe_3 ligands.[41] With regard to well-defined systems featuring aryl-halide oxidative addition processes, Nishiyama reported a low-spin aryl-Fe^{II} complex using a bisoxazoline aryl-Br pincer ligand and $Fe^0{}_2(CO)_9$.[42] Recently, Fout described the synthesis of an aryl-Fe^{II}-hydride stabilized within a bis(carbene) pincer CCC ligand, but no reactivity of the

Received: February 19, 2021
Published: March 9, 2021

https://dx.doi.org/10.1021/acs.organomet.1c00100
Organometallics 2021, 40, 1195−1200

Scheme 1. Relevant Examples of Iron-Mediated C−H Activation: (a) σ-Bond Metathesis at Fe^{II} and Oxidative Addition at Fe^{0}, (b) Low-Spin Aryl-Fe^{II} Trapped at Low Temperature, and (c) Reactivity of Well-Defined Aryl-Fe^{II} Species formed via C−H Activation or Cross-Coupling to Undergo C−C Coupling (This Work)

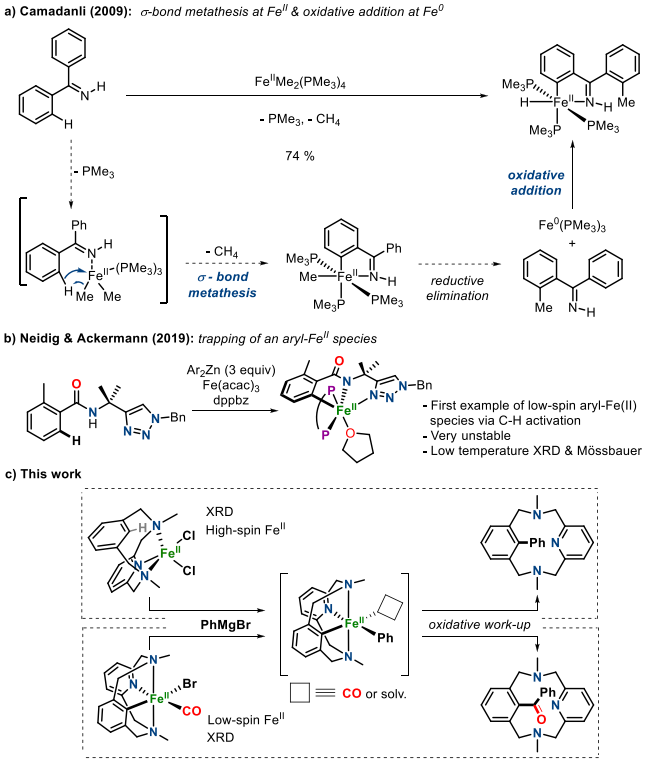

aryl-Fe^{II} was reported.[43] An alternative strategy to get access to well-defined aryl-Fe^{II} species consists of the use of macrocyclic aryl-X and aryl-H model substrates capable of stabilizing otherwise very reactive species. These size-tunable macrocyclic model substrates have been used by our group and others to stabilize square-planar aryl-Cu^{III},[44] aryl-Ag^{III},[45] and aryl-Ni^{II},[46] as well as octahedral aryl-Co^{III}[47] and aryl-Mn^{III} species.[48] Following this strategy, herein we report the reactivity of well-defined octahedral aryl-Fe^{II} species and their C−C cross-coupling reactivity with ArMgX reagents (Scheme 1c).

The model arene substrate $^{Me}\mathbf{L_H}$ was exposed to $FeCl_2$ in CH_3CN to obtain the coordination complex $[Fe^{II}(Cl)_2(^{Me}\mathbf{L_H})]$ (**1·Cl$_2$**) in 86% yield, which was isolated as a yellowish crystalline solid (Figure 1a). Paramagnetic ^{1}H NMR spectroscopy clearly indicated a high-spin Fe^{II} species, which was confirmed by X-ray crystallography (Figure 1b). The Fe^{II} center featured a pentacoordinated distorted-square-pyramidal geometry (τ = 0.46)[49] with long Fe−N distances (>2.1 Å). Noticeably, the sixth coordination site was occupied by an interaction with the inner aromatic C−H bond of $^{Me}\mathbf{L_H}$, which conformed to an incipient C_{Ar}-H···Fe interaction (Figure S59). The analogous structure with bromides as counterions was also obtained (**1·Br$_2$**, τ = 0.46; Figure 1b and Figure S60).

These structures suggested that an octahedral geometry featuring an organometallic aryl−Fe bond was feasible, provided the C_{Ar}−H activation could be executed. At this point we explored the reactivity of the complex **1·Cl$_2$** with PhMgBr Grignard reagent, seeking for a biaryl coupling product. By performing the reaction in THF at low

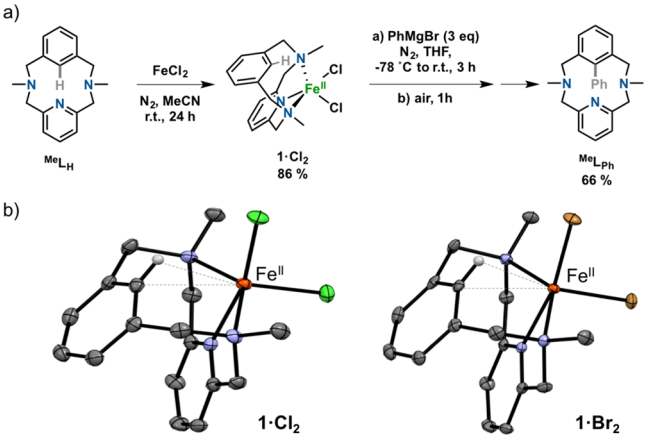

Figure 1. (a) Synthesis of the Fe^{II} complex **1·Cl$_2$** and subsequent reactivity with PhMgBr to obtain the biaryl C−C coupling product ($^{Me}\mathbf{L_{Ph}}$). (b) Crystal structures of **1·Cl$_2$** and **1·Br$_2$** (ellipsoids set at 50% probability and H atoms removed for clarity, except for inner Ar−H).

temperature (−78 °C) for 1 h and warming up the mixture to room temperature for an additional 2 h, we obtained a 66% yield of the C_{sp^2}−C_{sp^2} biaryl coupling product ($^{Me}\mathbf{L_{Ph}}$) after workup under aerobic conditions (Figure 1a). The product was fully characterized by NMR and HR-ESI-MS (see the Supporting Information). Despite no organoiron species derived from C−H activation could be isolated, the intermediacy of an aryl-iron species is clearly inferred by the obtained coupling product. Whether C−H activation proceeds via σ-bond metathesis or concerted metalation−deprotonation (CMD) at the iron(II) center is difficult to establish.[32−34,50] This prompted us to attempt another synthetic strategy to stabilize and isolate relevant aryl-iron species via aryl-halide oxidative addition at Fe^0. Thus, we prepared aryl-Br ligand analogues ($^{R}\mathbf{L_{Br}}$, R = H, Me, *t*Bu; Figure 2a) and reacted them

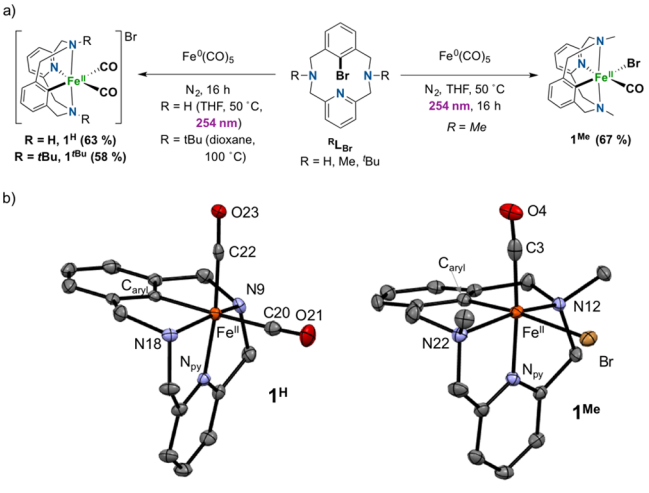

Figure 2. (a) Experimental conditions for the synthesis of **1^{tBu}**, **1^{Me}**, and **1^{H}** via aryl-Br oxidative addition at Fe^0. (b) Crystal structures of **1^{Me}** and **1^{H}** (monocation shown) (ellipsoids set at 50% probability and H atoms removed for clarity). Selected bond distances (Å): for **1^{H}**, Fe−C_{aryl} 1.925(2), Fe−N_{py} 1.928(2), Fe−N9 2.030(2), Fe−N18 2.034(2), Fe−C20 1.837(3), Fe−C22 1.759(3); for **1^{Me}**, Fe−C_{aryl} 1.904(3), Fe−N_{py} 1.935(3), Fe−N12 2.095(3), Fe−N22 2.102(3), Fe−Br 2.571(2), Fe−C3 1.785(4).

https://dx.doi.org/10.1021/acs.organomet.1c00100
Organometallics 2021, 40, 1195−1200

with $Fe^0(CO)_5$. In the case of $^{Me}L_{Br}$, upon overnight photoirradiation (254 nm) at 50 °C, the oxidative addition aryl-Fe^{II} product was obtained. The compound $[Fe^{II}(Br)(^{Me}L)(CO)]$ ($\mathbf{1}^{Me}$, Figure 2a) was characterized as a low-spin Fe^{II} species and displayed diamagnetic NMR spectra (Figures S19–S23), which was directly related to the coordination of the strong-field carbonyl ligand. The crystal structure of $\mathbf{1}^{Me}$ confirmed a distorted-octahedral structure of the Fe^{II} center, featuring a short Fe–aryl bond (1.904(3) Å) and a long Fe–Br bond (2.571(2) Å) *trans* to the aryl moiety, with a CO ligand completing the coordination sphere (Figure 2b). This *trans* disposition indicated that the reaction must entail an aryl-Br oxidative addition concomitant with a *cis* to *trans* rearrangement.[51,52] Indeed, the analogous $[Fe^{II}(^{H}L)(CO)_2]Br$ complex ($\mathbf{1}^{H}$) featured two CO ligands coordinated to the Fe^{II} center and a noncoordinating Br^- anion, clearly indicating that Br^- and CO ligands can easily exchange. Indeed, the *trans* effect of the aryl moiety is visualized by a longer Fe–CO bond *trans* to the aryl (1.837(3) Å) compared to the Fe–CO bond *trans* to the pyridine (1.759(3) Å). To evaluate the electronic effects of the tertiary amines, we also prepared the analogous complex $[Fe^{II}(^{tBu}L)(CO)_2]Br$ ($\mathbf{1}^{tBu}$) (Figure 2a), which was characterized by NMR and HR-ESI-MS.

At this point, we centered our efforts on investigating the intrinsic reactivity of $[Fe^{II}(Br)(^{Me}L)(CO)]$ ($\mathbf{1}^{Me}$) as a reference compound for well-defined low-spin aryl-Fe^{II} species. In order to determine whether this species could be involved in the reaction of the complex $\mathbf{1{\cdot}Cl_2}$ with the Grignard reagent, we reacted $\mathbf{1}^{Me}$ with PhMgBr under experimental conditions and workup analogous to those described above for $\mathbf{1{\cdot}Cl_2}$, obtaining a relevant 38% yield of the $^{Me}L_{COPh}$ product (Figure 3, top). NMR and HR-ESI-MS confirmed the nature of the

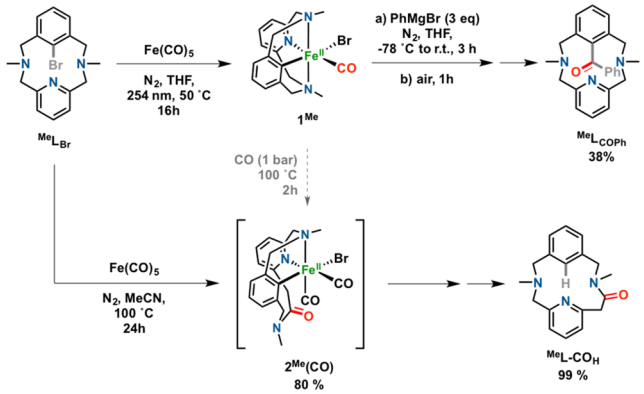

Figure 3. Synthesis of $^{Me}L_{COPh}$ from well-defined aryl-Fe^{II} (top) and synthesis of $^{Me}L\text{-}CO_H$ from $^{Me}L_{Br}$ via $\mathbf{2^{Me}(CO)}$ in an unprecedented amine-to-amide transformation (bottom).

coupling product, which stemmed from a putative $[Fe^{II}(^{Me}L)(Ph)(CO)]$ ($\mathbf{1^{Me}\text{-}Ph}$) followed by a CO migratory insertion and reductive elimination to form the aryl–COPh bond in $^{Me}L_{COPh}$.

It is worth noting here that the products $^{Me}L_{Ph}$ (derived from $\mathbf{1{\cdot}Cl_2}$) and $^{Me}L_{COPh}$ (derived from $\mathbf{1}^{Me}$) are obtained presumably via exposure of $[Fe^{II}(^{Me}L)(Ph)]$ and $[Fe^{II}(^{Me}L)(Ph)(CO)]$ to O_2 (or air) and a subsequent acid/base workup. An evident change in color (UV–vis monitoring, Figures S1 and S2) from dark green to reddish brown was observed upon contact with air, suggesting an oxidation to an Fe^{III} species that triggered the C–C reductive elimination, as reported in other examples.[26,53] Despite cryo-MS analysis at −40 °C of the mixture immediately after exposure to O_2, the decay was so fast that only the final coupling product $^{Me}L_{Ph}$ was detected as a single peak in the mass spectrum (Figure S2b). Moreover, when the crude mixture containing $[Fe^{II}(^{Me}L)(Ph)]$ was quenched with HCl prior to air exposure, $^{Me}L_H$ was solely obtained (85%) with no signs of biaryl coupling. Finally, since 1,2- dichloroisobutane (DCIB) is generally used as an oxidant in Fe-catalyzed C–H activations,[26] the addition of 2 equiv of DCIB under N_2 to the green species $[Fe^{II}(^{Me}L)(Ph)]$ afforded $^{Me}L_{Ph}$ in 45% yield, a value slightly lower than that with O_2 exposure (66%) (section 7.3 in the Supporting Information). Interestingly, DCIB addition at the beginning of the reaction only afforded a 9% yield of $^{Me}L_{Ph}$, suggesting that oxidation to Fe^{III} at the initial stages is detrimental to the observed chemistry. In line with the latter, catalytic attempts have been unfruitful.

On the basis of all these experimental observations, feasible mechanistic proposals are outlined in Figure 4a for the

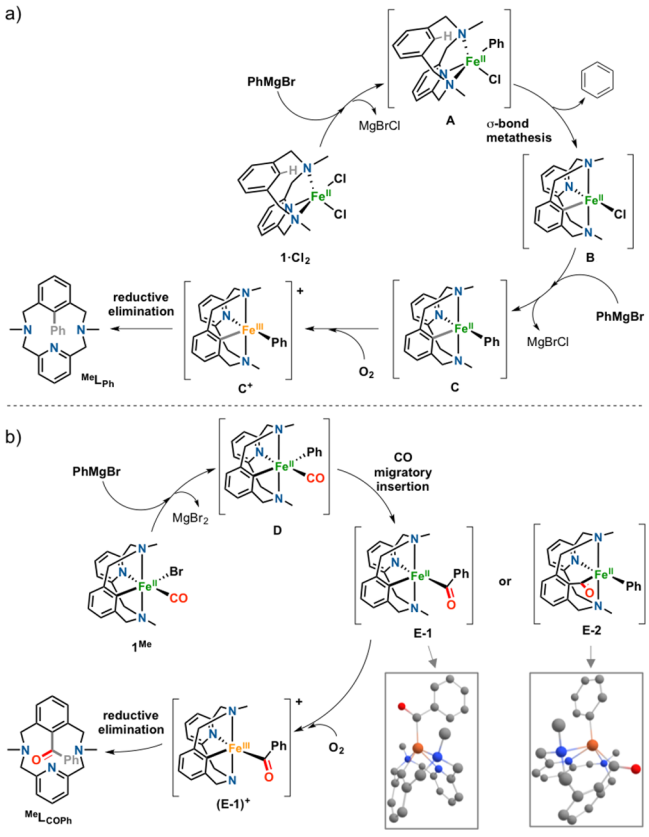

Figure 4. (a) Proposed mechanism for the synthesis of $^{Me}L_{Ph}$ via Fe^{II}-mediated C–H activation. (b) Proposed mechanism for the synthesis of $^{Me}L_{COPh}$ via the reaction of $\mathbf{1}^{Me}$ with PhMgBr (**E-1** and **E-2** quintuplet DFT optimized structures shown as insets; see the Supporting Information).

synthesis of $^{Me}L_{Ph}$ and in Figure 4b for the synthesis of $^{Me}L_{COPh}$. The reaction of $\mathbf{1{\cdot}Cl_2}$ with PhMgBr (Figure 4a) affords species **A**, which undergoes C–H activation, presumably via σ-bond metathesis, to give species **B**. A second equivalent of the Grignard reagent generates species **C**, which undergoes oxidative reductive elimination via $\mathbf{C}^+$ upon exposure to O_2. With regard to the reactivity of $\mathbf{1}^{Me}$ with PhMgBr (Figure 4b), first the Br^- ligand is exchanged by Ph^-

https://dx.doi.org/10.1021/acs.organomet.1c00100
Organometallics 2021, 40, 1195–1200

to afford **D**, and then a CO migratory insertion occurs to give **E-1** or **E-2**. Both species would form the final product $^{Me}L_{COPh}$ via reductive elimination. To discern between the two possibilities, the crude compound was treated with HCl(aq) prior to air exposure, and $^{Me}L_H$ was obtained as the product in 95% yield. This supports the idea that **E-1** is the most plausible intermediate, which is backed by DFT studies (Gibbs energies with respect to **D** are 6.19 kcal/mol for **E-1** and 9.72 kcal/mol for **E-2**; Figure 4b and the Supporting Information).

While exploring the reactivity of $^{Me}L_{Br}$ with $Fe(CO)_5$, we also performed the reaction under thermal conditions (100 °C) instead of via photoirradiation (Figure 3, bottom). Strikingly, the nature of the low-spin Fe^{II} complex $\mathbf{2^{Me}(CO)}$ obtained after 24 h was completely unexpected. A detailed diamagnetic 1D/2D NMR and FT-IR characterization concluded that a formal CO insertion occurred by amine to amide conversion at a pyridine-benzylic position, still holding the organoiron aryl-Fe^{II} moiety: i.e., $[Fe^{II}(Br)(^{Me}L\text{-}CO)(CO)_2]$ ($\mathbf{2^{Me}(CO)}$) (Figure 3). ^{13}C NMR integration of the coordinated CO signal and the lack of a HR-ESI-MS peak clearly points toward the coordination of two CO and one Br^- ligand to the Fe^{II} center, leaving the amide moiety uncoordinated. The amide moiety was corroborated upon protodemetalation, affording $^{Me}L\text{-}CO_H$ as the resulting macrocyclic compound (see the Supporting Information for characterization). To our knowledge, carbonylation into the ligand backbone to transform a tertiary amine to a tertiary amide is unprecedented and is reminiscent of an unreported inverse Curtius-like rearrangement.[54] Although it is not the same transformation, Cantat recently reported the iron-catalyzed amine to amide transformation of an *N*,*N*-dimethylaniline substrate by taking advantage of the acylation of a tertiary amine followed by the extrusion of Me^+ as MeI.[55] Also, the participation of Fe in Curtius-like rearrangements has only a few precedents, such as the work from Xia, forming isocyanates from hydroxamates through an Fe^{II}-nitrenoid complex.[56]

In order to gain insight into the mechanism of this unprecedented reactivity, the well-defined $\mathbf{1^{Me}}$ complex was heated under a CO atmosphere (1 bar). The reaction was monitored by ^1H NMR, and formation of $\mathbf{2^{Me}(CO)}$ was observed (14%) just after 2 h, together with the starting $\mathbf{1^{Me}}$ and protodemetalation byproduct ($^{Me}L_H$), thus suggesting that aryl-Br oxidative addition at Fe^0 takes place prior to the amine to amide conversion. Also, the nature of the tertiary amine is crucial, since a *t*Bu-N-substituted ligand ($^{tBu}L_{Br}$) did not undergo the amine to amide transformation, whereas $^HL_{Br}$ afforded $^HL\text{-}CO_H$ in a sluggish manner (section 8 in the Supporting Information).

In conclusion, model macrocyclic aryl-Fe^{II} species have been studied in detail by taking advantage of the stabilizing effect imposed by the macrocyclic N_3C-type ligands ^XL_Y (X = H, Me; Y = H, Br). The system affords the C−C biaryl cross-coupling products through C−H activation at a Fe^{II} complex using ArMgX reagents and the phenylcarbonylation cross-coupling products when well-defined aryl-Fe^{II} species are used, featuring C−C coupling with Grignard reagents, concomitantly with CO insertion. Furthermore, the overstabilized $\mathbf{1^{Me}}$ species undergoes at high temperatures an unprecedented CO insertion−carbonylation into the tertiary amine ligand backbone, rendering a tertiary amide quantitatively. Such model aryl-Fe^{II} complexes provide a neat mechanistic picture for C−H arylation and cross-coupling reactions that should inspire others in the design of improved Fe-catalyzed bond forming transformations.

■ ASSOCIATED CONTENT

Supporting Information

The Supporting Information is available free of charge at https://pubs.acs.org/doi/10.1021/acs.organomet.1c00100.

Spectroscopic characterization of all compounds, crystallographic data for $\mathbf{1{\cdot}Cl_2}$, $\mathbf{1{\cdot}Br_2}$, $\mathbf{1^{Me}}$, and $\mathbf{1^H}$, and DFT results for **D**, **E-1**, and **E-2** (PDF)

Accession Codes

CCDC 2046155−2046158 contain the supplementary crystallographic data for this paper. These data can be obtained free of charge via www.ccdc.cam.ac.uk/data_request/cif, or by emailing data_request@ccdc.cam.ac.uk, or by contacting The Cambridge Crystallographic Data Centre, 12 Union Road, Cambridge CB2 1EZ, UK; fax: +44 1223 336033.

■ AUTHOR INFORMATION

Corresponding Authors

Anna Company − *Institut de Química Computacional i Catàlisi (IQCC) and Departament de Química, Universitat de Girona, Girona E-17003, Catalonia, Spain;* orcid.org/0000-0003-4845-4418; Email: anna.company@udg.edu

Xavi Ribas − *Institut de Química Computacional i Catàlisi (IQCC) and Departament de Química, Universitat de Girona, Girona E-17003, Catalonia, Spain;* orcid.org/0000-0002-2850-4409; Email: xavi.ribas@udg.edu

Authors

Carla Magallón − *Institut de Química Computacional i Catàlisi (IQCC) and Departament de Química, Universitat de Girona, Girona E-17003, Catalonia, Spain*

Oriol Planas − *Institut de Química Computacional i Catàlisi (IQCC) and Departament de Química, Universitat de Girona, Girona E-17003, Catalonia, Spain;* orcid.org/0000-0003-2038-2678

Steven Roldán-Gómez − *Institut de Química Computacional i Catàlisi (IQCC) and Departament de Química, Universitat de Girona, Girona E-17003, Catalonia, Spain*

Josep M. Luis − *Institut de Química Computacional i Catàlisi (IQCC) and Departament de Química, Universitat de Girona, Girona E-17003, Catalonia, Spain;* orcid.org/0000-0002-2880-8680

Complete contact information is available at: https://pubs.acs.org/10.1021/acs.organomet.1c00100

Notes

The authors declare no competing financial interest.

■ ACKNOWLEDGMENTS

We acknowledge financial support from the MINECO-Spain for projects PID2019-104498GB-I00 to X.R., PID2019-106699GB-I00 to A.C., and PGC2018-098212-B-C22 to J.M.L. The Generalitat de Catalunya is also acknowledged for projects 2017SGR264 and 2017SGR39. We thank the UdG for a IFUdG Ph.D. grant to C.M. and the MINECO for an FPI grant to S.R.-G. We also thank COST Action CHAOS (CA15106). X.R. and A.C. are thankful for an ICREA Acadèmia award. The authors are grateful to STR-UdG for technical support.

https://dx.doi.org/10.1021/acs.organomet.1c00100
Organometallics 2021, 40, 1195−1200

REFERENCES

(1) Tamura, M.; Kochi, J. Iron catalysis in the reaction of grignard reagents with alkyl halides. *J. Organomet. Chem.* **1971**, *31*, 289−309.
(2) Tamura, M.; Kochi, J. K. Vinylation of Grignard reagents. Catalysis by iron. *J. Am. Chem. Soc.* **1971**, *93*, 1487−1489.
(3) Cahiez, G.; Avedissian, H. Highly Stereo- and Chemoselective Iron-Catalyzed Alkenylation of Organomagnesium Compounds. *Synthesis* **1998**, *1998*, 1199−1205.
(4) Sears, J. D.; Muñoz, S. B., III; Daifuku, S. L.; Shaps, A. A.; Carpenter, S. H.; Brennessel, W. W.; Neidig, M. L. The Effect of β-Hydrogen Atoms on Iron Speciation in Cross-Couplings with Simple Iron Salts and Alkyl Grignard Reagents. *Angew. Chem., Int. Ed.* **2019**, *58*, 2769−2773.
(5) Gärtner, D.; Stein, A. L.; Grupe, S.; Arp, J.; Jacobi von Wangelin, A. Iron-Catalyzed Cross-Coupling of Alkenyl Acetates. *Angew. Chem., Int. Ed.* **2015**, *54*, 10545−10549.
(6) Cahiez, G.; Duplais, C.; Moyeux, A. Iron-Catalyzed Alkylation of Alkenyl Grignard Reagents. *Org. Lett.* **2007**, *9*, 3253−3254.
(7) Hatakeyama, T.; Hashimoto, T.; Kondo, Y.; Fujiwara, Y.; Seike, H.; Takaya, H.; Tamada, Y.; Ono, T.; Nakamura, M. Iron-Catalyzed Suzuki−Miyaura Coupling of Alkyl Halides. *J. Am. Chem. Soc.* **2010**, *132*, 10674−10676.
(8) Hatakeyama, T.; Okada, Y.; Yoshimoto, Y.; Nakamura, M. Tuning Chemoselectivity in Iron-Catalyzed Sonogashira-Type Reactions Using a Bisphosphine Ligand with Peripheral Steric Bulk: Selective Alkynylation of Nonactivated Alkyl Halides. *Angew. Chem., Int. Ed.* **2011**, *50*, 10973−10976.
(9) Hatakeyama, T.; Hashimoto, T.; Kathriarachchi, K. K. A. D. S.; Zenmyo, T.; Seike, H.; Nakamura, M. Iron-Catalyzed Alkyl−Alkyl Suzuki−Miyaura Coupling. *Angew. Chem., Int. Ed.* **2012**, *51*, 8834−8837.
(10) Bedford, R. B.; Betham, M.; Bruce, D. W.; Danopoulos, A. A.; Frost, R. M.; Hird, M. Iron−Phosphine, − Phosphite, − Arsine, and − Carbene Catalysts for the Coupling of Primary and Secondary Alkyl Halides with Aryl Grignard Reagents. *J. Org. Chem.* **2006**, *71*, 1104−1110.
(11) Ghorai, S. K.; Jin, M.; Hatakeyama, T.; Nakamura, M. Cross-Coupling of Non-activated Chloroalkanes with Aryl Grignard Reagents in the Presence of Iron/N-Heterocyclic Carbene Catalysts. *Org. Lett.* **2012**, *14*, 1066−1069.
(12) Guisán-Ceinos, M.; Tato, F.; Buñuel, E.; Calle, P.; Cárdenas, D. J. Fe-catalysed Kumada-type alkyl−alkyl cross-coupling. Evidence for the intermediacy of Fe(i) complexes. *Chem. Sci.* **2013**, *4*, 1098−1104.
(13) Hatakeyama, T.; Nakamura, M. Iron-Catalyzed Selective Biaryl Coupling: Remarkable Suppression of Homocoupling by the Fluoride Anion. *J. Am. Chem. Soc.* **2007**, *129*, 9844−9845.
(14) Dongol, K. G.; Koh, H.; Sau, M.; Chai, C. L. L. Iron-Catalysed sp3−sp3 Cross-Coupling Reactions of Unactivated Alkyl Halides with Alkyl Grignard Reagents. *Adv. Synth. Catal.* **2007**, *349*, 1015−1018.
(15) Jin, M.; Adak, L.; Nakamura, M. Iron-Catalyzed Enantioselective Cross-Coupling Reactions of α-Chloroesters with Aryl Grignard Reagents. *J. Am. Chem. Soc.* **2015**, *137*, 7128−7134.
(16) Chua, Y.-Y.; Duong, H. A. Selective Kumada biaryl cross-coupling reaction enabled by an iron(iii) alkoxide−N-heterocyclic carbene catalyst system. *Chem. Commun.* **2014**, *50*, 8424−8427.
(17) O'Brien, H. M.; Manzotti, M.; Abrams, R. D.; Elorriaga, D.; Sparkes, H. A.; Davis, S. A.; Bedford, R. B. Iron-catalysed substrate-directed Suzuki biaryl cross-coupling. *Nat. Catal.* **2018**, *1*, 429−437.
(18) Przyojski, J. A.; Veggeberg, K. P.; Arman, H. D.; Tonzetich, Z. J. Mechanistic Studies of Catalytic Carbon−Carbon Cross-Coupling by Well-Defined Iron NHC Complexes. *ACS Catal.* **2015**, *5*, 5938−5946.
(19) Sherry, B. D.; Fürstner, A. The Promise and Challenge of Iron-Catalyzed Cross Coupling. *Acc. Chem. Res.* **2008**, *41*, 1500−1511.
(20) Nakamura, E.; Hatakeyama, T.; Ito, S.; Ishizuka, K.; Ilies, L.; Nakamura, M., Iron-Catalyzed Cross-Coupling Reactions. In *Organic Reactions*; Wiley: 2014; Vol. *83*, pp 1−210.
(21) Piontek, A.; Bisz, E.; Szostak, M. Iron-Catalyzed Cross-Couplings in the Synthesis of Pharmaceuticals: In Pursuit of Sustainability. *Angew. Chem., Int. Ed.* **2018**, *57*, 11116−11128.
(22) Lübken, D.; Saxarra, M.; Kalesse, M. Tris(acetylacetonato) Iron(III): Recent Developments and Synthetic Applications. *Synthesis* **2019**, *51*, 161−177.
(23) Ilies, L.; Asako, S.; Nakamura, E. Iron-Catalyzed Stereospecific Activation of Olefinic C−H Bonds with Grignard Reagent for Synthesis of Substituted Olefins. *J. Am. Chem. Soc.* **2011**, *133*, 7672−7675.
(24) Shang, R.; Ilies, L.; Asako, S.; Nakamura, E. Iron-Catalyzed C(sp2)−H Bond Functionalization with Organoboron Compounds. *J. Am. Chem. Soc.* **2014**, *136*, 14349−14352.
(25) Ilies, L.; Ichikawa, S.; Asako, S.; Matsubara, T.; Nakamura, E. Iron-Catalyzed Directed Alkylation of Alkenes and Arenes with Alkylzinc Halides. *Adv. Synth. Catal.* **2015**, *357*, 2175−2179.
(26) Shang, R.; Ilies, L.; Nakamura, E. Iron-Catalyzed C−H Bond Activation. *Chem. Rev.* **2017**, *117*, 9086−9139.
(27) Fürstner, A. Iron Catalysis in Organic Synthesis: A Critical Assessment of What It Takes To Make This Base Metal a Multitasking Champion. *ACS Cent. Sci.* **2016**, *2*, 778−789.
(28) Bauer, I.; Knölker, H.-J. Iron Catalysis in Organic Synthesis. *Chem. Rev.* **2015**, *115*, 3170−3387.
(29) Bedford, R. B.; Brenner, P. B.; Carter, E.; Cogswell, P. M.; Haddow, M. F.; Harvey, J. N.; Murphy, D. M.; Nunn, J.; Woodall, C. H. TMEDA in Iron-Catalyzed Kumada Coupling: Amine Adduct versus Homoleptic "ate" Complex Formation. *Angew. Chem., Int. Ed.* **2014**, *53*, 1804−1808.
(30) Liu, Y.; Xiao, J.; Wang, L.; Song, Y.; Deng, L. Carbon−Carbon Bond Formation Reactivity of a Four-Coordinate NHC-Supported Iron(II) Phenyl Compound. *Organometallics* **2015**, *34*, 599−605.
(31) Zhurkin, F. E.; Wodrich, M. D.; Hu, X. A Monometallic Iron(I) Organoferrate. *Organometallics* **2017**, *36*, 499−501.
(32) Camadanli, S.; Beck, R.; Flörke, U.; Klein, H.-F. C−H Activation of Imines by Trimethylphosphine-Supported Iron Complexes and Their Reactivities. *Organometallics* **2009**, *28*, 2300−2310.
(33) Shi, Y.; Li, M.; Hu, Q.; Li, X.; Sun, H. C−Cl Bond Activation of ortho-Chlorinated Imine with Iron Complexes in Low Oxidation States. *Organometallics* **2009**, *28*, 2206−2210.
(34) Wunderlich, S. H.; Knochel, P. Preparation of Functionalized Aryl Iron(II) Compounds and a Nickel-Catalyzed Cross-Coupling with Alkyl Halides. *Angew. Chem., Int. Ed.* **2009**, *48*, 9717−9720.
(35) Asako, S.; Ilies, L.; Nakamura, E. Iron-Catalyzed Ortho-Allylation of Aromatic Carboxamides with Allyl Ethers. *J. Am. Chem. Soc.* **2013**, *135*, 17755−17757.
(36) Matsubara, T.; Asako, S.; Ilies, L.; Nakamura, E. Synthesis of Anthranilic Acid Derivatives through Iron-Catalyzed Ortho Amination of Aromatic Carboxamides with N-Chloroamines. *J. Am. Chem. Soc.* **2014**, *136*, 646−649.
(37) Daifuku, S. L.; Al-Afyouni, M. H.; Snyder, B. E. R.; Kneebone, J. L.; Neidig, M. L. A Combined Mössbauer, Magnetic Circular Dichroism, and Density Functional Theory Approach for Iron Cross-Coupling Catalysis: Electronic Structure, In Situ Formation, and Reactivity of Iron-Mesityl-Bisphosphines. *J. Am. Chem. Soc.* **2014**, *136*, 9132−9143.
(38) Neidig, M. L.; Carpenter, S. H.; Curran, D. J.; DeMuth, J. C.; Fleischauer, V. E.; Iannuzzi, T. E.; Neate, P. G. N.; Sears, J. D.; Wolford, N. J. Development and Evolution of Mechanistic Understanding in Iron-Catalyzed Cross-Coupling. *Acc. Chem. Res.* **2019**, *52*, 140−150.
(39) Neate, P. G. N.; Greenhalgh, M. D.; Brennessel, W. W.; Thomas, S. P.; Neidig, M. L. Mechanism of the Bis(imino)pyridine-Iron-Catalyzed Hydromagnesiation of Styrene Derivatives. *J. Am. Chem. Soc.* **2019**, *141*, 10099−10108.
(40) Boddie, T. E.; Carpenter, S. H.; Baker, T. M.; DeMuth, J. C.; Cera, G.; Brennessel, W. W.; Ackermann, L.; Neidig, M. L. Identification and Reactivity of Cyclometalated Iron(II) Intermedi-

https://dx.doi.org/10.1021/acs.organomet.1c00100
Organometallics 2021, 40, 1195−1200

ates in Triazole-Directed Iron-Catalyzed C−H Activation. *J. Am. Chem. Soc.* **2019**, *141*, 12338−12345.
(41) Messinis, A. M.; Finger, L. H.; Hu, L.; Ackermann, L. Allenes for Versatile Iron-Catalyzed C−H Activation by Weak O-Coordination: Mechanistic Insights by Kinetics, Intermediate Isolation, and Computation. *J. Am. Chem. Soc.* **2020**, *142*, 13102−13111.
(42) Hosokawa, S.; Ito, J.-i.; Nishiyama, H. A Chiral Iron Complex Containing a Bis(oxazolinyl)phenyl Ligand: Preparation and Asymmetric Hydrosilylation of Ketones. *Organometallics* **2010**, *29*, 5773−5775.
(43) Jackson, B. J.; Najera, D. C.; Matson, E. M.; Woods, T. J.; Bertke, J. A.; Fout, A. R. Synthesis and Characterization of (DIPPCCC)Fe Complexes: A Zwitterionic Metalation Method and CO2 Reactivity. *Organometallics* **2019**, *38*, 2943−2952.
(44) Casitas, A.; King, A. E.; Parella, T.; Costas, M.; Stahl, S. S.; Ribas, X. Direct Observation of CuI/CuIII Redox Steps Relevant to Ullmann-Type Coupling Reactions. *Chem. Sci.* **2010**, *1*, 326−330.
(45) Font, M.; Acuña-Parés, F.; Parella, T.; Serra, J.; Luis, J. M.; Lloret-Fillol, J.; Costas, M.; Ribas, X. Direct observation of two-electron Ag(I)/Ag(III) redox cycles in coupling catalysis. *Nat. Commun.* **2014**, *5*, 4373.
(46) Rovira, M.; Roldán-Gómez, S.; Martin-Diaconescu, V.; Whiteoak, C. J.; Company, A.; Luis, J. M.; Ribas, X. Trifluoromethylation of a Well-Defined Square-Planar Aryl-NiII Complex involving NiIII/CF3. and NiIV−CF3 Intermediate Species. *Chem. - Eur. J.* **2017**, *23*, 11662−11668.
(47) Planas, O.; Roldán-Gómez, S.; Martin-Diaconescu, V.; Parella, T.; Luis, J. M.; Company, A.; Ribas, X. Carboxylate-Assisted Formation of Aryl-Co(III) Masked-Carbenes in Cobalt-Catalyzed C−H Functionalization with Diazo Esters. *J. Am. Chem. Soc.* **2017**, *139*, 14649−14655.
(48) Sarbajna, A.; He, Y.-T.; Dinh, M. H.; Gladkovskaya, O.; Rahaman, S. M. W.; Karimata, A.; Khaskin, E.; Lapointe, S.; Fayzullin, R. R.; Khusnutdinova, J. R. Aryl−X Bond-Forming Reductive Elimination from High-Valent Mn−Aryl Complexes. *Organometallics* **2019**, *38*, 4409−4419.
(49) Addison, A. W.; Rao, T. N.; Reedijk, J.; Van Rijn, J.; Verschoor, G. C. Synthesis, structure, and spectroscopic properties of copper(II) compounds containing nitrogen-sulfur donor ligands: the crystal and molecular structure of aqua[1,7-bis(N-methylbenzimidazol-2′-yl)-2,6-dithiaheptane]copper(II) perchlorate. *J. Chem. Soc., Dalton Trans.* **1984**, *7*, 1349−46.
(50) Beck, R.; Sun, H.; Li, X.; Camadanli, S.; Klein, H.-F. Cyclometalation of Thiobenzophenones with Mononuclear Methyl-iron and -cobalt Complexes. *Eur. J. Inorg. Chem.* **2008**, *2008*, 3253−3257.
(51) Tolman, C. A.; Ittel, S. D.; English, A. D.; Jesson, J. P. The chemistry of 2-naphthyl bis[bis(dimethylphosphino)ethane] hydride complexes of iron, ruthenium, and osmium. 1. Characterization and reactions with hydrogen and Lewis base ligands. *J. Am. Chem. Soc.* **1978**, *100*, 4080−4089.
(52) Tolman, C. A.; Ittel, S. D.; English, A. D.; Jesson, J. P. Chemistry of 2-naphthyl bis[bis(dimethylphosphino)ethane] hydride complexes of iron, ruthenium, and osmium. 3. Cleavage of sp2 carbon-hydrogen bonds. *J. Am. Chem. Soc.* **1979**, *101*, 1742−1751.
(53) Yoshikai, N.; Matsumoto, A.; Norinder, J.; Nakamura, E. Iron-Catalyzed Direct Arylation of Aryl Pyridines and Imines Using Oxygen as an Oxidant. *Synlett* **2010**, *2010*, 313−316.
(54) Ghosh, A. K.; Sarkar, A.; Brindisi, M. The Curtius rearrangement: mechanistic insight and recent applications in natural product syntheses. *Org. Biomol. Chem.* **2018**, *16*, 2006−2027.
(55) Nasr Allah, T.; Savourey, S.; Berthet, J.-C.; Nicolas, E.; Cantat, T. Carbonylation of C−N Bonds in Tertiary Amines Catalyzed by Low-Valent Iron Catalysts. *Angew. Chem., Int. Ed.* **2019**, *58*, 10884−10887.
(56) Li, D.; Wu, T.; Liang, K.; Xia, C. Curtius-like Rearrangement of an Iron−Nitrenoid Complex and Application in Biomimetic Synthesis of Bisindolylmethanes. *Org. Lett.* **2016**, *18*, 2228−2231.

https://dx.doi.org/10.1021/acs.organomet.1c00100
Organometallics 2021, 40, 1195−1200

Chapter VI. Organometallic Ni(II), Ni(III) and Ni(IV) Complexes Relevant to Carbon-Carbon and Carbon-Oxygen Bond Formation Reactions

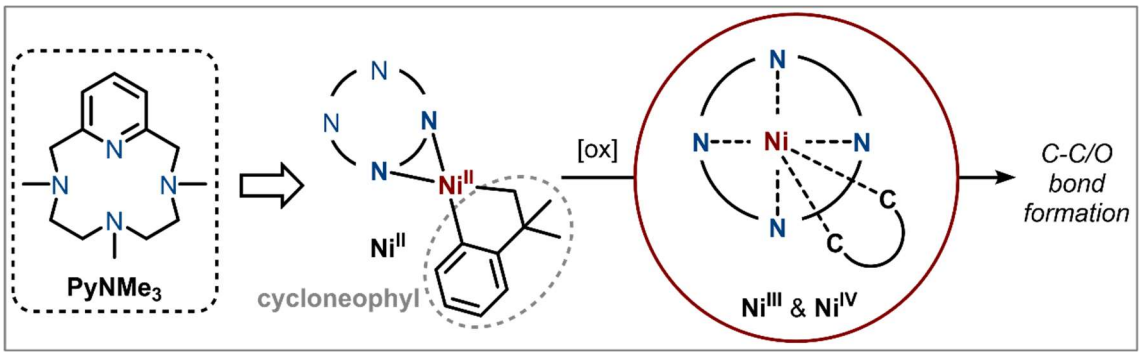

This chapter corresponds to the following publication:

Carla Magallón, Leonel Griego, Chi-Herng Hu, Anna Company*, Xavi Ribas*, Liviu M. Mirica* *Inorg. Chem. Front.*, **2022**, DOI: 10.1039/d1qi01486b.

Organometallic Ni(II), Ni(III), and Ni(IV) Complexes Relevant to Carbon-Carbon and Carbon-Oxygen Bond Formation Reactions

Carla Magallón,[a] Leonel Griego,[b] Chi-Herng Hu,[b] Anna Company,*[a] Xavi Ribas,*[a] Liviu M. Mirica*[b]

[a] *Institut de Química Computacional i Catàlisi (IQCC) and Departament de Química, Universitat de Girona, Campus Montilivi, Girona, E-17003, Catalonia, Spain.*
[b] *Department of Chemistry, University of Illinois at Urbana-Champaign, 600 S. Mathews Avenue, Urbana, Illinois 61801, USA.*
*Corresponding authors: anna.company@udg.edu; xavi.ribas@udg.edu; mirica@illinois.edu

Abstract: Pyridinophane tetradentate ligands have successfully been shown to stabilize uncommon high-valent organometallic nickel complexes. In this work, $PyNMe_3$ is used as a tetradentate *N*-based macrocyclic ligand which coordinates the nickel center through three aliphatic nitrogens and a pyridine. The synthesis and spectroscopic and structural characterization of well-defined organometallic Ni(II) and Ni(III) complexes bearing $PyNMe_3$ and the cycloneophyl ligand (an alkyl/aryl C-donor ligand) are described. Furthermore, spectroscopic and cryo-MS studies suggest the formation of a transient Ni(IV) organometallic complex, and its relevance to C-C and C-O bond formation reactions is discussed.

Introduction

The formation of new C-C and C-heteroatom bonds through transition-metal catalyzed cross-coupling reactions (i.e., Suzuki, Kumada, and Negishi reactions) are currently one of the most powerful tools in organic chemistry.[1-3] In this context, noble metal-based systems are the more commonly used catalysts for these transformations, due to their widely understood mechanism.[4-7] For example, Pd-catalyzed reactions usually occur via Pd^0/Pd^{II} catalytic cycles and mostly involve diamagnetic intermediate species, which makes their characterization more feasible.[8] In contrast, the mechanisms of Ni-catalyzed cross-coupling reactions are far less understood since this first-row transition-metal can easily undergo both one- and two-electron redox processes, often involving paramagnetic intermediate species that lead to more complex mechanistic pathways.[9-11] Although traditionally Ni-catalyzed cross-coupling reactions have been proposed to involve Ni^0, Ni^I and Ni^{II} intermediates,[12-14] recent studies suggest that high-

valent Ni^{III} and Ni^{IV} species are key intermediates in the C-C/C-heteroatom bond-forming step.[15-24]

In the past several years, Mirica and co-workers have employed a series of tetradentate pyridinophane ligands with different amine N-substituents (^{R}N4 ligands, R = Me, Ts, ^{i}Pr, ^{t}Bu, Np) as well as the tridentate 1,4,7-trimethyl-1,4,7-triazacyclononane ligand (Me_3tacn) to stabilize $Pd^{II/IV}$ and $Ni^{III/IV}$ complexes that undergo C-C/C-heteroatom bond formation reactions (Fig. 1a).[25-40] Recently, a macrocyclic N-based tetradentate ligand **PyNMe$_3$** has been employed by Costas, Company and coworkers to stabilize high-valent intermediate species and has proved successful to trap $Fe^{IV/V}$-oxo species and dinuclear Cu^{II} side-on peroxo species (Fig. 1b).[41-45] However, the use of the **PyNMe$_3$** ligand has never been employed to explore the reactivity of organometallic Ni complexes.

Herein we report the synthesis, characterization, and initial reactivity studies of a series of organometallic Ni^{II}, Ni^{III} and Ni^{IV} complexes supported by the **PyNMe$_3$** ligand and containing the cycloneophyl fragment, an alkyl/aryl C-donor ligand (Fig. 1c). The cycloneophyl ligand was developed by Carmona et al. as an ancillary ligand to isolate organonickel complexes, since the resulting Ni(cycloneophyl) complexes are less prone to reductive elimination or β-hydride elimination.[46-48] In addition, the cycloneophyl moiety has been widely and successfully employed together with N-based ligands independently by Sanford and Mirica in order to study C-C and C-heteroatom bond forming reactions.[31-33, 49-54] The current study reports the reactivity of the isolated [(PyNMe$_3$)Ni^{II}(cycl)] complex with oxidants to promote C-C or C-O reductive elimination through Ni^{IV} intermediate species is described.

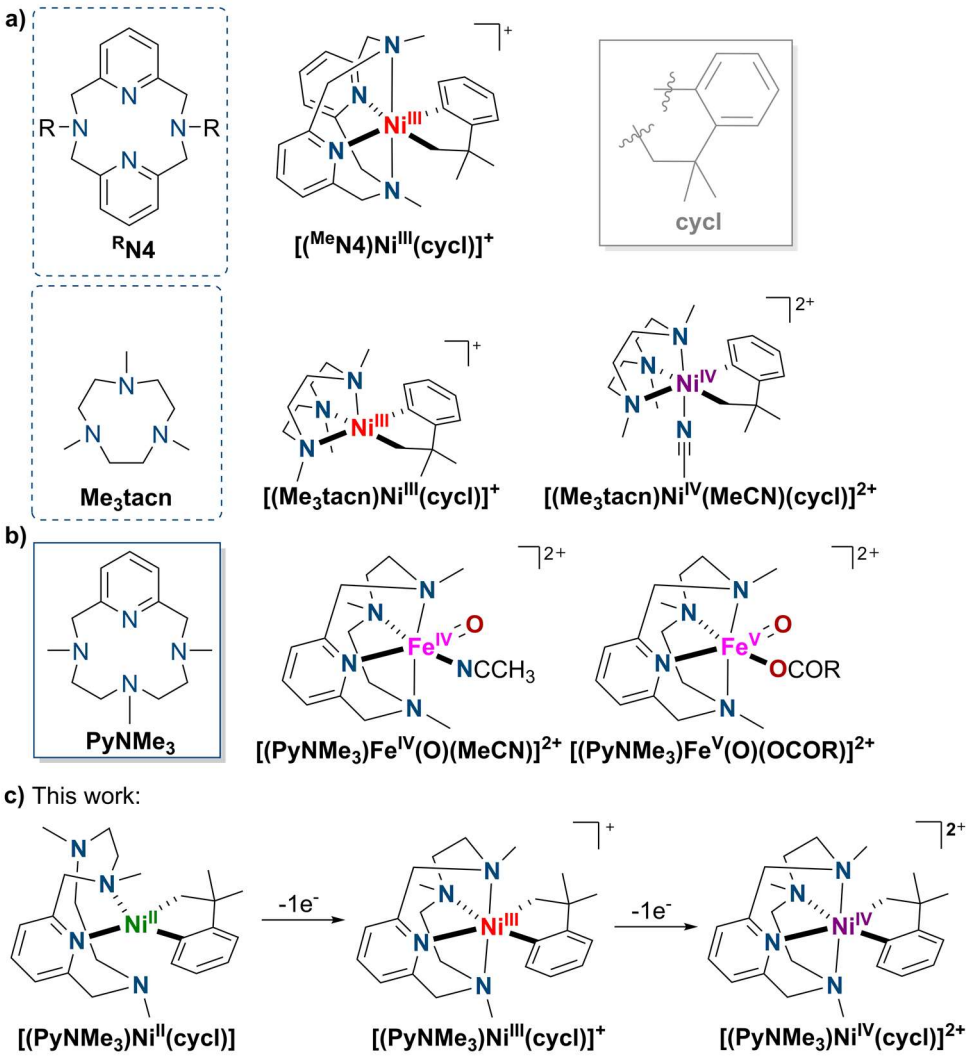

Fig. 1 (a) Isolated organometallic nickel complexes bearing tridentate or tetradentate *N*-donor ligands and cycloneophyl as the C-donor ligand; (b) spectroscopically characterized high-valent iron-oxo intermediate species relevant for O_2 activation chemistry bearing the tetradentate *N*-based **PyNMe$_3$** ligand, and (c) synthesis of well-defined organometallic nickel complexes bearing the **PyNMe$_3$** and the cycloneophyl ligands.

Results and Discussion

Our first attempt to isolate organometallic nickel complexes bearing the **PyNMe$_3$** ligand consisted of the *in situ* oxidative addition of 1-bromo-4-fluorobenzene using Ni(cod)$_2$. The putative [**(PyNMe$_3$)Ni^{II}(*p*F-Ph)(Br)**] complex could not be isolated due to fast decomposition and rapid ligand exchange that lead to the formation of 0.5 equiv. [(PyNMe$_3$)Ni^{II}Br$_2$] (**1-Br**) and 0.5 equiv. [**(PyNMe$_3$)Ni^{II}(*p*F-Ph)$_2$**]. The latter di-aryl complex then undergoes reductive elimination to afford the homocoupled product *p*F-Ph-Ph-*p*F (as detected via GC-MS), free ligand and Ni(0) (Fig. 2a). In addition, the reaction of the complex [(PyNMe$_3$)Ni^{II}(Cl)$_2$] (**1-Cl**) with MeMgCl in THF at -50°C led to an intractable mixture due

to fast decomposition of the desired nickel(II)-dimethyl complex (Fig. 2b). Nonetheless, the putative [(**PyNMe$_3$**)**Ni^{II}(Me)$_2$**] species could be detected via ^{1}H-NMR, which revealed two singlets below 0 ppm that integrated to three protons each and presumably correspond to the two inequivalent methyl groups directly attached to the Ni center (Fig. S1).

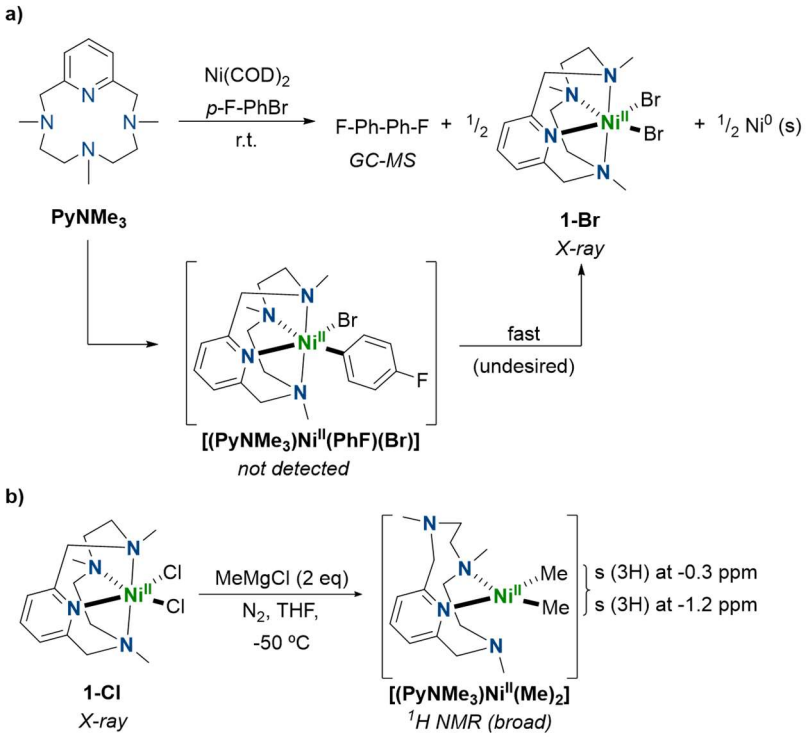

Fig. 2 (a) Attempt to synthesize complex [(**PyNMe$_3$**)**Ni^{II}(PhF)(Br)**] via oxidative addition at nickel(0), and (b) attempt to synthesize [(**PyNMe$_3$**)**Ni^{II}(Me)$_2$**] *via* transmetallation at the nickel(II)-chloride precursor, **1-Cl**.

Gratifyingly, the combination of **PyNMe$_3$** and cycloneophyl (CH_2CMe_2-*o*-C_6H_4-, or cycl) as ligands allows the stabilization and isolation of complex [(PyNMe$_3$)Ni^{II}(cycl)] (**2**) in 67 % yield. The complex was synthesized via ligand exchange of the Ni(II) precursor [(py)$_2$Ni^{II}(cycl)] with an equimolar amount of **PyNMe$_3$** in 1:1 toluene/pentane, for 16 hours at room temperature under a nitrogen atmosphere (Fig. 3a). The X-ray structure revealed a square planar geometry around the Ni(II) center, with the **PyNMe$_3$** ligand coordinated in a bidentate fashion (Fig. 3b). This new system allows for the observation the *trans* influence of the ligands. Interestingly, **PyNMe$_3$** ligand coordinates to the Ni(II) center through the pyridine moiety which is *trans* to the alkyl ligand, and one of the adjacent amines *trans* to the phenyl group. This type of coordination could not be observed with the previously reported systems bearing symmetric pyridinophane type ligands (^{R}N4). In addition, the ^{1}H-NMR spectrum confirms that **2** is a low-spin diamagnetic Ni(II) complex. Detailed NMR experiments were used to assign all proton and

carbon peaks for **2** (Fig. S2-S9). The broadness of the peaks, especially the methylene protons on the **PyNMe$_3$** ligand, is likely due to rapid ligand exchange of the four types of N donors. Furthermore, the unusual Ni(II) structure allows for an anagostic interaction of the methylene protons vicinal to the tertiary amine and the Ni metal center, with a Ni···H distance of 2.40 Å and a Ni···H-C angle of 170°.

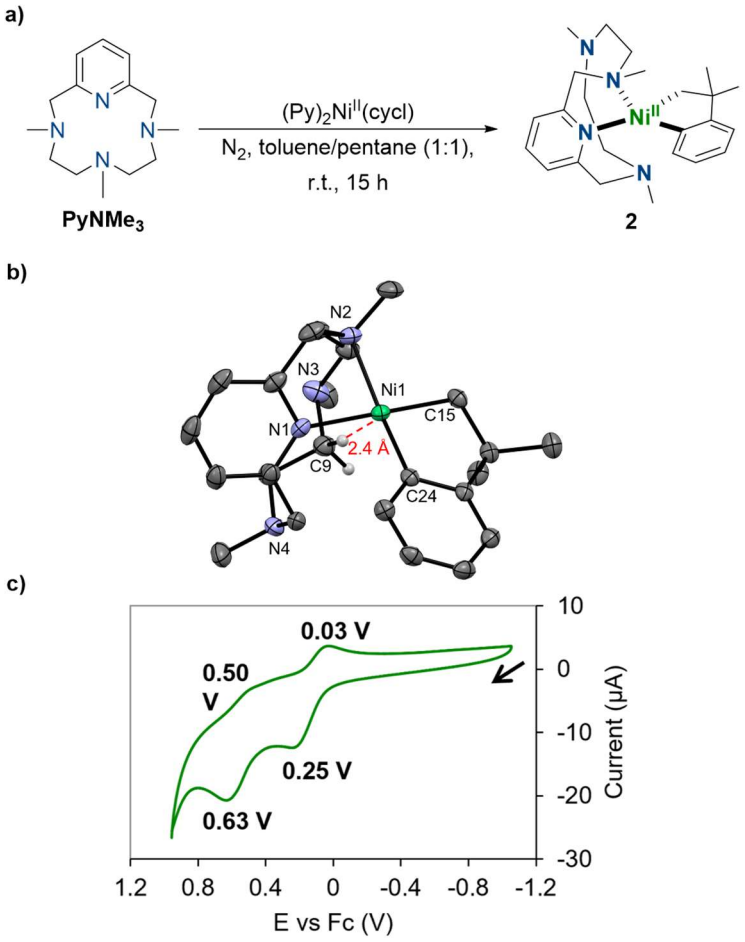

Fig. 3 (a) Synthesis and characterization of complex [(PyNMe$_3$)Ni^{II}(cycl)], **2**; (b) X-ray crystal structure of **2** (selected bond distances (Å): Ni-C1, 1.888(2); Ni-C2, 1.932(2); Ni-N1, 2.0535(19); Ni-N4, 1.9923(19), and (c) CV of **2** in 0.1 M NBu$_4$(PF$_6$)/MeCN at a scan rate of 100 mV/s.

The cyclic voltammogram (CV) of **2** in 0.1 M (nBu$_4$N)PF$_6$/MeCN reveals a quasi-reversible redox event at $E_{1/2}$ = 250 mV vs ferrocene (Fc), followed by another quasireversible oxidation at $E_{1/2}$ = 630 mV (Fig. 3c). These observed pseudo-reversible oxidations are presumably assigned to the Ni$^{III/II}$ and Ni$^{IV/III}$ redox couples, respectively. This result suggests accessible Ni(III) and Ni(IV) species, likely due to the stabilizing effect of the two anionic chelating C donors from the cycloneophyl ligand, as well as the tetradentate **PyNMe$_3$** ligand, as reported previously for high-valent iron-oxo species.[27, 33, 37]

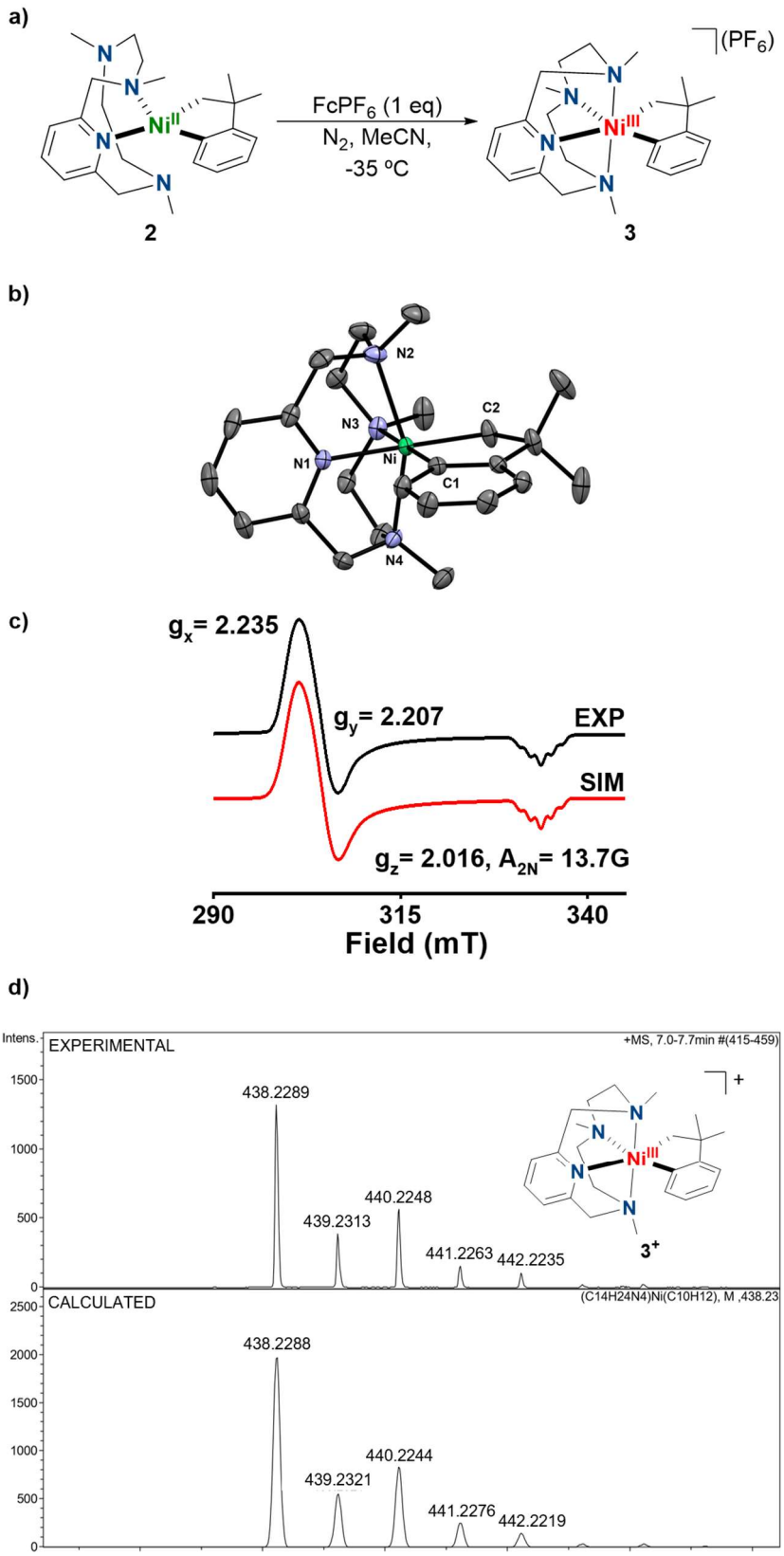

Fig. 4 (a) Synthesis and characterization of complex [(PyNMe$_3$)Ni^{III}(cycl)](PF$_6$), **3**; (b) ORTEP representation of **3** (50% probability thermal ellipsoids): Ni-C1, 1.9492 (12); Ni-C2, 1.9693 (14); Ni-N1, 1.9944 (11); Ni-N2, 2.2543 (13); Ni-N3, 2.1463 (12); Ni-N4, 2.2470 (12); (c) EPR spectra of complex **3** at 77 K 1:3 MeCN/PrCN (black: experimental; red: simulated), and (d) cryo-HR-MS of **3** showing the monocationic peak (**3**$^+$) at m/z = 438.2289 (top) and the simulation of its isotopic pattern (bottom).

In fact, **2** was rapidly oxidized with 1 equiv. of ferrocenium hexafluorophosphate ($FcPF_6$) in MeCN at -35 °C to yield the reddish product $[(PyNMe_3)Ni^{III}(cycl)](PF_6)$, **3** (Fig. 4a). The EPR spectrum of **3** in 1:3 MeCN/PrCN is consistent with a Ni (III) d^7 complex and exhibits a pseudoaxial signal with superhyperfine coupling to two nitrogen atoms in the g_z direction (A_{2N} = 13.7 G), indicating that two I = 1 nitrogen atoms, presumably from the ligand and/or solvent, coordinate to the Ni(III) center (Fig. 4c). Luckily, complex **3** was stable and isolated at low temperature in a 73 % yield.

The single crystal Xray structure of **3** confirmed the six-coordinate Ni(III) center in a distorted octahedral geometry where the 6 coordination positions are occupied by the **PyNMe$_3$** and cycloneophyl ligands, thus confirming the EPR data (Fig. 4b). Intriguingly, both the Ni-N and Ni-C bond distances in **3** are longer than those in **2**, as previously observed for similar complexes, and likely due to the change in the coordination number from 4 to 6 upon oxidation.[33, 37] Moreover, cryo-ESI-mass spectrometry at -40 °C was performed to further characterize this Ni(III) complex. The MS spectrum showed a major monocharged peak with a m/z = 438.2289 and an isotopic pattern fully consistent with the calculated values for **3**$^+$, $[(C_{14}H_{24}N_4)Ni^{III}(C_{10}H_{12})]^+$ (Fig. 4d).

Attempts to synthetize the corresponding Ni(IV) complex were conducted through a stepwise oxidation of **2**. The oxidation of complex **2** to obtain complex **3** was monitored by low temperature UV/vis spectroscopy (Fig. 5a and b). This experiment was performed at -40 °C using a 0.5 mM solution of complex **2** in MeCN. An initial spectrum was recorded for the starting Ni(II) complex, which exhibits an absorption band at λ_{max} = 462 nm. For the one-electron oxidation of each complex monitored by low-temperature UV/vis, $NO(SbF_6)$ was used as oxidant in order to obtain a cleaner spectrum, since Fc^+ exhibits two absorption bands at 325 nm and 440 nm that could interfere with the detection of the new species. Thus, addition of 1 equiv. of NO^+ to **2** immediately yields complex **3**$^+$, which exhibits an absorption band with λ_{max} = 513 nm. Afterwards, another equivalent of the same oxidant was added to generate the new Ni(IV) complex, **4**$^{2+}$. Upon addition of the second equivalent of oxidant the UV/vis spectrum instantly changed and showed the formation of two absorption bands with λ_{max} of 384 nm and 470 nm, and a shoulder at 620 nm (Fig. 5b). The subsequent injection of an aliquot into cryo-ESI-mass

spectrometer confirmed the generation of species $\mathbf{4}^{2+}$ with a dicationic major peak with a mass value of m/z = 219.1120 and an isotopic pattern fully consistent with the calculated value for $[(C_{14}H_{24}N_4)Ni^{IV}(C_{10}H_{12})]^{2+}$ (Fig. 5c). This novel complex was further characterized by NMR spectroscopy, where a stepwise injection of 2 equiv. NO^+ resulted in the observation of a new Ni(IV) species (Fig. S10-S11).

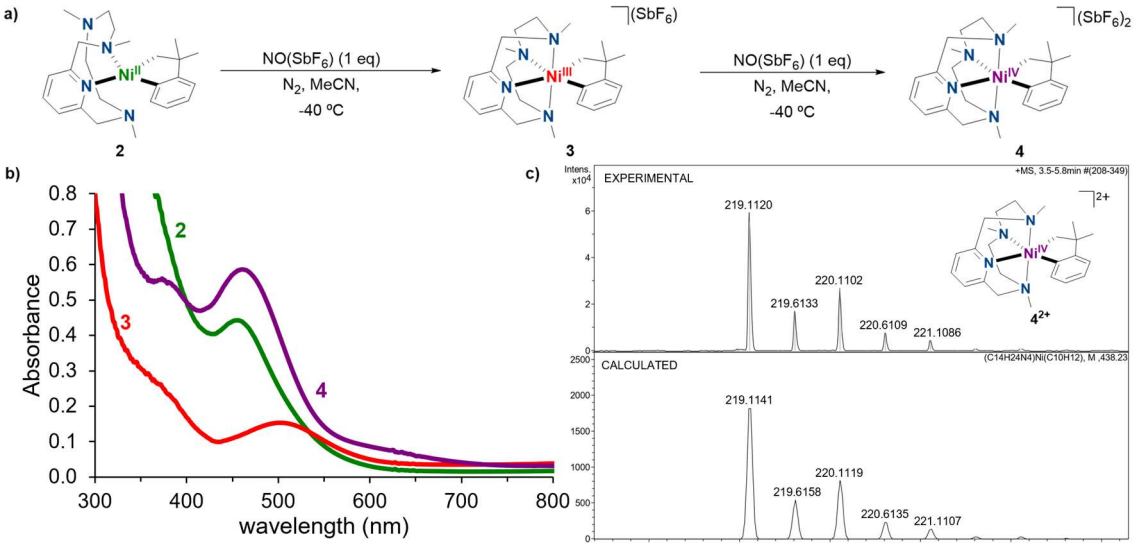

Fig. 5 (a) Step-wise one-electron oxidation to nickel(IV) from **2** using $NO(SbF_6)$ as an oxidant; (b) UV-vis characterization of complexes **2**, **3** and **4** obtained by the consecutive one-electron oxidation of **2** with $NO(SbF_6)$, respectively, and (c) cryo-HR-MS of **4** showing the dicationic peak ($\mathbf{4}^{2+}$) at m/z = 219.1120 (top) and simulation of its isotopic pattern (bottom).

In line with the UV-vis results, monitoring the oxidation by NMR provided complementary information. A color change from orange to red-pink was observed upon the addition of 1 equiv. of oxidant in CD_3CN at -35 °C, while the obtained paramagnetic NMR spectrum supports the formation of a Ni(III) species. Interestingly, a second equivalent of oxidant allowed the formation of a new diamagnetic species, tentatively assigned as a Ni(IV) complex. The inherent broadness of the NMR spectrum of the putative Ni(IV) species is likely caused by the residual Ni(III), which made peak assignment difficult. However, the obtained Ni(IV) spectrum closely resembles those of the recently reported Ni^{IV}-cycloneophyl complexes supported by the *N*-based macrocycles pyridinophane (^{Me}N4) and triazacyclononane (^{Me}tacn).[32,37] Due to the highly electrophilic nature of the Ni(IV) species, a key structural feature observed in both ^{Me}N4 and ^{Me}tacn Ni^{IV}-cyclonephyl systems is a large shift of the Ni^{IV}-CH_2- protons from ~2.10 ppm in their Ni^{II}-CH_2- counterparts to 5.33 ppm and 5.50 ppm, respectively. A similar shift was observed for

complex **4**, in which the Ni^{IV}-CH_2- protons shifted to 5.29 ppm, similar to what was observed for $[(^{Me}tacn)Ni^{IV}(cycl)]$.[32]

Next, we focused on the reactivity of **3** and **4** in C-C or C-O bond formation reactions. First, we exposed the Ni^{III} complex **3** to high temperatures (80 °C) to evaluate its stability, and it was found that the compound decomposed to an intractable mixture, which contains ~15% of the protodemetalation product *t*-butylbenzene. Then, since the Ni(IV) complex **4** was metastable, we studied its reactivity by generating it *in situ* through oxidation of **2** with a variety of two-electron oxidants such as XeF_2, NFTPT and $PhI(OAc)_2$, yet no promising reactivity was observed. On the contrary, interesting results were obtained when exploring its reactivity with green oxidants, such as O_2, H_2O_2, and ^{t}BuOOH (Fig. 6).

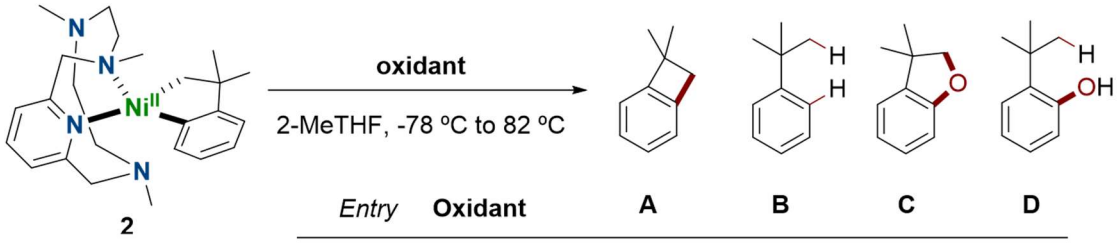

Entry	**Oxidant**	**A**	**B**	**C**	**D**
1	O_2	59 %	0 %	6 %	2 %
2	H_2O_2	9 %	1 %	11 %	2 %
3	$^tBuO_2H$	3 %	1 %	8 %	3 %

GC-MS

Fig. 6 Reactivity studies of complex **2** in front different two-electron oxidants, and the quantification of the respective organic products by GC-MS.

In these reactions, only trace amounts (<1%) of protodemetalation product t-butylbenzene, **B**, were observed in GC-MS, indicating a nearly full conversion of **2** into corresponding Ni^{III}/Ni^{IV} species. The reaction of **2** with 2 equiv. H_2O_2 in 2-MeTHF results in the formation of 11% **C** and 9% **A** as the primary organic products. The reaction of **2** with ^{t}BuOOH shows similar distribution of products. On the other hand, the reaction of complex **2** with dioxygen generated up to 59% of C-C coupled product **A**, exhibiting an appreciable C-C bond formation reactivity, which is proposed to occur *via* the intermediacy of the Ni(IV) species **4**. It is important to note that this tetradentate **PyNMe$_3$** ligand system displays a different reactivity from the structurally related pyridinophane ^{R}N4 system,[33] where C-O reductive elimination was greatly enhanced. In that case, it is likely that a Ni^{IV}-hydroxo transient, yet metastable intermediate was generated and

led to competing C-C/C-O reductive elimination steps, which has been observed for M^{IV} complexes (M = Pt, Pd) bearing ligands that are prone to reductive elimination.[32,33] By contrast, the [(PyNMe$_3$)Ni(cycl)] system seems to favor the C-C bond formation reactivity over the formation of any oxygen-containing products, possibly because the **PyNMe$_3$** ligand is flexible enough to strongly bind to the Ni(IV) species and complete the octahedral coordination geometry, without allowing the coordination of any additional oxidant-derived, O-donor ligand.

Conclusion

In summary, we have been able to explore the rich organometallic redox chemistry of Ni by characterizing spectroscopically Ni^{II} (**2**), Ni^{III} (**3**) and Ni^{IV} (**4**) complexes supported by the tetradentate N-donor ligand **PyNMe$_3$**. **2** features a square-planar geometry with two pendant aliphatic amine moieties, which enter into the coordination sphere of the metal upon oxidation to a Ni(III), **3**, that features a distorted octahedral geometry. Further reaction of **3** with another equivalent of oxidant affords the putative Ni(IV) complex **4**. Reactivity studies indicate that the *in situ* formed Ni(IV) complex, [(PyNMe$_3$)Ni^{IV}(cycl)](SbF$_6$)$_2$ (**4**), promotes C-C coupling over C-O coupling despite the use of O-based oxidants, in contrast to the related pyridinophane ^{R}N4 systems.[33] Overall, this new **PyNMe$_3$** ligand system provides important insight in understanding at a molecular level the electronic properties of dissymmetric macrocyclic ligands on well-defined Ni^{II} (**2**), Ni^{III} (**3**) and Ni^{IV} (**4**) organometallic complexes and their role in C-C and C-O bond formation transformations.

Acknowledgements

We acknowledge financial support from NSF CHE-1925751 to L.M., MINECO-Spain for projects PID2019-104498GB-I00 to X.R., PID2019-106699GB-I00 to A.C. Generalitat de Catalunya is also acknowledged for project 2017SGR264. We thank UdG for a IFUdG PhD grant to C.M. X.R. and A.C. are thankful for an ICREA Acadèmia award. The authors are grateful to STRUdG for technical support.

Notes and references

‡ CCDC 2118410 (**1-Br**), 2118413 (**1-Cl**), 2118411 (**2**), 2118412 (**3**) contains the supplementary crystallographic data for this paper. These data can be obtained free of charge

from The Cambridge Crystallographic Data Centre via www.ccdc.cam.ac.uk/data_request/cif. The Supporting Information also provides additional information.

1. F. Diederich and A. de Meijere, *Metal-Catalyzed Cross-* 31. *Coupling Reactions*, Wiley-VCH, Weinheim, Germany, 2nd edn., 2004.
2. J. F. Hartwig, *Organotransition Metal Chemistry: From Bonding to Catalysis*, University Science Books, Sausalito, 33. 2010.
3. J. Terao and N. Kambe, *Acc. Chem. Res.*, 2008, **41**, 1545-1554.
4. J. Magano and J. R. Dunetz, *Chem. Rev.*, 2011, **111**, 2177-2250.
5. J.-P. Corbet and G. Mignani, *Chem. Rev.*, 2006, **106**, 2651-2710.
6. C. C. C. Johansson Seechurn, M. O. Kitching, T. J. Colacot 37. and V. Snieckus, *Angew. Chem. Int. Ed.*, 2012, **51**, 5062-5085.
7. J. F. Hartwig, *Acc. Chem. Res.*, 1998, **31**, 852-860.
8. J. F. Hartwig, *Nature*, 2008, **455**, 314-322.
9. X. Hu, *Chem. Sci.*, 2011, **2**, 1867-1886.
10. V. B. Phapale and D. J. Cárdenas, *Chem. Soc. Rev.*, 2009, **38**, 1598-1607
11. T. T. Tsou and J. K. Kochi, *J. Am. Chem. Soc.*, 1978, **100**, 1634-1635.
12. T. T. Tsou and J. K. Kochi, *J. Am. Chem. Soc.*, 1979, **101**, 6319-6332.
13. J. Cornella, E. Gómez-Bengoa and R. Martin, *J. Am. Chem. Soc.*, 2013, **135**, 1997-2009.
14. C. A. Laskowski, D. J. Bungum, S. M. Baldwin, S. A. Del Ciello, V. M. Iluc and G. L. Hillhouse, *J. Am. Chem. Soc.*, 2013, **135**, 18272-18275.
15. L. M. Mirica, S. M. Smith and L. Griego, in *Nickel Catalysis in Organic Synthesis*, 2020, DOI: https://doi.org/10.1002/9783527813827.ch10, pp. 223-248.
16. A. Joshi-Pangu, C.-Y. Wang and M. R. Biscoe, *J. Am. Chem. Soc.*, 2011, **133**, 8478-8481.
17. A. S. Dudnik and G. C. Fu, *J. Am. Chem. Soc.*, 2012, **134**, 10693-10697.
18. N. D. Schley and G. C. Fu, *J. Am. Chem. Soc.*, 2014, **136**, 16588-16593.
19. J. C. Tellis, D. N. Primer and G. A. Molander, *Science*, 2014, **345**, 433-436.
20. Z. Zuo, D. T. Ahneman, L. Chu, J. A. Terrett, A. G. Doyle and D. W. C. MacMillan, *Science*, 2014, **345**, 437-440.
21. J. Cornella, J. T. Edwards, T. Qin, S. Kawamura, J. Wang, C.-M. Pan, R. Gianatassio, M. Schmidt, M. D. Eastgate, P. S. Baran, *J. Am. Chem. Soc.*, 2016, **138**, 2174-2177.
22. S. Z. Tasker, E. A. Standley and T. F. Jamison, *Nature*, 2014, **509**, 299-309.
23. J. R. Bour, N. M. Camasso, E. A. Meucci, J. W. Kampf, A. J. Canty and M. S. Sanford, *J. Am. Chem. Soc.*, 2016, **138**, 16105-16111.
24. N. M. Camasso and M. S. Sanford, *Science*, 2015, **347**, 1218-1220.
25. J. R. Khusnutdinova, N. P. Rath and L. M. Mirica, *J. Am. Chem. Soc.*, 2010, **132**, 7303-7305.
26. J. R. Khusnutdinova, N. P. Rath and L. M. Mirica, *Angew. Chem. Int. Ed.*, 2011, **50**, 5532-5536.

27. J. R. Khusnutdinova, N. P. Rath and L. M. Mirica, *J. Am. Chem. Soc.*, 2012, **134**, 2414-2422.
28. F. Tang, Y. Zhang, N. P. Rath and L. M. Mirica, *Organometallics*, 2012, **31**, 6690-6696.
29. F. Tang, F. Qu, J. R. Khusnutdinova, N. P. Rath and L. M. Mirica, *Dalton Trans.*, 2012, **41**, 14046-14050.
30. J. R. Khusnutdinova, N. P. Rath and L. M. Mirica, *Inorg. Chem.*, 2014, **53**, 13112-13129.
31. F. Qu, J. R. Khusnutdinova, N. P. Rath and L. M. Mirica, *Chem. Commun.*, 2014, **50**, 3036-3039.
32. M. B. Watson, N. P. Rath and L. M. Mirica, *J. Am. Chem. Soc.*, 2017, **139**, 35-38.
33. S. M. Smith, O. Planas, L. Gómez, N. P. Rath, X. Ribas, L. M. Mirica, *Chem. Sci.*, 2019, **10**, 10366-10372.
34. B. Zheng, F. Tang, J. Luo, J. W. Schultz, N. P. Rath and L. M. Mirica, *J. Am. Chem. Soc.*, 2014, **136**, 6499-6504.
35. F. Tang, N. P. Rath and L. M. Mirica, *Chem. Commun.*, 2015, **51**, 3113-3116.
36. W. Zhou, J. W. Schultz, N. P. Rath and L. M. Mirica, *J. Am. Chem. Soc.*, 2015, **137**, 7604-7607.
37. J. W. Schultz, K. Fuchigami, B. Zheng, N. P. Rath and L. M. Mirica, *J. Am. Chem. Soc.*, 2016, **138**, 12928-12934.
38. W. Zhou, S. Zheng, J. W. Schultz, N. P. Rath and L. M. Mirica, *J. Am. Chem. Soc.*, 2016, **138**, 5777-5780.
39. S. M. Smith, N. P. Rath and L. M. Mirica, *Organometallics*, 2019, **38**, 3602-3609.
40. H. Na, M. B. Watson, F. Tang, N. P. Rath and L. M. Mirica, *Chem. Commun.*, 2021, **57**, 7264-7267.
41. E. Andris, J. Jašík, L. Gómez, M. Costas and J. Roithová, *Angew. Chem. Int. Ed.*, 2016, **55**, 3637-3641.
42. J. Serrano-Plana, A. Aguinaco, R. Belda, E. García-España, M. G. Basallote, A. Company and M. Costas, *Angew. Chem. Int. Ed.*, 2016, **55**, 6310-6314.
43. J. Serrano-Plana, W. N. Oloo, L. Acosta-Rueda, K. K. Meier, B. Verdejo, E. García-España, M. G. Basallote, E. Münck, L. Que, A. Company and M. Costas, *J. Am. Chem. Soc.*, 2015, **137**, 15833-15842.
44. V. Dantignana, J. Serrano-Plana, A. Draksharapu, C. Magallón, S. Banerjee, R. Fan, I. Gamba, Y. Guo, L. Que, M. Costas and A. Company, *J. Am. Chem. Soc.*, 2019, **141**, 15078-15091.
45. C. Magallón, J. Serrano-Plana, S. Roldán-Gómez, X. Ribas, M. Costas and A. Company, *Inorg. Chim. Acta*, 2018, **481**, 166-170.
46. E. Carmona, F. González, M. L. Poveda, J. L. Atwood and R. D. Rogers, *J. Chem. Soc., Dalton Trans.*, 1981, 777-782.
47. E. Carmona, E. Gutierrez-Puebla, J. M. Marin, A. Monge, M. Paneque, M. L. Poveda and C. Ruiz, *J. Am. Chem. Soc.*, 1989, **111**, 2883-2891.

48. E. Carmona, P. Palma, M. Paneque, M. L. Poveda, E. Gutierrez-Puebla and A. Monge, *J. Am. Chem. Soc.*, 1986, **108**, 6424-6425.
49. N. M. Camasso, A. J. Canty, A. Ariafard and M. S. Sanford, *Organometallics*, 2017, **36**, 4382-4393.
50. A. J. Canty, A. Ariafard, N. M. Camasso, A. T. Higgs, B. F. Yates and M. S. Sanford, *Dalton Trans.*, 2017, **46**, 3742- 3748.
51. I. M. Pendleton, M. H. Pérez-Temprano, M. S. Sanford and P. M. Zimmerman, *J. Am. Chem. Soc.*, 2016, **138**, 6049- 6060.
52. N. M. Camasso, M. H. Pérez-Temprano and M. S. Sanford, *J. Am. Chem. Soc.*, 2014, **136**, 12771-12775.
53. M. H. Pérez-Temprano, J. M. Racowski, J. W. Kampf and M. S. Sanford, *J. Am. Chem. Soc.*, 2014, 136, 4097-4100.
54. J. M. Racowski, J. B. Gary and M. S. Sanford, *Angew. Chem. Int. Ed.*, 2012, **51**, 3414-3417.

Chapter VII. Results and discussion

VII.1 PREPARATION OF A COORDINATIVELY SATURATED μ-η²:η²-PEROXODICOPPER(II) COMPOUND

As explained in section I.3 (0), $Cu_n:O_2$ adducts are intermediates which play a key role in the catalytic cycle of O_2-activating copper-containing enzymes as they are directly involved in the oxidation/oxygenation of hydrocarbons.[1, 2] However, these copper-oxygen adducts are very reactive and for this reason these compounds are difficult to trap and characterize. In this regard, a useful strategy to gain insight into such elusive species involves the synthesis, characterization and reactivity studies towards dioxygen of discrete molecular bioinspired copper-based complexes.[3-5] In this context, we envisioned the use of the **PyNMe$_3$** ligand, which is a tetradentate nitrogen-based macrocyclic ligand that can coordinate the metal center through one pyridine and three aliphatic nitrogens. **PyNMe$_3$** was the ligand of choice as it was previously used in our laboratory for trapping high-valent iron-oxo species,[6-8] and later by Cho and co-workers for the synthesis and characterization of a mononuclear (hydro)peroxodicobalt(III) complex.[9]

The synthesis of the **PyNMe$_3$** ligand and its characterization was previously reported by our group.[8] Thus, we focused our attention to the synthesis of the corresponding mononuclear copper(I) complex, $[Cu^I(PyNMe_3)(CH_3CN)](OTf)$ (**1OTf**). The synthesis of **1OTf** was carried out under anaerobic conditions in a N_2-filled glovebox. The addition of 1 equivalent of $[Cu^I(CH_3CN)_4](OTf)$ to a solution of **PyNMe$_3$** in acetonitrile at room temperature afforded a yellow solution, indicating the coordination of the copper(I) center to the ligand (Figure VII.1). All the attempts to crystallize or isolate this compound were unsuccessful due to the tendency of copper(I) to disproportionate during the process. For this reason, everyday freshly prepared solutions of complex were used both to characterize the complex and to study its reactivity with molecular oxygen. Even though the X-Ray structure of this complex could not be obtained, DFT calculations suggested a C_s symmetric distorted square pyramidal geometry with the copper(I) center coordinated to the four nitrogens of the **PyNMe$_3$** ligand and to one CH_3CN ligand positioned in *trans* to the pyridine moiety (the optimized geometry without the coordination of CH_3CN ligand was 9.3 kcal mol^{-1} less stable) (Figure VII.1). The optimized geometry for $[Cu^I(PyNMe_3)(CH_3CN)]^+$ (**1**) is in agreement with previously reported copper(I) complexes

bearing tetradentate ligands and one CH_3CN molecule to complete the square-pyramidal pentadentate coordination environment.[10, 11]

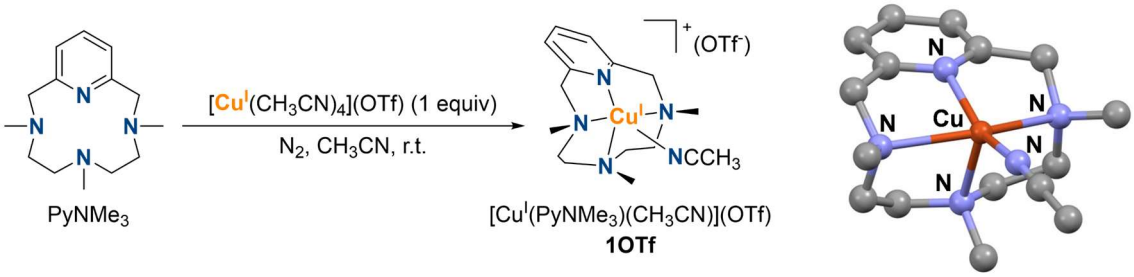

Figure VII.1 Synthesis of **1OTf** by reacting equimolar amounts of **PyNMe$_3$** ligand and $[Cu^I(CH_3CN)_4](OTf)$ in acetonitrile alongside with the DFT computed structure for compound **1**.

1OTf was characterized by several techniques such as high-resolution mass spectrometry (HR-MS) and NMR spectroscopy. Regarding the HR-MS, a clean spectrum was obtained with a very intense peak at m/z 311.1319 with a mass value and an isotopic pattern fully consistent with $[Cu^I(PyNMe_3)]^+$. Moreover, a small peak corresponding to the coordination of an CH_3CN molecule to the copper center was also observed ($[Cu^I(PyNMe_3)(CH_3CN)]^+$, m/z 352.1535), thus further supporting the formulation proposed by DFT (Figure VII.2).

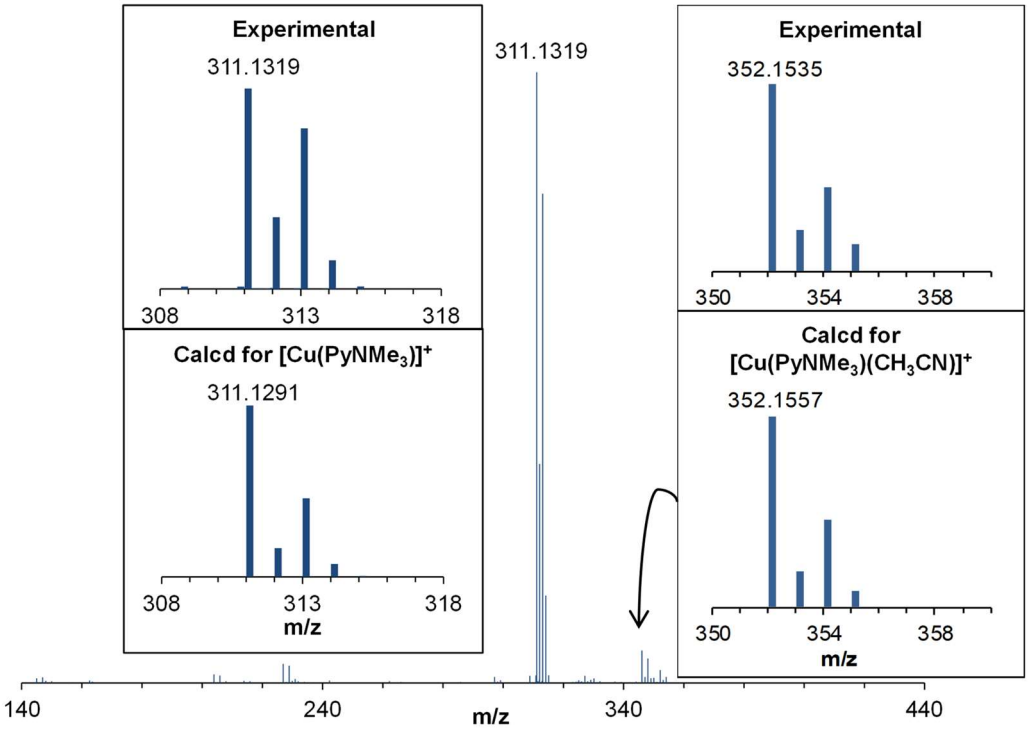

Figure VII.2 HR-ESI-MS spectra of $[Cu^I(PyNMe_3)](OTf)$ (**1OTf**). Left inset: the expanded view of the main peak at a m/z = 311.1319 corresponding to $[Cu^I(PyNMe_3)]^+$ and the expanded view of the corresponding calculated spectrum for this molecular formula. Right inset: the expanded view of the small peak at a m/z = 352.1535 corresponding to $[Cu^I(PyNMe_3)(CH_3CN)]^+$ and the expanded view of the corresponding calculated spectrum for this molecular formula.

1OTf could also be characterized by NMR spectroscopy by synthesizing the compound directly in CD_3CN. Luckily, ^{1}H-NMR of this diamagnetic complex exhibited well-resolved signals due to the rigidity provided by the **PyNMe$_3$** ligand which enabled its assignment with the help of ^{13}C-NMR and bidimensional experiments (Figure VII.3).

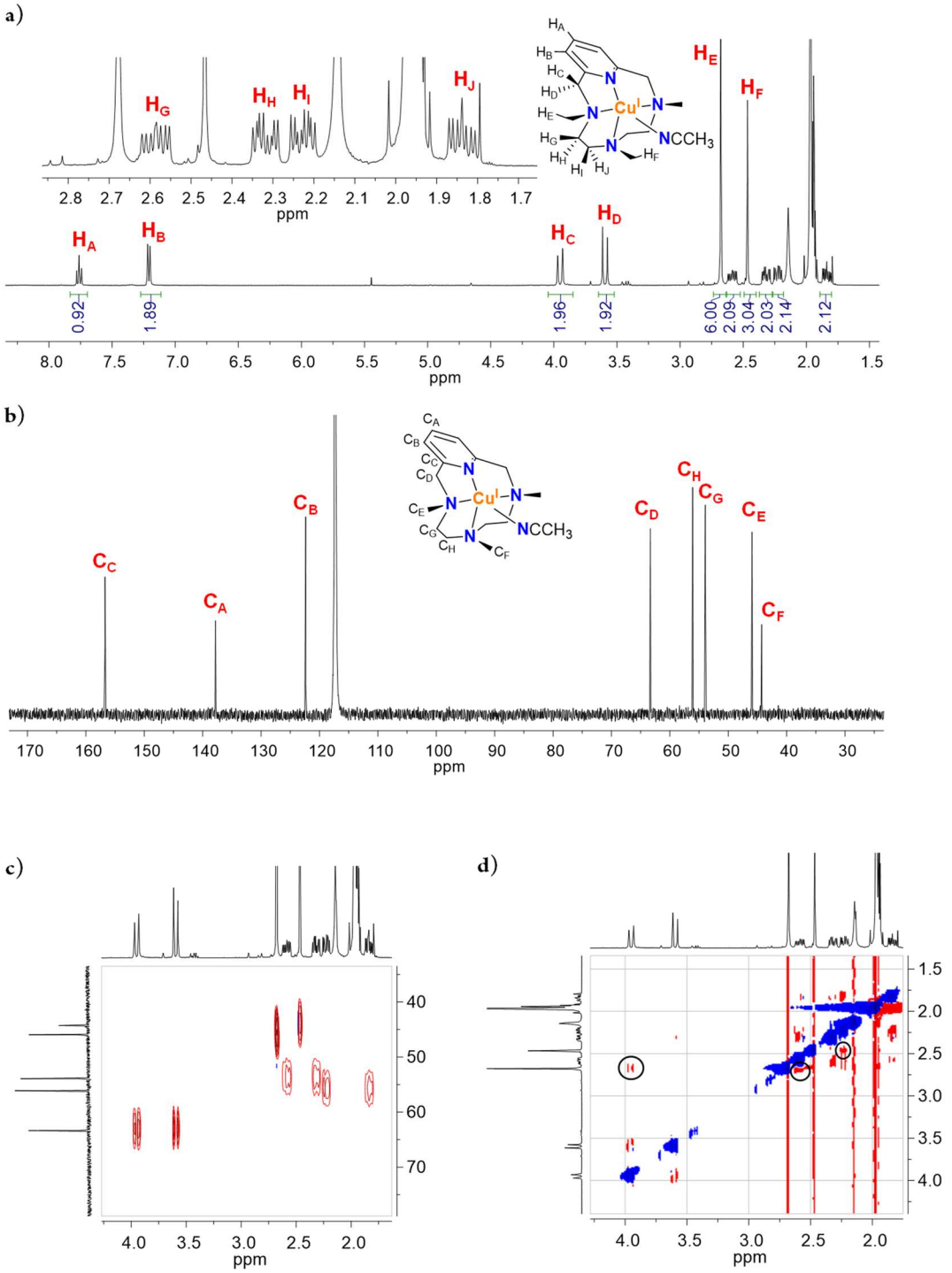

Figure VII.3 a) ^{1}H-NMR spectrum of **1OTf** in CD_3CN at room temperature; b) ^{13}C-NMR spectrum of **1OTf** in CD_3CN at room temperature; c) expanded view of the HSQC aliphatic region spectrum of **1OTf** in CD_3CN at room temperature, and d) expanded view of the NOESY aliphatic region spectrum of **1OTf** in CD_3CN at room temperature.

According to the NMR data, **1OTf** presents a C_s symmetry as predicted by the DFT calculations and in agreement with previously reported paramagnetic complexes bearing the **PyNMe$_3$** ligand.[6-9] Most of the protons were readily identified using either the chemical shift, the multiplicity of the signal or its integral. Hence, the signals corresponding to the pyridine γ proton and the two equivalent β protons are found in the aromatic region and consist of a triplet at 7.76 ppm and a doublet at 7.21 ppm, respectively. The four benzylic protons next to the pyridine appear as diastereotopic protons at 3.95 and 3.60 ppm as two sharp doublets. In the case of the N-methyl groups, the two equivalent methyl groups appear as a singlet at 2.68, while the other one appears at 2.47 ppm. However, methylenic protons between the aliphatic amines (H_I/H_J and H_H/H_G) in the 2.6 - 1.8 range could not be differentiated by monodimensional experiments and NOESY was necessary: H_I/H_J present a NOESY exchange peak with H_F (CH_3 group that integrates 3), while H_H/H_G present a NOESY exchange peak with H_E (CH_3 group that integrates 6). Moreover, HSQC was required which showed that H_I and H_J are attached to the same carbon (C_H), which is different from that bound to H_H and H_G (C_G).

At this point and with all the characterization data in hand, we wanted to study the reactivity of complex **1OTf** towards molecular oxygen. As well-established in literature, the metal-dioxygen species formed upon reaction of copper(I) complexes and dioxygen at low temperatures normally have very characteristic colors, ranging from purple, dark yellow to brown. For this reason, the reaction of **1OTf** towards O_2 was monitored by UV-vis spectroscopy at low temperature. But first, to evaluate the reactivity of **1OTf** towards oxygen, we performed qualitative experiments to detect if any color change was taking place.

Early attempts of visually monitoring the reaction of **1OTf** with molecular oxygen in acetonitrile at -40 °C did not show a clear color change that could be attributed to the formation of a transient Cu:O_2 intermediate. Thus, we tried to synthesize the initial complex with other solvents such as acetone or THF that would allow us to lower the temperature to -90 or -100 °C. However, all attempts failed (direct oxidation from Cu(I) to Cu(II) or disproportionation to Cu(II) and formation of copper mirror was observed). Consequently, based on previous experiences in the group, the presence of CH_3CN is required in order to stabilize the +1oxidation state. For this reason, we tried solvent mixtures containing CH_3CN and another solvent such as THF or acetone. A mixture of CH_3CN:THF (1:19) was found to be optimal for the formation of the

intermediate species. At this point, when a O_2 atmosphere was bubbled to the complex solution in CH_3CN:THF 1:19 at -100 °C, the color of the solution clearly turned from yellow to deep brown. This color change was indicative of the formation of copper-dioxygen intermediates. The color disappeared upon warming up the reaction mixture to room temperature.

In order to further study the nature of the copper-dioxygen intermediate species formed, the reaction was monitored by means of low-temperature UV/vis spectroscopy using a 0.1 mM solution of **1OTf** in CH_3CN:THF (1:19) at -100 °C. During the reaction, the formation of an intense absorption band at λ_{max} = 353 nm (ε = 17200 $M^{-1}cm^{-1}$) was observed in the UV-vis spectra (Figure VII.4). This new species (**2**) reached its maximum absorbance after 120 seconds and then it immediately decayed ($t_{1/2}$ = 6 min at -100 °C) (Figure VII.4). By analogy with previously reported Cu_n:O_2 species, compound **2** may correspond to a μ-η^2:η^2-peroxo (**^sP**) species which typically exhibits UV-vis spectra with a single high intensity band between 340 and 380 nm.[4] This species would form by reaction of two molecules of **1** with only one molecule of O_2. Nevertheless, rRaman experiments would be necessary to unequivocally establish the coordination mode of the bound O_2 in this transient compound. HR-ESI-MS analysis of the reaction mixture after the self-decay of **2** revealed the formation of a copper(II) complex coordinated to the **$PyNMe_3$** ligand.

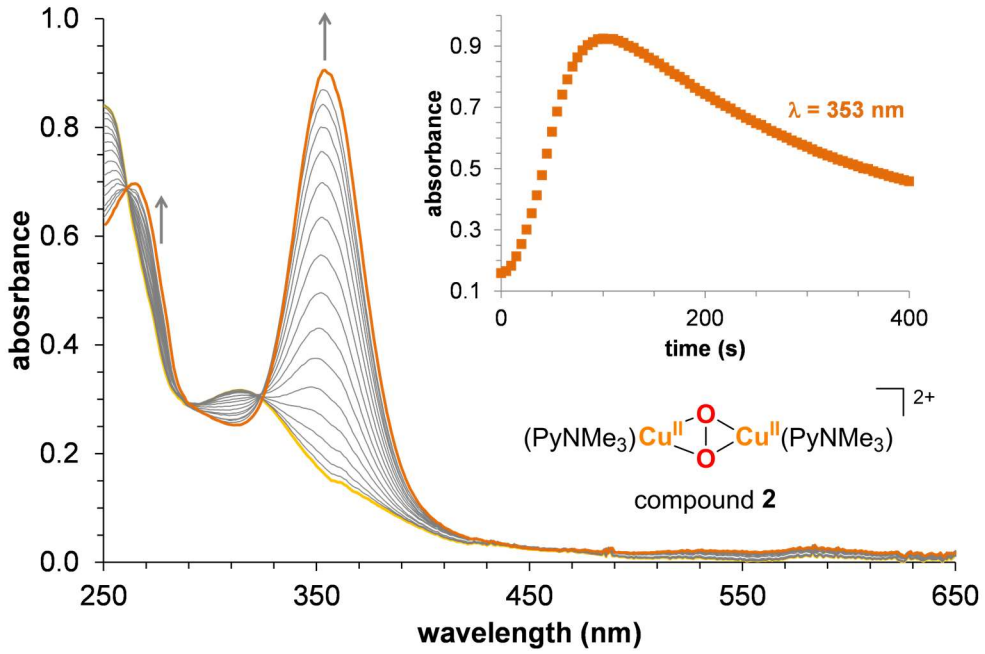

Figure VII.4 UV-vis spectra corresponding to the reaction of **1OTf** (0.1 mM) with O_2 in CH_3CN:THF (1:19) at -100 °C (yellow: **1OTf**; orange: **2**). Inset: time trace of the band at λ_{max} = 353 nm corresponding to the formation and self-decay of compound **2** at -100 °C.

As stated in section I.3.2 (0), tyrosinase carries out the *ortho*-hydroxylation of phenols to catechols and successive two-electron oxidation to *ortho*-quinones using molecular oxygen as oxidant. This reaction occurs via the involvement of a ^{S}**P** intermediate species.[12] Thus, with the idea of mimicking the activity of the enzyme, preliminary studies of the reactivity of **2** towards phenolates were performed, to test if this compound behaves as a functional model of tyrosinase. To do so, the reaction of **2** with sodium *para*-chlorophenolate was monitored by UV-vis at low temperature. In a typical experiment, and upon maximum formation of **2**, a solution containing 10 equivalents of sodium *para*-chlorophenolate in THF was added into the UV-vis cell, which caused the immediate decay of the intense band at 353 nm characteristic of **2**. This rapid decay of the band might be indicative of the coordination of the phenolate to the copper-dioxygen intermediate species. Sadly, no presence of neither catechol nor *ortho*-quinone was detected when analyzing the reaction crude, indicating that species **2** does not succeed in reproducing tyrosinase reactivity. This result could find an explanation in the rigidity given by the tetradentate **PyNMe$_3$** ligand which strongly coordinates the copper center and yields a coordinatively saturated ^{S}**P** compound **2**. This might preclude the phenolate from binding to the copper center in **2** and so the attack of the peroxide moiety to the aromatic ring is hampered (Scheme VII.1).[13]

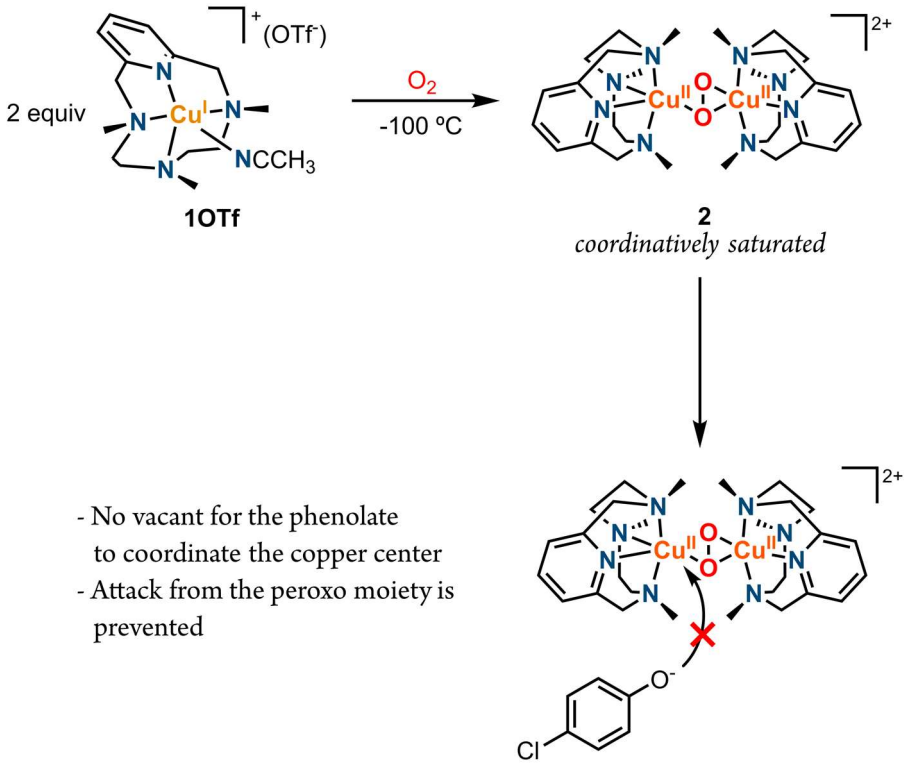

Scheme VII.1 O_2 activation by **1OTf** affording the ^{S}**P** species **2**, which is not able to oxidize phenolates.

In view of these results, we decided to test other substrates such as electrophilic sulfides as ^{S}**P** species are known to oxidize them. We tried the oxidation of 4-methoxythioanisole by compound **2**, although only a 2% of the corresponding sulfoxide oxidation product was obtained (Scheme VII.2).

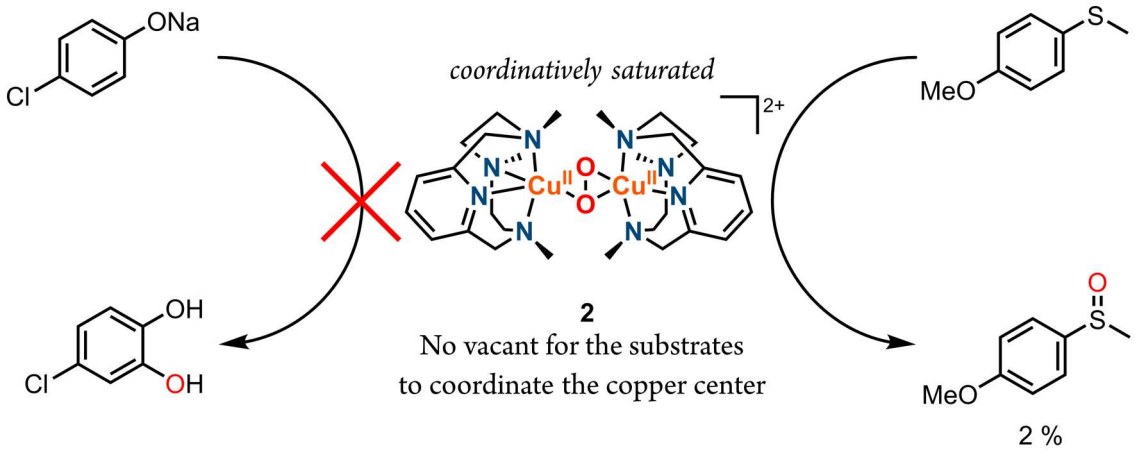

Scheme VII.2 Structure of compound **2**; its lack of reactivity towards phenolates (left), and its scarce reactivity to oxidize 4-methoxythianisole.

To summarize, we have been able to synthetize a bioinspired copper-based model system capable of performing O_2-binding and activation at low temperatures. Despite the formation of a ^{S}**P** species upon dioxygen exposure at low temperature, the tetradentate nitrogen-based environment provided by the **PyNMe$_3$** ligand does not allow the interaction of the copper center with the substrate, thus precluding reactivity with exogenous substrates. In fact, functional models of tyrosinase usually bear tri- or bidentate nitrogen-based ligands which enable the interaction of the copper center with the phenolic substrate.[5, 14]

VII.2 MECHANISTIC INSIGHTS INTO THE *ORTHO*-DEFLUORINAITON-HYDROXYLATION OF 2-HALOPHENOLATES PROMOTED BY A BIS(μ-OXO)DICOPPER(III) COMPLEX

Lots of efforts have been devoted towards the bioinspired oxidation/hydroxylation of C-H bonds. Nevertheless, much remains to be known and investigated to completely understand and control the mechanism by which these transformations occur. In the meantime, new challenges have arisen such as the need for cleaving C-F bonds.

Fluorinated organic molecules are used in a daily basis. For example, up to 30% of agrochemical products and 20% of pharmaceutical compounds used in our everyday routine contain fluorine.[15] Fluorinated compounds are interesting in medicinal chemistry and agrochemistry because they improve the lipophilicity and so present larger *in vivo* residence times in comparison with their nonfluorinated analogues.[15, 16] Nevertheless, the recent increase in the large-scale production and use of such compounds has led them to debate because of their high toxicity, ozone depletion and global warming potential, bioaccumulation and environmental endurance.[17, 18] All these advantages and drawbacks arise from the same fact: the inertness of C-F bonds (BDE of 130 kcal mol^{-1}). Their high bond dissociation energy is given by fluorine's electronegativity that strongly polarizes and shortens C-F bonds, increasing the ionic character of the chemical bond.[19] For this reason, C-F bonds are considered the strongest single bond to carbon and so the most inert functionality, which provides fluorinated organic molecules with high thermal stability. Hence, the need for the development of new strategies to cleave C-F bonds for the degradation of fluorinated organic compounds and further transformation of those into more reactive functionalities has emerged.

As mentioned in section I.3.2 (0), tyrosinase is a dicopper enzyme responsible for catalyzing the *ortho*-hydroxylation of phenols to catechols and their further oxidation to quinones using molecular oxygen.[2, 12, 14] Tyrosinase is known to operate through a side-on peroxo-dicopper(II) species (^{S}**P**) where the phenolate coordinates one of the copper centers and subsequent attack of the peroxo moiety over the arene ring affords the corresponding oxidation product. However, the substrate scope of this copper enzyme is restricted to the cleavage of C-H bonds. Indeed, replacement of the oxidizable C-H bonds in the substrate by C-F bonds is known to inhibit the

catalytic activity of tyrosinase.[20, 21] Nonetheless, other natural enzymes, such as cytochrome P450, chloroperoxidase and flavin adenine dinucleotide (FAD)-containing phenol hydroxylases, can carry out the defluorination of aromatic compounds.[22, 23] For instance, in analogy with tyrosinase's reactivity, (FAD)-containing phenol hydroxylases can transform 2-fluorophenols to catechols.[24-26]

Thanks to the many studies on model compounds, it has been demonstrated that usually the **P** species are in equilibrium with highly electrophilic bis(μ-oxo)dicopper(III) species (**O**).[27] This **O** species may unravel new oxidative transformations which are unattainable by the **P** isomer. Actually, our group demonstrated in 2014 the ability of the **O** species to catalyze the *ortho*-defluorination-hydroxylation of 2-fluorophenolates to yield the corresponding catechols and so selectively converting C_{Ar}-F bond into a C_{Ar}-OH functionality.[28] This result suggests that the **O** isomer is the key active species for the defluorination-hydroxylation of 2-fluorophenols. Given this precedent, we decided to explore both experimentally and computationally the selective defluorination-hydroxylation of 2-fluorophenolates with $[Cu_2O_2(DBED)_2]^{2+}$ (**1**), a compound first described by Stack and co-workers (Scheme VII.3).[29, 30] This system is particularly interesting because it corresponds to a **P** species, that upon addition of a phenolate transforms into a **O** compound which eventually hydroxylates the substrate. Thus, both **P** and **O** isomers are observed in the same system. Moreover, previous studies in our group have shown that **1** can also perform the *ortho*-defluorination-hydroxylation of 2-fluorophenolates, exhibiting selectivity for C-F over C-H or C-Cl bonds.[28] By using this complex, we wanted to give answer to three different questions: (i) which species **P** or **O** is responsible for the C-F bond cleavage and subsequent hydroxylation of the 2-fluorophenolic substrate; (ii) the origin of the selective hydroxylation at the *ortho*-C-F bond over the *ortho*-C-H bond upon reacting with 2-fluorophenols, and (iii) why C-Cl bonds remain unreactive despite being weaker than C-F bonds. The obtained experimental results will be explained in detail, and they will be briefly related to the computational results performed in this collaborative work by Mr. Pau Besalú and Dr. Josep M. Luís.

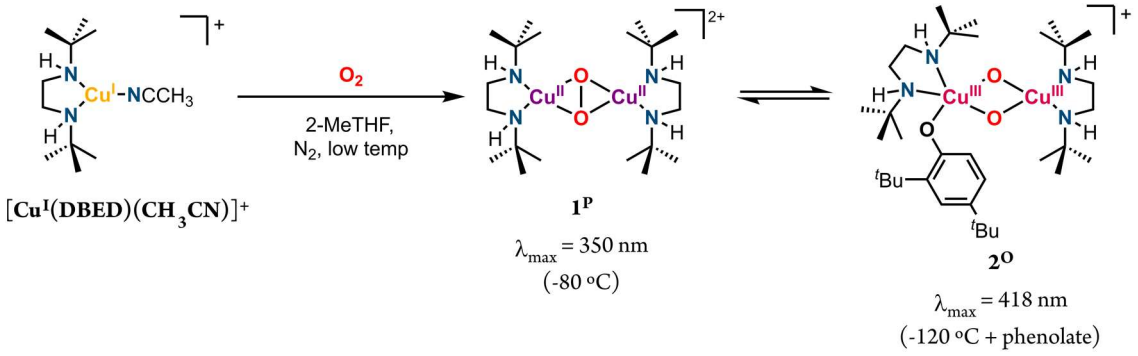

Scheme VII.3 System described by Stack and co-workers for the ortho-hydroxylation of phenolates.

Synthesis of the copper(I) precursor, **[Cu^{I}(DBED)(CH$_3$CN)](PF$_6$)**, was performed following a slightly modified procedure from the previously reported one in literature by Mirica *et al.*[29, 30] Under a N_2 atmosphere, 20 mM solutions of the **DBED** ligand and $[Cu^{I}(CH_3CN)_4](PF_6)$ in acetonitrile were prepared. Then equimolar amounts of the ligand and the copper(I) salt were mixed to give a 20 mM yellow solution of **[Cu^{I}(DBED)(CH$_3$CN)](PF$_6$)** after stirring for 1 hour at room temperature. As this copper(I) compound is very sensitive to oxygen and water, all the reactivity experiments were performed using freshly prepared **[Cu^{I}(DBED)(CH$_3$CN)](PF$_6$)** solutions everyday.

Since Cu_2O_2 adducts are thermally unstable species, low temperature UV-vis monitoring is required in order to avoid decomposition. As **[Cu^{I}(DBED)(CH$_3$CN)](PF$_6$)** seems to decompose in the absence of acetonitrile solvent, so a solvent mixture was required in order to lower the temperature below -80 °C. The optimal ratio to avoid decomposition of the copper(I) complex was found to be CH_3CN:2-MeTHF in a 1:19 solvent mixture. At this point the reaction of a 0.5 mM solution of **[Cu^{I}(DBED)(CH$_3$CN)](PF$_6$)** in CH_3CN:2-MeTHF 1:19 with O_2 at -80 °C was monitored by UV-vis spectroscopy giving an intense band at λ_{max} = 356 nm corresponding to the side-on peroxodicopper(II) species, **1^{P}**. This species **1^{P}** (ε =6400 $M^{-1}cm^{-1}$) was fully formed after ca. 15 min (Figure VII.5). Even though **1^{P}** is the most stable isomer, this species may be in equilibrium with the **1^{O}** isomer. Indeed, the relative Gibbs energies of both isomers were computed, and the result is in agreement with the experimental finding where the **1^{P}** isomer is ca. 4.1 kcal·mol^{-1} lower in energy than the corresponding **1^{O}** isomer (Figure VII.5).

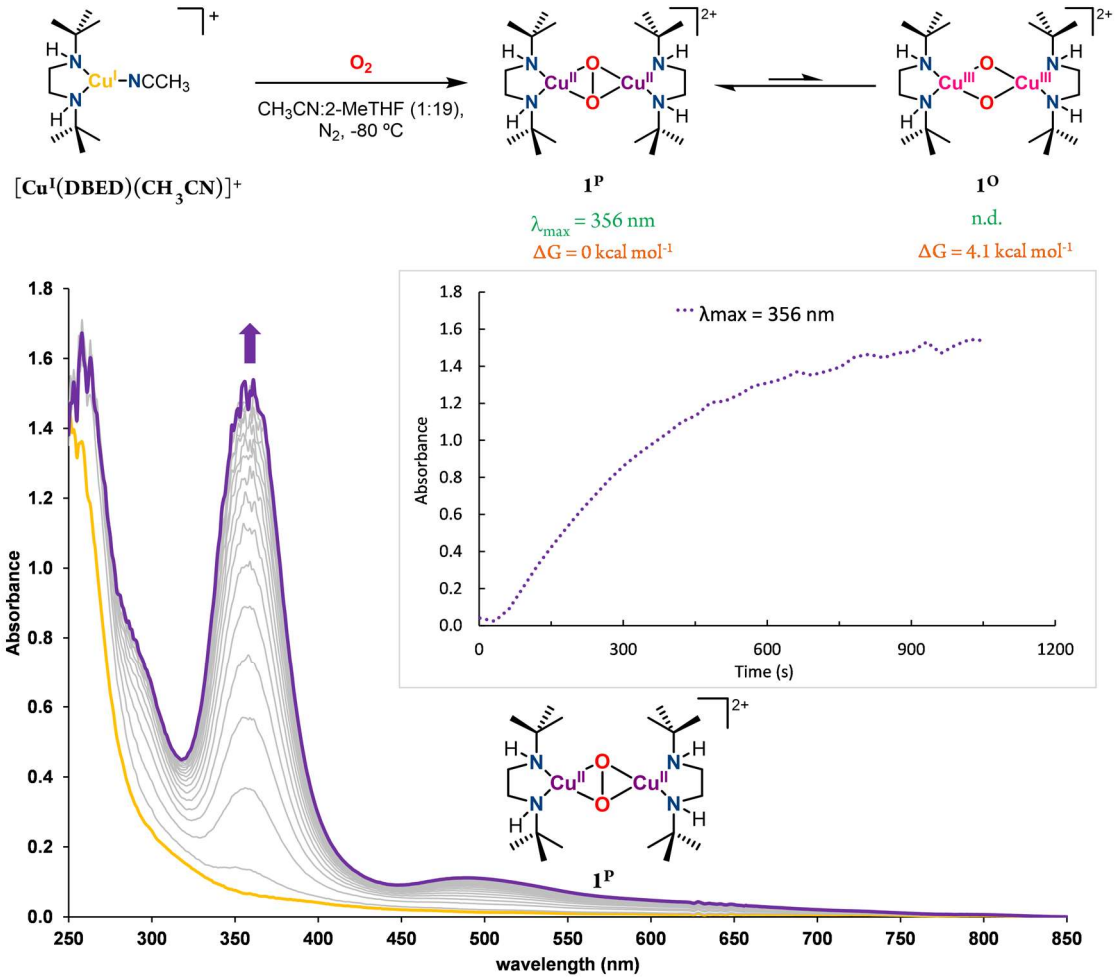

Figure VII.5 Top: Reaction of $[\mathbf{Cu^{I}(DBED)(CH_3CN)}]^+$ with O_2 to form $\mathbf{1^P}$ and $\mathbf{1^O}$ isomers along with the calculated Gibbs free energies (orange). Bottom: Reaction of $[\mathbf{Cu^{I}(DBED)(CH_3CN)}]^+$ (0.5 mM) with O_2 in CH_3CN:2-MeTHF 1:19 at -80 °C monitored by UV-vis spectroscopy. Inset: kinetic trace at λ_{max} = 356 nm.

In order to generate the corresponding **O** isomer, the previously $\mathbf{1^P}$ species was cooled down to -110 °C. When thermal equilibrium was reached, a new UV-vis spectrum of the $\mathbf{1^P}$ species was recorded. At this point, 1 equivalent (per Cu^I precursor) of sodium 2,6-difluorophenolate dissolved in 50 μL of acetone was added. This addition triggered the decay of the band at λ = 356 nm characteristic of $\mathbf{1^P}$, and the immediate generation of the bis(μ-oxo) species with the bound phenolate ($\mathbf{2^O}$·**a**) was observed with characteristic absorption bands at λ = 445 nm and λ = 560 nm (Figure VII.6). $\mathbf{2^O}$·**a** was not stable even at low temperatures and decomposed as shown in the kinetic traces (Figure VII.6). This result was further supported by ab initio calculations, which indicate that the **O** isomer ($\mathbf{2^O}$·**a**) is 3.6 kcal·mol^{-1} more stable than the **P** isomer ($\mathbf{2^P}$·**a**) upon phenolate coordination (Figure VII.6). Overall, these results are consistent with those previously reported by Stack and co-workers, indicating that the conversion to the **O** isomer occurs upon coordination of the phenolic substrate to the **P** isomer.[30]

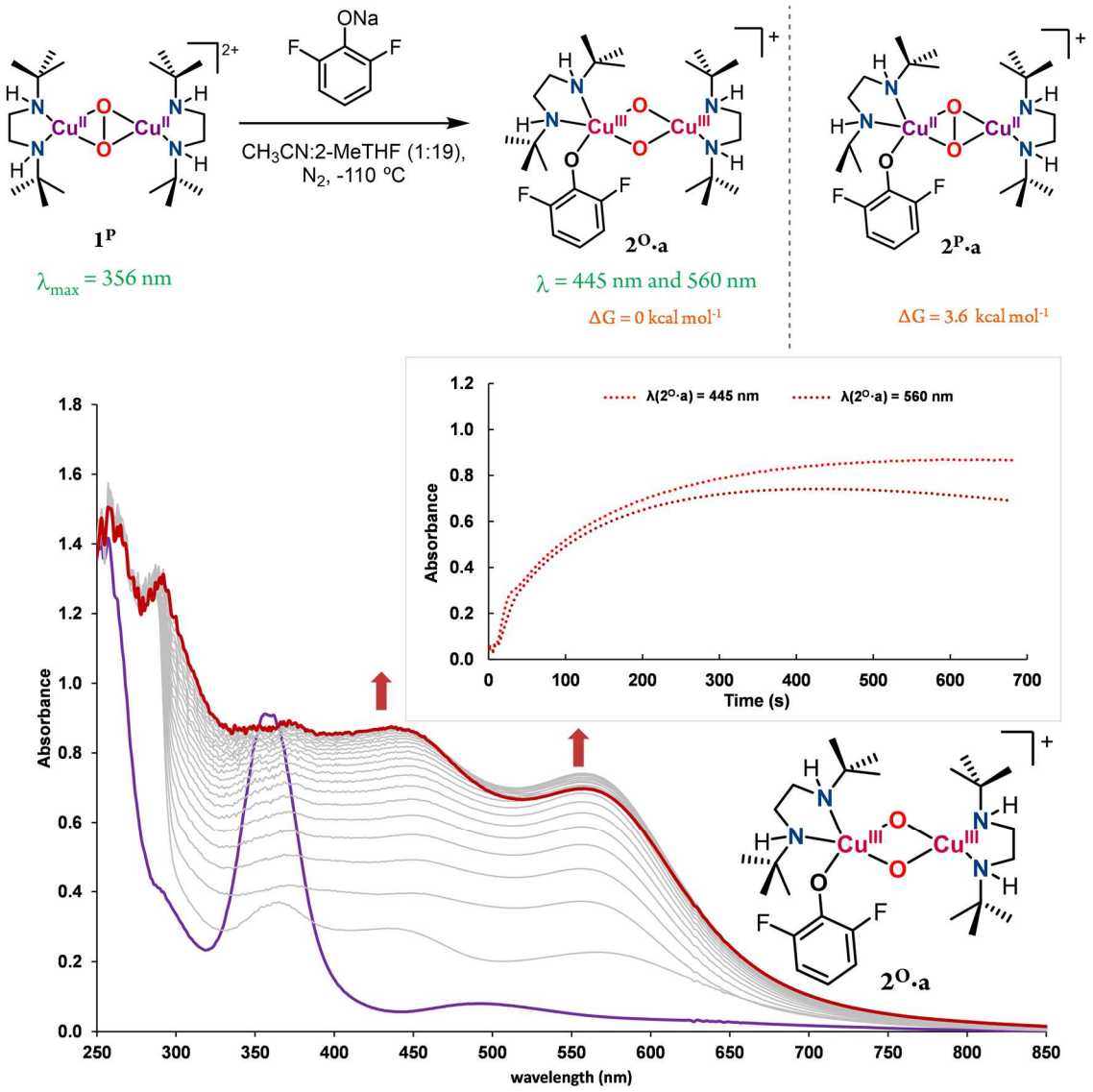

Figure VII.6 Top: Reaction of $\mathbf{1^P}$ with 2,6-difluorophenolate to form species $\mathbf{2^O}$**·a** with the corresponding calculated Gibbs free energies (orange) of the two possible isomers formed. Bottom: Reaction of $\mathbf{1^P}$ (0.25 mM) with 2 equivalents 2,6-difluorophenolate to form species $\mathbf{2^O}$**·a** in CH_3CN:2-MeTHF 1:19 at -110 °C monitored by UV-vis spectroscopy. Inset: kinetic traces of λ($\mathbf{2^O}$**·a**) = 445 nm, and λ($\mathbf{2^O}$**·a**) = 560 nm.

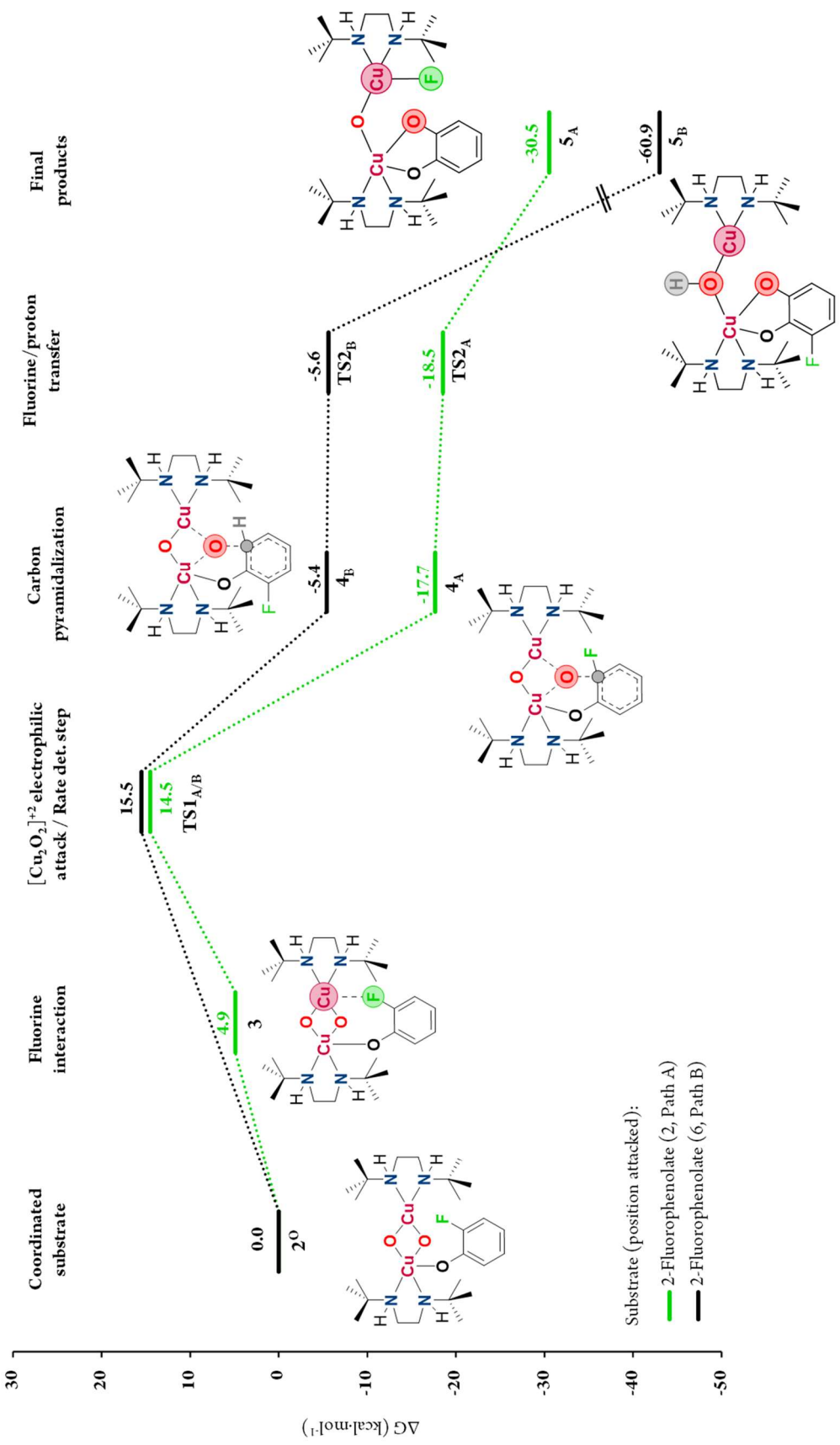

Figure VII.7 Proposed mechanism and calculated free-energy profiles at the UM06-L/cc-pVTZ-g ~ SMD//UM06-L/6-311G(d) level of theory for 2-fluorophenolate. Gibbs free energies (*G*, in kcal·mol^{-1}) are relative to **2°c**

Taking into account both the experimental and computational data, a mechanism for the *ortho*-defluorination-hydroxylation of 2-fluorophenolate was proposed. This substrate was used in the DFT calculations because it bears one *ortho*-C-F bond and one *ortho*-C-H bond, so that the preference for the attack over one bond or the other could be evaluated. After coordination of the phenolic substrate to species $\mathbf{1^P}$ to form the **O** isomer ($\mathbf{2^O}$), the first step consists in the attack over the *ortho*-C-X bond which can happen at both *ortho* positions giving two feasible reaction paths (Figure VII.7): Path A when the attack occurs at the *ortho*-C-F bond yielding the major product, and Path B when it occurs on the *ortho*-C-H bond yielding the minor product. For Path A there is an attractive noncovalent interaction between the lone pair of the fluorine atom and the less coordinatively saturated copper(III) center, giving intermediate **3** (observed on the NCIPLOT, Chapter III Figure 6). Such an interaction does not occur in the activation of the *ortho*-C-H bond (Path B) because the hydrogen atom does not have a lone pair to interact with the copper(III) center. The **O** moiety electrophilically attacks the aromatic ring, which involves the pyramidalization of the *ortho*-carbon giving intermediates $\mathbf{4_A}$ and $\mathbf{4_B}$, for Path A and Path B, respectively. This attack is followed by the rearomatization of the substrate that leads to the final catechol products either via transfer of the fluorine to the less coordinated copper center (Path A, *ortho*-defluorination-hydroxylation reaction, intermediate $\mathbf{5_A}$) or by the proton abstraction through the remaining oxygen atom of the **O** core (Path B, *ortho*-hydroxylation, intermediate $\mathbf{5_B}$).

As can be seen in the energy profile calculated for 2-fluorophenolate (Figure VII.7), the *ortho*-defluorination-hydroxylation (Path A) and the *ortho*-hydroxylation (Path B) are both possible. However, the attack on the fluoride is 1 kcal·mol^{-1} more favored than the attack on the hydrogen ($\Delta G(TS1_A)$ = 14.5 kcal·mol^{-1} versus $\Delta G(TS1_B)$ = 15.5 kcal·mol^{-1}). This theoretical result agrees well with the experimental data. Thus, quantification of the two possible catechol products for the reaction of $\mathbf{1^P}$ with sodium 2-fluorophenolate were carried out. In the glovebox, the copper(I) precursor was prepared in a Schlenk flask in a CH_3CN:acetone (1:19) solvent mixture. The solution was taken out of the glovebox and cooled down to -90 °C in an acetone/N_2 bath. Once thermal equilibrium was reached, an O_2 atmosphere was established, which was accompanied with an immediate observable color change from pale yellow to deep purple corresponding to the formation of $\mathbf{1^P}$. The mixture was left stirring at -90 °C for ca. 15 minutes

to ensure the full formation of $\mathbf{1^P}$. Then, the flask was purged via vacuum/N_2 cycles to remove the excess of dioxygen. After that, 1.5 equivalents (per Cu(I) precursor) of 2-fluorophenolate dissolved in 0.5 mL of acetone were added to the flask which caused an immediate substantial color change to a deep brown color corresponding to the formation of the bis(μ-oxo) dicopper(III) species with the bound phenolate ($\mathbf{2^O{\cdot}c}$). The mixture was left stirring for 30 minutes at -90 °C. Afterwards, the reaction was quenched with an aqueous solution of $HClO_4$ and it was let attain room temperature. At this point, 1,3,5-trimethoxybenzene was added as an internal standard and after working up the reaction crude, the sample was analyzed by HPLC which afforded a 36% yield of catechol formed via C-F activation (Path A) and a 2% yield of 3-fluorocatechol via C-H activation (Path B) with respect to the Cu_2O_2 core. Thus, both C-F and C-H activation products are obtained and the *ortho*-defluorination product constitutes the major one (18:1 C-F vs C-H oxygenation), which is in reasonable agreement with the theoretical results shown in Figure VII.7. Therefore, the *ortho*-C-F bond is more reactive against compound $\mathbf{2^O{\cdot}c}$, even in the presence of a presumably weaker bond such as the *ortho*-C-H bond.

At this point, further experimental mechanistic studies were performed in order to confirm the electrophilic attack of the Cu_2O_2 core to the aromatic ring as pointed out by DFT calculations. In order to do so, the kinetics of the reaction of $\mathbf{1^P}$ with a series of *para*-substituted sodium 2-fluorophenolates with tuned electronic properties (sodium 2-fluoro-4-Y-phenolate; Y = Cl, F, H and CH_3) were monitored by UV-vis spectroscopy. In a typical experiment, compound $\mathbf{1^P}$ was generated at -80 °C by reaction of the copper(I) precursor $\mathbf{[Cu^I(DBED)(CH_3CN)](PF_6)}$ and dioxygen in a CH_3CN:2-MeTHF 1:19 solvent mixture. Once compound $\mathbf{1^P}$ reached its maximum absorbance (λ_{max} = 356 nm; ε = 6400 $M^{-1}cm^{-1}$), the temperature was lowered to -110 °C and the appropriate amount of *para*-substituted sodium 2-fluorophenolate was added. This caused the conversion of $\mathbf{1^P}$ (λ_{max} = 356 nm) into the corresponding phenolate-bound **O** isomer with absorption bands between λ = 450 – 600 nm ($\mathbf{2^O{\cdot}x}$) (Figure VII.8). The UV-vis spectra of species $\mathbf{2^O{\cdot}x}$ were consistent with the analogues previously reported by Stack and co-workers[30] and in the group using the *m*-XYL^{MeAN} ligand.[28]

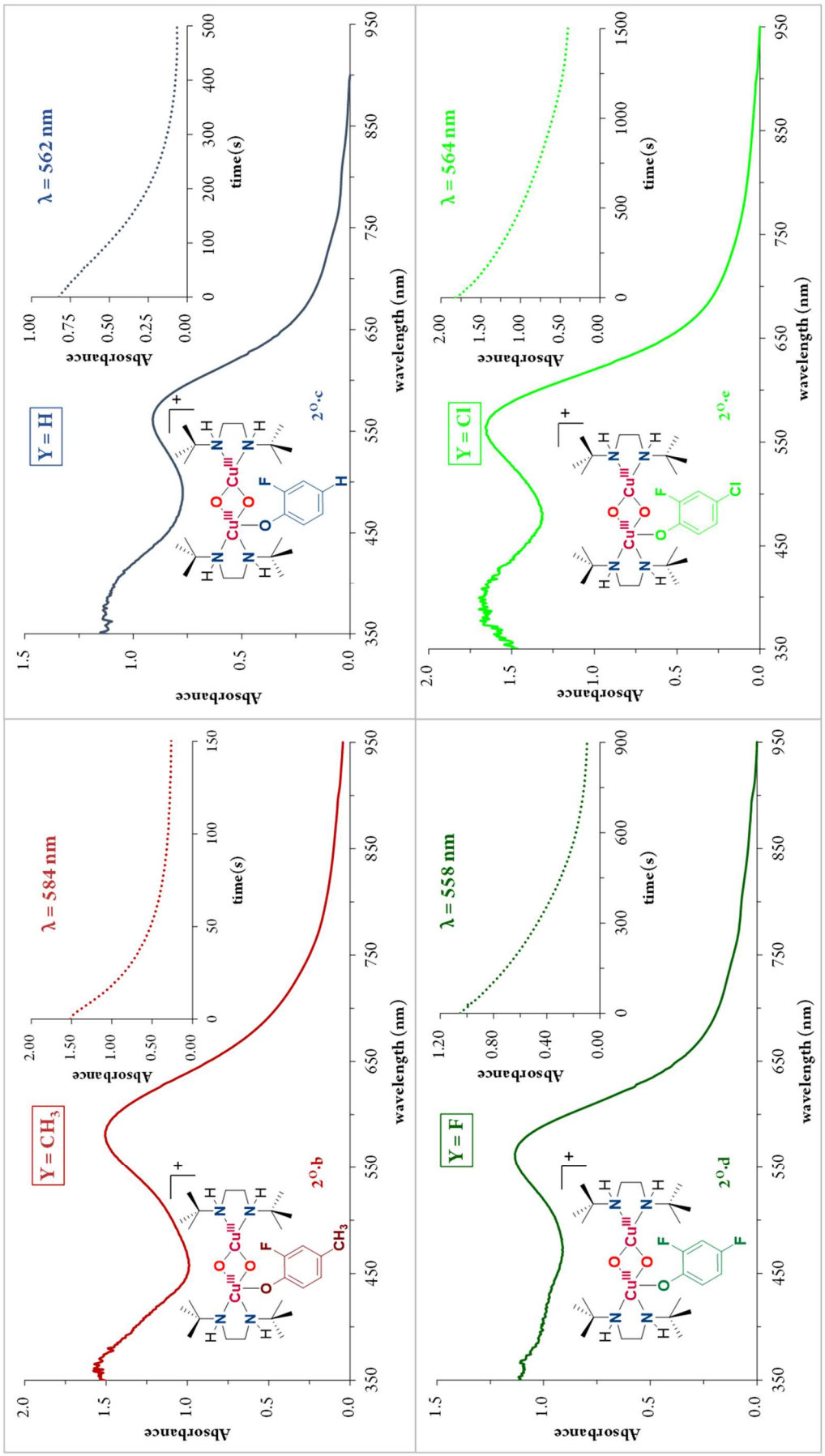

VII.8 UV-vis spectra of **2°-b-e** generated upon reaction of **1'** (0.25 mM) wih 2 equivalents of sodium 2-fluoro-4-Y-phenolate (Y = Cl, F, H and CH_3) at -110 °C in CH_3CN:2-MeTHF 1:19. Insets: kinetic traces corresponding to the self-decay of **2°-b-e** at -110 °C

The self-decays of compounds **2^{O}·x** were slow enough to be monitored by UV-vis spectroscopy at -110 °C and they showed a first-order behavior that could be satisfactorily fitted to a single exponential function by nonlinear regression methods. The decay rate (k) was dependent on the nature of the *para*-substituent Y, so the logarithm of k was plotted against the corresponding Hammett *para*-substituent constant (σ_p) affording a linear correlation (R^2 = 0.93) with a negative slope (ρ = -3.5) (Figure VII.9). A negative ρ value is indicative of an electrophilic attack on the aromatic ring of 2-fluoro-4-Y-phenolate, so that the self-decay is faster for more electron-donating Y *para*-substituents. This result agrees with the proposed mechanism based on DFT calculations performed on six frontier orbitals of compound **2^{O}·a** (Chapter III Figure 7).

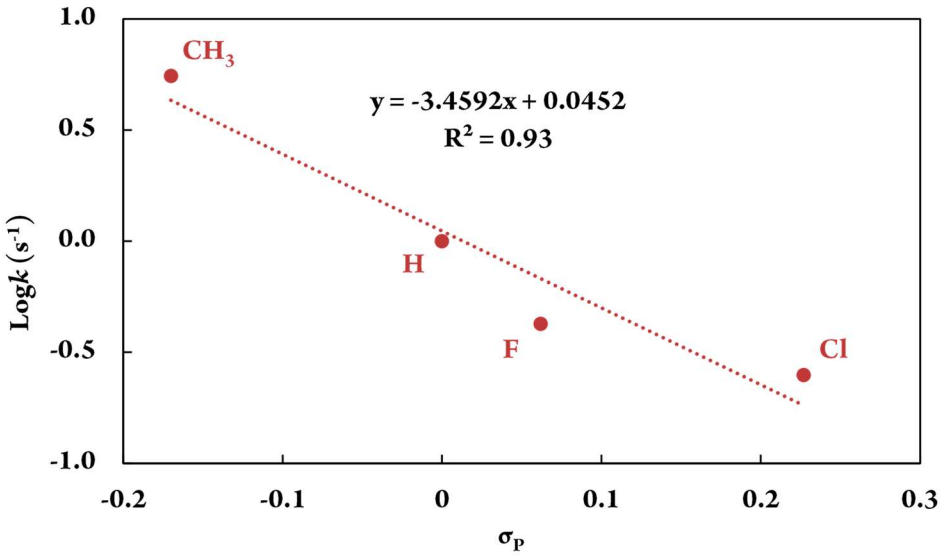

Figure VII.9 Experimental Hammett plot for the self-decay of **2^{O}·x** (x = b – e) at -110 °C in CH_3CN:2-MeTHF (1:19).

An Eyring plot was experimentally determined in order to check the precision of the computed reaction barriers for the reaction of **1^{P}** with 2,6-difluorophenolate. Thus, the decay rate of species **2^{O}·a** formed upon reaction of **1^{P}** with 2,6-difluorophenolate was measured at different temperatures. To do so, in a typical experiment, compound **1^{P}** was generated upon reaction of the copper(I) precursor and O_2 at -80 °C. Once **1^{P}** reached its maximum absorbance, the temperature was changed and set for each experiment (-110, -100, -95, -90, -85 and -80 °C). When the new thermal equilibrium was reached, a UV-vis spectrum of **1^{P}** was recorded and then 0.5 equivalents of sodium 2,6-difluorophenolate were added causing the immediate formation of compound **2^{O}·a** (λ = 445 nm and λ = 558 nm). The kinetic traces monitored at 558 nm were analyzed at the different temperatures and reaction rates (k) could be extracted by adjusting the

decays to single exponential functions through nonlinear regression methods. The obtained *k* values depend on the temperature and the Eyring plot analysis reveals a relatively small activation enthalpy ($\Delta H^{\ddagger}$ = 9.6 ± 0.3 kcal·mol^{-1}) and a negative activation entropy ($\Delta S^{\ddagger}$ = -12 ± 2 cal·K^{-1}mol^{-1}) (Figure VII.10). The experimentally obtained Gibbs free energy ($\Delta G^{\ddagger}_{exp}$ = 11.8 ± 0.6 kcal·mol^{-1}) nicely agrees with the computed value obtained for this parameter ($\Delta G^{\ddagger}_{calc}$ = 11.7 kcal·mol^{-1}).

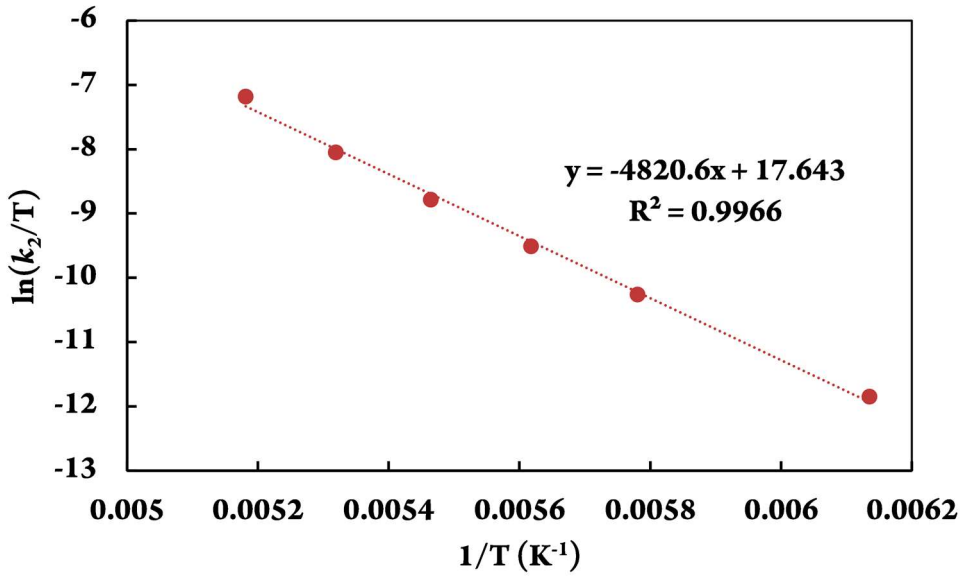

Figure VII.10 Experimental Eyring plot for the decay of $\mathbf{2^{O}}$**·a** in CH_3CN:2-MeTHF 1:19 at different temperatures.

The nice agreement between theory and experiments prompted us to also calculate the different reaction paths for the interaction of $\mathbf{1^{P}}$ with 6-chloro-2-fluorophenolate. Thus, both the attack at the *ortho*-C-F and *ortho*-C-Cl positions were calculated. In this case, the activation of the C-F bond is preferred over the C-Cl bond by an energy barrier difference of 6.3 kcal·mol^{-1}, and these DFT barriers are fully consistent with the exclusive activation of the C-F bond, which is experimentally observed for this substrate.[28]

In summary, we have been able to theoretically and experimentally investigate the reaction pathway of the *ortho*-defluorination-hydroxylation of 2-fluorophenolates by the $[(\mathbf{DBED})\mathbf{Cu^{I}}(\mathbf{CH_3CN})]^{+}$ system. This study reveals the **O** isomer as the responsible for the electrophilic attack of the phenolate-Cu_2O_2 core over the *ortho*-C-F position of the arene ring of the phenolic substrate. Moreover, the computed chemoselectivity towards the activation of the C-F bond over C-Cl or C-H bonds was also in agreement with previous experimental results.[28]

VII.3 WELL-DEFINED ARYL-Fe^{II} COMPLEXES IN CROSS-COUPLING AND C-H ACTIVATION PROCESSES

Since the development of many efficient and polyvalent iron-mediated cross-coupling and C-H activation methodologies to avoid the use of toxic and expensive noble metals such as palladium and platinum, the need for gaining deeper insight into the mechanistic features of iron-mediated cross-coupling and C-H activation reactions has naturally emerged.[31, 32] Indeed, detailed mechanistic comprehension of some fundamental steps is key to develop fruitful synthetic methodologies. Nevertheless, and referring back to section I.4.3 (0), due to a) the sensitivity to temperature, air and moisture of the complexes *in situ* formed in iron-mediated transformations, which in most cases lead to paramagnetic species, and b) the ability to undergo one and two-electron redox processes, and/or radical pathways, only few examples of isolated and characterized organoiron intermediates relevant for cross-coupling or C-H activation reactions have been described, which contrasts with the abundant number of methodology-type publications. In this line, our research group is highly trained in successfully trapping and characterizing important organometallic intermediates with macrocyclic model substrates (see section I.2 in 0).[33-37] To this end, we decided to combine two strategies to isolate and characterize aryl-iron(II) complexes relevant for C-X/H activation and functionalization. On the one hand, the use of a macrocyclic model substrate that would act as a ligand itself. On the other hand, the use of strong field ligands to enhance the stabilization of this otherwise elusive aryl-iron(II) complex. After isolating and characterizing the well-defined aryl-iron(II) complex, preliminary reactivity studies regarding the formation of new C_{Ar}-C bonds will be described, together with some unexpected and unprecedented reactivity towards the formation of tertiary amides.

For this project a 12-membered macrocyclic model substrate ($^{Me}\mathbf{L_H}$) was chosen, which is specially designed for the stabilization of octahedral metal geometries due to its bent arrangement. $^{Me}\mathbf{L_H}$ is a nitrogen-based tridentate ligand containing a pyridine group which connects symmetrically to two aliphatic amines bearing methyl substituents. These amines are connected to a phenyl moiety in positions 1 and 3, leaving the C-H bond in position 2 ready for activation (Scheme VII.4). This ligand platform was previously used in our group and has proven to be an outstanding architecture that enables the isolation of key organometallic aryl-cobalt(III) complexes for C-H activation and functionalization reactions.[36, 37] Moreover, the

group of Mirica used $^{R}\mathbf{L_H}$ for the synthesis and characterization of high-valent organometallic palladium and nickel complexes.[38-40]

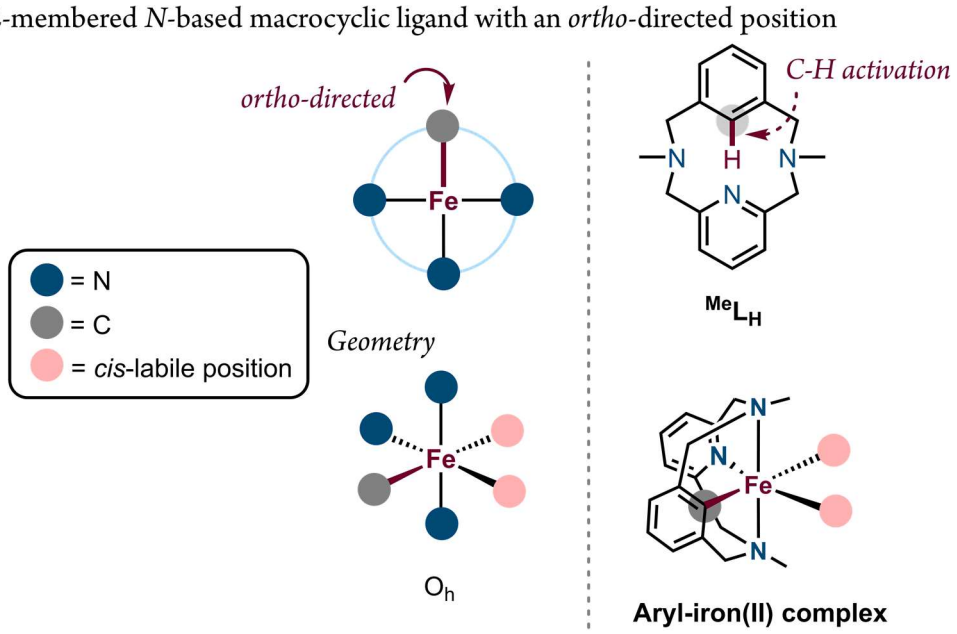

Scheme VII.4 Choice and design scheme of the model macrocyclic substrate $^{Me}\mathbf{L_H}$ for the formation of organometallic aryl-iron(II) complexes via C-H activation through an *ortho*-directing group strategy.

The synthesis of $^{Me}\mathbf{L_H}$ was carried out according to previously reported procedures.[37] Thus, the next goal was the synthesis of the corresponding iron(II) complexes to study the interaction of the iron center with the corresponding C_{Ar}-H bond. With this aim, equimolar amounts of $^{Me}\mathbf{L_H}$ and $FeCl_2$ were mixed in dry acetonitrile at room temperature under a N_2 atmosphere and the mixture was vigorously stirred for 24 hours. Compound $[(^{Me}L_H)Fe^{II}(Cl)_2]$ (**1·Cl₂**) was obtained in 86% after recrystallization (Figure VII.11a). The structure of **1·Cl₂** was first confirmed by HR-ESI-MS, ^{1}H-NMR (paramagnetic), FT-IR, elemental analysis and XRD analysis. The latter showed that the iron center was coordinated to both tertiary amines, the pyridine moiety and two chlorides, through a distorted-square-pyramidal geometry ($\tau = 0.46$).[41] The long Fe-N bond distances (>2.1 Å) confirmed the high-spin state of the iron(II) center in agreement with the observation of a paramagnetic ^{1}H-NMR. Even though the iron(II) center was pentacoordinated, a sixth coordination site, that would constitute the octahedral geometry, was occupied by an incipient interaction with the targeted inner C_{Ar}-H bond from the $^{Me}\mathbf{L_H}$ ligand, being this out-of-plane from the phenyl-ring-plane (torsion angle θ = 14.4º, Figure VII.11b). Additionally, the effective magnetic moment of the iron(II) complex was measured by the Evans' method with a result of μ_{eff} = 4.81 μ_B, consistent with 4 unpaired electrons for an iron(II) high-spin center.

Likewise, the analogous complex with bromides as counterions (**1·Br₂**) was also obtained in 82% yield with structural and spectroscopic features similar to **1·Cl₂** (Figure VII.11c).

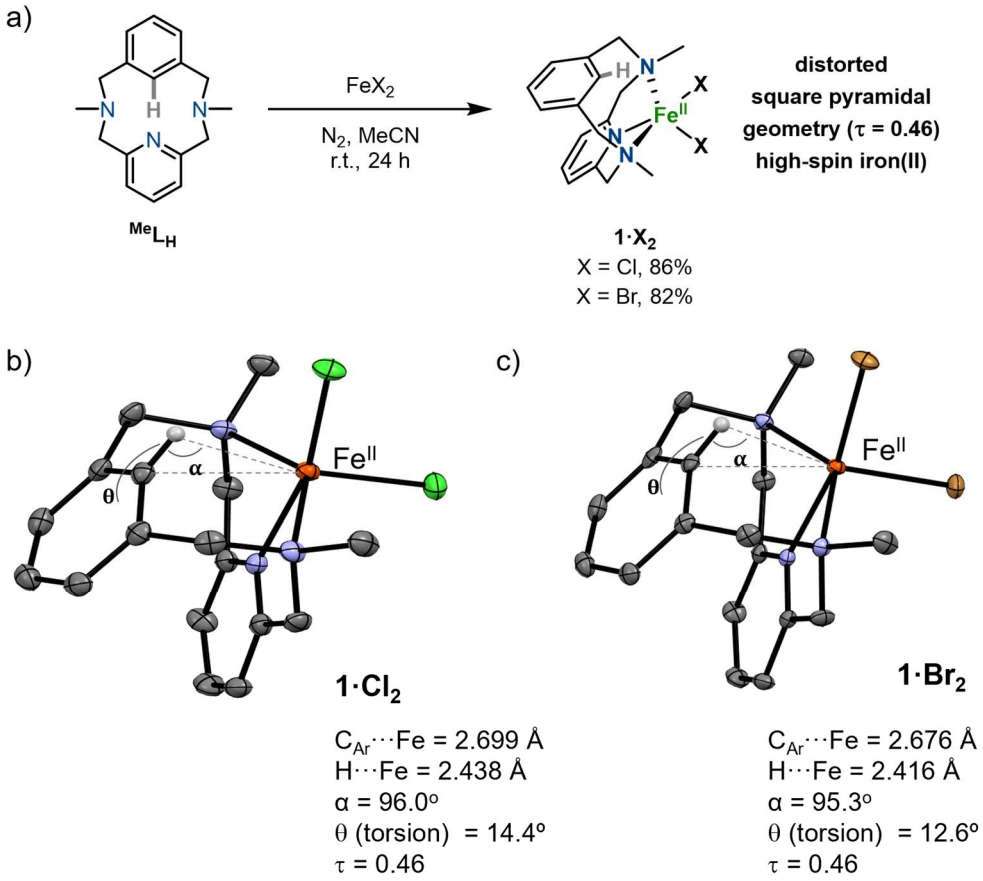

Figure VII.11 a) Synthesis of the iron(II) complex precursors **1·X₂** (X = Cl and Br), and effective magnetic moment determined by the Evans' method for complex **1·Cl₂** which is consistent with a high-spin iron(II) complex; b) and c) X-ray structures of **1·Cl₂** and **1·Br₂** determined at 100 K (CCDC 2046155 and CCDC 2046156) along with selected structural parameters.

The X-ray structures of **1·Cl₂** and **1·Br₂** suggested that an octahedral geometry was possible as long as the C_{Ar}-H bond activation occurred, affording an organometallic aryl-iron complex with a C_{Ar}-Fe bond occupying the sixth coordination site. With this aim, we decided to explore the reactivity of **1·Cl₂** towards a phenyl Grignard reagent. First, we sought for the formation of the biaryl coupling product (**$^{Me}L_{Ph}$**) by performing the reaction of **1·Cl₂** with 3 equivalents of PhMgBr in THF at -78 ºC under a N_2 atmosphere for 1 hour. The mixture was allowed to attain room temperature for 2 hours, and finally aerobic work up and purification of the reaction crude gave the desired C-C biaryl coupling product **$^{Me}L_{Ph}$** in a 66% yield (33% yield corresponds to the protodemetallation product or starting ligand, $^{Me}L_H$) (Figure VII.12a). The final C-C coupling product was fully characterized by HR-ESI-MS spectrometry (calcd. for $C_{23}H_{25}N_3$, $[M+H]^+$ 344.2121; exp 344.2133) and NMR spectroscopy. The compound could be fully assigned by

means of both 1D- and 2D-NMR experiments. Interestingly, from the ^{1}H-NMR spectrum it can be seen that the rotation between C_{Ar}-C_{Ph} is impeded as all protons corresponding to both phenyl rings are nonequivalent. Moreover, one of the *ortho*-protons from the phenyl moiety is strongly shifted down-field ($\delta(H_f)$ = 9.46 ppm) due to the shielding cone effect induced by its location between both the aryl and the pyridine rings from the ligand, and so due to perpendicular positioning of the phenyl ring with respect to the planes of the aryl and pyridine rings from the ligand (Figure VII.12b and c).

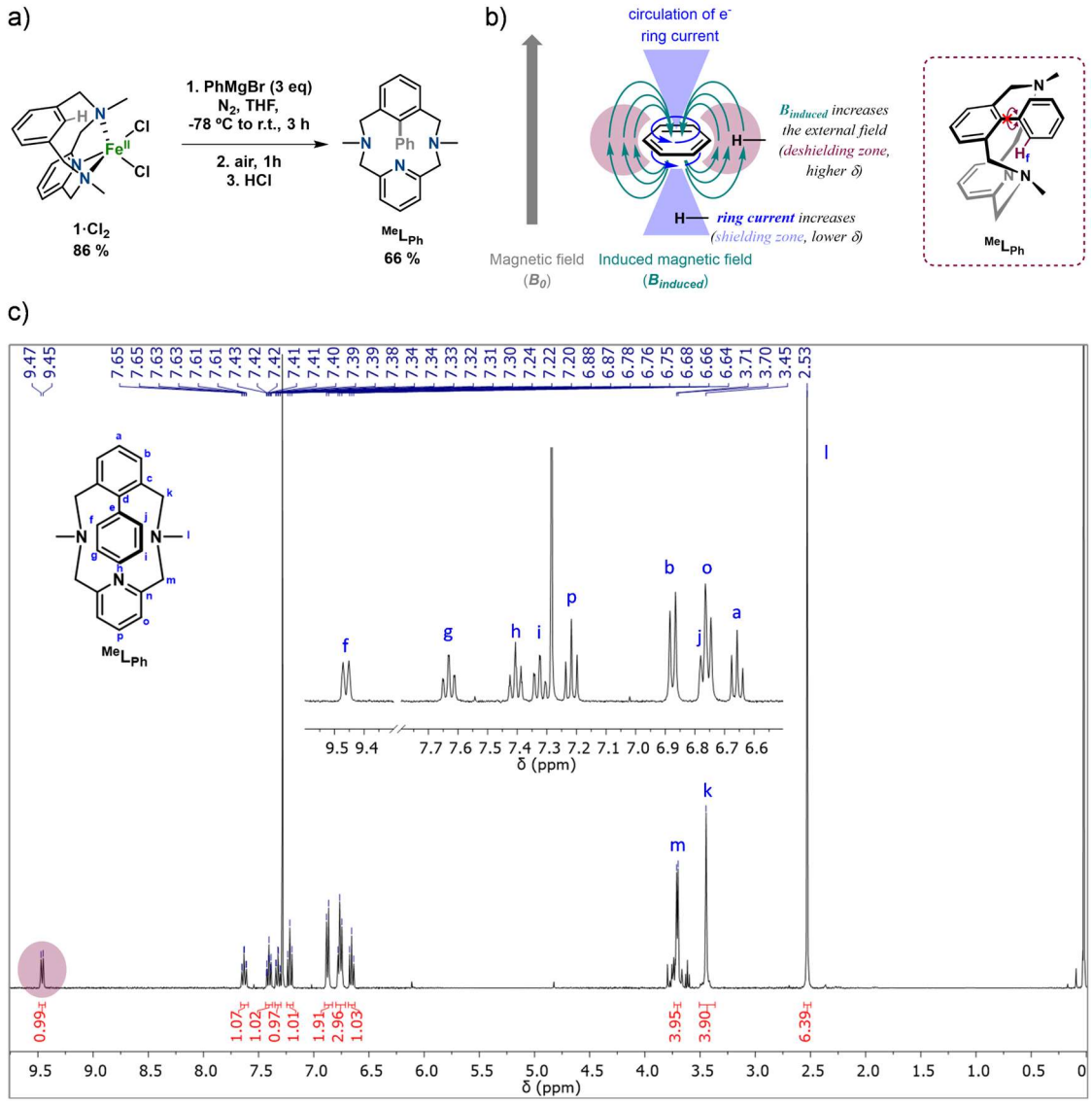

Figure VII.12 a) Reaction of **1·Cl$_2$** towards PhMgBr for the formation of biaryl C-C coupling product (^{Me}**L$_{Ph}$**); b) Representation of the shielding cone effect observed by ^{1}H-NMR for ^{Me}**L$_{Ph}$**, and c) ^{1}H-NMR spectrum of ^{Me}**L$_{Ph}$** in $CDCl_3$ at room temperature.

The formation of the desired C-C coupling product is clearly suggesting the involvement of an aryl-iron intermediate species. Hence, several attempts to isolate the organoiron species derived from the C-H activation were carried out by performing the reaction under severe inert and dry atmosphere, at low temperature and using only one equivalent of the phenyl Grignard reagent. Unfortunately, none of the attempts to isolate the organoiron species was successful. If we consider the C-H activation step occurs via a σ-bond metathesis, and if we analyze in more detail the structural and electronic properties that this putative aryl-iron complex (**B**) may have, the resulting organoiron would be a 16-electron pentacoordinated complex (Scheme VII.5).

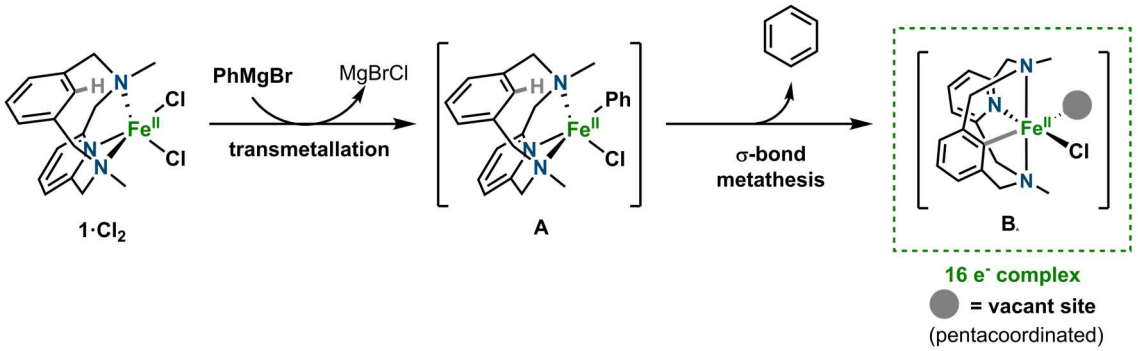

Scheme VII.5 Formation of the putative unstable species **B** upon C-H activation via σ-bond metathesis.

At this point we decided to change our synthetic strategy to stabilize and isolate a relevant aryl-iron complex by a formal two-electron oxidative addition to a C-Br bond was envisioned. To do so, the initial $^{Me}\mathbf{L_H}$ was modified, and the previous directed *ortho*-C_{Ar}-H bond was changed by the new targeted *ortho*-C_{Ar}-Br bond ($^{Me}\mathbf{L_{Br}}$) (Scheme VII.6).

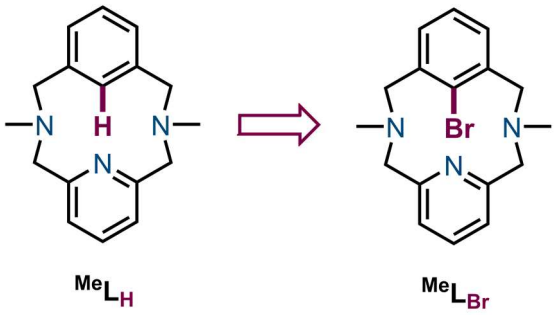

Scheme VII.6 New ligand design from C-H activation ($^{Me}\mathbf{L_H}$) to C-Br activation ($^{Me}\mathbf{L_{Br}}$).

The synthesis of this new macrocyclic model substrate was achieved through six reaction steps in good yields starting from the commercially available 2,6-bis(chloromethyl)pyridine (Scheme VII.7). First, the corresponding 2,6-bis(azidomethyl)pyridine (**i**) is formed with sodium azide refluxed in dimethylformamide. Then, **i** is hydrogenated in a H_2 atmosphere using palladium

over carbon catalyst in ethanol at room temperature to obtain 2,6-bis(aminomethyl)pyridine (**ii**). After that, tosylation with tosyl chloride and triethylamine yields 2,6-bis(tosylmethylamine)pyridine (**iii**). Next, after deprotonation of compound **iii** with excess of cesium carbonate, 1 equivalent of 2-bromo-1,3-bis(bromomethyl)benzene is slowly added dropwise. Once the addition is complete, the crude mixture is refluxed for 24 hours to afford the protected N-tosyl macrocyclic model substrate ($^{Ts}\mathbf{L}_{Br}$). Deprotection of the tosyl groups was performed using a phenol-assisted cleavage of the S-N bond under acidic conditions. This reaction resulted in the free-amine macrocyclic model substrate $^{H}\mathbf{L}_{Br}$ which is then further methylated with formaldehyde and formic acid to furnish the final macrocyclic model substrate $^{Me}\mathbf{L}_{Br}$.

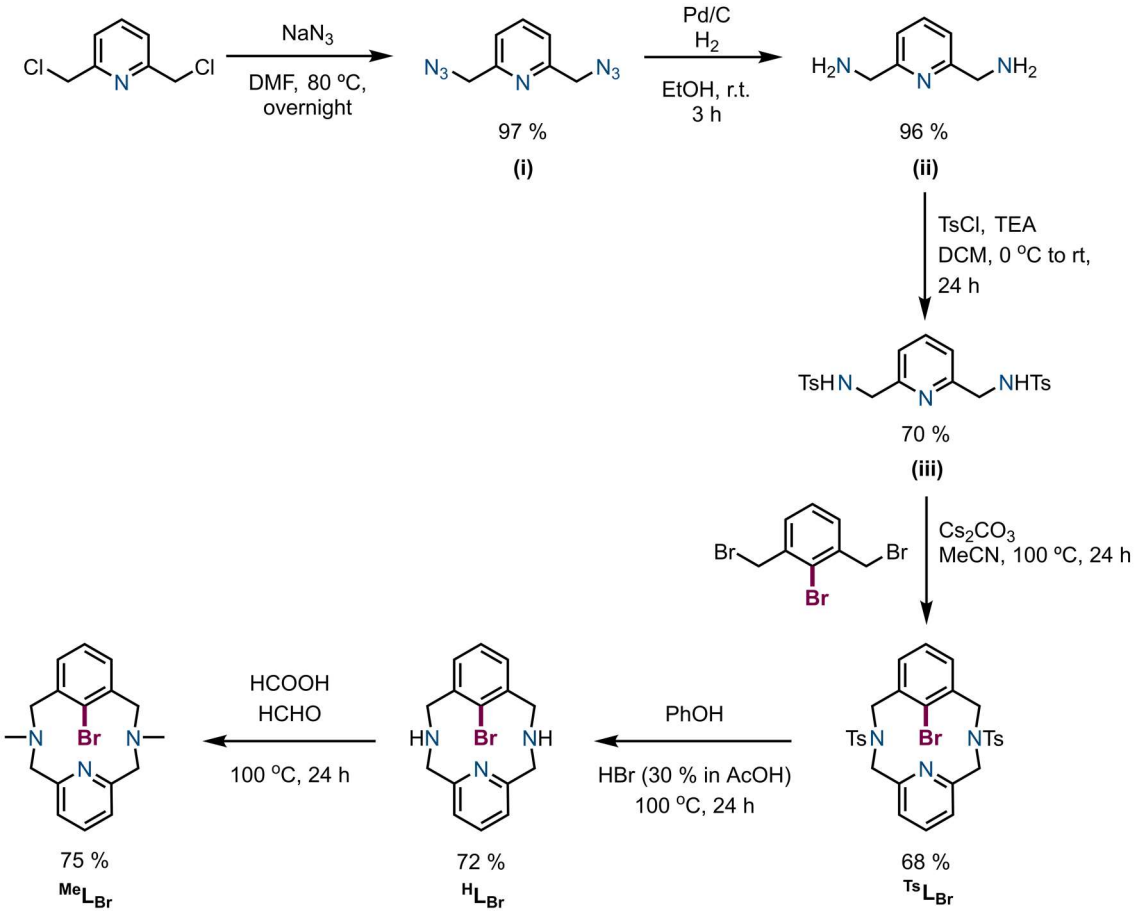

Scheme VII.7 Synthetic route for the synthesis of the new model substrate $^{Me}\mathbf{L}_{Br}$.

The new macrocycles $^{Me}\mathbf{L}_{Br}$ and $^{H}\mathbf{L}_{Br}$ were used for the synthesis of the corresponding aryl-iron(II) complexes via formal two-electron oxidative addition to an iron(0) source with strong-field ligands in order to stabilize the resulting organoiron complexes. In this line, $Fe(CO)_5$ was chosen as the iron(0) precursor. For both ligands equimolar amounts of the ligand and $Fe(CO)_5$

were mixed in anhydrous THF and photoirradiated with UV light (254 nm) at 50 °C overnight to yield the corresponding aryl-iron(II) complexes [(^{Me}L)Fe^{II}(CO)(Br)] (**1^{Me}**, 67%) and [(^{H}L)Fe^{II}(CO)$_2$](Br) (**1^{H}**, 63%), respectively (Scheme VII.8).

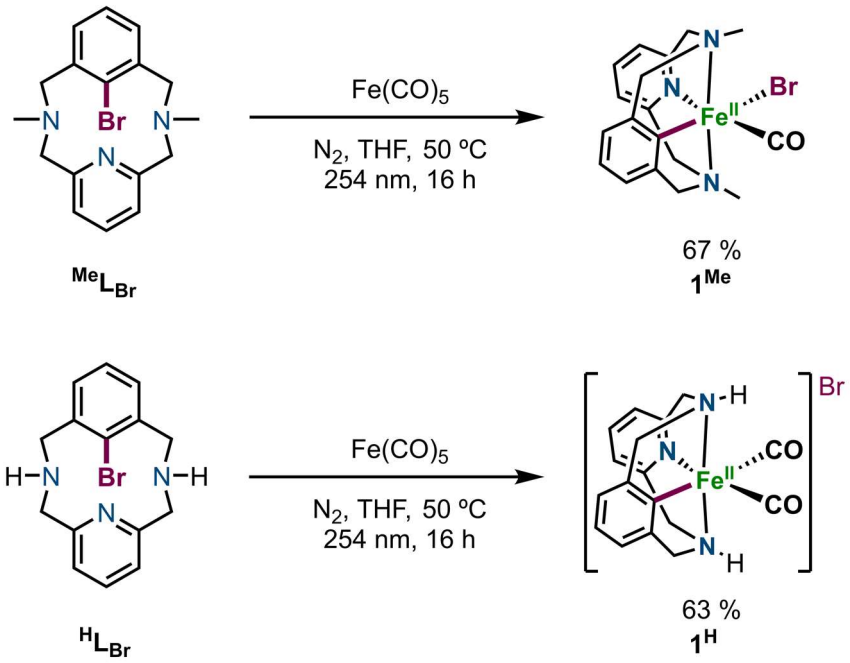

Scheme VII.8 Syntheses of the aryl-iron(II) complexes (**1^{Me}** top and **1^{H}** bottom) via photoinduced (254 nm) oxidative addition of the C-Br bond from the respective model substrates to the iron(0) precursor.

To our delight, X-ray quality crystals were obtained for both complexes **1^{Me}** and **1^{H}**, exhibiting distorted octahedral geometries around the iron(II) center (Figure VII.13). However, both structures present different features that require to individually analyze each aryl-iron(II) complex. Surprisingly, in the case of **1^{Me}** (Figure VII.13a), the bromide atom resulting from the C_{Ar}-Br bond addition to the initial iron(0) source is located *trans* to the aryl moiety, and so presents a shorter distance for the C_{Ar}-Fe bond (1.904 Å) and a longer distance for the Fe-Br bond (2.571 Å). This *cis* to *trans* rearrangement may take place simultaneously to the oxidative addition due to a *trans* effect that enhances the stability of the resulting complex.[42, 43] The sixth coordination position is occupied by a CO ligand.

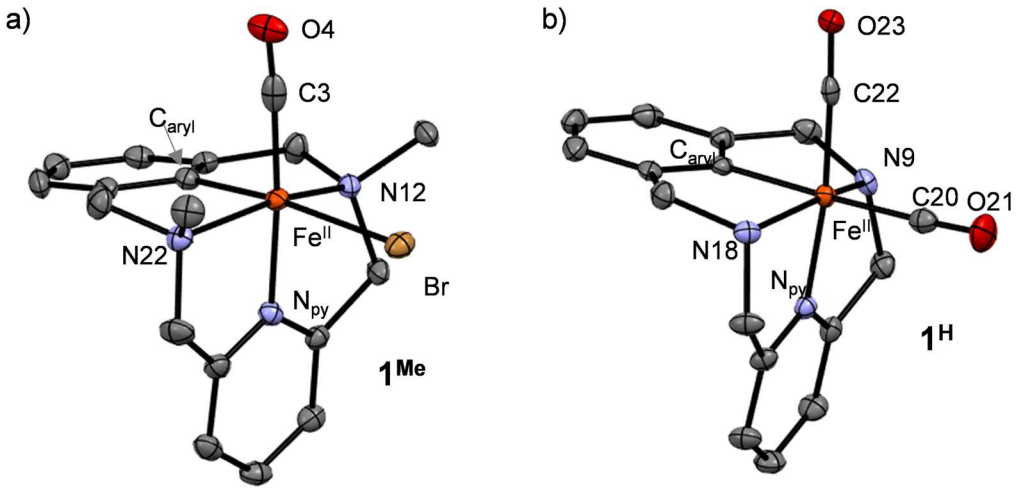

Figure VII.13 X-ray structures of complex a) $\mathbf{1^{Me}}$ and b) $\mathbf{1^{H}}$. Selected bond distances [Å] for $\mathbf{1^{Me}}$: Fe-C_{aryl} 1.904(3), Fe-N_{py} 1.935(3), Fe-N12 2.095(3), Fe-N22 2.102(3), Fe-Br 2.571(2), Fe-C3 1.785(4); for $\mathbf{1^{H}}$: Fe-C_{aryl} 1.925(2), Fe-N_{py} 1.928(2), Fe-N9 2.030(2), Fe-N18 2.034(2), Fe-C20 1.837(3), Fe-C22 1.759(3); (ellipsoids set at 50% probability and H atoms removed for clarity).

On the other hand, the X-ray crystal structure for $\mathbf{1^{H}}$ (Figure VII.13b) shows the bromide anion on the outer sphere of the complex (non-coordinated to the iron(II) center), but instead two CO ligands were completing the coordination sphere, thus confirming the hypothesis that the bromide anion and CO ligands can easily exchange. Actually, in this case the *trans* effect caused by the aryl moiety is observed by the longer Fe-CO bond *trans* to the aryl (1.837 Å) in comparison to the shorter Fe-CO bond *trans* to the pyridine moiety (1.759 Å).

The structures of both complexes were also confirmed by HR-ESI-MS and NMR. Interestingly, the HR-ESI-MS spectrum of $\mathbf{1^{Me}}$ showed a main peak at a m/z ratio and isotopic pattern corresponding to the complex $\mathbf{1^{Me}}$ with the addition of one CO ligand and loss of the bromide counterion (calcd. for $C_{19}H_{20}N_3O_2Fe^+$, $[M+CO-Br^-]^+$ 378.0900; exp 378.0905), together with another peak consistent with just the loss of the bromide anion (calcd. for $C_{18}H_{20}N_3OFe^+$, $[M-Br^-]^+$ 350.0950; exp 350.0888). This supports the idea observed by X-ray diffraction that some ligand exchange between the bromide and free CO molecules present in the media takes place. Gratifyingly, both $\mathbf{1^{Me}}$ and $\mathbf{1^{H}}$ complexes exhibit diamagnetic ^{1}H-NMR spectra which enabled their full characterization together with bidimensional NMR experiments. The fact that both complexes are characterized as low-spin aryl-iron(II) complexes is directly attributed to the coordination of strong-field carbonyl ligands.

The number of CO ligands present in both complexes, was further confirmed by FT-IR (Figure VII.14), as only one band corresponding to the CO stretching was observed for complex $\mathbf{1}^{Me}$ ($\tilde{\upsilon}$ = 1899 cm^{-1}), while two bands corresponding to the two inequivalent CO ligands were detected for complex $\mathbf{1}^{H}$ ($\tilde{\upsilon}$ = 2019 cm^{-1} and $\tilde{\upsilon}$ = 1963 cm^{-1}).

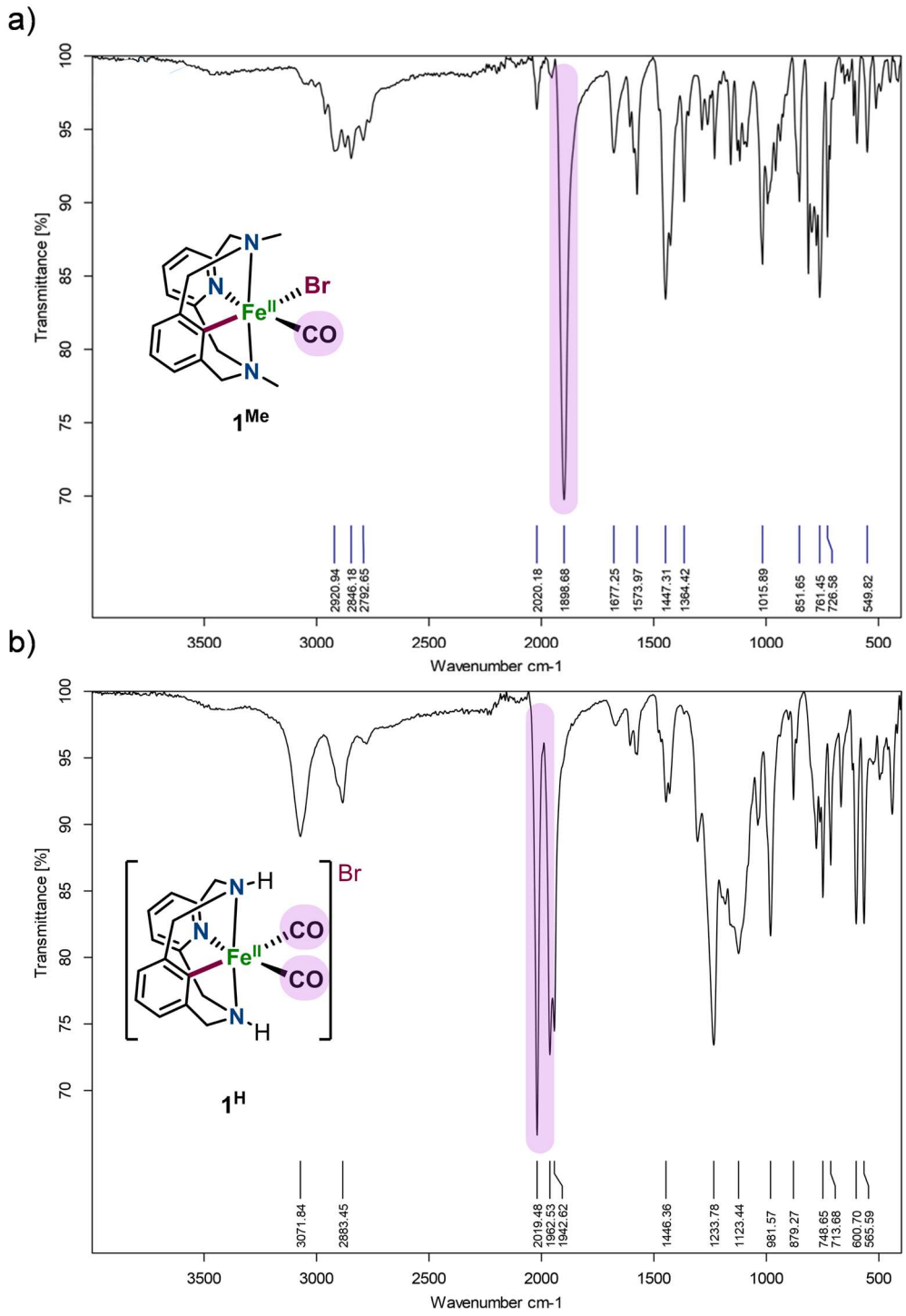

Figure VII.14 ATR-FT-IR spectrum of a) $\mathbf{1}^{Me}$ and b) $\mathbf{1}^{H}$ at room temperature. Shaded in purple, the bands corresponding to the CO stretchings one single band (1899 cm^{-1}) for complex $\mathbf{1}^{Me}$, and two bands (2019 $cm^{-1}$and 1963 cm^{-1}) for the two inequivalent CO ligands of $\mathbf{1}^{H}$.

After the synthesis and characterization of these well-defined aryl-iron(II) complexes, we then focused our attention on investigating the reactivity of $\mathbf{1}^{Me}$. In order to establish whether an aryl-iron(II) species could be participating in the reaction of $\mathbf{1{\cdot}Cl_2}$ with a phenyl Grignard reagent described above, $\mathbf{1}^{Me}$ was reacted with PhMgBr under the same experimental conditions followed by an aerobic workup analogous to the reaction of $\mathbf{1{\cdot}Cl_2}$. As a result, a significant 38% yield of the new coupling product that contained a carbonyl group between the aryl and the phenyl moieties ($^{Me}\mathbf{L}_{COPh}$) was obtained. The nature of this new coupling product was confirmed by HR-ESI-MS spectrometry, NMR and FT-IR spectroscopy. All techniques confirmed that the new C-C coupling product came from a putative $[(^{Me}L)Fe^{II}(Ph)(CO)]$ ($\mathbf{1}^{Me}$**-Ph**) followed by a CO migratory insertion and reductive elimination to form the aryl-COPh bond in $^{Me}\mathbf{L}_{COPh}$ (Scheme VII.9).

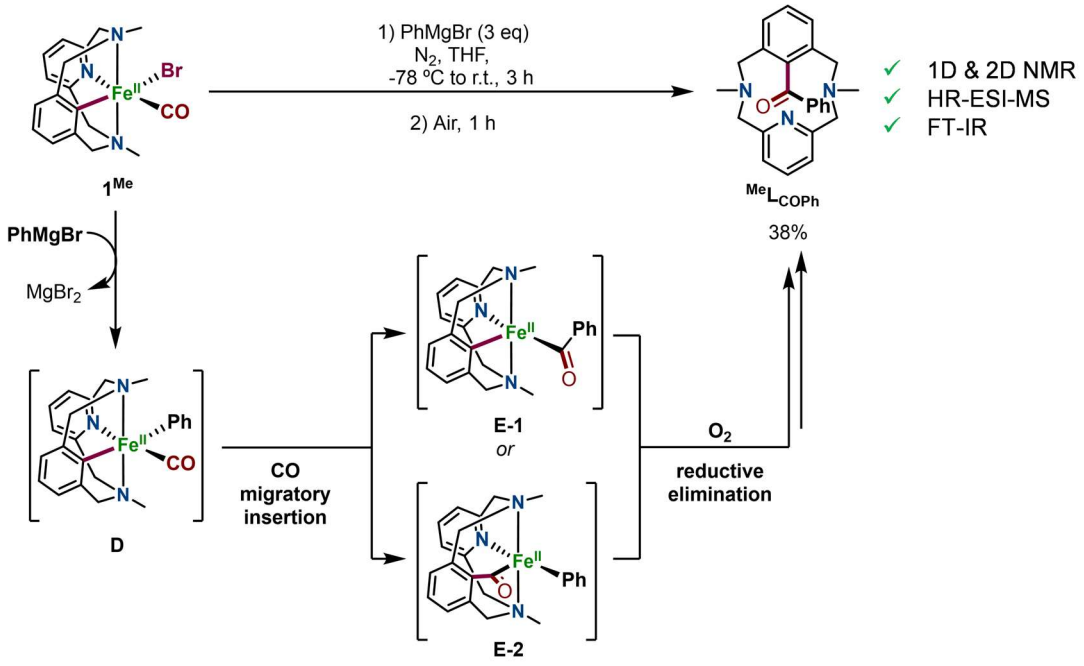

Scheme VII.9 Synthesis of the organic coupling product $^{Me}\mathbf{L}_{COPh}$ from the reaction of $\mathbf{1}^{Me}$ with PhMgBr, along with a putative mechanism for the CO insertion step.

The HR-ESI-MS spectrum of $^{Me}\mathbf{L}_{COPh}$ showed a main peak at a m/z ratio of 372.2070 (calcd. for $C_{24}H_{25}N_3O$, $[M+H]^+$ = 372.2071) which shifted 28 units higher with respect to $^{Me}\mathbf{L}_{Ph}$, further supporting the incorporation of a carbonyl group to the new coupling product. NMR experiments not only revealed the type of carbonyl group being this a ketone, but also how it was connected to the rest of the ligand. Mono- and bidimensional NMR experiments confirmed that the carbonyl unit was located between the aryl and the phenyl moiety. Moreover, the ^{1}H-NMR

spectrum showed that the presence of the carbonyl unit between the aryl and the phenyl ring, enabled the free rotation of the phenyl ring as only 3 signals for this moiety were observed and no shielding cone effect was present. This contrasts with the analogous non-carbonylated coupling product $^{Me}\mathbf{L_{Ph}}$ (Figure VII.15). Finally, the FT-IR spectrum further confirmed the ketone-type carbonyl group with a band at 1672 cm^{-1}, being this less energetic than that expected for an aliphatic ketone ($\bar{\upsilon}(C\text{-}O)_{str} \approx 1700\ cm^{-1}$) due to the conjugation generated by both aromatic ring substituents.

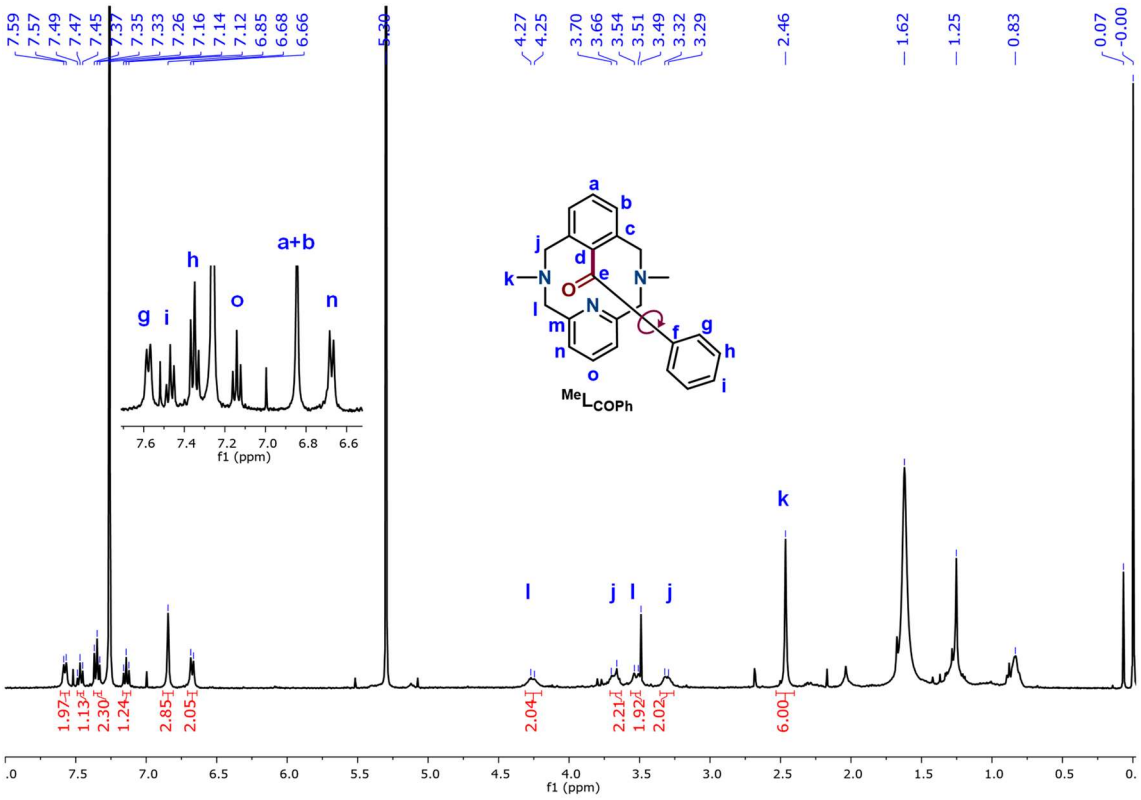

Figure VII.15 ^{1}H-NMR spectrum of $^{Me}\mathbf{L_{COPh}}$ with its corresponding assignment.

With this positive result in our hands, we decided to gain more insight into the mechanism of this reaction. First, it is worth stating that both organic products $^{Me}\mathbf{L_{Ph}}$ and $^{Me}\mathbf{L_{COPh}}$, resulting from $\mathbf{1{\cdot}Cl_2}$ and $\mathbf{1}^{Me}$ respectively, are obtained after an oxidative workup with O_2 (or air). So this suggests that the reductive elimination step that leads to the formation of $^{Me}\mathbf{L_{Ph}}$ and $^{Me}\mathbf{L_{COPh}}$ occurs only after the oxidation of the putative $[(^{Me}L)Fe^{II}(Ph)]$ or $[(^{Me}L)Fe^{II}(COPh)]$ intermediate species to the corresponding iron(III) species.[44, 45] This hypothesis is also supported by the observed visual color change from dark green to reddish-brown upon providing an air atmosphere when performing the reaction with $\mathbf{1{\cdot}Cl_2}$.

With this observation, UV-vis monitoring at low temperature was done in tandem with cryo-MS. To do so, after some optimization, we prepared a UV cell with a 0.5 mM solution of **1·Cl₂** in anhydrous THF under a N_2 atmosphere and set the UV cell-holder at 0 °C. Once thermal equilibrium was reached, a first spectrum of the starting complex was recorded and then 6 equivalents of PhMgBr were added via syringe. This caused the rapid formation of two new bands at λ_{max} = 520 nm and λ_{max} = 635 nm which are attributed to the formation of the proposed species **C** ([(^{Me}L)Fe^{II}(Ph)]). This new species was fully formed after ca. 13 minutes (Figure VII.16). Following, O_2 bubbling into the UV cell to prompt the oxidation of the iron(II) species **C** to the corresponding iron(III) species (**C**$^+$). Exposing **C** to dioxygen caused immediate decay of the two bands at λ_{max} = 520 nm and λ_{max} = 635 nm. Consecutive formation of the putative short-lived species **C**$^+$ was observed for less than 20 seconds and fast evolution to the final reaction mixture occurs (Figure VII.17 a and b). Sadly, all attempts to characterize species **C**$^+$ with cryo-MS after following its generation via low temperature UV-vis monitoring were unsuccessful due to the extreme reactivity of such species. Nonetheless, a clean mass spectrum of the final coupling product was obtained ^{Me}**L**$_{Ph}$ (Figure VII.17c).

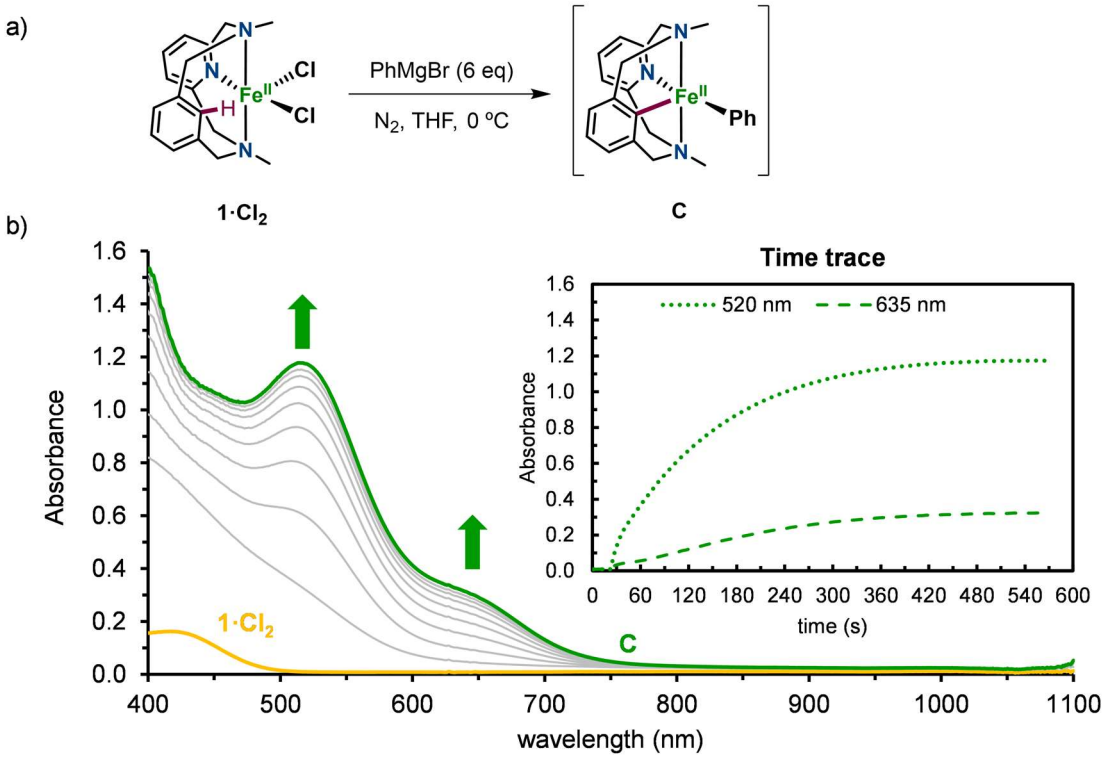

Figure VII.16 a) Reaction of **1·Cl₂** with PhMgBr and b) UV-vis monitoring of this reaction at 273 K to form the intermediate species **C** (green) with characteristic bands at 520 and 635 nm (Inset: time traces of the bands at 520 and 635 nm).

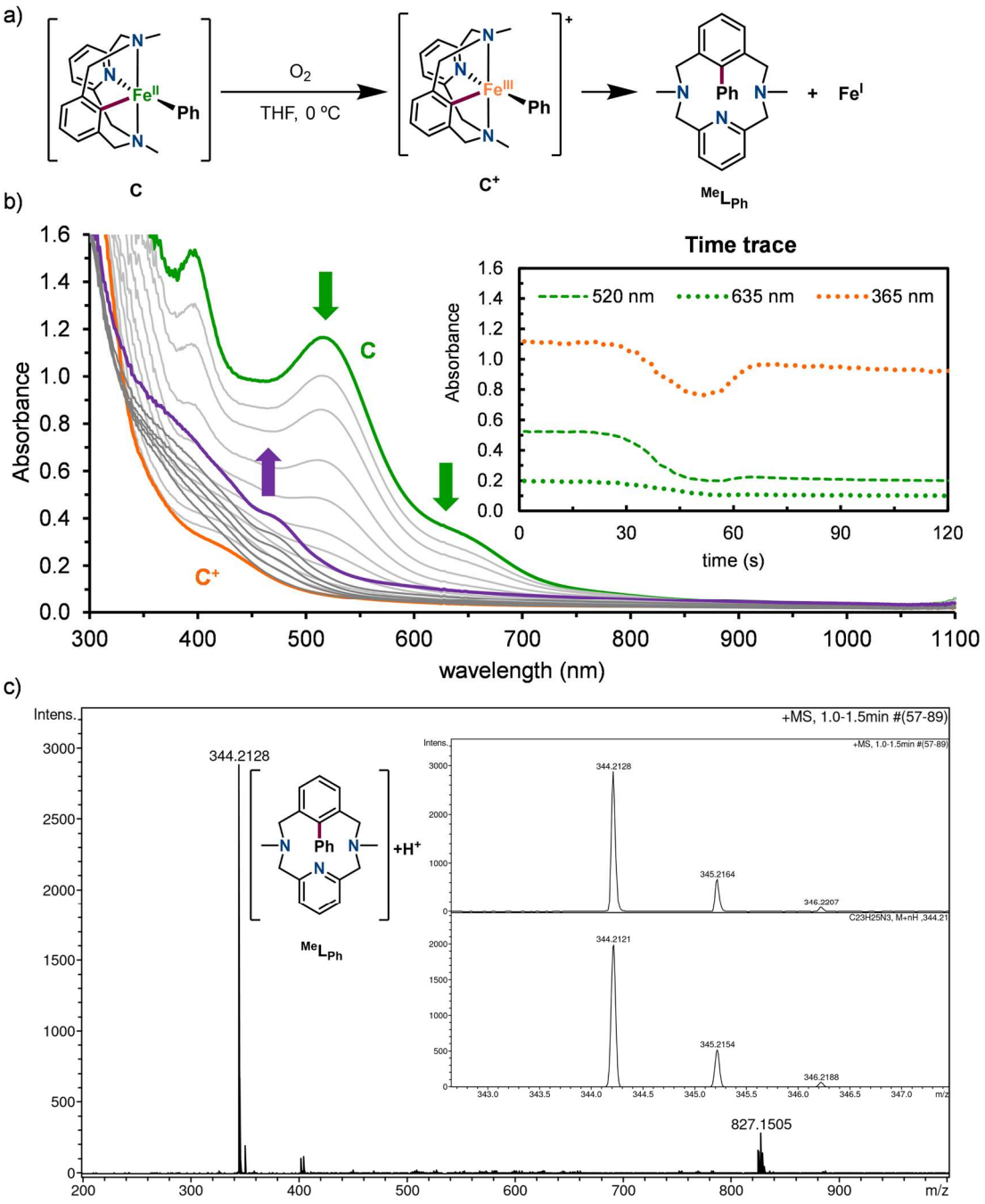

Figure VII.17 a) Reaction of **C** towards O_2 affording $^{Me}\mathbf{L_{Ph}}$; b) UV-vis monitoring of the reaction of **C** (green) towards dioxygen at 273 K yielding the decay of the bands at 520 and 635 nm to form unstable species $\mathbf{C}^+$ (orange) and immediate formation of the new band at 365 nm (purple) corresponding to the final mixture. Inset: time traces at 365, 520 and 635 nm. c) Attempt to detect species $\mathbf{C}^+$ by Cryo-HR-MS analysis. The obtained spectra only showed the presence of $^{Me}\mathbf{L_{Ph}}$. Inset: expanded view of the experimental peak at a m/z = 344.2128 corresponding to the monocharged $[C_{23}H_{25}N_3+H]^+$. Inset: expanded view of this peak along with the corresponding calculated spectrum.

Yet, regarding the information that can be drawn from the UV-vis monitoring, species **C** seems to be a bit more stable than species $\mathbf{C}^+$, so further attempts to isolate and characterize intermediate **C** were performed. Again, taking a deeper look into the electron count for the

putative compound **C**, we are once more in front of a pentacoordinated 16-electron complex, which makes it highly unstable. In order to elevate the coordination number to form an octahedral complex with 18 electrons, we envisioned the addition of a strong-field ligand such as triphenyl phosphine in order to enhance the stability of this intermediate species (**C'**) (Figure VII.18a). After some optimization of the process and different attempts, we came up with the best result with the following methodology. First, under a N_2 atmosphere, a Schlenk flask was charged with a solution of **1·Cl₂** and 1.5 equivalents of triphenyl phosphine in dry THF. The solution was stirred at room temperature for 1 hour and then the temperature was lowered to -78 ºC. Once thermal equilibrium was reached, 1.8 equivalents of PhMgBr were added dropwise. When the addition was completed, the temperature was increased at 65 ºC generating a color change to deep-red and the mixture was left stirring for 2 hours. After that, the crude mixture was cooled down to -40 ºC and the solution was cannulated at this temperature to remove the precipitate formed in the reaction media (Figure VII.18b). Unfortunately, although no crystals could be obtained neither a peak corresponding to species **C'** by mass spectrometry, the HR-ESI-MS spectrum of the cannulated solution showed a relevant peak corresponding to the formation of tetraphenyl phosphonium salt (PPh_4^+) (Figure VII.18c). This interesting result may stem from the P-C reductive elimination and so this would indicate the formation and involvement of complex **C'**. In fact, a blank reaction was carried out with phenyl Grignard reagent and triphenyl phosphine and no formation of the tetraphenyl phosphonium salt was detected, thus further confirming the role of iron for the previous result.[46]

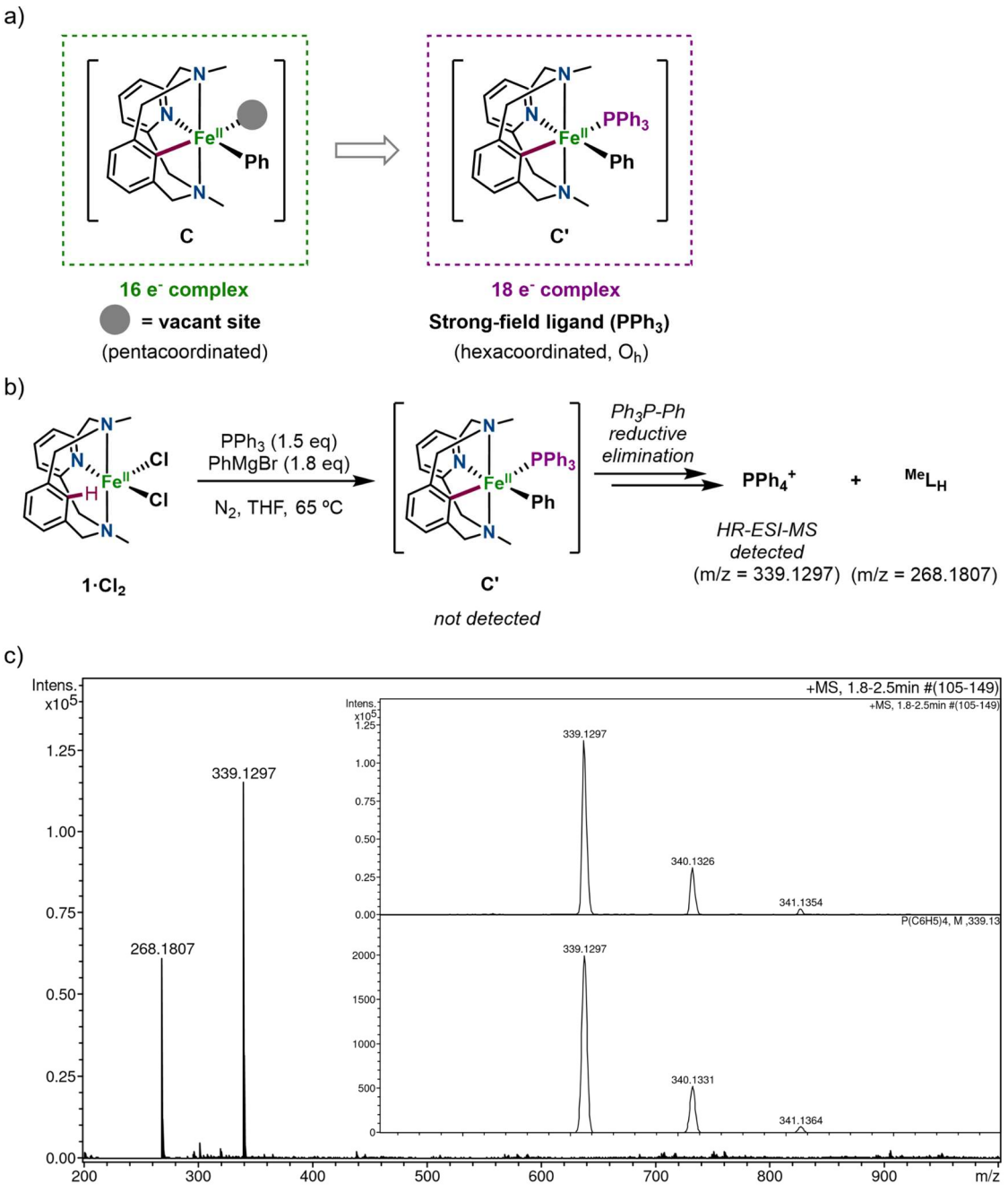

Figure VII.18 a) Scheme of the putative intermediate **C** (16 eletron complex) versus the corresponding intermediate **C'** containing 18 electrons by addition of a strong-field ligand (triphenyl phosphine); b) Reaction scheme for the synthesis of the new complex **C'**, and c) HR-ESI-MS spectrum of the reaction crude containing a main peak at a m/z = 339.1297 with a mass value and an isotopic pattern fully consistent with the P-C reductive elimination product $[PC_{24}H_{20}]^+$ (Inset: expanded view of this peak (top) and the calculated one for this formula (bottom)).

With the aim to gain more knowledge on the need for the oxidation from iron(II) to iron(III) to prompt the reductive elimination, a typical experiment for the obtention of $^{Me}\mathbf{L}_{Ph}$ was carried out but quenching directly with HCl before air exposure (Figure VII.19a). As a result, the biaryl coupling product was not detected, but only the protodemetallation product $^{Me}\mathbf{L}_{H}$ was obtained

in a relevant 85% yield. Thus, it seems clear that an oxidation step to iron(III) is required to trigger the reductive elimination step to form the final biaryl coupling product. The same experiment avoiding air exposure before acidic work-up was done for the reaction of $\mathbf{1^{Me}}$ with PhMgBr. In this case, 95% of the protodemetallation product $^{Me}\mathbf{L_H}$ and traces of $^{Me}\mathbf{L_{COPh}}$ were obtained. Interestingly, this result supports the formation of intermediate **E-1** upon CO migratory insertion into the phenyl moiety instead of the aryl moiety that would lead to the formation of the aldehyde product ($^{Me}\mathbf{L_{COH}}$) coming from intermediate **E-2**. This result was further validated by DFT calculations which suggest that intermediate **E-1** is 3.53 kcal·mol^{-1} lower in energy (Gibbs free energy) than **E-2** with respect to intermediate **D** (Figure VII.19b).

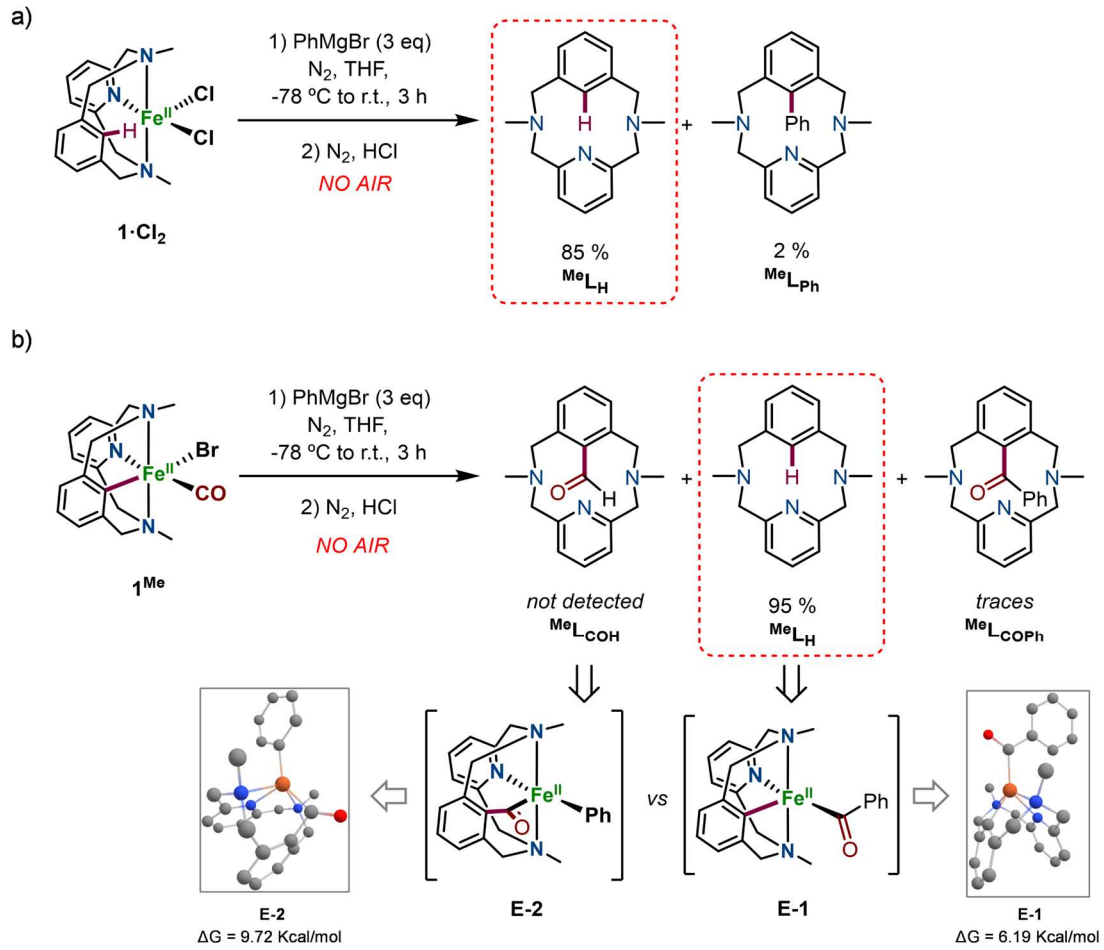

Figure VII.19 a) Reaction of $\mathbf{1{\cdot}Cl_2}$ with PhMgBr under anaerobic conditions, and b) reaction of $\mathbf{1^{Me}}$ with PhMgBr under anaerobic conditions and the corresponding computed Gibbs free energies of the structures for the putative intermediates **E-1** and **E-2**.

1,2-dichloroisobutane (DCIB) is a widely used oxidant in iron-mediated C-H activation/functionalization and cross-coupling reactions[44] and it was used to test if better results in terms of coupling product yield could be obtained. To do so, the reaction of $\mathbf{1{\cdot}Cl_2}$ with

PhMgBr was performed as previously described. Under a N_2 atmosphere, 2 equivalents of DCIB were added and, after the typical acid/base workup, $^{Me}\mathbf{L}_{Ph}$ was obtained in a 45% yield (lower than the 66% yield obtained with O_2) (Scheme VII.10). Finally, attempts to add DCIB at the beginning of the reaction, with the purpose of trying to make this transformation catalytic, only afforded 9% of $^{Me}\mathbf{L}_{Ph}$. This result suggests that the formation of the iron(III) species at the beginning of the reaction is unfavorable for this system and for this reason all attempts to make this system catalytic failed.

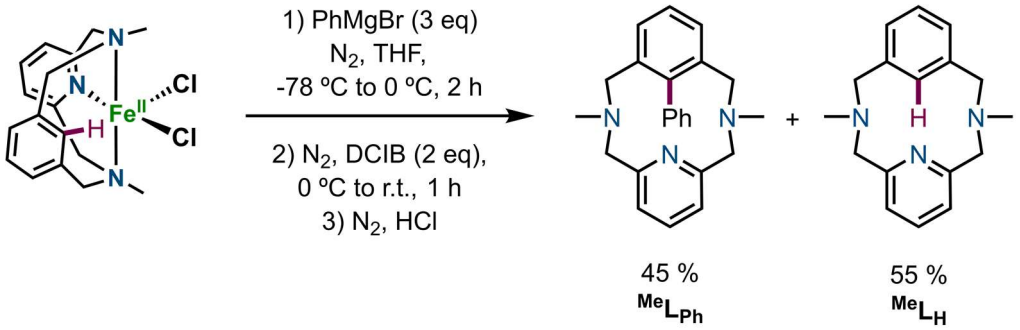

Scheme VII.10 Reaction of **1·Cl₂** with PhMgBr using DCIB as oxidant.

With all these results in hand, one mechanism was proposed for each reaction. In the case of the C-H activation/functionalization transformation, reaction of **1·Cl₂** with the first equivalent of phenyl Grignard reagent affords intermediate **A** via transmetallation. Then, C-H activation takes place, presumably via σ-bond metathesis where the coordinated phenyl moiety acts as an internal base to deprotonate the target hydrogen atom from the aryl moiety of the ligand, generating the new aryl-iron bond (species **B**) and releasing benzene. After that, transmetallation of the second equivalent of phenyl Grignard reagent takes place to give species **C** (bisaryl-iron(II)). At this point, an oxidation step is required to generate $\mathbf{C}^+$ and trigger the final reductive elimination step and release of the final aryl-phenyl coupling product, $^{Me}\mathbf{L}_{Ph}$ (Scheme VII.11).

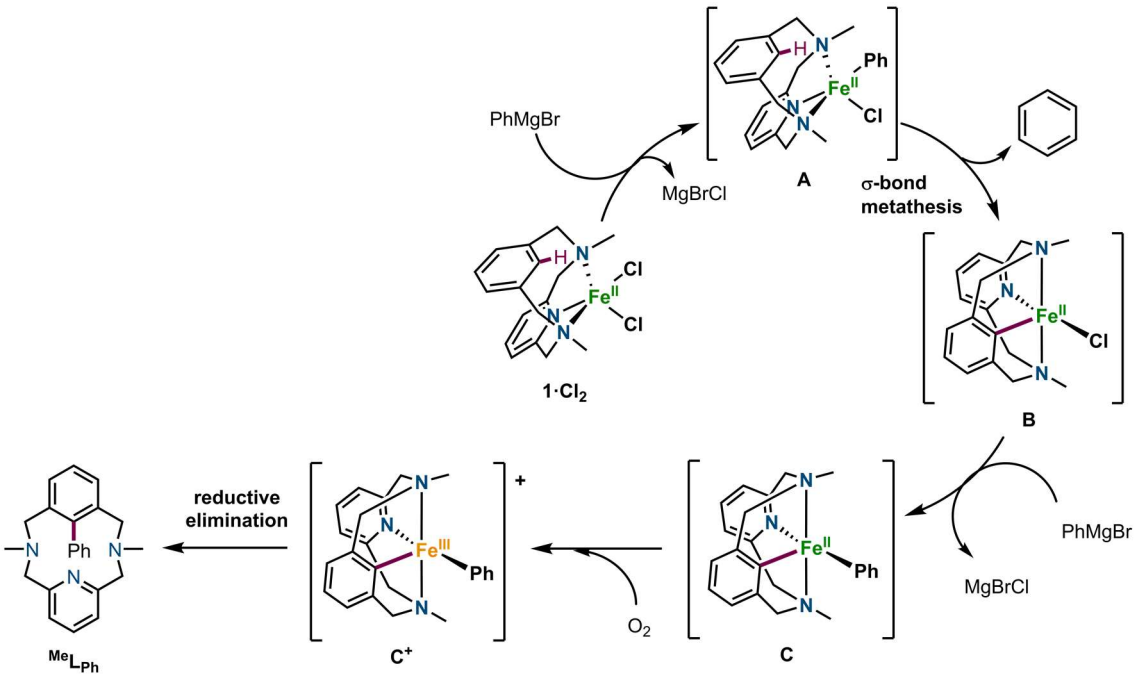

Scheme VII.11 Proposed mechanism for the reaction of **1·Cl$_2$** with PhMgBr for the obtention of the biaryl C-C coupling product (^{Me}**L$_{Ph}$**) via C-H activation.

A similar reaction pathway could be depicted for the cross-coupling reaction transformation, which started with the oxidative addition of the C_{Ar}-Br bond from the ligand (^{Me}**L$_{Br}$**) to the iron(0), $Fe(CO)_5$, to give **1^{Me}**. Then, transmetallation of the first equivalent of phenyl Grignard occurs to form the bisaryl-iron(II) complex (**D**). After that, a CO migratory insertion takes place most likely on the phenyl ring to give **E-1** (supported both by DFT calculations and experimental results previously explained). Finally, oxidation of **E-1** to **E-1**$^+$ with O_2 to trigger the reductive elimination step occurs and the aryl-COPh coupling product ^{Me}**L$_{COPh}$** is released (Scheme VII.12).

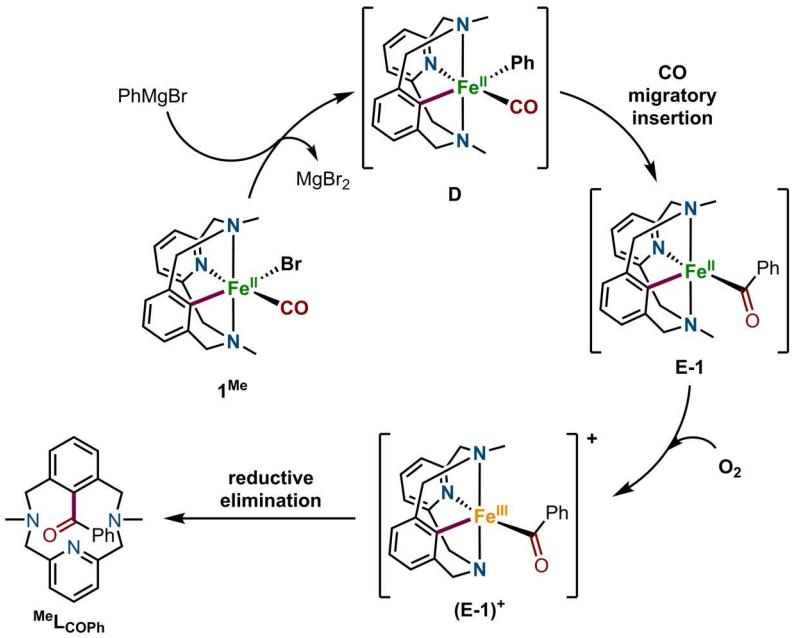

Scheme VII.12 Proposed mechanism for the reaction of $\mathbf{1}^{Me}$ with PhMgBr to obtain the CO-inserted C-C coupling product $^{Me}\mathbf{L}_{COPh}$.

In order to see if the CO insertion between the aryl and the phenyl moieties could be prevented, complex $\mathbf{1}^{Me}$ was reacted with PhMgBr under a N_2 atmosphere and UV-light photoirradiation (254 nm) to facilitate CO dissociation from the iron complex. However, HR-ESI-MS and NMR analysis of the reaction crude after aerobic acidic treatment, resulted in the formation of an 8% yield of the arylated product ($^{Me}\mathbf{L}_{Ph}$), a 10% of aryl-COPh coupling product ($^{Me}\mathbf{L}_{COPh}$), and a 52% of protodemetallation product ($^{Me}\mathbf{L}_{H}$) (Scheme VII.13a). In the same direction, to see if the CO insertion between the aryl and the phenyl moieties could be promoted, complex $\mathbf{1{\cdot}Cl_2}$ was reacted with phenyl Grignard under a CO atmosphere. Nevertheless, after the typical aerobic acidic treatment, the protodemetallation product was obtained in a 95% yield and less than a 3% yield of the desired CO-inserted coupling product ($^{Me}\mathbf{L}_{COPh}$) was obtained. No biaryl coupling product $^{Me}\mathbf{L}_{Ph}$ was detected (Scheme VII.13b). This result indicates that providing a CO atmosphere to the reaction of $\mathbf{1{\cdot}Cl_2}$ with phenyl Grignard is completely unfavorable for the formation of new C-C bonds.

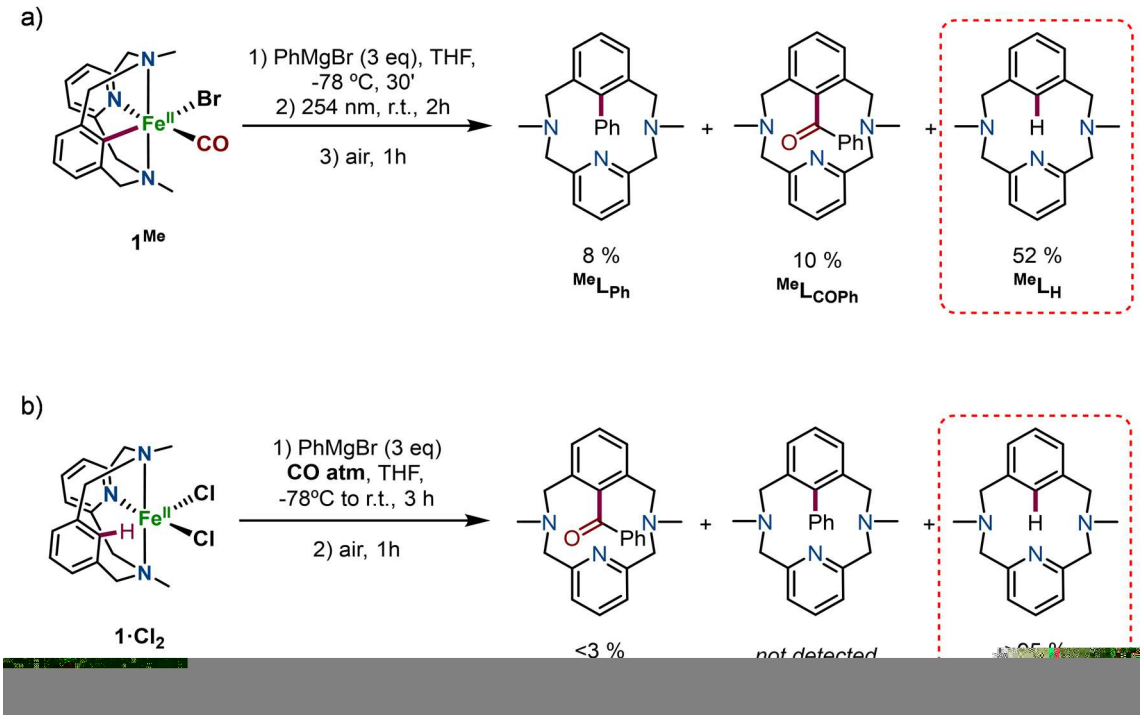

Scheme VII.13 a) Reaction of $\mathbf{1}^{Me}$ with PhMgBr in the presence of UV-light (254 nm) photoirradiation in order to avoid the insertion of CO into the coupling product, and b) reaction of $\mathbf{1{\cdot}Cl_2}$ with PhMgBr in the presence of a CO atmosphere to favour the CO insertion into the organic coupling product.

Interestingly, while exploring the reactivity of $^{Me}\mathbf{L_{Br}}$ we came up with an unexpected reactivity. when the reaction was performed under thermal conditions without UV-light irradiation. Under a N_2 atmosphere equimolar amounts of the ligand and $Fe(CO)_5$ were reacted in acetonitrile at 100 °C for 24 hours. After workup under an inert atmosphere, an unexpected aryl-iron(II) complex was obtained in 80% yield (Figure VII.20a). All attempts to isolate the complex failed, thus after exhaustive NMR and FT-IR characterization the structure of the new iron complex was unraveled. The new compound ($\mathbf{2^{Me}(CO)}$) presented a diamagnetic ^{1}H-NMR indicative of a low-spin aryl-iron(II) complex. Oddly, with the combination of 2D NMR experiments (Figure VII.20b) and FT-IR (Figure VII.20c) we concluded that one of the CO ligands from the starting iron(0) precursors had inserted between one of the tertiary amines and one of the pyridine-benzylic carbon atoms. This involves a tertiary amine to a tertiary amide conversion.

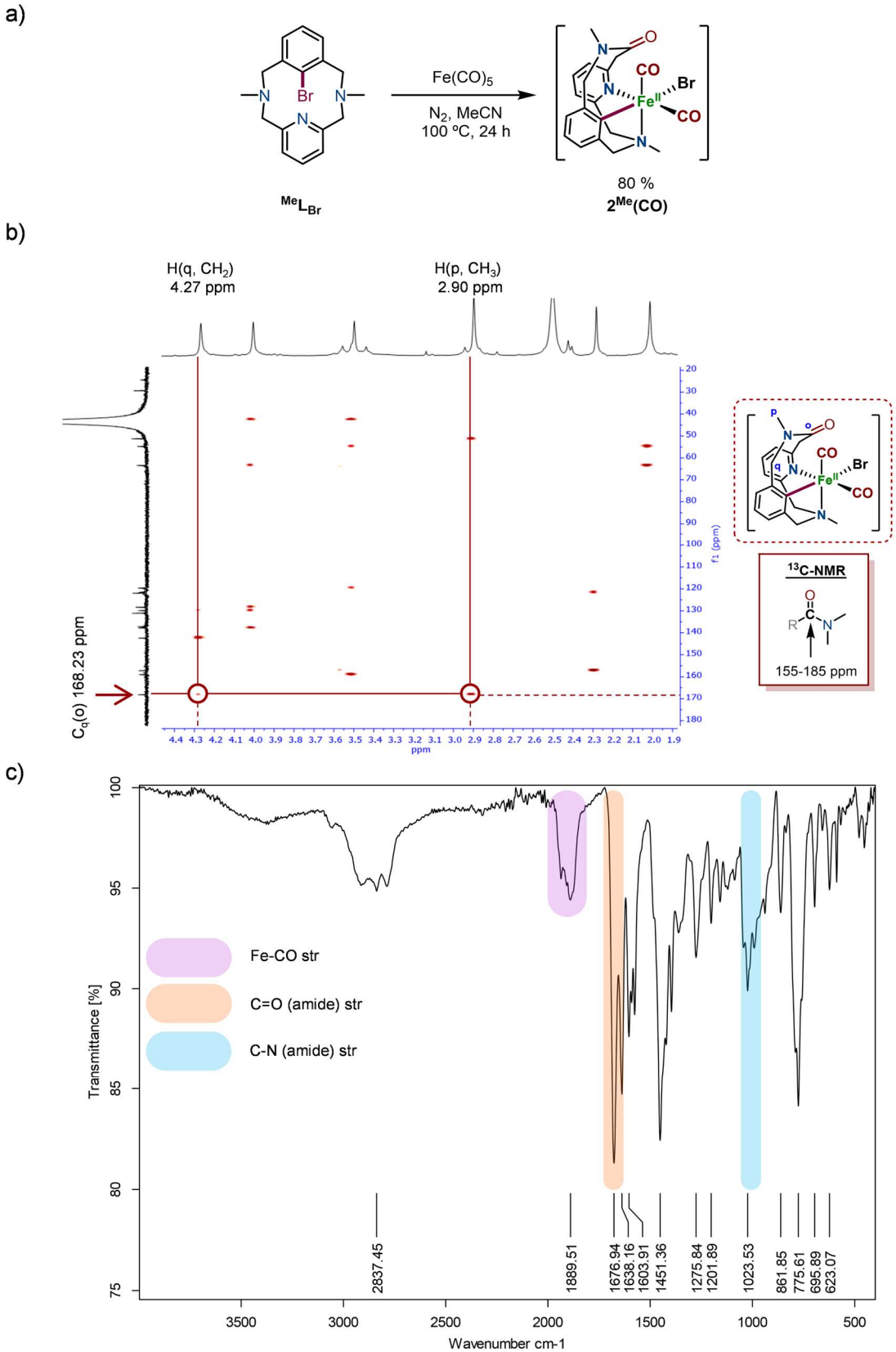

Figure VII.20 a) Synthesis of complex $\mathbf{2^{Me}(CO)}$; b) expansion of the aliphatic (^{1}H) region vs full range (^{13}C) ^{1}H-^{13}C HMBC spectrum of $\mathbf{2^{Me}(CO)}$ in DMSO-d_6 at room temperature (400 MHz), and c) ATR-FT-IR spectrum of $\mathbf{2^{Me}(CO)}$ at room temperature.

This new complex **2^{Me}(CO)** was submitted to HR-ESI-MS, but no peaks were obtained with an isotopic pattern containing iron, thus suggesting that this new complex was neutral (and so the bromide is directly coordinated to the iron(II) center). The only peak that was obtained had an m/z value and an isotopic pattern fully consistent with the hydrogenated ligand ($^{Me}L_H$) plus a CO moiety (calcd. for $C_{18}H_{21}N_3O$, $[M+H]^+$ = 296.1757; exp 296.1775).

The nature of the new amide product obtained was corroborated by isolating the organic product via protodemetallation from the iron complex with acidic treatment with HCl. The reaction proceeded smoothly and after a basic workup a quantitative yield of the organic product was obtained (**^{Me}L-CO$_H$**) and it was characterized by NMR, HR-ESI-MS and FT-IR. The ^{13}C-NMR presented a signal at 169.21 ppm corresponding to a quaternary carbon consistent with the carbonyl moiety of an amide group. Moreover, by FT-IR the C=O stretching frequency was observed at 1679 cm^{-1} which further supports the amide nature of **^{Me}L-CO$_H$** (Scheme VII.14b). Based on our knowledge, the carbonylation reaction to transform a tertiary amine to a tertiary amide is an uncommon transformation and is evocative of an unreported inverse Curtius-like rearrangement (Scheme VII.14a).[47] Xia and co-workers reported an iron-mediated Curtius-like rearrangement for the formation of isocyanates from hydroxamates through an iron(II)-nitrenoid complex.[48] Despite not being exactly the same mechanism, Cantat and co-workers, recently reported the iron-catalyzed tertiary amine acylation to tertiary amide by extrusion of methyl iodide.[49]

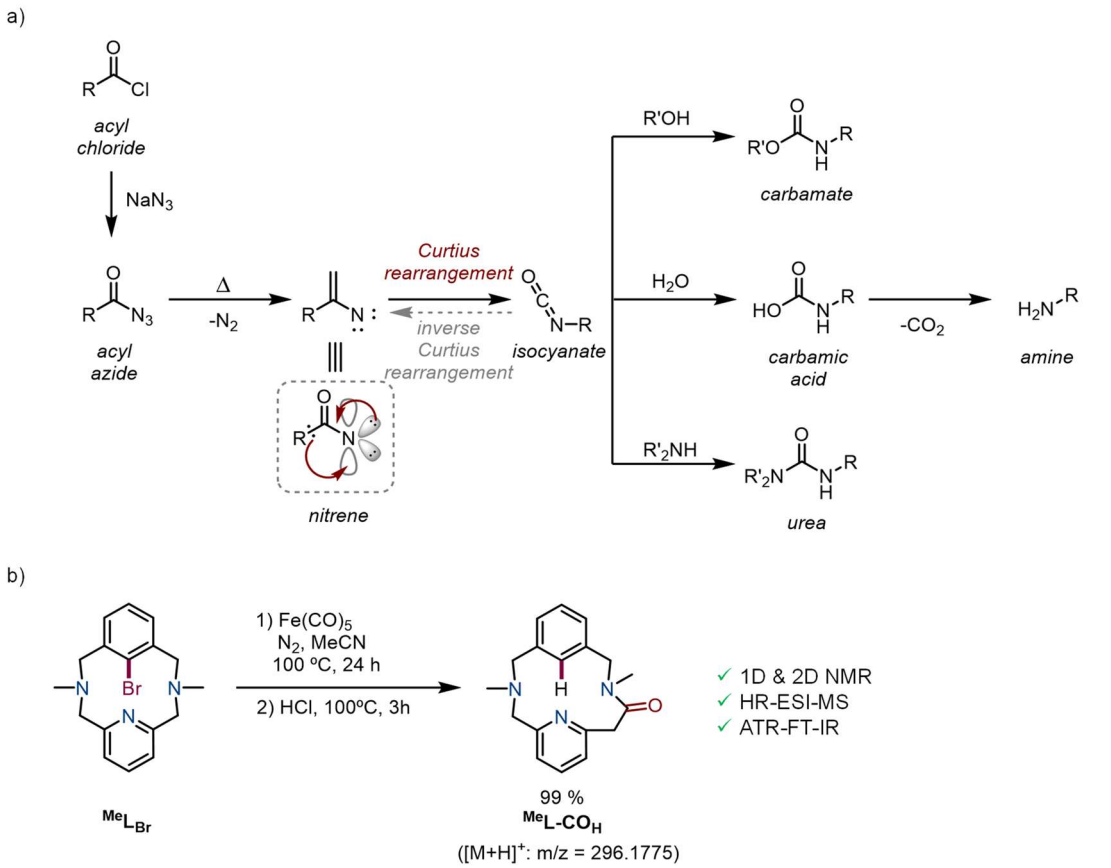

Scheme VII.14 a) The Curtius rearrangement transformation mechanism, and b) Synthesis and characterization of ^{Me}**L-CO$_H$**.

Following this line, with the aim to get more insight into the mechanism of this novel reactivity, a CO atmosphere was provided to the well-defined **1^{Me}** complex dissolved in deuterated DMSO and then heated up to 100 ºC. After only 2 hours a ^{1}H-NMR was taken and a 14% of complex **2^{Me}(CO)** was formed together with a 14% of protodemetallation organic product (^{Me}**L$_H$**) and a 71% of starting complex (**1^{Me}**) (Figure VII.21). This result suggests that the oxidative addition from the C-Br bond to the iron(0) takes place before the amine to amide transformation.

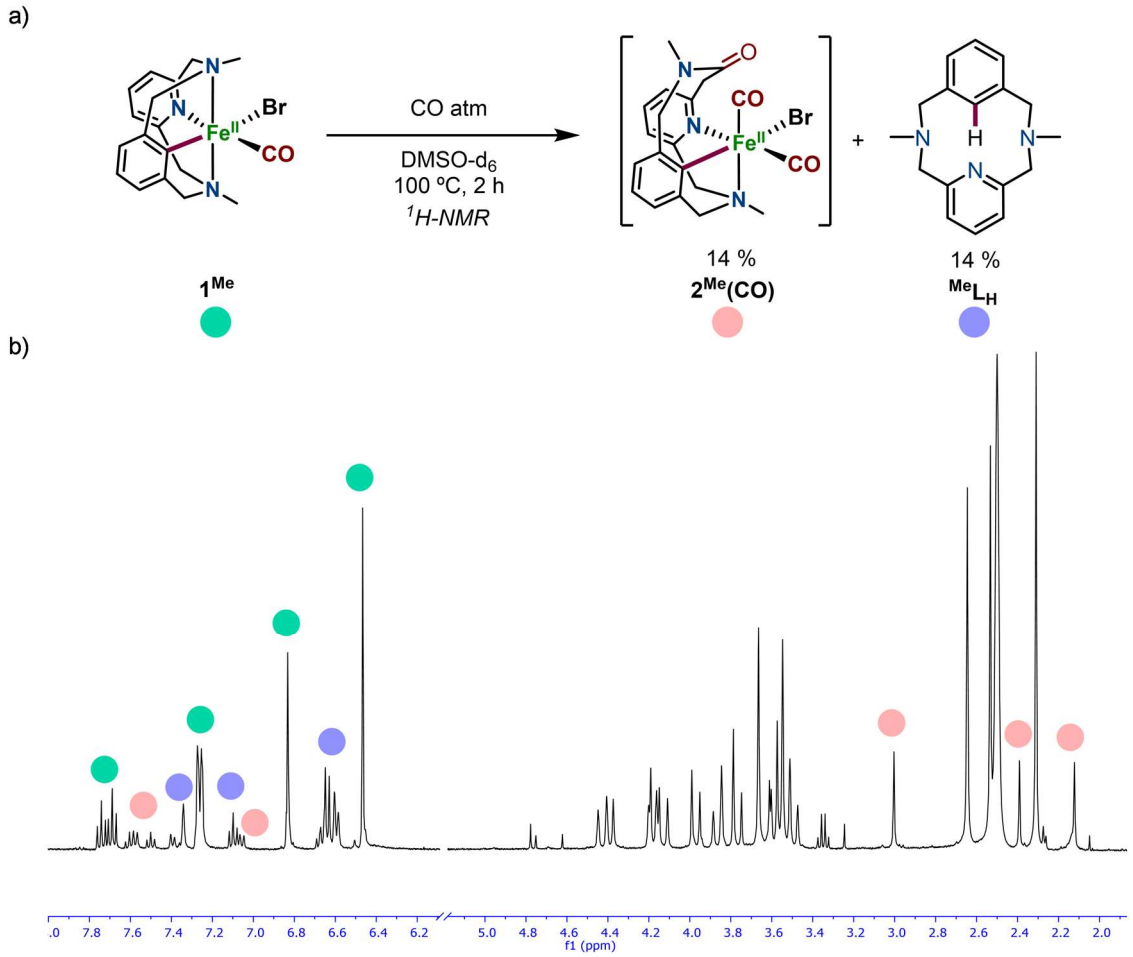

Figure VII.21 a) Reaction of the well-defined $\mathbf{1^{Me}}$ under thermal conditions for the synthesis of $\mathbf{2^{Me}(CO)}$, and b) ^{1}H-NMR spectrum of the crude after 2 hours of reaction.

Moreover, to explore the scope of the reaction by using different amine substituents on the starting ligand, the same reaction under thermal conditions was performed using the secondary amine version of the ligand ($\mathbf{^{H}L_{Br}}$) and the *tert*-butyl-*N*-substituted ligand ($\mathbf{^{tBu}L_{Br}}$), respectively. Under a N_2 atmosphere equimolar amounts of the ligands and $Fe(CO)_5$ were reacted at 100 °C for 24 hours. In the case of $\mathbf{^{tBu}L_{Br}}$, after inert atmosphere workup, the usual aryl-iron(II) complex, without the CO insertion into the ligand backbone, was obtained ($\mathbf{1^{tBu}}$, 58% yield, Scheme VII.15a). Nevertheless, all attempts to obtain a crystal structure suitable for X-ray diffraction analysis were unfruitful. On the other hand, when using the secondary amine version of the ligand, $\mathbf{^{H}L_{Br}}$, and after an acidic treatment, the outcome of the reaction was totally different, obtaining a 27% yield of the amide product ($\mathbf{^{H}L\text{-}CO_H}$) together with a 22% of the protodemetallation product ($\mathbf{^{H}L_H}$) and a 51% of unreacted starting ligand ($\mathbf{^{H}L_{Br}}$) (Scheme VII.15b). The scope of the reaction was further confirmed by analyzing the crude by HR-ESI-MS.

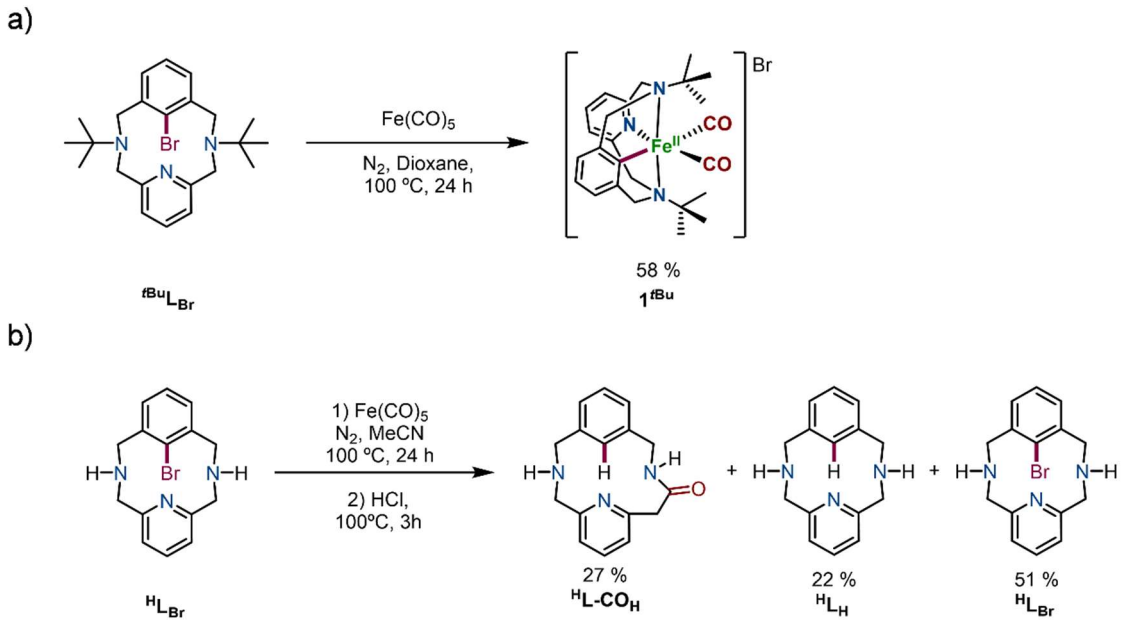

Scheme VII.15 a) Thermal reaction of $^{tBu}\mathbf{L_{Br}}$ with $Fe(CO)_5$ to form complex $\mathbf{1}^{tBu}$, and b) Thermal reaction of $^{H}\mathbf{L_{Br}}$ with $Fe(CO)_5$ to form $^{H}\mathbf{L\text{-}CO_H}$.

To sum up, we have been able to isolate well-defined aryl-iron(II) complexes via C-Br bond activation through a net two-electron oxidative addition which is a challenging transformation considering the facility for iron to undergo one-electron processes.[50] These well-defined organometallic iron complexes have shed light into the mechanism of C-H activation and C-C bond forming cross-coupling reactions, and constitute a powerful platform for developing new transformations in the field of iron organometallic chemistry. Furthermore, upon submitting the system to thermal conditions a tertiary amine to tertiary amide conversion has been observed on a macrocyclic substrate for the first time.

VII.4 ORGANOMETALLIC Ni(II), Ni(III) AND Ni(IV) COMPLEXES RELEVANT TO CARBON-CARBON AND CARBON-OXYGEN BOND FORMATION REACTIONS

As explained in the introduction, the formation of new C-C and C-heteroatom bonds via transition-metal mediated cross-coupling transformations, and the replacement of noble metals like palladium by first-row transition metals such as nickel, is nowadays one of the most potent strategies in organic chemistry. In order to develop more efficient reactions, mechanistic studies are very important to gain insight on how these reactions work and thus to improve them. However, first-row transition metals are far less mechanistically studied than their precious metals counterparts. For instance, it is well-known that palladium-mediated transformations occur via Pd^0/Pd^{II} or Pd^{II}/Pd^{IV} catalytic cycles, that involve in most of the cases diamagnetic species which are easier to characterize.[51, 52] In contrast, nickel-mediated transformations can undergo both one- and two-electron processes yielding more complex mechanistic cycles, as the +I and +III oxidation states are also feasible.[53-55] These species are paramagnetic and thus, they are more difficult to characterize, which makes their mechanistic understanding more challenging. Moreover, high-valent nickel(III) and nickel(IV) species have only recently been invoked in cross-coupling transformations, thus triggering an emerging need to gain more knowledge into the nature of high-valent organonickel complexes relevant for cross-coupling reactions.[56]

Based on that, we envisioned the use of the **PyNMe$_3$** ligand, which was previously employed in our group to stabilize high-valent iron-oxo[6-8] and side-on peroxodicopper(II)[57] intermediates, but it had never been used to stabilize organometallic compounds. To do this, a collaboration with Mirica's research group at University of Illinois at Urbana-Champaign was established to perform a detailed study on organonickel complexes bearing the **PyNMe$_3$** ligand. Mirica and co-workers are experts in the field of high-valent organometallic nickel complexes, but all the ligands they have employed for the mechanistic studies of high-valent nickel complexes are highly symmetric.[58-63] Thus, the **PyNMe$_3$** ligand would allow for a deeper study in terms of ligands distribution around the nickel center.

The first attempt to isolate an organonickel complex supported by **PyNMe$_3$** consisted in the oxidative addition of the C-Br bond from the 1-bromo-4-fluorobenzene substrate at an *in situ* prepared Ni^0 complex. To do so, under a N_2 atmosphere, equimolar amounts of **PyNMe$_3$** and $Ni(COD)_2$ were dissolved in 1-bromo-4-fluorobenzene at room temperature, and stirred for 4 hours. The formation of a green precipitate was observed together with a black solid. After work up and recrystallization complex $[(PyNMe_3)Ni^{II}(Br)_2]$ **(1-Br)**was obtained instead of the desired organonickel compound, **$[(PyNMe_3)Ni^{II}(PhF)(Br)]$**. Nevertheless, upon GC-MS analysis of the supernatant from the crystallization set-up, 4,4-difluorobiphenyl was detected, which corresponds to the homocoupling product resulting from a C-C bond reductive elimination. This result suggests that the desired **$[(PyNMe_3)Ni^{II}(PhF)(Br)]$** complex formed upon oxidative addition of the C-Br bond at the nickel(0) center rapidly transmetallates with another molecule of the same complex to generate **1-Br** and **$[(PyNMe_3)Ni^{II}(PhF)_2]$** which eventually undergoes reductive elimination to yield the homocoupling biphenyl derivative and nickel(0) (black solid) (Figure VII.22).

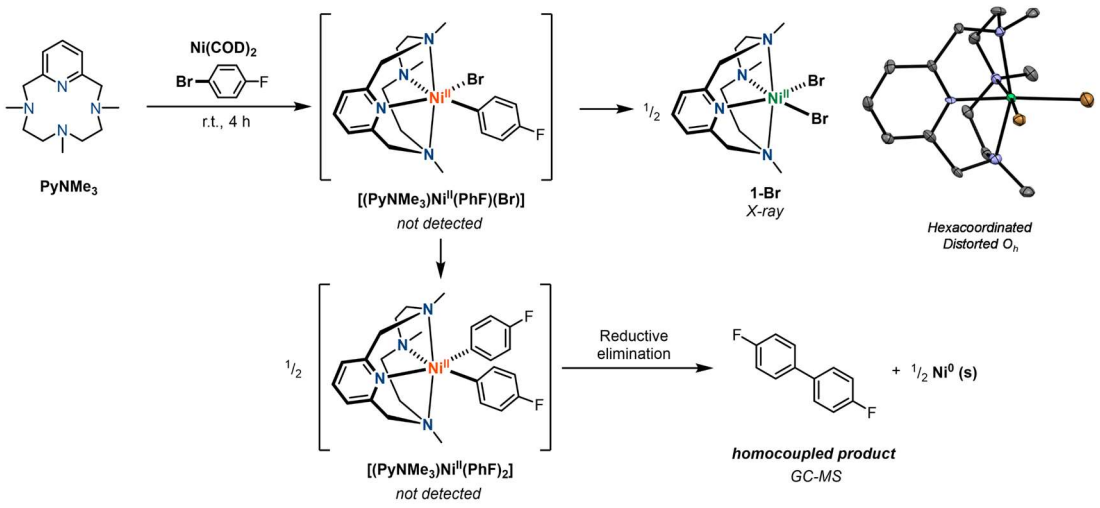

Figure VII.22 Attempted reaction to synthesise the desired complex **$[(PyNMe_3)Ni^{II}(PhF)(Br)]$**. On the right, X-ray structure for **1-Br** (hydrogen atoms have been omitted for clarity).

After that, we designed a different attempt to isolate a dimethylnickel(II) complex via transmetallation to a nickel(II) precursor. To synthetise the nickel(II) precursor, **PyNMe$_3$** and 0.8 equivalents of $Ni^{II}(DME)Cl_2$ were dissolved in THF and stirred at room temperature for 24 hours in the glovebox, which resulted in a green suspension. After work up and crystallization, X-ray quality crystals of $[(PyNMe_3)Ni^{II}(Cl)_2]$ **(1-Cl)** were obtained in 85% yield (Figure VII.23a). The structure of complex **1-Cl** presented the same features as its analogue complex

bearing bromides (**1-Br**) obtained in the previous reaction. Once **1-Cl** was obtained, it was reacted with 2 equivalents of MeMgBr in THF at -50 °C. Upon dropwise addition of the Grignard reagent, a color change from green to orange was observed. The reaction work up was carefully done in the glovebox under rigorous low-temperature conditions to avoid the decomposition of the putative [(**PyNMe$_3$**)**Ni^{II}(Me)$_2$**] complex formed (Figure VII.23b). Unfortunately, all the attempts to isolate or characterize this compound failed due to its high instability. The obtained orange-black solid was dissolved in deuterated benzene to take a ^{1}H-NMR at room temperature. Interestingly, despite being a very broad spectrum, two signals below 0 ppm could be detected that could correspond to the methyl groups directly attached to the nickel(II) center (Figure VII.23c).[59]

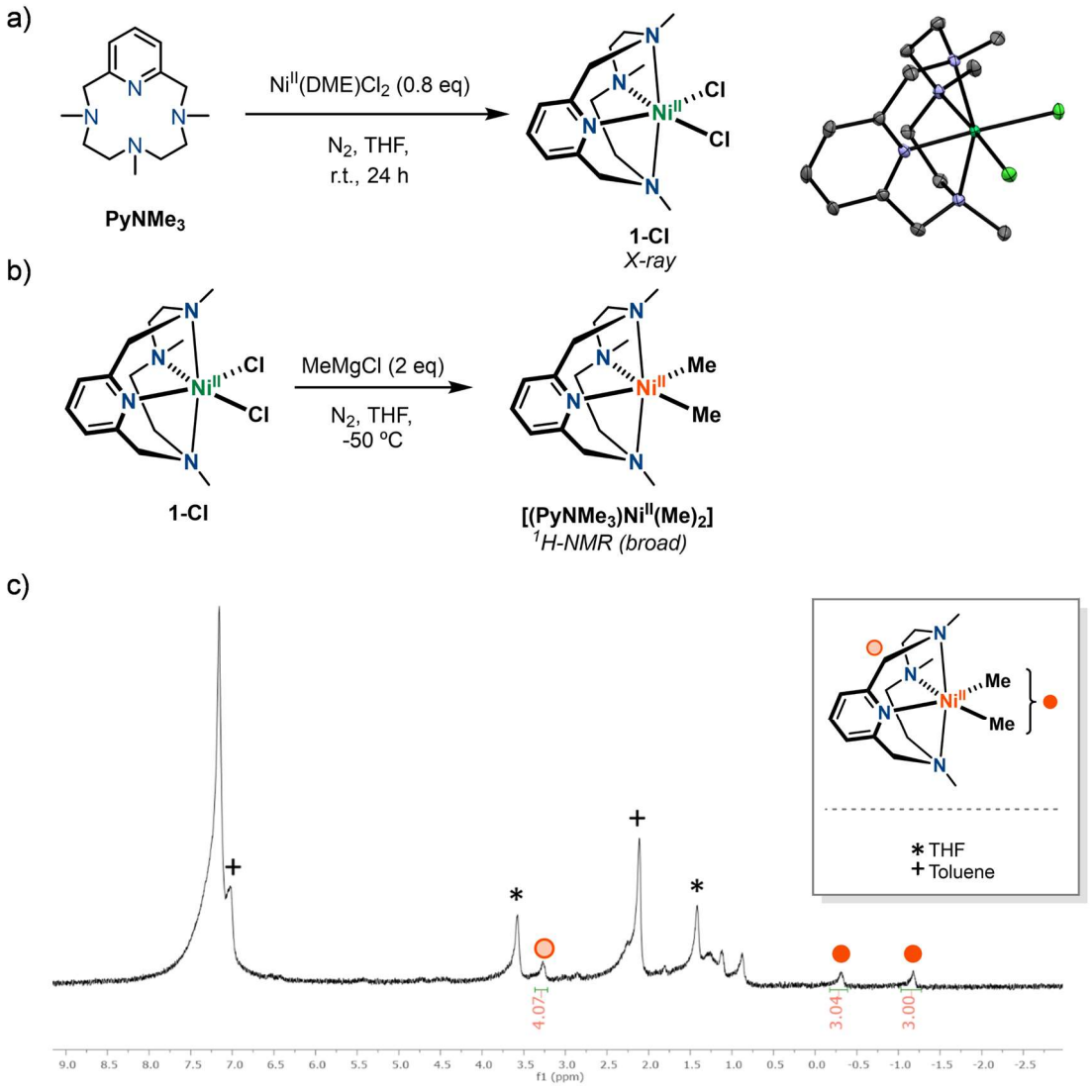

Figure VII.23 a) Synthesis of **1-Cl** along with its X-ray structure (hydrogen atoms have been omitted for clarity); b) synthesis of complex [(**PyNMe$_3$**)**Ni^{II}(Me)$_2$**], and c) ^{1}H-NMR spectrum of complex [(**PyNMe$_3$**)**Ni^{II}(Me)$_2$**].

At this point we decided to switch our strategy and enhance the stability of the organometallic nickel complex by using the cycloneophyl ligand (cycl, -$CH_2CMe_2C_6H_4$-) as the carbon-donor ligand. The cycloneophyl ligand is a bidentate ligand containing an alkyl and an aryl anchoring groups. Moreover, this alkyl/aryl-donor ligand was designed to decrease the probability of reductive elimination and avoids the possibility of β-hydride elimination (Scheme VII.16).[64-66]

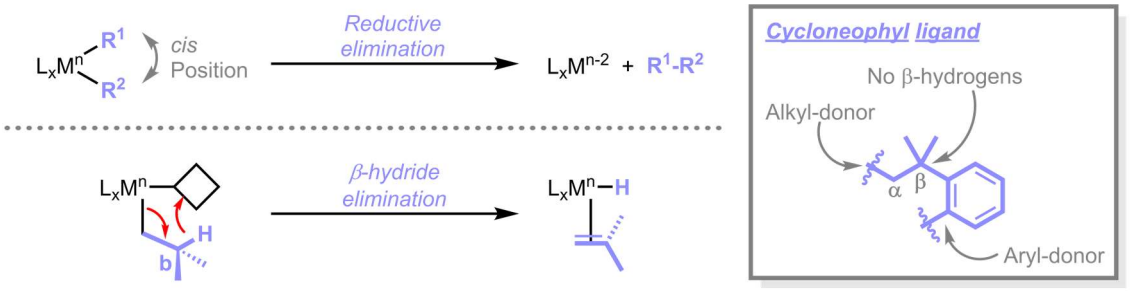

Scheme VII.16 Reductive elimination step (top) and β-hydride elimination step (bottom). Inset: the cycloneophyl ligand structure which hampers both processes.

For all these reasons we decided to synthesize a nickel(II)-cycloneophyl complex bearing the **PyNMe$_3$** ligand. To do so, equimolar amounts of **PyNMe$_3$** and the nickel(II)-cycloneopyl precursor, [$(Py)_2Ni^{II}$(cycl)], were dissolved in a toluene/pentane (1:1) solvent mixture, under an anaerobic atmosphere, and the mixture was stirred overnight at room temperature, resulting in an orange suspension. After work up and crystallization, X-ray quality crystals were obtained in a 71% yield corresponding to the desired complex [$(PyNMe_3)Ni^{II}$(cycl)] (**2**, Figure VII.24a). Complex **2** was fully characterized by NMR which showed a diamagnetic low-spin nickel(II) complex. Interestingly, the ^{1}H-NMR spectrum exhibits broad peaks, especially the ones assigned to the methylene protons on **PyNMe$_3$**, presumably due to the fast coordination exchange of the four types of nitrogen-donors from the ligand (Figure VII.24b). The X-ray structure of complex **2** presents a square planar geometry around the nickel(II) center, thus confirming the low-spin nature of the nickel(II) complex. As above stated, **PyNMe$_3$** enables the observation of the *trans*-effect of the different chelating groups, which could not be observed with ^{R}N4 or ^{R}N3 type ligands previously employed by Mirica and co-workers.[58-63] Interestingly, **PyNMe$_3$** coordinates the nickel(II) center in **2** in a bidentate fashion through the pyridine motif *trans* to the alkyl moiety from the cycloneophyl, and one of the adjacent amines *trans* to the phenyl moiety from the same cycloneophyl ligand (Figure VII.24c). Furthermore, in order to study the redox properties of complex **2**, a cyclic voltammogram (CV) was performed, which reveals a pseudo-

reversible oxidation at $E_{1/2}$ = 250 mV (vs. ferrocene) followed by another pseudo-reversible oxidation event at $E_{1/2}$ = 630 mV (vs. ferrocene), assigned to the $Ni^{II/III}$ (ΔE = 220 mV) and $Ni^{III/IV}$ (ΔE = 130 mV) redox couples, respectively (Figure VII.24d). These redox potentials suggest that **2** might be oxidized to the corresponding nickel(III) and nickel(IV) organometallic complexes.

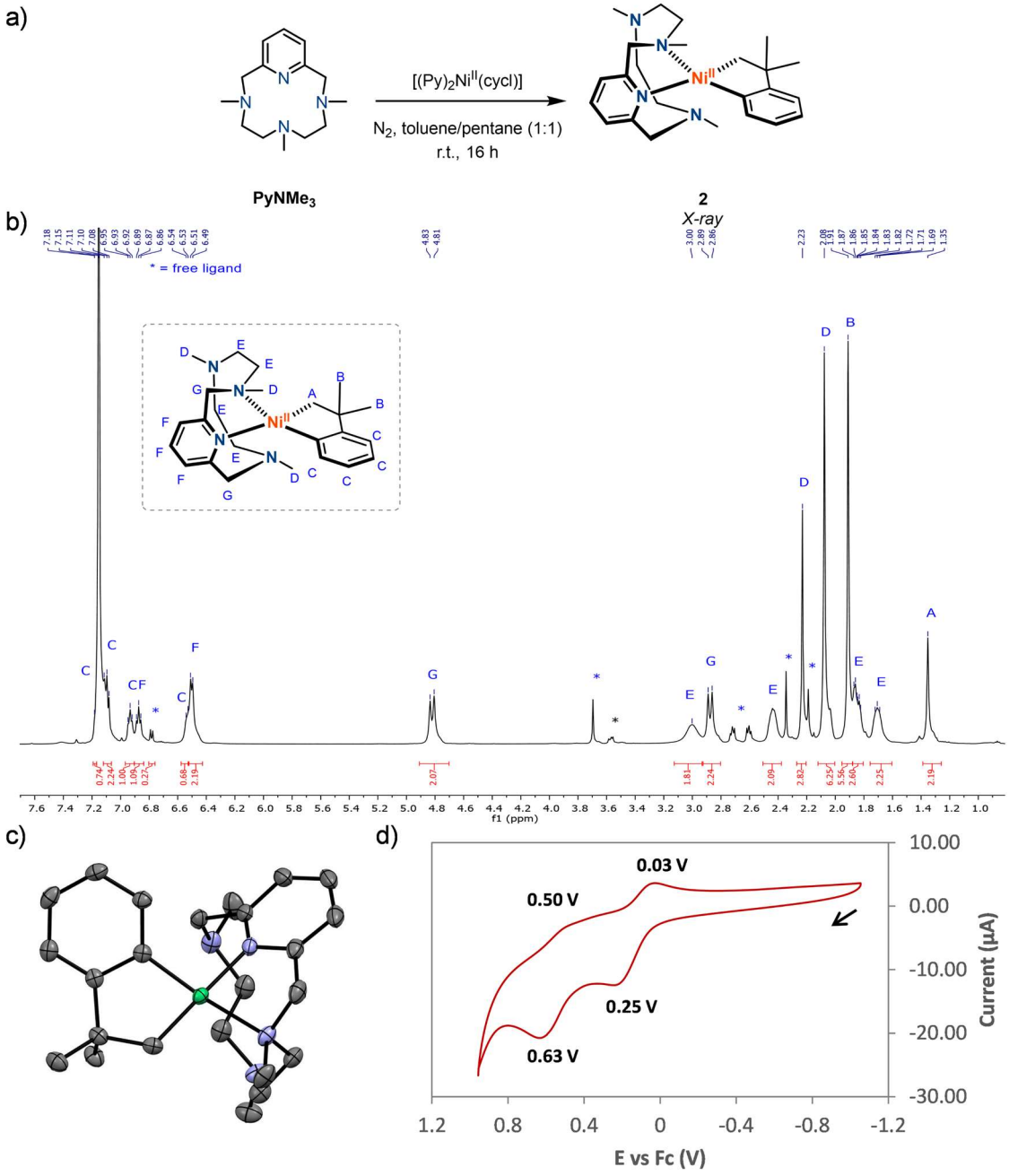

Figure VII.24 a) Synthesis of complex **2**; b) ^{1}H-NMR spectrum of complex **2** in benzene-d_6 at room temperature (inset: proton assignment); c) X-ray structure of **2** (hydrogen atoms omitted for clarity), and d) CV of **2** in a 0.1 M [nBu$_4$N](PF$_6$)/acetonitrile solution as electrolyte at a scan rate of100mV/s.

With the aim to obtain complex $[(PyNMe_3)Ni^{III}(cycl)]^+$ ($\mathbf{3}^+$), first an EPR analysis was done. To do so, a 0.1 mM solution of complex **2** in acetonitrile was prepared and cooled down to -35

°C. Subsequently, a cold suspension containing 1 equivalent of ferrocenium hexafluorophosphate ($FcPF_6$) in PrCN was layered over the complex **2** solution in an EPR tube, mixed for 5 seconds resulting in a 1:3 MeCN/PrCN mixture solution, and rapidly frozen in liquid N_2. Noteworthy, right after mixing the complex and the oxidant suspension, the dark color from the oxidant suspension completely vanished and everything became soluble. At this point, EPR at low temperature was measured obtaining the corresponding nickel(III) d^7 center which exhibits a pseudoaxial signal with hyperfine coupling in the g_z direction (A_{2N} = 13.7 G), suggesting that two *I*=1 nitrogen atoms, either from **PyNMe$_3$** or solvent (MeCN or PrCN), are coordinated to the nickel(III) center (Figure VII.25). Moreover, a second EPR spectrum was recorded after leaving the putative complex **3** at room temperature for 30 minutes without any significant changes, meaning that complex **3** is stable at room temperature.

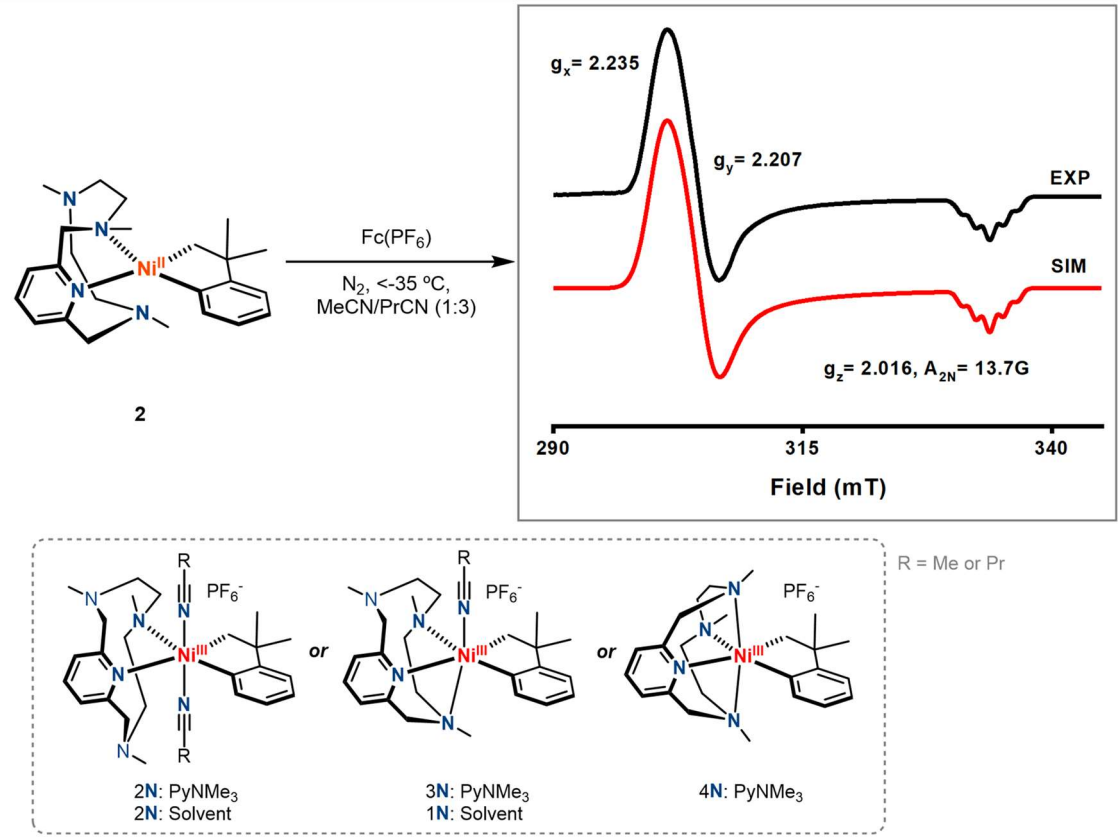

Figure VII.25 Top: Reaction of 2 with Fc(Pf6) to afford the corresponding nickel(III) complex (**3**) and its EPR spectrum at low temperature in a MeCN/PrCN 1:3 solvent mixture (black line: experimental; red line: simulated). Bottom: Possible structures of complex **3** based on the EPR spectrum.

With this positive result in hand, the reaction was performed at larger scale with the aim to isolate complex **3**. Complex **2** was dissolved in acetonitrile at -35 °C, and then 1 equivalent of ferrocenium hexafluorophosphate was added and mixed over a period of 3 hours. The resulting

solution was concentrated and stored at -35 °C giving after a few days red-colored crystals corresponding to $[(PyNMe_3)Ni^{III}(cycl)](PF_6)$ (**3**) in a 73% yield (Figure VII.26). The X-ray structure of complex **3** presents a distorted octahedral geometry of the nickel(III) center, where all the coordination positions are occupied by the four binding nitrogens from **PyNMe$_3$** and both the alkyl and aryl carbons from the cycloneophyl ligand. This result is in accordance with the six-coordinate complex observed by EPR and further supports the use of only one A(N) value as both nitrogen atoms are equivalent due to the symmetry provided by the **PyNMe$_3$** coordination mode. As shown in the X-ray structure of complex **3**, the pyridine moiety remains *trans* to the alkyl group, however this time the N3 amine is *trans* to the phenyl group, instead of the N2 amine as observed in complex **2**. Interestingly, as previously observed for other similar complexes reported by Mirica and co-workers, the Ni-C as well as the Ni-N bond distances are larger in complex **3** than those in complex **2**.[58, 59]

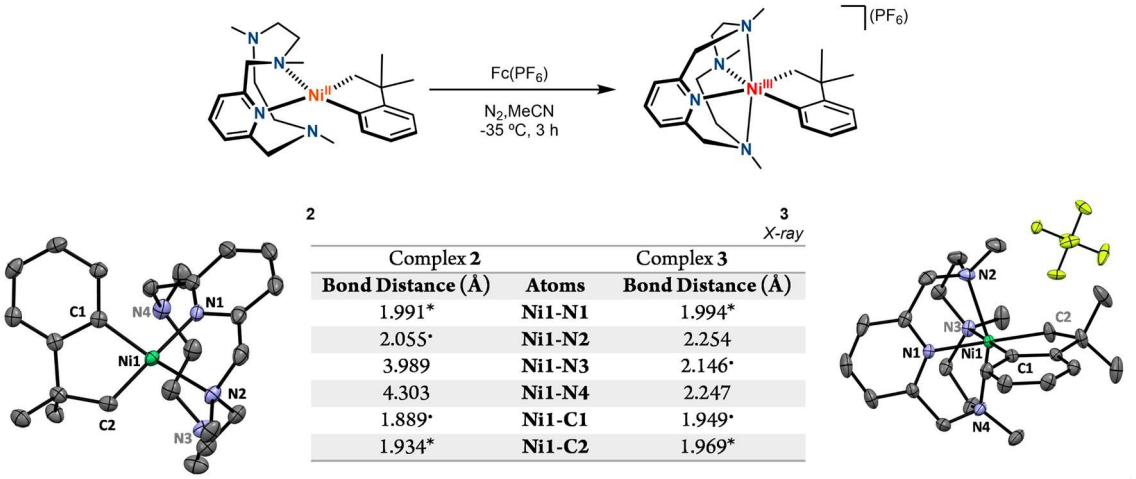

Complex **2**		Complex **3**
Bond Distance (Å)	**Atoms**	**Bond Distance (Å)**
1.991*	**Ni1-N1**	1.994*
2.055·	**Ni1-N2**	2.254
3.989	**Ni1-N3**	2.146·
4.303	**Ni1-N4**	2.247
1.889·	**Ni1-C1**	1.949·
1.934*	**Ni1-C2**	1.969*

Figure VII.26 Top: Synthesis of complex **3**. Bottom: Table with selected bond lengths for complex **2** and complex **3** (* and · are indicative of *trans* pairs), and their corresponding X-ray structures.

At this stage, and going back to the cyclic voltammogram performed for complex **2**, we decided to go further and try to synthesize and characterize the corresponding nickel(IV) complex. To do so, the reaction was monitored via low temperature UV-vis spectroscopy in tandem with cryo-MS experiments to detect the different species formed upon stepwise one-electron oxidation (Figure VII.27). It is worth mentioning that for this experiment, the oxidant of choice was a nitrosonium salt (NO^+) instead of the previously used ferrocenium salt, because nitrosonium is a cleaner oxidant (release of NO gas as by-product) compared to ferrocenium

salts which presents absorption bands (ca. λ = 325 and 440 nm for Fc^+; ca. λ = 450 nm for Fc) that could interfere with the UV-vis monitoring.

Hence, a 0.5 mM solution of complex **2** in acetonitrile was placed in a UV-vis cell set up at -40 °C, and once thermal equilibrium was reached, a first UV-vis spectrum was recorded. The UV-vis spectrum corresponding to complex **2** exhibited a band at a λ_{max} = 462 nm (ε = 880 $M^{-1}cm^{-1}$). Subsequently, 1 equivalent of $NO(SbF_6)$ was injected into the UV-cuvette through the septum, which caused the immediate disappearance of the band corresponding to complex **2** and a completely new UV-vis spectrum was obtained with a broad band at a λ_{max} = 513 nm (ε = 300 $M^{-1}cm^{-1}$) assigned to complex **3**. This result was further confirmed upon injecting an aliquot of this solution for cryo-MS analysis, which showed a monocharged main peak with a mass value and isotopic pattern fully consistent with complex $\mathbf{3}^+$ (calcd. for $C_{24}H_{36}N_4Ni^+$: m/z = 438.2288; exp: m/z = 438.2289) (Figure VII.27b). After that, a second equivalent of the same oxidant was injected into the UV-cuvette which caused the disappearance of the band corresponding to complex **3**, and the formation of two new bands at 384 nm and 470 nm (ε = 1200 $M^{-1}cm^{-1}$) assigned to $[(PyNMe_3)Ni^{IV}(cycl)](SbF_6)_2$ (**4**). To further support this result, an aliquot of the solution was analyzed by cryo-MS and to our delight a discharged main peak with a mass value and isotopic pattern fully consistent with complex $\mathbf{4}^{2+}$ was observed (calcd. for $C_{24}H_{36}N_4Ni^{2+}$: m/z = 219.1141; exp: m/z = 219.1129) (Figure VII.27c).

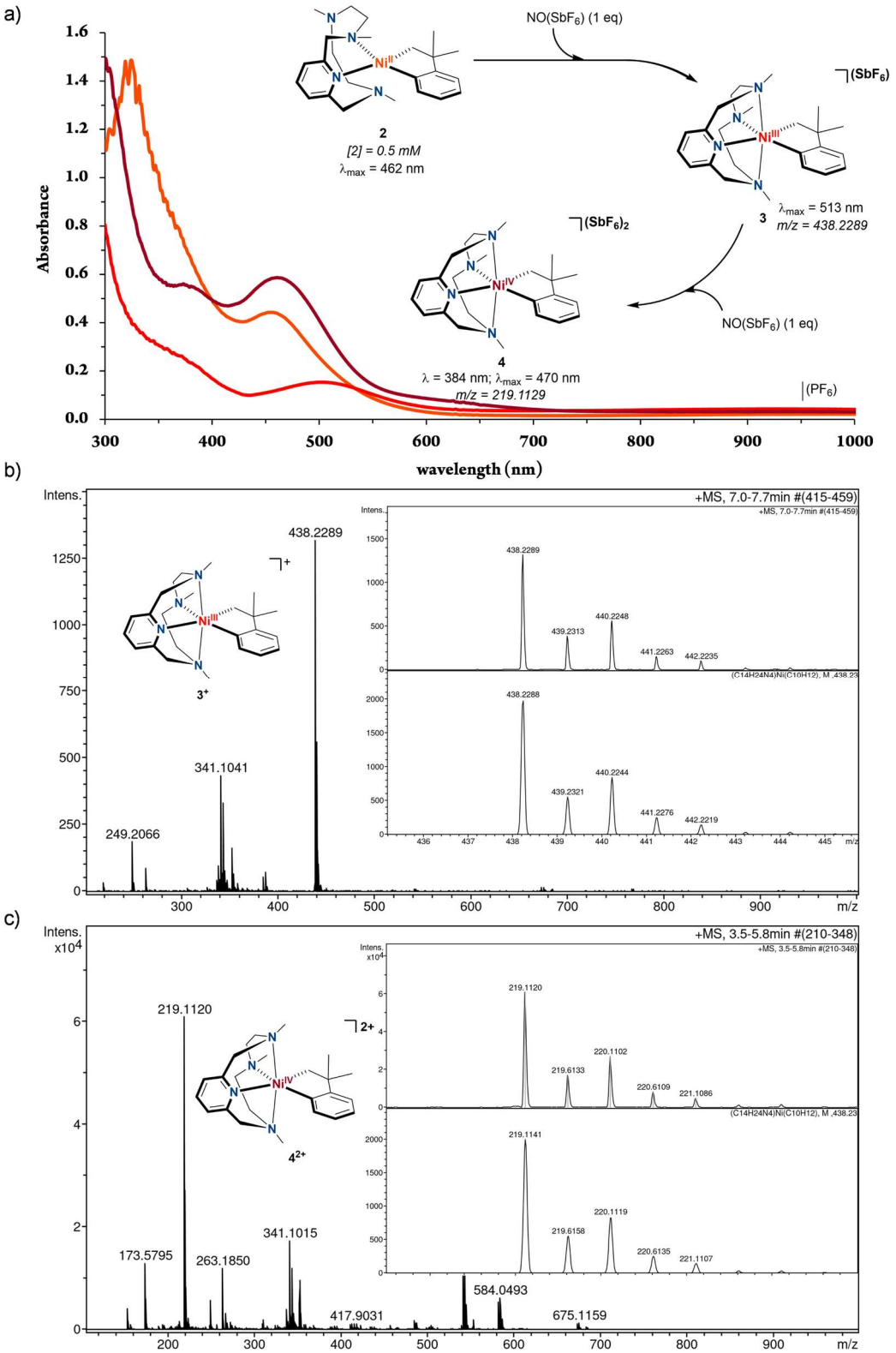

Figure VII.27 a) UV-vis spectra and reaction scheme for the synthesis and characterization of complexes **2** (orange), **3** (red) and **4** (burgundy) in MeCN at -40 °C; b) cryo-MS spectrum of the reaction crude after the addition of 1 equivalent of NO^+ to a solution of **1** containing a main monocationic peak at a m/z = 438.2289 with a mass value and an isotopic pattern fully consistent with complex $\mathbf{3}^+$ (Inset: expanded view of this peak (top) and the calculated one for this formula (bottom)), and c) cryo-MS spectrum of the reaction crude after the addition of 2 equivalents of NO^+ to a solution of **1** containing a main dicationic peak at a m/z = 219.1120 with a mass value and an isotopic pattern fully consistent with complex $\mathbf{4}^{2+}$ (Inset: expanded view of this peak (top) and the calculated one for this formula (bottom)).

Species **4** was further characterized by ^{1}H-NMR spectroscopy in a similar manner as previously done by UV-vis monitoring. Thus, 2 equivalents of NO^{+} were added in a stepwise manner at -35 °C into a solution of **2** in deuterated acetonitrile. Prior to oxidant addition, the initial ^{1}H-NMR spectrum corresponding to **2** was diamagnetic. After that, the first equivalent of oxidant was added directly in the NMR tube which triggered a color change from orange to red and the formation of a paramagnetic species attributed to complex **3**. Finally, the second equivalent of oxidant was added to the NMR tube, causing a change to a diamagnetic spectrum different to the one observed for **2**. This diamagnetic species was assigned to the nickel(IV) complex **4** (Figure VII.28). It is noteworthy that the spectrum corresponding to **4** presents some broadness most likely due to residual amounts of the paramagnetic complex **3**.

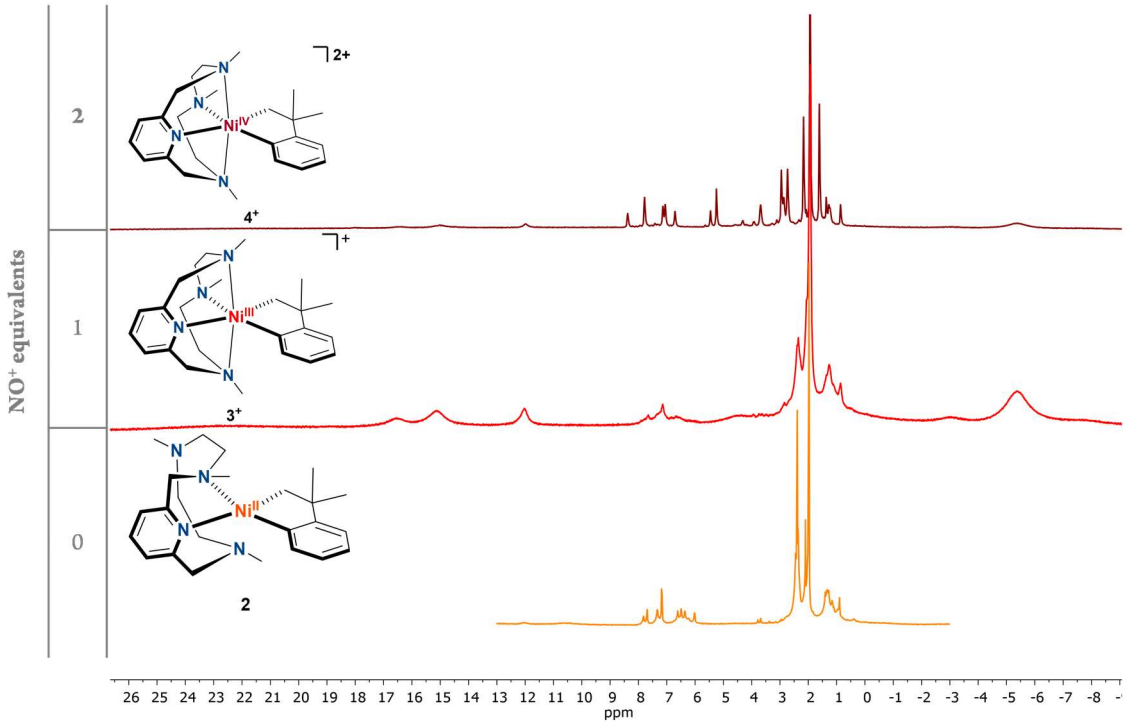

Figure VII.28 Stacked view of the ^{1}H-NMR spectra of complex **2** (orange), **3** (red) and **4** (burgundy) in CD_3CN.

Despite the slightly broadening of the ^{1}H-NMR spectrum, complex **4** could be fully assigned by comparison with nickel(IV)-cycloneophyl complexes bearing ^{R}N4 and ^{R}N3 type ligands previously reported by Mirica and co-workers (Figure VII.29).[59, 61] Remarkably, a huge downfield shift is observed for the Ni^{IV}-C**H**$_2$- protons to 5.29 ppm in contrast to their Ni^{II}-C**H**$_2$- counterparts found at ~2.10 ppm. This trend was also observed for the previously reported nickel(IV)-cycloneophyl complexes and it is presumably explained by the highly electrophilic

character of the nickel(IV) center which results in a weaker interaction of the metal center with the nearby protons.

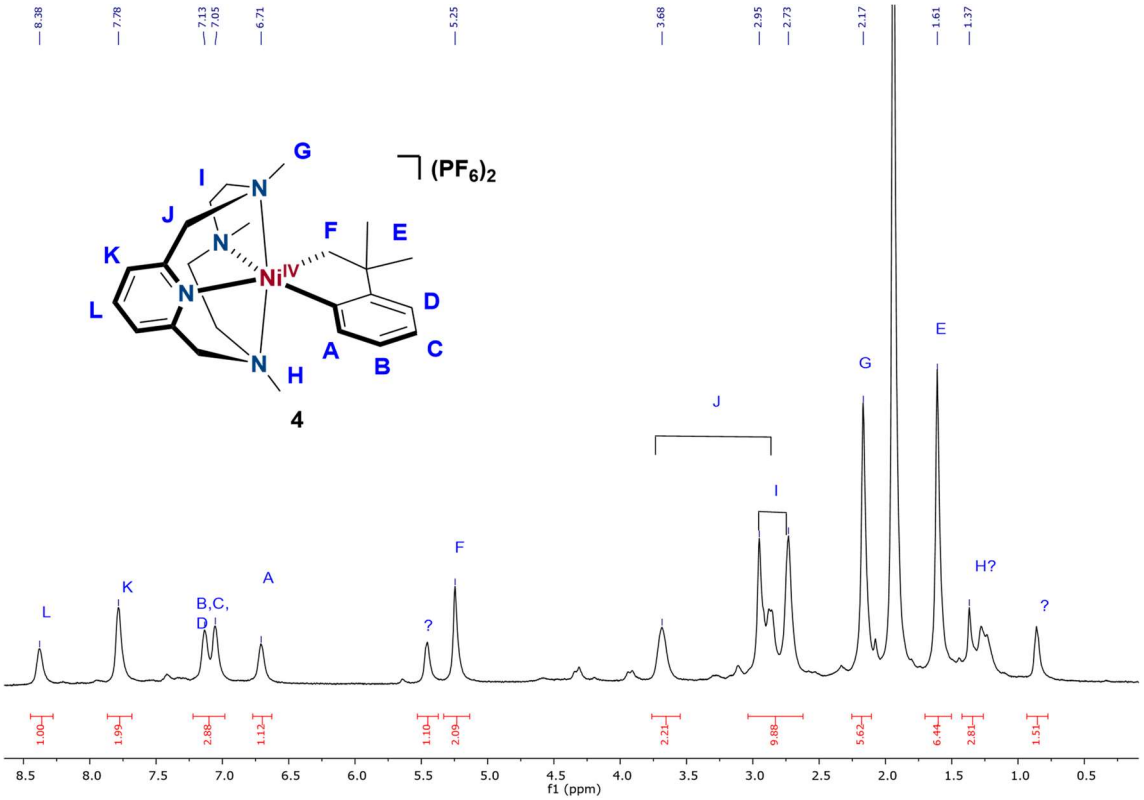

Figure VII.29 ^{1}H-NMR spectrum of complex **4** in CD_3CN at -35 °C. Inset: complex **4** ^{1}H-NMR assignment.

Next, we decided to study the reactivity of complexes **3** and **4** towards the formation of new C-C and C-O bonds. On a first experiment, complex **3** was exposed to high temperature (80 °C) for 24 hours in acetonitrile. After acidic treatment to ensure the protodemetallation and basic workup to remove the nickel center, the organic layer was analyzed by GC-MS. As a result, complex **3** decomposed in a troublesome mixture and only a 14.5% yield corresponding to the protodemetallation product (*tert*-butylbenzene, **B**) was detected (Scheme VII.17).

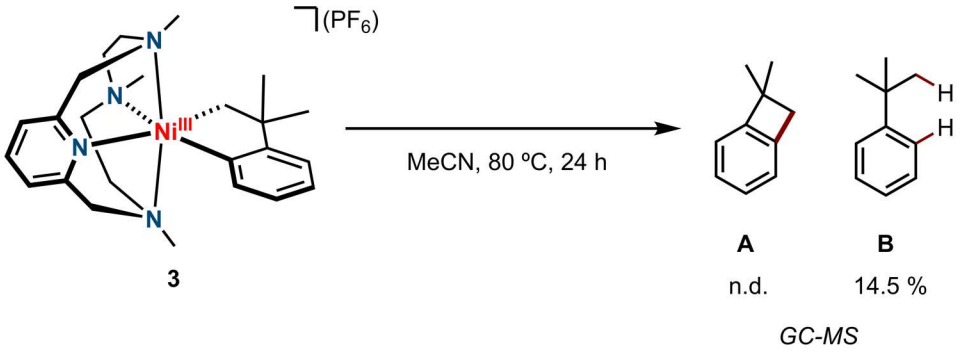

Scheme VII.17 Thermal treatment of complex **3** for the formation of C-C coupling products. The corresponding reductive elimination C-C product (**A**) was not detected by GC-MS, while the protodemetallation product (**B**) was detected in a 14.5% yield.

After that, and using a similar protocol, the reactivity of complex **2** was tested towards two-electron oxidants, such as XeF_2, NFTPT and $PhI(OAc)_2$, to form *in situ* complex **4**, but without any positive results. Then, we studied the reactivity of complex **4** formed *in situ* by the oxidation of **2**, but this time by using two-electron and oxygen transfer oxidants such as O_2, H_2O_2 and $^tBuO_2H$. In order to do so, complex **2** was dissolved in 2-MeTHF and cooled down to -78 °C. Then the oxidant is added, and the reaction crude is progressively heated to 82 °C for 48 hours. Finally, the crude is treated with acid to guarantee the protodemetallation of the organic fragments and subsequent basic work up is done to separate the metal from the organic layer, which is then injected into the GC-MS together with 1,3,5-trimethoxybenzene as internal standard (Scheme VII.18).

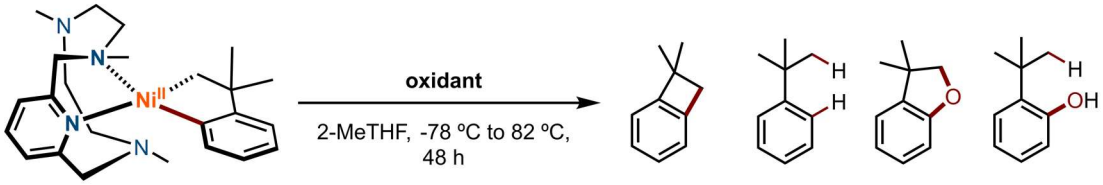

2

Entry	**Oxidant**	**A**	**B**	**C**	**D**
1	O_2	59 %	0 %	6 %	2 %
2	H_2O_2	9 %	1 %	11 %	2 %
3	$^tBuO_2H$	3 %	1 %	8 %	3 %

GC-MS

Scheme VII.18 Reactivity of **2** towards two-electron, oxygen-transfer oxidants for the formation of C-C and C-O coupling products. Table: results obtained for the different oxidants after GC-MS analysis using 1,3,5-trimethoxybenzene as internal standard.

Using this protocol, less than 1% of product **B** (protodemetallation product) was obtained in all cases, which is indicative of nearly quantitative oxidation of complex **2** to the corresponding nickel(III) or nickel(IV) reactive species. When bubbling dry dioxygen in the reaction mixture, the major product was the reductive elimination product **A** in a relevant 59% yield. Regarding C-O coupling products, only a 6% of product **C** and a 2% of product **D** were obtained. For this reaction the reactivity is clearly better towards the C-C than the C-O bond forming products. On the other hand, the reactivity with hydrogen peroxide results in a 9% yield of product **A** (C-C bond forming) and an 11% yield of product **C** (C-O bond forming). The reaction using *tert*-butyl hydroperoxide yields a 3% of C-C cross-coupling product **A**, and a total yield of 11% regarding the C-O bond forming products (8% of **C** and 3% of **D**). Overall, taking into account these results, and despite using oxygen-transfer oxidants, this system clearly favors the C-C bond

forming reactivity over the C-O bond forming transformations, presumably due to the flexibility of the **PyNMe$_3$** ligand which allows for the strong binding to the nickel(IV) center. Thus, this prevents the coordination of any O-donor ligand coming from the oxidant to the nickel(IV) core.

As a summary, we have been able to study the redox chemistry of well-defined organometallic nickel(II), nickel(III) and nickel(IV) complexes bearing the cycloneophyl moiety and, for the first time, the tetradentate nitrogen-based **PyNMe$_3$** ligand. Furthermore, upon exploring the reactivity of the *in situ* generated nickel(IV) species with oxygen-transfer oxidants, C-C bond forming product is promoted over the formation of C-O coupling products. This result given by this new system is in contrast with the outcome previously obtained by Mirica and co-workers for a system bearing ^{R}N4 type ligand.[58]

VII.5 REFERENCES

1. J. P. Klinman, *Chem. Rev.*, 1996, **96**, 2541-2562.
2. E. I. Solomon, U. M. Sundaram and T. E. Machonkin, *Chem. Rev.*, 1996, **96**, 2563-2606.
3. E. A. Lewis and W. B. Tolman, *Chem. Rev.*, 2004, **104**, 1047-1076.
4. L. M. Mirica, X. Ottenwaelder and T. D. P. Stack, *Chem. Rev.*, 2004, **104**, 1013-1046.
5. C. E. Elwell, N. L. Gagnon, B. D. Neisen, D. Dhar, A. D. Spaeth, G. M. Yee and W. B. Tolman, *Chem. Rev.*, 2017, **117**, 2059-2107.
6. V. Dantignana, J. Serrano-Plana, A. Draksharapu, C. Magallón, S. Banerjee, R. Fan, I. Gamba, Y. Guo, L. Que, M. Costas and A. Company, *J. Am. Chem. Soc.*, 2019, **141**, 15078-15091.
7. J. Serrano-Plana, A. Aguinaco, R. Belda, E. García-España, M. G. Basallote, A. Company and M. Costas, *Angew. Chem. Int. Ed.*, 2016, **55**, 6310-6314.
8. J. Serrano-Plana, W. N. Oloo, L. Acosta-Rueda, K. K. Meier, B. Verdejo, E. García-España, M. G. Basallote, E. Münck, L. Que, A. Company and M. Costas, *J. Am. Chem. Soc.*, 2015, **137**, 15833-15842.
9. B. Shin, K. D. Sutherlin, T. Ohta, T. Ogura, E. I. Solomon and J. Cho, *Inorg. Chem.*, 2016, **55**, 12391-12399.
10. H. Börzel, P. Comba, K. S. Hagen, M. Kerscher, H. Pritzkow, M. Schatz, S. Schindler and O. Walter, *Inorg. Chem.*, 2002, **41**, 5440-5452.
11. Z. Tyeklar, R. R. Jacobson, N. Wei, N. N. Murthy, J. Zubieta and K. D. Karlin, *J. Am. Chem. Soc.*, 1993, **115**, 2677-2689.
12. Y. Matoba, T. Kumagai, A. Yamamoto, H. Yoshitsu and M. Sugiyama, *J. Biol. Chem.*, 2006, **281**, 8981-8990.
13. G. J. Karahalis, A. Thangavel, B. Chica, J. Bacsa, R. B. Dyer and C. C. Scarborough, *Inorg. Chem.*, 2016, **55**, 1102-1107.
14. M. Rolff, J. Schottenheim, H. Decker and F. Tuczek, *Chem. Soc. Rev.*, 2011, **40**, 4077-4098.
15. K. Müller, C. Faeh and F. Diederich, *Science*, 2007, **317**, 1881-1886.
16. B. E. Smart, *J. Fluor. Chem.*, 2001, **109**, 3-11.
17. M. Houde, J. W. Martin, R. J. Letcher, K. R. Solomon and D. C. G. Muir, *Environ. Sci. Technol.*, 2006, **40**, 3463-3473.
18. B. D. Key, R. D. Howell and C. S. Criddle, *Environ. Sci. Technol.*, 1997, **31**, 2445-2454.
19. D. M. Lemal, *J. Org. Chem.*, 2004, **69**, 1-11.
20. G. Battaini, E. Monzani, L. Casella, E. Lonardi, A. W. J. W. Tepper, G. W. Canters and L. Bubacco, *J. Biol. Chem.*, 2002, **277**, 44606-44612.
21. A. Spada, S. Palavicini, E. Monzani, L. Bubacco and L. Casella, *Dalton Trans.*, 2009, DOI: 10.1039/B911946A, 6468-6471.
22. R. Natarajan, R. Azerad, B. Badet and E. Copin, *J. Fluor. Chem.*, 2005, **126**, 424-435.
23. C. D. Murphy, *Biotechnol. Lett*, 2010, **32**, 351-359.
24. V. S. Bondar, M. G. Boersma, E. L. Golovlev, J. Vervoort, W. J. H. Van Berkel, Z. I. Finkelstein, I. P. Solyanikova, L. A. Golovleva and I. M. C. M. Rietjens, *Biodegradation*, 1998, **9**, 475-486.
25. S. Peelen, I. M. C. M. Rietjens, M. G. Boersma and J. Vervoort, *Eur. J. Biochem.*, 1995, **227**, 284-291.

26. V. S. Bondar, M. G. Boersma, W. J. H. van Berkel, Z. I. Finkelstein, E. L. Golovlev, B. P. Baskunov, J. Vervoort, L. A. Golovleva and I. M. C. M. Rietjens, *FEMS Microbiol. Lett.*, 1999, **181**, 73-82.
27. W. B. Tolman, *Acc. Chem. Res.*, 1997, **30**, 227-237.
28. J. Serrano-Plana, I. Garcia-Bosch, R. Miyake, M. Costas and A. Company, *Angew. Chem. Int. Ed.*, 2014, **53**, 9608-9612.
29. L. M. Mirica, M. Vance, D. J. Rudd, B. Hedman, K. O. Hodgson, E. I. Solomon and T. D. P. Stack, *J. Am. Chem. Soc.*, 2002, **124**, 9332-9333.
30. L. M. Mirica, M. Vance, D. J. Rudd, B. Hedman, K. O. Hodgson, E. I. Solomon and T. D. P. Stack, *Science*, 2005, **308**, 1890.
31. B. D. Sherry and A. Fürstner, *Acc. Chem. Res.*, 2008, **41**, 1500-1511.
32. E. Nakamura, T. Hatakeyama, S. Ito, K. Ishizuka, L. Ilies and M. Nakamura, in *Organic Reactions*, 2014, 1-210.
33. A. Casitas, A. E. King, T. Parella, M. Costas, S. S. Stahl and X. Ribas, *Chem. Sci.*, 2010, **1**, 326-330.
34. M. Font, F. Acuña-Parés, T. Parella, J. Serra, J. M. Luis, J. Lloret-Fillol, M. Costas and X. Ribas, *Nat. Commun.*, 2014, **5**, 4373.
35. M. Rovira, S. Roldán-Gómez, V. Martin-Diaconescu, C. J. Whiteoak, A. Company, J. M. Luis and X. Ribas, *Chem. Eur. J.*, 2017, **23**, 11662-11668.
36. O. Planas, S. Roldán-Gómez, V. Martin-Diaconescu, T. Parella, J. M. Luis, A. Company and X. Ribas, *J. Am. Chem. Soc.*, 2017, **139**, 14649-14655.
37. O. Planas, C. J. Whiteoak, V. Martin-Diaconescu, I. Gamba, J. M. Luis, T. Parella, A. Company and X. Ribas, *J. Am. Chem. Soc.*, 2016, **138**, 14388-14397.
38. W. Zhou, J. W. Schultz, N. P. Rath and L. M. Mirica, *J. Am. Chem. Soc.*, 2015, **137**, 7604-7607.
39. W. Zhou, S. Zheng, J. W. Schultz, N. P. Rath and L. M. Mirica, *J. Am. Chem. Soc.*, 2016, **138**, 5777-5780.
40. N. P. Ruhs, J. R. Khusnutdinova, N. P. Rath and L. M. Mirica, *Organometallics*, 2019, **38**, 3834-3843.
41. A. W. Addison, T. N. Rao, J. Reedijk, J. van Rijn and G. C. Verschoor, *J. Chem. Soc., Dalton Trans.*, 1984, 1349-1356.
42. C. A. Tolman, S. D. Ittel, A. D. English and J. P. Jesson, *J. Am. Chem. Soc.*, 1978, **100**, 4080-4089.
43. C. A. Tolman, S. D. Ittel, A. D. English and J. P. Jesson, *J. Am. Chem. Soc.*, 1979, **101**, 1742-1751.
44. R. Shang, L. Ilies and E. Nakamura, *Chem. Rev.*, 2017, **117**, 9086-9139.
45. N. Yoshikai, A. Matsumoto, J. Norinder and E. Nakamura, *Synlett*, 2010, **2010**, 313-316.
46. A. C. Vetter, K. Nikitin and D. G. Gilheany, *Chem. Commun.*, 2018, **54**, 5843-5846.
47. A. K. Ghosh, A. Sarkar and M. Brindisi, *Org. Biomol. Chem.*, 2018, **16**, 2006-2027.
48. D. Li, T. Wu, K. Liang and C. Xia, *Org. Lett.*, 2016, **18**, 2228-2231.
49. T. Nasr Allah, S. Savourey, J.-C. Berthet, E. Nicolas and T. Cantat, *Angew. Chem. Int. Ed.*, 2019, **58**, 10884-10887.
50. S. M. Rummelt, P. O. Peterson, H. Zhong and P. J. Chirik, *J. Am. Chem. Soc.*, 2021, **143**, 5928-5936.
51. J. F. Hartwig, *Nature*, 2008, **455**, 314-322.
52. A. J. Hickman and M. S. Sanford, *Nature*, 2012, **484**, 177-185.

53. X. Hu, *Chem. Sci.*, 2011, **2**, 1867-1886.
54. V. B. Phapale and D. J. Cárdenas, *Chem. Soc. Rev.*, 2009, **38**, 1598-1607.
55. T. T. Tsou and J. K. Kochi, *J. Am. Chem. Soc.*, 1978, **100**, 1634-1635.
56. L. M. Mirica, S. M. Smith and L. Griego, in *Nickel Catalysis in Organic Synthesis*, 2020, 223-248.
57. C. Magallón, J. Serrano-Plana, S. Roldán-Gómez, X. Ribas, M. Costas and A. Company, *Inorg. Chim. Acta*, 2018, **481**, 166-170.
58. S. M. Smith, O. Planas, L. Gómez, N. P. Rath, X. Ribas and L. M. Mirica, *Chem. Sci.*, 2019, **10**, 10366-10372.
59. J. W. Schultz, K. Fuchigami, B. Zheng, N. P. Rath and L. M. Mirica, *J. Am. Chem. Soc.*, 2016, **138**, 12928-12934.
60. B. Zheng, F. Tang, J. Luo, J. W. Schultz, N. P. Rath and L. M. Mirica, *J. Am. Chem. Soc.*, 2014, **136**, 6499-6504.
61. M. B. Watson, N. P. Rath and L. M. Mirica, *J. Am. Chem. Soc.*, 2017, **139**, 35-38.
62. H. Na, M. B. Watson, F. Tang, N. P. Rath and L. M. Mirica, *Chem. Commun.*, 2021, **57**, 7264-7267.
63. F. Tang, N. P. Rath and L. M. Mirica, *Chem. Commun.*, 2015, **51**, 3113-3116.
64. E. Carmona, F. González, M. L. Poveda, J. L. Atwood and R. D. Rogers, *J. Chem. Soc., Dalton Trans.*, 1981, 777-782.
65. E. Carmona, E. Gutierrez-Puebla, J. M. Marin, A. Monge, M. Paneque, M. L. Poveda and C. Ruiz, *J. Am. Chem. Soc.*, 1989, **111**, 2883-2891.
66. E. Carmona, P. Palma, M. Paneque, M. L. Poveda, E. Gutierrez-Puebla and A. Monge, *J. Am. Chem. Soc.*, 1986, **108**, 6424-6425.

Chapter VIII. General Conclusions

The organic synthetic and research community has devoted many efforts to the use of first-row transition metals towards the development of new synthetic tools to produce biologically relevant organic and natural products, such as pharmaceuticals, agrochemicals, polymers, etc., in a more sustainable and efficient manner. Two very powerful strategies to fulfill this objective are oxidation/oxygenation reactions via dioxygen activation (Chapter III and IV), and C-H activation and/or cross-coupling transformations (Chapter V and VI). However, despite all the improvements achieved over the past years in the field of organic chemistry, there are still issues to address such as gaining more insight into the fundamental mechanism of these transformations mediated by first-row transition-metals. These metals, such as copper, iron and nickel can undergo both one- and two-electron processes, resulting in the formation of transient paramagnetic species which are difficult to trap and characterize. In order to gain more insight into the reactive intermediate species involved in such transformations, our group takes advantage of the *macrocyclic approach* to enhance the stability of these otherwise elusive species.

In Chapters III and IV, the focus is directed towards gaining mechanistic insights in the oxidation of phenolic derivatives by means of bioinspired copper model systems. In Chapter III, we tried to synthesize a tyrosinase bioinspired model system using the **PyNMe$_3$** platform which was previously successfully used in our group to stabilize high-valent iron-oxo species. To do so, the corresponding copper(I) complex, [(PyNMe$_3$)Cu^{I}(CH$_3$CN)](OTf) (**1OTf**), was prepared and characterized which rapidly reacts upon dioxygen exposure at low temperature (-100 °C) to generate the corresponding μ-η^2:η^2-peroxodicopper(II) (**2**) as detected by UV-vis monitoring. Even though side-on peroxodicopper(II) species (^{S}**P**) are believed to be key species in the *ortho*-hydroxylation of phenols to catechols performed by the enzyme tyrosinase, no reactivity was observed upon reaction of compound **2** towards *ortho*-phenolates. Our hypothesis is that the rigidity and robustness of the **PyNMe$_3$** ligand provide a coordinatively saturated ^{S}**P** species precluding any interaction with exogenous substrates. This fact together with previously coordinatively saturated reported examples, confirms that to develop a functional model of tyrosinase the nitrogenated ligand must provide a low coordination environment to the copper center in order to leave available positions for the exogenous substrates to interact with the ^{S}**P** species formed.

In Chapter IV, we focused our attention into the copper(I) system $[Cu^{I}(DBED)(MeCN)]^{+}$ reported by Stack and co-workers in 2005 which exhibited a tyrosinase-like reactivity by performing the *ortho*-hydroxylation of phenolates using molecular oxygen as oxidant through a ^{S}**P** speciesthat converts into a **O** species upon coordination to a phenolic substrate, which is eventually *ortho*-hydroxylated. Interestingly, a previous work in our group indicates that **O** species are competent to perform the *ortho*-defluorination-hydroxylation of 2-fluorophenolates. Thus, Stack's system is a good candidate to study whether the *ortho*-defluorination-hydroxylation of 2-fluorophenolates occurs via a ^{S}**P** or a **O** species as both isomers are detected. Based in our experimental and theoretical results, the existing equilibrium between the ^{S}**P** and **O** isomers is displaced towards the **O** species upon coordination of the phenolic substrate. Moreover, DFT calculations indicate that the **O** isomer is the responsible for the *ortho*-defluorination-hydroxylation reactivity. This is also a strong indication of why Cu_2O_2 adducts for which ^{S}**P** species are the only isomer observed are unreactive towards 2-fluorophenols. Remarkably, this system is selective towards *ortho*-C-F bonds over *ortho*-C-X (X = H and Cl) in phenolic substrates. Nevertheless, for all cases, the rate-determining step was the electrophilic attack of one of the oxygens from the Cu_2O_2 core to the aromatic ring of the phenolic substrate. Overall, this $[Cu^{I}(DBED)(MeCN)]^{+}$ complex is a potential candidate to cleave C-F bonds over weaker bonds (C-H/Cl) and find future application in the degradation of fluorinated compounds coming from the bioaccumulation of pharmaceuticals and agrochemicals. This work validates that only the **O** isomer is the responsible for the *ortho*-defluorination-hydroxylation of 2-fluorophenolates. Moreover, this would also explain why tyrosinase enzyme, for which only the ^{S}**P** has been detected so far, would not be able to perform such reaction in the presence of C-F bonds.

In Chapters V and VI, we shifted our attention to trap and characterize the reactive species involved in organometallic reactions (such as C-H activation and cross-coupling transformations) using iron and nickel bound to macrocyclic ligands. Studies conducted in these two chapters are both successful evidence of the use of specially designed macrocyclic model ligands to stabilize otherwise unstable and highly reactive intermediate key species.

In Chapter V, we envisioned the use of the $^{Me}L_H$ model substrate, effectively employed in our group for the isolation of aryl-cobalt(III) complexes via C-H activation and relevant to the

formation of new C-C bonds, to stabilize and isolate an aryl-iron complex and to further study its reactivity towards the formation of new coupling products. At first, the reaction of complex $[(^{Me}L_H)Fe^{II}(Cl)_2]$ (**1-Cl$_2$**) towards phenyl Grignard reagent afforded the desired bisaryl coupling product, $^{Me}L_{Ph}$, in a good yield via C-H activation (presumably through a σ-bond metathesis). However, all attempts to isolate the aryl-iron(II) complex involved after the C-H cleavage were unsuccessful. Nonetheless, we changed our approach by synthesizing a new family of model substrates bearing an *ortho*-directing C-Br bond, $^{R}L_{Br}$ (R = H, Me, ^{t}Bu) in combination with strong-field ligands (CO) with the aim of activating such bond via a formal two electron oxidative addition to an iron(0) source. The resulting well-defined aryl-iron(II) complexes were obtained after irradiation of 254 nm UV-light (for complexes **1^{Me}** and **1^{H}**) or heating (for **1^{tBu}**). All complexes were fully characterized as low-spin aryl-iron(II) complexes. The high stability of the aryl-iron(II) complexes is mainly attributed to the strong-field CO ligands that complete the coordination sphere of the metal center. The reactivity of complex **1^{Me}** was tested towards phenyl Grignard reagents obtaining the phenylcarbonylation product, $^{Me}L_{COPh}$, coming from the insertion of one CO ligand to the phenyl group prior to the reductive elimination step to release the final organic coupling product. Oxidant-free experiments suggest that an oxidant is required for the obtention of the new C-C cross-coupling product. Furthermore, when submitting the $^{Me}L_{Br}$ model substrate with $Fe^0(CO)_5$ under thermal conditions, an unprecedented CO insertion into the ligand backbone occurs, providing a tertiary amine to amide conversion at the pyridine-benzylic position in a quantitative manner.

In Chapter VI, we used the **PyNMe$_3$** ligand for the first time in the field of organometallic chemistry, to isolate a series of organonickel complexes bearing an alkyl/aryl-donor cycloneophyl ligand (cycl). We were able to isolate the corresponding low-valent nickel(II) (**2**), the high-valent nickel(III) (**3**), and to detect the high-valent nickel(IV) (**4**) species with spectroscopic and spectrometric techniques, through step-wise one electron oxidation. Complex **2** was diamagnetic and presented a square planar geometry around the nickel(II) center, where the pyridine is located *trans* to the alkyl group and the amine adjacent to the pyridine coordinates trans to the phenyl moiety. In contrast, complex **3** is a paramagnetic compound and exhibits a distorted octahedral geometry around the nickel(III) center. The nature of complex **4** was elucidated by low-temperature UV-vis spectroscopy in tandem with Cryo-MS spectrometry and it was acknowledged as low-spin nickel(IV) by ^{1}H-NMR. The

reactivity of the metastable complex **4** was studied by its *in situ* formation through the two-electron oxidation of complex **2** by means of oxygen-transfer type oxidants (O_2, H_2O_2 and $^tBuO_2H$), yielding up to 59% of C-C reductive elimination product (**A**) versus an 11% C-O forming product (**C**). This result is clearly indication that this novel system favors the formation of new C-C bonds over C-O coupling regardless of the use of oxygen-transfer oxidants.

ANNEX. Supporting information

ANNEX 1. Supporting information Chapter IV

SUPPORTING INFORMATION

Mechanistic insights into the *ortho*-defluorination-hydroxylation of 2-halophenolates promoted by a bis(μ-oxo)dicopper(III) complex

Pau Besalú-Sala,[‡] Carla Magallón,[‡] Miquel Costas,* Anna Company,* Josep M. Luis*

Institut de Química Computacional i Catàlisi and Departament de Química, Universitat de Girona, C/Maria Aurèlia Capmany 69, 17003, Girona, Catalonia, Spain

Contents

I. Instrumentation

All the spectroscopic and chromatographic analyses were carried out in *Serveis Tècnics de Recerca UdG* (STR-UdG) or in the laboratories of *Grup de Química Bioinspirada Supramolecular i Catàlisi* (QBIS-Cat Group) at the University of Girona.

UV/Vis spectroscopy was performed with an Agilent 8453 UV/Vis spectrophotometer with 1 cm quartz cells. Low temperature control was achieved with a cryostat from Unisoku Scientific Instruments, Japan. HPLC analyses were performed on an Agilent Technologies LC 1200 series using an Eclipse XDB - C18 analytical column (4.6 x 150 mm, 5 µm Agilent Technologies). Spectrophotometric detection of the HPLC elution profile in the range 190-400 nm was performed with an Agilent 1200 Series G1315D diode array detector. Quantification of the catechol in the reaction mixtures was performed at 215 nm and using 1,3,5-trimethoxybenzene as internal standard. For HPLC-DAD analyses elution was carried out using 0.1% H_3PO_4 in milliQ water (solvent A) and methanol (solvent C), with a flow rate of 0.5 mL/min. Elution started with 40% solvent A for 2 minutes, the eluting solvent decreased to 30% A over 11 min, and to 0% A over 3 min and stayed at 0% A for 2 additional min. Finally returned to 40% A over 4 min and remained stable for 8 min.

II. Materials

Reagents and solvents used were of commercially available reagent quality unless otherwise stated. Solvents were purchased from Scharlab, Acros or Sigma-Aldrich and used without further purification unless noted otherwise. 2-methyl-THF (2-MeTHF) was distilled from sodium /benzophenone. All solvents were stored under inert atmosphere Preparation and handling of air-sensitive materials and Cu(I) complexes were carried out in a N_2 drybox (Jacomex) with O_2 and H_2O concentrations <1.0 ppm. N,N′-di-tert-Butyl-ethylenediamine (DBED) was purchased from TCI Chemicals and used without further purification. The synthesis of the complexes were performed by following a slightly modified procedure previously reported in the literature. [1,2] Dry sodium salts of 2-fluorophenols were prepared according to reported procedures. All phenols were synthesized following previously described procedures.[1]

III. Synthesis of $[Cu^I(DBED)](PF_6)$

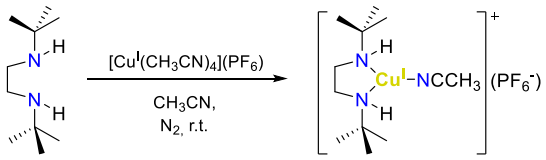

$[Cu^I(DBED)](PF_6)$

In the glovebox, **DBED** ligand (6.9 mg, 0.04 mmols) was dissolved in anhydrous CH_3CN (2 mL) leading to a 20 mM solution of the ligand. After that, $[Cu^I(CH_3CN)_4](PF_6)$ (15.0 mg, 0.04 mmols) was dissolved also in anhydrous CH_3CN (2 mL) leading to a 20 mM solution of the Cu(I) salt. Then, 0.5 mL of the 20 mM solution of the ligand and 0.5 mL of the 20 mM solution of de $[Cu^I(CH_3CN)_4]^+$ complex were mixed to give a 20 mM yellow solution of **$[Cu^I(DBED)](PF_6)$** after ca. 1 hour of stirring at room temperature.

IV. Preparation and reactivity of Cu_2O_2 species for UV/Vis experiments

Generation of $[Cu^{II}_2(\mu\text{-}\eta^2\text{:}\eta^2\text{-}O_2)(DBED)_2]^{2+}$ (1^P) monitored by UV/Vis spectroscopy

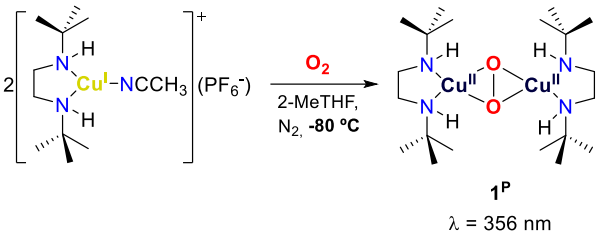

The preparation of the Cu(I) complex for the UV/Vis spectroscopy was performed under an inert atmosphere in the glovebox. All the UV/Vis experiments were performed in CH_3CN/2-MeTHF (1:19) as a solvent mixture. A freshly prepared 20 mM solution of $[Cu^I(DBED)](PF_6)$ in CH_3CN was diluted 10 times with CH_3CN to give a 2 mM stock solution. For the preparation of a 0.5 mM sample, a UV/Vis cell was charged with 125 µL of the 2 mM $[Cu^I(DBED)](PF_6)$ solution together with 2.2 mL of dry MeTHF (CH_3CN/2-MeTHF 1:19). The quartz cell was capped with a septum, taken out of the glovebox and placed in a Unisoku thermostated cell holder designed for low-temperature experiments at 193 K. Once the thermal equilibrium was reached, a UV/Vis spectrum of the starting complex was recorded. Dioxygen was injected into the cell with a balloon and a needle through the septum causing immediate formation of a band at λ_{max} = 356 nm corresponding to the generation of the side-on peroxo species (**1^P**). Full formation of **1^P** (ε = 28000 $M^{-1}cm^{-1}$) was reached after ca. 15 minutes (Figure 1).

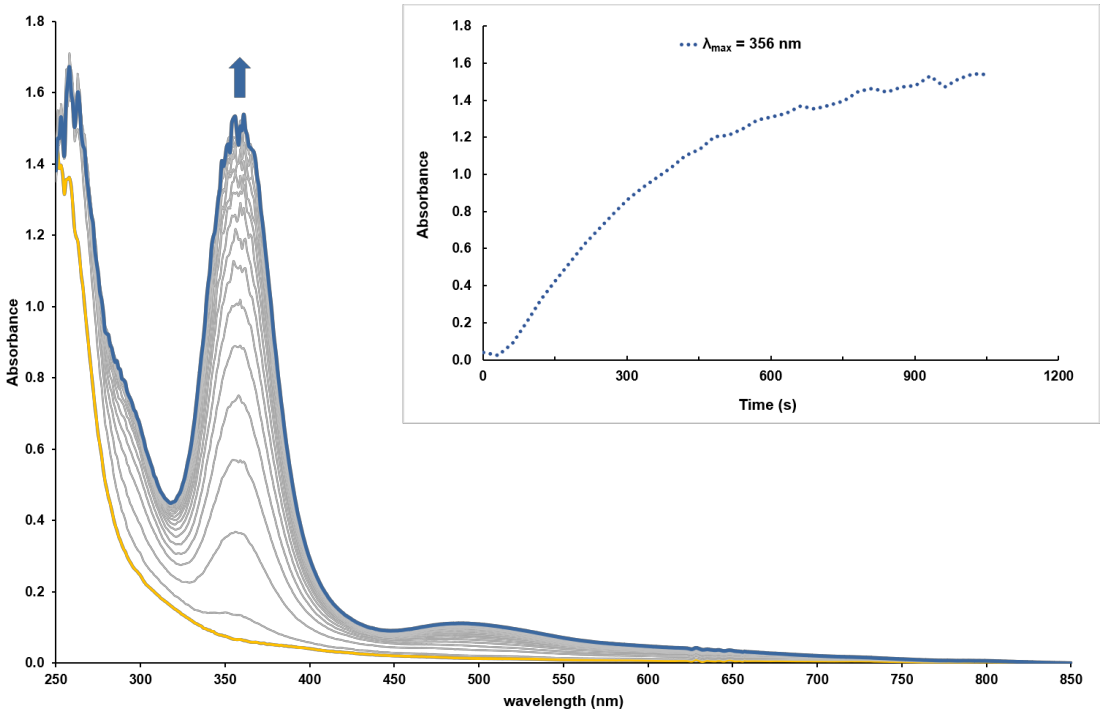

Figure 1. Formation of **1^P** (1 mM, MeCN/2MeTHF 1:19) monitored by UV/Vis spectroscopy at 193 K (yellow: **$[Cu^I(DBED)](PF_6)$**; blue: **1^P**). Inset: time trace of λ_{max} = 356 nm.

Generation of $[Cu^{III}_2(\mu\text{-}O)_2(DBED)_2]^{2+}$ (2^O) and reactivity with 2-fluorophenolates monitored by UV/Vis spectroscopy

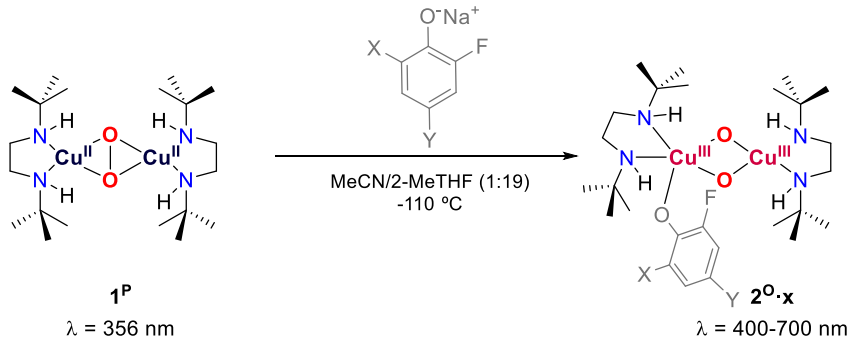

A solution of the pre-formed $\mathbf{1^P}$ species (see section above) was cooled down to 163 K. Again, when thermal equilibrium was reached, a UV/Vis spectrum of the $\mathbf{1^P}$ was recorded. Then, 1 equivalent of the desired sodium phenolate (0.02 mmol, 50 µL in acetone) was added via syringe causing immediate disappearance of the characteristic band of $\mathbf{1^P}$ at λ = 356 nm, and it was accompanied by the formation of the new bis-oxo species ($\mathbf{2^O \cdot x}$) with absorption bands between 400 and 600 nm depending on the added phenolate.

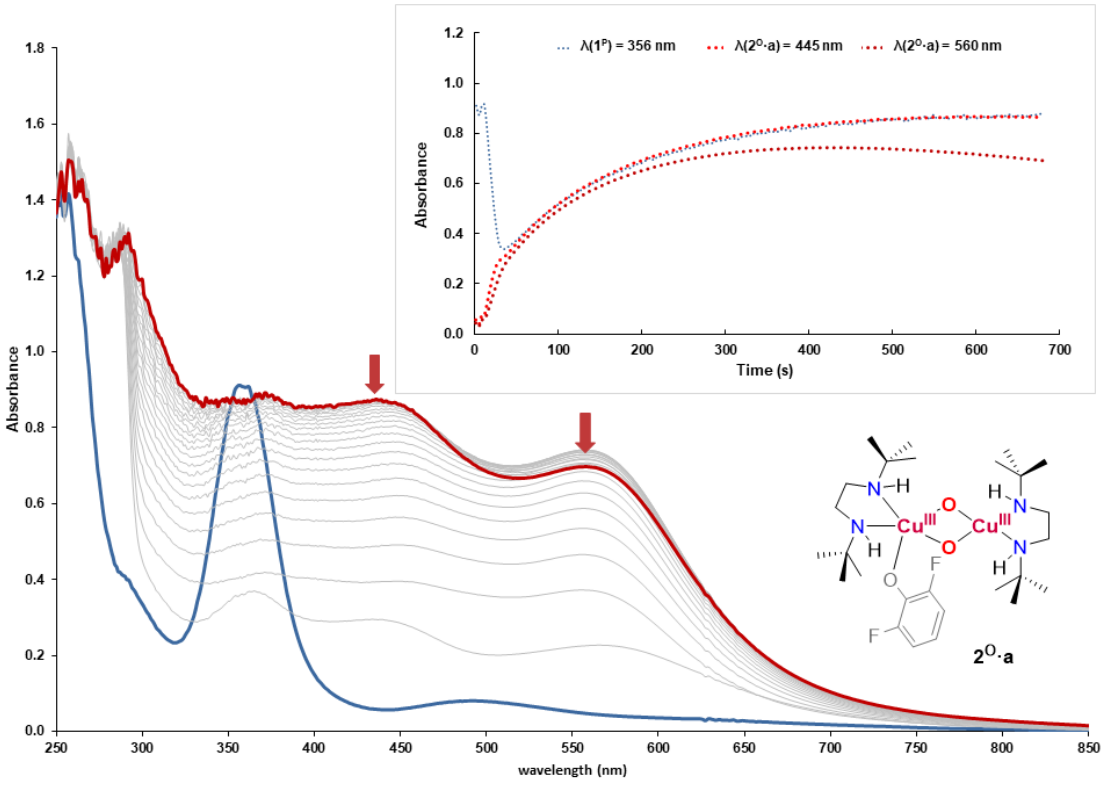

Figure 2. Generation of $\mathbf{2^O \cdot a}$ (0.5 mM, MeCN/2MeTHF 1:19) monitored by UV/Vis spectroscopy at 163 K (blue: $\mathbf{1^P}$; red: $\mathbf{2^O \cdot a}$) using *o*,*o*-difluorophenolate. Inset: time trace of λ($\mathbf{1^P}$) = 356 nm; λ($\mathbf{2^O \cdot a}$) = 445 nm; λ($\mathbf{2^O \cdot a}$) = 560 nm.

These new intermediate species were not stable even at low temperatures and decomposed as shown by the kinetic traces (Figure 3).

Hammett plot

In a typical experiment, 1 mL of a 10 mM solution of the starting Cu(I) complex **[Cu^{I}(DBED)](PF$_6$)** in MeCN was prepared in situ inside the glovebox and diluted in 2-MeTHF. From this 2.3 mL of a 0.5 mM solution of the starting **[Cu^{I}(DBED)](PF$_6$)** in MeCN/2-MeTHF (1:19) was placed in a UV/Vis cuvette which was sealed with a septum, taken out of the glovebox and cooled down to 193 K in a Unisoku thermostated cell holder designed for low-temperature experiments. Once the thermal equilibrium was reached, a UV/Vis spectrum of the starting complex was recorded. Dioxygen was injected into the cell with a balloon and a needle through the septum causing immediate formation of a band at λ_{max} = 356 nm corresponding to the generation of the side-on peroxo species (**1^{P}**). Upon maximum formation of the side-on peroxo species (after ca. 15 minutes, see section above), the temperature was lowered to 163 K. Again, when thermal equilibrium was reached, a UV/Vis spectrum of the **1^{P}** was recorded. Then, 1 equivalent (for Cu(I) complex) of the desired *para*-substituted sodium phenolate in 50 µL acetone was added via syringe causing immediate disappearance of the characteristic band of **1^{P}** at λ = 356 nm, and it was accompanied by the formation of the new bis-oxo species (**2^{O}·x**) with absorption bands between λ = 450 – 600 nm (Figure 3).

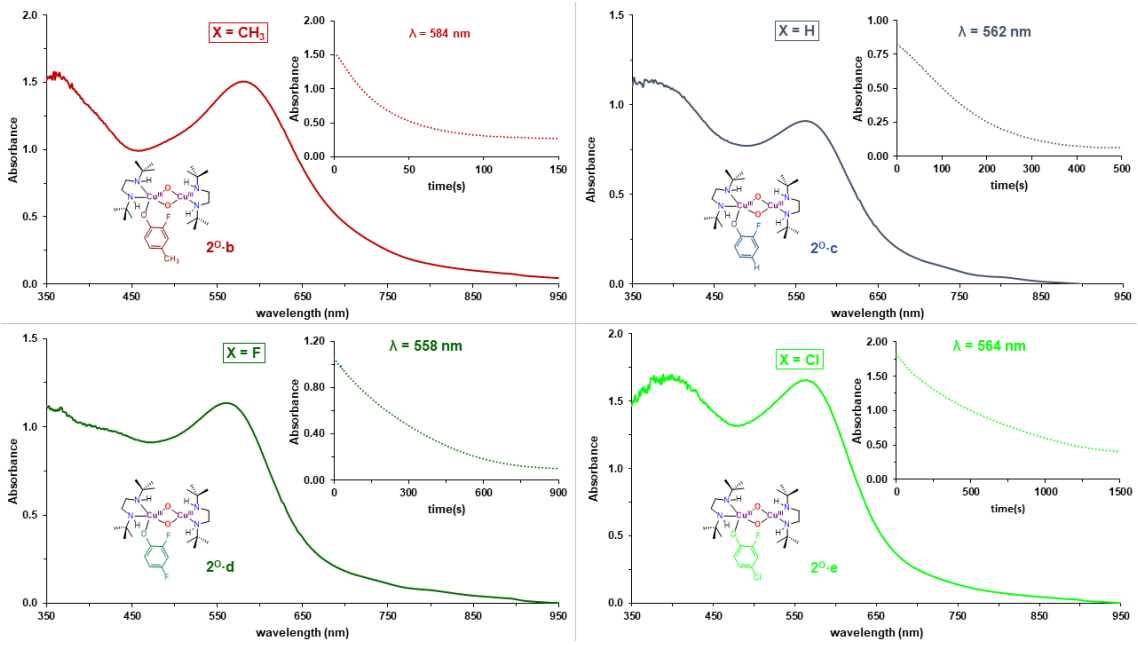

Figure 3. Generation of **2^{O}·b-e** (0.5 mM, MeCN/2MeTHF 1:19) monitored by UV/Vis spectroscopy at 163 K using *para*-substituted *o*-difluorophenolates. Inset: time traces of **2^{O}·b-e**.

Eyring plot

In a typical experiment, 1 mL of a 10 mM solution of the starting Cu(I) complex **[Cu^{I}(DBED)](PF$_6$)** in MeCN was prepared in situ inside the glovebox by mixing equimolar amounts of ligand (DBED) and copper(I) salt solutions From this 2.3 mL of a 0.5 mM solution of the starting Cu(I) in MeCN/2-MeTHF (1:19) was placed in a UV/Vis cuvette which was sealed with a septum, taken out of the glovebox and cooled down to 193 K in a Unisoku thermostated cell holder designed for low-temperature experiments. Once the thermal equilibrium was reached, a UV/Vis spectrum of the starting complex was recorded. Dioxygen was injected into the cell with a balloon and a needle through the septum causing immediate formation of a band at λ_{max} = 356 nm corresponding to the generation of the side-on peroxo species (**1^{P}**). Upon maximum

formation of the side-on peroxo species (after ca. 15 minutes, see section above), the temperature was changed and set (163, 173, 178, 183, 188 and 193 K). Again, when thermal equilibrium was reached, a UV/Vis spectrum of the $\mathbf{1^P}$ was recorded. Then, 1 equivalent (for Cu(I) complex) of *o*,*o*-difluorophenolate in 50 µL acetone was added via syringe causing immediate disappearance of the characteristic band of $\mathbf{1^P}$ at λ = 356 nm, and it was accompanied by the formation of the new bis-oxo species ($\mathbf{2^O}$**·a**) with absorption bands at λ = 445 nm and λ = 558 nm.

Analysis of the reaction rates of $\mathbf{2^O}$**·a** as a function of the temperature via kinetic traces for the decay of λ = 558 nm, show a pseudo-first order behavior and can be fitted to single exponentials. The corresponding k_2 are dependent on the temperature (Figure 4) and an Eyring analysis reveals a relatively small activation enthalpy ($\Delta H^{\ddagger}$ = 9.58 ± 2.80×10^{-1} Kcal·mol^{-1}) and a negative activation entropy ($\Delta S^{\ddagger}$ = -12.17 ± 1.56 cal·mol^{-1}).

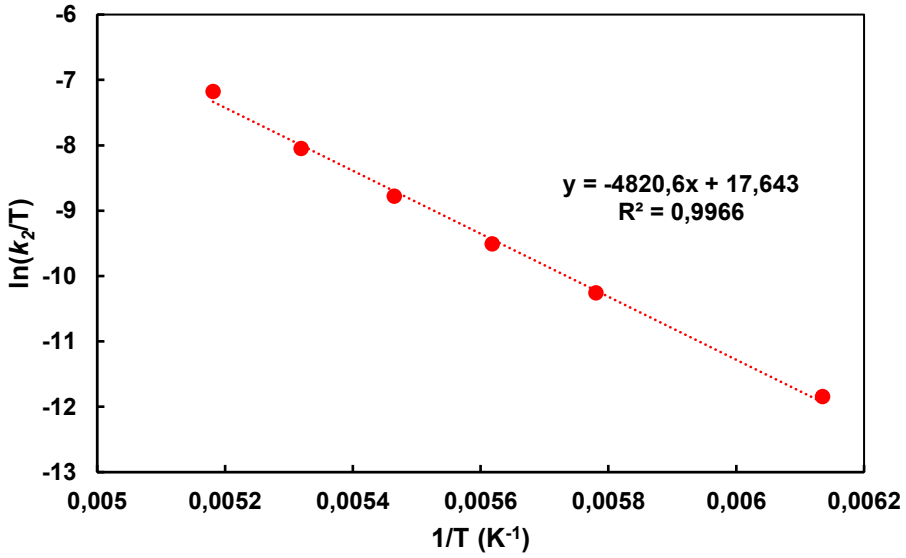

Figure 4. Eyring plot for the thermal decay of $\mathbf{1^P}$ with sodium *o*,*o*-difluorophenolate in MeCN/2-MeTHF (1:19).

Table 1. Second order rate constants (k_2) for the reaction of $\mathbf{1^P}$ with sodium *o*,*o*-difluorophenolate in MeCN/2-MeTHF (1:19) at different temperatures.

Entry	T (K)	k_2 ($M^{-1}\cdot s^{-1}$)
1	193	1.47×10^{-1}
2	188	6.00×10^{-2}
3	183	2.81×10^{-2}
4	178	1.32×10^{-2}
5	173	6.07×10^{-3}
6	163	1.17×10^{-3}

V. Analysis and quantification of the final oxidized products for C-H vs C-F activation

In the glovebox, a 50 mL schlenk flask was charged with 20 mL of an in-situ prepared 1 mM solution of the starting Cu(I) complex, **[Cu^{I}(DBED)](PF$_6$)** (20 µmols), in MeCN/acetone (1:19) by mixing equimolar amounts of DBED ligand and copper(I) salt solution. This solution was taken out of the glovebox and cooled down to 183 K in an acetone/N_2 bath. Then, an O_2

atmosphere was provided by using a balloon filled with dioxygen, which caused an immediate color change from colorless to dark, leading to the formation of $\mathbf{1^P}$. Upon maximum formation of the side-on peroxo species (after ca. 15 minutes, see section above), excess O_2 was removed by several vacuum/N_2 cycles and 1.5 equivalents (for Cu(I) complex) of 2-fluorophenolate (4.15 mg, 31 µmols) in 500 µL acetone were added which caused a substantial color change to even darker corresponding to the formation of $\mathbf{2^O{\cdot}c}$. The mixture was stirred for 30 minutes at 183 K, quenched with 10 mL of $HClO_4$ 0.5 M in water and it was let attain room temperature. Then, 1,3,5-trimethoxybenzene (1.94 mg, 12 µmols) was added as an internal standard. Acetone was removed under reduced pressure and the resulting aqueous mixture was extracted using dichloromethane (3x15 mL). The organic layers were combined and dried over anhydrous $MgSO_4$. The solvent was removed under reduced pressure to obtain the final sample which was analyzed by HPLC to quantify the amount and ratio (C-H vs C-F activation) of catechol formed.

Quantification analysis of the products formed by HPLC evidenced that the reaction of $\mathbf{1^P}$ in MeCN/Acetone (1:19) at 183 K with sodium 2-fluorophenolate afforded 36% of catechol (attack at the C-F bond) and a 2% of 3-fluorocatechol (attack at the C-H bond) with respect to Cu_2O_2 species. $\mathbf{1^P}$ proved to be highly selective in the defluorination of unsymmetric phenoates bearing a hydrogen in the *ortho* position. Thus, the *ortho*-C_{arene}-F bond is more reactive against $\mathbf{2^O{\cdot}c}$ even in the presence of presumably weaker bonds.

VI. Non-covalent interaction plots

The Cu-X interactions present in intermediates **3** had been characterized and visualized by means of non-covalent interactions (NCI) plots.[3] The output of this calculation, based on the electron density and its derivatives, localizes the NCIs in the real space. Focusing on the Cu_2O_2 core of **3** species it is clear that on the basis of NCI analysis, noncovalent interaction exists between one of the coppers and the heteroatoms of 2-fluorophenolate, 2,6-fluorophenolate and 6-chloro-2-fluorophenolate. Two figures for each interaction are displayed herein.

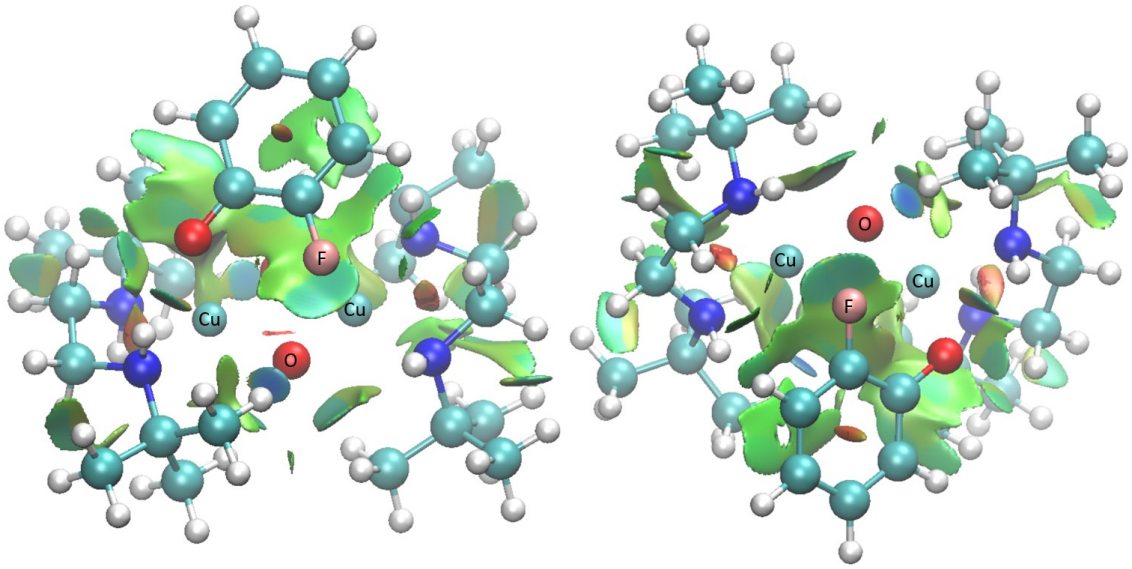

Figure 5. Two perspectives for the NCIs of the intermediate **3** with 2-fluorophenolate as substrate. Blue/Dark green surfaces indicates strong non-covalent attractive interactions; light green surfaces indicate weak non-covalent attractive interactions.

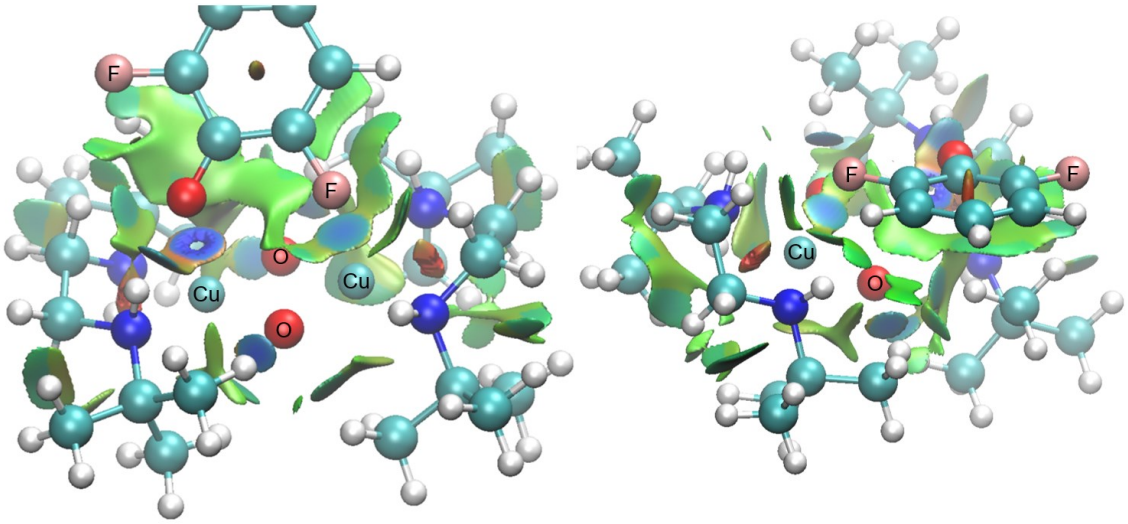

Figure 6. Two perspectives for the NCIs of the intermediate **3** with 2,6-difluorophenolate as substrate. Blue/Dark green surfaces indicates strong non-covalent attractive interactions; light green surfaces indicate weak non-covalent attractive interactions.

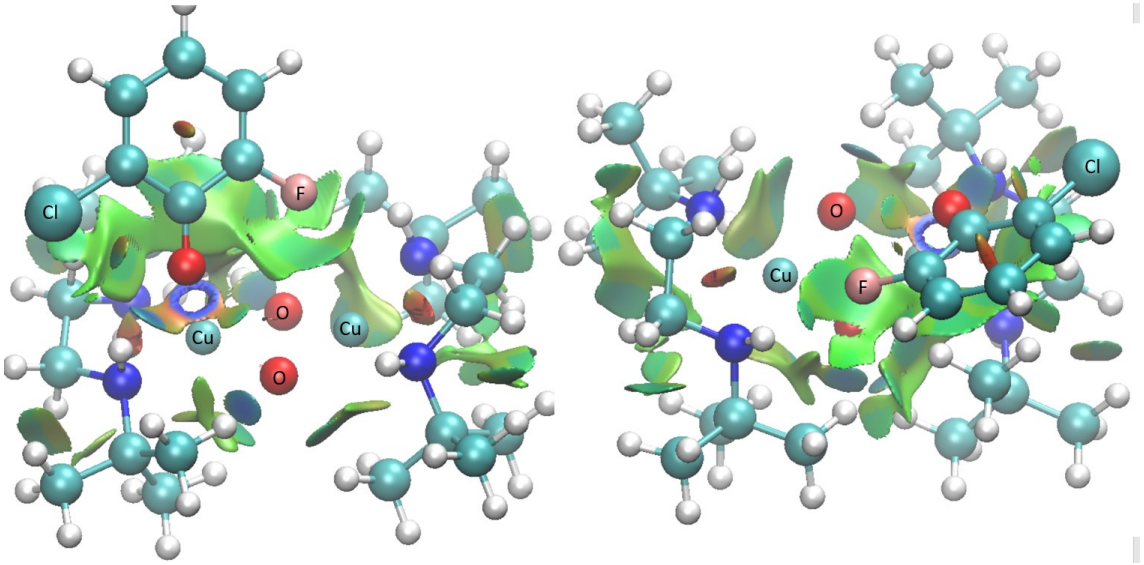

Figure 7. Two perspectives for the NCIs of the intermediate **3** with 6-chloro-2-fluorophenolate as substrate. Cu-F interaction. Blue/Dark green surfaces indicates strong non-covalent attractive interactions; light green surfaces indicate weak non-covalent attractive interactions.

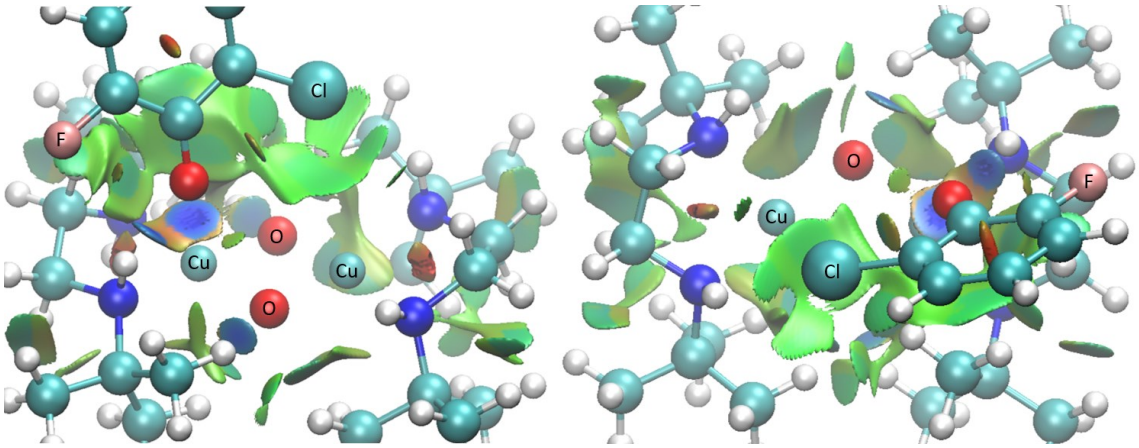

Figure 8. Two perspectives for the NCIs of the intermediate **3** with 6-chloro-2-fluorophenolate as substrate. Cu-Cl interaction. Blue/Dark green surfaces indicates strong non-covalent attractive interactions; light green surfaces indicate weak non-covalent attractive interactions.

VII. Cartesian coordinates of the DFT-optimized structures.

Charge, multiplicity and cartesian coordinates for the most stable species necessary for the construction of the manuscript are the following:

1^{o} +2, singlet

29	1.414053000	0.082562000	-0.531733000
29	-1.414294000	-0.082921000	-0.532612000
8	0.067457000	-1.124987000	-0.598890000
8	-0.067653000	1.124675000	-0.597637000
7	2.692046000	1.579480000	-0.440984000
1	2.281005000	2.255742000	-1.084976000
6	3.932756000	1.058811000	-1.075896000
1	4.790049000	1.707500000	-0.868924000
1	3.765995000	1.074907000	-2.157382000
6	4.193155000	-0.354552000	-0.614182000
1	5.023666000	-0.789946000	-1.178341000
1	4.459316000	-0.388335000	0.441418000
6	2.862072000	2.344654000	0.866672000
6	3.471900000	3.701710000	0.531808000
1	2.838415000	4.265227000	-0.162154000
1	3.576659000	4.297957000	1.443102000
1	4.467579000	3.608720000	0.087656000
6	3.753883000	1.591967000	1.838055000
1	3.357654000	0.600008000	2.073093000
1	3.799751000	2.152262000	2.776252000
1	4.781978000	1.487368000	1.479958000
6	1.481640000	2.523060000	1.478038000
1	1.035758000	1.555973000	1.732380000
1	1.559649000	3.116071000	2.394309000
1	0.792424000	3.029976000	0.797652000
7	2.957929000	-1.159303000	-0.800057000
1	2.896170000	-1.381501000	-1.796192000
6	2.935373000	-2.484930000	-0.057085000
6	4.315816000	-3.133495000	-0.073607000
1	5.058443000	-2.576911000	0.504629000
1	4.244922000	-4.132297000	0.367701000
1	4.693629000	-3.253243000	-1.094598000
6	1.950765000	-3.386419000	-0.788080000
1	0.966156000	-2.916966000	-0.863854000
1	1.842894000	-4.335328000	-0.254072000
1	2.303875000	-3.614646000	-1.800510000
6	2.481376000	-2.215826000	1.369287000
1	1.492717000	-1.745492000	1.377332000
1	2.412196000	-3.152396000	1.930882000
1	3.184001000	-1.569002000	1.904595000
7	-2.957973000	1.159338000	-0.800074000
6	-2.934981000	2.484984000	-0.057151000
6	-2.481252000	2.215790000	1.369282000
1	-1.492961000	1.744704000	1.377518000
1	-2.411407000	3.152427000	1.930687000
1	-3.184408000	1.569621000	1.904680000
6	-4.315216000	3.134024000	-0.073776000
1	-4.692929000	3.253912000	-1.094788000
1	-4.244003000	4.132796000	0.367550000
1	-5.058059000	2.577689000	0.504419000
6	-1.950047000	3.386127000	-0.788140000
1	-2.302992000	3.614309000	-1.800638000
1	-1.842013000	4.335079000	-0.254242000
1	-0.965550000	2.916423000	-0.863749000
6	-4.193322000	0.354883000	-0.613579000
1	-5.023969000	0.790428000	-1.177419000
1	-4.459029000	0.388860000	0.442135000
6	-3.933562000	-1.058584000	-1.075260000
1	-4.790919000	-1.706989000	-0.867658000
1	-3.767486000	-1.074880000	-2.156846000
1	-2.896675000	1.381548000	-1.796235000
7	-2.692589000	-1.579540000	-0.441092000
6	-2.862012000	-2.344526000	0.866761000
6	-3.472464000	-3.701435000	0.532459000
1	-2.839581000	-4.265304000	-0.161761000
1	-3.576905000	-4.297493000	1.443915000
1	-4.468371000	-3.608206000	0.088869000
6	-3.752980000	-1.591465000	1.838654000

1	-3.356426000	-0.599503000	2.073134000
1	-3.798204000	-2.151530000	2.777021000
1	-4.781339000	-1.486812000	1.481327000
6	-1.481270000	-2.523247000	1.477325000
1	-1.035066000	-1.556249000	1.731428000
1	-1.558886000	-3.116254000	2.393632000
1	-0.792538000	-3.030284000	0.796544000
1	-2.282281000	-2.256028000	-1.085315000

1^{P} +2, singlet

29	1.752780000	0.078134000	-0.591095000
29	-1.752785000	-0.078143000	-0.591102000
8	0.039225000	-0.740605000	-0.707567000
8	-0.039229000	0.740591000	-0.707563000
7	3.140069000	1.522781000	-0.511393000
1	2.978253000	2.146816000	-1.300676000
6	4.426217000	0.821141000	-0.767112000
1	5.278028000	1.378531000	-0.364741000
1	4.552746000	0.784864000	-1.853777000
6	4.421535000	-0.592113000	-0.216478000
1	5.331249000	-1.111053000	-0.538311000
1	4.416428000	-0.594283000	0.875027000
6	3.057371000	2.395585000	0.719545000
6	4.082459000	3.520737000	0.639529000
1	3.937271000	4.124851000	-0.262861000
1	3.977418000	4.185493000	1.502378000
1	5.112777000	3.154840000	0.641904000
6	3.273508000	1.540550000	1.957438000
1	2.635393000	0.648010000	1.932982000
1	3.018492000	2.109643000	2.856152000
1	4.313101000	1.215803000	2.064129000
6	1.653179000	2.985385000	0.729096000
1	0.892364000	2.218037000	0.889528000
1	1.556736000	3.726065000	1.528499000
1	1.427472000	3.488286000	-0.218459000
7	3.207595000	-1.301852000	-0.681490000
1	3.347096000	-1.518663000	-1.669987000
6	2.908176000	-2.607751000	0.014702000
6	4.173830000	-3.444912000	0.160634000
1	4.894867000	-2.996560000	0.850316000
1	3.920708000	-4.434272000	0.553876000
1	4.669553000	-3.591104000	-0.805296000
6	1.903997000	-3.345421000	-0.859524000
1	1.017865000	-2.737430000	-1.060351000
1	1.574333000	-4.265163000	-0.367483000
1	2.346951000	-3.625147000	-1.822146000
6	2.303341000	-2.301847000	1.377154000
1	1.380697000	-1.720363000	1.272134000
1	2.050690000	-3.230439000	1.898179000
7	-3.207588000	1.301860000	-0.681486000
6	-2.908147000	2.607760000	0.014694000
6	-2.303362000	2.301859000	1.377169000
1	-1.380746000	1.720325000	1.272188000
1	-2.050678000	3.230451000	1.898177000
1	-2.989175000	1.743215000	2.021791000
6	-4.173778000	3.444965000	0.160577000
1	-4.669467000	3.591161000	-0.805369000
1	-3.920635000	4.434321000	0.553815000
1	-4.894851000	2.996645000	0.850243000
6	-1.903919000	3.345384000	-0.859515000
1	-2.346836000	3.625103000	-1.822156000
1	-1.574245000	4.265126000	-0.367482000
1	-1.017798000	2.737364000	-1.060303000
6	-4.421527000	0.592136000	-0.216451000
1	-5.331242000	1.111086000	-0.538266000
1	-4.416400000	0.594307000	0.875055000
6	-4.426237000	-0.821118000	-0.767083000
1	-5.278044000	-1.378498000	-0.364692000
1	-4.552792000	-0.784842000	-1.853745000
1	-3.347101000	1.518666000	-1.669983000
7	-3.140091000	-1.522772000	-0.511390000
6	-3.057391000	-2.395593000	0.719535000
6	-4.082491000	-3.520733000	0.639509000
1	-3.937311000	-4.124839000	-0.262887000
1	-3.977457000	-4.185500000	1.502351000
1	-5.112804000	-3.154823000	0.641889000
6	-3.273515000	-1.540574000	1.957443000
1	-2.635384000	-0.648046000	1.933006000
1	-3.018512000	-2.109688000	2.856147000
1	-4.313102000	-1.215810000	2.064136000
6	-1.653205000	-2.985407000	0.729069000
1	-0.892380000	-2.218072000	0.889517000
1	-1.556768000	-3.726106000	1.528455000
1	-1.427505000	-3.488289000	-0.218497000
1	-2.978292000	-2.146799000	-1.300683000
1	2.989108000	-1.743151000	2.021780000

2$^{P}_{F}$ +1, singlet

29	1.647406000	0.158226000	-0.286742000
29	-1.831867000	-0.026392000	-0.070866000
8	-0.147529000	0.822582000	-0.339972000
8	-0.076484000	-0.633595000	-0.563354000
7	3.148411000	-1.174192000	-0.124836000
1	2.957721000	-1.618284000	0.775670000
6	4.384363000	-0.363820000	0.038986000
1	5.263928000	-0.887098000	-0.347219000
1	4.542449000	-0.224124000	1.114357000
6	4.247664000	0.986415000	-0.631071000
1	5.136974000	1.594599000	-0.428708000
1	4.162053000	0.874494000	-1.715433000
6	3.202987000	-2.286461000	-1.139106000
6	4.251668000	-3.314990000	-0.724804000
1	4.027013000	-3.726578000	0.266319000
1	4.266397000	-4.149129000	-1.433148000
1	5.263509000	-2.900134000	-0.696553000
6	3.512782000	-1.701297000	-2.507225000
1	2.796010000	-0.912188000	-2.766901000
1	3.443079000	-2.478737000	-3.273993000
1	4.522150000	-1.280759000	-2.563610000
6	1.829202000	-2.944093000	-1.144834000
1	1.068242000	-2.296306000	-1.586609000
1	1.853903000	-3.872477000	-1.723828000
1	1.505483000	-3.196108000	-0.128102000
7	3.017225000	1.634888000	-0.135190000
1	3.162663000	1.839728000	0.854549000
6	2.627149000	2.929109000	-0.798274000
6	3.828040000	3.861206000	-0.914246000
1	4.581292000	3.483402000	-1.612101000
1	3.507772000	4.841347000	-1.281129000
1	4.310404000	4.014368000	0.057684000
6	1.563661000	3.551511000	0.094880000
1	0.731971000	2.861756000	0.253080000
1	1.165583000	4.466037000	-0.355210000
1	1.972877000	3.814459000	1.077927000
6	2.049107000	2.622266000	-2.173283000
1	1.166422000	1.979096000	-2.093823000
1	1.741745000	3.547887000	-2.669535000
7	-3.178713000	-1.512540000	-0.007449000
6	-2.928829000	-2.687763000	-0.905736000
6	-2.597621000	-2.170122000	-2.299241000

1	-1.693763000	-1.551158000	-2.285009000
1	-2.418900000	-3.004207000	-2.984941000
1	-3.413247000	-1.573817000	-2.721855000
6	-4.139949000	-3.613585000	-0.952120000
1	-4.454316000	-3.911608000	0.054247000
1	-3.891847000	-4.526141000	-1.503445000
1	-4.996739000	-3.154523000	-1.454915000
6	-1.733427000	-3.420457000	-0.311595000
1	-1.988792000	-3.873743000	0.653251000
1	-1.393438000	-4.219892000	-0.977256000
1	-0.898258000	-2.734187000	-0.148085000
6	-4.482521000	-0.843020000	-0.136791000
1	-5.309339000	-1.499027000	0.162799000
1	-4.631188000	-0.588124000	-1.189567000
6	-4.478655000	0.396061000	0.735480000
1	-5.414306000	0.949012000	0.607666000
1	-4.422871000	0.096769000	1.786725000
1	-3.064180000	-1.815736000	0.962683000
7	-3.294125000	1.254397000	0.465916000
6	-3.505899000	2.448139000	-0.426109000
6	-4.531231000	3.397349000	0.186134000
1	-4.219918000	3.721955000	1.185425000
1	-4.633102000	4.292797000	-0.434783000
1	-5.526322000	2.951670000	0.269677000
6	-3.949203000	1.965390000	-1.797188000
1	-3.260546000	1.199597000	-2.176973000
1	-3.952264000	2.796255000	-2.509345000
1	-4.959859000	1.544829000	-1.785049000
6	-2.160938000	3.156485000	-0.526918000
1	-1.430181000	2.562911000	-1.081892000
1	-2.272701000	4.117260000	-1.038807000
1	-1.743697000	3.356705000	0.466912000
1	-2.967579000	1.613706000	1.362113000
1	2.774808000	2.130708000	-2.829467000
6	2.482106000	-0.864316000	3.113420000
6	1.708037000	-2.015687000	2.954839000
6	1.862034000	0.380573000	2.938827000
1	2.166805000	-2.996685000	3.084331000
1	2.414394000	1.311651000	3.067823000
6	0.356580000	-1.933288000	2.633940000
6	0.519267000	0.441885000	2.630560000
1	-0.232509000	-2.843110000	2.514585000
6	-0.328241000	-0.694672000	2.451008000
8	-1.569151000	-0.590894000	2.154709000
1	3.536392000	-0.921620000	3.373308000
9	-0.059543000	1.674422000	2.497715000

2$^{O}_{F}$ +1, singlet

29	-1.249334000	0.105818000	-0.341611000
29	1.518541000	-0.113169000	-0.083212000
8	0.073264000	-1.139312000	-0.450905000
8	0.226667000	1.139662000	-0.374665000
7	-2.502725000	1.661501000	-0.347644000
1	-2.141269000	2.296458000	0.363552000
6	-3.781355000	1.109098000	0.170027000
1	-4.625079000	1.774492000	-0.025046000
1	-3.669267000	1.042014000	1.255319000
6	-4.020936000	-0.264676000	-0.394030000
1	-4.908752000	-0.712277000	0.064499000
1	-4.190392000	-0.232460000	-1.473473000
6	-2.521561000	2.460389000	-1.654507000
6	-3.835453000	3.214619000	-1.811489000
1	-4.062248000	3.830943000	-0.935232000
1	-3.757530000	3.886013000	-2.671814000
1	-4.685810000	2.552054000	-1.998331000
6	-2.302884000	1.532522000	-2.843884000
1	-1.353295000	0.991711000	-2.752076000
1	-2.260190000	2.116421000	-3.768023000
1	-3.106761000	0.799986000	-2.958118000
6	-1.368561000	3.452248000	-1.559873000
1	-0.414285000	2.933102000	-1.444234000
1	-1.325684000	4.061532000	-2.467351000
1	-1.494213000	4.132908000	-0.709059000
7	-2.820323000	-1.101034000	-0.132403000
1	-2.810029000	-1.301816000	0.874624000
6	-2.818682000	-2.437579000	-0.855407000
6	-4.221190000	-3.038798000	-0.857889000
1	-4.925535000	-2.476968000	-1.477823000
1	-4.173284000	-4.054926000	-1.261274000
1	-4.632262000	-3.107462000	0.155375000
6	-1.879882000	-3.365450000	-0.097219000
1	-0.895382000	-2.909669000	0.030429000
1	-1.762626000	-4.305375000	-0.646171000
1	-2.281501000	-3.608915000	0.892951000
6	-2.331189000	-2.210132000	-2.278094000
1	-1.310994000	-1.815422000	-2.281326000
1	-2.330163000	-3.154882000	-2.830465000
1	-2.976837000	-1.516734000	-2.826912000
7	2.993242000	1.090132000	0.507156000
6	3.152608000	2.452191000	-0.126690000
6	2.996925000	2.294274000	-1.632655000
1	1.997850000	1.925486000	-1.885342000
1	3.138302000	3.257136000	-2.133827000
1	3.736076000	1.599661000	-2.046352000
6	4.516947000	3.051685000	0.205948000
1	4.693621000	3.081499000	1.286459000
1	4.552340000	4.082981000	-0.158836000
1	5.346215000	2.515078000	-0.263832000
6	2.060525000	3.344397000	0.447826000
1	2.213631000	3.509469000	1.521119000
1	2.072842000	4.322007000	-0.044725000
1	1.076072000	2.892345000	0.308860000
6	4.222704000	0.263371000	0.549614000
1	4.957725000	0.695488000	1.236756000
1	4.670694000	0.257198000	-0.447102000
6	3.839204000	-1.120852000	0.999432000
1	4.702990000	-1.789141000	1.029274000
1	3.415483000	-1.070974000	2.005247000
1	2.660966000	1.204900000	1.470982000
7	2.752049000	-1.653319000	0.138338000
6	3.116777000	-2.405386000	-1.135228000
6	4.385858000	-3.226141000	-0.940297000
1	4.322014000	-3.872858000	-0.058775000
1	4.531404000	-3.872409000	-1.811300000
1	5.281901000	-2.605390000	-0.848814000
6	3.294909000	-1.427271000	-2.288070000
1	2.392921000	-0.822853000	-2.444120000
1	3.484040000	-1.975871000	-3.215997000
1	4.137299000	-0.748150000	-2.136506000
6	1.945794000	-3.335649000	-1.429502000
1	1.018691000	-2.772767000	-1.565502000
1	2.142978000	-3.907471000	-2.341028000
1	1.791238000	-4.052647000	-0.614181000
1	2.213705000	-2.300726000	0.713010000
6	-2.722661000	-0.559665000	3.408120000
6	-1.927647000	-1.687278000	3.192851000
6	-2.143770000	0.702425000	3.229586000
1	-2.353305000	-2.681723000	3.326900000
1	-2.714707000	1.615882000	3.392338000
6	-0.596578000	-1.562284000	2.811382000

6	-0.822792000	0.806924000	2.849305000
1	0.009485000	-2.452160000	2.636933000
6	0.046599000	-0.302727000	2.623239000
1	-3.762807000	-0.648776000	3.712273000
8	1.273451000	-0.167629000	2.286006000
9	-0.298699000	2.058113000	2.694373000

2^{O}_{FF} +1, singlet

29	-1.523486000	0.257338000	-0.210280000
29	1.257070000	0.770162000	-0.473694000
8	-0.035552000	-0.389375000	-1.004665000
8	-0.292580000	1.534642000	0.129639000
7	-2.985428000	1.148985000	0.783565000
1	-2.482548000	1.526529000	1.587668000
6	-3.863013000	0.051977000	1.275256000
1	-4.842480000	0.429667000	1.586159000
1	-3.383333000	-0.369736000	2.162570000
6	-4.006692000	-1.011691000	0.213671000
1	-4.542762000	-1.878059000	0.615340000
1	-4.571471000	-0.647531000	-0.645095000
6	-3.687025000	2.343858000	0.155788000
6	-4.369982000	3.129376000	1.270337000
1	-3.643269000	3.480562000	2.010927000
1	-4.871546000	4.008879000	0.855377000
1	-5.129447000	2.538636000	1.791360000
6	-4.702599000	1.895704000	-0.880768000
1	-4.241851000	1.282634000	-1.662048000
1	-5.125596000	2.778954000	-1.368151000
1	-5.538880000	1.340958000	-0.445702000
6	-2.627073000	3.206241000	-0.510988000
1	-2.155633000	2.686929000	-1.351116000
1	-3.088492000	4.121927000	-0.893909000
1	-1.832192000	3.487657000	0.185107000
7	-2.659129000	-1.405421000	-0.265826000
1	-2.240106000	-1.989595000	0.461908000
6	-2.653918000	-2.230228000	-1.540487000
6	-3.839126000	-3.190490000	-1.569281000
1	-4.801422000	-2.678036000	-1.654050000
1	-3.745640000	-3.850271000	-2.437366000
1	-3.864431000	-3.826113000	-0.677597000
6	-1.359421000	-3.030994000	-1.544297000
1	-0.495054000	-2.377061000	-1.421823000
1	-1.252806000	-3.576544000	-2.487154000
1	-1.349706000	-3.766465000	-0.730580000
6	-2.714594000	-1.267608000	-2.716876000
1	-1.844452000	-0.602855000	-2.722530000
1	-2.724571000	-1.818274000	-3.662454000
1	-3.620583000	-0.652413000	-2.689652000
7	2.564553000	2.016759000	0.387091000
6	2.214552000	3.484371000	0.486587000
6	1.644859000	3.917813000	-0.856580000
1	0.713412000	3.385895000	-1.072602000
1	1.432033000	4.991349000	-0.857168000
1	2.349852000	3.725404000	-1.673734000
6	3.445277000	4.315109000	0.840387000
1	3.931117000	3.948236000	1.750675000
1	3.137374000	5.348526000	1.027897000
1	4.189431000	4.339993000	0.039344000
6	1.181377000	3.622424000	1.596454000
1	1.621412000	3.386914000	2.572768000
1	0.806024000	4.649759000	1.639777000
1	0.337869000	2.946899000	1.427957000
6	3.897891000	1.728225000	-0.185828000
1	4.690835000	1.986008000	0.523503000
1	4.031805000	2.354788000	-1.074215000
6	3.964188000	0.273262000	-0.564873000
1	4.925283000	0.050306000	-1.038512000
1	3.836838000	-0.366732000	0.312354000
1	2.534676000	1.600727000	1.321659000
7	2.832040000	0.016770000	-1.484063000
6	0.224491000	-3.982205000	2.735625000
6	1.601253000	-3.818828000	2.563734000
6	-0.607880000	-2.873636000	2.575888000
1	2.292905000	-4.648886000	2.692789000
1	-1.683930000	-2.942244000	2.730586000
6	2.102603000	-2.575848000	2.236821000
6	-0.053024000	-1.654425000	2.239785000
6	1.326488000	-1.404842000	1.998265000
1	-0.189397000	-4.951844000	2.996516000
8	1.813865000	-0.291544000	1.611516000
1	2.938999000	0.670271000	-2.264867000
6	2.785981000	-1.359266000	-2.111697000
6	2.383753000	-2.370282000	-1.052630000
1	1.441113000	-2.083867000	-0.583933000
1	2.259334000	-3.359512000	-1.505602000
1	3.141884000	-2.458336000	-0.271040000
6	1.765364000	-1.288460000	-3.240589000
1	2.086574000	-0.582941000	-4.016618000
1	1.657530000	-2.269710000	-3.712948000
1	0.786350000	-0.974599000	-2.871684000
6	4.151373000	-1.715152000	-2.696872000
1	4.058850000	-2.626460000	-3.295847000
1	4.529192000	-0.926268000	-3.357591000
1	4.904740000	-1.911317000	-1.929169000
9	-0.900035000	-0.575419000	2.123812000
9	3.452423000	-2.443039000	2.073910000

2^{O}_{FCl} +1, singlet

29	1.840777000	0.001257000	-0.047534000
29	-0.726223000	0.840289000	0.820522000
8	0.563287000	-0.390750000	1.170125000
8	0.674902000	1.369954000	-0.217520000
7	3.109042000	0.673152000	-1.413390000
1	2.478591000	1.010739000	-2.141202000
6	3.791922000	-0.538922000	-1.940711000
1	4.697607000	-0.279676000	-2.498981000
1	3.102591000	-1.013516000	-2.646505000
6	4.106859000	-1.485337000	-0.808571000
1	4.507878000	-2.426921000	-1.196872000
1	4.852107000	-1.065151000	-0.133780000
6	4.003771000	1.861493000	-1.088810000
6	4.474870000	2.464612000	-2.408081000
1	3.626835000	2.788411000	-3.021453000
1	5.098915000	3.342714000	-2.216455000
1	5.072868000	1.762761000	-2.997347000
6	5.191699000	1.439395000	-0.241287000
1	4.876511000	0.968470000	0.695628000
1	5.770797000	2.329109000	0.022086000
1	5.869893000	0.760633000	-0.766579000
6	3.170377000	2.874408000	-0.320979000
1	2.841919000	2.471577000	0.641790000
1	3.767604000	3.771786000	-0.131391000
1	2.273523000	3.169682000	-0.872118000
7	2.869959000	-1.725186000	-0.024855000
1	2.288855000	-2.356648000	-0.579561000
6	3.078169000	-2.397683000	1.320243000
6	4.212293000	-3.415717000	1.250294000
1	5.193614000	-2.955181000	1.106555000
1	4.251569000	-3.971133000	2.192613000
1	4.053119000	-4.145675000	0.449496000

6	1.777724000	-3.118596000	1.649498000
1	0.921969000	-2.448099000	1.553294000
1	1.804369000	-3.506610000	2.672230000
1	1.624627000	-3.969731000	0.974820000
6	3.397520000	-1.310539000	2.336205000
1	2.572412000	-0.595890000	2.416483000
1	3.566909000	-1.748008000	3.324754000
1	4.306432000	-0.761317000	2.064656000
7	-2.025047000	2.272145000	0.292092000
6	-1.508712000	3.668207000	0.039582000
6	-0.529245000	4.016952000	1.152366000
1	0.337803000	3.350857000	1.127675000
1	-0.171706000	5.045851000	1.043392000
1	-0.998574000	3.938511000	2.139910000
6	-2.657711000	4.672723000	0.007280000
1	-3.424309000	4.385686000	-0.720441000
1	-2.269621000	5.650689000	-0.294479000
1	-3.139227000	4.802419000	0.980687000
6	-0.821888000	3.650775000	-1.319595000
1	-1.547179000	3.470471000	-2.121875000
1	-0.342345000	4.615404000	-1.514403000
1	-0.061178000	2.865788000	-1.361275000
6	-3.166701000	2.181849000	1.224542000
1	-4.073605000	2.601807000	0.776088000
1	-2.933216000	2.770842000	2.118708000
6	-3.375969000	0.739678000	1.593321000
1	-4.190671000	0.649255000	2.318015000
1	-3.623796000	0.144572000	0.711330000
1	-2.312828000	1.838997000	-0.592658000
7	-2.101729000	0.231151000	2.148318000
6	-4.164919000	-2.953099000	-2.958724000
6	-4.730359000	-1.739652000	-2.552958000
6	-2.805489000	-3.168970000	-2.750597000
1	-5.787559000	-1.526808000	-2.699016000
1	-2.339618000	-4.102354000	-3.058320000
6	-3.930196000	-0.790376000	-1.959261000
6	-2.035666000	-2.184690000	-2.144583000
6	-2.532943000	-0.921878000	-1.701123000
1	-4.776577000	-3.715688000	-3.432290000
8	-1.845504000	-0.016388000	-1.134954000
1	-1.903673000	0.788905000	2.983400000
6	-2.125635000	-1.215982000	2.602753000
6	-2.050259000	-2.116560000	1.379383000
1	-1.199127000	-1.856542000	0.748107000
1	-1.951194000	-3.161799000	1.691561000
1	-2.957936000	-2.043311000	0.770641000
6	-0.929728000	-1.398249000	3.529357000
1	-1.050054000	-0.799290000	4.440255000
1	-0.843388000	-2.445760000	3.833547000
1	0.002747000	-1.103278000	3.043572000
6	-3.403081000	-1.502468000	3.389182000
1	-3.330582000	-2.499356000	3.835137000
1	-3.546715000	-0.787301000	4.207032000
1	-4.298705000	-1.494697000	2.762142000
9	-4.493501000	0.393387000	-1.564826000
17	-0.311559000	-2.481830000	-1.894738000

3$_F$ +1, triplet

29	-1.393697000	0.376918000	-0.206472000
29	1.517132000	0.238256000	-0.176410000
8	-0.074164000	-0.769023000	-0.634238000
8	0.067182000	1.405068000	0.083947000
7	-2.684661000	1.795103000	0.363317000
1	-2.205485000	2.211744000	1.161114000
6	-3.861318000	1.048423000	0.876890000
1	-4.746742000	1.686714000	0.960488000
1	-3.609079000	0.717525000	1.890577000
6	-4.151634000	-0.155581000	0.009572000
1	-4.947665000	-0.756113000	0.463076000
1	-4.490665000	0.137444000	-0.984793000
6	-2.972887000	2.949166000	-0.576344000
6	-3.731071000	4.034037000	0.182810000
1	-3.159937000	4.382552000	1.050315000
1	-3.901254000	4.896616000	-0.468671000
1	-4.711249000	3.698733000	0.533389000
6	-3.776651000	2.467580000	-1.773251000
1	-3.287715000	1.619480000	-2.266157000
1	-3.854882000	3.274941000	-2.507373000
1	-4.797147000	2.175900000	-1.508250000
6	-1.637028000	3.502437000	-1.050866000
1	-1.089430000	2.771363000	-1.651159000
1	-1.808879000	4.393461000	-1.663146000
1	-0.991404000	3.780022000	-0.212475000
7	-2.911646000	-0.949621000	-0.149289000
1	-2.746273000	-1.421310000	0.743070000
6	-2.976041000	-2.038765000	-1.203148000
6	-4.357396000	-2.686763000	-1.226990000
1	-5.142527000	-2.001997000	-1.561096000
1	-4.347332000	-3.533001000	-1.921133000
1	-4.638836000	-3.075896000	-0.242140000
6	-1.934119000	-3.086199000	-0.830059000
1	-0.951934000	-2.623638000	-0.700795000
1	-1.868395000	-3.847303000	-1.614565000
1	-2.208969000	-3.597793000	0.100625000
6	-2.659762000	-1.403681000	-2.547833000
1	-1.661118000	-0.956148000	-2.528973000
1	-2.684084000	-2.155654000	-3.342910000
1	-3.388755000	-0.629196000	-2.812100000
7	3.113116000	1.386468000	0.574671000
6	2.977312000	2.882238000	0.612804000
6	2.510574000	3.349282000	-0.759764000
1	1.548137000	2.889966000	-1.006428000
1	2.386688000	4.437093000	-0.777744000
1	3.229159000	3.093192000	-1.546730000
6	4.296191000	3.551175000	0.993453000
1	4.684833000	3.161254000	1.941124000
1	4.146297000	4.628358000	1.120045000
1	5.070550000	3.421364000	0.231053000
6	1.924057000	3.191652000	1.668723000
1	2.265751000	2.887260000	2.665920000
1	1.718015000	4.266439000	1.704276000
1	0.991291000	2.664138000	1.441806000
6	4.352093000	0.882059000	-0.050236000
1	5.217694000	1.001210000	0.612046000
1	4.552121000	1.477034000	-0.948495000
6	4.184019000	-0.569658000	-0.440133000
1	5.098183000	-0.922636000	-0.931524000
1	4.006104000	-1.191357000	0.442856000
1	3.104305000	1.053748000	1.538615000
7	3.001919000	-0.671829000	-1.316604000
6	-1.180971000	-3.272237000	3.147316000
6	0.030242000	-3.827390000	2.723021000
6	-1.370506000	-1.891708000	3.060596000
1	0.188595000	-4.901068000	2.804748000
1	-2.290291000	-1.422092000	3.404175000
6	1.030123000	-3.025370000	2.200795000
6	-0.358408000	-1.103994000	2.554954000
1	1.973367000	-3.457672000	1.875721000
6	0.889268000	-1.613101000	2.087865000
1	-1.967820000	-3.902116000	3.554624000
8	1.815040000	-0.845457000	1.631640000
1	3.156160000	-0.013920000	-2.084207000

6	2.756911000	-2.006324000	-1.966827000
6	2.258366000	-2.974961000	-0.909670000
1	1.374711000	-2.565470000	-0.413191000
1	1.988130000	-3.933815000	-1.365361000
1	3.020409000	-3.176600000	-0.150188000
6	1.679631000	-1.774358000	-3.018790000
1	2.024856000	-1.079960000	-3.795048000
1	1.418809000	-2.716200000	-3.512589000
1	0.778157000	-1.364767000	-2.552370000
6	4.023791000	-2.533774000	-2.635796000
1	3.788367000	-3.423030000	-3.229313000
1	4.459020000	-1.792272000	-3.316101000
1	4.793137000	-2.825202000	-1.914492000
9	-0.536542000	0.234221000	2.518160000

3$_{FF}$ +1, singlet

29	-1.523486000	0.257338000	-0.210280000
29	1.257070000	0.770162000	-0.473694000
8	-0.035552000	-0.389375000	-1.004665000
8	-0.292580000	1.534642000	0.129639000
7	-2.985428000	1.148985000	0.783565000
1	-2.482548000	1.526529000	1.587668000
6	-3.863013000	0.051977000	1.275256000
1	-4.842480000	0.429667000	1.586159000
1	-3.383333000	-0.369736000	2.162570000
6	-4.006692000	-1.011691000	0.213671000
1	-4.542762000	-1.878059000	0.615340000
1	-4.571471000	-0.647531000	-0.645095000
6	-3.687025000	2.343858000	0.155788000
6	-4.369982000	3.129376000	1.270337000
1	-3.643269000	3.480562000	2.010927000
1	-4.871546000	4.008879000	0.855377000
1	-5.129447000	2.538636000	1.791360000
6	-4.702599000	1.895704000	-0.880768000
1	-4.241851000	1.282634000	-1.662048000
1	-5.125596000	2.778954000	-1.368151000
1	-5.538880000	1.340958000	-0.445702000
6	-2.627073000	3.206241000	-0.510988000
1	-2.155633000	2.686929000	-1.351116000
1	-3.088492000	4.121927000	-0.893909000
1	-1.832192000	3.487657000	0.185107000
7	-2.659129000	-1.405421000	-0.265826000
1	-2.240106000	-1.989595000	0.461908000
6	-2.653918000	-2.230228000	-1.540487000
6	-3.839126000	-3.190490000	-1.569281000
1	-4.801422000	-2.678036000	-1.654050000
1	-3.745640000	-3.850271000	-2.437366000
1	-3.864431000	-3.826113000	-0.677597000
6	-1.359421000	-3.030994000	-1.544297000
1	-0.495054000	-2.377061000	-1.421823000
1	-1.252806000	-3.576544000	-2.487154000
1	-1.349706000	-3.766465000	-0.730580000
6	-2.714594000	-1.267608000	-2.716876000
1	-1.844452000	-0.602855000	-2.722530000
1	-2.724571000	-1.818274000	-3.662454000
1	-3.620583000	-0.652413000	-2.689652000
7	2.564553000	2.016759000	0.387091000
6	2.214552000	3.484371000	0.486587000
6	1.644859000	3.917813000	-0.856580000
1	0.713412000	3.385895000	-1.072602000
1	1.432033000	4.991349000	-0.857168000
1	2.349852000	3.725404000	-1.673734000
6	3.445277000	4.315109000	0.840387000
1	3.931117000	3.948236000	1.750675000
1	3.137374000	5.348526000	1.027897000
1	4.189431000	4.339993000	0.039344000
6	1.181377000	3.622424000	1.596454000
1	1.621412000	3.386914000	2.572768000
1	0.806024000	4.649759000	1.639777000
1	0.337869000	2.946899000	1.427957000
6	3.897891000	1.728225000	-0.185828000
1	4.690835000	1.986008000	0.523503000
1	4.031805000	2.354788000	-1.074215000
6	3.964188000	0.273262000	-0.564873000
1	4.925283000	0.050306000	-1.038512000
1	3.836838000	-0.366732000	0.312354000
1	2.534676000	1.600727000	1.321659000
7	2.832040000	0.016770000	-1.484063000
6	0.224491000	-3.982205000	2.735625000
6	1.601253000	-3.818828000	2.563734000
6	-0.607880000	-2.873636000	2.575888000
1	2.292905000	-4.648886000	2.692789000
1	-1.683930000	-2.942244000	2.730586000
6	2.102603000	-2.575848000	2.236821000
6	-0.053024000	-1.654425000	2.239785000
6	1.326488000	-1.404842000	1.998265000
1	-0.189397000	-4.951844000	2.996516000
8	1.813865000	-0.291544000	1.611516000
1	2.938999000	0.670271000	-2.264867000
6	2.785981000	-1.359266000	-2.111697000
6	2.383753000	-2.370282000	-1.052630000
1	1.441113000	-2.083867000	-0.583933000
1	2.259334000	-3.359512000	-1.505602000
1	3.141884000	-2.458336000	-0.271040000
6	1.765364000	-1.288460000	-3.240589000
1	2.086574000	-0.582941000	-4.016618000
1	1.657530000	-2.269710000	-3.712948000
1	0.786350000	-0.974599000	-2.871684000
6	4.151373000	-1.715152000	-2.696872000
1	4.058850000	-2.626460000	-3.295847000
1	4.529192000	-0.926268000	-3.357591000
1	4.904740000	-1.911317000	-1.929169000
9	-0.900035000	-0.575419000	2.123812000
9	3.452423000	-2.443039000	2.073910000

3$_{CIF}$ +1, singlet

29	-1.599996000	-0.054491000	0.253000000
29	1.120770000	-0.483224000	-0.315466000
8	-0.365404000	-1.383676000	0.325975000
8	-0.073567000	0.852994000	-0.047820000
7	-3.331270000	-1.036515000	0.477200000
7	-2.682132000	1.548912000	-0.050640000
7	1.904218000	-0.818108000	1.950927000
7	2.350895000	-2.018502000	-0.704854000
6	-4.393216000	-0.239302000	-0.223147000
6	-3.831988000	1.037017000	-0.829884000
6	-3.371490000	-2.526847000	0.183649000
6	-2.814820000	-2.744517000	-1.213981000
6	-2.515866000	-3.204975000	1.245290000
6	-4.800408000	-3.055296000	0.297226000
6	-2.948825000	2.474345000	1.118492000
6	-1.659200000	2.526298000	1.922910000
6	-4.091051000	1.958183000	1.976145000
6	-3.288997000	3.851819000	0.560433000
6	2.316988000	-2.212011000	1.790682000
6	3.114219000	-2.412246000	0.509830000
6	2.675920000	0.044263000	2.875162000
6	4.125709000	0.115997000	2.412869000
6	2.020734000	1.418966000	2.782865000
6	2.614620000	-0.453889000	4.320142000

6	1.779274000	-3.149587000	-1.531374000
6	0.950081000	-2.500769000	-2.631588000
6	0.907176000	-4.045408000	-0.666724000
6	2.923298000	-3.943038000	-2.156365000
1	-3.515094000	-0.953730000	1.477402000
1	-5.203870000	-0.044244000	0.481764000
1	-4.814671000	-0.838718000	-1.029718000
1	-4.613967000	1.796954000	-0.945555000
1	-3.440174000	0.822255000	-1.829198000
1	-2.078018000	2.072809000	-0.685578000
1	-3.421453000	-2.244256000	-1.977664000
1	-1.791392000	-2.365807000	-1.275095000
1	-2.800743000	-3.811239000	-1.458945000
1	-1.502511000	-2.795944000	1.259497000
1	-2.959284000	-3.080069000	2.240515000
1	-2.452565000	-4.279115000	1.046019000
1	-5.253349000	-2.786233000	1.257868000
1	-5.458500000	-2.704260000	-0.502173000
1	-4.783503000	-4.147874000	0.238514000
1	-1.418226000	1.541255000	2.337819000
1	-0.808758000	2.824267000	1.301408000
1	-1.754416000	3.235303000	2.750838000
1	-5.047665000	1.963805000	1.445741000
1	-3.906728000	0.949610000	2.361019000
1	-4.204108000	2.611868000	2.845584000
1	-2.460982000	4.255071000	-0.033532000
1	-4.182224000	3.828475000	-0.071860000
1	-3.483561000	4.553687000	1.376897000
1	0.932961000	-0.808507000	2.248992000
1	1.412287000	-2.827730000	1.751280000
1	2.915098000	-2.588869000	2.633238000
1	3.442434000	-3.454325000	0.429280000
1	4.017935000	-1.798761000	0.531825000
1	3.002425000	-1.536558000	-1.324341000
1	4.634409000	-0.849244000	2.516003000
1	4.193101000	0.426536000	1.365835000
1	4.685697000	0.838578000	3.016118000
1	1.933690000	1.728807000	1.738649000
1	1.007830000	1.398233000	3.202623000
1	2.591733000	2.175961000	3.331141000
1	1.576317000	-0.529002000	4.664769000
1	3.078152000	-1.439060000	4.440084000
1	3.137770000	0.230380000	4.998211000
1	0.112831000	-1.938934000	-2.206029000
1	1.551739000	-1.806359000	-3.229025000
1	0.540488000	-3.257486000	-3.307778000
1	1.484279000	-4.563398000	0.106587000
1	0.114988000	-3.464882000	-0.187850000
1	0.441506000	-4.814501000	-1.291802000
1	3.566452000	-3.300863000	-2.768677000
1	3.550743000	-4.435149000	-1.407098000
1	2.523955000	-4.726965000	-2.807571000
8	2.400920000	0.659787000	-1.145970000
6	2.006585000	1.891207000	-1.319129000
6	0.961481000	2.287509000	-2.196235000
6	0.554695000	3.605140000	-2.348886000
6	1.199728000	4.608185000	-1.631816000
6	2.254546000	4.286932000	-0.779284000
6	2.627915000	2.966449000	-0.644293000
1	2.790388000	5.049666000	-0.220401000
1	-0.256548000	3.843560000	-3.031448000
1	0.888069000	5.642849000	-1.745716000
9	3.659071000	2.665477000	0.174810000
17	0.185926000	1.043335000	-3.148478000

$TS1_F$ +1, singlet

29	-1.587192000	0.122910000	0.119463000
29	1.272928000	0.557007000	-0.051315000
8	-0.334706000	1.447942000	0.136378000
8	-0.009453000	-0.820932000	-0.248716000
7	-3.195572000	1.308921000	0.320419000
1	-2.893569000	2.021416000	0.983939000
6	-4.241683000	0.480379000	0.981099000
1	-5.244377000	0.870945000	0.780373000
1	-4.088599000	0.550482000	2.061227000
6	-4.144439000	-0.957369000	0.521617000
1	-4.858946000	-1.581143000	1.066686000
1	-4.402693000	-1.039730000	-0.535567000
6	-3.655982000	2.071706000	-0.910604000
6	-4.653806000	3.144636000	-0.482057000
1	-4.205191000	3.835756000	0.240154000
1	-4.966453000	3.733258000	-1.349989000
1	-5.560303000	2.727296000	-0.033707000
6	-4.287970000	1.122548000	-1.915444000
1	-3.608796000	0.306329000	-2.184015000
1	-4.516642000	1.671829000	-2.833641000
1	-5.228855000	0.691924000	-1.559729000
6	-2.439190000	2.735645000	-1.534213000
1	-1.718716000	1.999553000	-1.898004000
1	-2.755474000	3.360456000	-2.375593000
1	-1.914067000	3.370845000	-0.815288000
7	-2.755547000	-1.457034000	0.643648000
7	3.027802000	-0.502642000	0.191518000
6	3.085948000	-1.493845000	1.334784000
6	2.352944000	-0.898099000	2.526940000
1	1.308011000	-0.687278000	2.275128000
1	2.357515000	-1.598007000	3.368911000
1	2.814611000	0.032002000	2.872576000
6	4.527140000	-1.825513000	1.710506000
1	5.098611000	-2.176178000	0.844246000
1	4.532952000	-2.629996000	2.453001000
1	5.058252000	-0.976055000	2.149896000
6	2.385496000	-2.756657000	0.858025000
1	3.000976000	-3.299029000	0.133754000
1	2.190152000	-3.429312000	1.699329000
1	1.433461000	-2.510339000	0.380877000
6	4.089459000	0.531177000	0.208828000
1	5.066604000	0.102809000	-0.041557000
1	4.164175000	0.936062000	1.222236000
6	3.716466000	1.605216000	-0.778681000
1	4.492301000	2.372732000	-0.851254000
1	3.595694000	1.156252000	-1.769682000
1	3.155062000	-1.039183000	-0.668423000
7	2.392885000	2.177549000	-0.433539000
6	2.319235000	3.308002000	0.582581000
6	3.591399000	4.144095000	0.589110000
1	3.836513000	4.524451000	-0.408276000
1	3.446807000	5.009904000	1.242812000
1	4.458403000	3.595189000	0.970421000
6	2.058926000	2.724414000	1.964314000
1	1.138816000	2.130153000	1.958921000
1	1.938192000	3.526480000	2.699854000
1	2.881837000	2.092323000	2.306799000
6	1.131504000	4.163224000	0.159658000
1	0.233600000	3.540635000	0.093529000
1	0.956764000	4.961560000	0.887316000
1	1.306941000	4.633625000	-0.815377000
1	1.999717000	2.543105000	-1.298982000
6	0.561088000	-3.951274000	-2.054034000
6	1.872952000	-3.572469000	-2.407662000

6	-0.420254000	-2.988151000	-1.931607000
1	2.631115000	-4.343425000	-2.536372000
1	-1.459245000	-3.250049000	-1.741447000
6	2.213483000	-2.247444000	-2.582474000
6	-0.086728000	-1.630712000	-2.077412000
1	3.227157000	-1.964374000	-2.867118000
6	1.261542000	-1.187966000	-2.442662000
1	0.313874000	-5.001123000	-1.915524000
8	1.533514000	0.034578000	-2.570188000
9	-1.109149000	-0.800436000	-2.432745000
6	-2.303010000	-2.016925000	1.992084000
6	-3.464864000	-2.602461000	2.781731000
1	-3.074663000	-3.096956000	3.676710000
1	-4.176231000	-1.842262000	3.119535000
1	-4.014036000	-3.355201000	2.206198000
6	-1.618039000	-0.915765000	2.795791000
1	-2.289567000	-0.083566000	3.028318000
1	-1.243102000	-1.311259000	3.745042000
1	-0.761414000	-0.515367000	2.243897000
6	-1.288338000	-3.104635000	1.670467000
1	-1.755999000	-3.947321000	1.147242000
1	-0.494876000	-2.699590000	1.039114000
1	-0.837173000	-3.491090000	2.589916000
1	-2.654606000	-2.214016000	-0.028235000

TS1$_{H}$ +1, singlet

29	-1.615152000	-0.029383000	-0.179557000
29	1.217437000	0.635868000	-0.315236000
8	-0.485023000	1.382655000	-0.329163000
8	0.065506000	-0.846810000	-0.564593000
7	-3.403836000	0.941795000	0.112491000
1	-3.476916000	0.979150000	1.128210000
6	-4.478245000	0.018208000	-0.362702000
1	-5.039910000	0.495370000	-1.166221000
1	-5.189063000	-0.161262000	0.448802000
6	-3.897510000	-1.273097000	-0.904841000
1	-4.661270000	-2.057435000	-0.951403000
1	-3.546490000	-1.106259000	-1.929850000
6	-3.549238000	2.377870000	-0.349649000
6	-4.989981000	2.862373000	-0.184850000
1	-5.356781000	2.691568000	0.833618000
1	-5.030779000	3.940554000	-0.369088000
1	-5.690835000	2.395346000	-0.882080000
6	-3.110485000	2.445272000	-1.802676000
1	-2.067763000	2.126527000	-1.893839000
1	-3.196391000	3.467262000	-2.185599000
1	-3.730608000	1.806799000	-2.442854000
6	-2.648492000	3.215704000	0.547941000
1	-1.626604000	2.827699000	0.527392000
1	-2.638249000	4.257054000	0.210346000
1	-3.014185000	3.209265000	1.582369000
7	-2.700713000	-1.702742000	-0.153403000
7	2.776065000	-0.202960000	0.868190000
6	2.328992000	-0.927058000	2.112483000
6	1.092695000	-0.214026000	2.649996000
1	0.307956000	-0.180864000	1.884364000
1	0.691854000	-0.728568000	3.529995000
1	1.316390000	0.818251000	2.942753000
6	3.426076000	-0.968496000	3.173614000
1	4.346570000	-1.415480000	2.781690000
1	3.099139000	-1.582641000	4.019011000
1	3.671659000	0.021213000	3.570380000
6	1.986430000	-2.347178000	1.690938000
1	2.885329000	-2.887110000	1.371810000
1	1.544494000	-2.902446000	2.524618000
1	1.275949000	-2.339235000	0.861146000
6	3.678124000	0.945125000	1.092157000
1	4.684623000	0.620751000	1.384671000
1	3.283873000	1.544748000	1.916571000
6	3.744483000	1.751679000	-0.180516000
1	4.465101000	2.569995000	-0.098149000
1	4.077649000	1.102291000	-0.996433000
1	3.288807000	-0.864898000	0.287013000
7	2.396316000	2.239541000	-0.572667000
6	1.922512000	3.575598000	-0.023427000
6	3.060188000	4.588584000	0.031010000
1	3.579776000	4.670332000	-0.930310000
1	2.652139000	5.576510000	0.267027000
1	3.800177000	4.356531000	0.802685000
6	1.310722000	3.383450000	1.357847000
1	0.557921000	2.590982000	1.327646000
1	0.817578000	4.307198000	1.679616000
1	2.058964000	3.140837000	2.117491000
6	0.858457000	4.061034000	-1.002578000
1	0.064007000	3.316812000	-1.106611000
1	0.413925000	4.996457000	-0.648924000
1	1.293235000	4.254730000	-1.990707000
1	2.425229000	2.357909000	-1.584484000
6	1.029871000	-4.224292000	-1.516447000
6	2.394635000	-3.897278000	-1.338017000
6	0.131735000	-3.258516000	-1.903763000
1	3.116387000	-4.648091000	-1.024320000
1	-0.904102000	-3.529292000	-2.104302000
6	2.804258000	-2.608663000	-1.534278000
6	0.538374000	-1.906225000	-2.082881000
6	1.949882000	-1.545054000	-1.953545000
1	0.708427000	-5.252589000	-1.368166000
8	2.356220000	-0.357879000	-2.105016000
6	-2.865564000	-2.376124000	1.192067000
6	-3.919976000	-3.471463000	1.116462000
1	-3.928392000	-4.045085000	2.048571000
1	-4.929090000	-3.071917000	0.974824000
1	-3.712395000	-4.172075000	0.299942000
6	-3.215263000	-1.358767000	2.269899000
1	-4.212342000	-0.925923000	2.153386000
1	-3.198972000	-1.846547000	3.249240000
1	-2.476448000	-0.548330000	2.301641000
6	-1.496204000	-2.957959000	1.509526000
1	-1.205719000	-3.736049000	0.793524000
1	-0.739384000	-2.172518000	1.462298000
1	-1.485370000	-3.398670000	2.510784000
1	-2.215603000	-2.380187000	-0.739250000
9	4.105731000	-2.278391000	-1.301905000
1	-0.058631000	-1.268556000	-2.729420000

TS1$_{FF}$ +1, singlet

29	-1.579625000	0.076015000	0.014674000
29	1.258024000	0.614521000	-0.165927000
8	-0.396626000	1.446436000	-0.164523000
8	0.043457000	-0.815668000	-0.347746000
7	-3.349235000	1.093693000	0.163321000
1	-3.421309000	1.316641000	1.155260000
6	-4.436045000	0.109765000	-0.139708000
1	-5.055628000	0.478997000	-0.957362000
1	-5.089554000	0.018897000	0.732192000
6	-3.863156000	-1.229663000	-0.551072000
1	-4.627172000	-2.014297000	-0.512527000
1	-3.512576000	-1.172217000	-1.588467000
6	-3.462392000	2.423454000	-0.560413000
6	-4.902154000	2.937413000	-0.548421000

1	-5.327955000	2.917016000	0.461047000
1	-4.913244000	3.978388000	-0.885746000
1	-5.570952000	2.384047000	-1.212996000
6	-2.966529000	2.222696000	-1.982053000
1	-1.913440000	1.927320000	-1.979351000
1	-3.065792000	3.147792000	-2.558585000
1	-3.544802000	1.450859000	-2.504302000
6	-2.592203000	3.408725000	0.208037000
1	-1.580138000	3.013917000	0.331618000
1	-2.533044000	4.360636000	-0.329324000
1	-3.019522000	3.614874000	1.197114000
7	-2.666311000	-1.570047000	0.242692000
7	2.866072000	-0.356838000	0.771022000
6	2.499429000	-1.103824000	2.032581000
6	1.380014000	-0.332205000	2.725937000
1	0.527952000	-0.202565000	2.048707000
1	1.031040000	-0.865039000	3.616674000
1	1.710314000	0.662797000	3.044096000
6	3.697988000	-1.258361000	2.965779000
1	4.540179000	-1.743130000	2.459973000
1	3.421798000	-1.888603000	3.817192000
1	4.047463000	-0.304286000	3.371056000
6	2.021828000	-2.482447000	1.602791000
1	2.845283000	-3.060933000	1.167856000
1	1.641817000	-3.043731000	2.462369000
1	1.226114000	-2.400075000	0.859960000
6	3.862852000	0.721800000	0.942444000
1	4.869463000	0.319434000	1.106710000
1	3.597566000	1.300857000	1.831091000
6	3.838493000	1.585381000	-0.292617000
1	4.604974000	2.363831000	-0.254422000
1	4.042415000	0.962788000	-1.168736000
1	3.260626000	-1.024769000	0.109470000
7	2.482655000	2.157456000	-0.505771000
6	2.134391000	3.485381000	0.151531000
6	3.347506000	4.403988000	0.230382000
1	3.833993000	4.525277000	-0.743590000
1	3.025017000	5.396353000	0.560951000
1	4.096415000	4.054618000	0.947856000
6	1.566880000	3.238696000	1.542355000
1	0.703392000	2.569403000	1.488225000
1	1.237336000	4.185418000	1.983814000
1	2.309245000	2.809779000	2.221208000
6	1.073182000	4.109256000	-0.747676000
1	0.246632000	3.409954000	-0.902800000
1	0.672991000	5.021802000	-0.294743000
1	1.494305000	4.380000000	-1.723298000
1	2.398942000	2.315934000	-1.509022000
6	0.420456000	-4.086773000	-1.730754000
6	1.817226000	-3.950443000	-1.593685000
6	-0.364618000	-2.986222000	-1.999343000
1	2.447503000	-4.808483000	-1.374036000
1	-1.434194000	-3.077138000	-2.178542000
6	2.386668000	-2.710302000	-1.724009000
6	0.227248000	-1.708049000	-2.074000000
6	1.673035000	-1.514943000	-2.032609000
1	-0.030656000	-5.071362000	-1.643584000
8	2.201649000	-0.378226000	-2.161773000
9	-0.481375000	-0.755270000	-2.731051000
6	-2.818482000	-2.063670000	1.668992000
6	-3.965770000	-3.057638000	1.772586000
1	-3.974312000	-3.508654000	2.769782000
1	-4.941652000	-2.585242000	1.623412000
1	-3.863022000	-3.868520000	1.043374000
6	-3.022792000	-0.899034000	2.632462000
1	-3.985667000	-0.396691000	2.505911000
1	-2.995264000	-1.268989000	3.661830000
1	-2.219908000	-0.155647000	2.533323000
6	-1.488788000	-2.730621000	1.989328000
1	-1.307660000	-3.604251000	1.351364000
1	-0.671025000	-2.026792000	1.824198000
1	-1.460371000	-3.061357000	3.031387000
1	-2.185562000	-2.318865000	-0.252884000
9	3.729416000	-2.569831000	-1.557609000

TS1$_{FCI}$+1, singlet

29	-1.566044000	0.072265000	0.085571000
29	1.268305000	0.628453000	-0.154535000
8	-0.394324000	1.445797000	-0.133182000
8	0.058022000	-0.814216000	-0.340622000
7	-3.333723000	1.091885000	0.282206000
1	-3.375719000	1.320245000	1.274722000
6	-4.432678000	0.111586000	0.013724000
1	-5.073725000	0.481832000	-0.786623000
1	-5.062686000	0.027080000	0.903147000
6	-3.879700000	-1.231071000	-0.412922000
1	-4.645823000	-2.011789000	-0.347284000
1	-3.567767000	-1.177841000	-1.462485000
6	-3.464242000	2.418287000	-0.446475000
6	-4.903934000	2.931752000	-0.407181000
1	-5.311369000	2.912222000	0.609807000
1	-4.921117000	3.972388000	-0.745243000
1	-5.584902000	2.378374000	-1.059259000
6	-2.998288000	2.211549000	-1.877621000
1	-1.944024000	1.921969000	-1.895399000
1	-3.116949000	3.132660000	-2.457190000
1	-3.581850000	1.432220000	-2.383263000
6	-2.578647000	3.408705000	0.297114000
1	-1.563941000	3.015033000	0.399949000
1	-2.531902000	4.357152000	-0.247507000
1	-2.984417000	3.620688000	1.294027000
7	-2.658359000	-1.575529000	0.340085000
7	2.870374000	-0.292008000	0.867137000
6	2.481635000	-1.009324000	2.138132000
6	1.331002000	-0.239655000	2.780221000
1	0.498718000	-0.130565000	2.074995000
1	0.959316000	-0.759767000	3.669422000
1	1.639078000	0.765179000	3.089730000
6	3.654747000	-1.118590000	3.109512000
1	4.518662000	-1.603829000	2.642079000
1	3.363225000	-1.729433000	3.969953000
1	3.977746000	-0.148475000	3.498428000
6	2.042150000	-2.406751000	1.730045000
1	2.889584000	-2.979788000	1.335770000
1	1.643819000	-2.954478000	2.589981000
1	1.270755000	-2.357453000	0.959170000
6	3.845799000	0.806495000	1.034061000
1	4.854430000	0.424790000	1.232472000
1	3.552335000	1.404552000	1.900380000
6	3.838438000	1.638177000	-0.222610000
1	4.592331000	2.428867000	-0.185633000
1	4.074032000	0.997925000	-1.078039000
1	3.298261000	-0.972575000	0.239878000
7	2.480825000	2.185492000	-0.482441000
6	2.100082000	3.522243000	0.139236000
6	3.294563000	4.466783000	0.200738000
1	3.786066000	4.569937000	-0.772881000
1	2.949940000	5.461638000	0.500104000
1	4.044630000	4.153557000	0.933398000
6	1.526372000	3.304030000	1.532773000
1	0.688292000	2.602437000	1.493236000

1	1.157398000	4.253493000	1.935235000
1	2.274855000	2.927880000	2.235379000
6	1.035409000	4.103024000	-0.784739000
1	0.220207000	3.388112000	-0.926349000
1	0.618614000	5.021894000	-0.360744000
1	1.459569000	4.352762000	-1.764652000
1	2.424329000	2.328123000	-1.490173000
6	0.568883000	-4.136074000	-1.510471000
6	1.961819000	-3.953612000	-1.379444000
6	-0.245866000	-3.079357000	-1.843351000
1	2.615748000	-4.780427000	-1.113753000
1	-1.310649000	-3.225695000	-2.011307000
6	2.492427000	-2.707168000	-1.568039000
6	0.300861000	-1.780102000	-1.998059000
6	1.748094000	-1.544736000	-1.933362000
1	0.143689000	-5.125760000	-1.367451000
8	2.262712000	-0.408570000	-2.086823000
6	-2.771707000	-2.076761000	1.766842000
6	-3.905942000	-3.082846000	1.895112000
1	-3.881573000	-3.541082000	2.888717000
1	-4.890656000	-2.620330000	1.777016000
1	-3.815202000	-3.887557000	1.157465000
6	-2.962488000	-0.918549000	2.740444000
1	-3.930198000	-0.421102000	2.637544000
1	-2.910351000	-1.294006000	3.766895000
1	-2.166478000	-0.170352000	2.628244000
6	-1.427962000	-2.730537000	2.050772000
1	-1.260143000	-3.608988000	1.415927000
1	-0.623848000	-2.020533000	1.851185000
1	-1.361804000	-3.050082000	3.094706000
1	-2.196445000	-2.323966000	-0.173748000
9	3.826799000	-2.515007000	-1.392296000
17	-0.619938000	-0.678873000	-3.039409000

TS1$_{\mathbf{CIF}}$ +1, singlet

29	-1.566044000	0.072265000	0.085571000
29	1.268305000	0.628453000	-0.154535000
8	-0.394324000	1.445797000	-0.133182000
8	0.058022000	-0.814216000	-0.340622000
7	-3.333723000	1.091885000	0.282206000
1	-3.375719000	1.320245000	1.274722000
6	-4.432678000	0.111586000	0.013724000
1	-5.073725000	0.481832000	-0.786623000
1	-5.062686000	0.027080000	0.903147000
6	-3.879700000	-1.231071000	-0.412922000
1	-4.645823000	-2.011789000	-0.347284000
1	-3.567767000	-1.177841000	-1.462485000
6	-3.464242000	2.418287000	-0.446475000
6	-4.903934000	2.931752000	-0.407181000
1	-5.311369000	2.912222000	0.609807000
1	-4.921117000	3.972388000	-0.745243000
1	-5.584902000	2.378374000	-1.059259000
6	-2.998288000	2.211549000	-1.877621000
1	-1.944024000	1.921969000	-1.895399000
1	-3.116949000	3.132660000	-2.457190000
1	-3.581850000	1.432220000	-2.383263000
6	-2.578647000	3.408705000	0.297114000
1	-1.563941000	3.015033000	0.399949000
1	-2.531902000	4.357152000	-0.247507000
1	-2.984417000	3.620688000	1.294027000
7	-2.658359000	-1.575529000	0.340085000
7	2.870374000	-0.292008000	0.867137000
6	2.481635000	-1.009324000	2.138132000
6	1.331002000	-0.239655000	2.780221000
1	0.498718000	-0.130565000	2.074995000
1	0.959316000	-0.759767000	3.669422000
1	1.639078000	0.765179000	3.089730000
6	3.654747000	-1.118590000	3.109512000
1	4.518662000	-1.603829000	2.642079000
1	3.363225000	-1.729433000	3.969953000
1	3.977746000	-0.148475000	3.498428000
6	2.042150000	-2.406751000	1.730045000
1	2.889584000	-2.979788000	1.335770000
1	1.643819000	-2.954478000	2.589981000
1	1.270755000	-2.357453000	0.959170000
6	3.845799000	0.806495000	1.034061000
1	4.854430000	0.424790000	1.232472000
1	3.552335000	1.404552000	1.900380000
6	3.838438000	1.638177000	-0.222610000
1	4.592331000	2.428867000	-0.185633000
1	4.074032000	0.997925000	-1.078039000
1	3.298261000	-0.972575000	0.239878000
7	2.480825000	2.185492000	-0.482441000
6	2.100082000	3.522243000	0.139236000
6	3.294563000	4.466783000	0.200738000
1	3.786066000	4.569937000	-0.772881000
1	2.949940000	5.461638000	0.500104000
1	4.044630000	4.153557000	0.933398000
6	1.526372000	3.304030000	1.532773000
1	0.688292000	2.602437000	1.493236000
1	1.157398000	4.253493000	1.935235000
1	2.274855000	2.927880000	2.235379000
6	1.035409000	4.103024000	-0.784739000
1	0.220207000	3.388112000	-0.926349000
1	0.618614000	5.021894000	-0.360744000
1	1.459569000	4.352762000	-1.764652000
1	2.424329000	2.328123000	-1.490173000
6	0.568883000	-4.136074000	-1.510471000
6	1.961819000	-3.953612000	-1.379444000
6	-0.245866000	-3.079357000	-1.843351000
1	2.615748000	-4.780427000	-1.113753000
1	-1.310649000	-3.225695000	-2.011307000
6	2.492427000	-2.707168000	-1.568039000
6	0.300861000	-1.780102000	-1.998059000
6	1.748094000	-1.544736000	-1.933362000
1	0.143689000	-5.125760000	-1.367451000
8	2.262712000	-0.408570000	-2.086823000
6	-2.771707000	-2.076761000	1.766842000
6	-3.905942000	-3.082846000	1.895112000
1	-3.881573000	-3.541082000	2.888717000
1	-4.890656000	-2.620330000	1.777016000
1	-3.815202000	-3.887557000	1.157465000
6	-2.962488000	-0.918549000	2.740444000
1	-3.930198000	-0.421102000	2.637544000
1	-2.910351000	-1.294006000	3.766895000
1	-2.166478000	-0.170352000	2.628244000
6	-1.427962000	-2.730537000	2.050772000
1	-1.260143000	-3.608988000	1.415927000
1	-0.623848000	-2.020533000	1.851185000
1	-1.361804000	-3.050082000	3.094706000
1	-2.196445000	-2.323966000	-0.173748000
9	3.826799000	-2.515007000	-1.392296000
17	-0.619938000	-0.678873000	-3.039409000

4$_{\mathbf{F}}$ +1, triplet

29	-1.485544000	0.099022000	-0.098772000
29	1.408628000	0.368904000	-0.127962000
8	-0.146136000	1.350604000	-0.270153000
8	0.066406000	-1.220624000	-0.500736000
7	-3.144815000	1.447187000	0.211604000
1	-3.014213000	1.769206000	1.168197000
6	-4.379995000	0.622516000	0.185561000

1	-5.119038000	1.050986000	-0.493284000
1	-4.840459000	0.627482000	1.177889000
6	-4.092421000	-0.792688000	-0.266983000
1	-4.967587000	-1.433235000	-0.102366000
1	-3.891640000	-0.796441000	-1.345678000
6	-3.151336000	2.683318000	-0.654229000
6	-4.496835000	3.410457000	-0.630242000
1	-4.850000000	3.571011000	0.394939000
1	-4.382363000	4.396366000	-1.092610000
1	-5.286242000	2.895517000	-1.185175000
6	-2.799454000	2.249618000	-2.069095000
1	-1.800325000	1.801941000	-2.083461000
1	-2.810385000	3.099832000	-2.759324000
1	-3.516516000	1.510855000	-2.447988000
6	-2.088817000	3.611230000	-0.078342000
1	-1.144561000	3.071220000	0.033465000
1	-1.931080000	4.470440000	-0.738768000
1	-2.402548000	4.000065000	0.899037000
7	-2.869141000	-1.328882000	0.356260000
7	2.917464000	-0.736834000	0.785401000
6	2.432141000	-1.520028000	1.984807000
6	1.294105000	-0.725357000	2.618317000
1	0.485351000	-0.550094000	1.898174000
1	0.867066000	-1.254615000	3.476858000
1	1.638683000	0.253478000	2.972009000
6	3.543624000	-1.757840000	3.002276000
1	4.403559000	-2.262764000	2.548779000
1	3.173756000	-2.402825000	3.805798000
1	3.898329000	-0.834224000	3.468751000
6	1.939739000	-2.867133000	1.470400000
1	2.767670000	-3.449615000	1.048199000
1	1.508933000	-3.454334000	2.287792000
1	1.176028000	-2.746396000	0.700338000
6	3.975957000	0.254702000	1.062657000
1	4.931804000	-0.226080000	1.304036000
1	3.678237000	0.837521000	1.938463000
6	4.136440000	1.152602000	-0.143512000
1	4.972058000	1.844815000	0.002341000
1	4.384427000	0.537173000	-1.015152000
1	3.305468000	-1.405781000	0.120925000
7	2.872614000	1.848561000	-0.465098000
6	2.610137000	3.201991000	0.152314000
6	3.879420000	4.036895000	0.275517000
1	4.416721000	4.103215000	-0.677537000
1	3.619099000	5.057415000	0.575022000
1	4.572154000	3.650119000	1.029763000
6	1.958422000	3.019997000	1.518733000
1	1.071382000	2.385595000	1.425842000
1	1.647619000	3.988704000	1.925468000
1	2.642525000	2.571740000	2.245923000
6	1.634986000	3.884991000	-0.800459000
1	0.777315000	3.230906000	-0.983981000
1	1.271909000	4.827832000	-0.378766000
1	2.119081000	4.113795000	-1.758010000
1	2.864308000	1.989150000	-1.472533000
6	0.147799000	-4.123849000	-2.269311000
6	1.551436000	-4.061102000	-2.603324000
6	-0.529822000	-3.020712000	-1.904479000
1	2.049589000	-4.983932000	-2.896389000
1	-1.594343000	-3.059766000	-1.683375000
6	2.257618000	-2.900793000	-2.572054000
6	0.144557000	-1.700088000	-1.752748000
6	1.617739000	-1.665841000	-2.205089000
1	-0.355724000	-5.085895000	-2.329535000
8	2.200139000	-0.577539000	-2.154589000
9	-0.558513000	-0.792871000	-2.653262000
6	-2.897914000	-1.746578000	1.811513000
6	-4.208918000	-2.431310000	2.170531000
1	-4.152599000	-2.833530000	3.187185000
1	-5.060130000	-1.743125000	2.143439000
1	-4.425679000	-3.267666000	1.496804000
6	-2.657638000	-0.546302000	2.725553000
1	-3.496168000	0.155391000	2.743188000
1	-2.513708000	-0.889829000	3.755141000
1	-1.753249000	0.006362000	2.438383000
6	-1.729979000	-2.714996000	1.955268000
1	-1.886549000	-3.625036000	1.363348000
1	-0.809844000	-2.244169000	1.603723000
1	-1.591418000	-3.012490000	2.999008000
1	-2.644022000	-2.176182000	-0.158472000
1	3.312434000	-2.866091000	-2.836018000

4$_{H}$ +1, triplet

29	-1.485751000	-0.146014000	-0.277911000
29	1.208958000	0.693070000	-0.268421000
8	-0.443122000	1.232933000	-0.948696000
8	0.287221000	-1.144395000	-0.450577000
7	-3.375939000	0.810173000	0.047114000
1	-3.297830000	1.125868000	1.011798000
6	-4.415619000	-0.252630000	0.019737000
1	-5.178524000	-0.018315000	-0.725159000
1	-4.930587000	-0.289663000	0.985560000
6	-3.814308000	-1.599044000	-0.331656000
1	-4.534112000	-2.403761000	-0.136558000
1	-3.592051000	-1.622447000	-1.405930000
6	-3.685869000	2.040436000	-0.765706000
6	-5.124059000	2.515486000	-0.559989000
1	-5.359583000	2.628460000	0.504725000
1	-5.256859000	3.496288000	-1.028398000
1	-5.871734000	1.851171000	-1.002804000
6	-3.421367000	1.702813000	-2.224535000
1	-2.376033000	1.399322000	-2.348594000
1	-3.613028000	2.567497000	-2.868555000
1	-4.068097000	0.888832000	-2.574238000
6	-2.730910000	3.118770000	-0.274022000
1	-1.704107000	2.750373000	-0.346282000
1	-2.831175000	4.026565000	-0.878310000
1	-2.949031000	3.390114000	0.767370000
7	-2.523805000	-1.810980000	0.341574000
7	2.856401000	0.097664000	0.892302000
6	2.518450000	-0.710163000	2.119559000
6	1.199174000	-0.173290000	2.663704000
1	0.412655000	-0.229700000	1.900923000
1	0.862846000	-0.742532000	3.536689000
1	1.290479000	0.876091000	2.966905000
6	3.606002000	-0.618626000	3.186480000
1	4.581058000	-0.928605000	2.794724000
1	3.362622000	-1.285880000	4.019743000
1	3.710536000	0.388764000	3.600149000
6	2.383568000	-2.161228000	1.674153000
1	3.340936000	-2.543134000	1.298033000
1	2.084164000	-2.795947000	2.514468000
1	1.636047000	-2.260313000	0.884332000
6	3.615862000	1.337280000	1.144705000
1	4.637506000	1.128580000	1.484859000
1	3.116255000	1.890858000	1.945456000
6	3.642857000	2.146589000	-0.130131000
1	4.268652000	3.037156000	-0.013772000
1	4.095722000	1.544424000	-0.926006000
1	3.440583000	-0.484523000	0.291521000
7	2.272713000	2.467678000	-0.575135000
6	1.600636000	3.711131000	-0.024197000

6	2.601370000	4.810437000	0.308663000
1	3.241143000	5.057062000	-0.545957000
1	2.061405000	5.721822000	0.585555000
1	3.246927000	4.551418000	1.154314000
6	0.787321000	3.350294000	1.215860000
1	0.095816000	2.535076000	0.980251000
1	0.198779000	4.211790000	1.550766000
1	1.421757000	3.047172000	2.053944000
6	0.664631000	4.175749000	-1.133175000
1	0.014297000	3.347439000	-1.430882000
1	0.041093000	5.010045000	-0.795959000
1	1.232677000	4.516720000	-2.007396000
1	2.314352000	2.595506000	-1.583281000
6	0.458217000	-4.060957000	-2.046193000
6	1.899624000	-4.112542000	-1.953140000
6	-0.200124000	-2.889383000	-1.990542000
1	2.408601000	-5.074022000	-1.943552000
1	-1.285953000	-2.857054000	-2.070129000
6	2.626880000	-2.978399000	-1.876493000
6	0.507910000	-1.593188000	-1.779371000
6	2.026129000	-1.661309000	-1.910413000
1	-0.075437000	-5.001451000	-2.161398000
8	2.690175000	-0.625817000	-1.936991000
6	-2.508950000	-2.132579000	1.817162000
6	-3.665866000	-3.040938000	2.209251000
1	-3.561962000	-3.345628000	3.255831000
1	-4.637593000	-2.545861000	2.112863000
1	-3.687126000	-3.952472000	1.601922000
6	-2.535344000	-0.846004000	2.637536000
1	-3.505258000	-0.341500000	2.606210000
1	-2.329715000	-1.066946000	3.689897000
1	-1.764096000	-0.146014000	2.291352000
6	-1.176385000	-2.835513000	2.041360000
1	-1.139687000	-3.798877000	1.518029000
1	-0.365268000	-2.217761000	1.653741000
1	-1.000428000	-3.022944000	3.104803000
1	-2.088291000	-2.609677000	-0.115034000
9	3.969724000	-3.016427000	-1.767085000
1	0.147387000	-0.828819000	-2.493684000

4_{FF} +1, singlet

29	-1.612729000	-0.069903000	-0.149575000
29	1.224738000	0.695026000	-0.104313000
8	-0.476763000	1.352606000	-0.369924000
8	0.202124000	-1.086125000	-0.458802000
7	-3.430313000	0.979153000	0.125111000
1	-3.364699000	1.339437000	1.075036000
6	-4.520309000	-0.034391000	0.107605000
1	-5.324315000	0.276644000	-0.560617000
1	-4.963582000	-0.104104000	1.104895000
6	-4.016156000	-1.382038000	-0.356364000
1	-4.777324000	-2.154396000	-0.193302000
1	-3.821467000	-1.347273000	-1.435285000
6	-3.627670000	2.182339000	-0.773046000
6	-5.076189000	2.671651000	-0.778774000
1	-5.470603000	2.779522000	0.237958000
1	-5.117865000	3.658364000	-1.251167000
1	-5.756566000	2.027224000	-1.342722000
6	-3.188047000	1.780901000	-2.172890000
1	-2.124999000	1.518942000	-2.165509000
1	-3.341141000	2.598462000	-2.885059000
1	-3.760345000	0.918396000	-2.535924000
6	-2.742558000	3.284467000	-0.207258000
1	-1.722341000	2.909602000	-0.081555000
1	-2.725683000	4.145604000	-0.883537000
1	-3.126521000	3.633471000	0.760051000
7	-2.720717000	-1.722998000	0.262538000
7	2.846676000	-0.094384000	0.947983000
6	2.449116000	-0.920048000	2.149984000
6	1.148698000	-0.337308000	2.695203000
1	0.361989000	-0.338691000	1.931415000
1	0.784479000	-0.912749000	3.552769000
1	1.285646000	0.699499000	3.025786000
6	3.525283000	-0.910518000	3.232491000
1	4.490709000	-1.252636000	2.844057000
1	3.239314000	-1.591057000	4.040894000
1	3.668900000	0.077614000	3.679250000
6	2.252429000	-2.351415000	1.667541000
1	3.197925000	-2.773542000	1.305477000
1	1.901209000	-2.986190000	2.487243000
1	1.520570000	-2.405459000	0.860110000
6	3.664031000	1.098798000	1.248610000
1	4.674595000	0.829190000	1.577582000
1	3.187746000	1.639622000	2.071308000
6	3.731392000	1.956962000	0.007338000
1	4.408113000	2.803901000	0.153437000
1	4.142521000	1.360923000	-0.814892000
1	3.408669000	-0.687594000	0.337590000
7	2.379254000	2.383490000	-0.417674000
6	1.827106000	3.687665000	0.123947000
6	2.915119000	4.741093000	0.296195000
1	3.505031000	4.872439000	-0.617846000
1	2.452181000	5.705719000	0.528452000
1	3.601580000	4.510967000	1.117136000
6	1.121432000	3.433623000	1.450668000
1	0.377486000	2.640366000	1.329328000
1	0.604844000	4.340036000	1.785415000
1	1.821675000	3.153319000	2.243509000
6	0.821642000	4.152837000	-0.923001000
1	0.100612000	3.355458000	-1.126466000
1	0.278193000	5.036496000	-0.573678000
1	1.327702000	4.423332000	-1.857994000
1	2.414692000	2.496097000	-1.428750000
6	0.823976000	-4.111817000	-1.752710000
6	2.250383000	-3.917008000	-1.824807000
6	-0.027962000	-3.070261000	-1.713785000
1	2.915711000	-4.777161000	-1.834609000
1	-1.105152000	-3.218913000	-1.690203000
6	2.776175000	-2.672162000	-1.883128000
6	0.463006000	-1.666126000	-1.648043000
6	1.967585000	-1.481246000	-1.905429000
1	0.452098000	-5.132991000	-1.737442000
8	2.425855000	-0.342051000	-2.003853000
9	-0.215527000	-0.938160000	-2.699891000
6	-2.686649000	-2.164151000	1.712585000
6	-3.873486000	-3.056275000	2.047144000
1	-3.759698000	-3.462791000	3.057081000
1	-4.824616000	-2.514712000	2.022959000
1	-3.947712000	-3.904541000	1.357486000
6	-2.641700000	-0.957813000	2.647103000
1	-3.569946000	-0.380182000	2.650167000
1	-2.475668000	-1.295479000	3.675183000
1	-1.817038000	-0.280651000	2.391203000
6	-1.380342000	-2.936303000	1.851719000
1	-1.382417000	-3.848666000	1.243072000
1	-0.544436000	-2.316766000	1.522131000
1	-1.206610000	-3.227896000	2.891903000
1	-2.360538000	-2.514662000	-0.264209000
9	4.109633000	-2.483074000	-1.941757000

4_{FCI} +1, singlet

29	-1.678610000	-0.201835000	-0.163234000
29	1.031897000	0.862278000	0.005030000
8	-0.700716000	1.325685000	-0.405900000
8	0.225331000	-1.052290000	-0.326779000
7	-3.639137000	0.612019000	-0.089269000
1	-3.705305000	0.961113000	0.864867000
6	-4.580343000	-0.534902000	-0.206299000
1	-5.306221000	-0.351445000	-0.999706000
1	-5.154560000	-0.630284000	0.720307000
6	-3.848730000	-1.819131000	-0.528262000
1	-4.515588000	-2.681945000	-0.411419000
1	-3.526139000	-1.801462000	-1.576873000
6	-3.921609000	1.793074000	-0.988238000
6	-5.413647000	2.121474000	-1.051251000
1	-5.849026000	2.203178000	-0.048780000
1	-5.549157000	3.089154000	-1.544785000
1	-6.000920000	1.394178000	-1.619113000
6	-3.378060000	1.450939000	-2.365626000
1	-2.298646000	1.274814000	-2.303006000
1	-3.558473000	2.264750000	-3.075470000
1	-3.855672000	0.550662000	-2.772038000
6	-3.186440000	2.979903000	-0.379452000
1	-2.135850000	2.721237000	-0.215539000
1	-3.241854000	3.846256000	-1.046902000
1	-3.643080000	3.270550000	0.575474000
7	-2.607878000	-1.950557000	0.258480000
7	2.637020000	0.296302000	1.208499000
6	2.246785000	-0.515965000	2.422883000
6	0.860442000	-0.054010000	2.861224000
1	0.132506000	-0.164527000	2.047770000
1	0.499811000	-0.637470000	3.714749000
1	0.864606000	1.001044000	3.159372000
6	3.245484000	-0.348143000	3.564364000
1	4.262014000	-0.610833000	3.251285000
1	2.975983000	-1.014556000	4.390033000
1	3.264712000	0.669954000	3.963701000
6	2.228434000	-1.977985000	1.994951000
1	3.233173000	-2.314124000	1.710303000
1	1.890826000	-2.614794000	2.818681000
1	1.558830000	-2.135161000	1.147798000
6	3.309903000	1.580383000	1.496115000
1	4.309157000	1.429674000	1.921422000
1	2.716440000	2.117709000	2.241573000
6	3.404017000	2.368930000	0.210500000
1	3.978053000	3.288141000	0.361087000
1	3.948231000	1.773064000	-0.531277000
1	3.298381000	-0.262241000	0.669012000
7	2.062364000	2.628064000	-0.358259000
6	1.348567000	3.906978000	0.024964000
6	2.307339000	5.088367000	0.126440000
1	2.922088000	5.190637000	-0.774972000
1	1.733432000	6.014143000	0.237271000
1	2.975854000	5.024610000	0.990602000
6	0.615383000	3.699740000	1.344665000
1	-0.006112000	2.800665000	1.283397000
1	-0.035514000	4.553970000	1.560097000
1	1.307187000	3.601750000	2.187155000
6	0.347894000	4.157623000	-1.098026000
1	-0.284520000	3.275590000	-1.238562000
1	-0.290632000	5.014082000	-0.859711000
1	0.863951000	4.381602000	-2.039936000
1	2.175030000	2.664531000	-1.369116000
6	1.182889000	-4.009984000	-1.593974000
6	2.583831000	-3.685452000	-1.631871000
6	0.239040000	-3.049931000	-1.575377000
1	3.308556000	-4.496121000	-1.640700000
1	-0.820064000	-3.297814000	-1.589836000
6	3.013492000	-2.396522000	-1.670064000
6	0.598471000	-1.609260000	-1.494552000
6	2.093218000	-1.283476000	-1.694041000
1	0.906482000	-5.060932000	-1.593394000
8	2.425069000	-0.102011000	-1.766863000
9	-0.091244000	-0.953874000	-2.585898000
6	-2.694667000	-2.305063000	1.728821000
6	-3.802218000	-3.314552000	1.990718000
1	-3.765241000	-3.645602000	3.033416000
1	-4.798244000	-2.892651000	1.821880000
1	-3.696760000	-4.203652000	1.359459000
6	-2.900587000	-1.050593000	2.573236000
1	-3.894881000	-0.610626000	2.453022000
1	-2.792133000	-1.297011000	3.634419000
1	-2.150750000	-0.283136000	2.338714000
6	-1.331910000	-2.900507000	2.058913000
1	-1.156011000	-3.834121000	1.510354000
1	-0.543246000	-2.198477000	1.782176000
1	-1.244918000	-3.115542000	3.128054000
1	-2.084353000	-2.711077000	-0.166599000
17	4.716972000	-2.017818000	-1.733125000

$TS2_F$ +1, triplet

29	1.531342000	0.105340000	-0.043109000
29	-1.332451000	0.463622000	0.410678000
8	0.309303000	1.320371000	0.592820000
8	-0.160671000	-1.190046000	-0.066045000
7	3.205373000	1.324829000	0.119116000
1	2.798991000	2.246476000	-0.028454000
6	4.060686000	1.001601000	-1.044739000
1	5.111111000	1.262049000	-0.868002000
1	3.725807000	1.617017000	-1.885620000
6	3.950159000	-0.469392000	-1.401087000
1	4.550247000	-0.687138000	-2.290746000
1	4.356481000	-1.081591000	-0.592477000
6	3.884012000	1.384422000	1.461982000
6	4.809251000	2.596737000	1.513697000
1	4.252392000	3.525683000	1.345733000
1	5.290971000	2.673850000	2.493838000
1	5.606490000	2.542109000	0.765508000
6	4.667254000	0.105338000	1.713461000
1	4.022769000	-0.776445000	1.638796000
1	5.083430000	0.124286000	2.725475000
1	5.508442000	-0.016465000	1.023271000
6	2.781311000	1.521938000	2.501399000
1	2.125389000	0.647149000	2.489464000
1	3.212030000	1.628613000	3.502436000
1	2.150387000	2.393218000	2.300418000
7	2.539383000	-0.886957000	-1.551381000
7	-3.228051000	-0.403323000	0.043197000
6	-3.462663000	-1.252281000	-1.189141000
6	-2.759040000	-0.588006000	-2.363684000
1	-1.698874000	-0.424821000	-2.140877000
1	-2.818797000	-1.216077000	-3.258810000
1	-3.205560000	0.379787000	-2.613356000
6	-4.952604000	-1.417776000	-1.482115000
1	-5.487253000	-1.844656000	-0.626035000
1	-5.086567000	-2.103252000	-2.324826000
1	-5.441054000	-0.477564000	-1.752310000
6	-2.868366000	-2.631686000	-0.930658000
1	-3.294957000	-3.090228000	-0.029841000
1	-3.090382000	-3.297484000	-1.770153000
1	-1.785636000	-2.594347000	-0.819589000
6	-4.204142000	0.698489000	0.215550000

1	-5.200164000	0.315163000	0.464716000
1	-4.297901000	1.234429000	-0.733383000
6	-3.724536000	1.621815000	1.310733000
1	-4.462569000	2.408674000	1.502135000
1	-3.622073000	1.052623000	2.242370000
1	-3.371521000	-1.021105000	0.842770000
7	-2.386714000	2.153839000	1.001259000
6	-2.266915000	3.344588000	0.068772000
6	-3.493765000	4.244411000	0.137561000
1	-3.699891000	4.576264000	1.161048000
1	-3.323862000	5.139687000	-0.469054000
1	-4.395543000	3.759212000	-0.250962000
6	-2.050459000	2.861425000	-1.361804000
1	-1.174546000	2.205533000	-1.416324000
1	-1.875390000	3.711862000	-2.029457000
1	-2.912981000	2.316600000	-1.752255000
6	-1.028260000	4.104298000	0.529286000
1	-0.170436000	3.422397000	0.548666000
1	-0.813679000	4.937178000	-0.147818000
1	-1.168860000	4.520725000	1.534308000
1	-1.960825000	2.433569000	1.881188000
6	0.214631000	-4.511786000	1.129428000
6	-0.508730000	-4.409489000	2.376479000
6	0.496839000	-3.416628000	0.398793000
1	-0.679367000	-5.322090000	2.945103000
1	1.039253000	-3.473756000	-0.543256000
6	-0.988977000	-3.230592000	2.847538000
6	0.069645000	-2.079395000	0.843526000
1	-1.560230000	-3.175522000	3.771383000
6	-0.817128000	-2.014390000	2.089225000
1	0.526474000	-5.496668000	0.790027000
8	-1.352527000	-0.942203000	2.378894000
9	1.501690000	-1.563911000	1.594027000
6	1.847639000	-0.637119000	-2.887872000
6	2.835330000	-0.528685000	-4.040884000
1	2.284062000	-0.435269000	-4.981857000
1	3.484119000	0.349610000	-3.961429000
1	3.470179000	-1.417287000	-4.121518000
6	1.009454000	0.636797000	-2.791071000
1	1.616814000	1.524945000	-2.583963000
1	0.466258000	0.815455000	-3.725579000
1	0.266308000	0.554383000	-1.989728000
6	0.919839000	-1.824892000	-3.118986000
1	1.485720000	-2.757953000	-3.225894000
1	0.219335000	-1.939464000	-2.287865000
1	0.336893000	-1.683924000	-4.034617000
1	2.523948000	-1.892283000	-1.401359000

$TS2_H$ +1, singlet

29	-1.610655000	-0.344209000	0.124702000
29	1.496340000	0.012523000	0.219925000
8	-0.173245000	0.510770000	0.815521000
8	1.012520000	0.860000000	-1.414727000
7	-3.634183000	-0.164689000	0.605176000
1	-3.857554000	-0.842615000	1.330773000
6	-4.423551000	-0.497376000	-0.603016000
1	-5.231668000	0.224037000	-0.760285000
1	-4.913995000	-1.465040000	-0.461127000
6	-3.533979000	-0.520340000	-1.835975000
1	-4.095000000	-0.892392000	-2.702531000
1	-3.228156000	0.505350000	-2.074644000
6	-3.872470000	1.198048000	1.213930000
6	-5.324243000	1.353934000	1.653437000
1	-5.603697000	0.595913000	2.393278000
1	-5.480775000	2.330480000	2.119629000
1	-6.030935000	1.286975000	0.821352000
6	-3.481726000	2.246965000	0.183927000
1	-2.460799000	2.067171000	-0.172164000
1	-3.500873000	3.249767000	0.618105000
1	-4.149409000	2.260488000	-0.684362000
6	-2.948685000	1.287470000	2.422549000
1	-1.895033000	1.266758000	2.129496000
1	-3.127192000	2.213061000	2.976002000
1	-3.121917000	0.458177000	3.119773000
7	-2.281239000	-1.265816000	-1.603707000
7	3.449388000	-0.328378000	-0.262645000
6	3.824566000	-0.832182000	-1.643049000
6	2.754630000	-1.825015000	-2.078211000
1	1.774524000	-1.340920000	-2.130999000
1	2.978571000	-2.229577000	-3.069705000
1	2.689109000	-2.679817000	-1.395538000
6	5.200445000	-1.492502000	-1.643791000
1	5.980408000	-0.814591000	-1.282810000
1	5.469918000	-1.767252000	-2.667201000
1	5.242296000	-2.409744000	-1.048970000
6	3.843721000	0.379929000	-2.566732000
1	4.635288000	1.081463000	-2.280334000
1	4.043659000	0.069681000	-3.595913000
1	2.888443000	0.905050000	-2.540263000
6	4.029601000	-1.050142000	0.886880000
1	5.117900000	-0.928582000	0.942421000
1	3.839276000	-2.121614000	0.759574000
6	3.375030000	-0.528381000	2.147814000
1	3.793228000	-0.997520000	3.043460000
1	3.558082000	0.548754000	2.231308000
1	3.738117000	0.650746000	-0.197884000
7	1.905552000	-0.689802000	2.054932000
6	1.270967000	-2.025613000	2.422660000
6	2.152542000	-2.836225000	3.362568000
1	2.378126000	-2.295944000	4.286964000
1	1.633043000	-3.754687000	3.648156000
1	3.098861000	-3.138903000	2.904031000
6	0.998599000	-2.789975000	1.133770000
1	0.317696000	-2.203059000	0.506828000
1	0.514170000	-3.751136000	1.334565000
1	1.904130000	-2.993777000	0.557524000
6	-0.067155000	-1.714148000	3.086816000
1	-0.710489000	-1.160287000	2.395194000
1	-0.575312000	-2.641221000	3.367726000
1	0.050739000	-1.115943000	3.996551000
1	1.462112000	0.023587000	2.629229000
6	-0.662017000	4.094384000	-1.663847000
6	0.104336000	4.831861000	-0.722314000
6	-0.426557000	2.763713000	-1.852356000
1	-0.079109000	5.893465000	-0.574672000
1	-0.970104000	2.180332000	-2.594396000
6	1.091572000	4.236440000	0.011456000
6	0.541215000	2.076684000	-1.029927000
6	1.468228000	2.862463000	-0.166242000
1	-1.413924000	4.612648000	-2.252283000
8	2.392499000	2.285690000	0.445079000
6	-2.316424000	-2.775785000	-1.578802000
6	-3.354904000	-3.348356000	-2.534607000
1	-3.280295000	-4.438970000	-2.564268000
1	-4.380712000	-3.111351000	-2.235578000
1	-3.210052000	-2.988093000	-3.558142000
6	-2.586642000	-3.240484000	-0.149464000
1	-3.585967000	-2.970002000	0.200794000
1	-2.511084000	-4.329170000	-0.072065000
1	-1.857523000	-2.812281000	0.548683000
6	-0.916469000	-3.212174000	-1.996372000
1	-0.714293000	-2.974537000	-3.046524000

1	-0.158865000	-2.708449000	-1.389631000
1	-0.781371000	-4.289637000	-1.871835000
1	-1.645246000	-1.001365000	-2.353442000
9	1.837679000	4.966011000	0.850207000
1	-0.134923000	1.699325000	-0.019781000

TS2$_{FF}$ +1, triplet

29	-1.488494000	0.231045000	0.099210000
29	1.471974000	0.290368000	0.126375000
8	-0.040167000	1.332186000	0.000067000
8	0.037409000	-1.304126000	0.081945000
7	-3.071213000	1.692036000	0.002509000
1	-3.076791000	2.091633000	0.938201000
6	-4.336460000	0.931193000	-0.161716000
1	-4.875074000	1.277839000	-1.045334000
1	-4.992437000	1.126047000	0.692527000
6	-4.078109000	-0.553736000	-0.332015000
1	-5.008087000	-1.121019000	-0.204622000
1	-3.724309000	-0.742367000	-1.351250000
6	-2.845319000	2.841262000	-0.946689000
6	-4.123185000	3.638206000	-1.209865000
1	-4.617420000	3.926139000	-0.274919000
1	-3.872177000	4.560625000	-1.743861000
1	-4.850998000	3.105380000	-1.828737000
6	-2.289628000	2.260676000	-2.237464000
1	-1.346002000	1.745240000	-2.031273000
1	-2.107421000	3.044519000	-2.980317000
1	-2.986352000	1.539753000	-2.683217000
6	-1.830120000	3.754402000	-0.270696000
1	-0.944291000	3.182152000	0.018385000
1	-1.526450000	4.558669000	-0.949083000
1	-2.264796000	4.224238000	0.621029000
7	-2.993463000	-1.045058000	0.539096000
7	2.976833000	-0.805838000	1.010716000
6	2.575932000	-1.399056000	2.347625000
6	1.553792000	-0.458168000	2.977889000
1	0.677901000	-0.344196000	2.326334000
1	1.203346000	-0.840190000	3.942096000
1	1.974188000	0.539655000	3.147917000
6	3.776486000	-1.578662000	3.272238000
1	4.552666000	-2.198710000	2.810553000
1	3.458308000	-2.084602000	4.189268000
1	4.231010000	-0.629667000	3.569503000
6	1.954082000	-2.764373000	2.083362000
1	1.078666000	-2.691494000	1.437758000
1	2.677086000	-3.442653000	1.614567000
1	1.640186000	-3.223124000	3.026354000
6	4.114753000	0.137734000	1.063204000
1	5.058065000	-0.377784000	1.278780000
1	3.938639000	0.842534000	1.880546000
6	4.212141000	0.869250000	-0.256875000
1	5.093553000	1.517852000	-0.270223000
1	4.351236000	0.137038000	-1.060693000
1	3.260824000	-1.577569000	0.406659000
7	2.964070000	1.600478000	-0.560662000
6	2.832940000	3.043833000	-0.135060000
6	4.154116000	3.797886000	-0.234175000
1	4.613444000	3.686970000	-1.222957000
1	3.979158000	4.866597000	-0.072787000
1	4.882561000	3.477265000	0.517420000
6	2.291385000	3.107288000	1.288562000
1	1.345526000	2.560436000	1.357133000
1	2.107976000	4.147163000	1.580631000
1	2.995042000	2.690442000	2.016069000
6	1.819611000	3.645606000	-1.103072000
1	0.913388000	3.032781000	-1.116842000
1	1.549867000	4.663245000	-0.803219000
1	2.230170000	3.696983000	-2.119135000
1	2.858649000	1.592464000	-1.572147000
6	-0.389251000	-4.233823000	-1.887592000
6	0.553703000	-3.978702000	-2.951793000
6	-0.703389000	-3.296323000	-0.973738000
1	0.756741000	-4.749728000	-3.691000000
1	-1.387986000	-3.509772000	-0.155586000
6	1.203375000	-2.798616000	-3.027020000
6	-0.089123000	-1.958190000	-1.017943000
6	1.025881000	-1.751879000	-2.044178000
1	-0.832141000	-5.224884000	-1.834860000
8	1.711316000	-0.733898000	-2.007026000
9	-1.259283000	-1.087889000	-1.907817000
6	-3.250771000	-1.245248000	2.014256000
6	-4.597066000	-1.914282000	2.253790000
1	-4.710952000	-2.160345000	3.314380000
1	-5.437440000	-1.268017000	1.981306000
1	-4.687893000	-2.847282000	1.686297000
6	-3.172681000	0.086062000	2.756006000
1	-3.999837000	0.759334000	2.513951000
1	-3.213686000	-0.088735000	3.835576000
1	-2.228511000	0.605539000	2.543211000
6	-2.117651000	-2.139879000	2.505623000
1	-2.134968000	-3.120796000	2.016362000
1	-1.143543000	-1.684354000	2.305639000
1	-2.201173000	-2.306292000	3.583703000
1	-2.746181000	-1.960643000	0.171098000
9	2.114071000	-2.559300000	-3.984477000

TS2$_{FCl}$ +1, triplet

29	1.711351000	-0.032197000	0.011926000
29	-1.150893000	-0.753574000	-0.050735000
8	0.545643000	-1.375934000	-0.448583000
8	-0.097599000	0.987338000	0.519851000
7	3.434748000	-0.988175000	-0.610736000
1	3.186686000	-1.968652000	-0.492413000
6	4.484312000	-0.648465000	0.376952000
1	5.489562000	-0.732398000	-0.052840000
1	4.429074000	-1.380807000	1.188555000
6	4.275591000	0.752826000	0.920921000
1	5.022005000	0.971742000	1.691264000
1	4.421123000	1.487794000	0.126062000
6	3.795432000	-0.823693000	-2.064665000
6	4.826112000	-1.878185000	-2.456436000
1	4.437589000	-2.890096000	-2.294524000
1	5.083458000	-1.789475000	-3.516909000
1	5.757268000	-1.778938000	-1.888982000
6	4.339925000	0.573483000	-2.316406000
1	3.624802000	1.341039000	-2.003324000
1	4.518644000	0.707480000	-3.387738000
1	5.292289000	0.753481000	-1.807052000
6	2.513052000	-1.021836000	-2.859630000
1	1.780357000	-0.247933000	-2.612601000
1	2.720465000	-0.976766000	-3.933829000
1	2.047866000	-1.986962000	-2.637285000
7	2.890871000	0.949925000	1.402765000
7	-3.022419000	-0.188907000	0.706596000
6	-3.130383000	0.273412000	2.144098000
6	-2.216349000	-0.600384000	2.990311000
1	-1.181129000	-0.550327000	2.631778000
1	-2.221942000	-0.271982000	4.034703000
1	-2.527798000	-1.649667000	2.976392000
6	-4.568013000	0.190645000	2.651810000
1	-5.251414000	0.769194000	2.020253000
1	-4.625019000	0.608165000	3.661855000
1	-4.942102000	-0.835700000	2.706146000

6	-2.679185000	1.727682000	2.202637000
1	-3.278010000	2.357359000	1.532762000
1	-2.806826000	2.118847000	3.216511000
1	-1.629469000	1.841695000	1.933481000
6	-3.922797000	-1.314580000	0.361314000
1	-4.973102000	-1.003260000	0.368474000
1	-3.812021000	-2.092014000	1.123164000
6	-3.555916000	-1.840996000	-1.005993000
1	-4.253228000	-2.625470000	-1.317620000
1	-3.645617000	-1.030064000	-1.738173000
1	-3.328908000	0.596532000	0.130582000
7	-2.149269000	-2.282359000	-1.042917000
6	-1.805076000	-3.680733000	-0.570098000
6	-2.959010000	-4.654259000	-0.773231000
1	-3.306960000	-4.663752000	-1.811798000
1	-2.625744000	-5.668517000	-0.531194000
1	-3.816649000	-4.436442000	-0.128327000
6	-1.404584000	-3.634010000	0.901168000
1	-0.552116000	-2.960406000	1.042249000
1	-1.109065000	-4.629907000	1.248882000
1	-2.223070000	-3.297710000	1.542979000
6	-0.603125000	-4.111659000	-1.402020000
1	0.196376000	-3.370972000	-1.297070000
1	-0.233463000	-5.086600000	-1.068996000
1	-0.866623000	-4.200470000	-2.463244000
1	-1.838617000	-2.217407000	-2.009268000
6	-0.489653000	4.432913000	-0.135034000
6	-1.507838000	4.366432000	-1.148571000
6	0.164414000	3.330812000	0.286028000
1	-2.000068000	5.284894000	-1.458677000
1	0.925081000	3.376105000	1.061626000
6	-1.868590000	3.182644000	-1.712147000
6	-0.155286000	2.011385000	-0.267921000
6	-1.251485000	1.934820000	-1.326765000
1	-0.267114000	5.405863000	0.295436000
8	-1.572373000	0.830160000	-1.767613000
9	1.191596000	1.787472000	-1.300382000
6	2.537875000	0.476658000	2.809095000
6	3.757144000	0.404441000	3.718028000
1	3.438356000	0.143294000	4.731959000
1	4.473733000	-0.360118000	3.400898000
1	4.283175000	1.363048000	3.779267000
6	1.865379000	-0.892086000	2.727087000
1	2.517861000	-1.651211000	2.282484000
1	1.582090000	-1.241275000	3.725740000
1	0.953926000	-0.847100000	2.121499000
6	1.538740000	1.484574000	3.364262000
1	1.987234000	2.479742000	3.466672000
1	0.665637000	1.565599000	2.711946000
1	1.191102000	1.173078000	4.354288000
1	2.724503000	1.952413000	1.386532000
17	-3.139932000	3.095775000	-2.901273000

5$_F$ +1, triplet

29	-1.471309000	-0.284545000	-0.429707000
29	1.276759000	0.466443000	0.437009000
8	-0.547066000	0.863770000	0.639421000
7	-2.414674000	-1.940732000	0.519982000
1	-2.011881000	-2.734189000	0.025409000
6	-3.820188000	-1.828588000	0.080719000
1	-4.478312000	-2.500475000	0.643550000
1	-3.835743000	-2.153234000	-0.962172000
6	-4.348192000	-0.408033000	0.159985000
1	-5.349739000	-0.382755000	-0.288912000
1	-4.453682000	-0.071235000	1.191279000
6	-2.150147000	-2.167209000	1.981093000
6	-2.832196000	-3.447021000	2.461658000
1	-2.521318000	-4.311523000	1.864467000
1	-2.558440000	-3.648429000	3.502289000
1	-3.923247000	-3.382696000	2.424622000
6	-2.610200000	-0.968078000	2.797357000
1	-2.248246000	-0.036525000	2.348092000
1	-2.202783000	-1.032672000	3.811127000
1	-3.697925000	-0.913663000	2.893145000
6	-0.643685000	-2.317943000	2.116466000
1	-0.135236000	-1.399883000	1.809025000
1	-0.365955000	-2.532054000	3.153058000
1	-0.266110000	-3.133027000	1.489147000
7	-3.434672000	0.509698000	-0.539773000
1	-3.517685000	0.303528000	-1.536568000
6	-3.701558000	1.971029000	-0.363670000
6	-5.143608000	2.296911000	-0.743398000
1	-5.862610000	1.842681000	-0.054825000
1	-5.306158000	3.379346000	-0.716539000
1	-5.377787000	1.951214000	-1.756766000
6	-2.735435000	2.673786000	-1.305425000
1	-1.707961000	2.401378000	-1.056386000
1	-2.829826000	3.761426000	-1.234356000
1	-2.917105000	2.388817000	-2.348870000
6	-3.421490000	2.374441000	1.077761000
1	-2.415491000	2.068611000	1.376787000
1	-3.490530000	3.462482000	1.179545000
1	-4.140446000	1.941708000	1.780999000
7	3.209209000	-0.159533000	0.756647000
6	3.376773000	-1.223257000	1.812103000
6	2.631065000	-0.775421000	3.062800000
1	1.591004000	-0.516381000	2.828454000
1	2.615693000	-1.577327000	3.807092000
1	3.092832000	0.096672000	3.536630000
6	4.852473000	-1.460097000	2.117821000
1	5.412261000	-1.717070000	1.211539000
1	4.958317000	-2.295868000	2.816727000
1	5.331419000	-0.591170000	2.578474000
6	2.762384000	-2.494863000	1.249400000
1	3.291486000	-2.824655000	0.347051000
1	2.815952000	-3.304987000	1.982522000
1	1.715373000	-2.342772000	0.988865000
6	4.025866000	1.054076000	0.991543000
1	5.071197000	0.888825000	0.709988000
1	4.010942000	1.272661000	2.063865000
6	3.451611000	2.223359000	0.234874000
1	4.047206000	3.119167000	0.441962000
1	3.479341000	2.041975000	-0.843596000
1	3.520176000	-0.560227000	-0.127851000
7	2.041256000	2.402430000	0.636374000
6	1.041782000	-3.424479000	-3.271968000
6	1.993171000	-2.673683000	-4.023052000
6	0.508973000	-2.926650000	-2.108227000
1	2.388792000	-3.098556000	-4.943380000
1	-0.228513000	-3.486714000	-1.536654000
6	2.407353000	-1.440211000	-3.606517000
6	0.902104000	-1.654032000	-1.636146000
1	3.132954000	-0.860739000	-4.173779000
6	1.900337000	-0.867195000	-2.389181000
1	0.734883000	-4.402929000	-3.634760000
8	2.277519000	0.239057000	-1.933394000
9	-1.951204000	-1.067375000	-2.091521000
1	2.036333000	2.641428000	1.629278000
6	1.313252000	3.507818000	-0.092824000
6	0.901671000	2.987961000	-1.462912000
1	0.311928000	2.072189000	-1.365282000
1	0.294561000	3.732779000	-1.987482000

1	1.765377000	2.756544000	-2.091630000
6	0.095331000	3.860347000	0.748487000
1	0.394901000	4.264083000	1.723588000
1	-0.507429000	4.623843000	0.246813000
1	-0.524963000	2.977656000	0.913154000
6	2.196550000	4.744217000	-0.244632000
1	1.602458000	5.566776000	-0.655412000
1	2.595283000	5.078172000	0.719838000
1	3.037416000	4.582888000	-0.925224000
8	0.431795000	-1.160316000	-0.538944000

5_H +1 singlet

29	-1.633774000	-0.421134000	0.100484000
29	1.494774000	-0.007192000	0.238890000
8	-0.221841000	0.467673000	0.943808000
8	0.989026000	0.856256000	-1.494911000
7	-3.711835000	-0.250345000	0.625506000
1	-3.947954000	-0.930611000	1.343885000
6	-4.471171000	-0.576083000	-0.599543000
1	-5.285430000	0.136730000	-0.768435000
1	-4.955032000	-1.549981000	-0.478252000
6	-3.568347000	-0.578683000	-1.825698000
1	-4.122441000	-0.947594000	-2.698192000
1	-3.269175000	0.450891000	-2.054303000
6	-3.949488000	1.110594000	1.226010000
6	-5.414454000	1.316420000	1.598039000
1	-5.757114000	0.556976000	2.309055000
1	-5.556628000	2.290382000	2.074827000
1	-6.083152000	1.291423000	0.733036000
6	-3.480947000	2.152797000	0.219578000
1	-2.452506000	1.942792000	-0.099314000
1	-3.494208000	3.157071000	0.651027000
1	-4.107385000	2.182264000	-0.678686000
6	-3.094110000	1.169794000	2.485310000
1	-2.036628000	1.015254000	2.259896000
1	-3.200488000	2.136577000	2.984081000
1	-3.394036000	0.401060000	3.207991000
7	-2.307367000	-1.316435000	-1.602681000
7	3.441729000	-0.412756000	-0.260108000
6	3.808906000	-0.911886000	-1.644315000
6	2.725742000	-1.888746000	-2.082438000
1	1.749298000	-1.395797000	-2.119637000
1	2.936561000	-2.284300000	-3.080521000
1	2.657443000	-2.749942000	-1.408552000
6	5.177617000	-1.588628000	-1.657170000
1	5.966617000	-0.922611000	-1.293393000
1	5.440233000	-1.857962000	-2.683860000
1	5.211973000	-2.510714000	-1.069964000
6	3.848797000	0.301487000	-2.565916000
1	4.640710000	0.997767000	-2.267610000
1	4.064146000	-0.009520000	-3.591730000
1	2.900048000	0.836347000	-2.562829000
6	4.010182000	-1.173417000	0.871120000
1	5.101826000	-1.079767000	0.918172000
1	3.796572000	-2.236395000	0.715697000
6	3.393885000	-0.682680000	2.166569000
1	3.842104000	-1.193435000	3.026438000
1	3.613231000	0.385065000	2.284464000
1	3.773202000	0.551525000	-0.185118000
7	1.925196000	-0.797416000	2.123582000
6	1.260916000	-2.119008000	2.440025000
6	2.109007000	-2.982263000	3.364820000
1	2.341379000	-2.469689000	4.303574000
1	1.568355000	-3.896891000	3.622845000
1	3.053000000	-3.293068000	2.906551000
6	0.977620000	-2.834928000	1.123823000
1	0.315696000	-2.209413000	0.510294000
1	0.465307000	-3.789190000	1.287140000
1	1.879219000	-3.042282000	0.543863000
6	-0.083420000	-1.805394000	3.094822000
1	-0.730362000	-1.261719000	2.399091000
1	-0.590465000	-2.731680000	3.380309000
1	0.025195000	-1.199516000	4.000779000
1	1.528247000	-0.100044000	2.746227000
6	-0.727669000	4.033030000	-1.652219000
6	0.041599000	4.782258000	-0.728613000
6	-0.469864000	2.700308000	-1.888941000
1	-0.180260000	5.828514000	-0.538035000
1	-1.048106000	2.130927000	-2.615095000
6	1.078206000	4.186523000	-0.062639000
6	0.648438000	2.076587000	-1.286206000
6	1.447022000	2.821420000	-0.281003000
1	-1.535488000	4.532982000	-2.180662000
8	2.317437000	2.208002000	0.393685000
6	-2.338768000	-2.828682000	-1.579598000
6	-3.377942000	-3.400420000	-2.535316000
1	-3.300896000	-4.490759000	-2.567486000
1	-4.403768000	-3.166350000	-2.234380000
1	-3.235250000	-3.037933000	-3.558427000
6	-2.605067000	-3.295335000	-0.150770000
1	-3.604324000	-3.028842000	0.201818000
1	-2.523785000	-4.383731000	-0.074535000
1	-1.876247000	-2.862763000	0.545166000
6	-0.939422000	-3.263293000	-2.000085000
1	-0.735671000	-3.016907000	-3.048006000
1	-0.182139000	-2.766716000	-1.387079000
1	-0.806969000	-4.342123000	-1.885226000
1	-1.684635000	-1.051702000	-2.363651000
9	1.795958000	4.873183000	0.832344000
1	-0.297388000	1.429661000	0.875540000

5_{FF} +1, triplet

29	-1.506284000	-0.338706000	-0.437672000
29	1.102372000	0.612894000	0.639298000
8	-0.757840000	0.897353000	0.674404000
7	-2.422118000	-2.015125000	0.505889000
1	-1.925199000	-2.801770000	0.092197000
6	-3.784677000	-2.020815000	-0.068723000
1	-4.450579000	-2.708658000	0.465028000
1	-3.677381000	-2.396415000	-1.089277000
6	-4.408484000	-0.638950000	-0.120365000
1	-5.354948000	-0.705496000	-0.672411000
1	-4.646879000	-0.259469000	0.872745000
6	-2.285455000	-2.155722000	1.995357000
6	-2.923315000	-3.459801000	2.472330000
1	-2.494159000	-4.324676000	1.954076000
1	-2.743653000	-3.593367000	3.543892000
1	-4.006587000	-3.477386000	2.324356000
6	-2.908960000	-0.958773000	2.697551000
1	-2.562973000	-0.024196000	2.241971000
1	-2.611444000	-0.949799000	3.750525000
1	-4.002060000	-0.979139000	2.674706000
6	-0.793556000	-2.193033000	2.288223000
1	-0.312258000	-1.257810000	1.988966000
1	-0.615950000	-2.341194000	3.357837000
1	-0.299204000	-3.007966000	1.748219000
7	-3.488183000	0.305358000	-0.773624000
1	-3.447773000	0.040921000	-1.759673000
6	-3.867238000	1.751432000	-0.715962000
6	-5.273629000	1.953294000	-1.275569000
1	-6.041321000	1.497611000	-0.642548000
1	-5.501823000	3.021873000	-1.344659000

1	-5.366693000	1.528992000	-2.281758000
6	-2.848052000	2.471788000	-1.585211000
1	-1.843596000	2.305218000	-1.193504000
1	-3.034155000	3.549768000	-1.606390000
1	-2.872817000	2.105853000	-2.618865000
6	-3.780199000	2.250118000	0.719978000
1	-2.793277000	2.042019000	1.142466000
1	-3.940849000	3.332886000	0.747599000
1	-4.538233000	1.797151000	1.367370000
7	3.046927000	0.124590000	1.074163000
6	3.228042000	-0.896855000	2.172599000
6	2.361157000	-0.485146000	3.354422000
1	1.318739000	-0.356126000	3.039889000
1	2.382841000	-1.253603000	4.132973000
1	2.694205000	0.452035000	3.811209000
6	4.693841000	-0.999549000	2.581578000
1	5.334654000	-1.222381000	1.721235000
1	4.820331000	-1.811342000	3.304680000
1	5.063699000	-0.085126000	3.054367000
6	2.760182000	-2.231626000	1.614446000
1	3.348104000	-2.525419000	0.735900000
1	2.870055000	-3.018837000	2.365890000
1	1.710905000	-2.194211000	1.321180000
6	3.764928000	1.398111000	1.313009000
1	4.837706000	1.289166000	1.122650000
1	3.648157000	1.664747000	2.368392000
6	3.182030000	2.486143000	0.450382000
1	3.708456000	3.427980000	0.640965000
1	3.298941000	2.245650000	-0.610648000
1	3.441737000	-0.279334000	0.225313000
7	1.738595000	2.600367000	0.741954000
6	1.497484000	-3.624181000	-2.654525000
6	2.479834000	-2.909951000	-3.393891000
6	0.793281000	-3.033585000	-1.632179000
1	3.029524000	-3.391951000	-4.197787000
1	0.041066000	-3.584970000	-1.072641000
6	2.726898000	-1.607786000	-3.088154000
6	1.035383000	-1.685726000	-1.292426000
6	2.042543000	-0.904789000	-2.032422000
1	1.310636000	-4.663249000	-2.913458000
8	2.288491000	0.281493000	-1.722344000
9	-1.770473000	-1.208957000	-2.108302000
1	1.649486000	2.903359000	1.713402000
6	0.996675000	3.602338000	-0.110919000
6	0.733156000	2.968244000	-1.469725000
1	0.208116000	2.015001000	-1.356010000
1	0.115672000	3.628005000	-2.087239000
1	1.658614000	2.768021000	-2.016166000
6	-0.303534000	3.915303000	0.614400000
1	-0.107883000	4.405872000	1.575729000
1	-0.922551000	4.592284000	0.017742000
1	-0.868083000	2.999593000	0.800592000
6	1.804363000	4.887125000	-0.277688000
1	1.192834000	5.637976000	-0.788011000
1	2.098835000	5.307593000	0.690537000
1	2.707178000	4.743834000	-0.878167000
8	0.426820000	-1.102218000	-0.312632000
9	3.646338000	-0.905040000	-3.772331000

5$_{\mathbf{FCI}}$ +1, triplet

29	1.554583000	-0.419294000	0.479292000
29	-0.971079000	0.608734000	-0.748916000
8	0.851649000	0.955887000	-0.469604000
7	2.693121000	-1.901433000	-0.531350000
1	2.216951000	-2.762665000	-0.269731000
6	3.984638000	-1.888495000	0.187333000
1	4.756127000	-2.451090000	-0.351475000
1	3.805536000	-2.401307000	1.134720000
6	4.485480000	-0.484527000	0.473018000
1	5.371803000	-0.556736000	1.116362000
1	4.794476000	0.026573000	-0.437693000
6	2.721074000	-1.857160000	-2.031827000
6	3.477305000	-3.059960000	-2.592182000
1	3.053313000	-4.001678000	-2.226489000
1	3.409894000	-3.068827000	-3.684755000
1	4.540360000	-3.043325000	-2.336647000
6	3.344030000	-0.553048000	-2.506368000
1	2.902958000	0.297207000	-1.973876000
1	3.154103000	-0.417338000	-3.575470000
1	4.428327000	-0.529762000	-2.366633000
6	1.269929000	-1.914451000	-2.480757000
1	0.715772000	-1.056179000	-2.090312000
1	1.199191000	-1.902202000	-3.572494000
1	0.773967000	-2.821752000	-2.119487000
7	3.432574000	0.317736000	1.119096000
1	3.319853000	-0.049186000	2.065320000
6	3.708603000	1.784972000	1.241304000
6	5.024276000	2.011162000	1.982721000
1	5.887373000	1.656835000	1.410777000
1	5.173046000	3.080021000	2.167609000
1	5.027686000	1.502725000	2.953651000
6	2.550392000	2.356675000	2.044702000
1	1.607102000	2.158497000	1.532761000
1	2.652633000	3.438810000	2.171299000
1	2.496431000	1.906598000	3.043417000
6	3.756606000	2.423104000	-0.140795000
1	2.848520000	2.197991000	-0.705880000
1	3.831238000	3.510849000	-0.041080000
1	4.622479000	2.097019000	-0.725923000
7	-2.811310000	0.051321000	-1.479101000
6	-2.765763000	-0.843138000	-2.695530000
6	-1.803715000	-0.219684000	-3.698367000
1	-0.828826000	-0.022349000	-3.236459000
1	-1.640866000	-0.895288000	-4.543590000
1	-2.176535000	0.725131000	-4.106046000
6	-4.156382000	-1.009286000	-3.301136000
1	-4.869461000	-1.391328000	-2.562210000
1	-4.118055000	-1.730880000	-4.123126000
1	-4.555371000	-0.076213000	-3.708227000
6	-2.252848000	-2.198117000	-2.235264000
1	-2.923641000	-2.644784000	-1.491275000
1	-2.190950000	-2.887718000	-3.082227000
1	-1.261896000	-2.119500000	-1.790425000
6	-3.601481000	1.290036000	-1.680515000
1	-4.673277000	1.096796000	-1.568729000
1	-3.441114000	1.633886000	-2.706857000
6	-3.149971000	2.361273000	-0.723936000
1	-3.716591000	3.279042000	-0.914731000
1	-3.329343000	2.063736000	0.313043000
1	-3.269832000	-0.475757000	-0.736249000
7	-1.697739000	2.569190000	-0.900155000
6	-1.572696000	-3.770349000	2.288068000
6	-2.565444000	-3.048671000	3.003356000
6	-0.816281000	-3.173055000	1.309794000
1	-3.144175000	-3.549843000	3.774328000
1	-0.047098000	-3.722367000	0.772118000
6	-2.787567000	-1.729446000	2.724310000
6	-1.017295000	-1.813499000	0.994701000
6	-2.046568000	-1.025502000	1.704083000
1	-1.418724000	-4.817798000	2.534816000
8	-2.236902000	0.168870000	1.393042000
9	1.719655000	-1.533787000	2.006682000

1	-1.548682000	2.870698000	-1.865392000
6	-1.100112000	3.628999000	-0.007160000
6	-0.986241000	3.057684000	1.397514000
1	-0.419548000	2.123379000	1.382334000
1	-0.469746000	3.762898000	2.056428000
1	-1.963435000	2.843266000	1.839399000
6	0.273685000	3.956015000	-0.573785000
1	0.192679000	4.383047000	-1.581083000
1	0.781561000	4.692740000	0.056798000
1	0.888908000	3.056348000	-0.626296000
6	-1.958979000	4.891896000	-0.002857000
1	-1.429713000	5.690434000	0.526253000
1	-2.156268000	5.248308000	-1.020439000
1	-2.918639000	4.752521000	0.502772000
8	-0.340913000	-1.213515000	0.071807000
17	-3.996133000	-0.822197000	3.590713000

5$_{CIF}$ +1, singlet

29	1.517805000	0.034580000	-0.152914000
29	-1.454211000	0.428193000	-0.379539000
8	0.148504000	1.236970000	-0.161614000
7	2.841424000	-1.415576000	-0.503652000
1	2.486944000	-2.240433000	-0.018556000
6	4.096622000	-1.024919000	0.188679000
1	4.962536000	-1.559877000	-0.216890000
1	3.980281000	-1.329198000	1.232898000
6	4.322609000	0.471596000	0.124689000
1	5.151433000	0.736103000	0.792066000
1	4.601839000	0.798667000	-0.877941000
6	2.968293000	-1.805809000	-1.964515000
6	3.658335000	-3.160837000	-2.060302000
1	3.093121000	-3.933285000	-1.526580000
1	3.739528000	-3.473965000	-3.105873000
1	4.672079000	-3.138584000	-1.648983000
6	3.750309000	-0.749106000	-2.726288000
1	3.301084000	0.243408000	-2.608883000
1	3.739151000	-0.991188000	-3.792848000
1	4.798257000	-0.697608000	-2.417468000
6	1.558901000	-1.895460000	-2.534795000
1	1.043858000	-0.928677000	-2.489905000
1	1.595161000	-2.206754000	-3.583137000
1	0.950206000	-2.620952000	-1.988292000
7	3.089512000	1.184069000	0.517042000
1	2.953738000	1.028978000	1.520562000
6	3.097943000	2.669343000	0.269992000
6	4.463460000	3.270323000	0.597884000
1	5.248657000	2.934078000	-0.085402000
1	4.408780000	4.360548000	0.518755000
1	4.772577000	3.030377000	1.620975000
6	2.047247000	3.268721000	1.192193000
1	1.081372000	2.784944000	1.035951000
1	1.936427000	4.341139000	1.003940000
1	2.329805000	3.142609000	2.244466000
6	2.747490000	2.908564000	-1.190940000
1	1.774734000	2.464586000	-1.428404000
1	2.694701000	3.980637000	-1.406411000
1	3.496985000	2.478569000	-1.864594000
7	-3.160574000	-0.583472000	-0.891387000
6	-3.131733000	-1.354403000	-2.198972000
6	-2.485853000	-0.466309000	-3.252119000
1	-1.456509000	-0.206133000	-2.975312000
1	-2.443573000	-0.987735000	-4.213141000
1	-3.038081000	0.465239000	-3.414410000
6	-4.546185000	-1.759660000	-2.609630000
1	-5.042531000	-2.331923000	-1.818477000
1	-4.495860000	-2.400414000	-3.494879000
1	-5.181618000	-0.908364000	-2.865494000
6	-2.303855000	-2.615043000	-1.992567000
1	-2.691842000	-3.218839000	-1.163436000
1	-2.343298000	-3.232321000	-2.894494000
1	-1.258107000	-2.387687000	-1.789509000
6	-4.268671000	0.404229000	-0.808255000
1	-5.194049000	-0.073761000	-0.474725000
1	-4.449660000	0.803543000	-1.809900000
6	-3.878428000	1.535580000	0.099066000
1	-4.665533000	2.295363000	0.105185000
1	-3.722034000	1.198245000	1.126670000
1	-3.310709000	-1.263771000	-0.145867000
7	-2.602298000	2.092548000	-0.411944000
6	-0.143918000	-4.040989000	1.985123000
6	-0.978836000	-3.614845000	3.045498000
6	0.121386000	-3.231862000	0.899874000
1	-1.169827000	-4.256534000	3.900976000
1	0.758842000	-3.581888000	0.090590000
6	-1.549356000	-2.380564000	2.982875000
6	-0.469116000	-1.960576000	0.809222000
6	-1.369608000	-1.484549000	1.871691000
1	0.288313000	-5.037236000	2.031309000
8	-1.933474000	-0.370216000	1.787617000
1	-2.741396000	2.312858000	-1.401909000
6	-2.139675000	3.371195000	0.256333000
6	-1.644860000	3.041461000	1.655618000
1	-0.876237000	2.267804000	1.622617000
1	-1.218441000	3.936331000	2.120050000
1	-2.457971000	2.695930000	2.302110000
6	-1.043623000	3.953326000	-0.626718000
1	-1.444702000	4.231930000	-1.609051000
1	-0.635241000	4.860576000	-0.171415000
1	-0.231423000	3.240337000	-0.769495000
6	-3.293862000	4.372004000	0.325308000
1	-2.899419000	5.345203000	0.633304000
1	-3.773363000	4.507704000	-0.650749000
1	-4.060273000	4.092368000	1.052687000
8	-0.258732000	-1.166963000	-0.207308000
17	1.641748000	-0.608284000	2.773155000
9	-2.349957000	-1.946701000	3.967911000

VIII. References

[1] J. Serrano-Plana, I. Garcia-Bosch, R. Miyake, M. Costas, A. Company, *Angew. Chem. Int. Ed.* **2014**, *53*, 9608-9612.

[2] a) L. M. Mirica, M. Vance, D. J. Rudd, B. Hedman, K. O. Hodgson, E. I. Solomon, T. D. P. Stack, *Science* **2005**, *308*, 1890-1892; b) L. M. Mirica, M. Vance, D. J. Rudd, B. Hedman, K. O. Hodgson, E. I. Solomon, T. D. P. Stack, *J. Am. Chem. Soc.* **2002**, *124*, 9332-9333.

[3] E. R. Johnson, S. Keinan, P. Mori-Sánchez, J. Contreras-García, A. J. Cohen, W. Yang, *J. Am. Chem. Soc.* **2010**, *132*, 6498-6506.

ANNEX 2. Supporting information Chapter V

Supporting Information for

Well-Defined Aryl-Fe^{II} Complexes in Cross-Coupling and C-H Activation Processes

Carla Magallon, Oriol Planas, Steven Roldán-Gómez, Josep M. Luis, Anna Company,* Xavi Ribas*

†Institut de Química Computacional i Catàlisi (IQCC) and Departament de Química, Universitat de Girona, Campus Montilivi, Girona, E-17003, Catalonia, Spain

Table of contents

1. General considerations

Materials and methods

All reagents and solvents were purchased from Sigma Aldrich, Fisher Scientific or Fluorochem and used without further purification. NMR data concerning product identity were collected with a Bruker Ultrashield AVANCE III400 and a Bruker Ultrashield ASCEND Nanobay 400MHz (Serveis Tècnics, Universitat de Girona) spectrometers ($CDCl_3$, THF-d_8, CD_3CN and DMSO-d_6) and calibrated relative the residual protons of the solvent. All NMR experiments (^1H, $^{13}C^1$, COSY, HSQC, HMBC, NOESY and TOCSY) were recorded and processed using standard parameters and no more details are given, unless otherwise stated. Quantification of reaction yields through integration of peaks was performed using an internal standard (1,3,5-trimethoxybenzene). Preparation and handling of air-sensitive materials were carried out in a N_2 drybox with O_2 and H_2O concentrations < 1 ppm. High resolution mass spectra (HRMS) were recorded on a Bruker MicrOTOF-Q IITM instrument using ESI as ionization source or CMS (cryospray ionization, for low temperature experiments) at Serveis Tècnics University of Girona. IR Spectra (FTIR) were recorded on a FT-IR Alpha spectrometer from Bruker with a PLATINUM-ATR attachment using OPUS software to process the data. UV-vis spectroscopy was performed with an Agilent 8453 UV-vis spectrophotometer with 1 cm quartz cells. Low temperature control was achieved with a cryostat from Unisoku Scientific Instruments, Japan. Monocrystal X-Ray diffraction was performed with a Bruker D8 QUEST ECO diffractometer. Ligands $^{Me}L_H$ [2] and $^{tBu}L_{Br}$ [3-4] were synthesized following previously described procedures. For $^{Me}L_{Br}$ ligand, the synthesis was carried out following a slightly modified previously reported procedure.[2, 5-7]

2. Synthesis of ligand $^{Me}L_{Br}$

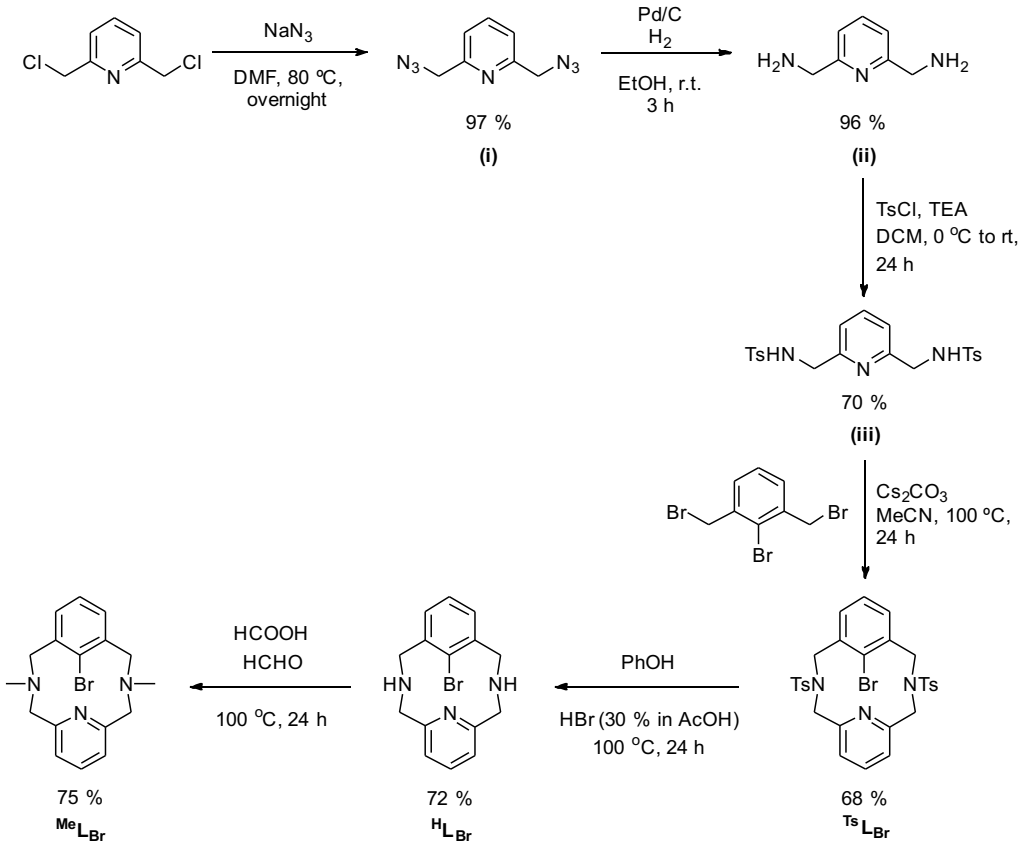

Scheme S1. Synthesis protocol for $^{Me}L_{Br}$ macrocyclic ligand.

2.1. Synthesis of 2,6-bis(azidomethyl)pyridine (i)

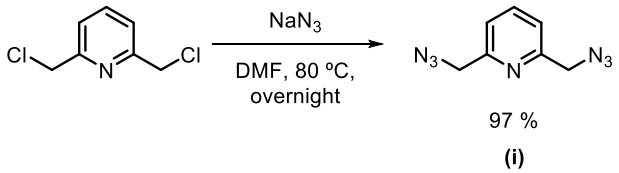

Scheme S2. Synthesis of 2,6-bis(azidomethyl)pyridine **(i)**.

Sodium azide (9.59 g, 146.0 mmol) and 2,6-bis(chloromethyl)pyridine (2.5 g, 14.0 mmol), were dissolved in DMF (130 ml) and refluxed overnight at 80 ºC. After that, the solvent was removed under reduced pressure, then the residue was extracted using water (4x60 ml) and EtOAc (100 ml). The organic layer was washed with brine (3x60 ml), dried over $MgSO_4$, filtered and the solvent was removed under vacuum to yield a colorless oil corresponding to 2,6-bis(azidomethyl)pyridine **(i)** (2.56 g, 13.5 mmol, 97 %).

^{1}H-NMR ($CDCl_3$, 400 MHz, 298 K) δ (ppm): 7.75 (t, J = 8 Hz, 1 H**a**), 7.30 (d, J = 8 Hz, 2 H**b**), 4.48 (s, 4 H**c**).

2.2. Synthesis of 2,6-bis(aminomethyl)pyridine (ii)

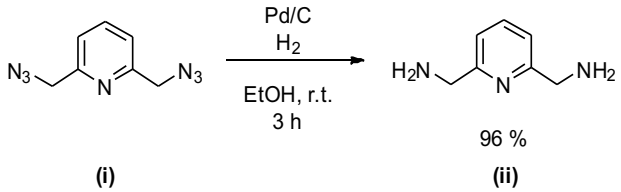

Scheme S3. Synthesis of 2,6-bis(aminomethyl)pyridine **(ii)**.

Under N_2, a 1 L round flask was charged with 2,6-bis(azidomethyl)pyridine (2.50 g, 13.2 mmol) and Pd/C (0.25 g, 10%) and then diluted in ethanol (280 ml). After that, the reaction was purged with H_2 to remove N_2. The reaction was left stirring at room temperature for 3 hours under a H_2 atmosphere. The reaction solution was filtered using a celite® pad and rinsed with ethanol (the solid was discarded) and the filtrates were dried under reduced pressure to yield an orange oil corresponding to 2,6-bis(aminomethyl)pyridine **(ii)** (1.75 g, 12.7 mmol, 96%).

^{1}H-NMR (CD_3OD, 400 MHz, 298 K) δ (ppm): 7.75 (t, J = 8 Hz, 1 H**a**), 7.28 (d, J = 8 Hz, 2 H**b**), 3.92 (s, 4 H**c**).

2.3. Synthesis of 2,6-bis(tosylaminomethyl)pyridine (iii)

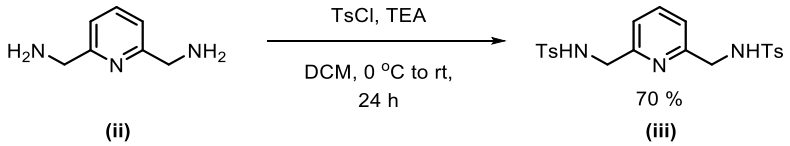

Scheme S4. Synthesis of 2,6-bis(tosylaminomethyl)pyridine **(iii)**.

Triethylamine (4.0 ml, 28.3 mmol) and 2,6-bis(aminomethyl)pyridine (1.85 g, 13.5 mmol) were dissolved in DCM (75 ml) and chilled to 0 °C. To this solution, TsCl (5.56 g, 28.6 mmol) diluted in DCM (100 ml) was added dropwise. During addition, the reaction mixture was vigorously stirred and maintained at 0 °C in an ice-bath. Upon completion of the addition, the reaction mixture was left stirring for an additional 24 hours allowing the solution to attain room temperature. The organic layer was washed with water and brine (2x175 ml each), dried with anhydrous $MgSO_4$, and solvent was removed under reduced pressure to yield a brownish oil. The crude product was purified by silica gel column chromatography (DCM:EtOAc, 95:5) to obtain 2,6-bis(tosylmethylamine)pyridine **(iii)** as white powder (4.21 g, 9.4 mmol, 70 %).

^{1}H-NMR ($CDCl_3$, 400 MHz, 298 K) δ (ppm): 7.72 (d, J = 12 Hz, 4 H**d**), 7.53 (t, J = 8 Hz, 1 H**a**), 7.25 (d, J = 12 Hz, 4 H**e**), 7.06 (d, J = 8 Hz, 2 H**b**), 5.50 (t, J = 6 Hz, 2 **N**H), 4.17 (d, J = 4 Hz, 4 H**c**), 2.41 (s, 6 H**f**).

2.4. Synthesis of $^{Ts}L_{Br}$

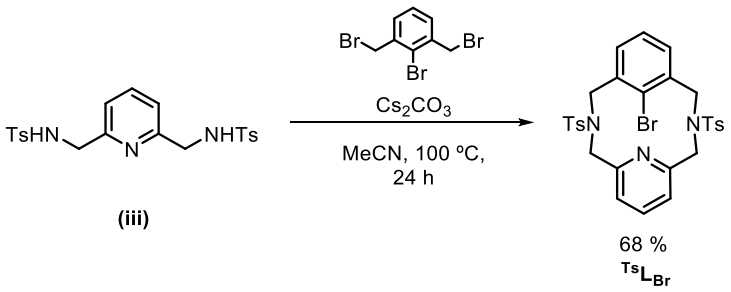

Scheme S5. Synthesis of $^{Ts}L_{Br}$.

Cs_2CO_3 (4.16 g, 12.6 mmol) and 2,6-bis(tosylaminomethyl)pyridine (2.60 g, 5.83 mmol) were dissolved in MeCN (150 ml) in a 500 ml 2-necked round-bottom flask. Once the mixture started refluxing, then a solution of 2-bromo-1,3-bis(bromomethyl)benzene (2.19 g, 6.25 mmol) in MeCN (100 ml) was slowly added dropwise. After heating at 100 °C for 24 hours, the crude was cooled down to room temperature and filtered. The filtrates were evaporated under reduced pressure and the resulting pale-brown solid was purified by recrystallization in $CHCl_3$:EtOH (1:3) in the freezer. $^{Ts}L_{Br}$ (2.5 g, 3.99 mmol, 68 % yield) was obtained.

^{1}H-NMR ($CDCl_3$, 400 MHz, 298 K) δ (ppm): 7.79 (d, *J* = 8 Hz, 4 H**d**), 7.39 (d, *J* = 8 Hz, 4 H**e**), 7.37 (t, *J* = 8 Hz, 1 H**i**), 7.21 (d, *J* = 8 Hz, 2 H**h**), 7.17 (d, *J* = 8 Hz, 2 H**b**), 6.86 (t, *J* = 8 Hz, 1 H**a**), 4.88 (d, *J* = 20 Hz, 2 H**g**), 4.83 (d, *J* = 20 Hz, 2 H**g**), 4.49 (d, *J* = 16 Hz, 2 H**c**), 3.92 (d, *J* = 16 Hz, 2 H**c**), 2.48 (s, 6 H**f**).

2.5. Synthesis of $^{H}L_{Br}$

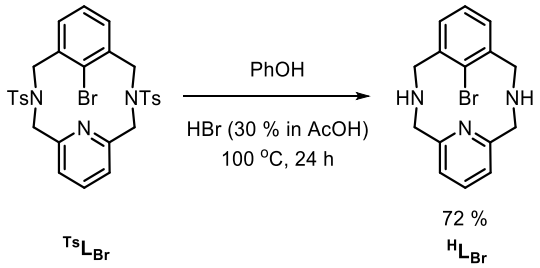

Scheme S6. Synthesis of $^{H}L_{Br}$.

$^{Ts}L_{Br}$ (2.10 g, 3.35 mmol) and phenol (7.88 g, 82.9 mmol) were added as solid to a 250 ml round-bottom flask, then HBr (30 wt % in AcOH, 100 ml) was added, the resulting solution was stirred and heat up to 100 °C for 24 hours. The crude was concentrated as much as possible and then 40 ml of H_2O were added. Extractions using $CHCl_3$ (3 x 40 ml) were performed. The organic layer was discarded, and the aqueous layer was basified with 50 % NaOH (~40 ml) until pH 14. After that, extractions with $CHCl_3$ (3 x 40 ml) were done again. The organic layer was then dried with $MgSO_4$, filtered and the solvent removed under reduced pressure. $^{H}L_{Br}$ (0.77 g, 2.42 mmol, 72 % yield) was obtained as a white solid.

^{1}H-NMR ($CDCl_3$, 400 MHz, 298 K) δ (ppm): 7.20 (t, *J* = 8 Hz, 1H**f**), 6.62 – 6.54 (m, 5H**a,b,e**), 4.60 (d, *J* = 16 Hz, 2H**d**), 4.22 (d, *J* = 16 Hz, 2H**d**), 3.81 (d, *J* = 16 Hz, 2H**c**), 3.58 (d, *J* = 16 Hz, 2H**c**), 1.66 (br.s, **N**H).

2.6. Synthesis of $^{Me}L_{Br}$

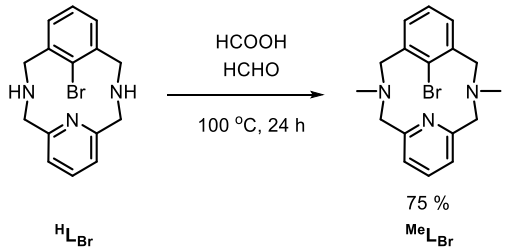

Scheme S7. Synthesis of $^{Me}L_{Br}$.

$^{H}L_{Br}$ (770 mg, 2.42 mmol), formaldehyde (58 ml, 774 mmol) and formic acid (10 ml, 242 mmol) were mixed in a 100 ml round-bottom flask and heat up to 100 °C for 24 hours. Then the crude mixture was cooled down to room temperature and the solvent was removed under reduced pressure. After that, NaOH(aq) 30% (50 ml) was added to the crude and the aqueous phase was extracted using DCM (3 x 40 ml). The organic layer was washed with NaOH(aq) 30% (50 ml) and the solvent removed under reduced pressure. The brownish solid obtained was further purified by stirring overnight in hexane. The colorless solution was decanted and dried to obtain $^{Me}L_{Br}$ (630 mg, 1.81 mmol, 75 % yield) as a white solid.

^{1}H-NMR ($CDCl_3$, 400 MHz, 298 K) δ (ppm): 7.15 (t, *J* = 8 Hz, 1H**g**), 6.78 (d, *J* = 8 Hz, 2H**f**), 6.69 (d, *J* = 8 Hz, 2H**b**), 6.61 (t, *J* = 8 Hz, 1H**a**), 4.26 (d, *J* = 12 Hz, 2H**e**), 3.94 (d, *J* = 12 Hz, 2H**e**), 3.65 (d, *J* = 12 Hz, 2H**c**), 3.53 (d, *J* = 12 Hz, 2H**c**), 2.70 (s, 6H**d**).
HR-ESI-MS: calcd. for $C_{17}H_{20}N_3Br$ $[M+H]^+$ 346.0913; exp 346.0914.

3. Synthesis of Iron(II) complexes: 1·Cl_2 and 1·Br_2

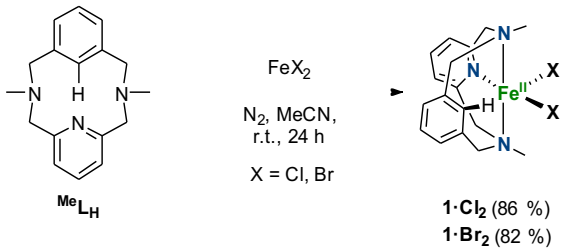

Scheme S8. Synthesis of **1·X_2** (X = Cl, Br).

In the glovebox, $^{Me}L_H$ (75.3 mg, 0.28 mmol) and $FeCl_2$ (36.1 mg, 0.28 mmol) were dissolved in dry MeCN (2.0 ml). The mixture was left stirring 24 hours at room temperature. After that, the mixture was filtered over celite®. Slow Et_2O diffusion over a concentrated solution in MeCN/DCM at room temperature afforded yellow crystals corresponding to $[(^{Me}L_H)Fe^{II}(Cl)_2]$ (94.9 mg, 0.24 mmol, 86 % yield).

^{1}H-NMR (CD_3CN, 400 MHz, 298 K) δ (ppm): 139.33, 90.10, 65.63, 41.64, 32.26, 18.29, -5.72, -7.82, -39.45.
Evans' method: μ_{eff} = 4.81 MB (3.92 unpaired electrons).
HR-ESI-MS: calcd. for $C_{17}H_{21}N_3FeCl^+$, $[M\text{-}Cl^-]^+$ 358.0768; exp 358.0787.
EA: calcd. for $C_{17}H_{21}N_3FeCl_2$, C 51.10, N 10.66, H 5.37 %; exp. C 51.74, N 10.40, H 5.09 %.

FT-IR (ATR) $\tilde{\upsilon}$ (cm^{-1}) = 2877 (C_{sp3}-H str), 1604 (C_{sp2}-C_{sp2} str), 1446 (C_{sp3}-H bend), 1001 (C_{sp3}-N str), 797 (Fe-Cl str).

The analogous procedure using $FeBr_2$ was followed for the synthesis of **1·Br₂** (82% yield). HR-ESI-MS: calcd. for $C_{17}H_{21}N_3FeBr^+$, $[M\text{-}Br^-]^+$ 402.0264; exp 402.0267.

4. Reactivity of 1·Cl₂ towards PhMgBr reagent

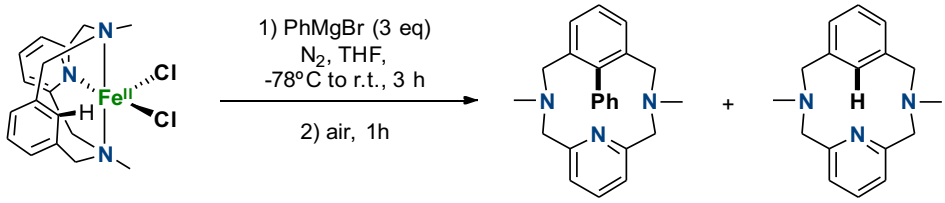

1·Cl₂ 66 % $^{Me}L_{Ph}$ 33 % $^{Me}L_{H}$

Scheme S9. Synthesis of $^{Me}L_{Ph}$.

In the Schlenk line, complex **1·Cl₂** (31.10 mg, 0.1 mmol) was dissolved in anhydrous THF (1.5 ml). The yellow suspension was stirred below -78 ºC and 3 equivalents of PhMgBr (236 µl of a 1.0 M solution in THF) were dropwise added via syringe. The mixture was left stirring below 78 ºC for 30 min and then the temperature was increased to 0 ºC for 1 hour. After that, the reaction was let to attain room temperature for 1 more hour and finally it was stirred under air for an additional hour. Next, concentrated HCl was added (together with the internal standard) and solvent was removed under reduced pressure. Ammonium hydroxide was used until pH >14 was reached, and extractions were performed using DCM. The product was dried over a $MgSO_4$ plug and the solvent was removed. The final organic product was purified by silica gel chromatography using DCM:MeOH:NH_3 (95:5:1) as eluent. $^{Me}L_{Ph}$ was obtained in a 66 % yield (^{1}H-NMR calculated using TMB as internal standard, 33% $^{Me}L_{H}$ corresponding to the protodemetallation product).

^{1}H-NMR ($CDCl_3$, 400 MHz, 298 K) δ (ppm): 9.46 (d, *J* = 8 Hz, 1H**f**), 7.63 (td, *J* = 8, 1.5 Hz, 1H**g**), 7.41 (tt, *J* = 7.4, 1.4 Hz, 1H**h**), 7.32 (td, *J* = 7.4, 1.2 Hz, 1H**i**), 7.22 (t, *J* = 7.7 Hz, 1H**p**), 6.87 (d, *J* = 7.5 Hz, 2H**b**), 6.76 (t, *J* = 7.0 Hz, 3H**j,o**), 6.66 (t, *J* = 7.5 Hz, 1H**a**), 3.71 (d, *J* = 4 Hz, 4H**m**), 3.45 (s, 4H**k**), 2.53 (d, 6H**l**).
^{13}C-NMR ($CDCl_3$, 400 MHz, 298 K) δ (ppm): 158.90 (C**n**), 144.53 (C**d**), 140.47 (C**e**), 135.76 (C**c**), 135.08 (C**p**), 132.78 (C**f**), 131.61 (C**j**), 130.51 (C**b**), 127.23 (C**g**), 127.19 (C**i**), 126.67 (C**h**), 126.43 (C**a**), 120.63 (C**o**), 64.64 (C**m**), 61.83 (C**k**), 49.00 (C**l**).
HR-ESI-MS: calcd. for $C_{23}H_{25}N_3$ $[M+H]^+$ 344.2121; exp 344.2133.

5. Synthesis of Aryl-Iron(II) complexes

5.1. Synthesis of 1^{Me}

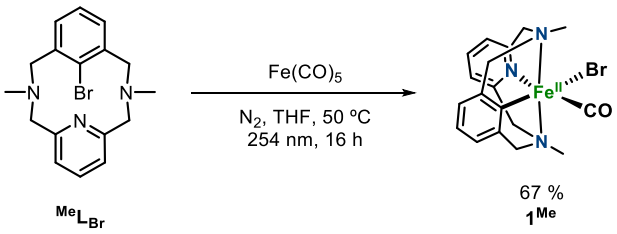

Scheme S10. Synthesis of $\mathbf{1^{Me}}$.

In the glovebox, $^{Me}\mathbf{L_{Br}}$ (53.2 mg, 0.15 mmol) and $Fe^0(CO)_5$ (20.21 µl, 0.15 mmol) were dissolved in dry THF (1.5 ml). The mixture was left stirring overnight at 50 °C under UV light (254 nm) in a 8-lamp photoreactor. After that, rapidly, vacuum was applied to remove any CO present in the atmosphere and to remove the solvent from the reaction mixture. The mixture was filtered over celite® and slow Et_2O diffusion over a concentrated solution in THF at room temperature afforded green crystals corresponding to $\mathbf{1^{Me}}$ (44.3 mg, 0.10 mmol, 67 %).

^{1}H-NMR (THF-d_8, 400 MHz, 298 K) δ (ppm): 7.57 (t, *J* = 8 Hz, 1H**j**), 7.16 (d, *J* = 4 Hz, 2H**i**), 6.47 (s br, 3H**a,b**), 4.06 (d, *J* = 16 Hz, 2H**d**), 3.60 (m, 4H**g,d**), 3.50 (d, *J* = 16 Hz, 2H**g**), 2.42 (s, 6H**e**).
^{13}C-NMR (THF-d_8, 400 MHz, 298 K) δ (ppm): 223.59 (C**k**), 183.99 (C**f**), 160.09 (C**h**), 146.86 (C**c**), 136.67 (C**j**), 120.89 (C**a**), 118.76(C**i**), 118.35(C**b**), 76.46 (C**g**), 72.30 (C**d**), 54.89 (C**e**).
HR-ESI-MS: calcd. for $C_{19}H_{20}N_3O_2Fe^+$ 378.0900; exp 378.0905. Calcd for $C_{18}H_{20}N_3OFe^+$ 350.0950; exp 350.0888.
EA: calcd. for $C_{18}H_{20}N_3OFeBr{\cdot}0.25C_{17}H_{21}N_3$, C 53.77, N 10.57, H 5.12 %; exp. C 54.05, N 10.10, H 5.14 %.
FT-IR (ATR) $\bar{\upsilon}$ (cm^{-1})= 2846 (C_{sp3}-H str), 1899 (Fe-CO str), 1447 (C_{sp3}-H bend), 1015 (C_{sp3}-N str), 761 (Fe-Br str).

5.2. Synthesis of 1^{H}

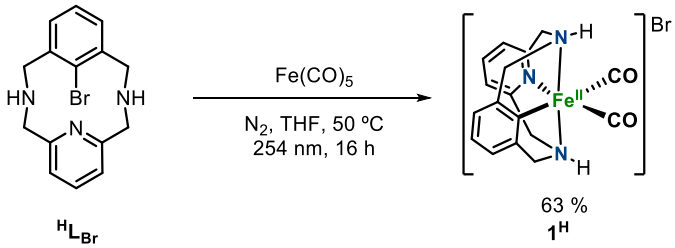

Scheme S11. Synthesis of $\mathbf{1^{H}}$.

In the glovebox, $^{H}L_{Br}$ (53.0 mg, 0.17 mmol) and $Fe^0(CO)_5$ (22.00 µl, 0.17 mmol) were dissolved in dry THF (1.5 ml). The mixture was left stirring overnight at 50 °C under UV light (254 nm). After that, a green solid was formed and vacuum was applied to remove any CO present in the atmosphere. The solvent was decanted-off and the solid residue was redissolved in MeCN. Slow pentane diffusion over a

concentrated solution in MeCN afforded pale green crystals corresponding to $\mathbf{1^{H}}$ (46.1 mg, 0.11 mmol, 63 %).

^{1}H-NMR (DMSO-d$_6$, 400 MHz, 298 K) δ (ppm): 7.76 (t, *J* = 8 Hz, 1H**i**), 7.33 (d, *J* = 8 Hz, 2H**h**), 6.94-6.87 (m, 3H**a,b**), 5.63 (br, 2H**N**H), 4.32 (d, *J* = 16 Hz, 2H**f**), 4.16 (m, 4H**f,d**), 3.93 (d, *J* = 16 Hz, 2H**d**).
^{13}C-NMR (DMSO-d$_6$, 400 MHz, 298 K): 184.73 (C**e**), 158.41 (C**g**), 145.70 (C**c**), 138.59 (C**i**), 124.43 (C**a**), 121.09 (C**b**), 120.23 (C**h**), 67.34 (C**d**), 64.47 (C**f**).
HR-ESI-MS: calcd. for $C_{16}H_{16}N_3OFe^+$ 322.0637; exp 322.0643.
EA: calcd. for $C_{17}H_{16}N_3O_2FeBr{\cdot}1.5H_2O$, C 44.67, N 9.19, H 4.19 %; exp. C 44.52, N 9.32, H 3.29 %.
FT-IR (ATR) $\tilde{\upsilon}$ (cm^{-1})= 3072 (N-H str), 2883 (C_{sp3}-H str), 2019 (Fe-CO str), 1963 (Fe-CO str), 1446 (C_{sp3}-H bend), 1234 (C_{sp3}-N str).

5.3. Synthesis of $\mathbf{1^{tBu}}$

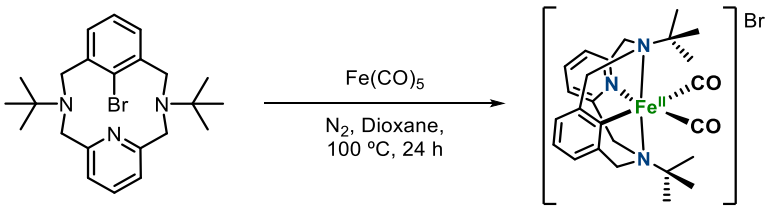

$^{tBu}\mathbf{L_{Br}}$ — 58 % — $\mathbf{1^{tBu}}$

Scheme S12. Synthesis of $\mathbf{1^{tBu}}$.

In the glovebox, $^{tBu}\mathbf{L_{Br}}$ (31.3 mg, 0.07 mmol) and $Fe^0(CO)_5$ (9.6 µl, 0.07 mmol) were dissolved in dry dioxane (1.0 ml). The mixture was left stirring for 24 hours at 100 °C. After that, rapidly, vacuum was applied to remove any CO present in the atmosphere and to remove the solvent from the reaction mixture. $\mathbf{1^{tBu}}$ (20.9 mg, 0.04 mmol, 58 %) was obtained as a greenish foam.

^{1}H-NMR (DMSO-d$_6$, 400 MHz, 298 K) δ (ppm): 8.02 (t, *J* = 8 Hz, 1H**g**), 7.52 (d, *J* = 8 Hz, 2H**f**), 7.08 (s, 3H**a,b**), 4.44 (d, *J* = 16 Hz, 2H**c**), 4.31 (d, *J* = 16 Hz, 2H**c**), 3.91 (d, *J* = 16 Hz, 2H**e**), 3.63 (d, *J* = 16 Hz, 2H**e**), 1.23 (br, 18H**d**).
HR-ESI-MS: calcd. for $C_{24}H_{32}N_3OFe^+$ 434.1890; exp 434.1905.

6. Reactivity of $\mathbf{1^{Me}}$ with phenyl Grignard (PhMgBr)

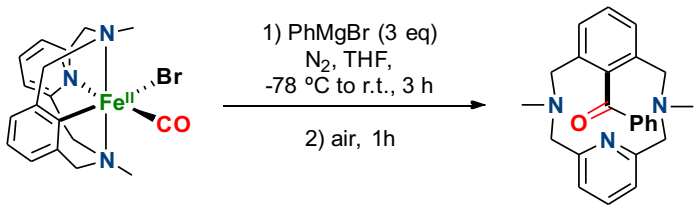

$\mathbf{1^{Me}}$ — 38 % — $^{Me}\mathbf{L_{Ph}}$

Scheme S13. Synthesis of $^{Me}\mathbf{L_{COPh}}$.

In the Schlenk line, complex $\mathbf{1^{Me}}$ (26.0 mg, 0.06 mmol) was dissolved in anhydrous THF (1.5 ml). The yellow suspension was stirred below -78 °C and 3 equivalents of PhMgBr (181 µl of a 1.0 M solution

inTHF) were dropwise added via syringe. The mixture was left stirring below 78 ºC for 30 min and then the temperature was increased to 0 ºC for 1 hour. After that, the reaction was let to attain room temperature for 1 more hour and finally it was stirred under air for an additional hour. Next, concentrated HCl was added (together with the internal standard) and solvent was removed under reduced pressure. Ammonium hydroxide was used until pH >14 was reached, and extractions were performed using DCM. The product was dried over a $MgSO_4$ plug and the solvent was removed. The final organic product was purified by silica gel chromatography using DCM:MeOH:NH_3 (95:5:1) as eluent. $^{Me}L_{COPh}$ was obtained in a 38 % yield (^{1}H-NMR calculated using TMB as internal standard, 7% $^{Me}L_{Ph}$ and 5% $^{Me}L_H$ corresponding to the protodemetallation product).

^{1}H-NMR ($CDCl_3$, 400 MHz, 298 K) δ (ppm): 7.58 (d, *J* = 8 Hz, 2H**g**), 7.47 (t, *J* = 8, Hz, 1H**i**), 7.35 (t, *J* = 8 Hz, 2H**h**), 7.14 (t, *J* = 8 Hz, 1H**o**), 6.85 (br, 3H**a,b**), 6.67 (d, *J* = 8 Hz, 2H**n**), 4.26 (br, 2H**l**), 3.68 (br, 2H**j**), 3.53 (br, 2H**l**), 3.31 (br, 2H**j**), 2.46 (s, 6H**k**).
^{13}C-NMR ($CDCl_3$, 400 MHz, 298 K) δ (ppm): 195.00 (C**e**), 158.12 (C**m**), 140.49 (C**f**), 139.00 (C**d**), 137.61 (C**c**), 135.32 (C**o**), 132.04 (C**i**), 130.46 (C**b**), 129.05 (C**g**), 128.75 (C**a**), 128.22 (C**h**), 121.58 (C**n**), 64.86 (C**l**), 61.38 (C**j**), 48.91 (C**k**).

HR-ESI-MS: calcd. for $C_{24}H_{25}N_3O$, $[M+H]^+$ 372.2071; exp 372.2070.

FT-IR (ATR) $\tilde{\upsilon}$ (cm^{-1})= 2922 (C_{sp3}-H str), 1672 (C_{sp2}-O str), 1447 (C_{sp3}-H bend), 1122 (C_{sp3}-N str).

7. Mechanistic insights

7.1. UV-vis monitoring of 1·Cl_2 with PhMgBr

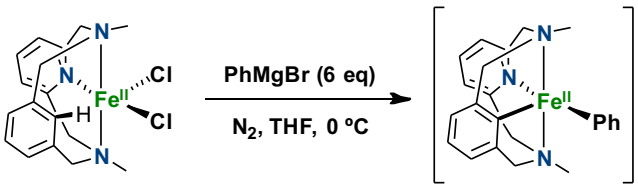

1·Cl_2 **C**

Scheme S14. Reaction of **1·Cl_2** towards PhMgBr monitored by UV-vis spectroscopy at 0 ºC.

A. A UV-vis cell was charged with 2.2 ml of a 0.5 mM solution of **1·Cl_2** in anhydrous THF prepared in the glovebox. The quartz cell was capped with a septum, taken out of the glovebox, and placed in a Unisoku thermostated cell holder designed for low-temperature experiments at 273 K. Once the thermal equilibrium was reached, a UV-vis spectrum of the starting complex was recorded. PhMgBr (10 equiv) was injected into the cell through the septum causing immediate formation of two bands at λ_{max} = 520 nm and λ_{max} = 635 nm corresponding to the generation of the green (C) species proposed (Figure S1). Maximum formation of such species is formed after ca. 13 min.

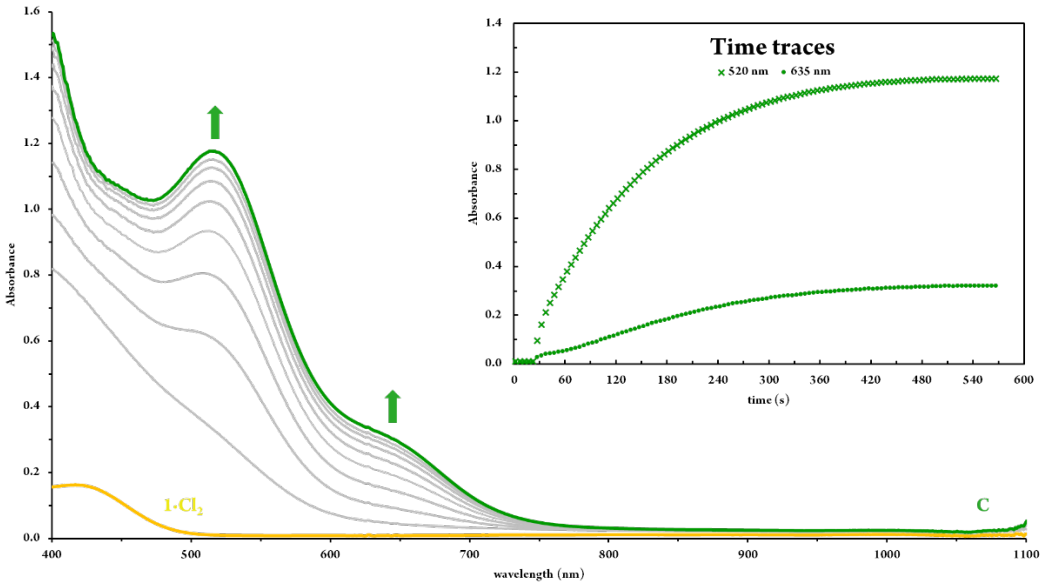

Figure S1. UV-vis spectra of the reaction of **1·Cl$_2$** (yellow) towards PhMgBr at 0 °C to form species **C** (green) with the corresponding bands at 520 and 635 nm.

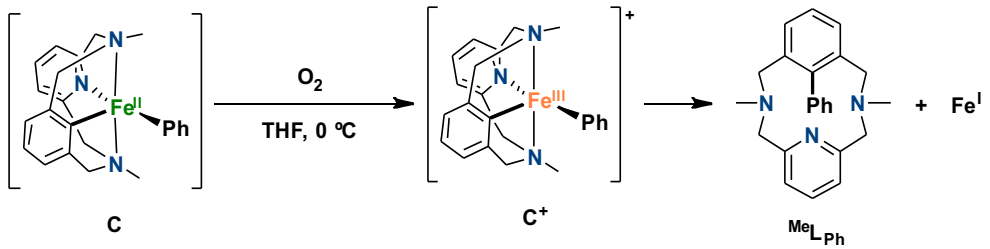

Scheme S15. Reaction of **C** towards dioxygen monitored by UV-vis spectroscopy at room temperature.

B. A first UV-vis spectrum of the new formed species **C** was recorded. Dioxygen was bubbled into the cell through the septum causing immediate decay of the two bands at λ_{max} = 520 nm and λ_{max} = 635 assigned to green species (C). Subsequent formation of new species was rapidly observed (< 20 seconds, orange trace in Figure S2a) corresponding to the putative C^+ species that rapidly evolves (< 10 seconds) to the final reaction mixture (purple trace in Figure S2a).

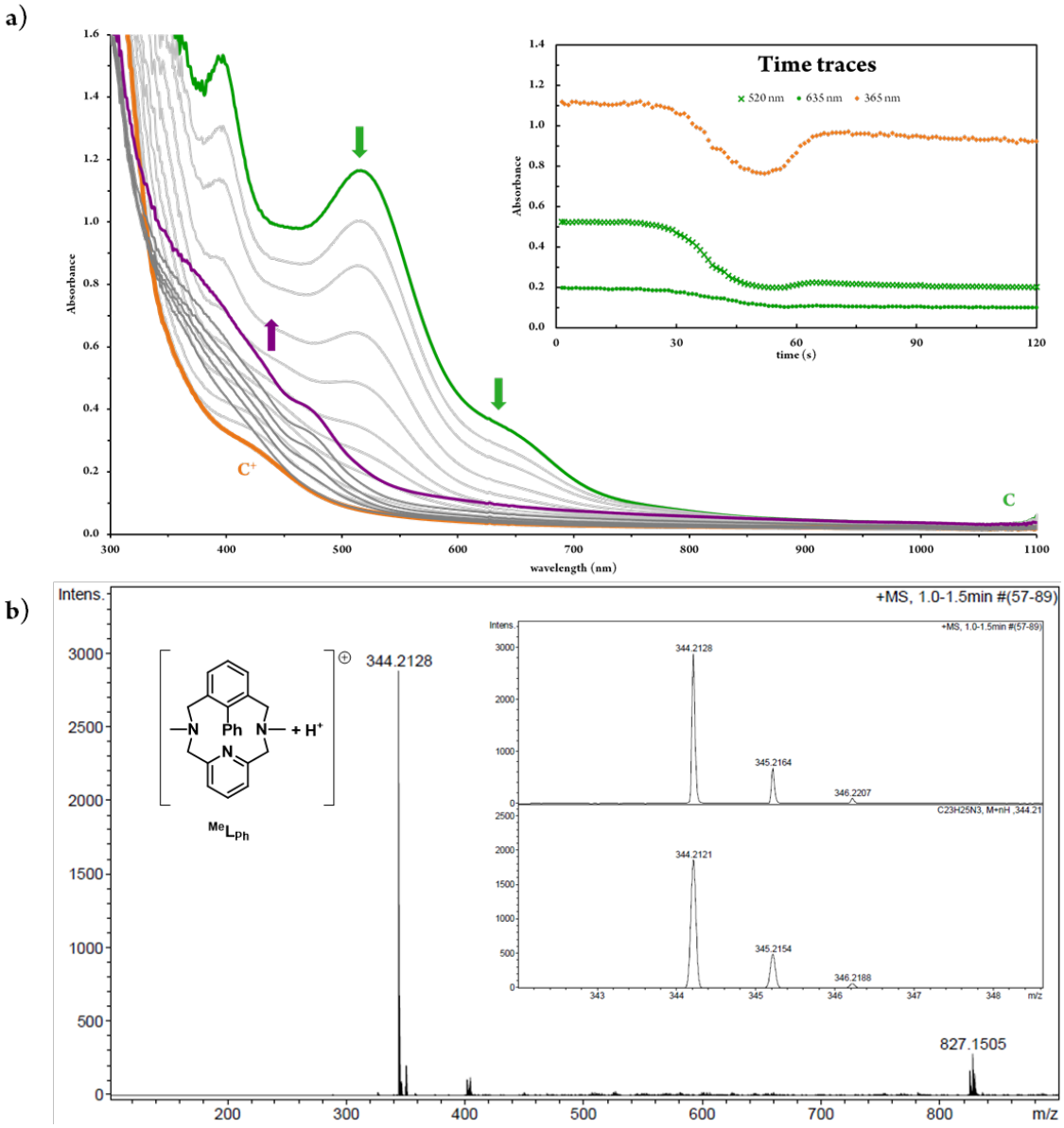

Figure S2. a)UV-vis spectra of the reaction of species **C** (green) towards dioxygen at 0 ºC. Decay of the bands at 520 and 635 nm to form unstable species **C**$^{+}$ (orange) and immediate formation of the new band at 365 nm (purple) corresponding to the final mixture. b) Cryo-HR-MS spectra of $^{Me}\mathbf{L}_{Ph}$. Inset: expanded view of the experimental peak at a m/z = 344.2128 corresponding to the monocharged $[C_{23}H_{25}N_3+H]^+$ (top) and the expanded view of the corresponding calculated spectrum for this molecular formula (bottom).

Attempts to characterize **C**$^{+}$ by Cryospray ionization/HR-MS

In order to perform HR-MS analysis, in a typical UV-vis experiment, the generation of species **C** was monitored at 0 ºC. Once it was fully formed the sample was cooled down to -45 ºC. On a separated vial containing DCM, previously cooled down and purged with dioxygen, an aliquot from the UV-vis cuvette was added and then it was immediately injected into the mass spectrometer equipped with cryospray ionization at -45 ºC. However, all attempts to gain information about the nature of species **C**$^{+}$ were unfruitful due to its extremely high reactivity. Nevertheless, a clean mass spectrum of the final coupling biaryl product $^{Me}\mathbf{L}_{Ph}$ was obtained (m/z = 344.2128 corresponding to $[C_{23}H_{25}N_3+H]^+$) as shown in Figure S2b.

7.2. Inert atmosphere work-up for 1·Cl$_2$ and 1^{Me} towards phenyl Grignard

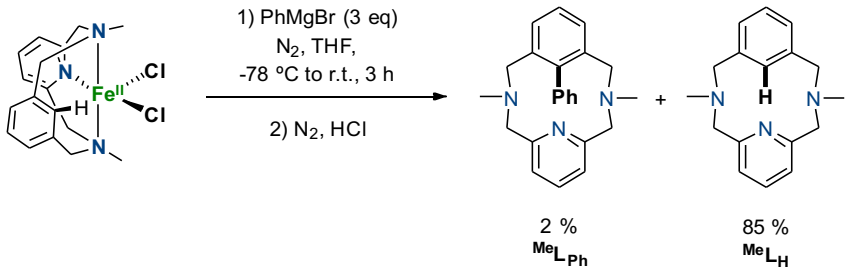

Scheme S16. Reaction of **1·Cl$_2$** towards PhMgBr in absence of oxidant.

In the Schlenk line, complex **1·Cl$_2$** (12.00 mg, 0.03 mmol) was dissolved in anhydrous THF (1.0 ml). The yellow suspension was stirred at -78 ºC and 3 equivalents of PhMgBr (120 µl of a 1.0 M solution in THF) were dropwise added via syringe. The mixture was left stirring at -78 ºC for 30 min and then the temperature was increased to 0 ºC for 1 hour. After that, the reaction was let to attain room temperature for 1 more hour. Next, concentrated HCl was added (together with the internal standard) under N_2 atmosphere and solvent was removed under vacuum. Ammonium hydroxide was used until pH >14 was reached, and extractions were performed using DCM. The product was dried over a $MgSO_4$ plug, filtered and the solvent was removed. **^{Me}L$_{Ph}$** was obtained in a 2% yield (^{1}H-NMR calculated using TMB as internal standard, 85% ^{Me}L$_H$ corresponding to the protodemetallation product).

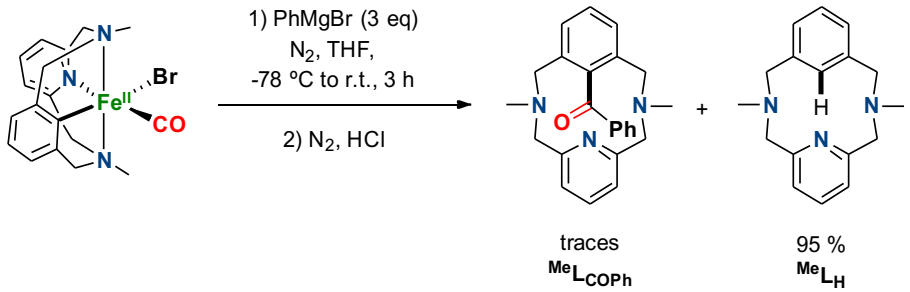

Scheme S17. Reaction of **1^{Me}** towards PhMgBr in absence of oxidant.

In the Schlenk line, complex **1^{Me}** (26.00 mg, 0.06 mmol) was dissolved in anhydrous THF (1.5 ml). The yellow suspension was stirred at -78 ºC and 3 equivalents of PhMgBr (181 µl of a 1.0 M solution in THF) were added dropwise. The mixture was left stirring at -78 ºC for 30 min and then the temperature was increased to 0 ºC for 1 hour. After that, the reaction was let to attain room temperature for 1 more hour. Next, concentrated HCl was added (together with the internal standard) under N_2 atmosphere and solvent was removed under vacuum. Ammonium hydroxide was used until pH >14 was reached, and extractions were performed using DCM. The product was dried over a $MgSO_4$ plug, filtered and the solvent was removed. **^{Me}L$_{COPh}$** was obtained in a trace amounts (^{1}H-NMR calculated using TMB as internal standard, 95% **^{Me}L$_H$** corresponding to the protodemetallation product).

7.3. Use of DCIB as oxidant for the reaction of 1·Cl_2 with PhMgBr

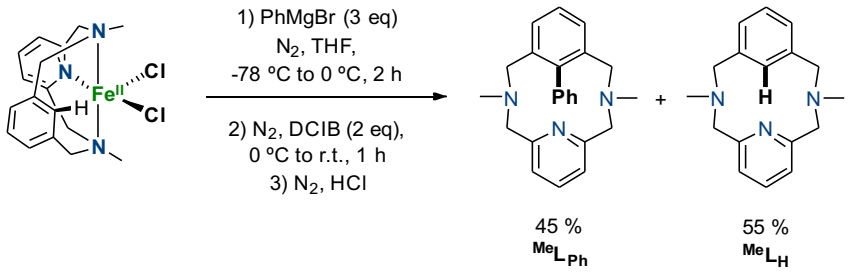

Scheme S18. Reaction of **1·Cl_2** towards PhMgBr in presence of DCIB as oxidant.

In a typical experiment, in the Schlenk line, complex **1·Cl_2** (32.90 mg, 0.08 mmol) was dissolved in anhydrous THF (1.6 ml). The yellow suspension was stirred below -78 ºC and 3 equivalents of PhMgBr (251 µl of a 1.0 M solution in THF) were added dropwise via syringe. The mixture was left stirring below 78 ºC for 30 min and then the temperature was increased to 0 ºC for 1.5 hour. After that, 2 equivalents of DCIB, 1,2-dichloroisobutane (20.4 µl), were added the reaction was let to attain room temperature for 1 more hour. Next, concentrated HCl was added (together with the internal standard) under N_2 atmosphere and solvent was removed under vacuum. Ammonium hydroxide was used until pH >14 was reached, and extractions were performed using DCM. The product was dried over a $MgSO_4$ plug, filtered and the solvent was removed. $^{Me}L_{Ph}$ was obtained in a 45% yield (^{1}H-NMR calculated using TMB as internal standard, 55% $^{Me}L_H$ corresponding to the protodemetallation product).

Noteworthy, addition of DCIB with the rest of reagents at the beginning of the reaction only afforded 9% yield of $^{Me}L_{Ph}$. Attempts to conduct a catalysis with DCIB under N_2 using 20 mol% of $FeCl_2$ were unfruitful, and only 4% yield of $^{Me}L_{Ph}$ was obtained.

7.4. Use of CO atmosphere for the reaction of 1·Cl_2 with PhMgBr

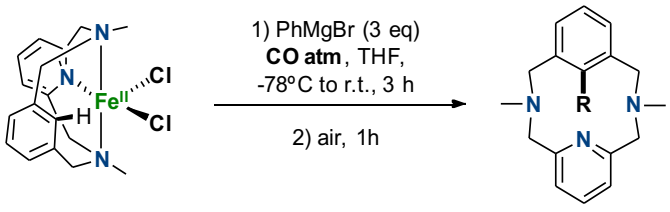

Scheme S19. Reaction of **1·Cl_2** towards PhMgBr in presence of CO atmosphere.

In a typical experiment, in the Schlenk line, complex **1·Cl_2** (38.90 mg, 0.10 mmol) was dissolved in anhydrous THF (1.5 ml). Once dissolved, a CO atm was provided. The yellow suspension was stirred below -78 ºC and 3 equivalents of PhMgBr (300 µl of a 1.0 M solution in THF) were added dropwise via syringe. The mixture was left stirring below 78 ºC for 30 min and then the temperature was increased to 0 ºC for 1 hour. After that, the reaction was let to attain room temperature for 1 more hour and finally it was stirred under air for an additional hour. Next, concentrated HCl was added (together with the internal standard) and solvent was removed under reduced pressure. Ammonium hydroxide was used until pH >14 was reached, and extractions were performed using DCM. The product was dried over a

$MgSO_4$ plug and the solvent was removed. $^{Me}L_{COPh}$ was obtained in less than a 3 % yield (^{1}H-NMR calculated using TMB as internal standard, >95 % $^{Me}L_H$ corresponding to the protodemetallation product and $^{Me}L_{Ph}$ was not observed).

7.5. Reaction of 1^{Me} with PhMgBr under photoirradiation (254 nm).

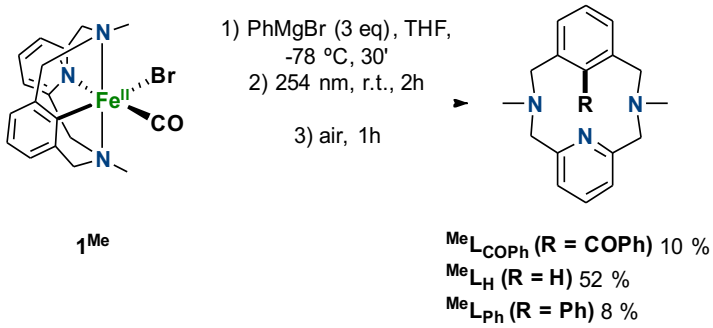

Scheme S20. Reaction of $\mathbf{1^{Me}}$ towards PhMgBr in presence of CO atmosphere.

In the Schlenk line, complex $\mathbf{1^{Me}}$ (31.9 mg, 0.07 mmol) was dissolved in anhydrous THF (1.5 ml). The solution was stirred at -78 ºC and 3 equivalents of PhMgBr (230 µl of a 1.0 M solution in THF) were added dropwise. The mixture was left stirring at -78 ºC for 30 min. After that, the mixture was irradiated with 254 nm lamps and then the temperature was increased to room temperature for 2 hours and opened to air for 1 more hour. Next, concentrated HCl was added (together with the internal standard) and solvent was removed under vacuum. Ammonium hydroxide was used until pH >14 was reached, and extractions were performed using DCM. The product was dried over a $MgSO_4$ plug, filtered and the solvent was removed. $^{Me}L_{Ph}$ was obtained in an 8 % yield (^{1}H-NMR calculated using TMB as internal standard, 52 % $^{Me}L_H$ corresponding to the protodemetallation product and a 10 % corresponding to $^{Me}L_{COPh}$).

7.6. Attempts to isolate species C' ([Fe^{II}(MeL)(Ph)(PPh_3)])

Attempt 1

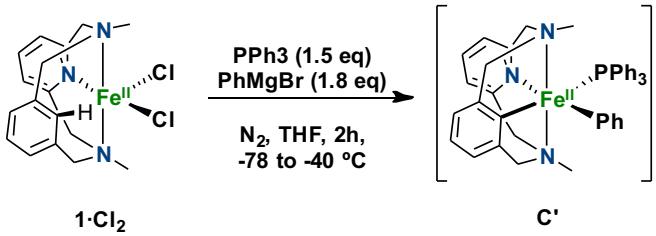

Scheme S21. Attempt to synthetize intermediate **C'** with PPh_3 at low temperature.

Under a nitrogen atmosphere, $\mathbf{1{\cdot}Cl_2}$ (37.4 mg, 0.09mmol) and THF (2 mL) were added to a 25 mL round bottom flask stirring at -78 ºC. Once thermal equilibrium was reached, PhMgBr (170 µL, 1.8 eq) was added dropwise and stirred for 30 min. Then temperature was increased to -40 ºC generating a red-colored solution. At this point 1.5 eq of PPh_3 (37.7 mg in 0.5 mL THF) were added. After that, the solution was cannulated at -40 ºC to remove the precipitate salts. Crystallization by slow diffusion over hexane at -40 ºC did not afford crystalline material but decomposition of the complex. HR-ESI-MS of the crude shows the 344.21 peak corresponding to the $^{Me}L_{Ph}$ biaryl formation via C-C reductive elimination.

Attempt 2

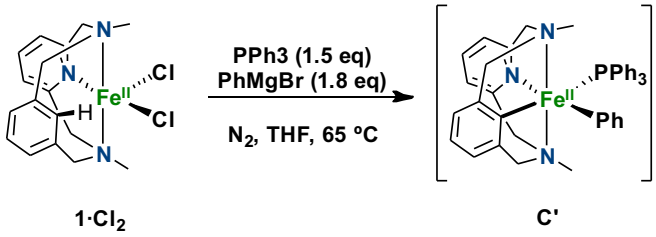

Scheme S22. Attempt to synthetize intermediate **C'** with PPh_3 at 65 °C.

Under a nitrogen atmosphere, **1·Cl₂** (35.4 mg, 0.09mmol), PPh_3 (35.4 mg, 1.5 eq) and THF (3 mL) were added to a 25 mL round bottom flask stirring at RT for 1 hour. Temperature was lowered to -78°C. Once thermal equilibrium was reached, PhMgBr (150 µL, 1.8 eq) was added to the vial containing the iron/PPh_3 solution dropwise generating a red-colored solution after heating at 65 °C for 2 hours. After that, temperature was lowered to -40°C and the solution was cannulated to remove the precipitate salts. Crystallization by slow diffusion over hexane at -40 °C. Compound **C'** was neither detected, although PPh_4^+ was detected by HR-ESI-MS, suggesting a P-C reductive elimination from **C'**.

8. Amine-to-amide CO insertion reactivity

8.1. Synthesis of $2^{Me}(CO)_H$ and $^{Me}L\text{-}CO_H$

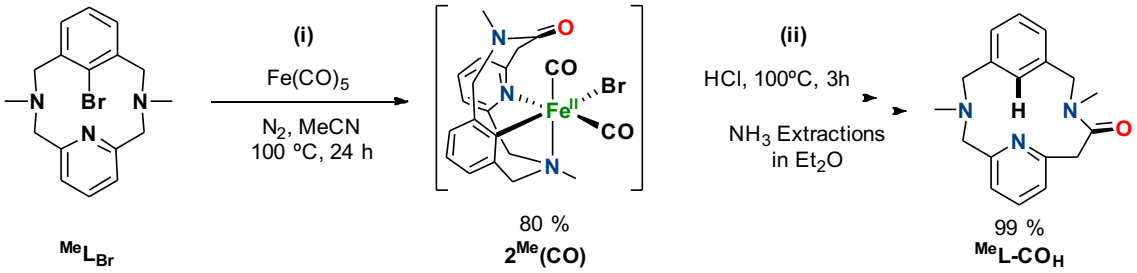

Scheme S23. (i) Synthesis of $2^{Me}(CO)$. **(ii)** Synthesis of $^{Me}L\text{-}CO_H$

(i) In the glovebox, $^{Me}L_{Br}$ (31.8 mg, 0.09 mmol) and $Fe^0(CO)_5$ (12.13 µl, 0.09 mmol) were dissolved in dry MeCN (1 ml). The mixture was left stirring for 24 hours at 100 °C. After that, rapidly, vacuum was applied to remove any CO present in the atmosphere and to remove the solvent from the reaction mixture. $2^{Me}(CO)$ was obtained as a red-brown foam (33.7 mg, 0.07 mmol, 80 %).

^{1}H-NMR (DMSO-d_6, 400 MHz, 298 K) δ (ppm): 7.50 (t, *J* = 8 Hz, 1H**k**), 7.47 (d, *J* = 8 Hz, 1H**c**), 7.40 (t, *J* = 8 Hz, 1H**b**), 7.29 (d, *J* = 8 Hz, 1H**a**), 7.17 (d, *J* = 8 Hz, 1H**j**), 6.95 (d, *J* = 8 Hz, 1H**l**), 4.27 (s, 2H**q**), 4.00 (s, 2H**f**), 3.50 (s, 2H**h**), 2.90 (s, 3H**p**), 2.28 (s, 2H**n**), 2.01 (s, 3H**g**).
^{13}C-NMR (DMSO-d_6, 400 MHz, 298 K) δ (ppm): 210.78 (C**s**), 168.23 (C**o**), 159.04 (C**i**), 157.22 (C**m**), 142.41 (C**r**), 137.82 (C**d**), 137.19 (C**k**), 131.11 (C**b**), 129.88 (C**e**), 128.37 (C**c**), 121.96 (C**a**), 121.64 (C**l**), 119.65 (C**j**), 63.42 (C**h**), 54.77 (C**f**), 51.26 (C**q**), 43.96 (C**g**), 29.37 (C**p**), 24.44 (C**n**).

FT-IR (ATR) $\bar{\upsilon}$ (cm^{-1})= 2837 (C_{sp3}-H str), 1890 (Fe-CO str), 1677 (C_{sp2}-O str), 1451 (C_{sp3}-H bend), 1024 (C_{sp3}-N str).

(ii) To **2^{Me}(CO)** HCl was added and the reaction was left stirring at 100 ºC for 3 additional hours. After that, NH_4OH was added until pH 14. Then extractions were performed in Et_2O. The organic layer was dried in $MgSO_4$, filtered and solvent was removed under vacuum to obtain **^{Me}L-CO$_H$** (99 %, NMR yield).

^{1}H-NMR ($CDCl_3$, 400 MHz, 298 K) δ (ppm): 7.68 (d, *J* = 8 Hz, 1H**a**), 7.53 (t, *J* = 8 Hz, 1H**l**), 7.47 (t, *J* = 8 Hz, 1H**b**), 7.39 (s, 1H**e**), 7.35 (d, *J* = 8 Hz, 1H**k**), 7.28 (d, *J* = 8 Hz, 1H**c**), 6.98 (d, *J* = 8 Hz, 1H**m**), 4.32 (s, 2H**f**), 4.27 (s, 2H**q**), 3.77 (s, 2H**i**), 3.16 (s, 3H**g**), 2.53 (s, 2H**o**), 2.29 (s, 3H**p**).
^{13}C-NMR ($CDCl_3$, 400 MHz, 298 K) δ (ppm): 169.21 (C**h**), 159.37 (C**j**), 157.66 (C**n**), 141.50 (C**d**), 138.88 (C**r**), 136.72 (C**l**), 130.94 (C**b**), 130.17 (C**c**), 128.88 (C**a**), 121.44 (C**m**), 121.06 (C**e**), 119.93 (C**k**), 63.85 (C**i**), 55.45 (C**q**), 51.60 (C**f**), 42.59 (C**p**), 29.45 (C**g**), 24.62 (C**o**).
HR-ESI-MS: calcd. for $C_{18}H_{21}N_3O$, $[M+H]^+$ 296.1757; exp 296.1775. (See Figure S57).

FT-IR (ATR) $\tilde{\upsilon}$ (cm^{-1})= 2942 (C_{sp3}-H str), 1679 (C_{sp2}-O str), 1453 (C_{sp3}-H bend), 1044 (C_{sp3}-N str).

8.2. Mechanistic insights

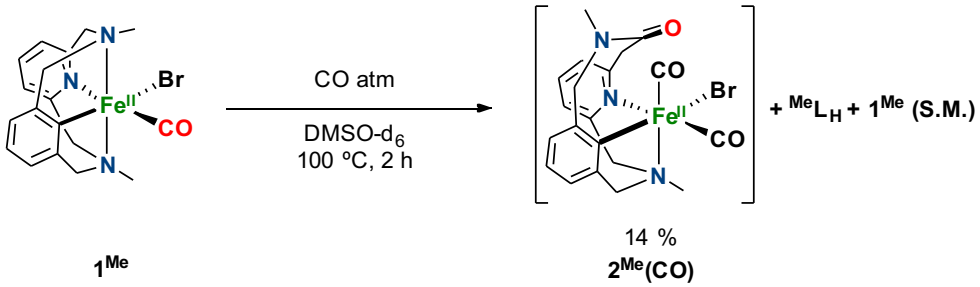

Scheme S24. Synthesis of **2^{Me}(CO)** starting from the well-defined **1^{Me}**.

In the glovebox, **1^{Me}** (19.6 mg, 0.05 mmol) were dissolved in dry DMSO-d_6 (1 ml). The mixture was left stirring for 2 hours at 100 ºC under a CO atmosphere. After that, rapidly, vacuum was applied to remove any CO present in the atmosphere and the reaction crude was checked by ^{1}H-NMR. After only 2 hours of reaction a 14 % of **2^{Me}(CO)** could be observed together with a 14 % of **^{Me}L$_H$** (protodemetallation by-product) and 71 % of starting complex (**1^{Me}**).

8.3. Amine-to-amide CO insertion reactivity using ^{H}L$_{Br}$

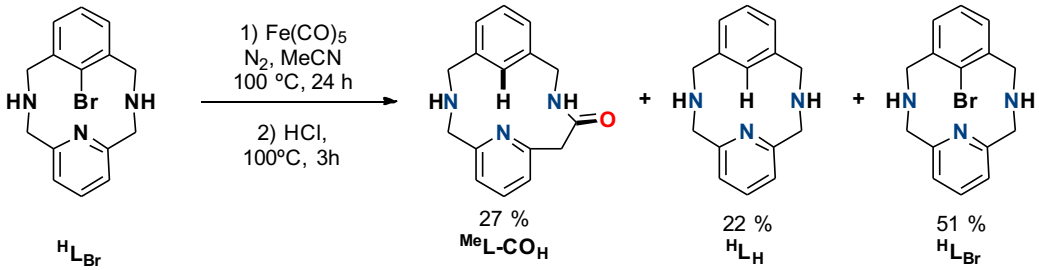

Scheme S25. Synthesis of **^{H}L-CO$_H$**

In the glovebox, $^{H}L_{Br}$ (32.6 mg, 0.10 mmol) and $Fe^{0}(CO)_5$ (13.48 µl, 0.10 mmol) were dissolved in dry MeCN (1 ml). The mixture was left stirring for 24 hours at 100 ºC. After that, HCl was added and the reaction was left stirring at 100 ºC for 3 additional hours. Then, NH_4OH was added until pH 14 and extractions were performed in Et_2O. The organic layer was dried in $MgSO_4$, filtered and solvent was removed under vacuum to obtain $^{H}L\text{-}CO_H$ (27 %, ^1H NMR yield). HR-ESI-MS: calcd. for $C_{16}H_{17}N_3O$ $[M+H]^+$: 268.1450; exp: 268.1446 (See Figure S3).

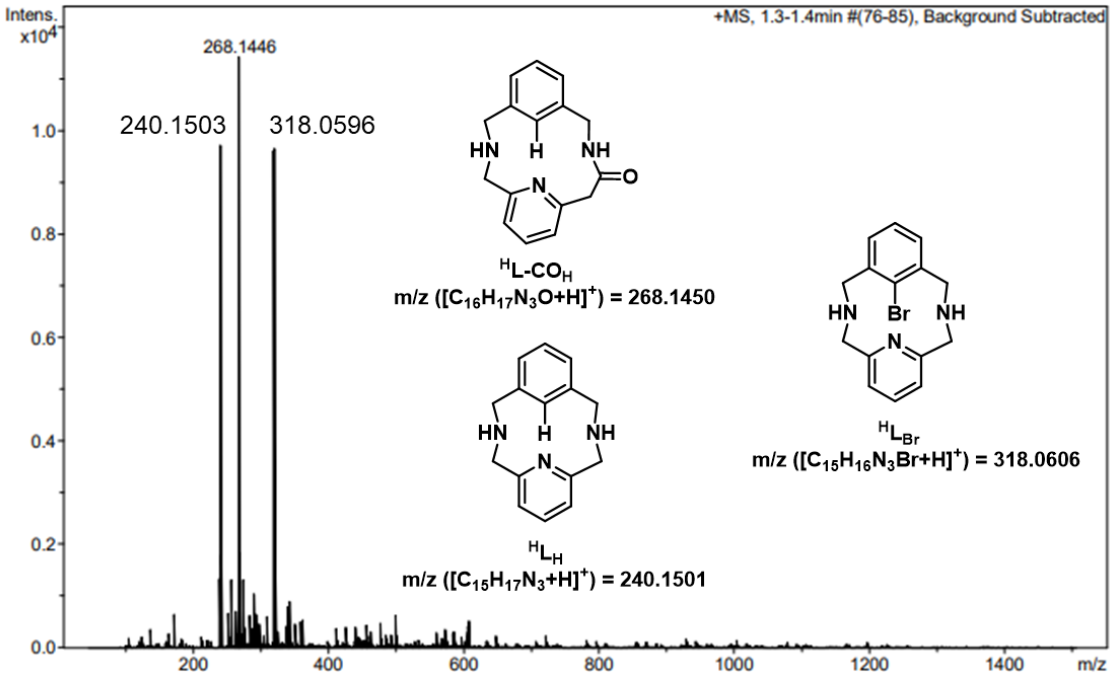

Figure S3. HR-ESI-MS of the reaction crude for the synthesis of $^{H}L\text{-}CO_H$. Three main peaks could be observed. The experimental peak at m/z = 268.1446 with a mass value and an isotopic pattern fully consistent with the monocharged $[C_{16}H_{18}N_3O]^+$. The experimental peak at m/z = 240.1503 with a mass value and an isotopic pattern fully consistent with the monocharged $[C_{15}H_{18}N_3]^+$. The experimental peak at m/z = 318.0596 with a mass value and an isotopic pattern fully consistent with the monocharged $[C_{15}H_{17}N_3Br]^+$.

9. Spectroscopic characterization

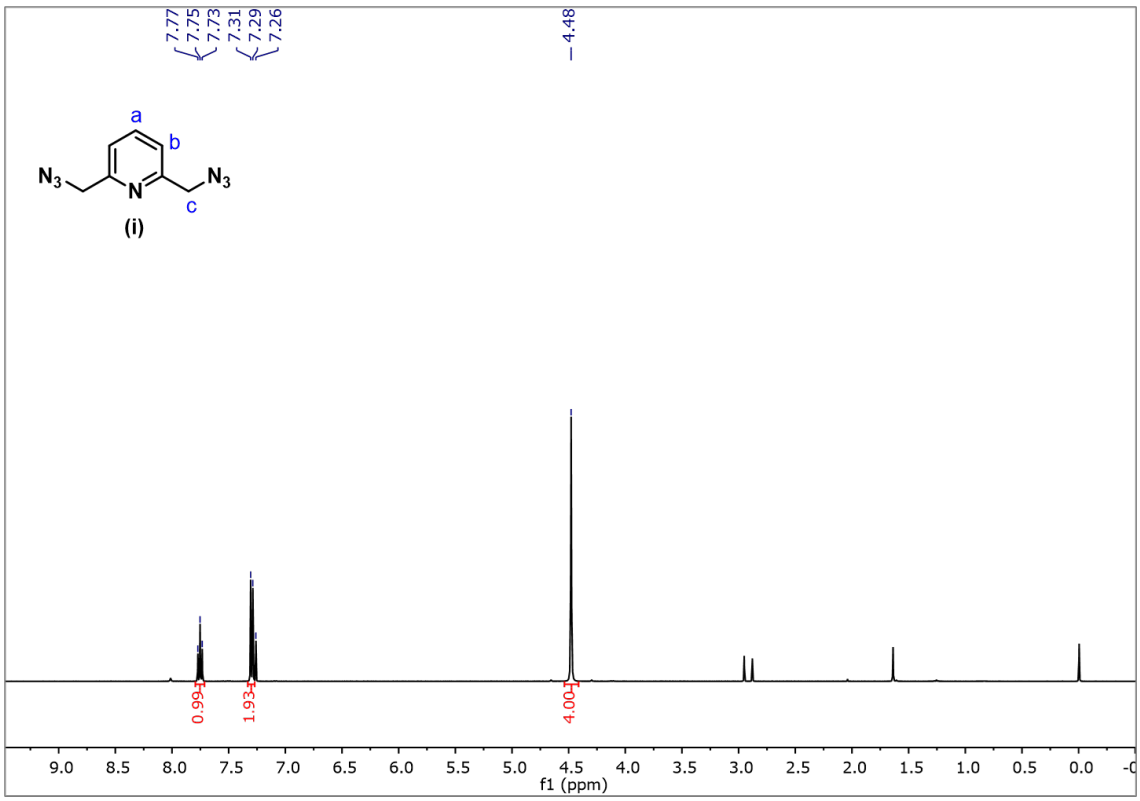

Figure S4. ^{1}H-NMR spectrum of **(i)** in $CDCl_3$ at room temperature (400 MHz).

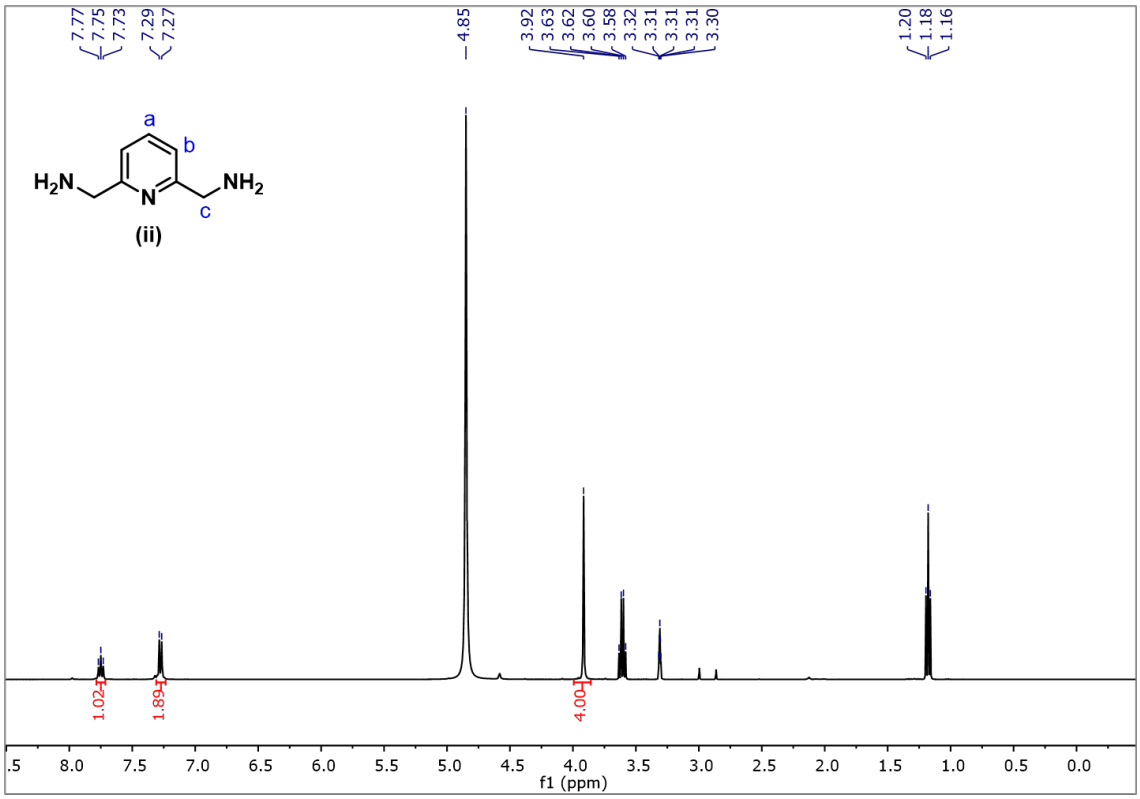

Figure S5. ^{1}H-NMR spectrum of **(ii)** in CD_3OD at room temperature (400 MHz).

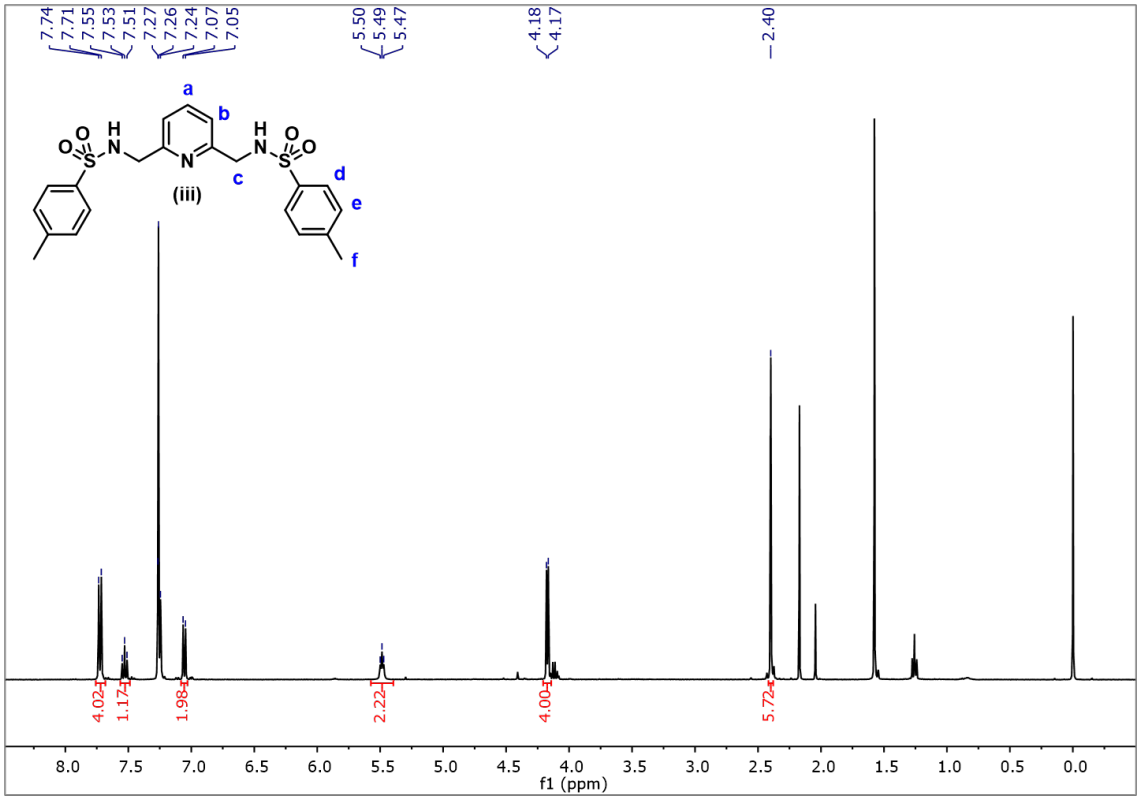

Figure S6. ^{1}H-NMR spectrum of **(iii)** in $CDCl_3$ at room temperature (400 MHz).

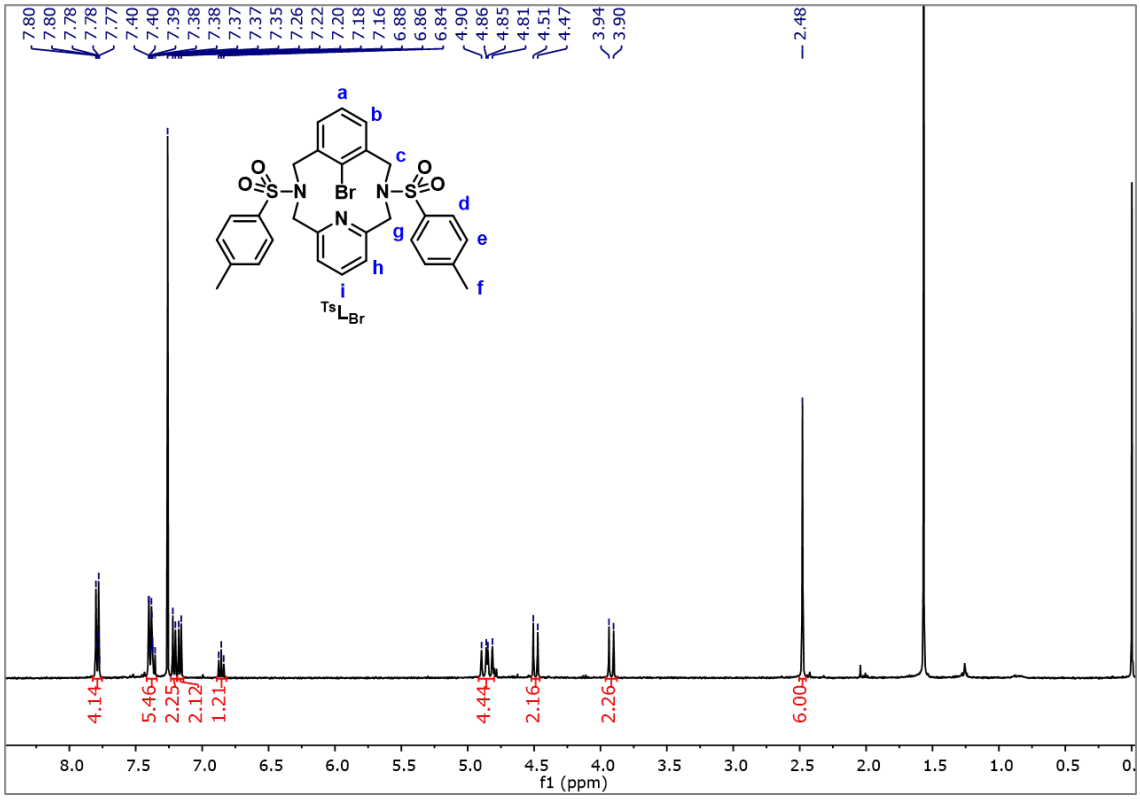

Figure S7. ^{1}H-NMR spectrum of $^{Ts}L_{Br}$ in $CDCl_3$ at room temperature (400 MHz).

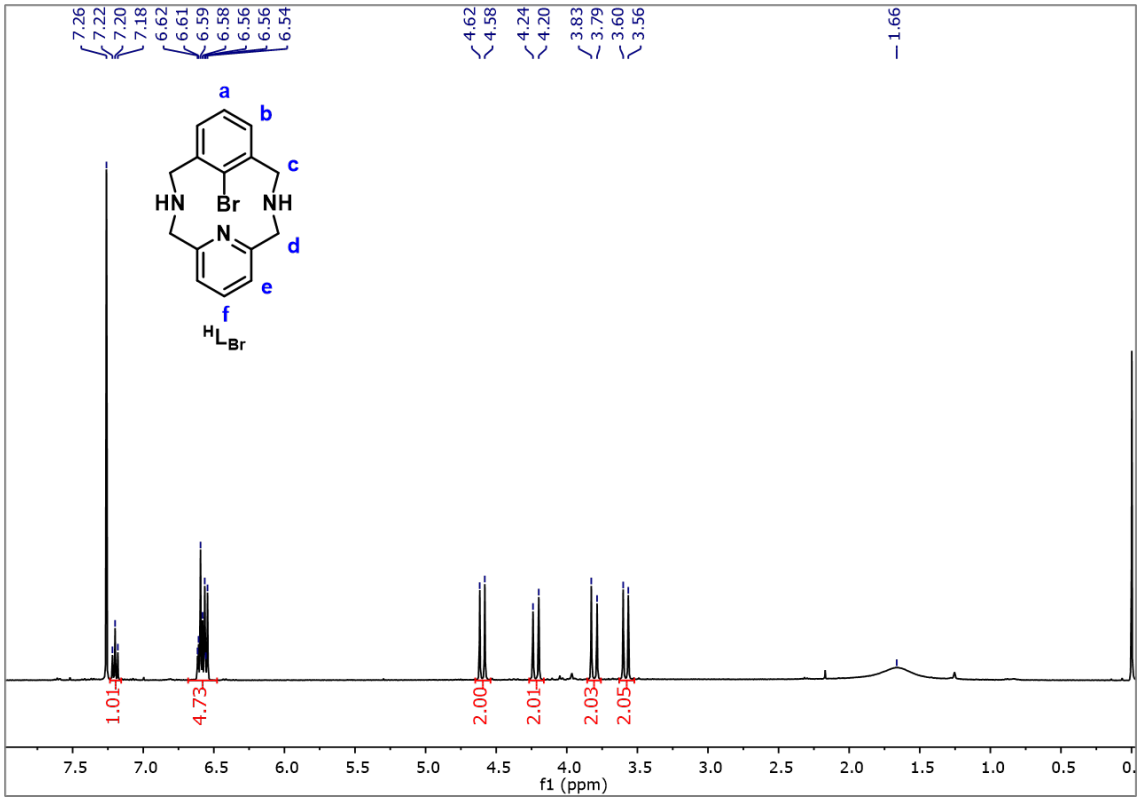

Figure S8. ^{1}H-NMR spectrum of $^{H}L_{Br}$ in $CDCl_3$ at room temperature (400 MHz).

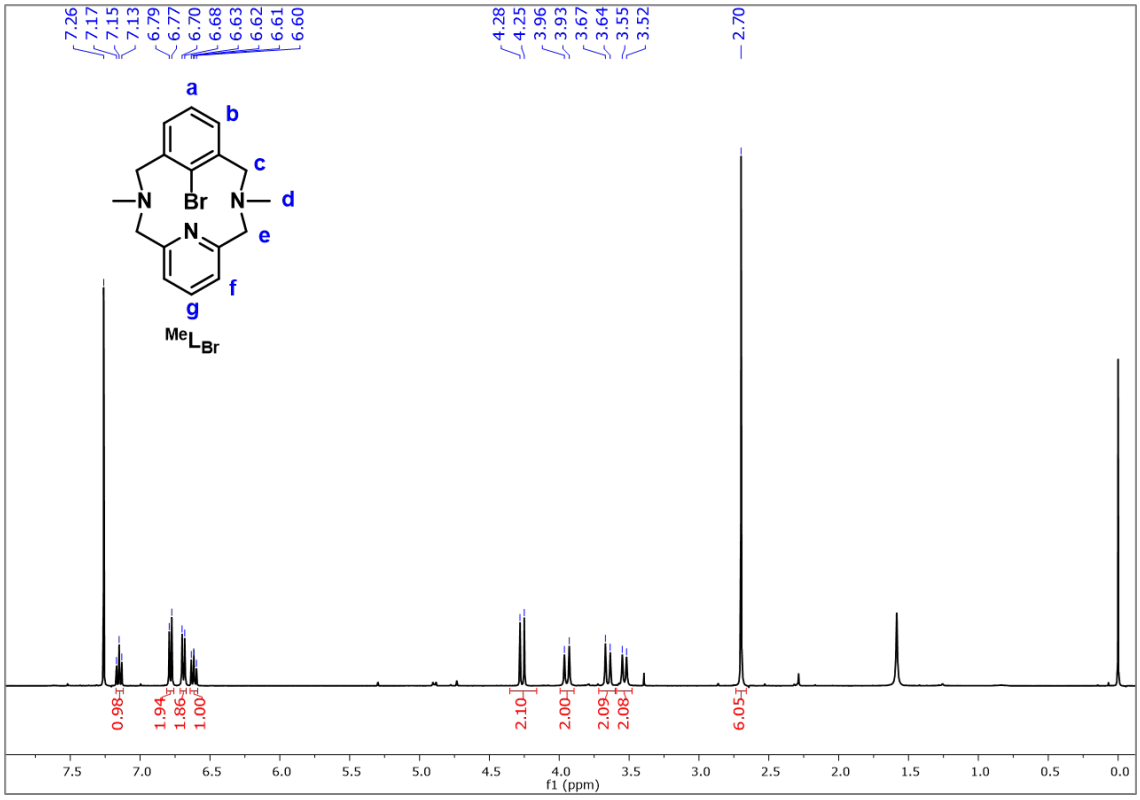

Figure S9. ^{1}H-NMR spectrum of $^{Me}L_{Br}$ in $CDCl_3$ at room temperature (400 MHz).

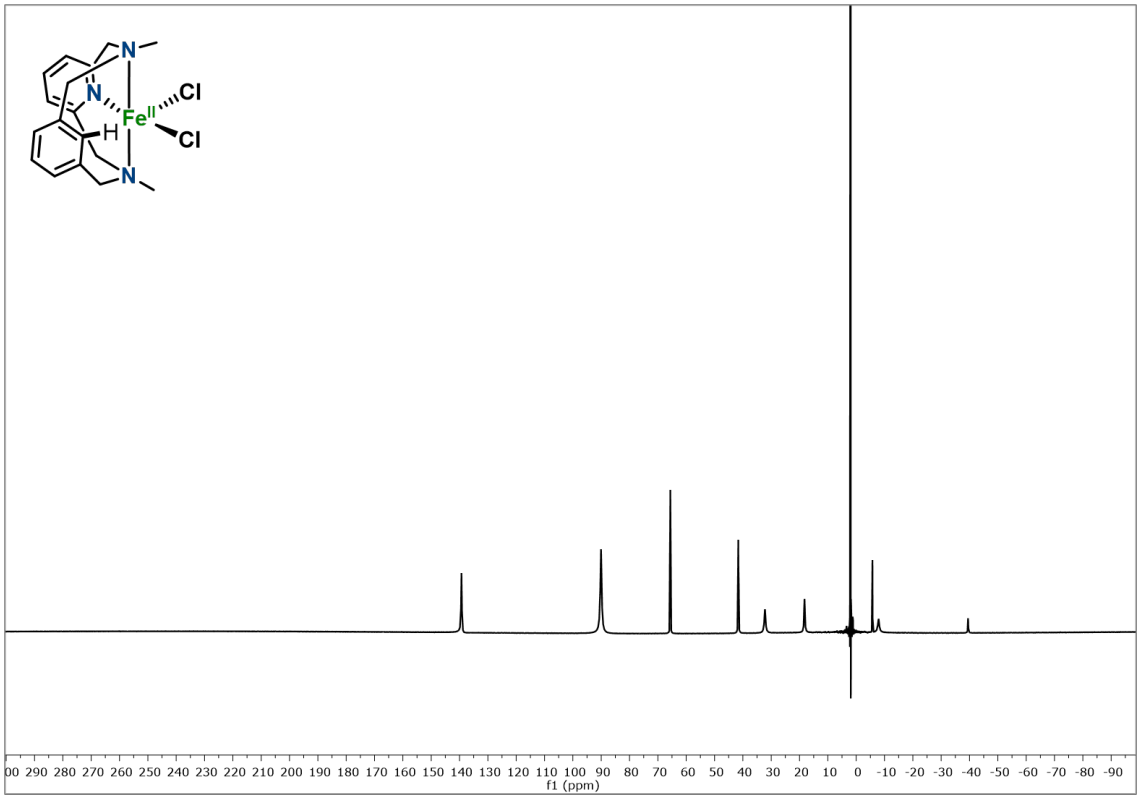

Figure S10. Paramagnetic ^{1}H-NMR spectrum of **1·Cl$_2$** in CD_3CN at room temperature (400 MHz).

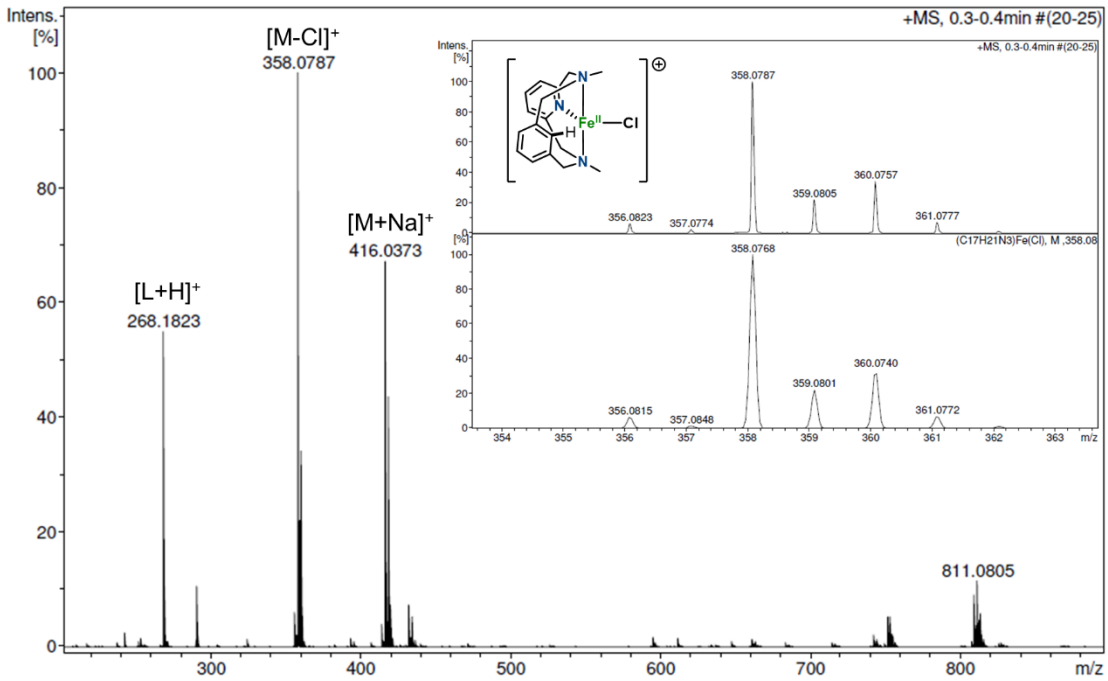

Figure S11. HR-ESI-MS of **1·Cl$_2$**. Inset: expanded view of the experimental peak at a m/z = 358.0787 with a mass value and an isotopic pattern fully consistent with the peak corresponding to the monocharged $[M\text{-}Cl^-]^+$ (top) and the expanded view of the corresponding calculated spectrum for this molecular formula (bottom). (M = $C_{17}H_{21}N_3FeCl_2$; L = $C_{17}H_{21}N_3$).

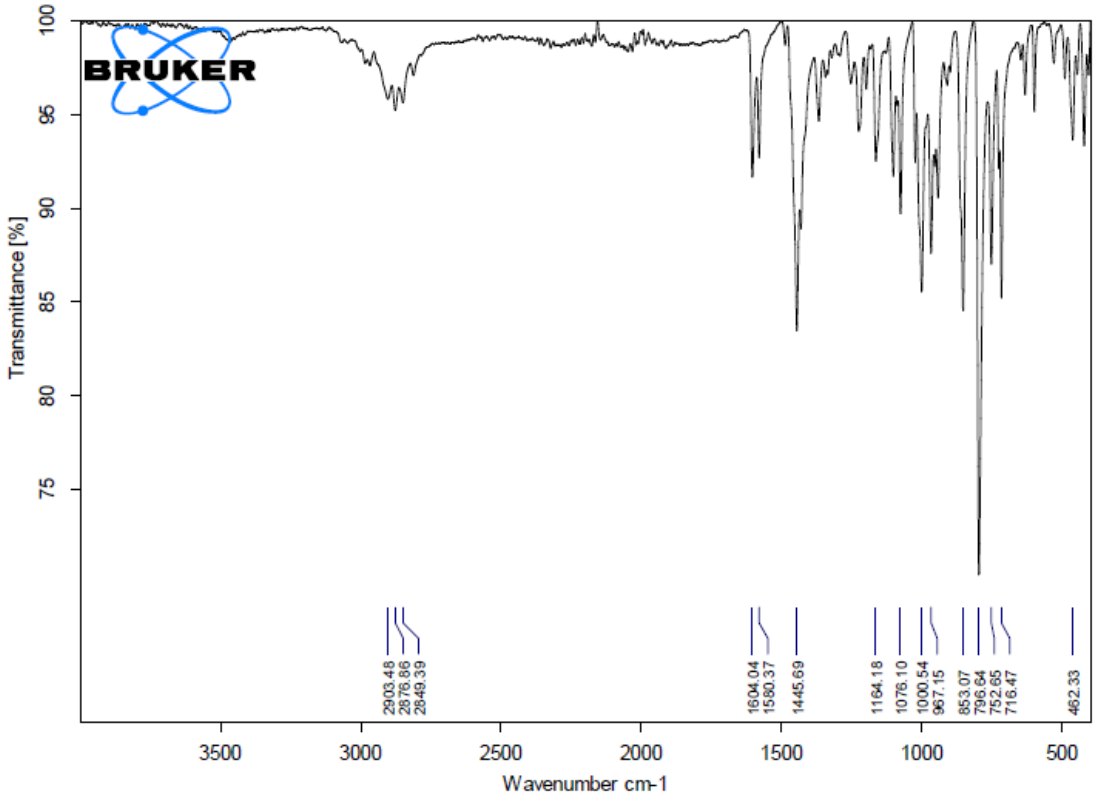

Figure S12. ATR-FT-IR spectrum of **1·Cl$_2$** at room temperature.

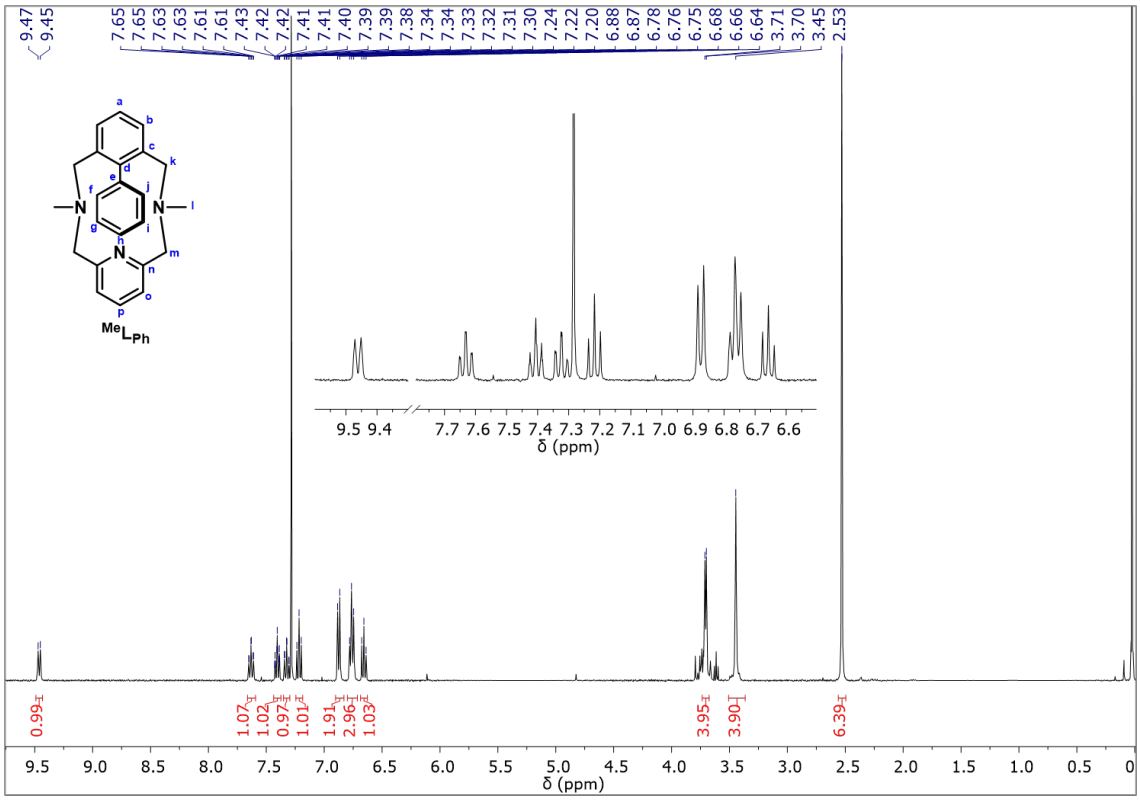

Figure S13. ^{1}H-NMR spectrum of ^{Me}**L$_{Ph}$** in $CDCl_3$ at room temperature (400 MHz).

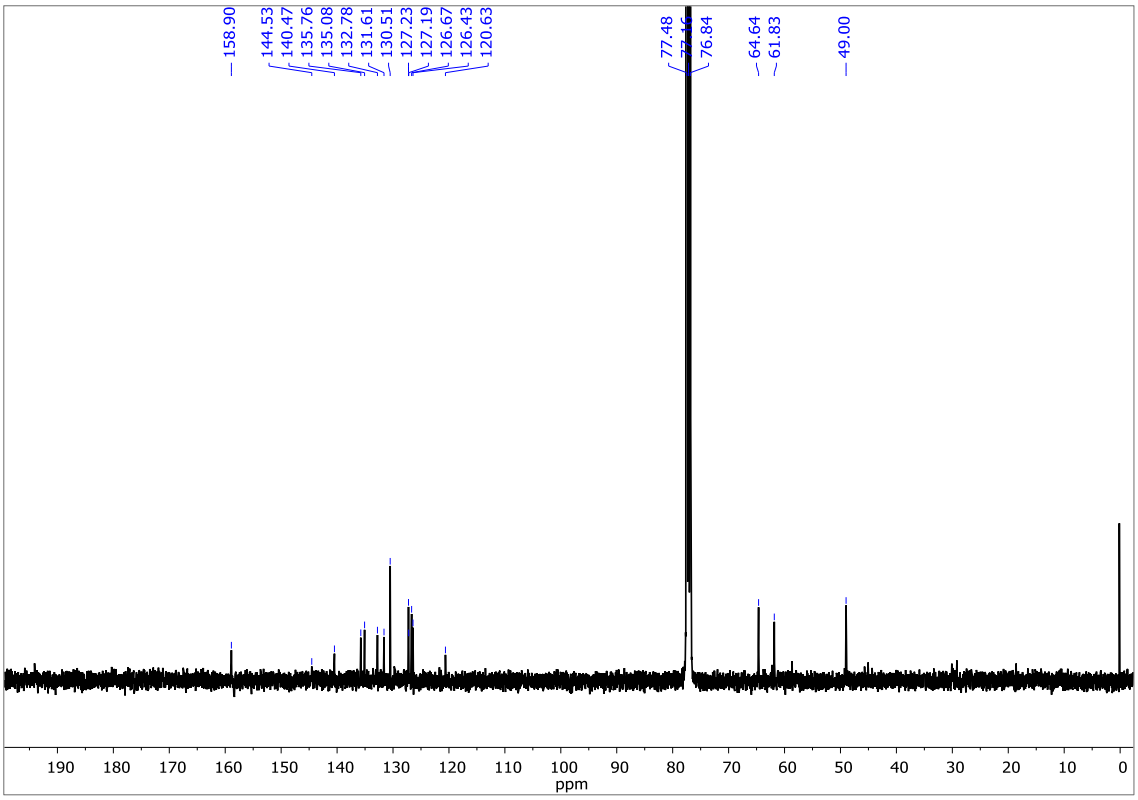

Figure S14. ^{13}C-NMR spectrum of $^{Me}L_{Ph}$ in $CDCl_3$ at room temperature (100 MHz).

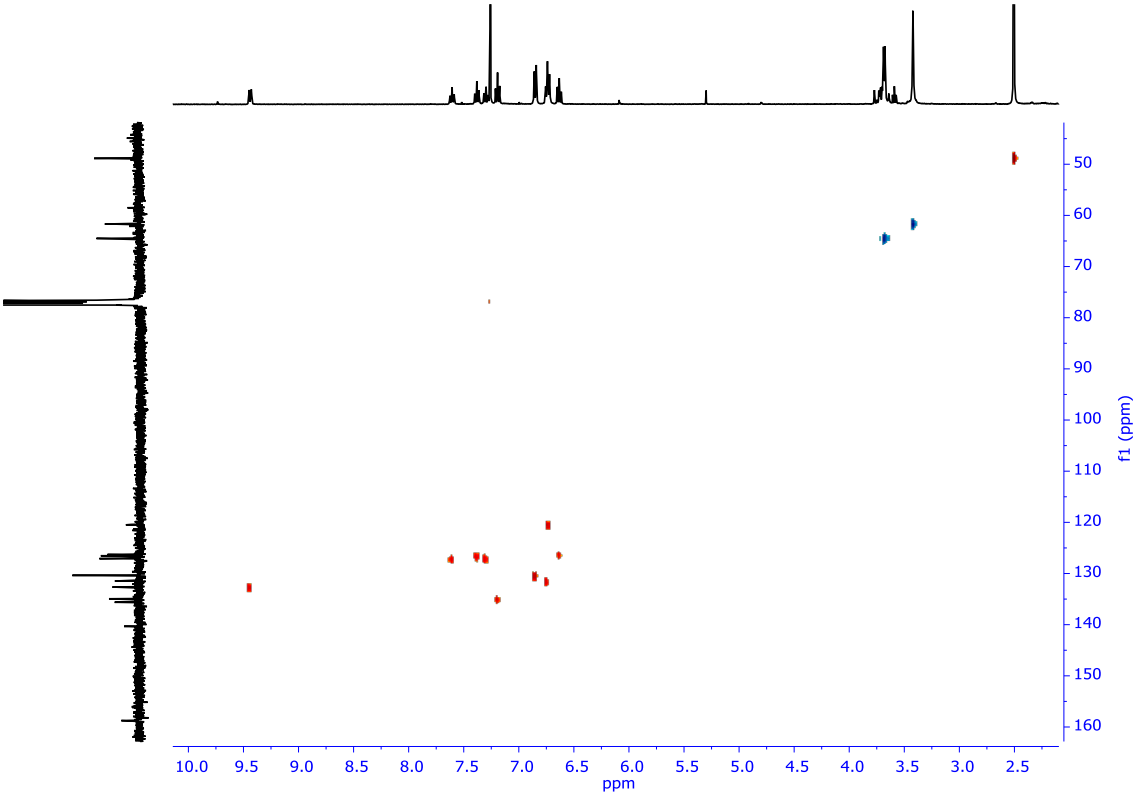

Figure S15. ^{1}H-13C HSQC spectrum of $^{Me}L_{Ph}$ in $CDCl_3$ at room temperature (400 MHz).

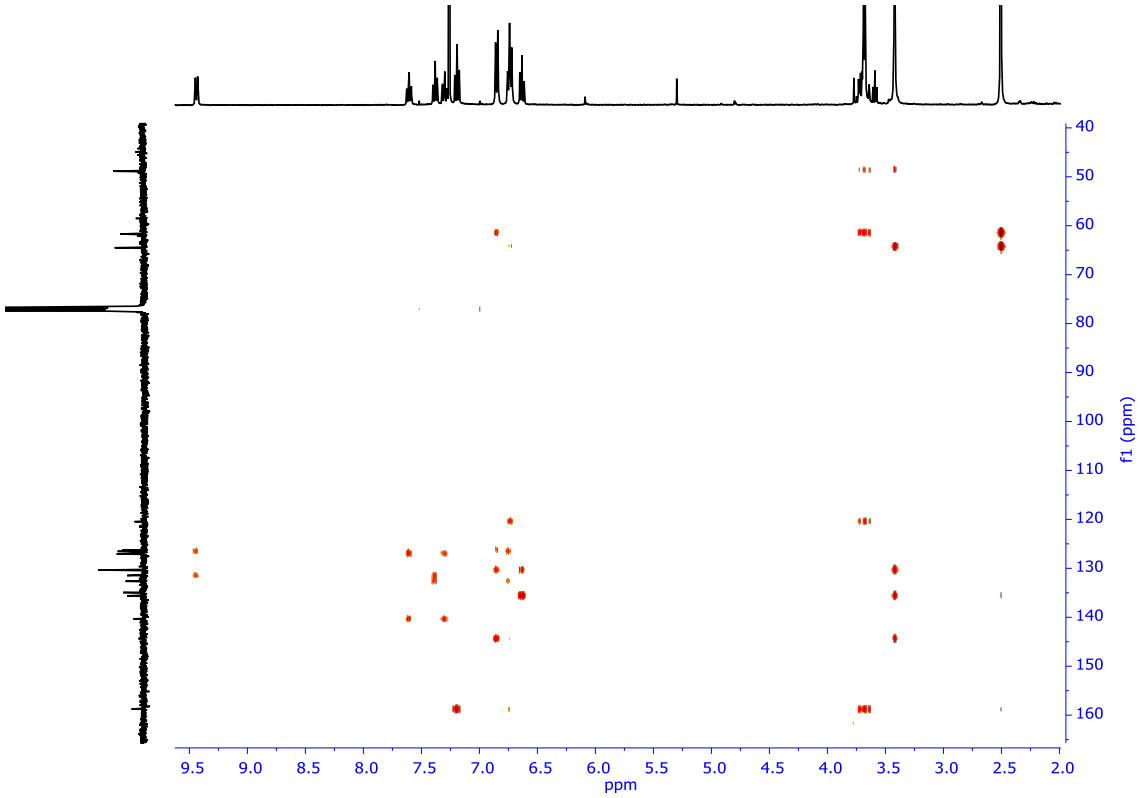

Figure S16. ^{1}H-^{13}C HMBC spectrum of $^{Me}L_{Ph}$ in $CDCl_3$ at room temperature (400 MHz).

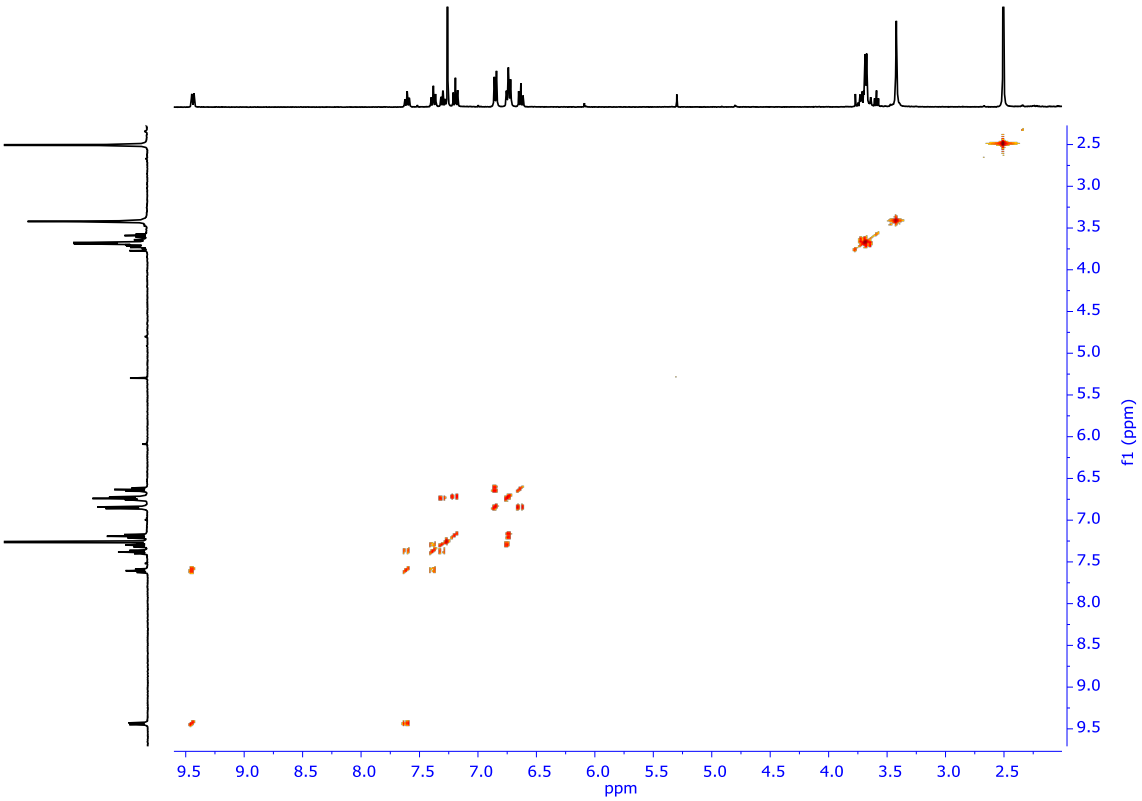

Figure S17. ^{1}H-^{1}H COSY spectrum of $^{Me}L_{Ph}$ in $CDCl_3$ at room temperature (400 MHz).

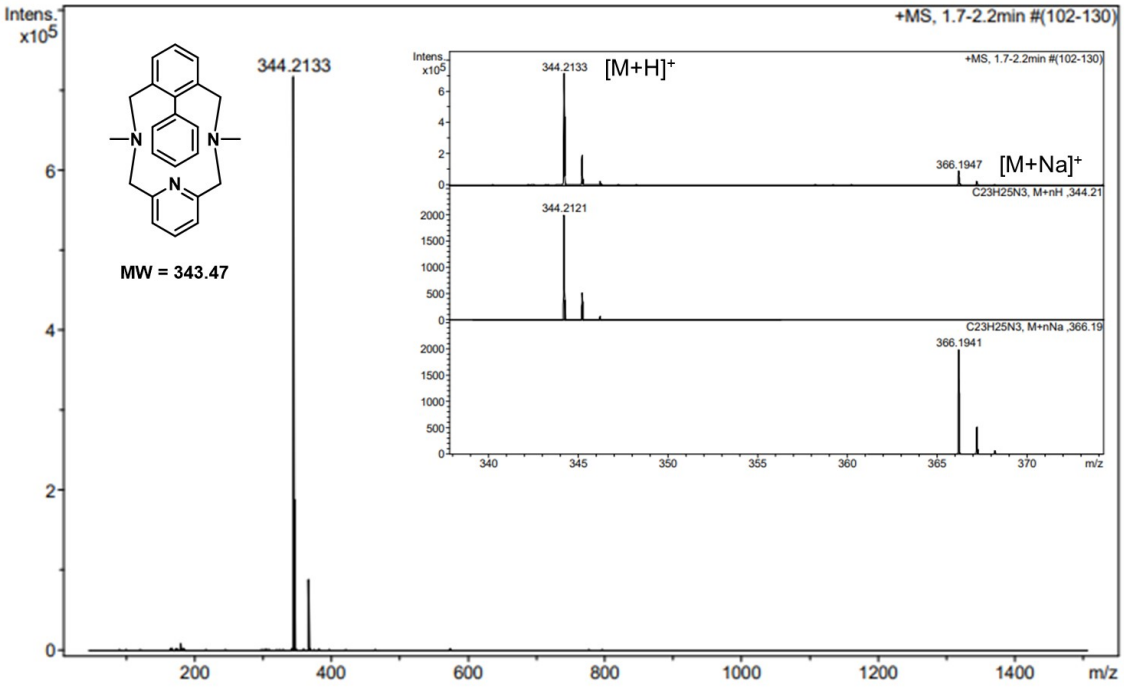

Figure S18. HR-ESI-MS of $^{Me}L_{Ph}$. Inset: expanded view of the experimental peak at a m/z = 344.2133 with a mass value and an isotopic pattern fully consistent with the monocharged $[M+H/Na]^+$ (top) and the corresponding calculated for these molecular formulas (middle $[M+H]^+$, bottom $[M+Na]^+$). ($M = C_{23}H_{25}N_3$).

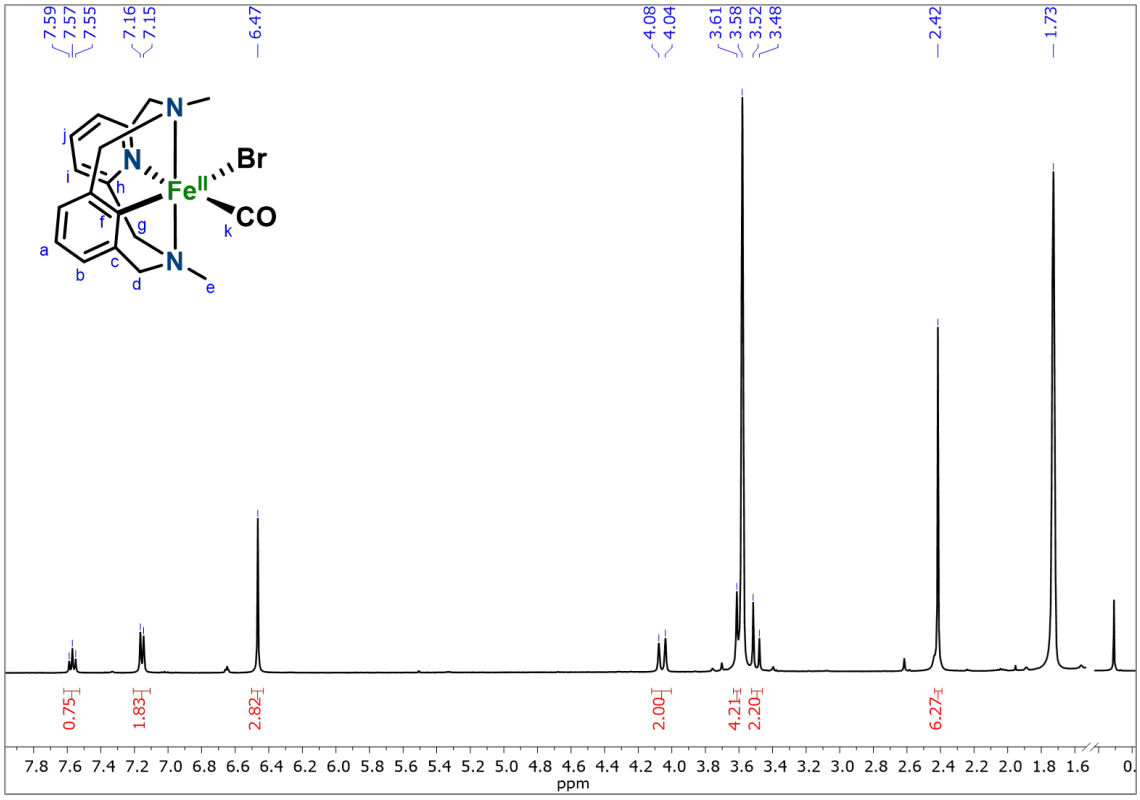

Figure S19. ^{1}H-NMR spectrum of $\mathbf{1^{Me}}$ in THF-d_8 at room temperature (400 MHz).

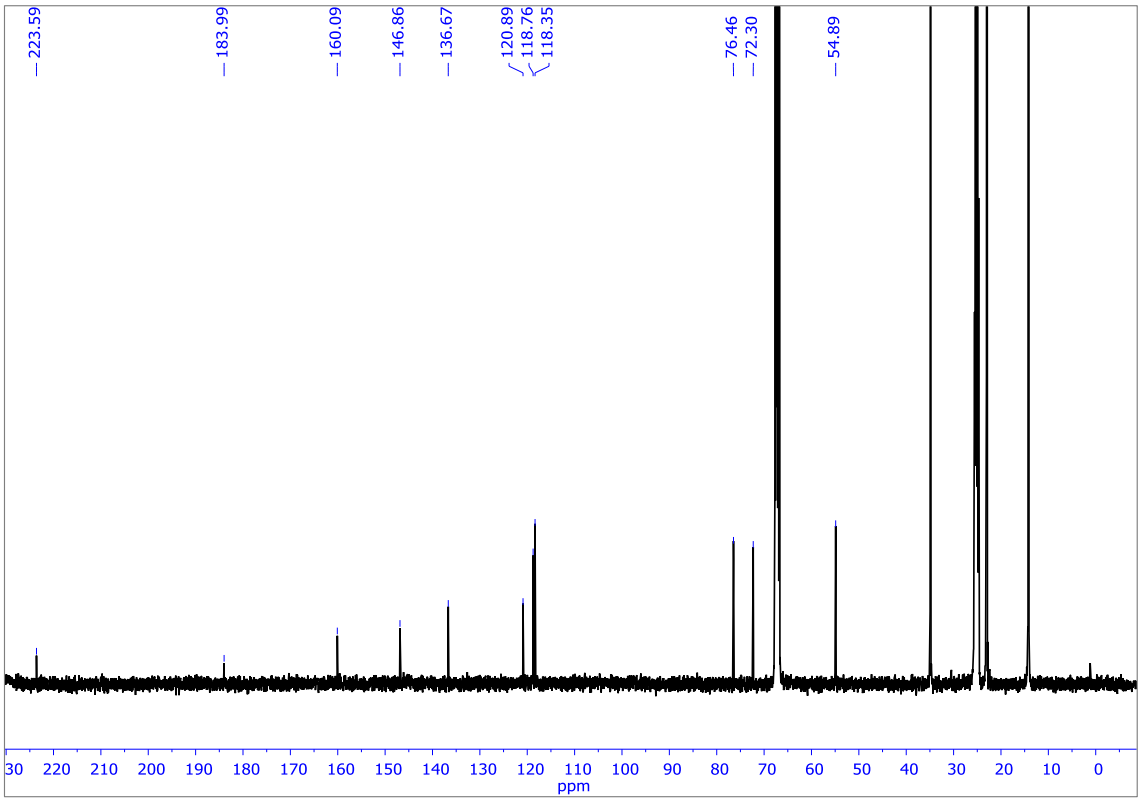

Figure S20. ^{13}C-NMR spectrum of **1^{Me}** in THF-d_8 at room temperature (100 MHz).

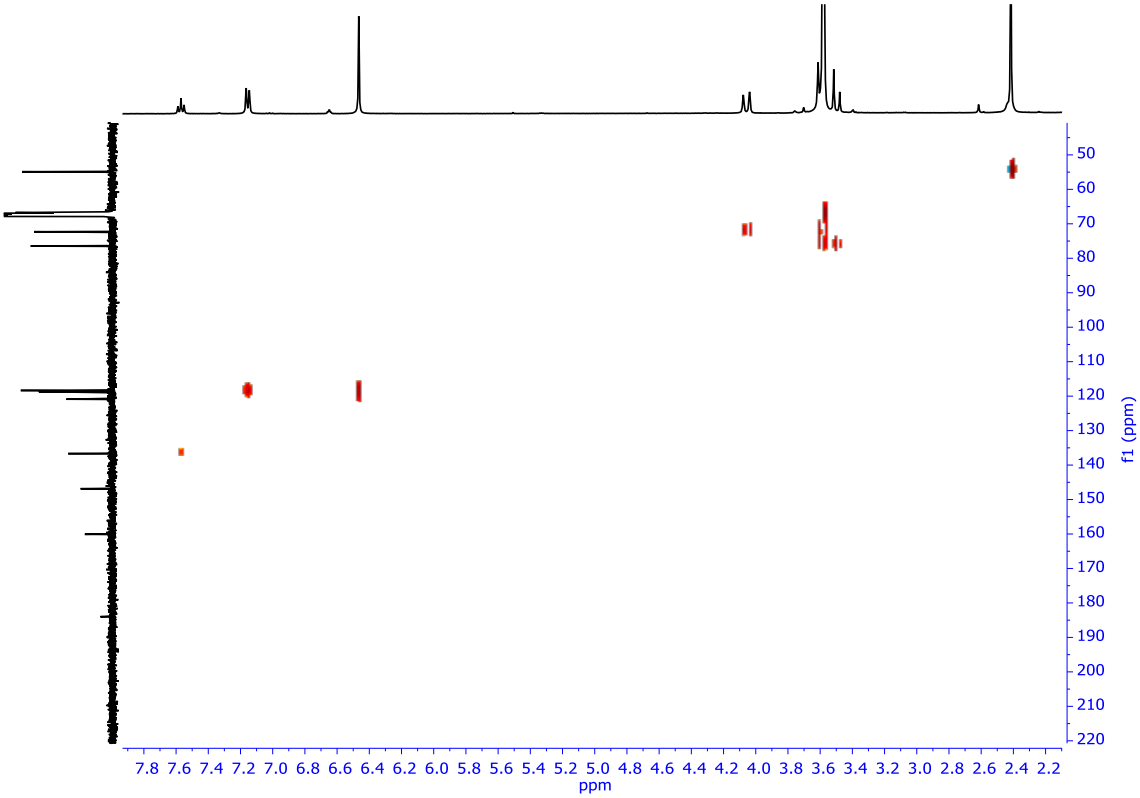

Figure S21. ^{1}H-^{13}C HSQC spectrum of **1^{Me}** in THF-d_8 at room temperature (400 MHz).

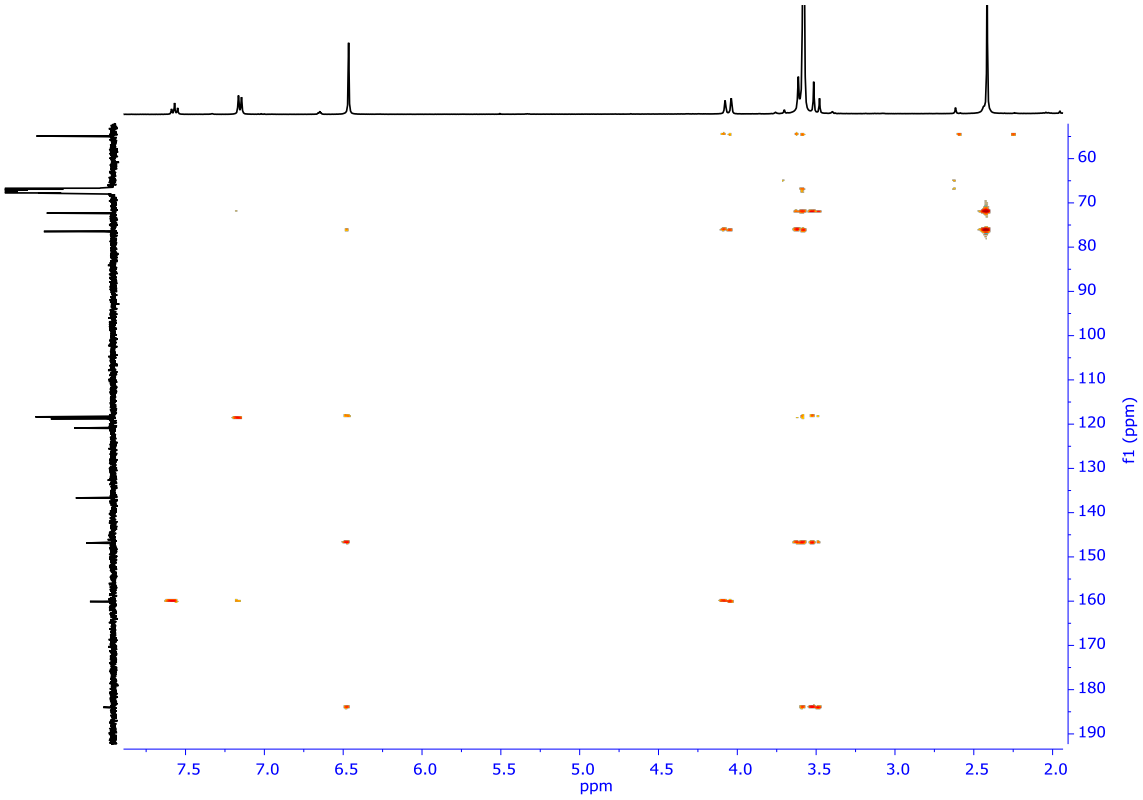

Figure S22. ^{1}H-^{13}C HMBC spectrum of $\mathbf{1^{Me}}$ in THF-d_8 at room temperature (400 MHz).

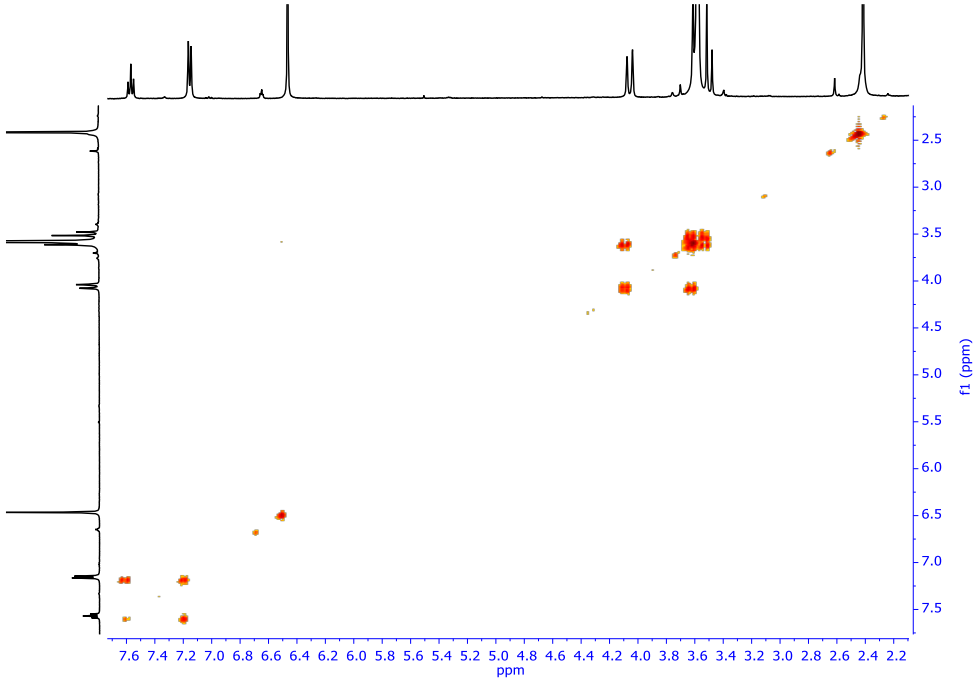

Figure S23. ^{1}H-^{1}H COSY spectrum of $\mathbf{1^{Me}}$ in THF-d_8 at room temperature (400 MHz).

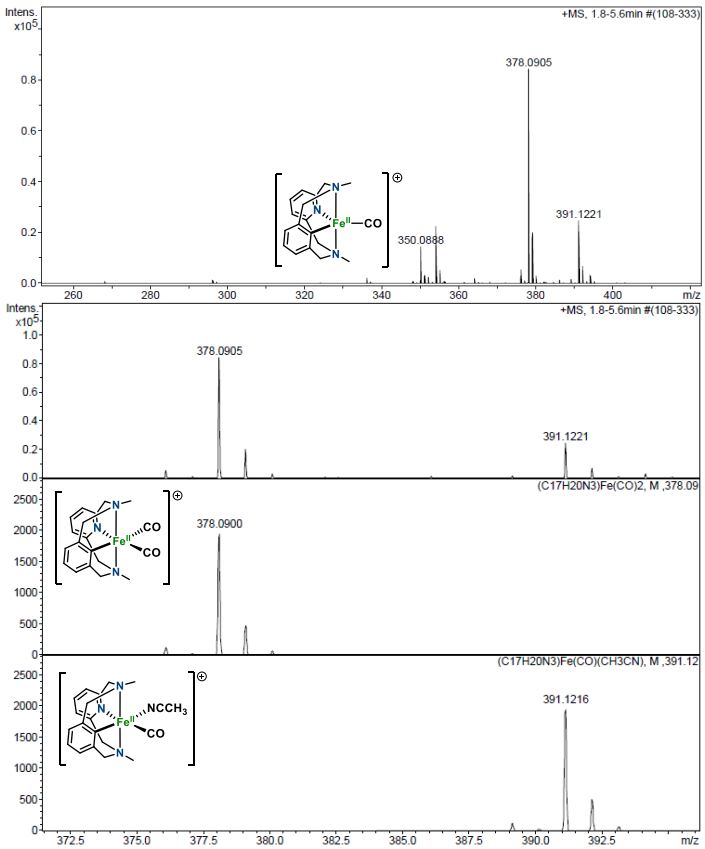

Figure S24. HR-ESI-MS of $\mathbf{1}^{Me}$. Expanded view of the experimental peaks with mass value and isotopic pattern fully consistent with the monocharged $[C_{19}H_{20}N_3O_2Fe]^+$ = 378.0905 and $[C_{20}H_{23}N_4OFe]^+$ = 391.1221 (top) and the corresponding calculated for these molecular formulas (middle $[C_{19}H_{20}N_3O_2Fe]^+$, bottom $[C_{20}H_{23}N_4OFe]^+$).

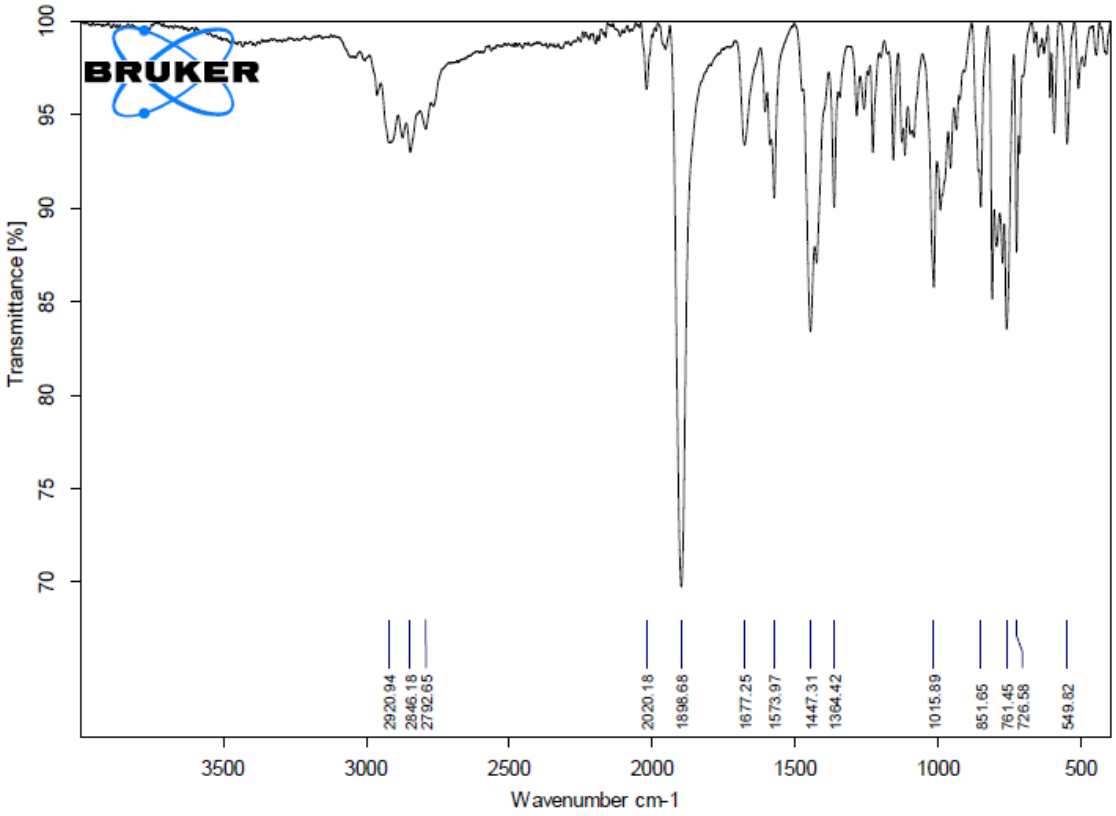

Figure S25. ATR-FT-IR spectrum of $\mathbf{1}^{Me}$ at room temperature.

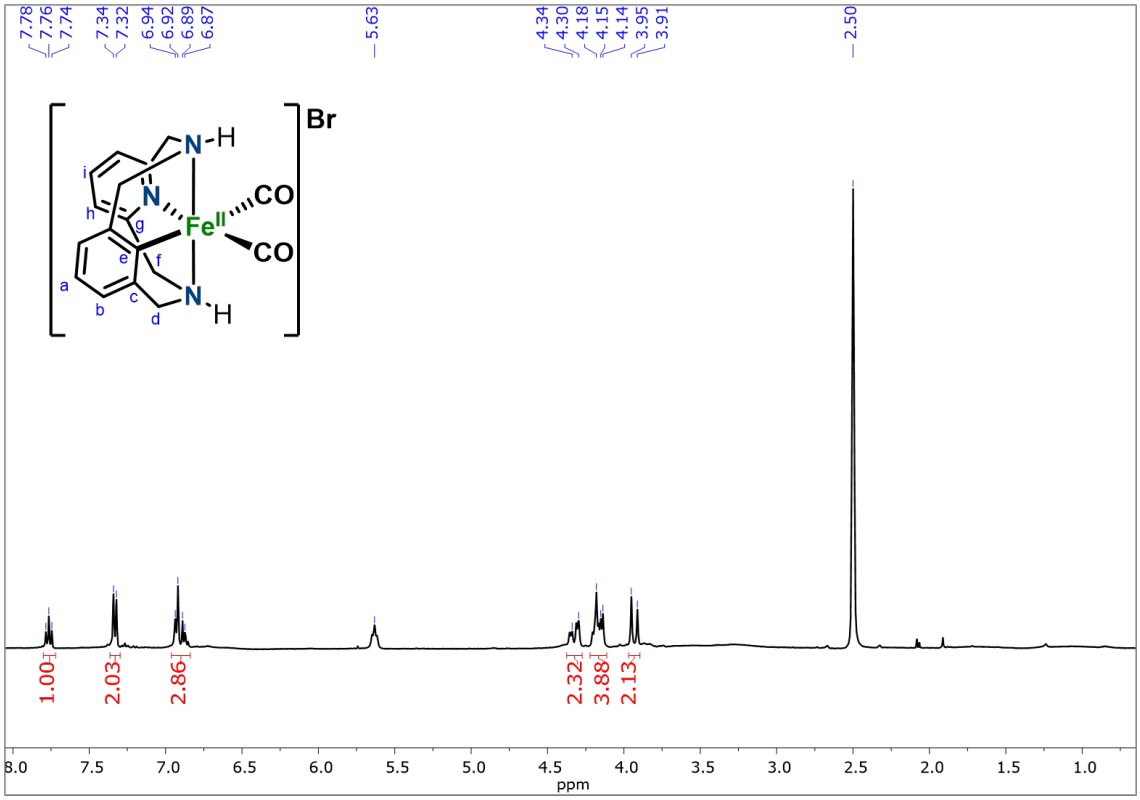

Figure S26. ^{1}H-NMR spectrum of $\mathbf{1^{H}}$ in DMSO-d_6 at room temperature (400 MHz).

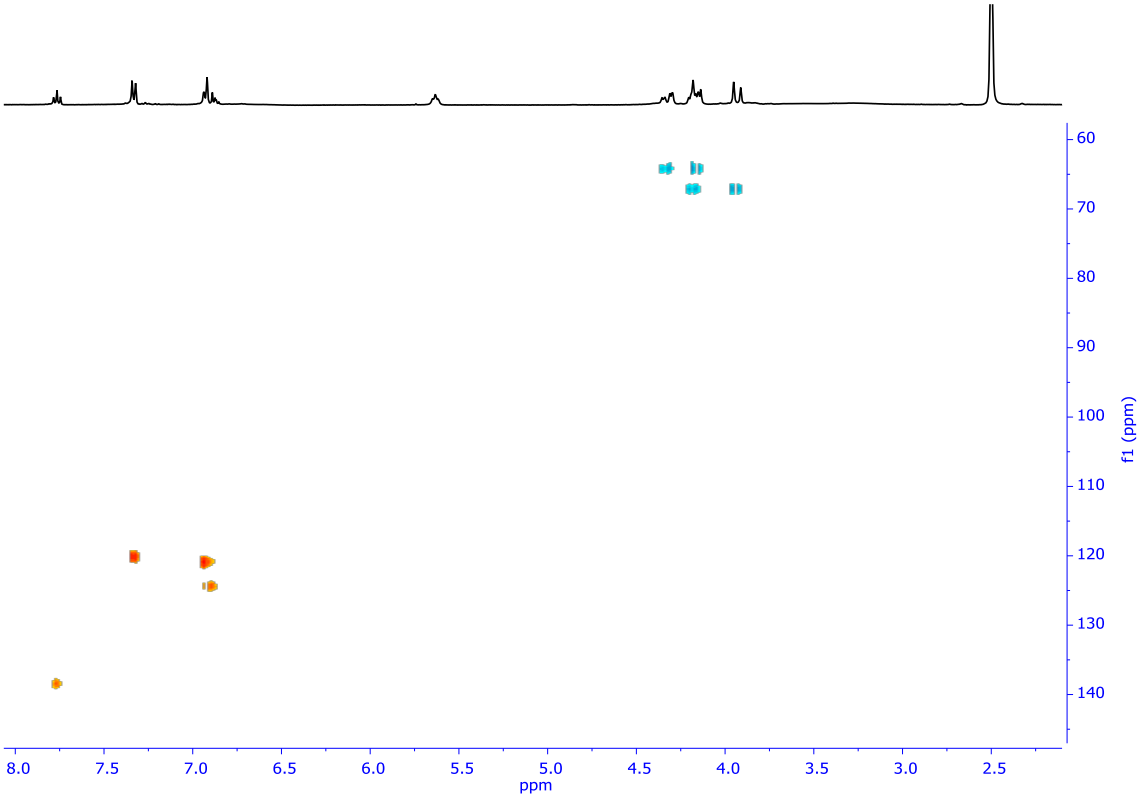

Figure S27. ^{1}H-^{13}C HSQCed spectrum of $\mathbf{1^{H}}$ in DMSO-d_6 at room temperature (400 MHz).

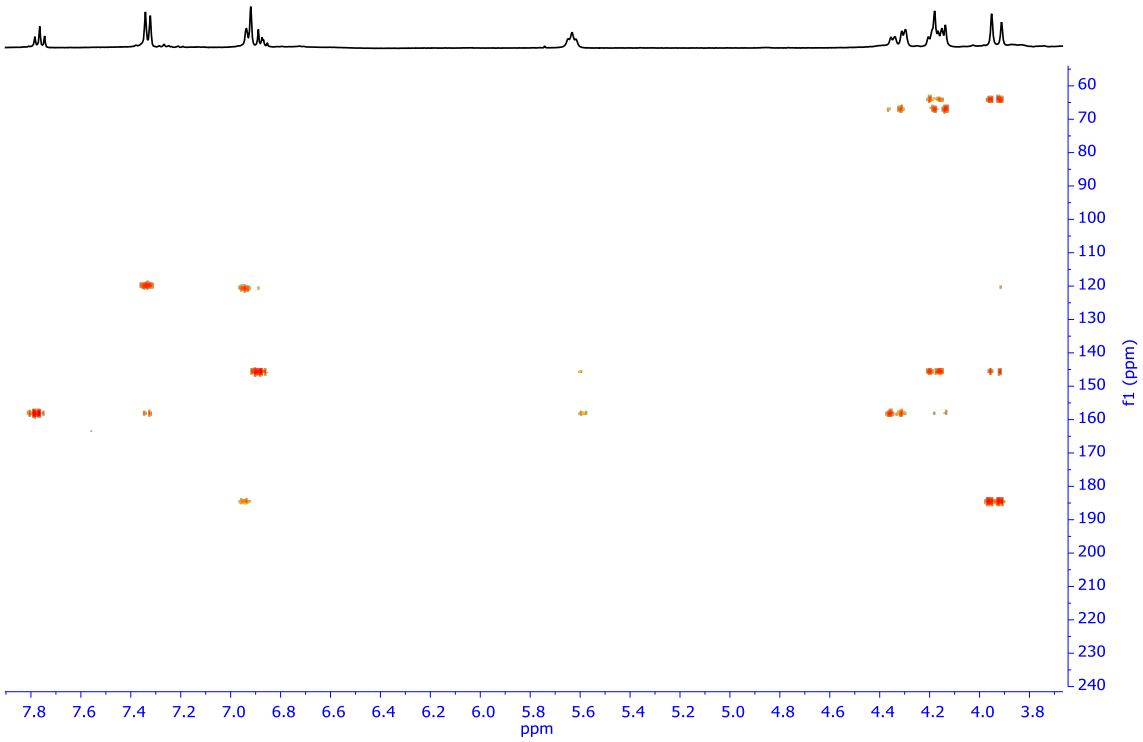

Figure S28. ^{1}H-^{13}C HMBC spectrum of $\mathbf{1^{H}}$ in DMSO-d_6 at room temperature (400 MHz).

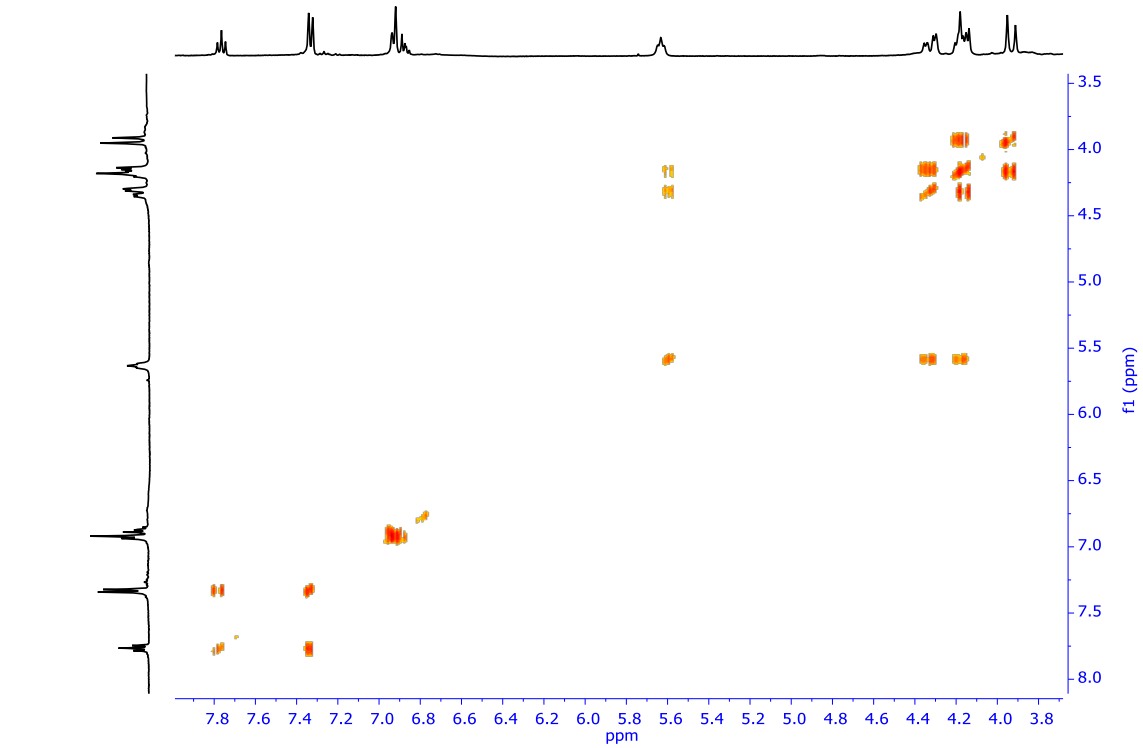

Figure S29. ^{1}H-^{1}H COSY spectrum of $\mathbf{1^{H}}$ in DMSO-d_6 at room temperature (400 MHz).

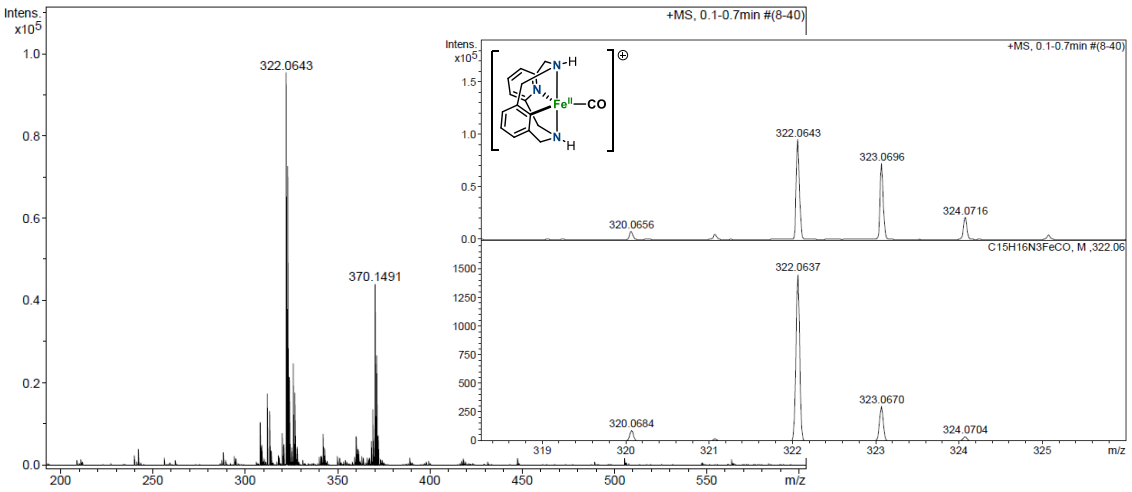

Figure S30. HR-ESI-MS of $\mathbf{1^H}$. Inset: expanded view of the experimental peak with mass value and isotopic pattern fully consistent with the monocharged $[C_{16}H_{16}N_3OFe]^+$ = 322.0643 (top) and the corresponding calculated for this molecular formula (bottom).

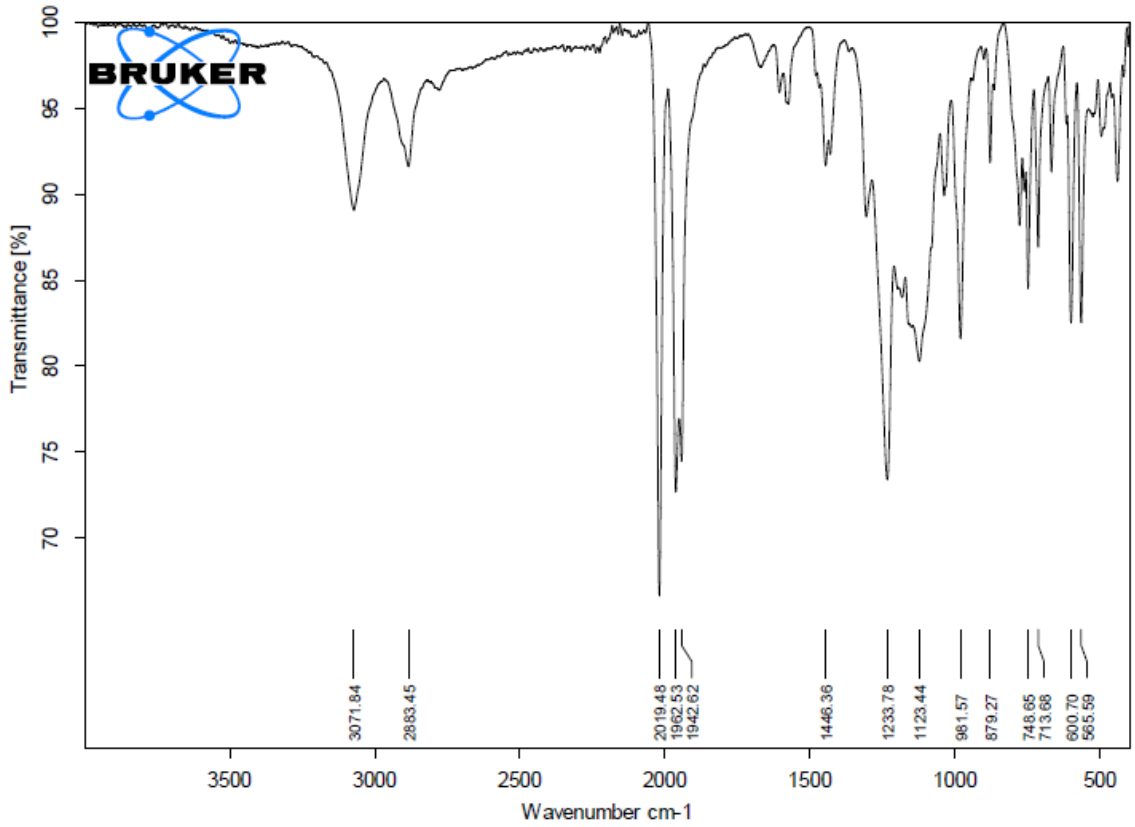

Figure S31. ATR-FT-IR spectrum of $\mathbf{1^H}$ at room temperature.

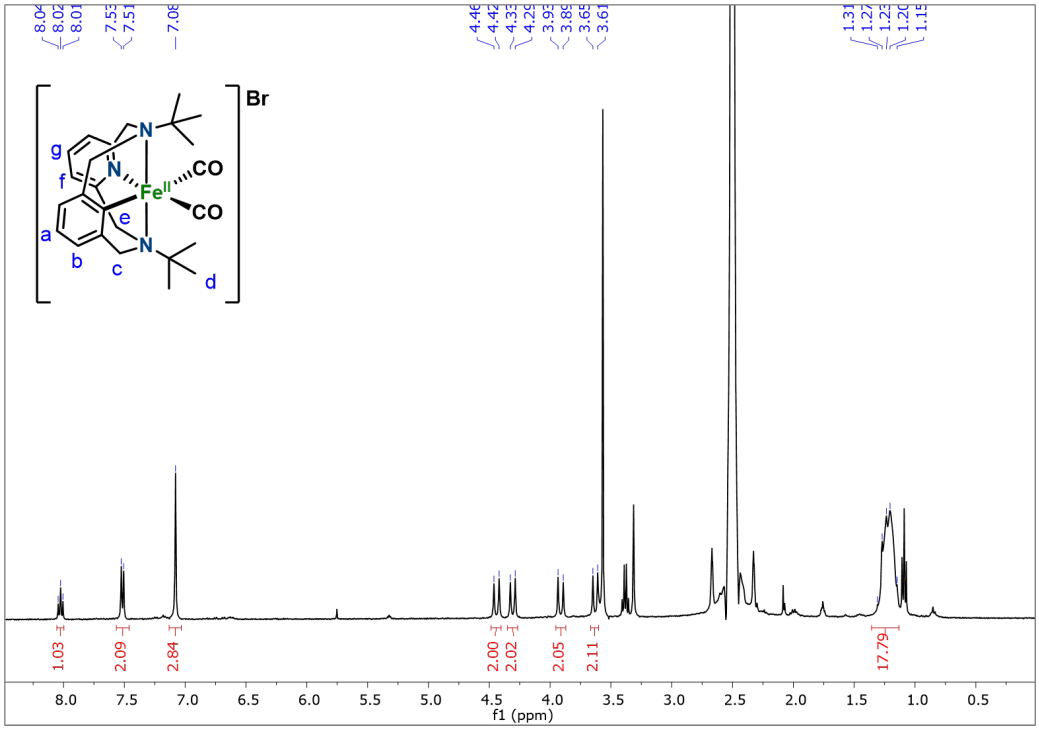

Figure S32. ^{1}H-NMR spectrum of $\mathbf{1^{tBu}}$ in DMSO-d_6 at room temperature (400 MHz).

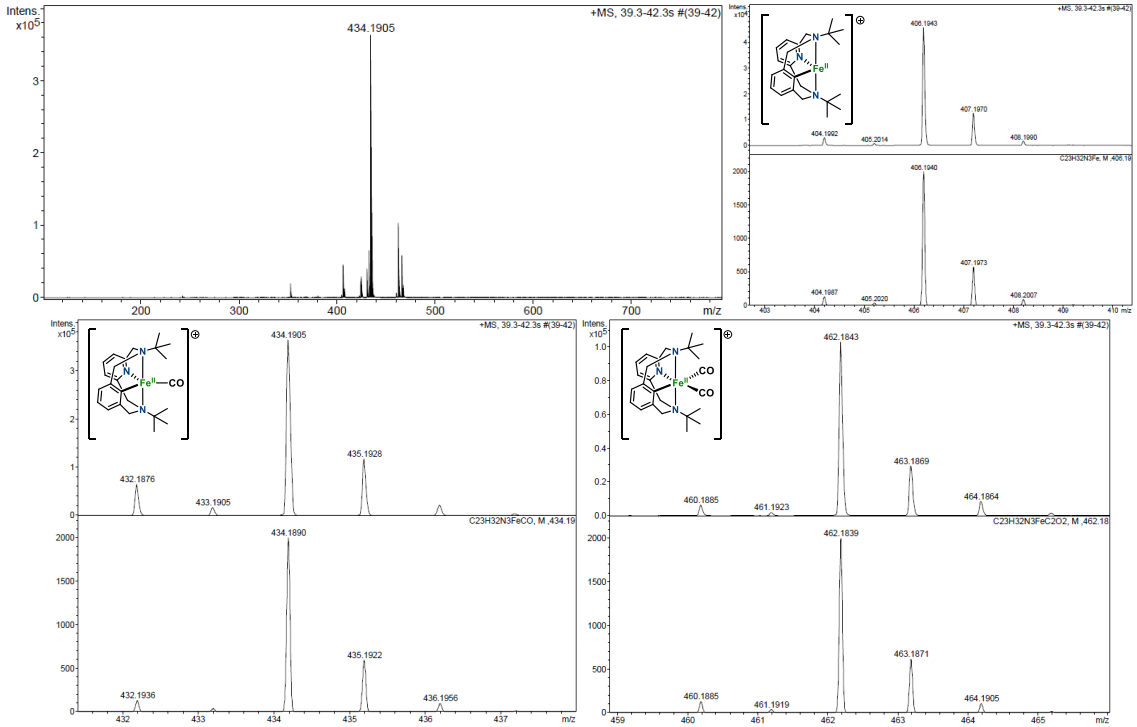

Figure S33. Top left: HR-ESI-MS of $\mathbf{1^{tBu}}$. Top right: expanded view of the experimental peak at m/z = 406.1943 with a mass value and an isotopic pattern fully consistent with the monocharged $[C_{23}H_{32}N_3Fe]^+$ (top) and the corresponding calculated for this molecular formula (bottom). Bottom left: expanded view of the experimental peak at m/z = 434.1905 with a mass value and an isotopic pattern fully consistent with the monocharged $[C_{24}H_{32}N_3OFe]^+$ (top) and the corresponding calculated for this molecular formula (bottom). Bottom right: expanded view of the experimental peak at m/z = 462.1843 with a mass value and an isotopic pattern fully consistent with the monocharged $[C_{25}H_{32}N_3O_2Fe]^+$ (top) and the corresponding calculated for this molecular formula (bottom).

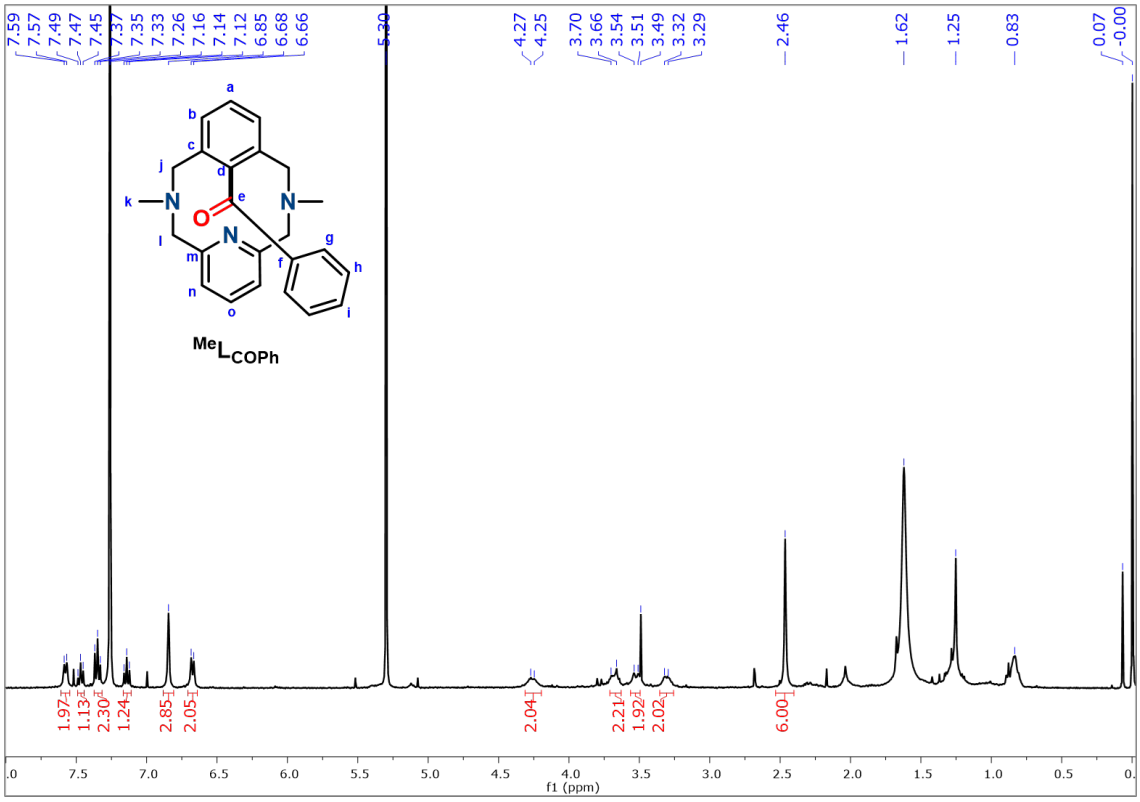

Figure S34. ^{1}H-NMR spectrum of $^{Me}L_{COPh}$ in $CDCl_3$ at room temperature (400 MHz).

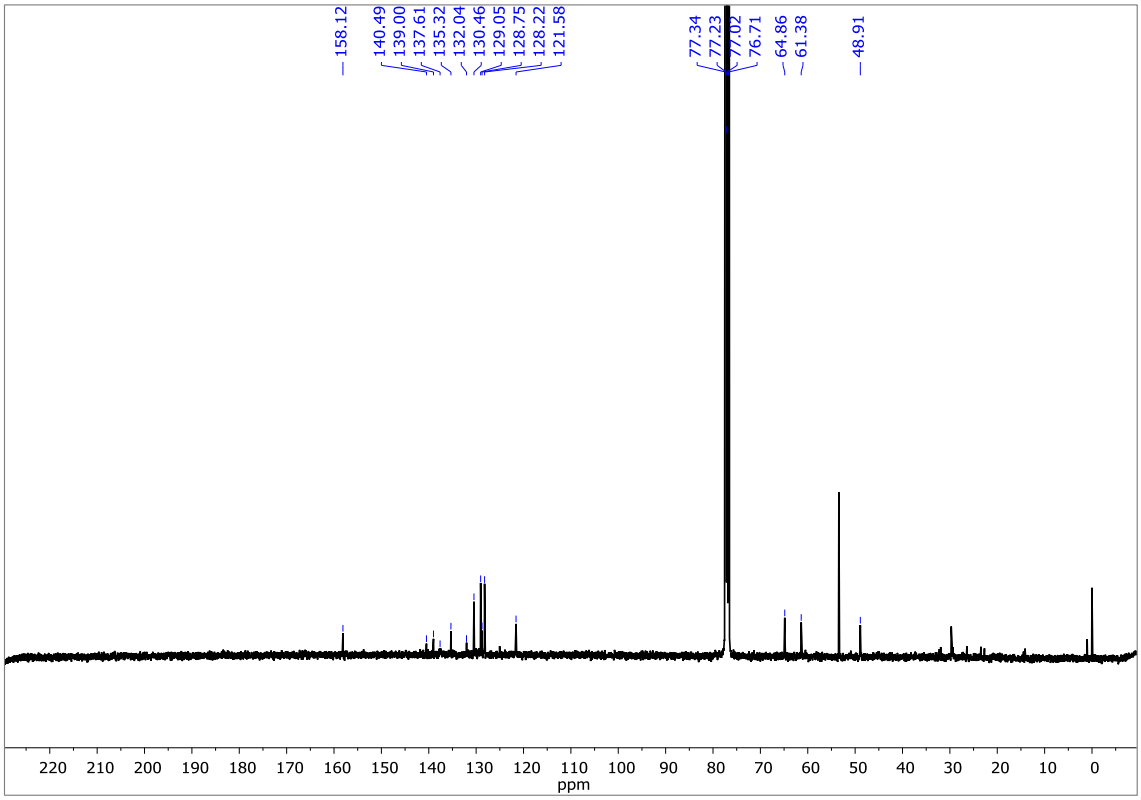

Figure S35. ^{13}C-NMR spectrum of $^{Me}L_{COPh}$ in $CDCl_3$ at room temperature (400 MHz).

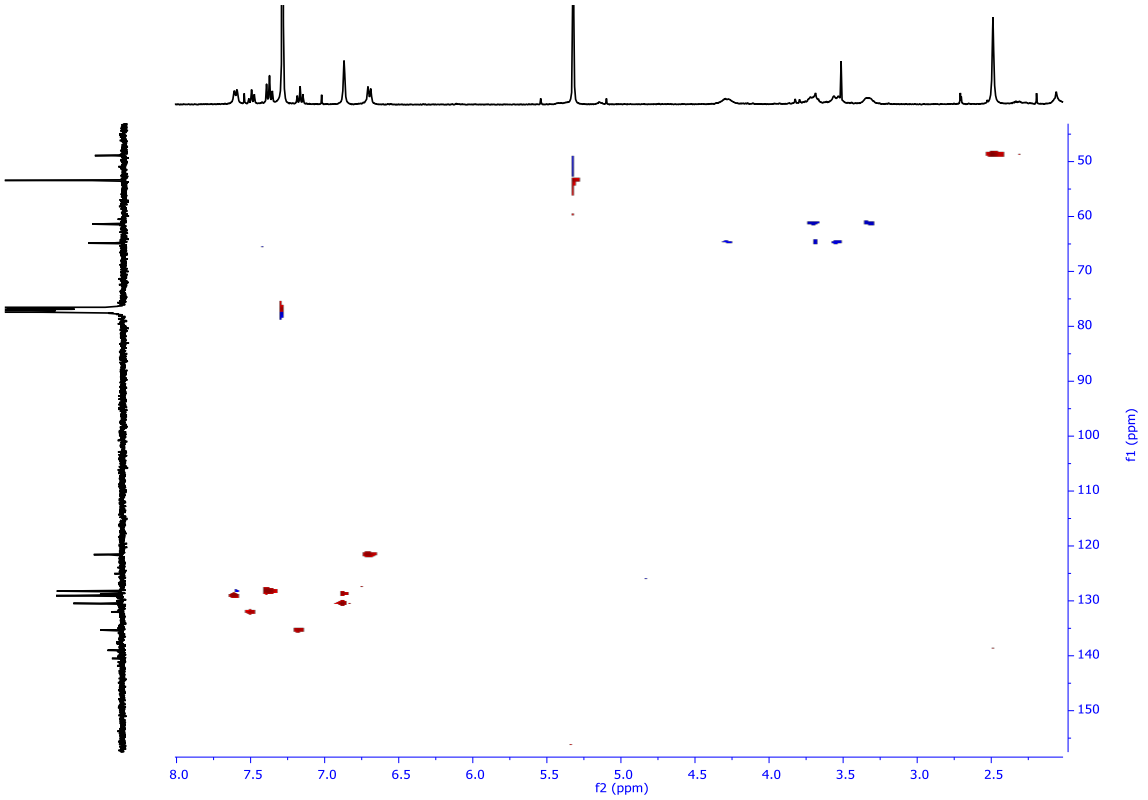

Figure S36. ^{1}H-^{13}C HSQCed spectrum of $^{Me}L_{COPh}$ in $CDCl_3$ at room temperature (400 MHz).

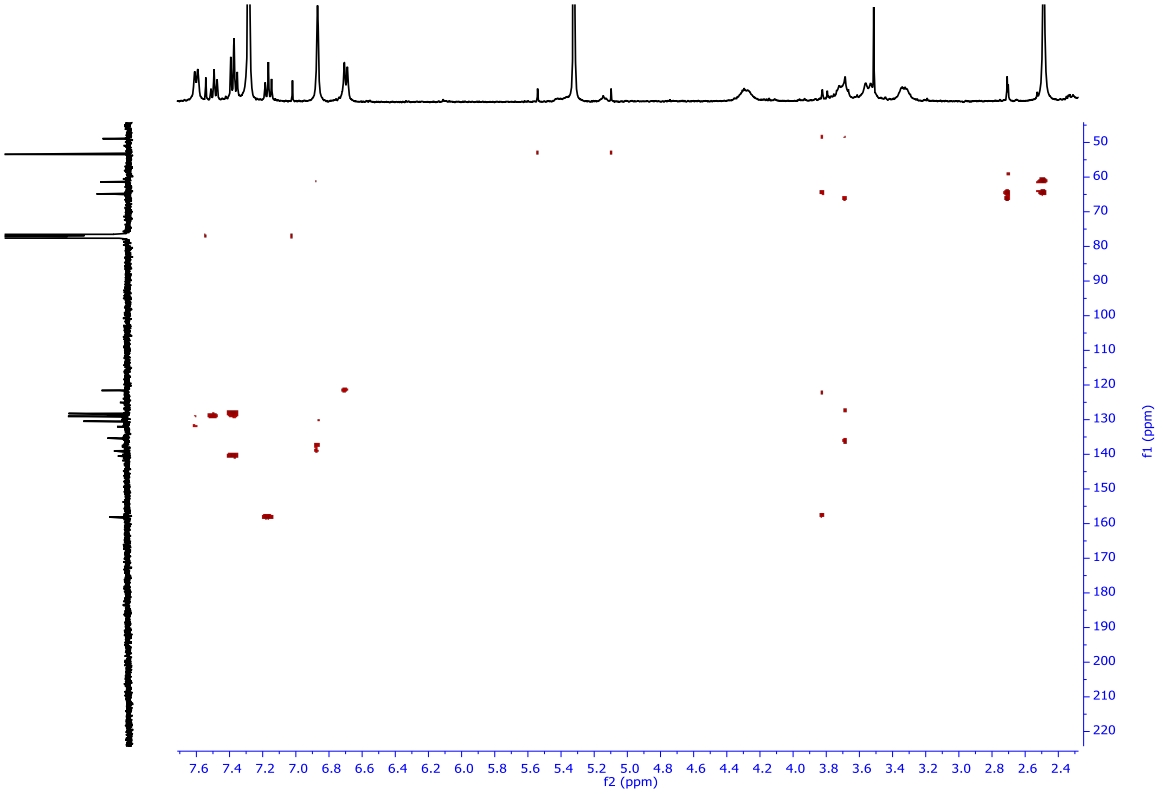

Figure S37. ^{1}H-^{13}C HMBC spectrum of $^{Me}L_{COPh}$ in $CDCl_3$ at room temperature (400 MHz).

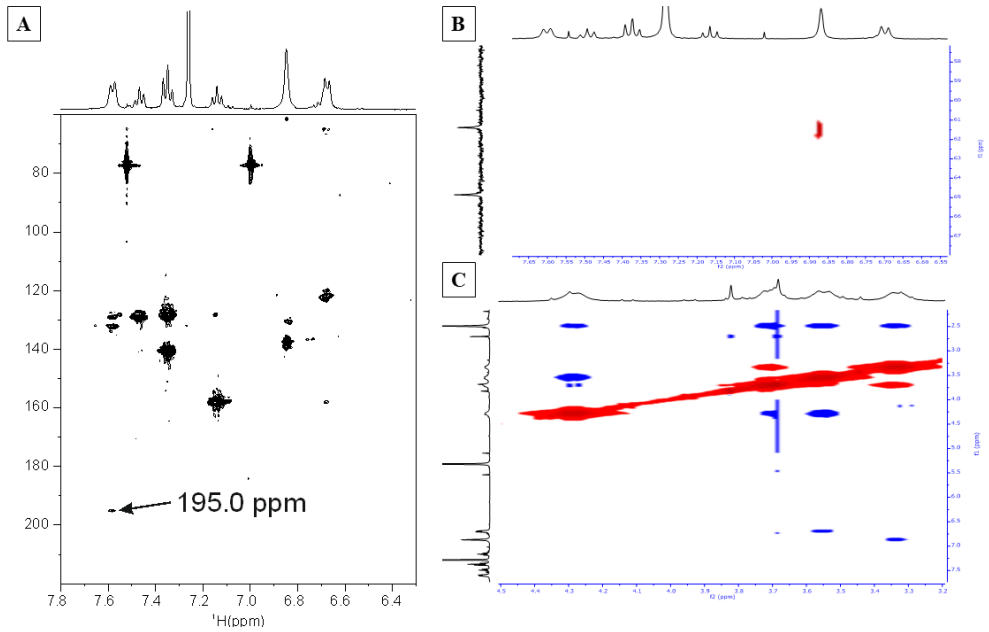

Figure S38. A: ^{1}H-^{13}C HMBC spectrum of $^{Me}L_{COPh}$ in $CDCl_3$ at room temperature (400 MHz), ampliation of the aromatic region for detection of the ketone CO. The presence of chemical exchange dynamics in combination with relaxation properties of carbonyl nuclei do not allow to detect CO with proper sensitivity. The presence of CO band in IR spectrum enforce us to optimize a HMBC spectra to improve the sensitivity provided by ^{13}C NMR spectra and be able to assign the carbonyl nucleus using conventional HMBC without low-pass filter spectrum optimized with a interscan delay of 3.5s. B: ^{1}H-^{13}C HMBC spectrum of $^{Me}L_{COPh}$ in $CDCl_3$ at room temperature (400 MHz), ampliation of the aromatic (^{1}H) and aliphatic (^{13}C) regions to assign the benzylic positions. C: ^{1}H-^{1}H NOESY spectrum of $^{Me}L_{COPh}$ in $CDCl_3$ at room temperature (400 MHz), ampliation of the aliphatic (f1) region to assign and further confirm the benzylic positions.

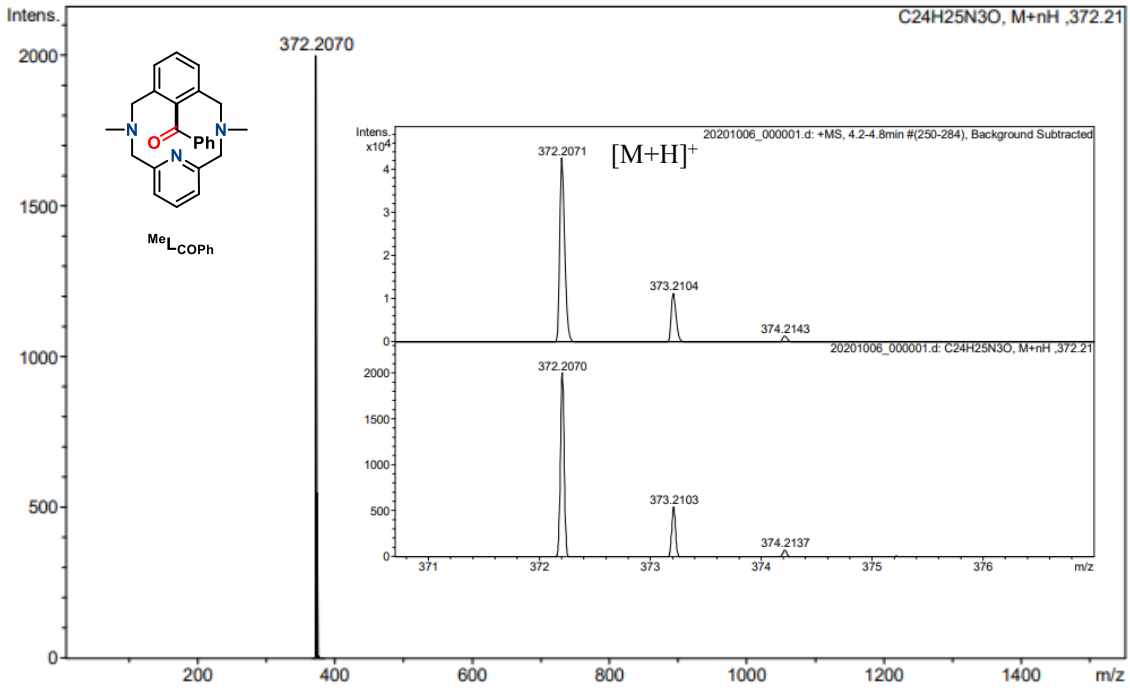

Figure S39. HR-ESI-MS of $^{Me}L_{COPh}$. Inset: expanded view of the experimental peak at m/z = 372.2070 with a mass value and an isotopic pattern fully consistent with $[M+H]^+$ (top) and the corresponding calculated for this molecular formula (bottom). ($M = C_{24}H_{25}N_3O$).

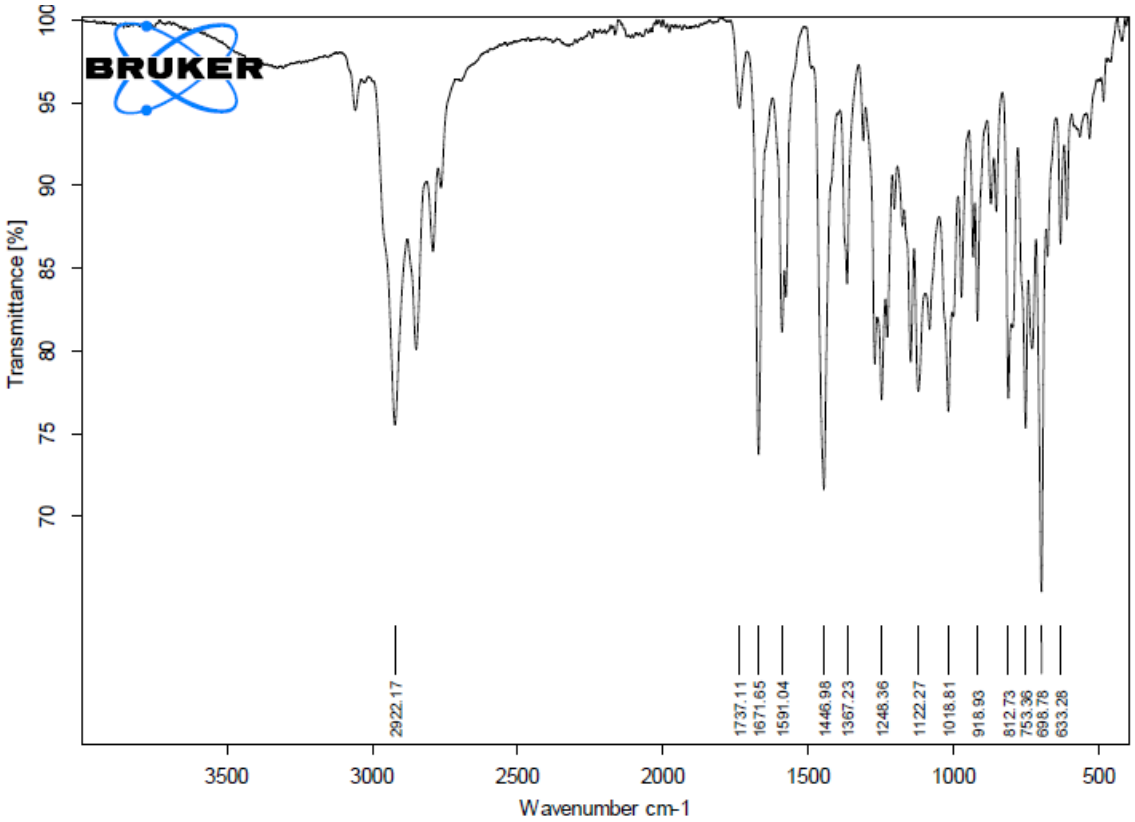

Figure S40. ATR-FT-IR spectrum of $^{Me}L_{COPh}$ at room temperature.

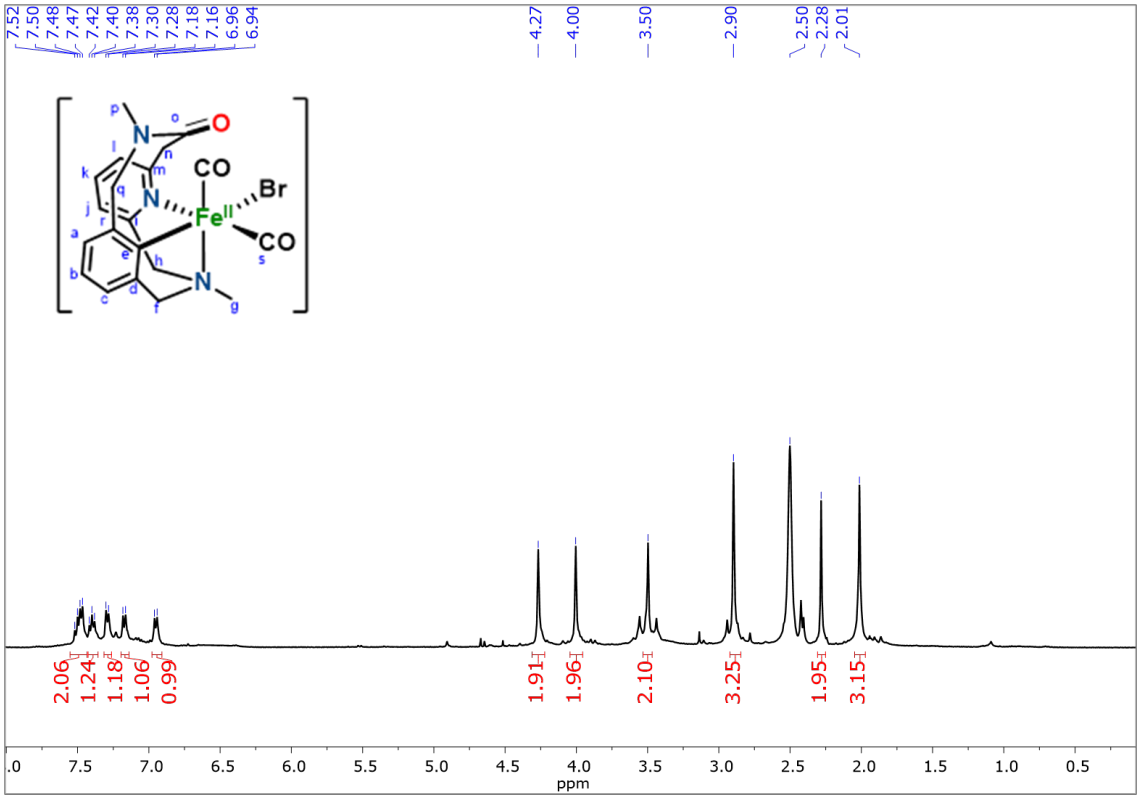

Figure S41. ^{1}H-NMR spectrum of **2^{Me}(CO)** in DMSO-d_6 at room temperature (400 MHz).

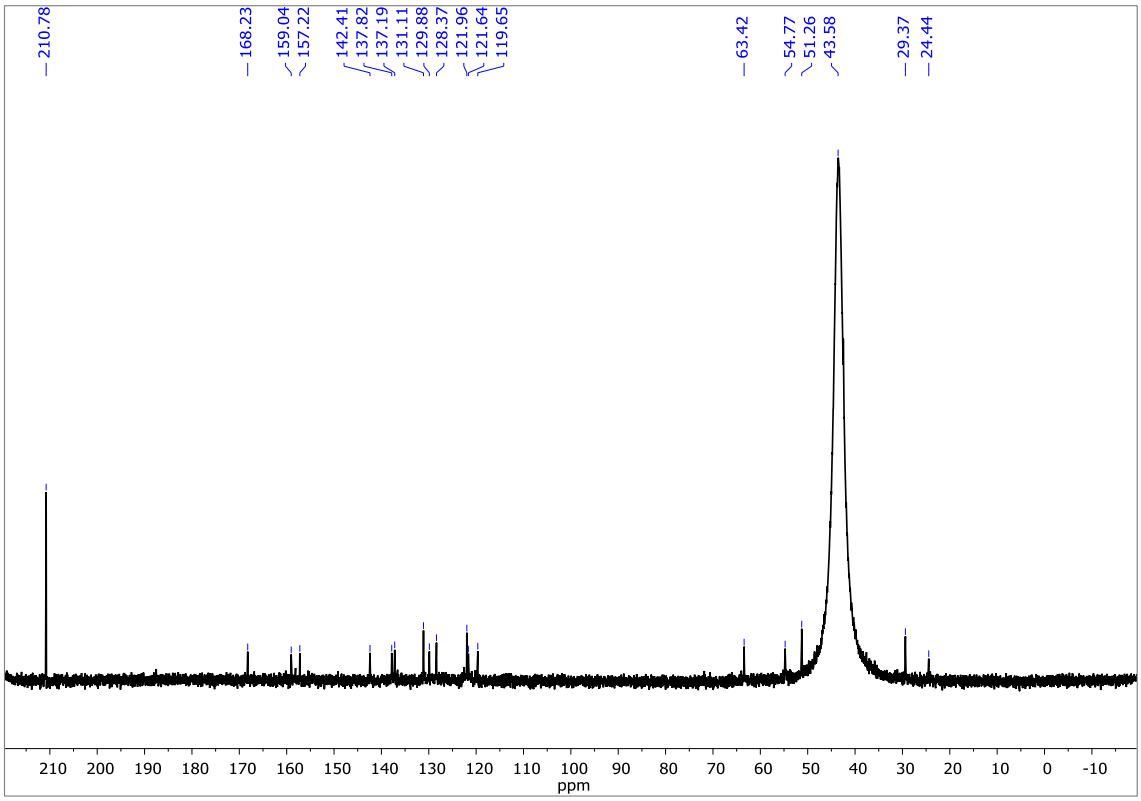

Figure S42. ^{13}C-NMR spectrum of **2^{Me}(CO)** in DMSO-d$_6$ at room temperature (100 MHz).

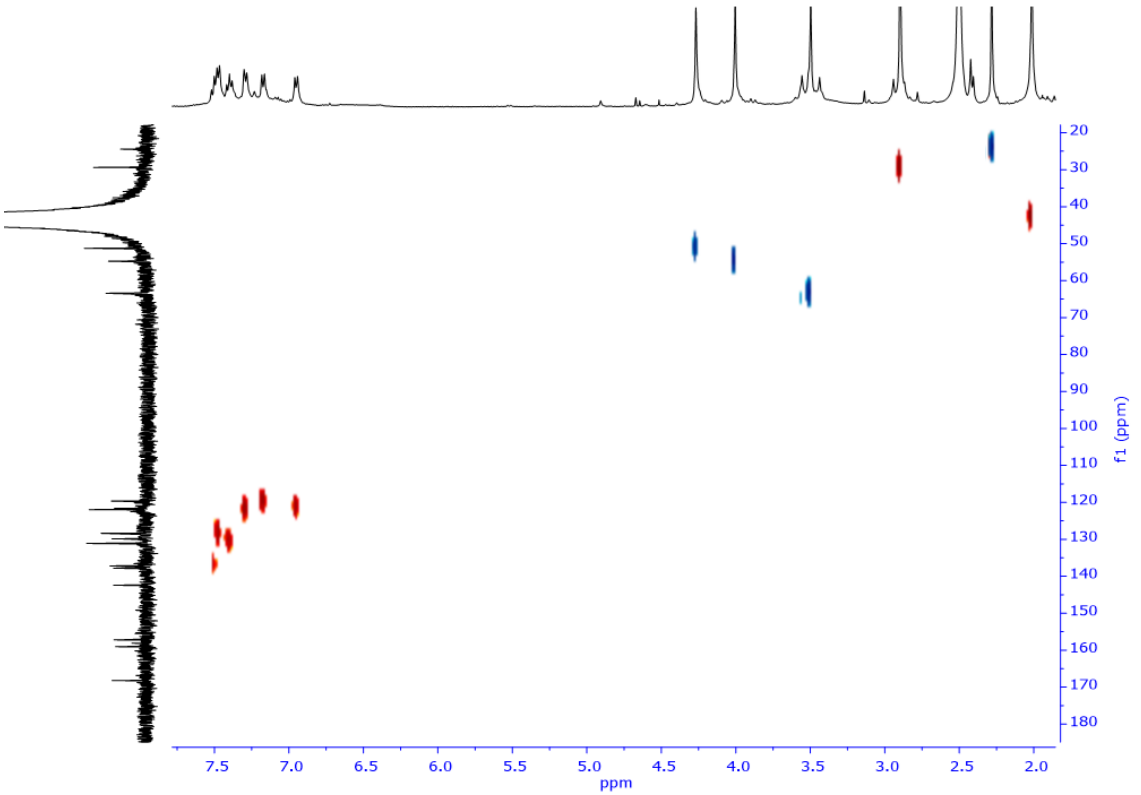

Figure S43. ^{1}H-^{13}C HSQC spectrum of **2^{Me}(CO)** in DMSO-d$_6$ at room temperature (400 MHz).

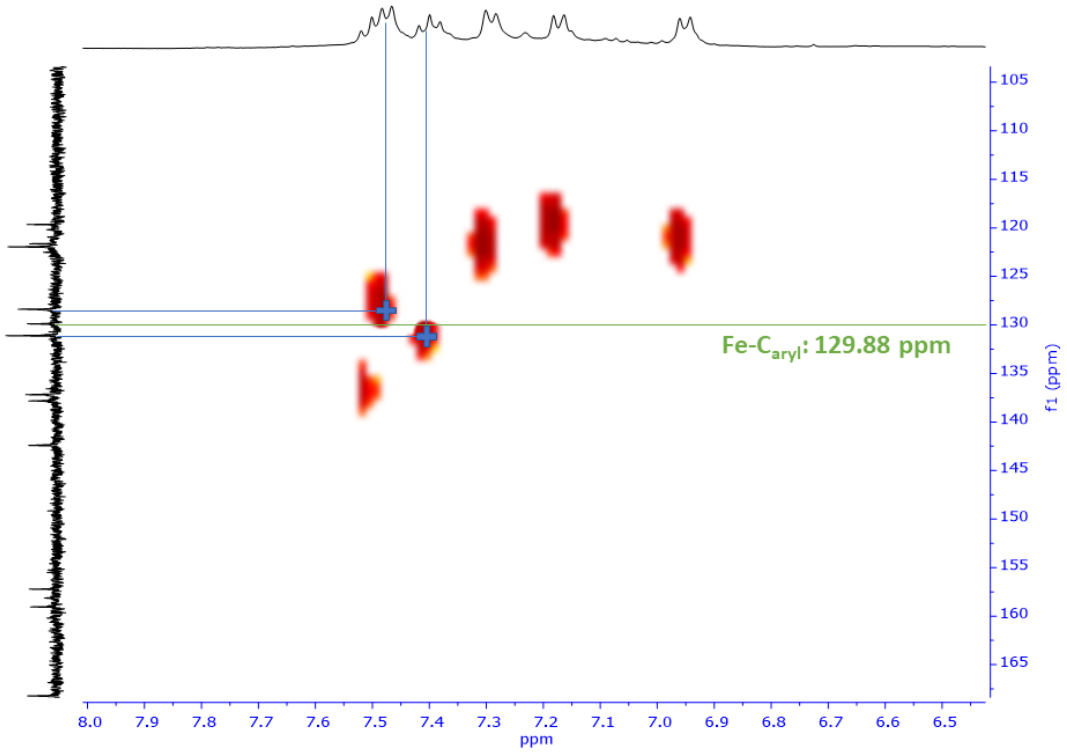

Figure S44. ^{1}H-^{13}C HSQCed spectrum of **2^{Me}(CO)** in DMSO-d$_6$ at room temperature (400 MHz). Ampliation of the aromatic regions.

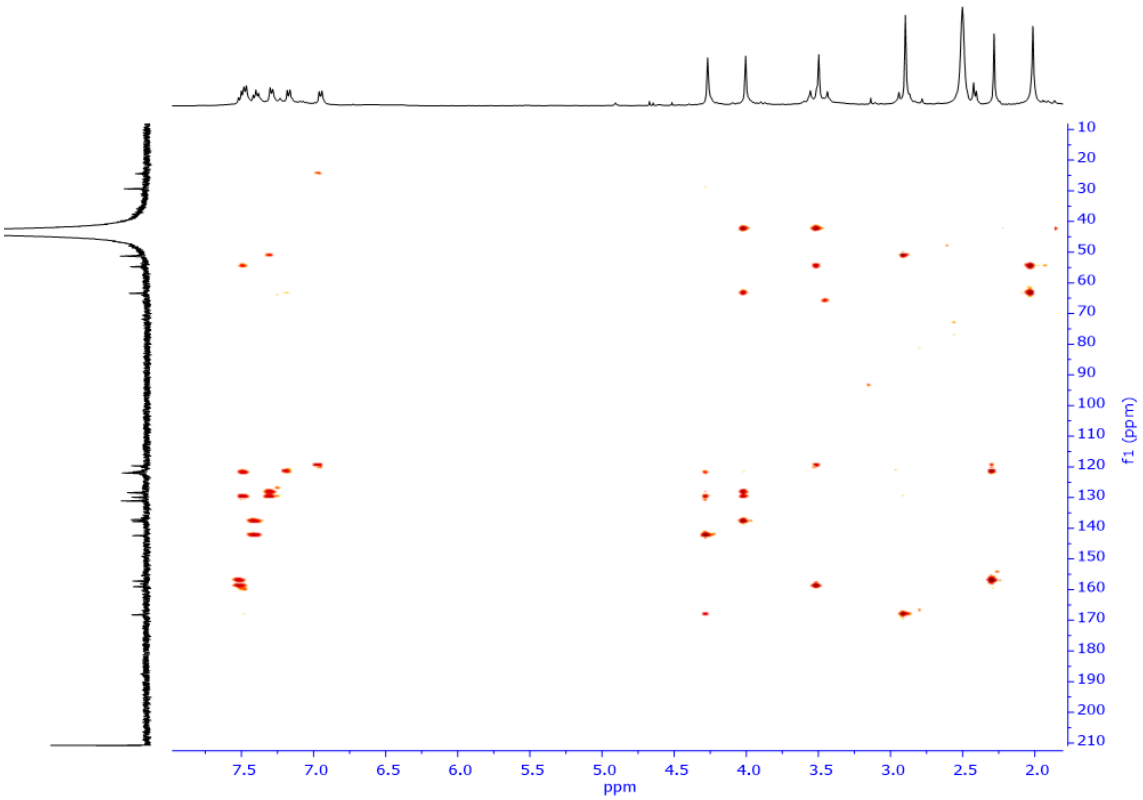

Figure S45. ^{1}H-^{13}C HMBC spectrum of **2^{Me}(CO)** in DMSO-d$_6$ at room temperature (400 MHz).

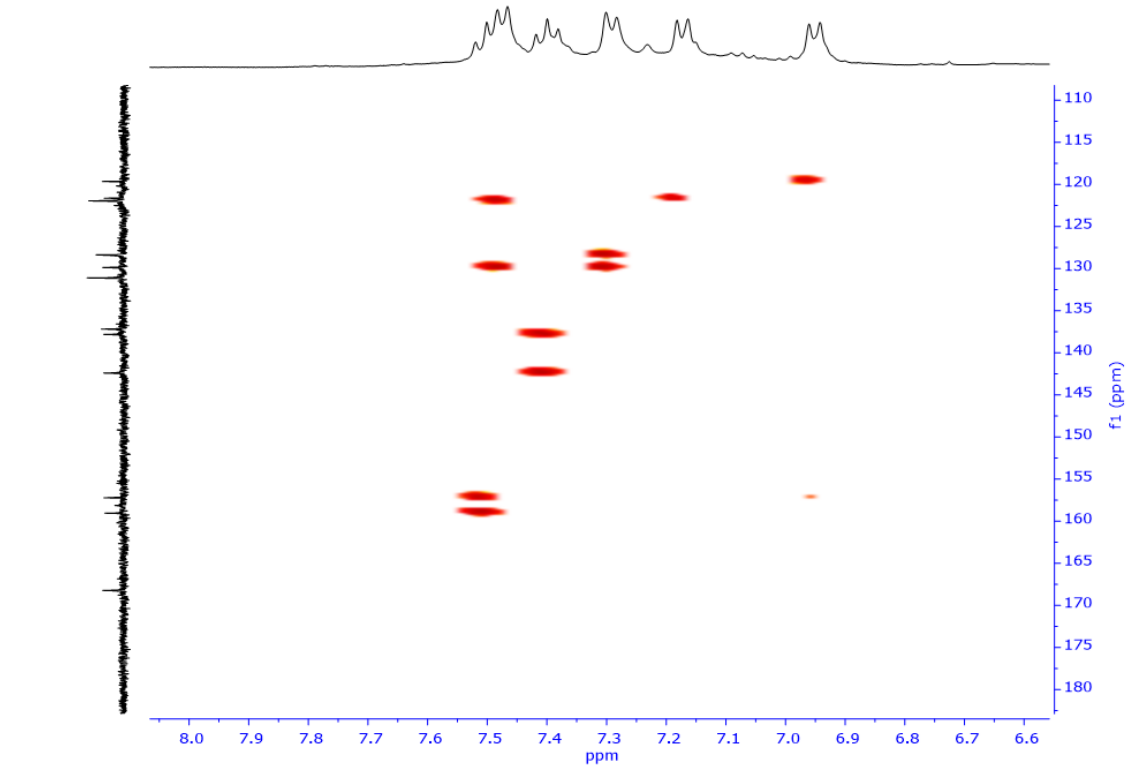

Figure S46. ^{1}H-^{13}C HMBC spectrum of **2^{Me}(CO)** in DMSO-d$_6$ at room temperature (400 MHz). Ampliation of the aromatic regions.

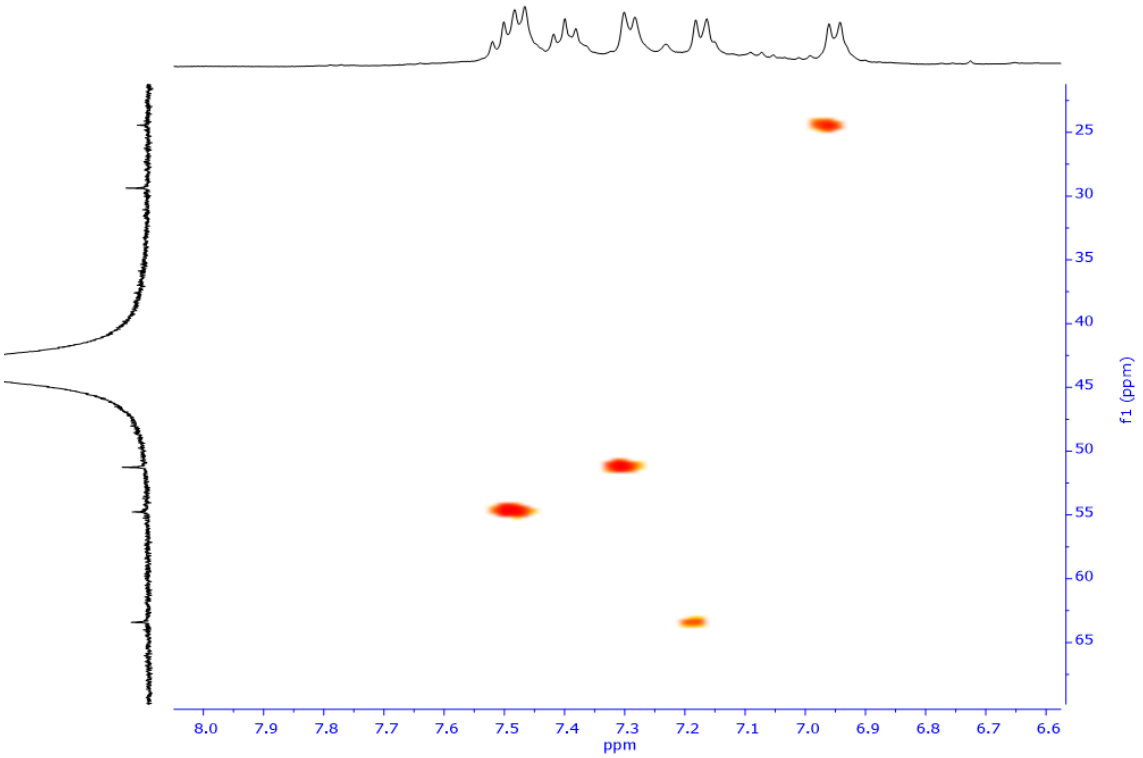

Figure S47. ^{1}H-^{13}C HMBC spectrum of **2^{Me}(CO)** in DMSO-d$_6$ at room temperature (400 MHz). Ampliation of the aromatic (^{1}H) and aliphatic (^{13}C) regions.

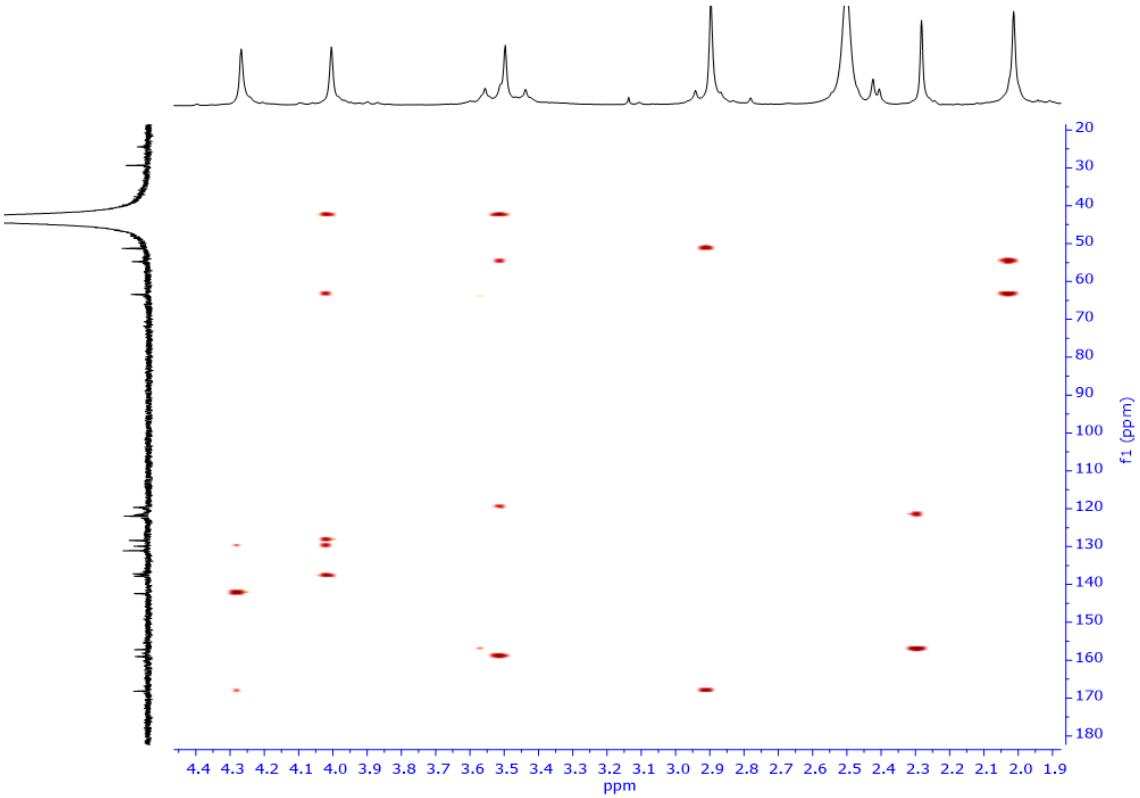

Figure S48. ^{1}H-^{13}C HMBC spectrum of **2^{Me}(CO)** in DMSO-d$_6$ at room temperature (400 MHz). Ampliation of the aliphatic (^{1}H) region vs full range (^{13}C).

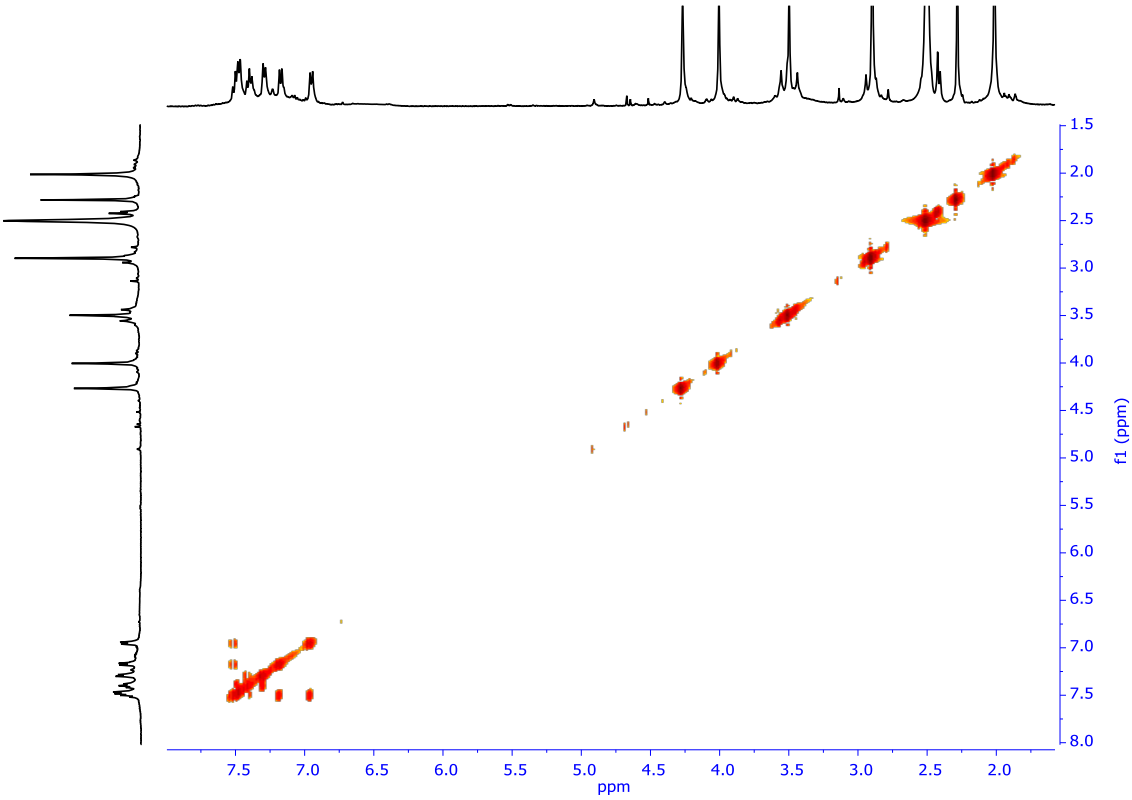

Figure S49. ^{1}H-^{1}H COSY spectrum of **2^{Me}(CO)** in DMSO-d$_6$ at room temperature (400 MHz).

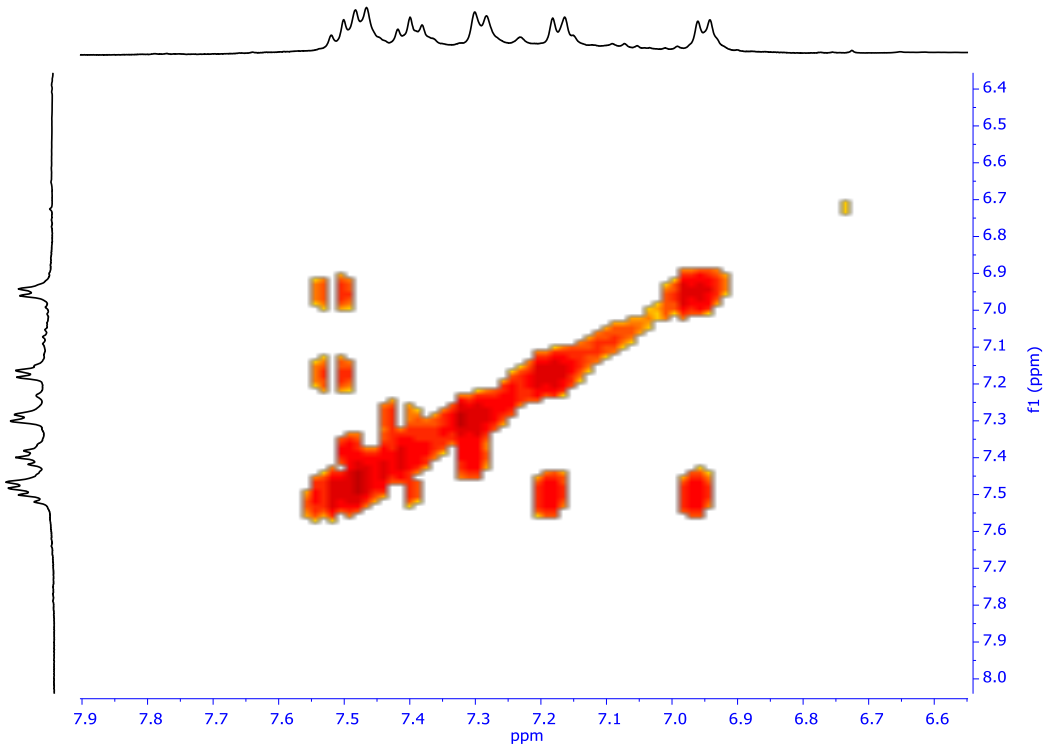

Figure S50. ^{1}H-^{1}H COSY spectrum of **2^{Me}(CO)** in DMSO-d_6 at room temperature (400 MHz). Ampliation of the aromatic region.

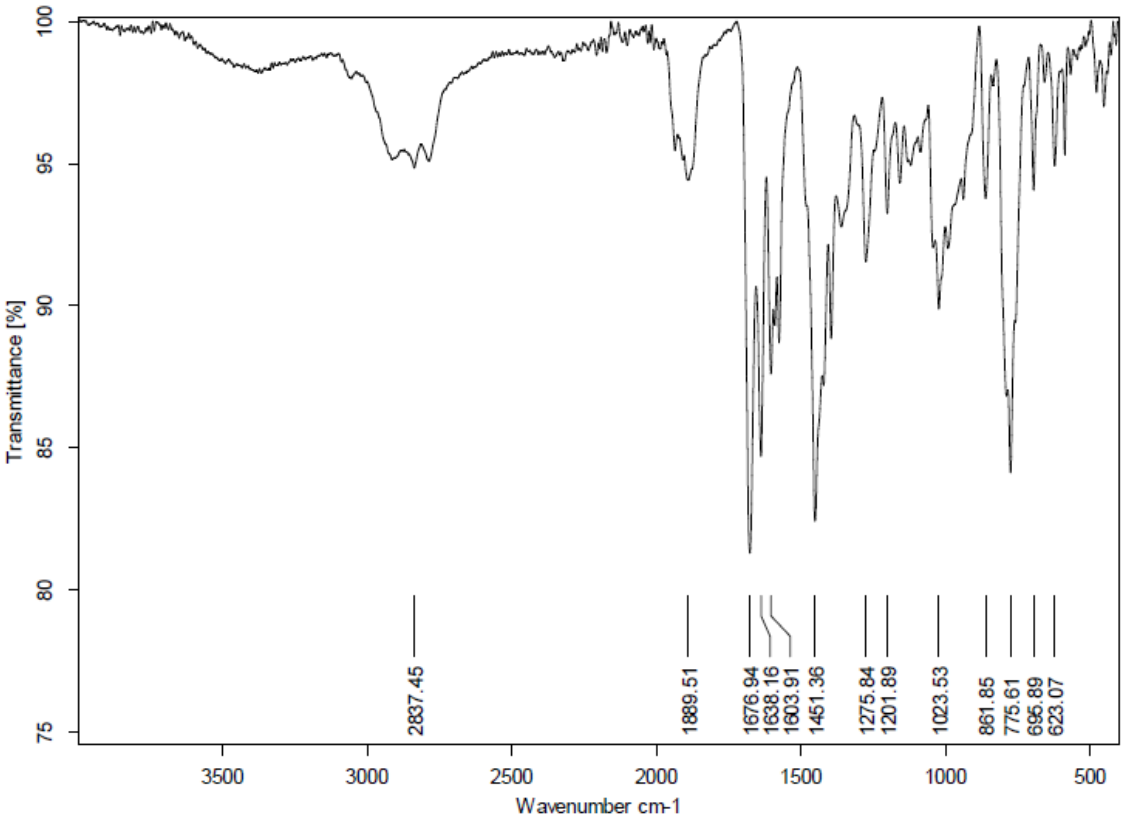

Figure S51. ATR-FT-IR spectrum of **2^{Me}(CO)** at room temperature.

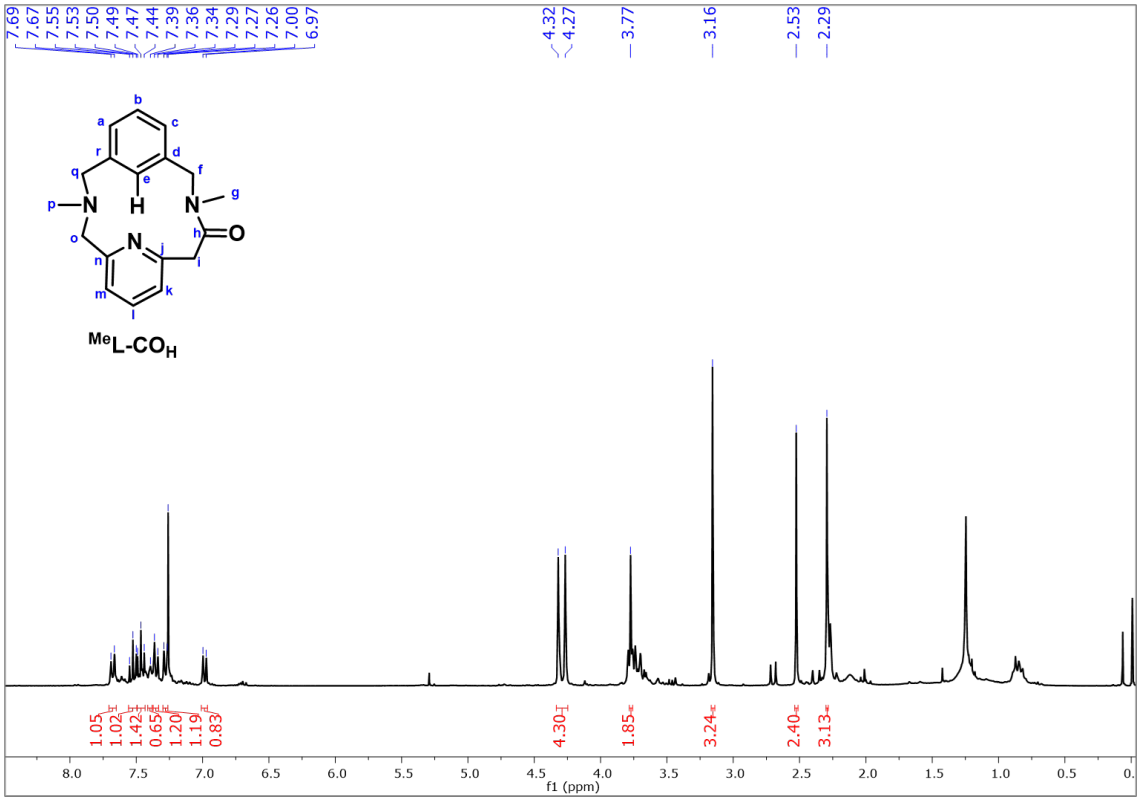

Figure S52. ^{1}H-NMR spectrum of ^{Me}**L-CO$_H$** in $CDCl_3$ at room temperature (400 MHz).

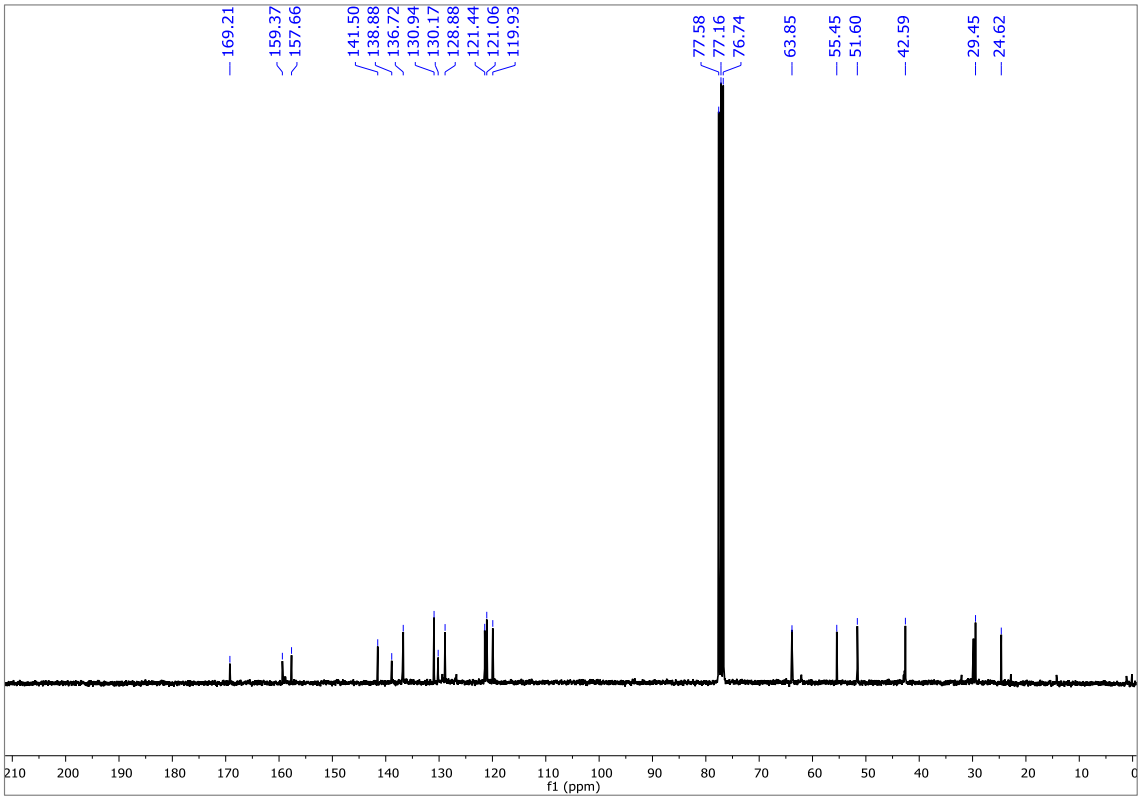

Figure S53. ^{13}C-NMR spectrum of ^{Me}**L-CO$_H$** in $CDCl_3$ at room temperature (400 MHz).

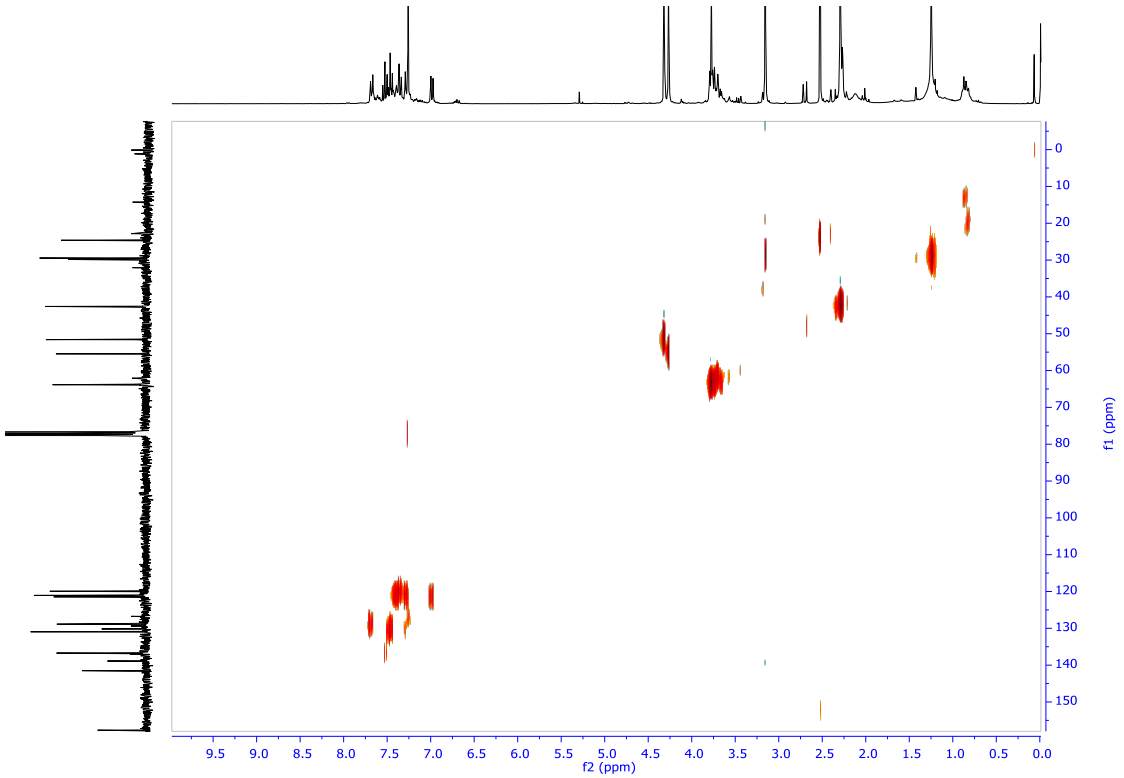

Figure S54. ^{1}H-^{13}C HSQC spectrum of ^{Me}**L-CO$_H$** in $CDCl_3$ at room temperature (400 MHz).

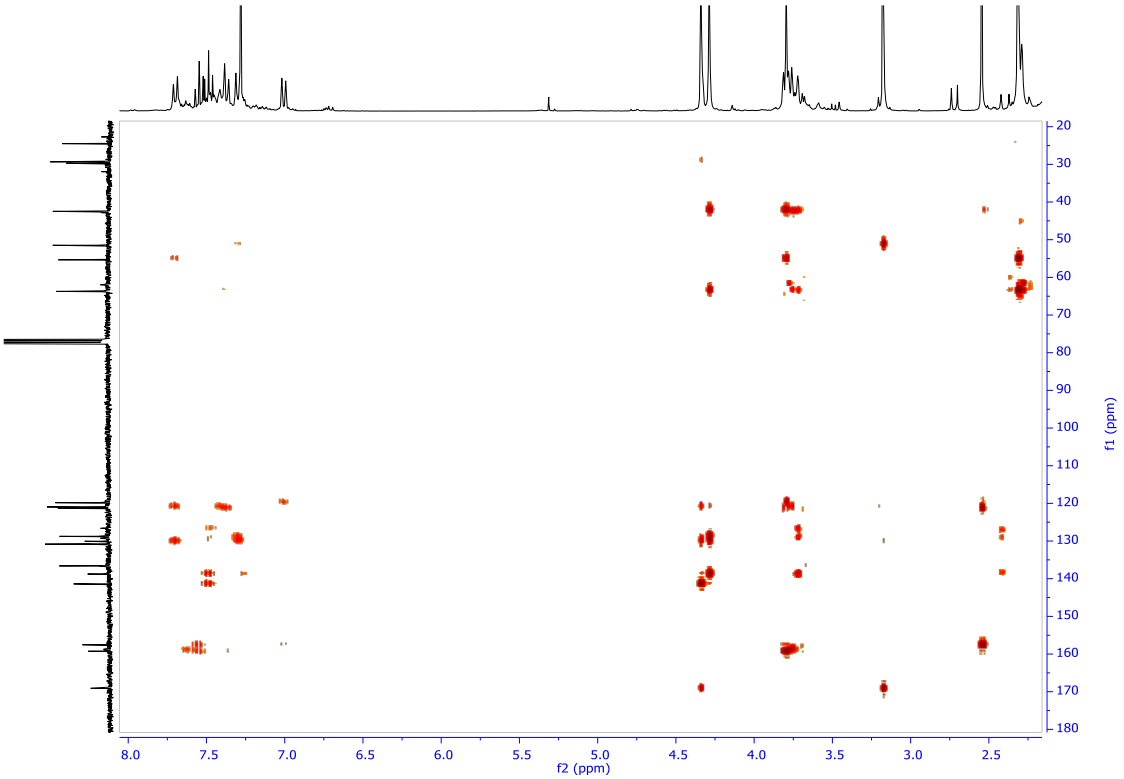

Figure S55. ^{1}H-^{13}C HMBC spectrum of ^{Me}**L-CO$_H$** in $CDCl_3$ at room temperature (400 MHz).

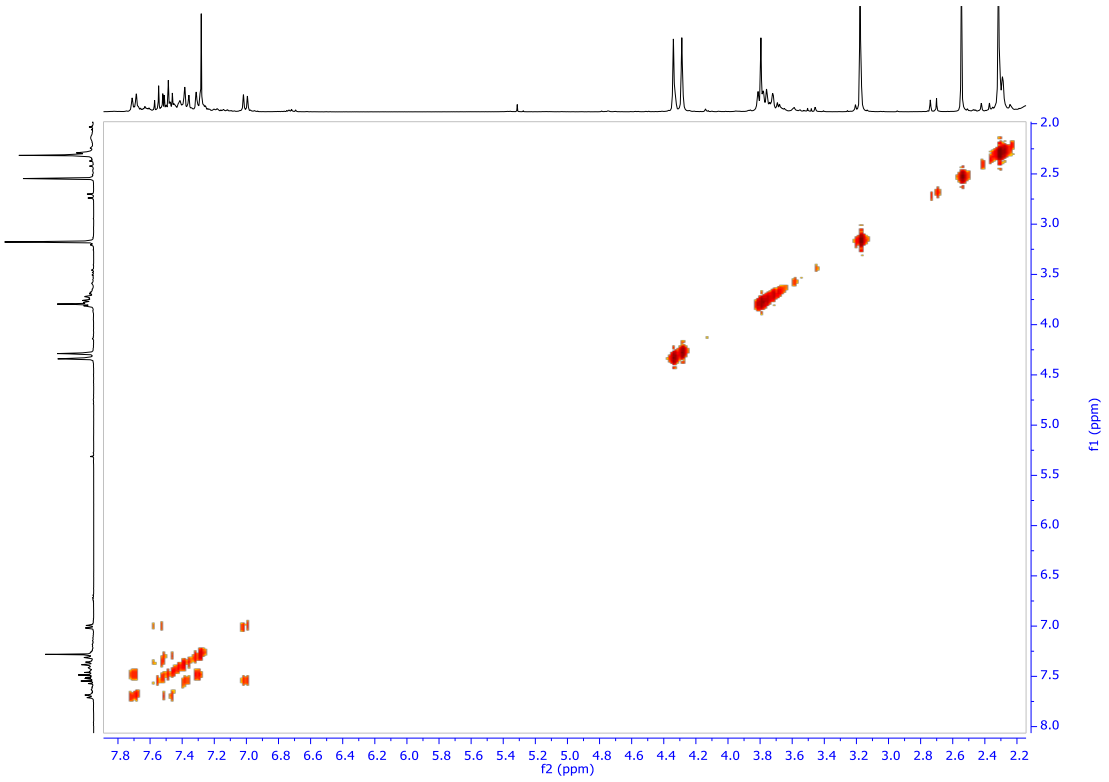

Figure S56. ^{1}H-^{1}H COSY spectrum of ^{Me}**L-CO$_H$** in $CDCl_3$ at room temperature (400 MHz).

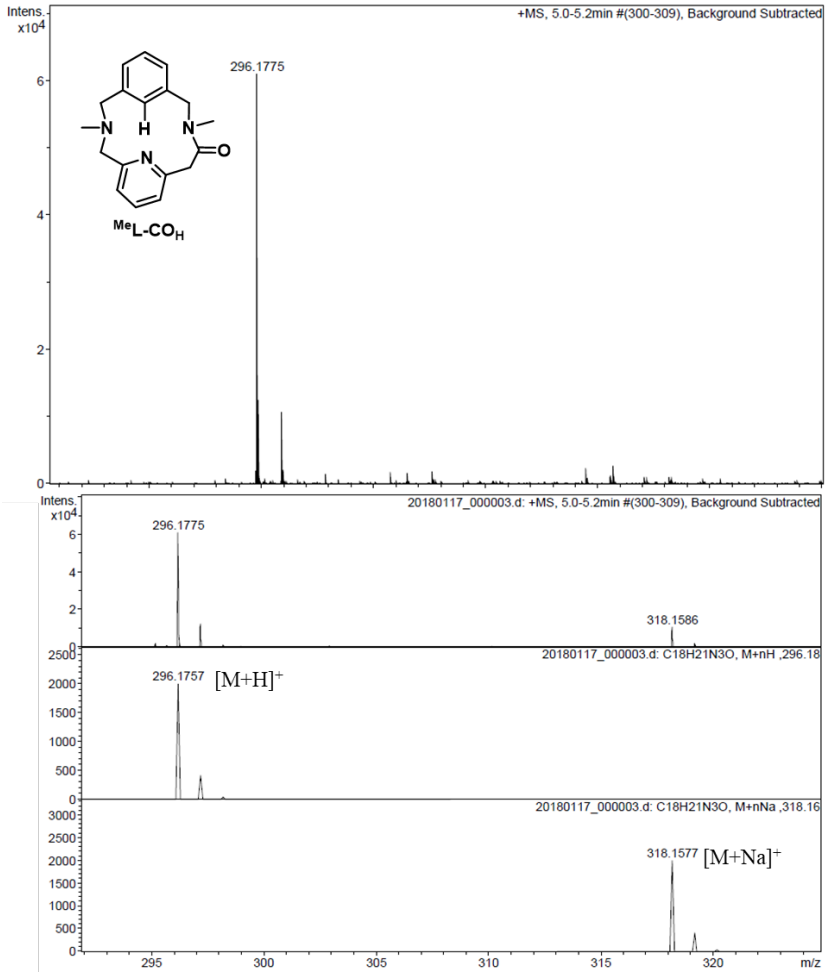

Figure S57. HR-ESI-MS of ^{Me}**L-CO$_H$**. Expanded view of the experimental peaks at m/z = 296.1775 and 318.1586 with a mass value and an isotopic pattern fully consistent with $[M+H/Na]^+$ (top) and the corresponding calculated for these molecular formulas (middle$[M+H]^+$; bottom$[M+Na]^+$). (M = $C_{18}H_{21}N_3O$).

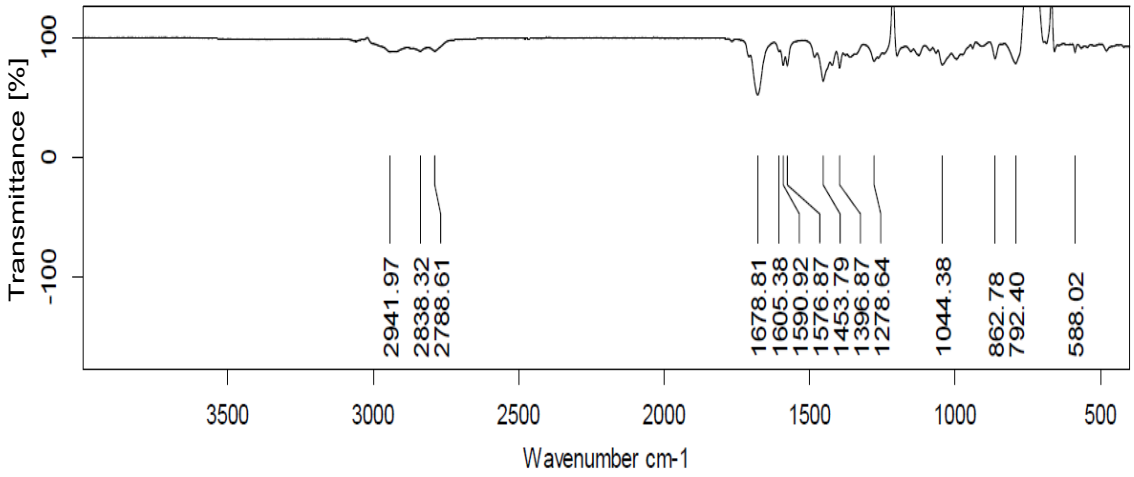

Figure S58. ATR-FT-IR spectrum of ^{Me}**L-CO$_H$** in DCM at room temperature.

10. X-ray Diffraction Analysis

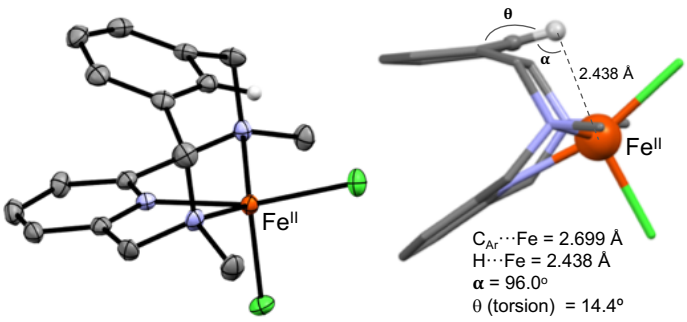

Figure S59. Crystal structure of **1·Cl₂** at 100 K (CCDC 2046155).

Table S1. Crystallographic parameters for **1·Cl₂**.

	1·Cl₂	
Chemical formula	$C_{17}H_{21}Cl_2FeN_3$	
Formula weight	394.12 g/mol	
Temperature	100(2) K	
Wavelength	0.71073 Å	
Crystal system	orthorhombic	
Space group	P b c a (61)	
Unit cell dimensions	a = 12.855(2) Å	α = 90°
	b = 14.842(2) Å	β = 90°
	c = 18.151(3) Å	γ = 90°
Volume	3463.2(9) Å^3	
Z, Density (calculated)	8, 1.512 g/cm^3	
Absorption coefficient	1.181 mm^{-1}	
F(000)	1632	
Crystal size	0.180 x 0.220 x 0.250 mm	
Theta range for data collection	2.38 to 26.08 °	
Index ranges	-16<=h<=17 -18<=k<=19 -24<=l<=24	
Reflections collected / Independent	35615 / 4299 [R(int) = 0.0458]	
Completeness to Theta	99.9% (Theta = 26.08°)	
Refinement method	Full-matrix least-squares on F^2	
Data / restraints / parameters	4299 / 0 / 210	
Goodness-of-fit on F^2	1.075	
Final R indices	3325 data I>2σ(I)	R1 = 0.0449, wR2 = 0.0911
	all data	R1 = 0.0635, wR2 = 0.1006
Largest diff. peak and hole	0.741 and -0.305 eÅ^{-3}	

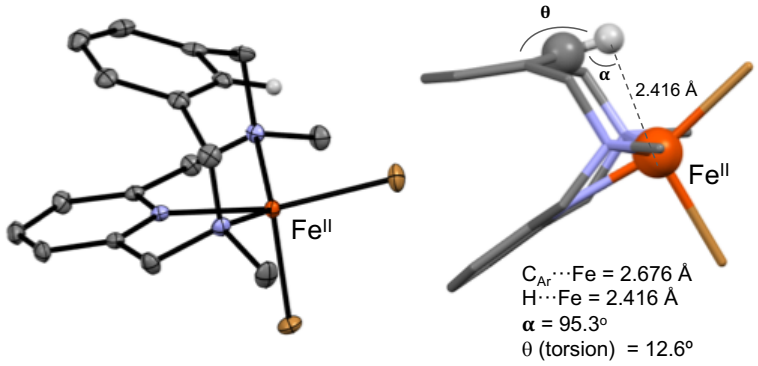

Figure S60. Crystal structure of **1·Br$_2$** at 100 K (CCDC 2046156).

Table S2. Crystallographic parameters for **1·Br$_2$**.

	1·Br$_2$
Chemical formula	$C_{17}H_{21}Br_2FeN_3$
Formula weight	483.04 g/mol
Temperature	100(2) K
Wavelength	0.71076 Å
Crystal system	orthorhombic
Space group	P b c a
Unit cell dimensions	a = 12.927(8) Å α = 90° b = 15.209(9) Å β = 90° c = 18.193(12) Å γ = 90°
Volume	3577(4) Å^3
Z, Density (calculated)	8, 1.794 g/cm^3
Absorption coefficient	5.313 mm^{-1}
F(000)	1920
Crystal size	0.090 x 0.110 x 0.220 mm
Theta range for data collection	3.05 to 30.08 °
Index ranges	-18<=h<=18 -21<=k<=12 -25<=l<=25
Reflections collected / Independent	83185 / 5245 [R(int) = 0.0788]
Completeness to Theta	99.9% (Theta = 30.08°)
Refinement method	Full-matrix least-squares on F^2
Data / restraints / parameters	5245 / 0 / 210
Goodness-of-fit on F^2	1.020
Final R indices	4148 data; I>2σ(I) R1 = 0.0282, wR2 = 0.0495 all data R1 = 0.0471, wR2 = 0.0543
Largest diff. peak and hole	0.518 and -0.465 eÅ^{-3}

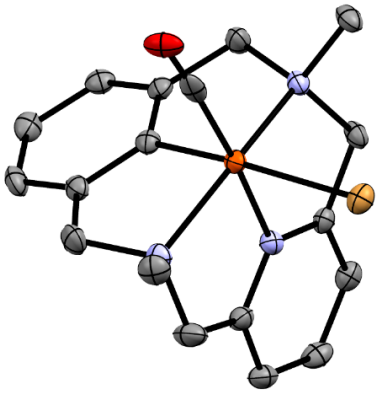

Figure S61. Crystal structure of $\mathbf{1^{Me}}$ at 100 K (CCDC 2046157).

Table S3. Crystallographic parameters for $\mathbf{1^{Me}}$.

	$\mathbf{1^{Me}}$
Chemical formula	$C_{18}H_{20}BrFeN_3O$
Formula weight	430.13 g/mol
Temperature	100(2) K
Wavelength	0.71076 Å
Crystal system	monoclinic
Space group	P 1 21/c 1
Unit cell dimensions	a = 14.751(14) Å α = 90° b = 9.565(8) Å β = 105.17(3)° c = 13.177(10) Å γ = 90°
Volume	1794(3) $Å^3$
Z, Density (calculated)	4, 1.592 g/cm^3
Absorption coefficient	3.076 mm^{-1}
F(000)	872
Crystal size	0.030 x 0.100 x 0.100 mm
Theta range for data collection	2.56 to 27.51 °
Index ranges	-19<=h<=19 -12<=k<=12 -17<=l<=17
Reflections collected / Independent	48846 / 4109 [R(int) = 0.0775]
Completeness to Theta	99.6% (Theta = 27.51°)
Refinement method	Full-matrix least-squares on F^2
Data / restraints / parameters	4109 / 0 / 219
Goodness-of-fit on F^2	1.062
Final R indices	3288 data; I>2σ(I) R1 = 0.0403, wR2 = 0.0805 all data R1 = 0.0598, wR2 = 0.0872
Largest diff. peak and hole	1.408 and -0.409 $eÅ^{-3}$

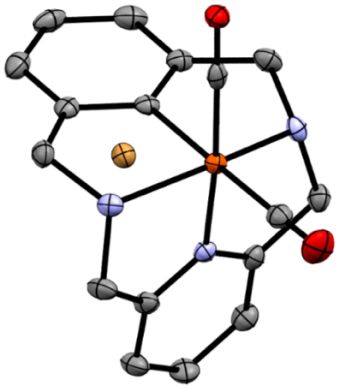

Figure S62. Crystal structure of $\mathbf{1^H}$ at 100 K (CCDC 2046158).

Table S4. Crystallographic parameters for $\mathbf{1^H}$.

	$\mathbf{1^H}$
Chemical formula	$C_{17}H_{16}BrFeN_3O_2$, CH_3CN
Formula weight	471.14 g/mol
Temperature	100(2) K
Wavelength	0.71076 Å
Crystal system	monoclinic
Space group	P 1 21/n 1
Unit cell dimensions	a = 12.717(8) Å α = 90° b = 10.223(7) Å β = 97.74(3)° c = 15.008(9) Å γ = 90°
Volume	1933(2) $Å^3$
Z, Density (calculated)	4, 1.619 g/cm^3
Absorption coefficient	2.868 mm^{-1}
F(000)	952
Crystal size	0.020 x 0.080 x 0.270 mm
Theta range for data collection	2.57 to 27.66 °
Index ranges	-16<=h<=16 -13<=k<=13 -19<=l<=19
Reflections collected / Independent	41971 / 4504 [R(int) = 0.0651]
Completeness to Theta	99.6% (Theta = 27.66°)
Refinement method	Full-matrix least-squares on F^2
Data / restraints / parameters	4504 / 0 / 253
Goodness-of-fit on F^2	1.020
Final R indices	3668 data; I>2σ(I) R1 = 0.0290, wR2 = 0.0545 all data R1 = 0.0452, wR2 = 0.0591
Largest diff. peak and hole	0.422 and -0.346 $eÅ^{-3}$

11. DFT Modelling

11.1. Computational details

All DFT calculations were performed with the Gaussian 16 Revision A.03 program.[8] Geometry optimizations were carried out using the long-range corrected ωB97X-D functional,[9] which includes empirical dispersion correction, along with the def2-SVP basis set.[10] Solvation effects were included as a Polarizable Continuum using the SMD model.[11] Subsequently, we performed frequency calculations to each of the optimized structures to ensure that all local minima have only real frequencies and compute the Gibbs energy (ΔG), i.e., to evaluate the entropic and enthalpic corrections, assuming temperature value of 298.15 K and a pressure of 1.0 atm. Finally, single point energy calculations on the equilibrium geometries, including solvent effects, were computed with the more flexible basis set def2-TZPV.[10] Therefore, the values of ΔG reported in the manuscript are calculated at ωB97X-D/def2TZVP//ωB97X-D/def2SVP level, including solvent effects (SMD) and empirical dispersion corrections.

11.2. Relative electronic and Gibbs energy values of D, E-1 and E-2

Table S1. Relative Electronic (ΔE) and Gibbs energy (ΔG) values in kcal/mol of **D**, **E-1** and **E-2** compounds optimized at ωB97X-D/def2TZVP//ωB97X-D/def2SVP level for the spin states S = 0, 1 and 2.

Compound	ΔE	ΔG
D Singlet	0.00	1.01
D triplet	2.18	0.00
D quintuplet	22.44	14.13
E-1 Singlet	18.17	17.56
E-1 triplet	19.20	15.51
E-1 quintuplet	11.69	6.19
E-2 Singlet	36.89	34.01
E-2 triplet	26.27	22.86
E-2 quintuplet	15.47	9.72

11.3. XYZ coordinates of DFT optimized structures

All Cartesian coordinates for the optimized structures can be found in the supplementary file "Magallon_Organometallics_Cartesian_coordinates.xyz".

12. References

1. *1H-NMR spectra compared to the commercial product.*

2. Planas, O.; Whiteoak, C. J.; Martin-Diaconescu, V.; Gamba, I.; Luis, J. M.; Parella, T.; Company, A.; Ribas, X., Isolation of Key Organometallic Aryl-Co(III) Intermediates in Cobalt-Catalyzed C(sp2)–H Functionalizations and New Insights into Alkyne Annulation Reaction Mechanisms. *J. Am. Chem. Soc.* **2016,** *138*, 14388-14397.

3. Zhou, W.; Schultz, J. W.; Rath, N. P.; Mirica, L. M., Aromatic Methoxylation and Hydroxylation by Organometallic High-Valent Nickel Complexes. *J. Am. Chem. Soc.* **2015,** *137*, 7604-7607.

4. Sarbajna, A.; He, Y.-T.; Dinh, M. H.; Gladkovskaya, O.; Rahaman, S. M. W.; Karimata, A.; Khaskin, E.; Lapointe, S.; Fayzullin, R. R.; Khusnutdinova, J. R., Aryl–X Bond-Forming Reductive Elimination from High-Valent Mn–Aryl Complexes. *Organometallics* **2019,** *38*, 4409-4419.

5. Zhan, C.; Wang, X.; Wei, Z.; Evans, D. J.; Ru, X.; Zeng, X.; Liu, X., Synthesis and characterisation of polymeric materials consisting of {Fe2(CO)5}-unit and their relevance to the diiron sub-unit of [FeFe]-hydrogenase. *Dalton Trans.* **2010,** *39*, 11255-11262.

6. Ouizem, S.; Rosario-Amorin, D.; Dickie, D. A.; Paine, R. T.; de Bettencourt-Dias, A.; Hay, B. P.; Podair, J.; Delmau, L. H., Synthesis and f-element ligation properties of NCMPO-decorated pyridine N-oxide platforms. *Dalton Trans.* **2014,** *43*, 8368-8386.

7. Wessel, A. J.; Schultz, J. W.; Tang, F.; Duan, H.; Mirica, L. M., Improved synthesis of symmetrically & asymmetrically N-substituted pyridinophane derivatives. *Org. Biomol. Chem.* **2017,** *15*, 9923-9931.

8. Frisch, M. J. T., G. W.; Schlegel, H. B.; Scuseria, G. E.; Robb, M. A.; Cheeseman, J. R.; Scalmani, G.; Barone, V.; Petersson, G. A.; Nakatsuji, H.; Li, X.; Caricato, M.; Marenich, A. V.; Bloino, J.; Janesko, B. G.; Gomperts, R.; Mennucci, B.; Hratchian, H. P.; Ortiz, J. V.; Izmaylov, A. F.; Sonnenberg, J. L.; Williams-Young, D.; Ding, F.; Lipparini, F.; Egidi, F.; Goings, J.; Peng, B.; Petrone, A.; Henderson, T.; Ranasinghe, D.; Zakrzewski, V. G.; Gao, J.; Rega, N.; Zheng, G.; Liang, W.; Hada, M.; Ehara, M.; Toyota, K.; Fukuda, R.; Hasegawa, J.; Ishida, M.; Nakajima, T.; Honda, Y.; Kitao, O.; Nakai, H.; Vreven, T.; Throssell, K.; Montgomery, J. A., Jr.; Peralta, J. E.; Ogliaro, F.; Bearpark, M. J.; Heyd, J. J.; Brothers, E. N.; Kudin, K. N.; Staroverov, V. N.; Keith, T. A.; Kobayashi, R.; Normand, J.; Raghavachari, K.; Rendell, A. P.; Burant, J. C.; Iyengar, S. S.; Tomasi, J.; Cossi, M.; Millam, J. M.; Klene, M.; Adamo, C.; Cammi, R.; Ochterski, J. W.; Martin, R. L.; Morokuma, K.; Farkas, O.; Foresman, J. B.; Fox, D. J. *Gaussian 16, Revision A.03*, Gaussian Inc.: Wallingford CT, 2016.

9. Chai, J.-D.; Head-Gordon, M., Long-range corrected hybrid density functionals with damped atom–atom dispersion corrections. *Phys. Chem. Chem. Phys.* **2008,** *10*, 6615-6620.

10. Weigend, F.; Ahlrichs, R., Balanced basis sets of split valence, triple zeta valence and quadruple zeta valence quality for H to Rn: Design and assessment of accuracy. *Phys. Chem. Chem. Phys.* **2005,** *7*, 3297-3305.

11. Marenich, A. V.; Cramer, C. J.; Truhlar, D. G., Universal solvation model based on solute electron density and on a continuum model of the solvent defined by the bulk dielectric constant and atomic surface tensions. *J. Phys. Chem. B* **2009,** *113*, 6378-6396.

ANNEX 3. Supporting information Chapter VI

Organometallic Ni(II), Ni(III) and Ni(IV) relevant to Carbon-Carbon and Carbon-Oxygen bond formation reactions

Carla Magallon,[a] Leonel Griego,[b] Daniel Hu,[b] Anna Company,*[,a] Xavi Ribas,*[,a] Liviu M. Mirica*[,b]

[a]Institut de Química Computacional i Catàlisi (IQCC) and Departament de Química, Universitat de Girona, Campus Montilivi, Girona, E-17003, Catalonia, Spain

[b]Department of Chemistry, University of Illinois at Urbana-Champaign, 600 S. Mathews Avenue, Urbana, Illinois 61801, USA.

*Corresponding author: mirica@illinois.edu

Table of contents

1. General considerations

Materials and methods

All manipulations were carried out under a nitrogen atmosphere using standard Schlenk and glove box (with O_2 and H_2O concentrations < 1 ppm) techniques unless otherwise indicated. All reagents for which synthesis is not given are commercially available from Sigma Aldrich, Acros or STREM and were used as received without further purification. Solvents were purified prior to use by passing through a column of activated molecular sieves using an MBRAUN SPS. **PyNMe$_3$** ligand,[1, 2] $(Py)_2Ni^{II}$(cycloneophyl),[3] were prepared according to previously reported protocols in the literature. Other abbreviations used throughout the paper and supporting information: ferrocenium hexafluorophosphate ($FcPF_6$), nitrosonium hexafluorophosphate ($NOPF_6$), nitrosonium hexafluoroantimonate ($NOSbF_6$), 1-Fluoro-2,4,6-trimethylpyridinium triflate (NFTPT), hydrogen peroxide (H_2O_2), *tert*-butyl hydroperoxide ($^tBuO_2H$), xenon difluoride (XeF_2) and (diacetoxyiodo)benzene ($PhI(OAc)_2$).

NMR data concerning product identity were collected with a Bruker 500 spectometer (500 MHz). Chemical shifts are reported in ppm and referenced to residual solvent resonance peaks. Abbreviations for the multiplicity of NMR signals are s (singlet), d (doublet), dd (doublet of doublets), t (triplet), m (multiplet). All NMR experiments were recorded and processed using standard parameters and no more details are given, unless otherwise stated. EPR spectra were recorded using a Bruker 10" EMXPlus X-band Continuous Wave EPR spectrometer at 77 K. EPR spectra simulation and analysis were performed using Bruker WINEPR SimFonia program, version 1.25. GC-MS data was collected using an Agilent 7890B GC Series System and an Agilent 5977B Mass Selective Detector. High resolution mass spectra (HRMS) were recorded on a Bruker MicrOTOF-Q IITM instrument using ESI as ionization source or CMS (cryospray ionization, for low temperature experiments) at Serveis Tècnics University of Girona. Samples were introduced into the mass spectrometer ion source by direct infusion and were externally calibrated using sodium triflate. The instrument was operated in the positive ion mode. Electrochemical-grade electrolytes from Fluka were used as the supporting electrolyte for electrochemical measurements. Cyclic voltammetry experiments were performed with a BASi EC Epsilon electrochemical workstation or a CHI 660D Electrochemical Analyzer. The

electrochemical measurements were taken in a glove box under nitrogen. A glassy carbon disk electrode (d = 1.6 mm) was used as the working electrode for cyclic voltammetry. The auxiliary electrode was a Pt wire for cyclic voltammetry measurements. The non-aqueous references electrode used was a silver wire. The reference electrodes were calibrated against ferrocene (Fc). UV-vis spectroscopy was performed with an Agilent 8453 UV-vis spectrophotometer with 1 cm quartz cells. Low temperature control was achieved with a cryostat from Unisoku Scientific Instruments, Japan. Elemental analysis was carried out by the Microanalysis Laboratory at UIUC using an Exeter Analytical - Model CE440 CHN Analyzer.

2. Synthesis of [(PyNMe$_3$)Ni^{II}(PhF)(Br)] and 1-Br Complexes

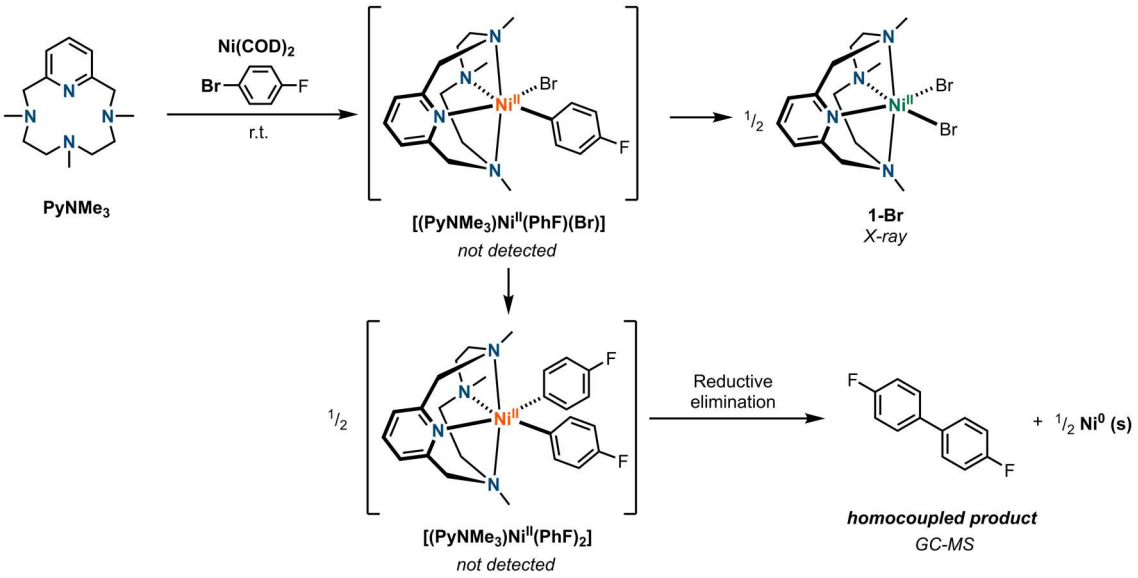

Scheme S1. Attempt to synthesize complex [(**PyNMe$_3$**)**Ni^{II}**(**PhF**)(**Br**)].

In a N_2-filled glovebox, **PyNMe$_3$** (38mg, 0.15 mmols) and Ni(COD)$_2$ (42.1 mg, 0.15 mmols) were dissolved in ~3 mL of 4-**f**luorobromobenzene. The mixture was stirred for 4 hours at room temperature, and a green solid formed with specs of a black solid. The mixture was collected and washed with diethylether to remove excess solvent and ligand. [(PyNMe$_3$)Ni^{II}(Br)$_2$] (1-Br) and Ni(0) (64.9 mg, 0.13 mmol, 88% yield).

X-ray quality crystals were obtained from the slow diethylether vapor diffusion over a concentrated solution of the complex in MeCN at -35 ºC. The solid-state structure revealed complex **1-Br**. In addition, the reaction solution contained homocoupled product 4,4-difluorobiphenyl, detected via GC-MS.

3. Synthesis of 1-Cl and [(PyNMe$_3$)Ni^{II}(Me)$_2$] Complexes

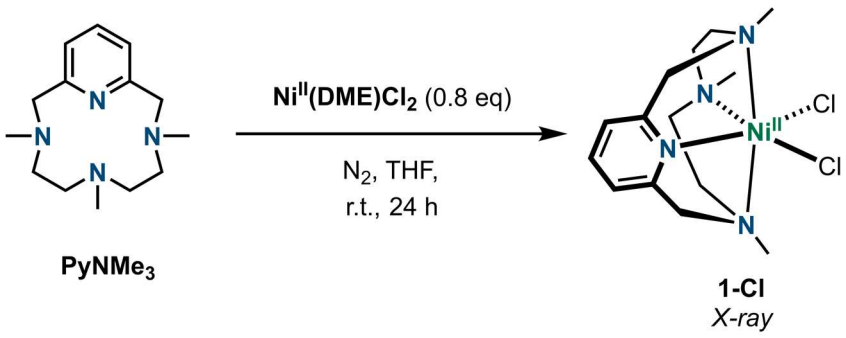

Scheme S2. Synthesis of complex **1-Cl**.

In the glovebox, **PyNMe$_3$** (29.2 mg, 0.12 mmol) was dissolved in THF (2 mL). Afterwards Ni^{II}(DME)Cl$_2$ (20.0 mg, 0.09 mmol) was added directly as a solid and the mixture was stirred for 24 hours. After that, the formation of a green suspension was observed. Then the suspension was crashed out with diethyl ether, filtered and dried under vacuum obtaining 28.5 mg of a green solid corresponding to [**(PyNMe$_3$)Ni^{II} (Cl)$_2$**], **1-Cl** (0.08 mmol, 85% yield). X-ray quality crystals were obtained after redissolving the green solid in MeCN and by slow diethyl ether diffusion at room temperature.

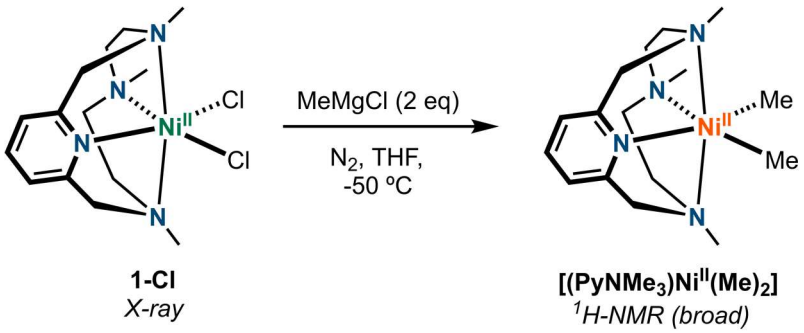

Scheme S3. Attempt to synthesize complex [**(PyNMe3)NiII(PhF)(Br)**].

In a N$_2$-filled glovebox, **1-Cl** (35.5 mg, 0.09 mmol) was suspended in THF and cooled down to -50 °C. Then 66 µL of a 3M solution of cold MeMgCl in THF was added dropwise and upon addition of the MeMgCl a color change from green to red was observed. The suspension was left stirring for an 1 hour at -50 °C in the glovebox freezer and then the solvent was evaporated under vacuum at -50 °C. After that toluene was added to precipitate the magnesium salts and the mixture (orange) was filtered twice through a celite® pad and once through a kim-wipe. The

solvent was removed under vacuum and the orange-black solid was dissolved in benzene-d_6 to take ^{1}H-NMR at r.t of the putative $[(\mathbf{PyNMe_3})\mathbf{Ni^{II}(Me)_2}]$ formed.

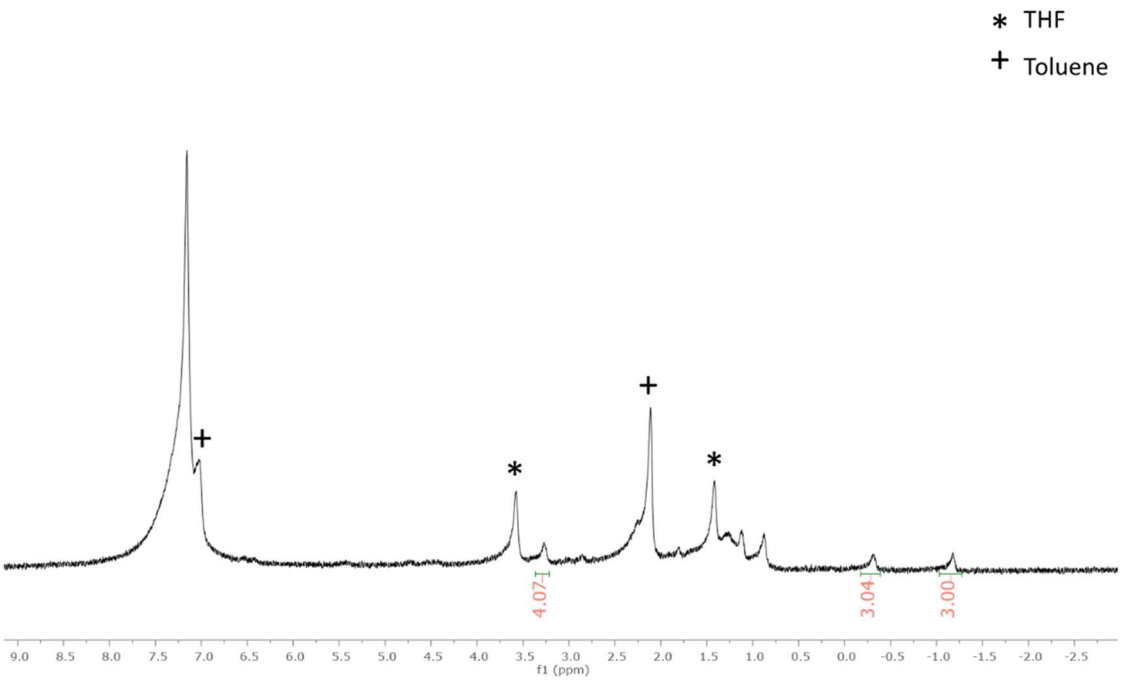

Figure S1. ^{1}H-NMR of the putative $[(\mathbf{PyNMe_3})\mathbf{Ni^{II}(Me)_2}]$ in C_6D_6.

4. Synthesis of $[(\mathbf{PyNMe_3})\mathbf{Ni(cycloneophyl)}]$ complexes

4.1. Preparation of $[(\mathbf{PyNMe_3})\mathbf{Ni^{II}(cycl)}$, 2

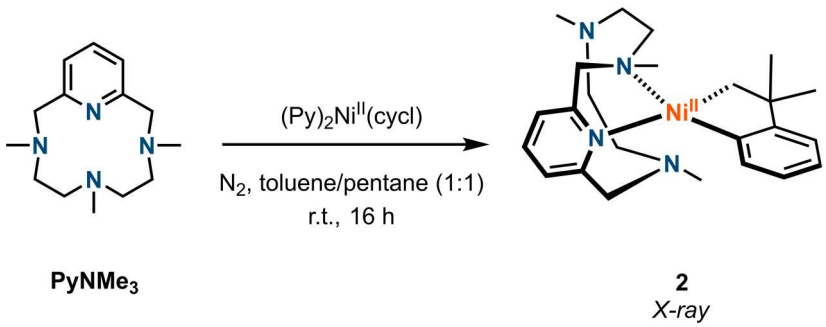

Scheme S4. Synthesis of complex **2**.

In the glovebox, **PyNMe$_3$** (70.9 mg, 0.28 mmol) and $(Py)_2Ni^{II}(cycl)$ (65.2 mg, 0.19 mmols) were dissolved in 3 mL toluene/pentane (1:1). The mixture was stirred for 16 hours at room temperature. After that the orange-red suspension was dried under vacuum. Then the orange solid obtained was washed with diethyl ether to remove any ligand in excess. The suspension

was filtered and the solid was redissolved in the minimum amount of THF. Slow pentane diffusion over a concentrated solution of the complex in THF at -35 ºC afforded orange crystals corresponding to [(**PyNMe$_3$**)**Ni^{II}**(**cycl**)], **2** (58.3 mg, 0.13 mmol, 71 % yield).

^{1}H-NMR (C_6D_6, 500 MHz, 298 K) δ (ppm): 7.19-7.10 (m, 2H, **C**), 6.93 (m, 1H, **C**), 6.86 (m, 1H, **F**), 6.54 (b, 1H, **C**), 6.50 (m, 2H, **F**), 4.82 (d, 2H, **G**), 3.00 (b, 2H, **E**), 2.87 (b, 2H, **G**), 2.44 (b, 2H, **E**), 2.22 (s, 3H, **D**), 2.07 (s, 6H, **D**), 1.90 (s, 6H, **B**), 1.85 (b, 3H,) 1.71 (b, 2H, **E**), 1.35 (s, 2H, **A**); Ligand Impurities: 6.78, 3.69, 3.56, 2.71, 2.60, 2.33, 2.18

^{13}C-NMR (C_6D_6, 500 MHz, 298 k), δ (ppm): 169.50 (**c**), 159.80 (**f**), 159.04 (**c**), 157.78 (**f**), 136.73 (**c**), 136.07 (**f**), 134.50 (**f**), 122.56 (**c**), 121.76 (**c**), 121.43 (**f**), 120.82 (**c**), 65.04 (**g**), 56.49 (**e**), 55.89 (**e**), 47.79 (**h**), 47.08 (**d**), 44.42 (**d**), 40.74 (**a**), 34.16 (**b**) ; Ligand Impurities: 62.52, 52.09, 51.43, 45.05, 44.12

EA: calcd. for $C_{24}H_{36}N_4Ni$, C 65.62, N 12.75, H 8.26 %; exp. C 66.01, N 12.83, H 8.37 %.

UV-vis(233 K): λ_{max} = 460 nm (ε = 880 $M^{-1}cm^{-1}$)

4.2. Preparation of [(PyNMe$_3$)Ni^{III}(cycl)](PF$_6$), 3

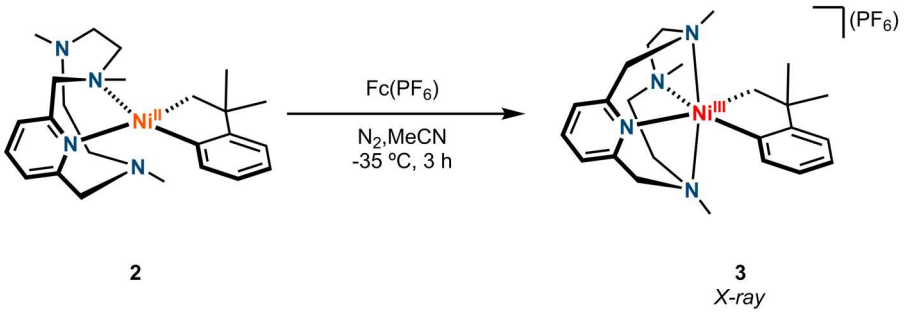

2 **3** *X-ray*

Scheme S5. Synthesis of complex **3**.

In the glovebox, complex **2** (23.4 mg, 0.05 mmol) was dissolved in 2 mL of MeCN and Fc(PF$_6$) (17.6 mg, 0.05 mmols) was added at -50 ºC. The mixture was stirred for 3 hours at -35 ºC. After that the mixture was concentrated under vacuum. X-ray quality crystals were obtained after a few days of storage of a concentrated solution in MeCN at -35 ºC corresponding to [(**PyNMe$_3$**)**Ni^{III}**(**cycl**)](**PF$_6$**), **3** (21.3 mg mg, 0.04 mmol, 73 % yield)

HR-CMS-MS (233 K): calcd. for $C_{24}H_{36}N_4Ni^+$ $[M\text{-}PF_6]^+$ 438.2288; exp 438.2289.

EPR $g_z = 2.235$; $g_y = 2.207$; $g_z = 2.016$, $A_{2N} = 13.7$ G

EA: calcd. for $C_{24}H_{36}N_4NiPF_6 \cdot 0.6(CH_3CN)$, C 48.53, N 10.58, H 6.26 %; exp. C 48.22, N 10.47, H 6.17 %.

UV-vis(233 K): $\lambda_{max} = 510$ nm ($\varepsilon = 300$ $M^{-1}cm^{-1}$)

4.3. NMR Scale Preparation of $[(PyNMe_3)Ni^{IV}(cycloneophyl)](SbF_6)_2$, 4

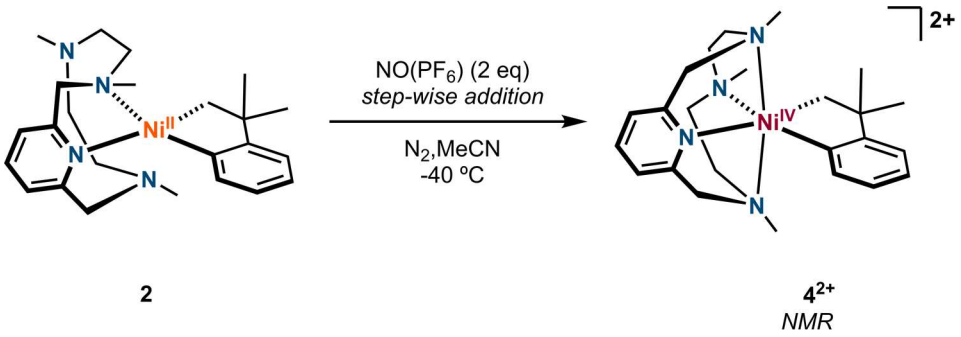

Scheme S6. NMR-scale synthesis of complex **4**.

In the glovebox, complex **2** (6.0 mg, 0.01 mmol) was dissolved in 200 µL CD_3CN, placed in an NMR tube and sealed with a septum cap. A separate solution of $NO(PF_6)$ (3.5 mg, 0.02 mmols) in 200 µL of CD_3CN was added at -40 ºC in a stepwise fashion. The first equivalent of oxidant was added and quickly mixed in the NMR tube to get a pink-red paramagnetic solution. The second equivalent of oxidant was then added and mixed to obtain a dark orange diamagnetic solution corresponding to complex $[(PyNMe_3)Ni^{IV}(cycl)](PF_6)_2$, **4**.

^{1}H-NMR (500 MHz, CD_3CN, -35 ºC), δ (ppm): 8.38 (b, 1H, **L**), 7.78 (b, 2H, **K**), 7.14-7.05 (d, 3H, **B,C,D**), 6.70 (b, 1H, **A**), 5.25 (s, 2H, **F**), 3.70-2.86 (d, 4H, **J**), 2.95-2.73 (d, 8H, **I**), 2.17 (s, 6H, **H**), 1.61 (s, 6H, **E**), 1.37 (s, 3H, **G**) Impurities: 5.45, 1.3, 0.86

HR-CMS-MS (233 K): calcd. for $C_{24}H_{36}N_4Ni^{2+}$ $[M\text{-}2SbF_6]^+$ 219.1141; exp 219.1120.

UV-vis(233 K): $\lambda_{max} = 470$ nm ($\varepsilon = 1200$ $M^{-1}cm^{-1}$)

5. NMR Spectra for [(PyNMe$_3$)Ni(cycloneophyl)] Complexes

5.1. NMR Characterization for complex 2

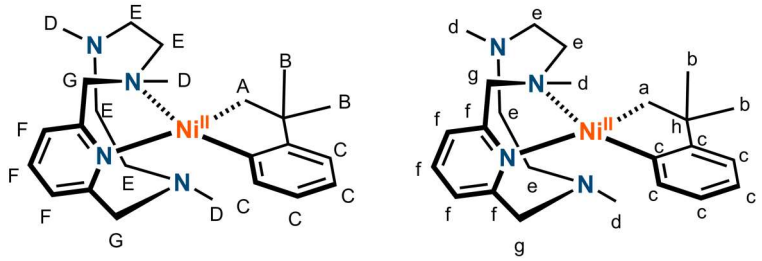

complex **2**

Scheme S7. ^{1}H-NMR (left) and ^{13}C-NMR (right) assignations for complex **2**.

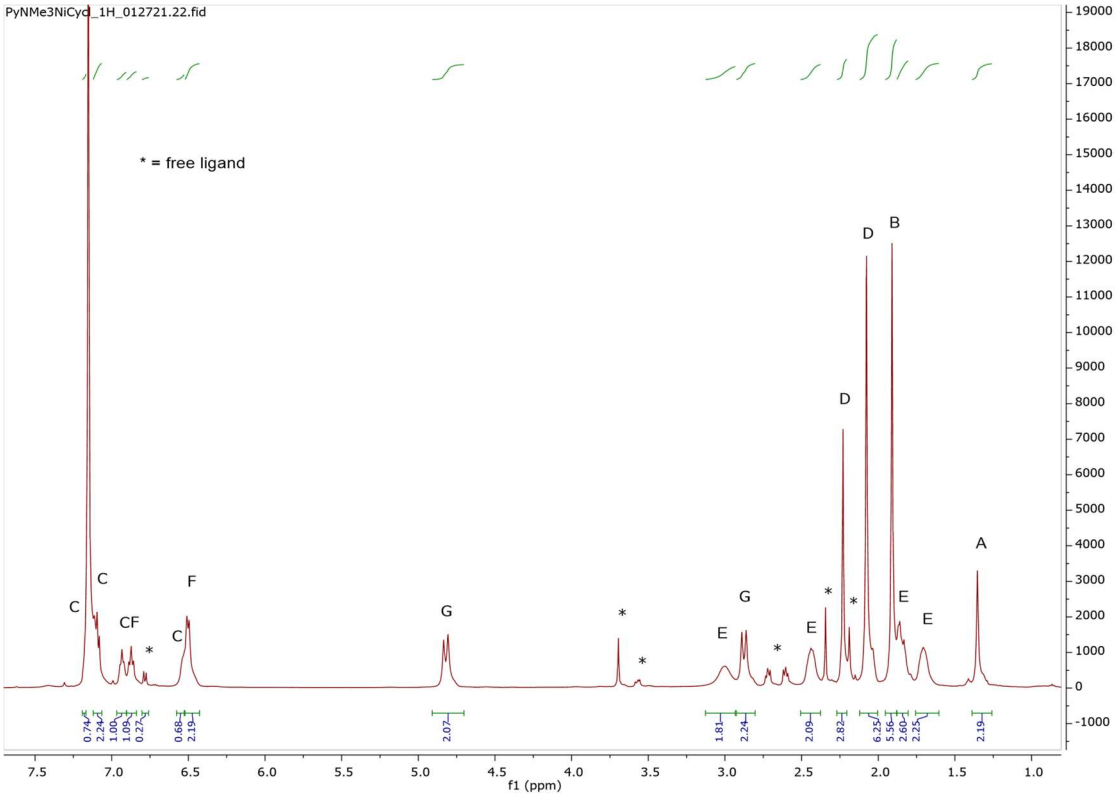

Figure S2. ^{1}H-NMR of complex **2** in C_6D_6 at room temperature.

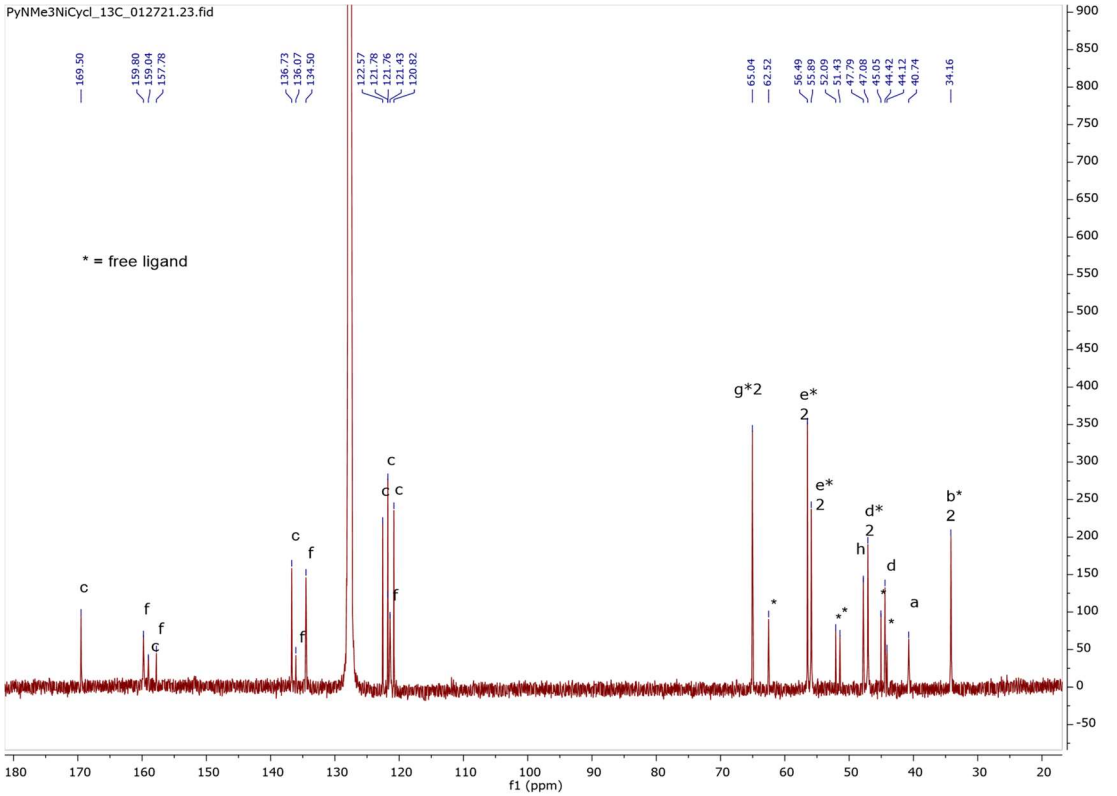

Figure S3. ^{13}C-NMR of complex **2** in C_6D_6 at room temperature.

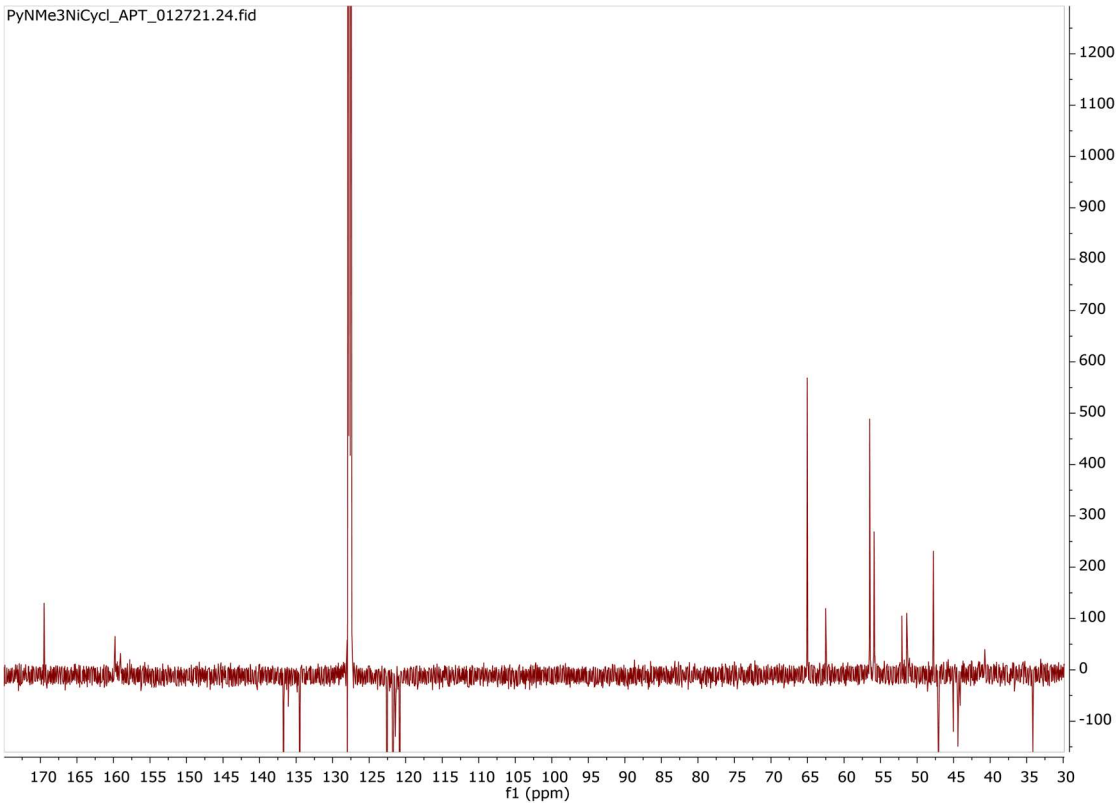

Figure S4. ^{13}C-APT of complex 2 in C_6D_6 at room temperature.

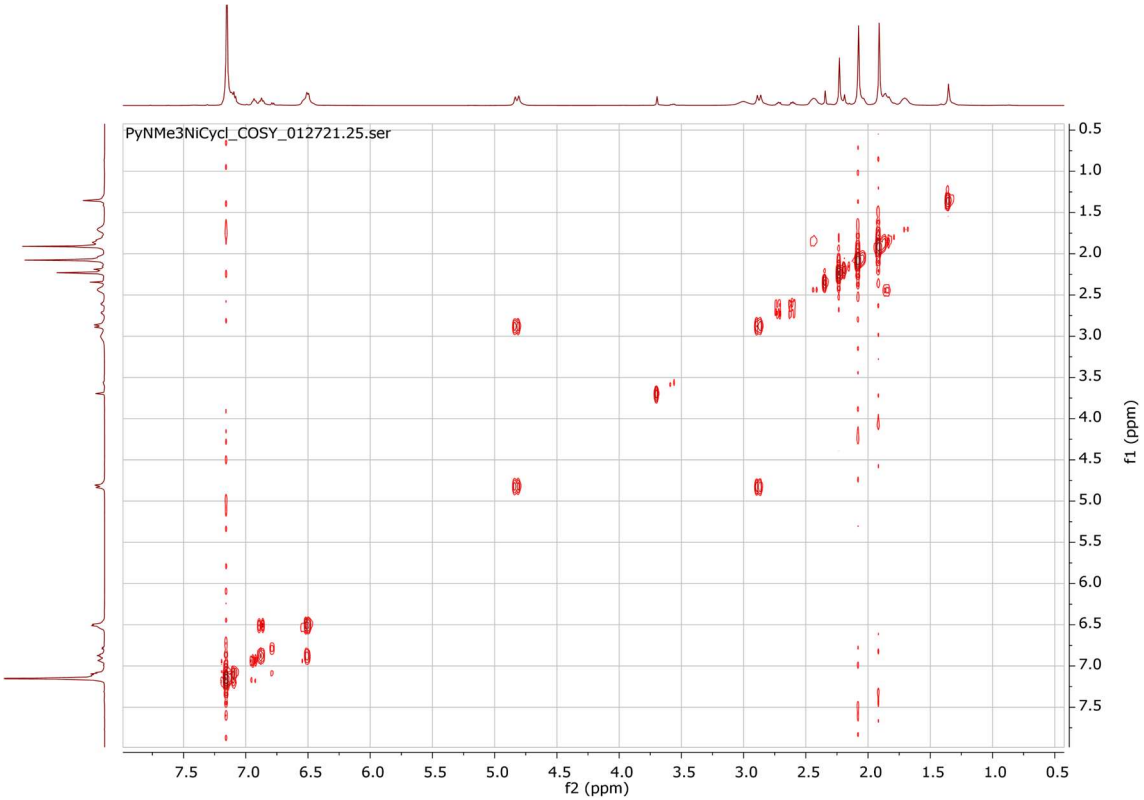

Figure S5. ^{1}H-^{1}H COSY NMR of complex **2** in C_6D_6 at room temperature.

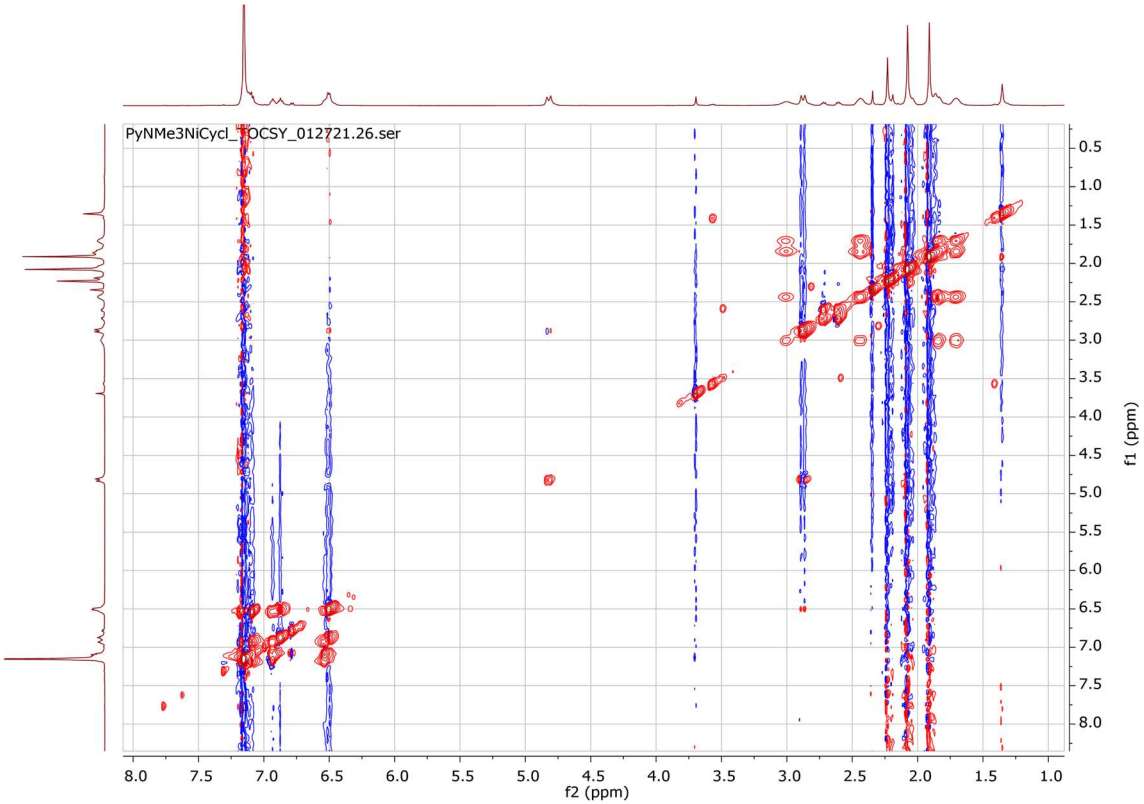

Figure S6. ^{1}H-^{1}H TOCSY NMR of complex **2** in C_6D_6 at room temperature.

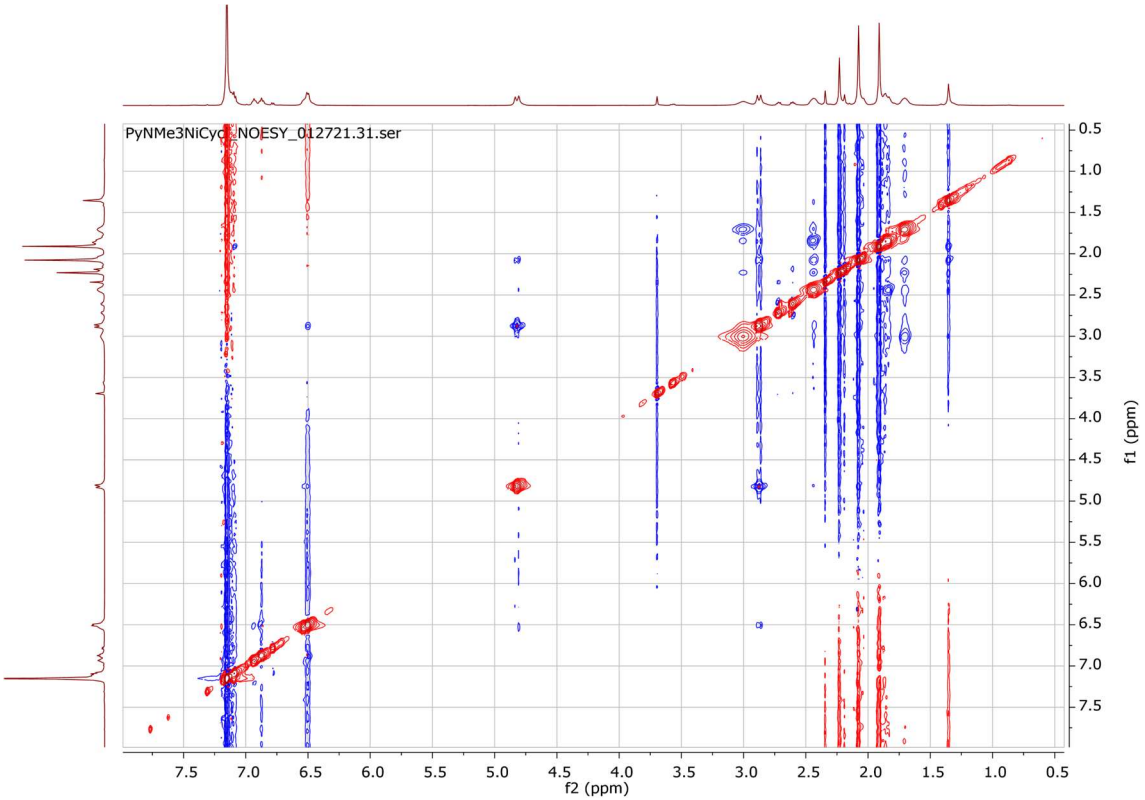

Figure S7. ^{1}H-^{1}H NOESY NMR of complex **2** in C_6D_6 at room temperature.

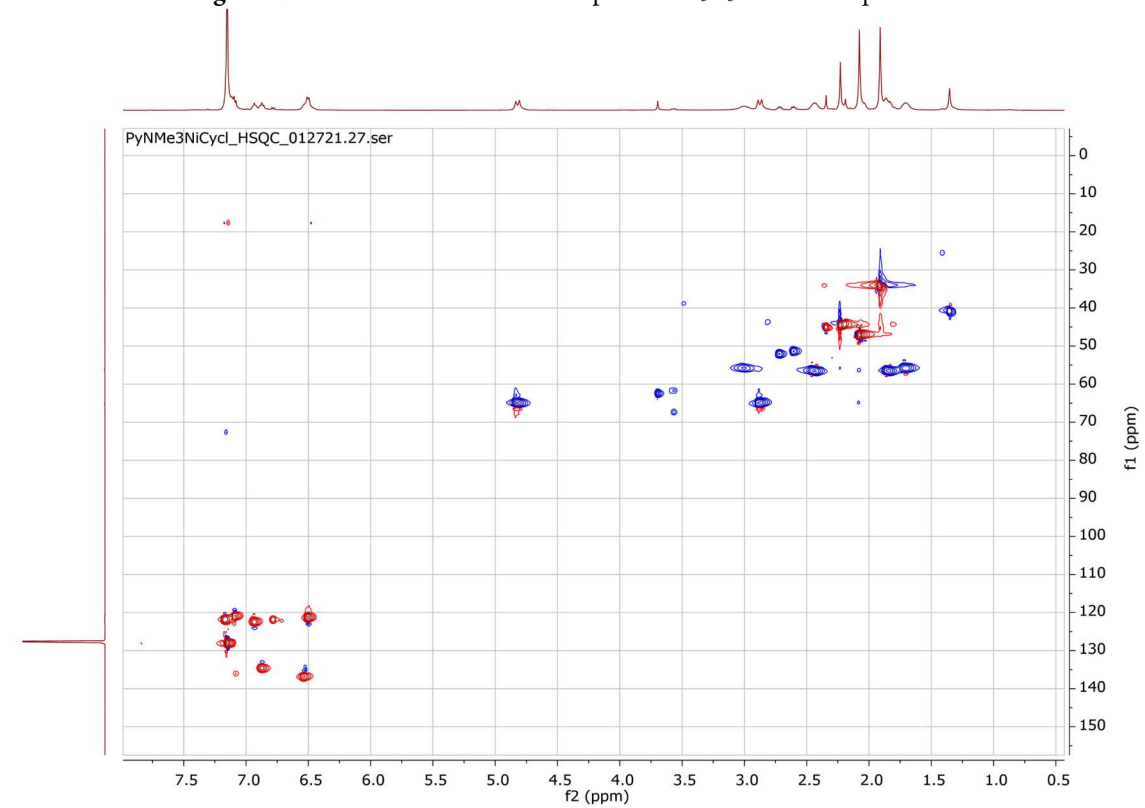

Figure S 8. ^{1}H-^{13}C HSQC NMR of complex **2** in C_6D_6 at room temperature.

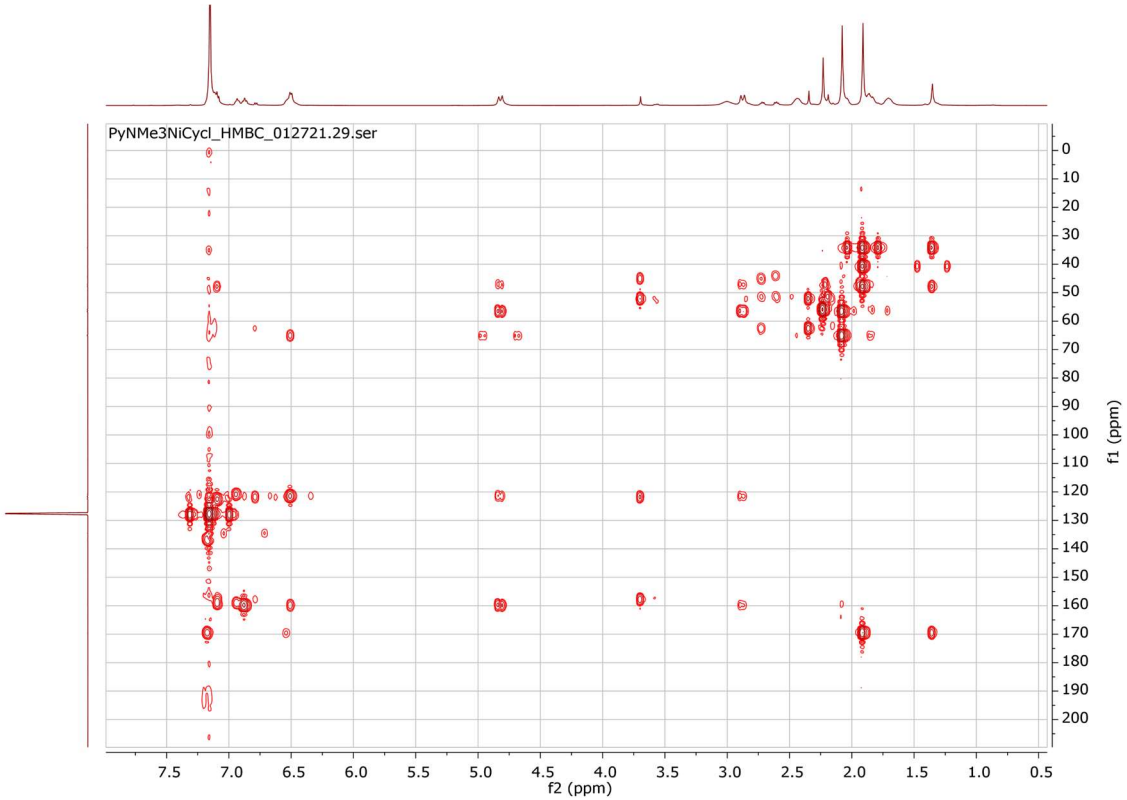

Figure S9. ^{1}H-^{13}C HMBC NMR of complex **2** in C_6D_6 at room temperature.

5.2. NMR Comparison for complexes 2, 3 and 4

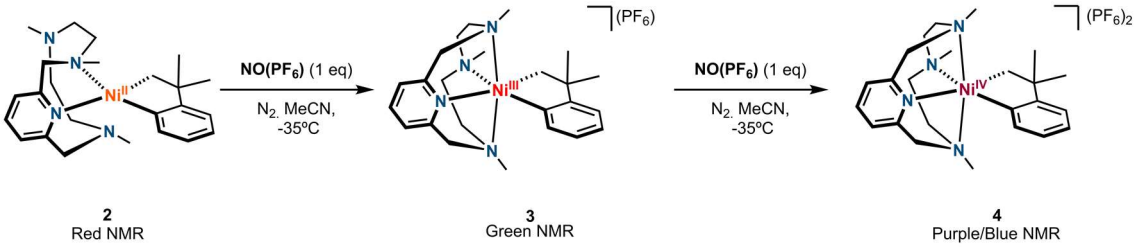

A stepwise 2e$^-$ oxidation of $NOPF_6$ to complex **2** in a N_2-filled NMR tube. The addition of one equiv. oxidant converted the diamagnetic Ni^{II} complex (Stacked: Red Spectra) to a paramagnetic Ni^{III} species (**3**) (Stacked: Green Spectra). Upon the addition of the second equiv. of oxidant, the NMR signal became diamagnetic to form the proposed Ni^{IV} species (**4**) (Stacked: Purple/Blue Spectra). Broad Ni^{IV} peaks were observed, which are likely due to a small amount residual of Ni^{III}.

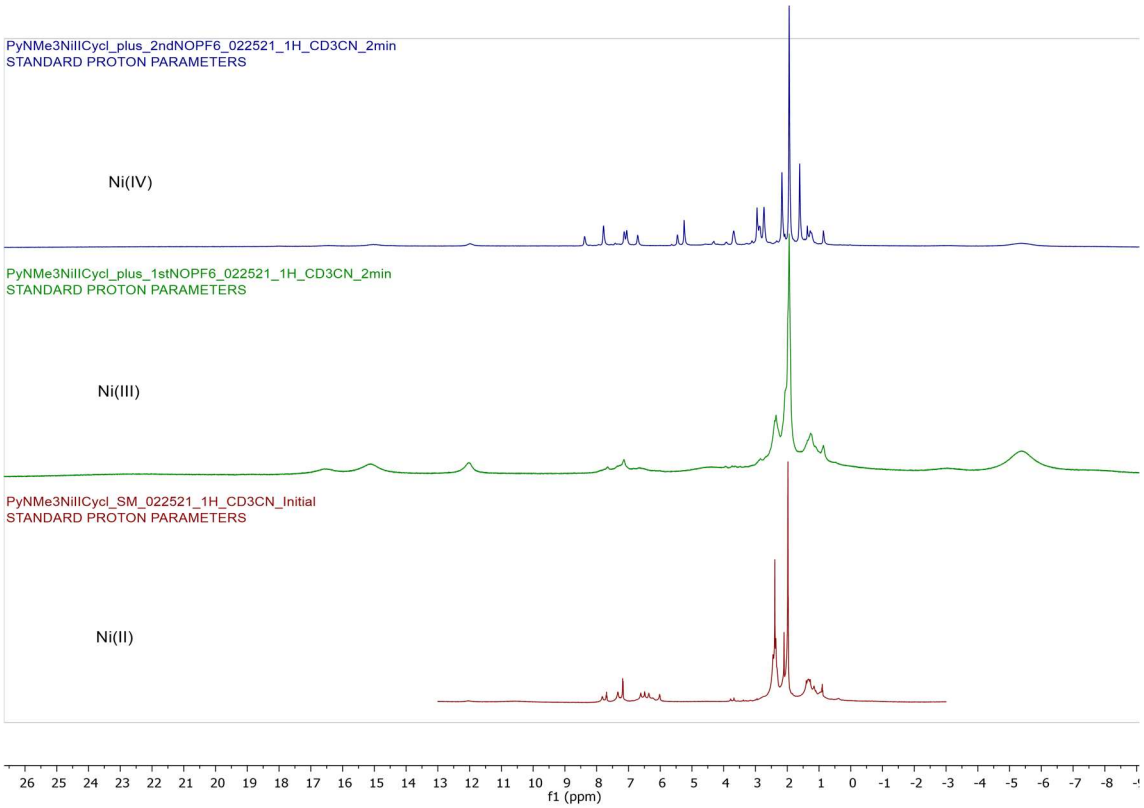

Figure S10. Stacked view of the ^{1}H NMR spectra of Ni^{II}/Ni^{III}/Ni^{IV} (complexes **2**/**3**/**4**, respectively) in CD_3CN at -35 ºC.

5.3. NMR Characterization of complex 4

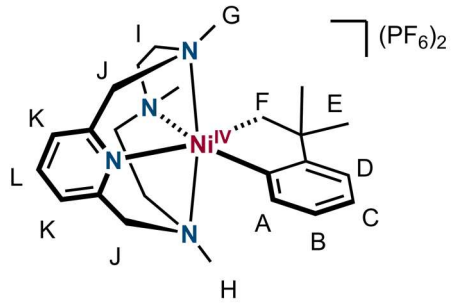

complex **4**

Scheme S 8. [1]H-NMR assignation for complex **4**.

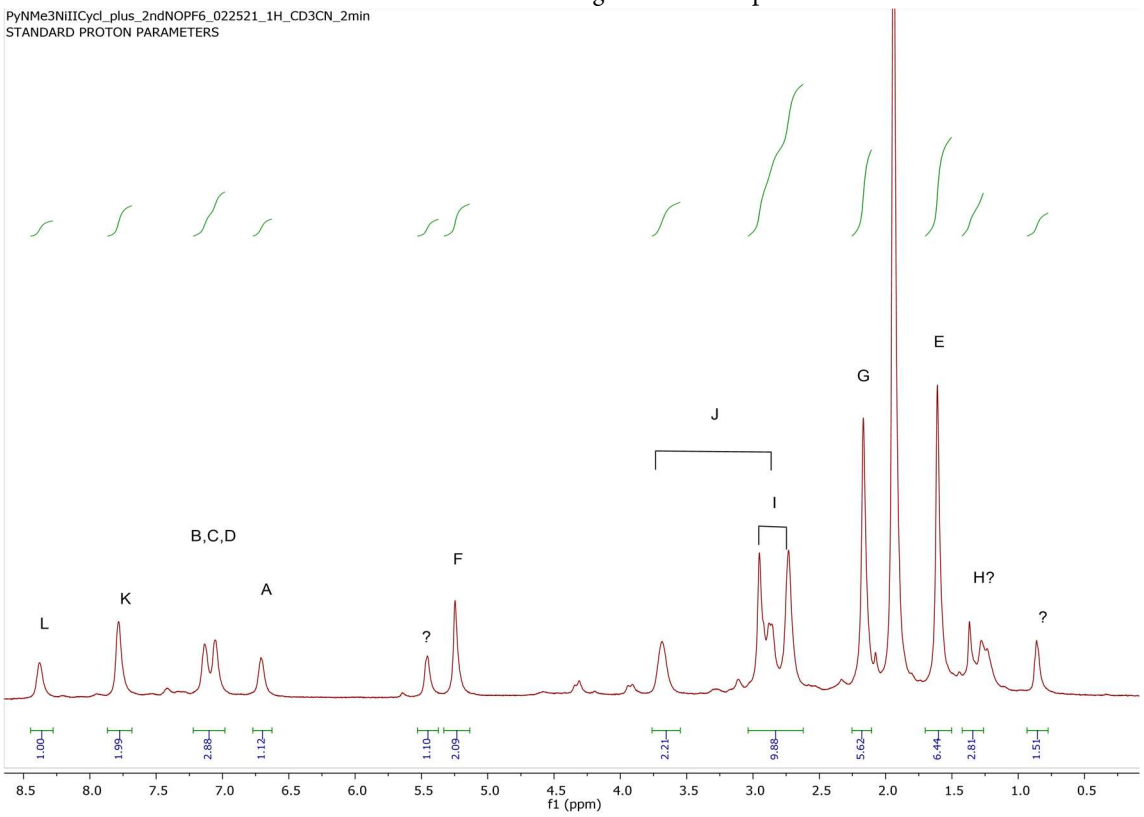

Figure S11. [1]H NMR of complex **4** in CD_3CN.

[1]H-NMR (500 MHz, CD_3CN), δ (ppm): 8.38 (b, 1H, **L**), 7.78 (b, 2H, **K**), 7.14-7.05 (d, 3H, **B,C,D**), 6.70 (b, 1H, **A**), 5.25 (s, 2H, **F**), 3.70-2.86 (d, 4H, **J**), 2.95-2.73 (d, 8H, **I**), 2.17 (s, 6H, **H**), 1.61 (s, 6H, **E**), 1.37 (s, 3H, **G**) Impurities: 5.45, 1.3, 0.86

Peaks were assigned based on the previously isolated Ni^{IV} complexes $[^{Me}N4Ni(Cycloneophyl)]^{2+}$ and $[^{Me}TACNNi(Cycloneophyl)]^{2+}$.[4, 5]

6. Cyclic Voltammogram (CV) of complex 2

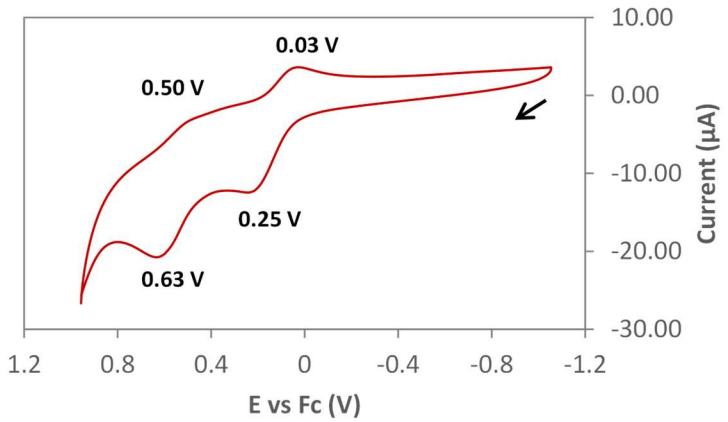

Figure S12. Cyclic voltammogram of complex **2**.

7. Simulation of EPR Spectra of Isolated complex 3

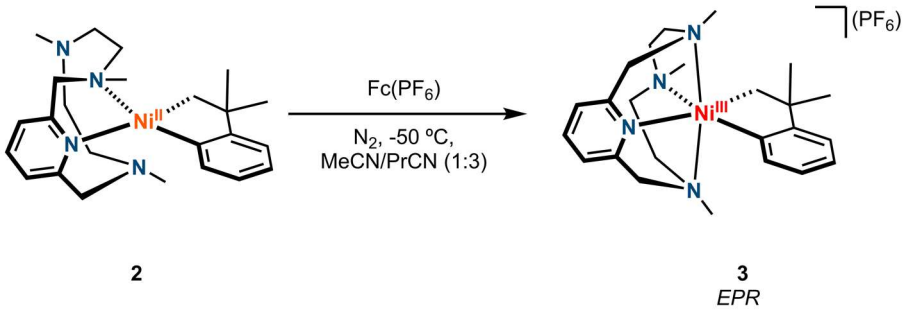

Scheme S9. Synthesis of complex **3** for EPR characterization.

In the glovebox, complex **2** (3.6 mg, 0.008 mmol) was dissolved in MeCN (100 µL) and cooled down to -50ºC. Then a cold suspension of $FcPF_6$ (2.7 mg, 0.008 mmol) in PrCN (300 µL) was layered over the complex solution. The resulting solution of 1:3 MeCN:PrCN was shaken for 5 seconds and then frozen in liquid nitrogen. After mixing, the dark blue colour of the oxidant suspension vanished immediately, and everything was in solution.

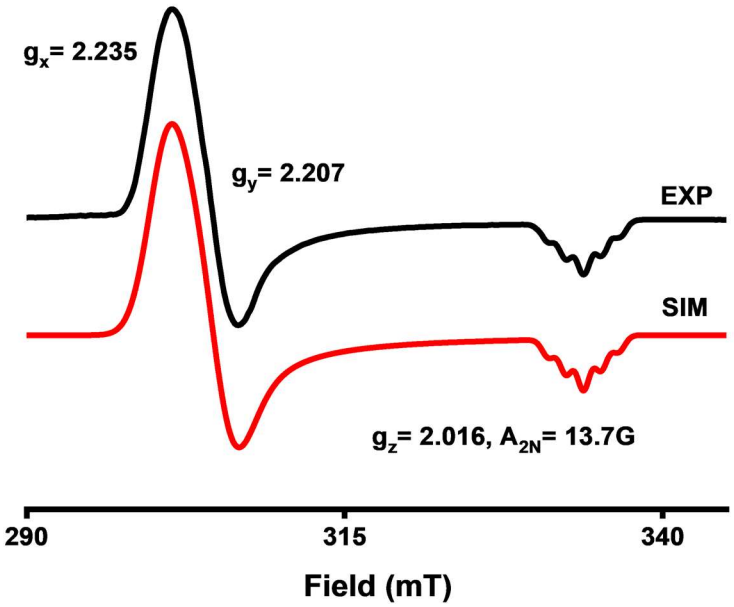

Figure S13. EPR spectra of complex **3** at low temperature (black line: experimental; red line: simulated).

Obs: The complex is stable at room temperature. Spectra of the initial complex (low temp, no warming up) and spectra of the complex after 30 min at room temperature remains the same.

8. UV/vis spectra of [(PyNMe$_3$)Ni(cycloneophyl)] complexes

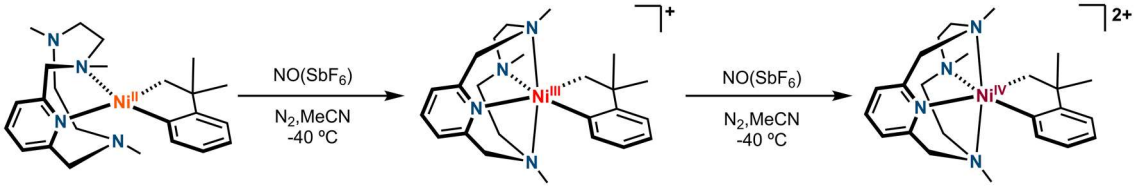

2 3^+ 4^{2+}

Scheme S10. Reaction scheme for the low-temperature UV/vis characterization of complexes **2**, **3** and **4**.

A UV-vis cell was charged with 2.2 ml of a 0.5 mM solution of **2** in anhydrous MeCN prepared in the glovebox. The quartz cell was capped with a septum, taken out of the glovebox, and placed in a Unisoku thermostated cell holder designed for low-temperature experiments at 233 K. Once the thermal equilibrium was reached, a UV/vis spectrum of the starting complex was recorded (orange line). Complex **2** exhibited a band at λ_{max} = 460 nm (ε = 880 $M^{-1}cm^{-1}$). After that, another equivalent of NO^+ was injected into the cell through the septum resulting in an immediate new spectrum corresponding to complex $\mathbf{3}^+$ which showed a band at λ_{max} = 510 nm (ε = 300 $M^{-1}cm^{-1}$). The nature of complex 3 was confirmed by HR-CMS-MS (calcd. for $C_{24}H_{36}N_4Ni^+$ $[M\text{-}SbF_6]^+$ 438.2288; exp 438.2289). Finally, another equivalent of the same oxidant was added as before stated to the cuvette and instantly afforded a different spectrum corresponding to complex $\mathbf{4}^{2+}$

that presents a band at λ_{max} = 470 nm (ε = 1200 $M^{-1}cm^{-1}$). Again, the nature of complex **4** was confirmed by HR-CMS-MS (calcd. for $C_{24}H_{36}N_4Ni^{2+}$ $[M\text{-}2SbF_6]^{2+}$ 219.1141; exp 219.1120, at 233 K).

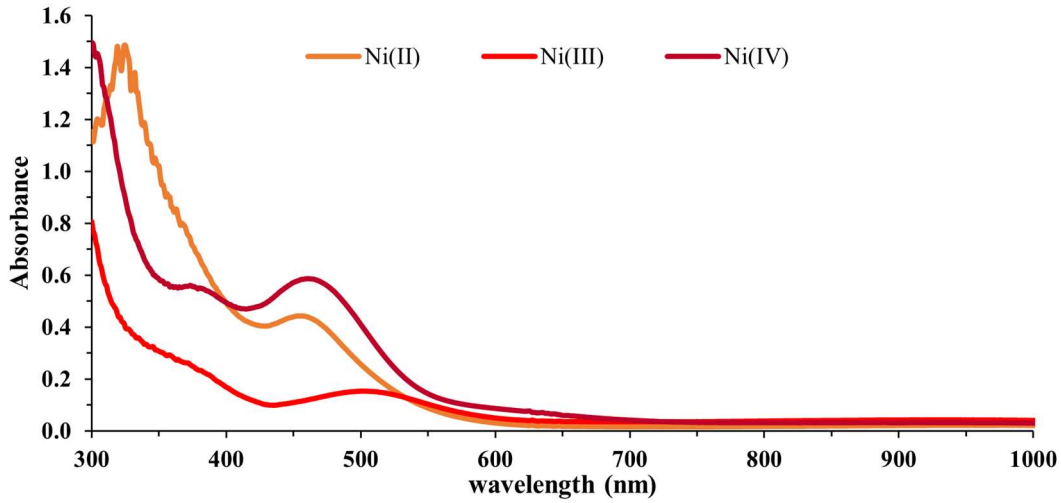

Figure S14. UV/Vis at -40 ºC, 0.5 mM solution of complexes **2**, **3** and **4** in MeCN.

9. Cryo-ESI-MS analysis of complexes 3 and 4

$[(PyNMe_3)Ni^{III}(cycl)]^+$, 3^+ (233 K)

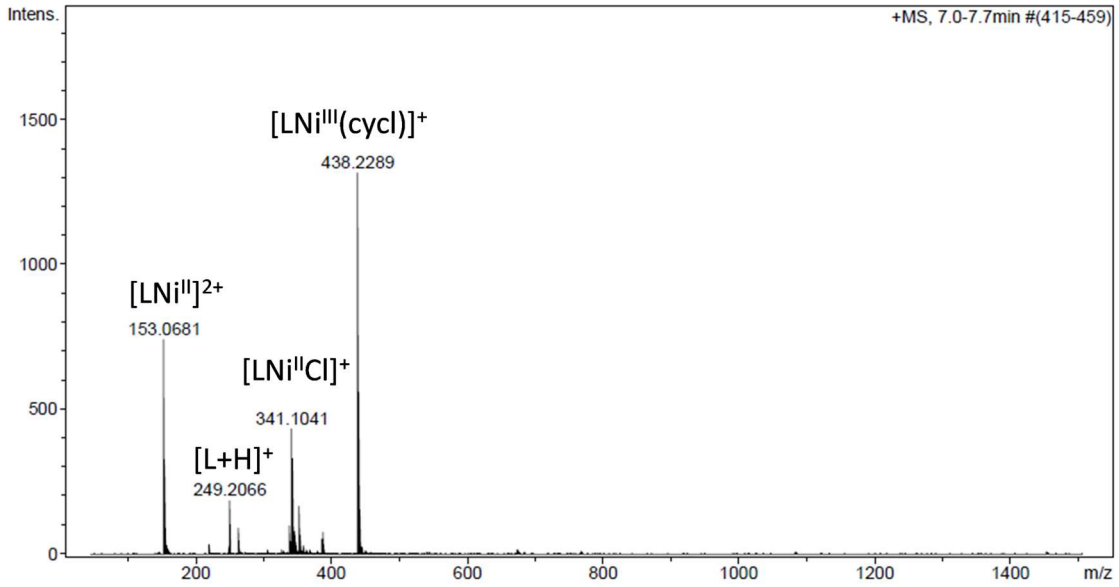

Figure S15. HR-cryo-MS of complex **3** at -40 ºC.

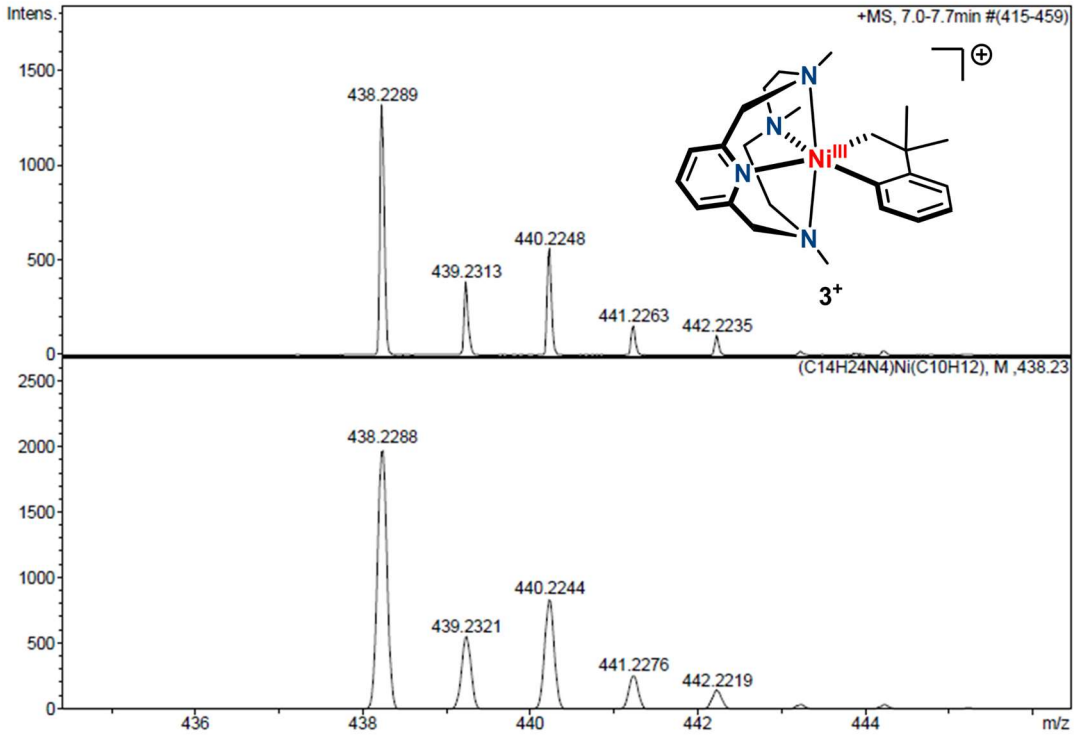

Figure S16. Zoom-in of the monocharged peak corresponding to complex $\mathbf{3}^{+}$.

$[(\mathbf{PyNMe_3})\mathbf{Ni^{IV}(cycl)}]^{2+}$, $\mathbf{4}^{2+}$ (233 K)

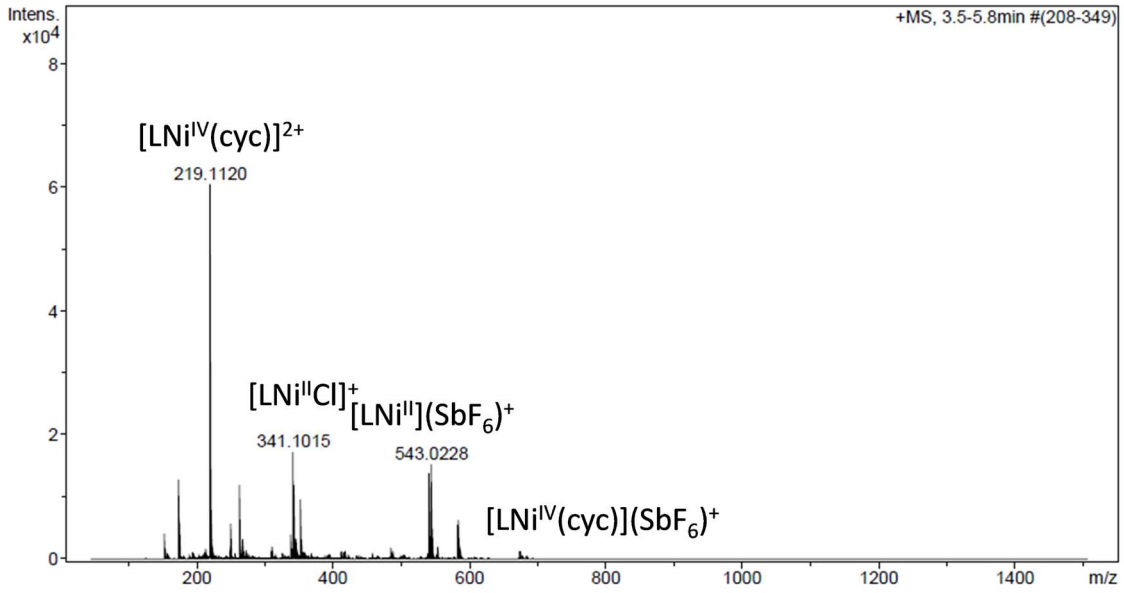

Figure S17. HR-cryo-MS of complex **4** at -40 °C.

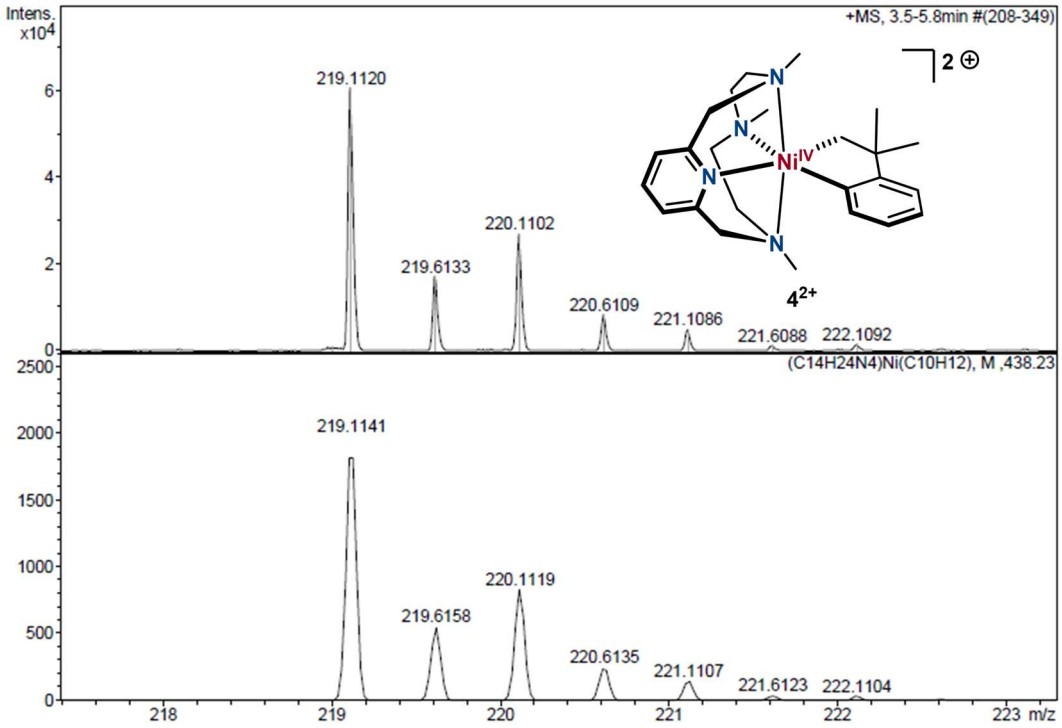

Figure S18. Zoom-in of the discharged peak corresponding to complex $\mathbf{4}^{2+}$.

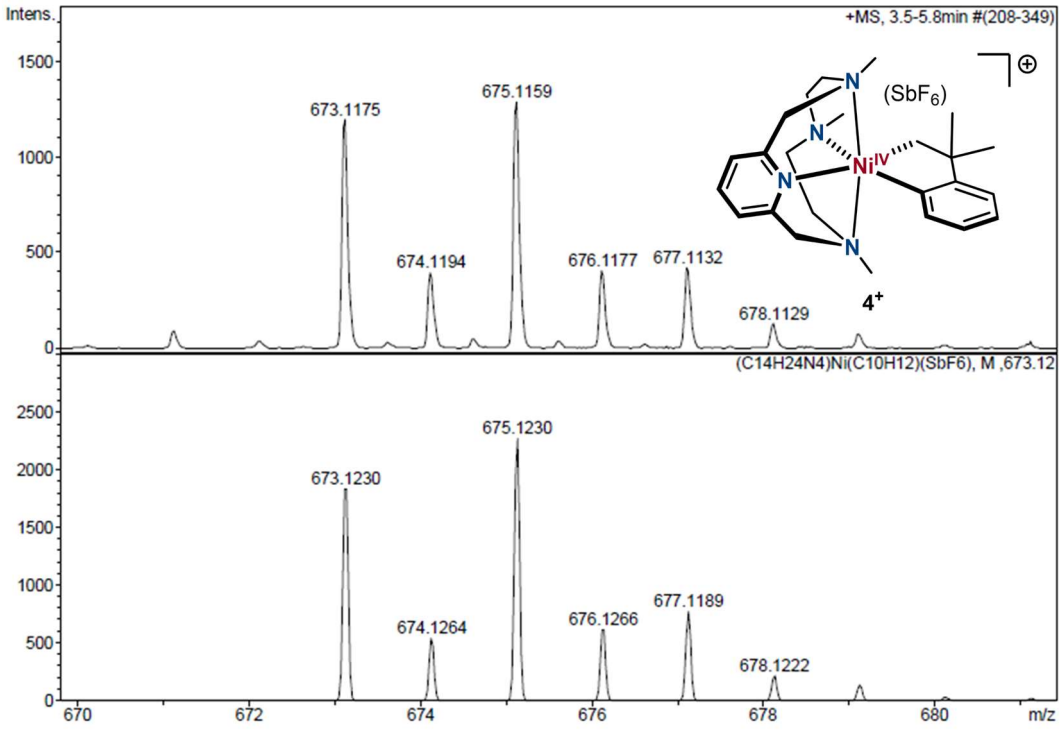

Figure S19. Zoom-in of the monocharged peak corresponding to complex $\mathbf{4}^{+}$.

10. Reactivity studies

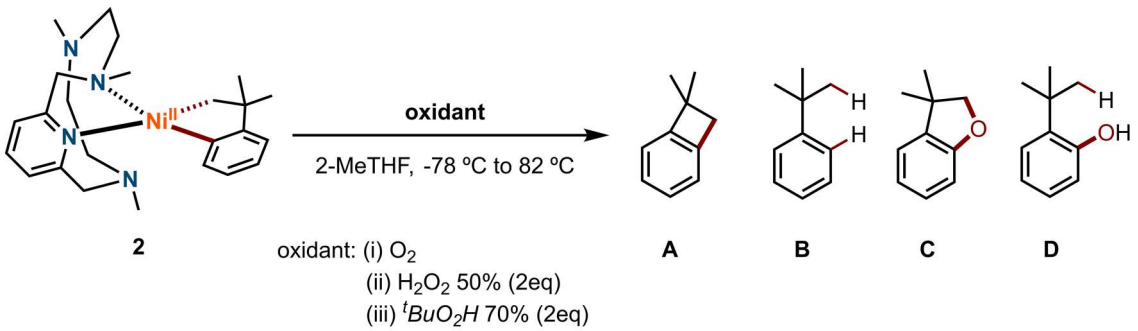

Scheme S11. Reactivity of complex **2** towards two-electron oxidants for the formation of C-C and C-O coupling products.

In a N_2-filled glovebox, complex **2** (2 mg) and 1.0 eq trimethoxybenzene were dissolved in 2 mL of 2-methyltetrahydrofuran. The mixture was allowed to cool down to -78 °C, and then bubbled with dry oxygen for 30 seconds, or injected with 2.0 eq H_2O_2 (50 wt%) or $^tBuO_2H$ (70 wt%). After 15 minutes, aliquots were taken from the reaction mixture for GC-MS analysis and the solution was allowed to warm up to 22 °C. After 1 hour at 22 °C, aliquots were taken again, and the solution was heated to 82 °C. After 24 and 48 hours at 82 °C, aliquots were also taken.

For GC-MS analysis, the aliquots taken were added to 200µL of 14wt% $HClO_4$ solution to completely protodemetallate the organic fragments. Then 1mL saturated K_2CO_3 solution was added to the mixture to neutralize, and the organic product was extracted twice with 0.5mL diethyl ether. The organic layer was dried over $MgSO_4$, filtered and injected into GC-MS for analysis. The product yield was calibrated with a calibration curve against trimethoxybenzene.

Entry	Oxidant	Time	A (%)	B (%)	C (%)	D (%)	Sum(%)	C-O Sum (%)
1	O_2 (30s bubbling)	15min	55	0	0	0	55	0
2		15min + 1h	41	0	1	1	43	2
3		15min + 1h + 24h	41	2	4	1	48	5
4		15min + 1h + 48h	59	0	6	2	67	8
5	H_2O_2 2eq	15min	13	0	1	1	15	2
6		15min + 1h	9	1	5	2	17	7
7		15min + 1h + 24h	8	0	9	2	19	11
8		15min + 1h + 48h	9	1	11	2	23	13
9	$tBuO_2H$ 2eq	15min	5	0	1	1	7	2
10		15min + 1h	3	0	4	2	9	6
11		15min + 1h + 24h	3	0	7	2	12	9
12		15min + 1h + 48h	3	1	8	3	15	11

11. X-ray Diffraction Analysis

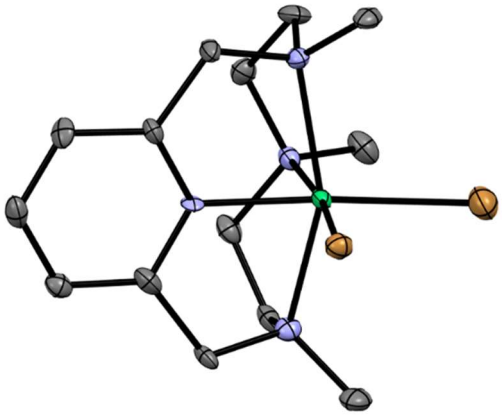

	1-Br
Chemical formula	$C_{14}H_{24}NiN_4Br_2$
Formula weight	466.90 g/mol
Temperature	100(2) K
Wavelength	0.71073
Crystal system	orthorhombic
Space group	$Pca2_1$
Unit cell dimensions	a = 14.5110(8) Å α = 90° b = 7.7903(5) Å β = 90° c = 30.1258(17) Å γ = 90°
Volume	3405.6(3) $Å^3$
Z, Density (calculated)	8, 1.821 g/cm^3
Absorption coefficient	5.831mm^{-1}
F(000)	1872
Crystal size	0.418 x 0.295 x 0.206 mm
Theta range for data collection	2.615 to 27.522°
Index ranges	-18≤h≤18, -10≤k≤6, -39≤l≤39
Reflections collected / Independent	32021/ 7798 [R(int) = 0.0466]
Completeness to Theta	99.9% (Theta = 25.242°)
Refinement method	Full-matrix least-squares on F^2
Data / restraints / parameters	7798 / 1 / 386
Goodness-of-fit on F^2	1.035
Final R indices	data R1 = 0.0461, wR2 = 0.11901 I>2σ(I) all data R1 = 0.0586, wR2 = 0.1259
Largest diff. peak and hole	and $eÅ^{-3}$ 1.286 and -1.612 $e.Å^{-3}$

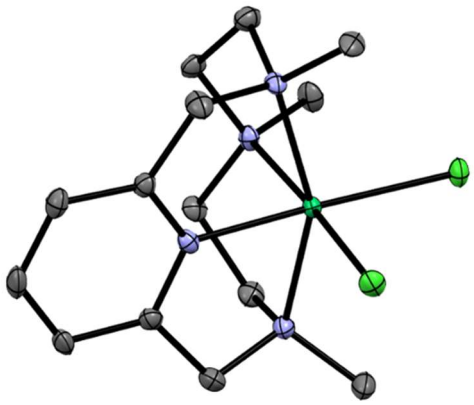

	1-Cl
Chemical formula	$C_{14}H_{24}NiN_4Cl_2$
Formula weight	377.98 g/mol
Temperature	100(2) K
Wavelength	0.71073
Crystal system	orthorhombic
Space group	$Pca2_1$
Unit cell dimensions	a = 25.5261(8) Å α = 90° b = 7.5526(2) Å β = 90° c = 34.2402(12) Å γ = 90°
Volume	6601.1(4) $Å^3$
Z, Density (calculated)	16, 1.521 g/cm^3
Absorption coefficient	$1.498mm^{-1}$
F(000)	3168
Crystal size	0.541 x 0.294 x 0.107 mm
Theta range for data collection	1.189 to 32.656°
Index ranges	-38≤h≤38, -5≤k≤11, -51≤l≤51
Reflections collected / Independent	24015/ 18871 [R(int) = 0.0447]
Completeness to Theta	99.9% (Theta = 25.242°)
Refinement method	Full-matrix least-squares on F^2
Data / restraints / parameters	7798 / 1 /770
Goodness-of-fit on F^2	1.012
Final R indices	data I>2σ(I) R1 = 0.0447, wR2 = 0.0741 all data R1 = 0.0671, wR2 = 0.0811
Largest diff. peak and hole	and $eÅ^{-3}$ 0.549 and -0.660 $e.Å^{-3}$

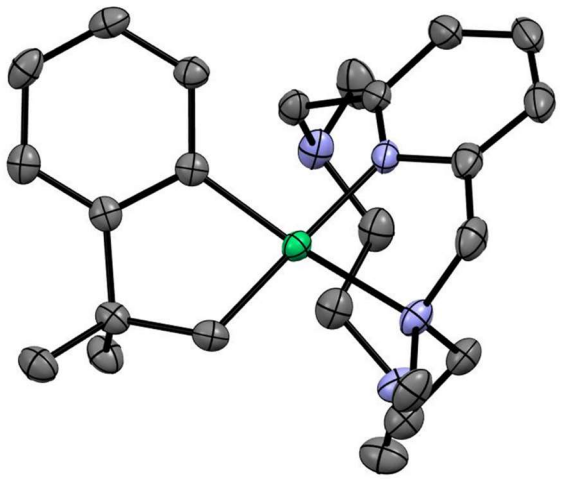

	2
Chemical formula	$C_{24}H_{36}NiN_4$
Formula weight	439.27 g/mol
Temperature	100(2) K
Wavelength	0.71073
Crystal system	orthorhombic
Space group	$P2_12_12_1$
Unit cell dimensions	a = 10.3930(4) Å α = 90° b = 13.3946(5) Å β = 90° c = 15.9835(6) Å γ = 90°
Volume	2225.06(15)Å^3
Z, Density (calculated)	4, g/cm^3
Absorption coefficient	0.889 mm^{-1}
F(000)	984.0
Crystal size	0.446 × 0.297 × 0.227 mm
Theta range for data collection	4.674 to 56.588 °
Index ranges	-13 ≤ h ≤ 13-16 ≤ k ≤ 17-21 ≤ l ≤ 21
Reflections collected / Independent	62710/ 5516 [R_{int} = 0.0344, R_{sigma} = 0.0164]
Completeness to Theta	1.77/1.00 (Theta = 28.294 º)
Refinement method	Solved with the ShelXT structure solution program using Intrinsic Phasing and refined with the XL refinement package using Least Squares minimization.
Data / restraints / parameters	5516/0/267
Goodness-of-fit on F²	1.123
Final R indices	data I>2σ(I) R1 = 0.0249, wR2 = 0.0641 all data R1 = 0.0259, wR2 = 0.0647
Largest diff. peak and hole	and eÅ^{-3} 0.57/-0.53

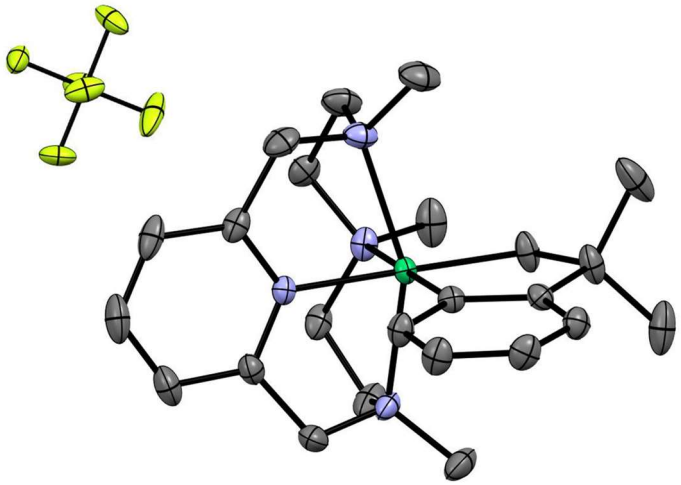

	3
Chemical formula	$C_{24}H_{36}NiN_4PF_6$
Formula weight	584. 25 g/mol
Temperature	100(2) K
Wavelength	0.71073
Crystal system	monoclinic
Space group	$P2_1/n$
Unit cell dimensions	a = 8.4822(2) Å α = 90° b = 10.1578(2) Å β = 97.0100(10) ° c = 29.7277(6) Å γ = 90°
Volume	2542.21(9) $Å^3$
Z, Density (calculated)	4, g/cm^3
Absorption coefficient	0.891 mm^{-1}
F(000)	1220.0
Crystal size	0.201 × 0.113 × 0.079 mm
Theta range for data collection	4.24 to 56.58°
Index ranges	-11 ≤ h ≤ 11-13 ≤ k ≤ 13-39 ≤ l ≤ 39
Reflections collected / Independent	83724/ 6326 [R_{int} = 0.0351, R_{sigma} = 0.0149]
Completeness to Theta	0.999% (Theta =28.290 °)
Refinement method	Solved with the ShelXT structure solution program using Intrinsic Phasing and refined with the XL refinement package using Least Squares minimization.
Data / restraints / parameters	6326/0/330
Goodness-of-fit on F^2	1.039
Final R indices	data R_1 = 0.0283, wR_2 = 0.0691 I>2σ(I) all data R_1 = 0.0315, wR_2 = 0.0716
Largest diff. peak and hole	and $eÅ^{-3}$ 0.50/-0.44

12. References

1. C. Magallón, J. Serrano-Plana, S. Roldán-Gómez, X. Ribas, M. Costas and A. Company, *Inorg. Chim. Acta*, 2018, **481**, 166-170.
2. J. Serrano-Plana, W. N. Oloo, L. Acosta-Rueda, K. K. Meier, B. Verdejo, E. García-España, M. G. Basallote, E. Münck, L. Que, A. Company and M. Costas, *Journal of the American Chemical Society*, 2015, **137**, 15833-15842.
3. J. Cámpora, M. a. del Mar Conejo, K. Mereiter, P. Palma, C. Pérez, M. L. Reyes and C. Ruiz, *J. Organomet. Chem.*, 2003, **683**, 220-239.
4. J. W. Schultz, K. Fuchigami, B. Zheng, N. P. Rath and L. M. Mirica, *Journal of the American Chemical Society*, 2016, **138**, 12928-12934.
5. M. B. Watson, N. P. Rath and L. M. Mirica, *Journal of the American Chemical Society*, 2017, **139**, 35-38.